HIGH STRAIN RATE PROPERTIES

OF STRUCTURAL ALUMINIUM

by

TALAL NAYEF MINWER AL-HADDID BSc

A thesis submitted to the **COUNCIL FOR NATIONAL ACADEMIC AWARDS** in partial fulfilment for the degree of **DOCTOR OF PHILOSOPHY**

Sponsoring Establishment: Department of Mechanical and Production Engineering
Sheffield City Polytechnic
Sheffield 1

Collaborating Establishment: Davy McKee PLC
Prince of Wales Road
Sheffield 9

October 1987

ACKNOWLEDGEMENTS

The author wishes to express his gratitude to Professor M S J Hashmi, Head of School of Mechanical Engineering, NIHE, Dublin, for his encouragement and helpful supervision during the course of this project. Thanks are also expressed to Dr T D Campbell, Senior Lecturer at the Mechanical and Production Engineering Department, Sheffield City Polytechnic, for his constructive suggestions, helpful advice and comments.

The technical assistance offered by Mr R Teasdale and his staff was much appreciated and in particular the author wishes to thank Messrs R Wilkinson, K Wright, M Jackson and R Sidebottom for their valued contributions at various stages of this work.

Thanks are also due to the many other people who I have not mentioned but whose help and advice has been invaluable and greatly appreciated throughout the project.

Finally, I would like to thank Mrs S Saunby for typing the thesis.

ABSTRACT

HIGH STRAIN RATE PROPERTIES

OF STRUCTURAL ALUMINIUM

T N M Al-Haddid

A number of theories and techniques have been used in the past to determine the stress-strain relationship of metals and alloys at high strain rates of up to 2.2×10^4 per second; some of these were approximate whilst others required expensive equipment. In the present study three aluminium alloys, HE15, HE30TF and DTD5044 have been investigated due to their importance in the aircraft, motor and construction industries. En-8 steel was also investigated for the purpose of comparison.

A simple new approach using high velocity compression testing in conjunction with a finite-difference numerical technique was adopted, developed, used and modified to suit different situations. Incremental compression tests were conducted on the materials to obtain the quasi-static stress-strain properties and used in the high strain rate (dynamic) deformation theoretical analysis and calculations. The final dimensions of the dynamically deformed specimens (diameter and height) obtained experimentally were plotted against impact velocity. These parameters were also predicted theoretically for given values of material constants and compared with the experimental ones. The material constants were then varied in a systematic manner to obtain the optimum agreement between theoretical and experimental results.

The temperature rise during deformation, specimen size and deformation history were investigated and found to alter the material constants and therefore affect the flow stress. However the radial inertia contribution to the flow stress was investigated and found negligible. Friction was investigated and its effect was minimised by using tallow-graphite lubricant, which proved to be adequate and effective.

The new approach caters for material inertia, strain hardening, strain rate sensitivity, friction and temperature rise during deformation. This technique provides a simple, inexpensive method of obtaining the stress-strain characteristics of materials at high strain rates without sacrificing accuracy.

CONTENTS Page

CONTENTS (cont) **Page**

INDEX TO FIGURES Page

INDEX TO PLATES

INDEX TO TABLES

NOMENCLATURE

ΔS	Link length in lumped parameter model
A	Cross-sectional area
D	Material strain-rate constant (per second)
N	Axial force
R	Diameter to height ratio of the link
V	Velocity during time δt
m_f	Frictional constant
P	Material strain-rate constant
δt	Time increment
u	Displacement
ε	Strain
ρ	Density
σ	Stress
$\dot{\varepsilon}$	Strain Rate
Do	Initial Diameter
Ho	Initial Height
T	Temperature rise within specimen during deformation
I	Radial Inertia
T + I	Theoretical analysis including the effect of temperature rise and radial inertia
T - I	Theoretical analysis including the temperature rise effect, excluding radial inertia
-T + I	Theoretical analysis excluding the temperature rise, including radial inertia
-T - I	Theoretical analysis excluding both temperature rise and radial inertia effects

Subscripts

i	The mass number and the number of the proceeding link
j	Instant of time
o	Initial or static values

Superscripts

(.)	Single differentiation with respect to time
(..)	Double differentiation with respect to time

CHAPTER ONE

1.0 Introduction

1.1 Importance of Stress-Strain Data at High Strain Rates

The mechanical properties of materials at high strain rates are of interest from two main points of view. The design engineeer who wishes to use the material under conditions where these may have to withstand sudden impact or shock loading needs to know their mechanical properties under the appropriate conditions. It is also of interest to the material scientist to know the variations of the stress-strain properties with loading rate, since it is related to the relaxation process taking place on the microscopic scale.

The design engineer, who is concerned with structures that are likely to be subjected to impact, is interested in material properties and how static properties are altered under dynamic loading conditions. Such data is used to predict the changes in the material plastic flow characteristics under high rates of strain and to cater for them in appropriate situations. The space age has increased the interest in high strain rates associated with impact problems or the hyper velocity impact range because of the concern for the protection of space vehicles against possible damage due to impact with foreign bodies. The aluminium industry responded to the requirements of the aerospace industry (1-4) for higher toughness, high strength alloys by producing new breeds of alloys, such as Al-Cu and Al-Zn, with superplasticity to accommodate formability by making

the grain size of such alloys smaller. Special structural problems may arise especially in the nuclear industry where radiation influences materials on the atomic scale. Large changes in static as well as dynamic plastic behaviour may take place due to continuous exposure to nuclear radiation which may create design problems in structures where failure can have most serious consequences.

Some of the main processes and areas involving high strain rates are as follows:

(i) Impact loading of structures

(ii) Powder metallurgy

(iii) Forming of metals.

1.1.1 Impact Loading of Structures

Materials used in the construction industry are often subjected to rapidly applied loading in certain structures and may undergo high intensity shock loading. The demand in recent years for large and relatively cheap building structures has promoted the development of several new varieties of design and the imaginative structural use of concrete which may be reinforced, prestressed or post-tensioned with steel bar. This has given rise to a considerable sophistication in the mechanics of structural design.

The assessment of the ability of these buildings and structures to withstand blast loading effects requires high strain rate data. In order to use the optimum material for reinforcing, accurate material properties

need to be known at both static and dynamic (impact) loading to provide adequate protection from collapse or excessive damage. The strain rate in such impact or impulsive loading situations can reach 10^4 per second. Demolishing these structures and buildings at the end of their useful life for salvaging purposes is a complex operation. The removal of some stressed elements in modern, large and continuous structures may lead to disastrous dynamic collapse. Many demolition techniques are in use for different purposes (such as blast explosive loading and lay on charges for cutting reinforced concrete structures) which involve high strain rates of up to 10^6 per second.

Finally the construction industry in general and the structural design engineer in particular require information on the behaviour of materials, in terms of stress-strain characteristics at low and high strain rates to achieve their targets of shock resistance and easy demolition when it is needed.

1.1.2 Powder Metallurgy

The volume of metal powder now used industrially is increasing at a great rate. In recent years, metal powders have been prepared and made commercially available on a large scale for conversion into engineering components directly by means of quasi-static compaction processes involving low strain rates. However, the dynamic compaction of metal powders by means of ballistic and explosive processes may involve strain rates of 10^2 and 10^3 per second respectively.

The dynamic compaction results in uniform material density and an increase in production rate. Therefore, fundamental information about the stress-strain characteristics of metal powders at high strain rates are necessary to secure better compaction systems.

1.1.3 Forming of Metals

Metal processing engineers are usually concerned with stress-strain data, to facilitate predictive calculations for tool pressures or loads developed in causing a certain operation or processes to take place. In the manufacturing industry the process design engineers who are concerned with large plastic strains at high rates of strains are interested in metal behaviour over a wide range of temperatures, where as in structures such as beams or frames the design engineers are usually concerned with small elastic-plastic strains.

It has been recognised that strain rate as well as temperature affect many material properties. The rate effect can be due to either mechanical (inertia) or metallurgical reasons such as ageing and change of failure modes. Strain rate has greater effect on the flow stress in the hot working range and relatively smaller effect in the cold working range; this applies especially when large strains are imposed.

In metal forming the loads to be applied to preform an operation depends upon the strength of the material being processed and the influence of strain rate on the strength. Many processes in metal forming such as drop and high-energy-rate forging involve high strain rates. High-energy-rate forging is a high strain

rate process which leads to faster forging cycles. The higher forging speed means larger energy requirements per unit volume due to high strain rate effects which can be very significant at higher temperatures.

High strain rates can also occur in dynamic punching, impact extrusion, high speed rolling and drawing, where strain rates up to 10^4 per second may be encountered. In machining processes strain rates of 10^6 per second may be experienced. In some of these processes the effect of strain rate on the yield stress may be counteracted to some extent by the influence of temperature rise.

In the present study, ballistic compression tests were carried out on three aluminium alloys and a structural steel. The dynamic stress-strain properties of these alloys and steel at room temperature and at strain rates of up to 2.2×10^4 per second were determined by a new technique.

This technique takes into account the effects of radial inertia and temperature rise during deformation. The technique is relatively inexpensive and simple but efficient for determining high strain rate properties of materials.

1.2 Selection of Materials

In the present study three high strength aluminium alloys were chosen for their structural application for general use, especially in the aircraft industry. Structural steel was also chosen and tested in phase two of the present investigation for the purpose of comparison with other techniques used by other researchers.

The materials investigated in the present study were as follows:

(i) HE15 (Aluminium)
(ii) HE30TF (Aluminium)
(iii) DTD5044 (Aluminium)
(iv) En-8 (Mild Steel)

HE15 is an Al-Cu-Si aluminium alloy with a copper content of 3.87%. This type of alloy is used in aircraft parts for its strength, very good machinability and fair corrosion resistance. It is a heat treatable alloy which is used also in rivets and bolts because of its slow ageing and high fracture toughness. At temperatures below room temperature its strength and hardness increases, while at high temperatures its impact resistance and notch toughness increases (1, 3).

HE30TF is an Al-Si-Mg aluminium alloy, with a silicon content of 1.4%. This type of aluminium alloy is used in general structures, road vehicles, rail roads, tubing and pipes carrying water, oil and petrol. It has a medium to high strength, good extrudability and when tempered good formability. It is a heat treatable alloy with good corrosion and creep resistance (1, 3).

DTD5044 is an Al-Zn-Mg aluminium alloy, with a zinc content of 5.4%. This alloy is extensively used in aircraft and other structures requiring high strength to weight ratios. Because of its fair to poor corrosion resistance, sheets of this alloy are often clad with other corrosion resistance materials (3, 4). It is also a heat treatable alloy and its machinability increases at below room temperature. Its strength and impact resistance increases as the temperature increases.

En-8 steel resembles one of the important varieties of steels which is subjected to stresses in machine parts. This type of medium carbon steel, with 0.41% carbon, is also used in both the

construction and transportation industries for making components which are directly or indirectly subjected to dynamic loading.

The main advantage of this steel is that it enables the construction of lighter but relatively high strength structures while retaining the highly desirable properties of easy workability. To the design engineer in the space technology, motor, aircraft and construction industries, requirements for lighter but stronger materials have become important and therefore, stress-strain data for such materials under static and dynamic loading conditions is essential.

1.3 Review of Previous Work

As early as the 1930s and possibly even earlier, many researchers have been investigating the behaviour and properties of metals undergoing deformation. High strain rate, its influence and importance in many manufacturing processes such as forging, punching, extrusion, rolling and machining was of interest to many. Pugh and Watkins (5) investigated the effects of strain rate within the range of 3.5×10^2 to 10^3 per second in the drop-forging of aluminium and copper. They reported that the percentage reduction seemed to decrease slightly with increasing strain rate. Dowling et al (6) investigated the dynamic punching of aluminium, copper and mild steel and the response of these materials to strain rates varying from 10^{-3} to 4×10^4 per second. They reported that at strain rates approaching 10^4 per second all three ductile materials showed a drop in load at the start of yielding, as a direct consequence of the increased rate-sensitivity shown by all materials at the highest loading rates.

Green et al (7) investigated material properties, including strain rate effects related to aluminium and steel sheet metal forming. Their tests were conducted at strain rates of up to 10^2 per second using a forming press. They concluded that the flow stress was very sensitive to strain rate while strain hardening showed only a slight change during forming. Oxley and Stevenson (9) determined the stress-strain properties of a low carbon steel at very high strain rates using machining tests. They conducted their tests over a strain rate range of 10^3 to 10^5 per second, suggesting that accurate stress-strain data at high strain rates can be obtained by their method.

Christopherson et al (10) investigated the effect of high strain rate in the strip-rolling of aluminium, copper and steel. Strain rates of up to 2×10^2 per second were reached using a rolling mill to carry out their tests. Ignoring friction, they reported that the flow stress and hardness of only the mild steel were affected by strain rate. Bittans and Whitton (11) reviewed the work of others in the field of high strain rate with particular reference to the stress-strain characteristics of materials in different manufacturing processes. They reported in their review that strain rates ranging from 10^3 to 10^5 per second can be experienced in metal cutting, wire drawing and dynamic blanking.

1.3.1 Effect of Specimen Size

Many researchers have investigated the effect of specimen size and the corresponding effect on stress-strain behaviour at different strain rates. Gunasekera et al (12) conducted compression tests under lubricated

conditions on steel cylindrical specimens at low strain rates of 2.2×10^{-3} per second. They reported that large aspect ratio test specimens (height/diameter) are desirable and kept their aspect ratio at 1.5 to avoid buckling and barrelling. Kramer (13) investigated the effect of specimen diameter on the flow stress of polycrystalline aluminium. He conducted his tests at a strain rate of 1.66×10^{-5} per second using an Instron tensile machine, reporting that the flow stress changes with specimen diameter. This change was associated with the surface layer stress, but it was not clear to him why the yield stress changed with specimen diameter. Haque (14) kept the aspect ratio of his test specimens less than unity to avoid buckling and barrelling.

Hauser (15) investigated the stress-strain relationship of aluminium at high strain rates. He conducted compression and tension tests using the split Hopkinson bar at strain rates of up to 10^4 per second. He reported that if the test specimen is small enough, the transit time for the elastic wave is too short, so equilibrium throughout the specimen is rapidly established and plastic deformation takes place uniformly within the specimen.

1.3.2 Effect of Radial Inertia

Many researchers have investigated radial inertia effects on the stress-strain characteristics of materials at high strain rate. Dharan and Hauser (16) determined the stress-strain relationship of aluminium at strain rates

up to 1.2×10^5 per second. They used a split Hopkinson bar to conduct compression tests on cylindrical specimens with aspect ratios of 1.0 and 0.5. They reported that during high velocity compression, in addition to the axial particle velocity, radial and tangential particle velocities exists. These velocities may achieve high values requiring high compressive stresses in three directions. The hydrostatic part of the stress tensor is therefore high and due to this fact they corrected their data. Holzer and Brown (17) investigated the behaviour of steel in compression at strain rates ranging from 10^{-3} to 10^4 per second. Their tests were conducted on a hydraulic testing machine and a drop forge to obtain strain rates of 10^{-3} to 10^2 and 10^2 to 10^4 per second respectively. They reported that if the radial inertia effect is significant it will lead to a much larger separation between the stress-strain curves for the high strain rate region than for the low one and this was not observed. Haque (14) also investigated this effect, and then ignored it using the argument that radial inertia and temperature effects will cancel each other.

1.3.3 Microstructural Changes

The change in the microstructure of materials has been investigated by many researchers. Their investigations have considered the effects of fine graining and grain orientation on deformation at low and high strain rates.

H J McQueen and J E Hockett (18) conducted compression tests on aluminium using a cam plastometer at strain

rates up to 2.2 x 10^4 per second. They reported that the flow stress increases as the subgrain size decreases at elevated temperatures. They also added that during hot working, aluminium deforms by a mechanism of dynamic recovery which tends to inhibit subsequent recrystallisation. Lloyd (19) examined fine grained aluminium alloy (Aℓ-6wt-%N) in tension and torsion at low strain rates. He reported that the initial yield stress is dependent on grain size, and that the latter is an important factor which affects work hardening at large strains and stresses.

1.3.4 Friction and Lubricant

Friction effects during deformation are of interest to many researchers. Friction is one of the important factors which may cause errors in static and dynamic compression testing of materials. The unsuitable lubricant will lead to high friction which will cause barrelling and inaccurate stress-strain data.

Osakada (20) investigated theoretically the mechanism of lubricant trapping in compression at low strain rates. He reported that this mechanism depends on the thickness of the lubricant film, speed of compression and the radius of billet undergoing test. Male and Cockcroft (21) developed a technique for studying the coefficient of friction between rigid tools and plastically deforming metals at elevated temperatures. Their technique only involved the measurement of the change in geometry of a flat ring after compression and not the mechanical

properties of the metal. It is applicable over a wide range of testing conditions with respect to temperature, amount of deformation, rate of deformation and lubricant. They conducted their compression tests by means of a drop-hammer giving an average strain rate of 1.2×10^3 per second on a variety of metals such as aluminium, copper, brass and mild steel. They indicated that at low strain rates the coefficient of friction (μ) increased as the amount of deformation increased. However, at intermediate and high strain rates, μ was not affected by moderate amounts of deformation. Only when a large amount of deformation was imposed at intermediate and high strain rates did the coefficient of friction increase.

1.3.5 Techniques and Equipment

Many investigations have been carried out on the dynamic deformation of metals. These investigations have involved different techniques and equipment. Clark (24) in his work dealt principally with the results of tension tests on sixteen metals and alloys most of which are employed extensively in aircraft construction. He discussed work done by many researchers employing different methods and testing equipment. Duffy (25) has also done the same in his report reviewing work done by others on the dynamic plastic deformation of metals and alloys. However, Eleiche's (26) report was involved with a literature survey of the combined effect of strain rate and elevated temperatures on the mechanical properties of metals. Ripperger (27) investigated the plastic

behaviour of aluminium, copper and iron at strain rates of up to 10^4 per second using a split Hopkinson bar. He reported that for aluminium and copper the dynamic yield stress is very sensitive to strain rate. His assertion was based on the fact that these metals sustain stresses considerably higher than the stress which could be associated with corresponding strains under static loading conditions.

Lengyel and Mohitpour (29) conducted incremental compression tests on aluminium using a high-energy-rate forging machine at strain rates of up to 10^3 per second. Comparisons were made between the results of stress-strain data which were obtained incrementally and those obtained under continuously applied loads to large deformations. They reported that much more accurate stress-strain data can be obtained by their method.

However, others have used the split Hopkinson bar extensively in their investigations of stress-strain characteristics at high strain rates. In some cases it has been modified to suit specific purposes and different accessory equipment has been connected to it for recording loads during deformation.

Yoshida and Nagata (30) investigated annealed polycrystalline aluminium using the split Hopkinson bar at strain rates ranging from 10^2 to 8×10^3 per second. They reported that the dynamic stress-strain curve for aluminium is parabolic (similar to the static one). They

also indicated that the dynamic flow stress is always higher than the static one showing strain rate dependence. Bell (32) determined in his investigation the approximate dynamic stress-strain data for aluminium at strain rates ranging from 1 to 10^4 per second. He used the split Hopkinson pressure bar to conduct his tests assuming in advance that the uniform stress and strain distribution of the quasi-static measurements apply during impact. Meanwhile, Lindholm and Yeakley (33) conducted compression tests on high purity single crystal and polycrystalline aluminium at strain rates up to 5 x 10^2 per second, using the split Hopkinson bar. They compared the dynamic behaviour of the two metals regarding strain rate dependency, indicating that impurities in aluminium lead to a reduction in rate sensitivity as evidenced by an increase in activation volume. Lindholm (34) in his investigation showed that strain gauges connected to the split Hopkinson pressure bar provided a method of measuring loads during deformation. He managed to simultaneously record strain against time, strain rate against time, stress against time and stress against strain. Wingrove (35), Wulf and Richardson (36) used a modified split Hopkinson bar with coaxial capacitors to determine the dynamic stress-strain relationship at strain rates of up to 10^5 per second. Maiden and Green (37) conducted compressive strain rate tests on six selected materials, including two aluminium alloys, at strain rates ranging from 10^{-3} to 10^4 per second. They used the split Hopkinson apparatus to

conduct their tests, reporting that both aluminium alloys (7075-T6 and 6061-T6) have been found to be insensitive to strain rate, at least up to 10^3 per second.

As early as 1947, Taylor (38) and Wiffens (39) looked extensively into ballistic compression to investigate material behaviour and dynamic yield strength at high strain rates. Taylor's (38) work was mainly theoretical analysis. Subsequently, he conducted tests to support his analysis by using flat ended transparent cylinders made from cast blocks of paraffin wax. The cylinders were projected by means of a catapult at a rigid anvil. He used the momentum equation, ignoring the radial inertia effect, so that the stress can be considered constant over any cross-section. Wiffens (39) followed in Taylor's (38) steps using the same approach theory. He conducted his tests on steel, copper and lead in the same manner as Taylor's (38), looking as well at the effect of pre-straining on the stress-strain characteristics. He reported that an increase in the dynamic strength of mild steel can be obtained by pre-straining either in tension or in compression. He also established equations relating stress ratio (dynamic strength/static strength) to the static strength of steel and duralumin.

Other researchers have investigated the stress-strain relationship with particular reference to dynamic yield strength. Hawkyard et al (40) obtained the mean dynamic yield strengths for copper and mild steel from strain measurements of "mushroomed" ends of flat ended

projectiles, impinged against a rigid anvil. They conducted their tests using air pressure to propel mild steel projectiles through a gun designed with a long barrel for these purposes. They carried out the tests at temperatures ranging from 20-700°C approaching a mean strain rate of 5×10^3 per second. The analysis they adopted for determining the mean dynamic stress equated the kinetic energy at impact with plastic work done. They reported that a "double frustum" was observed in tests conducted on annealed materials, suggesting that a suitable theory would include strain hardening from which it might be possible to deduce the actual form of the dynamic stress-strain curve. Finally they added that their method provides only a mean yield stress, averaged over a wide strain range.

Later on, Hawkyard (41) introduced strain hardening into the theory proposed in reference (40). He conducted his tests on mild steel and copper at elevated temperatures in the same manner as in his previous work with others (40). He reported that his new analysis appeared to predict with reasonable accuracy the profiles of projectiles after impact, thus providing better mean dynamic yield stress data. He suggested that the only remaining possibility of improvement was to introduce radial inertia forces into the theory. Finally he indicated that the use of the energy equilibrium equation across the plastic wave gives a closer overall approximation to actual conditions than does the momentum equation proposed by Taylor (38).

Balendra and Travis (42) investigated the "double-frustum" phenomenon in the mushrooming of cylindrical aluminium high velocity projectiles when impacted at strain rates up to 5.3×10^3 per second onto a rigid anvil. They explained that this phenomenon was due to the effects of a very high radial velocity imparted to the front face upon impact.

Others have investigated stress-strain characteristics at high strain rates by means of high speed ballistic tests. Ghosh (43) conducted his tests on copper, brass, aluminium alloy and mild steel billets. The billets were subjected to repeated dynamic compression at ambient temperature by a drop-hammer at strain rates of up to 2.0×10^2 per second. He stated that the discrepancies between the predicted and experimental data of reduction in height were due to the number of impacts involved, temperature rise and friction during deformation.

The work of Hutchins and O'Brien (44) involved impacting copper cylindrical projectiles against a rigid anvil at strain rates of up to 5×10^3 per second. The reduction in length after impact was then analysed in three different ways to provide the mean dynamic yield stress for copper. They reported that a theory which takes account of elastic strains in the projectiles provided the best agreement with the data at low strain rates, while theories which assume rigid-plastic behaviour give good agreement at higher velocities.

Gorham (45) used a modified Hopkinson bar system in which the projectile bar strikes the specimen directly, thus

achieving high strain rates of up to 10^5 per second. He used a high speed camera incorporating a novel optical system to accurately record the strain distribution along the specimen during the test. This was also done by Haque and Hashmi (46). They reported that the strain rate sensitivity for En-8 structural steel increases with the increase in strain rate over the temperature range -30 to 235°C. Hashmi and Thompson (47) suggested a numerical technique which enabled them to predict the final shape of projectiles after impact and the distribution of strain taking into account strain rate and strain hardening effects. Subsequently, the same technique was applied by Hashmi (48) on mild steel projectiles at room temperature and at strain rates of up to 10^5 per second. He used charges in a gun designed for this purpose to propel the projectiles, introducing material inertia in the technique proposed in (47) to obtain the material constants.

1.3.6 Effect of Temperature

Since the 1960s and possibly earlier, considerable effort has been devoted towards relating the effect of temperature change to metal deformation. Lahoti and Altan (50) used a numerical method to predict the temperature distribution in axisymmetric compression and torsion. They also devoted part of their work to the effects of friction, temperature and strain rate upon metal flow and temperature rise during torsion and compression.

Hockett (51) investigated the effect of strain, strain rate and temperature on the flow stress of aluminium. He conducted his tests using a cam-plastometer, achieving strain rates ranging from 10^{-3} to 10^{2} per second. He reported that the increase in flow stress with increase in strain rate is greatest at the highest temperature.

Baraya et al (52) dynamically compressed circular cylindrical billets of super-pure aluminium with different height/diameter ratios at temperatures ranging from 20 to 500°C. They conducted their tests using a drop-hammer and tallow-graphite as lubricant, investigating the temperature rise during deformation within the test specimen. Their work, based on the mean strain rate and the mean dynamic stress, reported that the percentage reduction in height obtained at a given temperature is a function of the deformation energy. This would be true provided that the impacting mass remains constant.

Samanta (54) investigated the dynamic deformation of aluminium and copper at elevated temperatures to determine their strain rate sensitivity. He used a modified Hopkinson bar to conduct his tests at strain rates of up to 2.2×10^{3} per second. He reported that for aluminium the dislocation density decreases with increasing temperature. Chiddister and Malvern (55) also investigated aluminium during compression-impact tests at elevated temperatures of up to 550°C. They also used a split Hopkinson pressure bar to obtain the stress-strain strain rate relationship over a strain rate range of

3.0×10^2 to 2.0×10^3 per second and reported that the strain rate sensitivity for aluminium was found to increase with temperature. However, the stress-strain curves were not obtained over a sufficiently large range of strain to determine the dependency of rate sensitivity on the level of strains.

Meanwhile, Dean and Sturges (56) investigated steel using compression tests at strain rates of up to 2.5×10^3 per second and elevated temperatures ranging from 600-1200°C. They reported that the strain rate sensitivity increases with increasing test temperature and the flow stress increases either with reduction in temperature or increase in strain rate. Finally, Alder and Phillips (57) looked into the effect of strain rate and temperature on the resistance to deformation of aluminium, copper and steel in compression. They conducted their tests using a plastometer at strain rates ranging from 1-40 per second at various sub-zero and elevated temperatures. They reported that the power law $\sigma = \sigma_o \dot{\varepsilon}^{\eta}$, where σ is the stress, σ_o is stress at unit strain and $\dot{\varepsilon}$ is the strain rate, fits the stress-strain curves fairly well. They also indicated that the power index (n) increases with temperature and at higher temperatures increases with strain.

1.4 Plan and Aim of the Present Work

The present investigation, consisting of three phases, was scheduled according to the following plan of work.

(a) Phase One:

1. To conduct incremental compression tests on the three aluminium alloys and the structural steel in order to obtain their quasi-static stress-strain characteristics.

2. To carry out ballistic tests, by firing cylindrical projectiles made from one of the three aluminium alloys onto a flat rigid anvil; the projectile velocity being measured just before impact. The final diameters at the impact ends and the heights of the deformed projectiles to be measured.

3. To predict theoretically the maximum final diameters and heights of the projectiles in conjunction with the quasi-static stress-strain properties, a chosen strain rate sensitivity equation, and a finite-difference numerical technique. The material constants of the strain rate sensitivity equation to be given arbitrary magnitudes.

4. To compare the experimental and theoretical curves of final diameter and height against impact velocity.

5. To improve the correlation between the theoretical and experimental results by systematically varying the magnitudes of the constants of the chosen strain rate sensitivity equation.

6. To ascertain the values of the constants for which agreement is the closest.

7. Repeat steps 2 to 6 for the other two aluminium alloys.

(b) Phase Two:

1. To undertake ballistic tests by firing cylindrical projectiles made of FMP-338 tool steel onto a small billet made from one of the aluminium alloys.

2. Repeat steps 2 to 6 as in phase one of the present work.

3. Repeat steps 1 to 2 in this phase for the other two aluminium alloys and also for the structural steel.

(c) Phase Three:

Due to the detection of a temperature rise within the test specimens in phase two during the dynamic deformation, an additional test programme was undertaken. This programme consists of the following:

1. To carry out incremental compression tests on the three aluminium alloys and the structural steel at elevated temperatures of up to 250°C in order to obtain the quasi-static stress-strain curves.

2. To formulate a temperature dependent quasi-static constitutive equation for each material.

3. To modify the numerical technique and software to cater for the temperature rise and radial inertia effects.

4. To repeat steps 2 to 6 as in phase one for each of the four materials undergoing the investigation.

Finally, the principal aim of the present work is to develop a simple technique to determine the stress-strain characteristics of any metal and alloy at high strain rates taking into account the strain-hardening, temperature rise, friction and radial inertia effects during dynamic deformations and to compare the results with those obtained using more sophisticated and expensive equipment.

CHAPTER TWO

2.0 Experimental Equipment, Preparation of Test Specimens and Test Procedure

2.1 Introduction

All the impact tests were carried out using a ballistic test rig originally designed and commissioned by Haque M M (14) and used by Haque M M et al (46), for determining the high strain rate behaviour of steel at sub-zero, room and elevated temperatures. In their work the rig was used in conjunction with a high speed IMACON camera operating at framing rates of up to one million per second to photographically record the deformation history.

In the present study, the same rig was used for the dynamic compression of small cylindrical billets but without making use of the high speed camera. The ballistic compression rig and its accessories are shown schematically in figure 2.1; whilst plate No 2.1 shows a photograph of the experimental set up.

The main items as indicated in figure 2.1 are as follows:

(i) Reservoir unit (17) and two-way ball valve (16)

(ii) Barrel (18) and Loading throat unit (19)

(iii) Rig frame (8).

The accessories consist of the following:

(i) Laser unit (7) and photocell (10)

(ii) Transient recorder (20) and oscilloscope (14)

(iii) Transducer unit (12).

The circuit diagram of accessories is shown in figure 2.2.

2.2 Detailed Description of the Ballistic Rig

2.2.1 Reservoir Unit and Two-Way Ball Valve

The main components of this section are:

(i) The high pressure reservoir

(ii) Two-way ball valve.

The top end of the pressure reservoir was connected by a flexible reinforced rubber hose to a compressed air cylinder which can provide the reservoir with a pressure of up to 2000 psi (13.78 MN/m^2). It was also fitted with a pressure transducer to monitor the pressure in the reservoir.

The bottom end of the reservoir is firmly fixed to the two-way ball valve by means of the valve nut. A copper gasket is used between the two components to make the assembly leak proof. The 1 inch BSP two-way ball valve (part No. 012-25-34) was suitable for operation at pressures of up to 4700 psi (32.383 MN/m^2) and at temperatures between -30 and 100°C. The valve is manually operated by turning its handle through 90°. The pressure reservoir and two-way ball valve section is rigidly fixed to the main frame of the rig.

2.2.2 Barrel and Loading Throat

This section of the ballistic rig, shown in figure 2.1, consists of the following parts: extension barrel, surge suppressor, coupling sleeve, loading unit, split cover, sliding collar, collar nut and projectile gripper mechanism.

The extension barrel is made of En-16 steel with 0.3-0.4% carbon content. It has a high tensile strength, good shock resistance properties and is easily machined when heat treated. It is used in gun parts, high tensile bolts and nuts and is suitable for low temperature applications.

The suppressor cap is attached to the end of the extension barrel to minimise noise. A wire mesh safety chamber around the anvil area provides additional protection from rebounding projectiles. The suppressor cap has vertical slots to permit the laser beam to pass through, normal to the line of travel of the projectile.

The other end of the extension barrel is attached to the loading throat by a threaded coupling sleeve. The loading throat is made from En-32 steel. This steel has 0.15% maximum carbon content and is extremely hard and wear resistant when suitably heat treated. It also has high strength and good resistance to shock. A cut-out segment in the loading throat allows the projectile to be inserted and pushed up and held by the gripping mechanism. A close fitting cover of En-32 steel is used to cover the cut-out segment, which in turn is held firmly to the assembly using a sliding collar and nut. The projectile gripper mechanism consists of three grip screws which can be adjusted to hold the projectile in position, thus preventing it from sliding down the barrel.

The coupling sleeve is provided with a stop pin to prevent the collar nut from sliding down. The barrel is attached by a circular bracket to the frame of the rig so that it remains positioned perpendicularly.

2.2.3 Anvil Unit

This section consists of the following parts as shown schematically in figure 2.3:

(i) Base plate

(ii) Back-up anvil

(iii) Holder plate

(iv) Robust support column

(v) Top anvil

(vi) Cover plate.

The support column or anvil column was made from a cylindrical alloy steel En-32 bar. The top anvil unit is made of tool steel FMP-338. The support column and the top anvil were heat treated to 970°C, oil quenched and tempered to 800 HV. These parts are held in place by the cover plate at the top and a holder plate, which is fastened to the base plate, at the bottom end of the support column.

The base plate is made of a rectangular solid En-12 steel plate which has 0.3-0.45% carbon content, with medium tensile strength and good impact properties. It is centrally recessed for the insertion of the back-up anvil and is also fixed by means of bolts onto the reinforced concrete foundation of the test rig.

2.2.4 Frame of the Rig

The frame is made of welded and bolted mild steel angles. It is two metres in height and about half a metre square in base area and is shown in plate No 2.1. A small safety chamber was built using wire mesh and thick perspex sheet to contain the projectile or the specimen after impact. Two opposite sides of the wire mesh chamber have small circular holes in them to allow the laser beam to pass through from the laser unit to the photo cell detector. The front panel can be easily opened and closed to gain access to the anvil as well as to remove the deformed projectiles (phase one) or billets (phase two) after impact. The steel frame is erected on a cubical reinforced concrete foundation unit.

2.2.5 The Laser Unit

The laser unit used was made by Spectra Physics (model 155, serial No 30996). It is operated from a 230 AC supply and is fitted with a beam attenuator. The laser unit is fixed to an adjustable stand which in turn is positioned on a table. The adjustable stand allowed the unit to be moved up and down vertically. The laser unit was then positioned at one side of the rig as shown in figure 2.1 and in plate No 2.1.

The beam passes through the circular holes in the wire mesh surrounding the safety chamber and suppressor cap to the photocell detector which is firmly fixed to the frame of the rig by means of screws. The photocell detector (sensor) is connected to a signal receptor unit which in

turn is connected to a transient recorder and oscilloscope unit as shown in figure 2.2. As the projectile passes through the suppressor cap, it cuts the laser beam and a change in voltage at the photocell detector is registered by the receptor unit, which amplifies and converts the signal into an electrical output. The output voltage is then passed onto the transient recorder and displayed on the oscilloscope screen.

2.2.6 Transient Recorder and Oscilloscope Unit

The transient recorder, made by Data Laboratories (model DL905), records the change in signal received from the photocell and charge amplifier units as the projectile passes through the laser beam. The change in signal is then amplified and transmitted to the transient recorder where it is amplified again and converted to digital data by an analog to digital convertor.

The digital data are then stored in a buffer store which can be recalled when needed. The main advantage of such a recorder is that the output digital data can be displayed on the oscilloscope screen at much slower speeds than the input signal.

The oscilloscope used was made by Telequipment Ltd (type D65, serial No 1035). The width of the approximately rectangular signal displayed on the oscilloscope screen gives the time elapsed for the projectile to pass through the laser beam.

2.2.7 Transducer Unit

This unit was used to control the air pressure and consists of the following three parts:

(i) Pressure transducer

(ii) Pressure transducer meter

(iii) Roband electric digital voltmeter.

The pressure transducer is of the differential inductive type, made by S E Labs (Eng) Ltd (Model No D59472000, Serial No 68722) and is fitted to the pressure reservoir. This facilitated a direct and accurate reading of the pressure. The pressure transducer is connected to a direct reading transducer meter, made by Sangams Weston Control Ltd (Type C52 and Serial No 05928/38), which has been calibrated by a dual range dead weight pressure gauge tester. The transducer was connected to an electronic digital voltmeter, made by Roband Electronics Limited - England (Serial No A044L6) to obtain an output reading of pressure in psi directly.

2.3 Preparation of Test Specimens

2.3.1 Introduction

The materials which have been investigated in the present study are HE15, HE30TF, DTD5044 aluminium alloys and En-8 structural steel.

Tests were only conducted on the three aluminium alloys, in the initial stage (phase one) of the present work. However in the main part of the investigation (phase two) En-8 structural steel was introduced in addition to the

three aluminium alloys mentioned previously. All materials have been tested as received from suppliers.

2.3.2 Materials Composition

Chemical composition tests were carried out on all materials involved in this study to find out the percentage weight of the alloying elements. These alloying elements affect the materials behaviour and characteristics regarding strength, strain-hardening and stress-strain relationship at different strain rates.

Table 2.1 shows the chemical composition of the three aluminium alloys together with the FMP-338 and En-8 steels. Heat treated FMP-338 tool steel projectiles were used to deform small billets in phase two of the present study.

2.3.3 Materials Hardness

A Vickers pyramid hardness testing machine was used to obtain the hardness of HE15, HE30TF, DTD5044 aluminium alloys and FMP-338, En-8 steels.

Hardness tests were conducted on all materials as received and after being machined to size, except the FMP-338 tool steel. This was heat treated to 970°C, oil quenched and tempered to 150°C then tested. The objective lens of the hardness testing machine was kept at 2/3" in all tests conducted. Table 2.2 shows the average hardness numbers of these materials.

2.3.4 Preparation of Test Specimens

(a) Phase One (Cylindrical projectiles fired onto a rigid anvil)

In the early stages of the research, ballistic test specimens were made of HE15, HE30TF and DTD5044 aluminium alloys. The specimen size was chosen to be 20mm in length and 9.52mm in diameter, in order to suit the firing device. Accuracy in length of the test specimen was important for correct impact velocity readings. Diametral accuracy was essential for close fit of the projectiles in the barrel; this prevented air from passing through the gap between the projectile and the barrel inside surface.

HE30TF and HE15 aluminium alloy specimens were machined to size from as received round bars, size 12.7mm and 15.87mm in diameter respectively. The DTD5044 specimens were machined from a rectangular cross-sectional bar 76mm x 50mm obtained from British Aerospace PLC, Aircraft Group, Weybridge Division.

Using such projectile dimensions it was possible to obtain strain rates ranging from 2.5×10^3 to 1.25×10^4 per second. The cylindrical ballistic test specimens were finely ground to obtain a smooth flight through the barrel, and the flat ends surfaces were polished resulting in a mirror finish to achieve uniform deformation across the diameter and to minimise friction.

(b) Phase Two (Tool steel projectiles fired onto small billets)

In this phase of the investigation the specimen size was kept to 5mm in length and 5.2mm in diameter in order to obtain strain rates of the order of 10^4 per second. Other dimensions were introduced later on for the three aluminium alloys in order to investigate radial inertia and size effects during deformation. The aspect ratio (length/diameter) was kept less than unity to avoid buckling and undesirable barrelling during deformation.

En-8 test specimens, 5mm in length and 5.2mm in diameter were machined to size from as received 25.4mm diameter round bars. All test specimens in this phase, including the FMP-338 tool steel projectiles, were finely ground and the ends polished resulting in surfaces as flat as possible in order to achieve homogenous deformation. Using such test specimens it was possible to achieve strain rates ranging from 4×10^3 to 2.2×10^4 per second.

2.3.5 Preparation of Tool Steel Projectiles for Phase Two Tests

The FMP-338 tool steel projectile dimensions were 19mm in length and 9.52mm in diameter and were initially machined to size from as received 76.2mm diameter round bars. The projectiles were then heat treated at a temperature of 970°C, oil quenched and tempered at a temperature of 150°C to increase the strength. The chemical composition and hardness of the projectile material are shown in tables 2.1 and 2.2 respectively. Mass of FMP-338 tool steel projectile is 10.2 grams.

The FMP-338 projectiles were machined to size to fit accurately in the loading throat of the test rig and all finely ground. Their flat surface were polished to a mirror finish. Other dimensions for the tool steel projectiles were considered to achieve higher impact velocities and consequently higher strain rates. However, it was not possible to use impact velocities higher than about 110m/s for the aluminium alloys and En-8 steel respectively, due to severe compression, fracture and noticeable barrelling. Thus all these tests were conducted with only one sized projectile.

2.4 Calibration of Test Equipment

2.4.1 Calibration of Pressure Transducer

The pressure transducer was calibrated using a dual range dead weight pressure gauge tester (Budenberg Gauge Tester). This tester uses hydraulic oil and ratio weights. Equal amounts of oil are pumped to the output end of the equipment where the pressure transducer is connected and to the other end where a piston carries the weight. Pumping was continued until the weights were rotating freely on the piston. The voltage reading corresponding to the pressure applied was noted.

Table 2.3 shows the pressures with their corresponding voltages for the pressure transducer.

2.4.2 Air Pressure - Impact Velocity Calibration

The ballistic rig was used to obtain air pressure-impact velocity calibration charts for FMP-338, HE15, HE30TF

and DTD5044 projectiles as shown in figure 2.4. This chart facilitates easy readings of the air pressure corresponding to a required impact velocity for initial guide only. The calibration chart was constructed from experiments carried out using the standard test procedure detailed in section 2.5. After selecting a certain air pressure (using the Roband Voltmeter) the projectile was fired and the velocity noted.

2.5 Experimental Procedure

2.5.1 Introduction

A number of preliminary tests were carried out involving full use of the experimental rig in order to obtain

(i) Calibration of test equipment

(ii) Impact velocity and air pressure relationship

(iii) Laser tests involving velocity readings corresponding to each aluminium alloy and tool steel projectile.

Several quasi-static compression tests were carried out using different lubricants such as oil, petroleum jelly and tallow-graphite (8/1 weight) to decide which of these lubricants was most suitable. These quasi-static compression tests were carried out at different compression speeds in the quasi-static range in order to gather information regarding stress-strain and strain rate characteristics.

These experiments have been conducted to establish and maintain an appropriate test procedure in order to obtain as similar conditions as possible in all tests.

2.5.2 Setting the Test Equipment and Loading the Projectiles

Before setting the equipment the whole rig was checked for horizontal levelling by means of a spirit level. Small steel wedges were used to make adjustments, these wedges were pushed and hammered in under the concrete base at different positions until the rig was level, thus ensuring a perpendicular impact between the projectiles and anvil or test specimens.

Setting the test equipment before loading was essential due to the fact that once the air reservoir was full, it was dangerous to load the projectile or pre-test the equipment. The triggering device on the transient recorder and the oscilloscope were set in conjunction with the charge amplifier which was connected to the photo-cell. The laser beam unit was checked to ensure that it was fully operational and that nothing was obstructing the path of its beam while passing through the suppressor cap to the photo-cell. A circuit operational check was then performed by obstructing the laser beam path and monitoring whether or not the other items of equipment were in operational mode.

After re-setting the equipment the projectile (aluminium alloy in phase one, FMP-338 tool steel in phase two) was placed inside the loading throat through the entrance slot and pushed up into the grip mechanism to be kept in suspension ready for firing to take place. The slot was then closed with the split cover and the collar slid over and clamped using the collar nut. The valve of the

compressed air cylinder was opened slowly, filling the air reservoir to the predetermined level as indicated by the pressure transducer meter and the Roband digital voltmeter.

2.5.3 Lubrication

It was essential to use a lubricant in order to reduce as much as possible the frictional effect during the deformation of the aluminium alloy projectiles impinging onto the rigid anvil or the heat treated tool steel ones impinging onto the small cylindrical billets.

It was decided not to lubricate the flat surface of the projectile so as to avoid accumulation of debris inside the barrel. For the tests in phase one, the anvil surface alone was lubricated, by spreading a thin film of tallow-graphite. However, in phase two where FMP-338 tool steel projectiles were fired onto small cylindrical billets made of the three aluminium alloys and En-8 steel, the anvil and both flat surfaces of the test specimens were lubricated, again by spreading a thin film of tallow-graphite.

Ring-compression tests were carried out at low (quasi-static) and high strain rates. Tests were conducted on HE15 rings with 1.7mm, 5.2mm inside and outside diameters respectively. This method has a particular advantage when applied to the study of friction at elevated temperatures or high strain rates. No direct measurement of force was required, and no yield strength values were

needed, hence the major difficulties of compression testing at high temperatures or strain rates were eliminated. Plate No 2.2 shows ring specimens of HE15 aluminium alloy which have been deformed statically and dynamically using tallow-graphite 8/1 weight as lubricant.

2.5.4 Firing the Projectile and Recording the Impact Velocity

Once the whole system was ready, the triggering device on, the transient recorder and the oscilloscope checked and set on and the laser unit in its correct position with the beam unobstructed, the projectile was fired.

Firing of the projectile was activated by turning the two-way ball valve handle through 90°. This allowed air to escape from the air reservoir through a convergent-divergent nozzle to propel the projectile down the barrel. In the course of its travel through the barrel at high velocity, the projectile passes through the laser beam, cutting off its path and the resulting signal is recorded.

This signal represents the elapsed time for the projectile to clear the laser beam. Knowing the length of the projectile and the elapsed time, the impact velocity was calculated and noted.

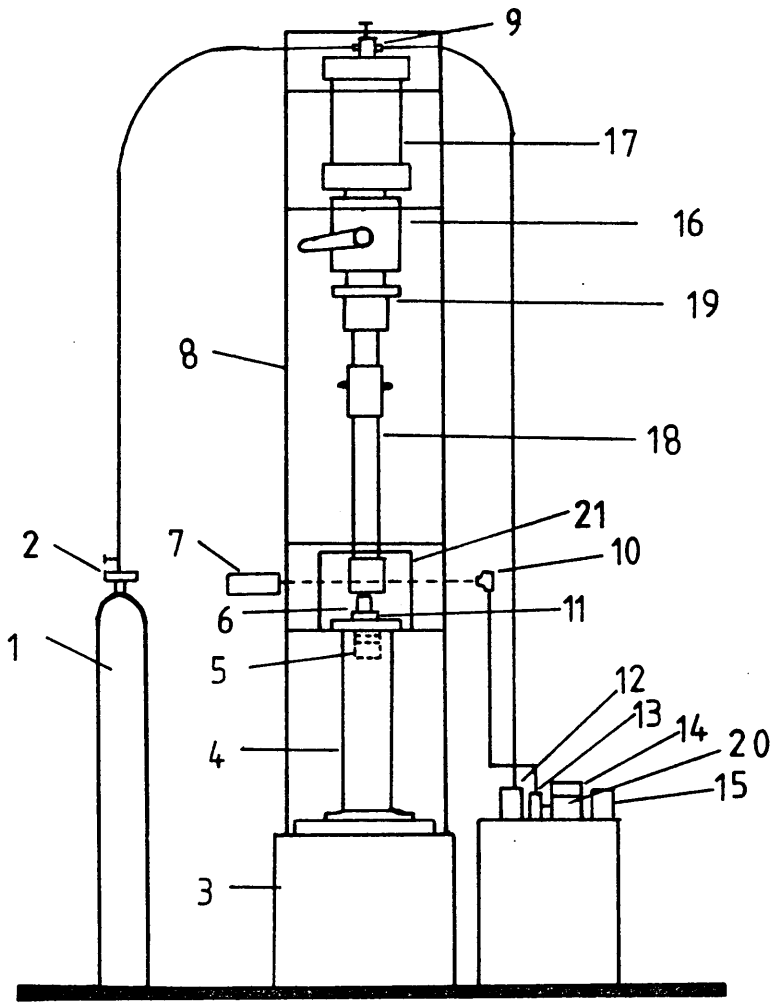

1. COMPRESSED AIR CYLINDER	11. TOP ANVIL
2. CYLINDER VALVE	12. PRESSURE TRANSDUCER METER
3. CONCRETE BASE	13. CONDITIONER UNIT
4. PRESSURE BAR	14. OSCILLOSCOPE
5. MIDDLE ANVIL	15. DIGITAL VOLTMETER
6. SPECIMEN	16. 2-WAY BALL VALVE
7. LASER	17. RESERVOIR UNIT
8. RIG FRAME	18. BARREL
9. PRESSURE TRANSDUCER	19. LOADING THROAT
10. PHOTO CELL	20. TRANSIENT RECORDER
	21. WIRE MESH

Fig [2.1] Experimental Ballistic Rig and Accessories

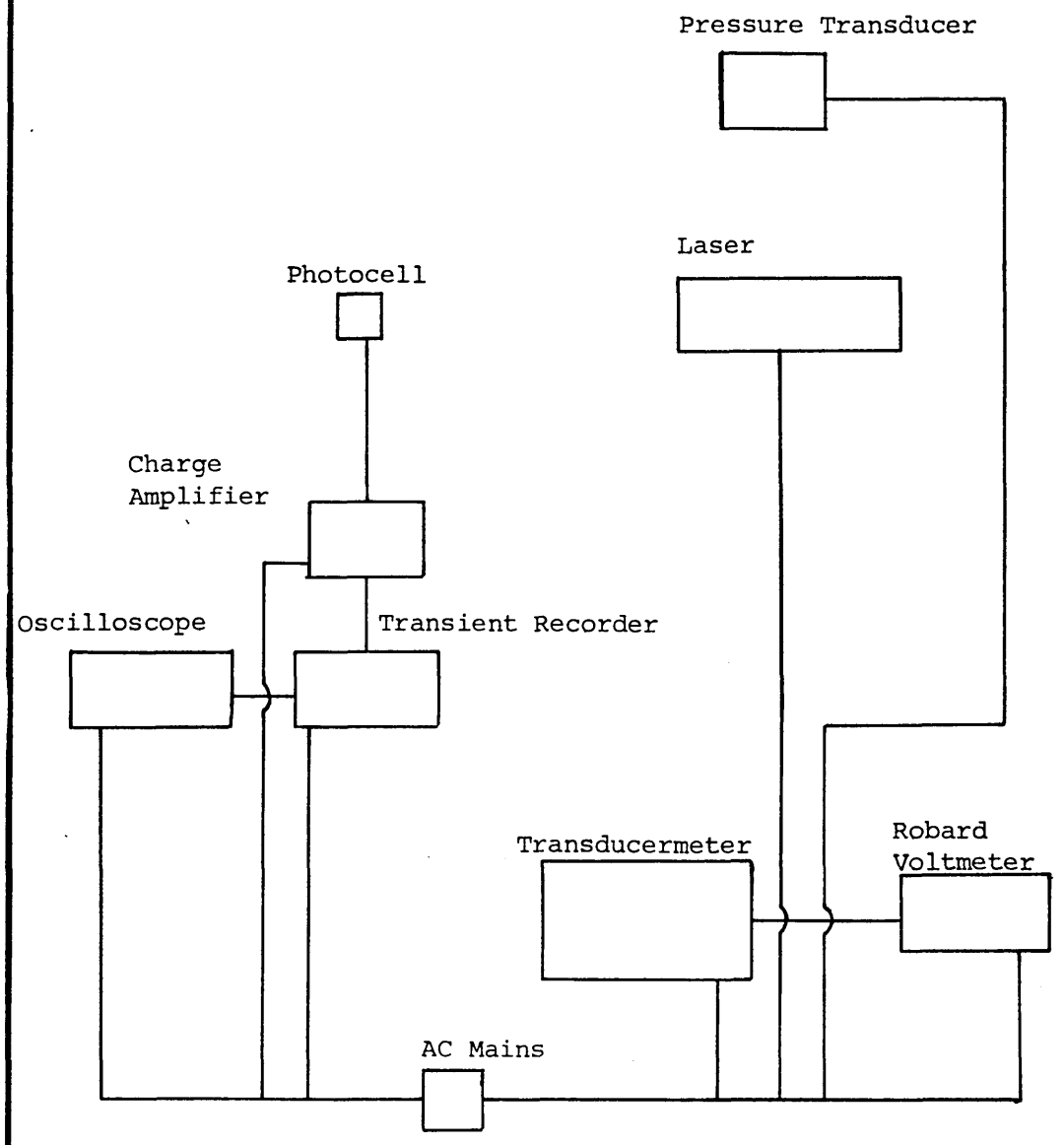

Fig [2.2] Accessories Circuit Diagram

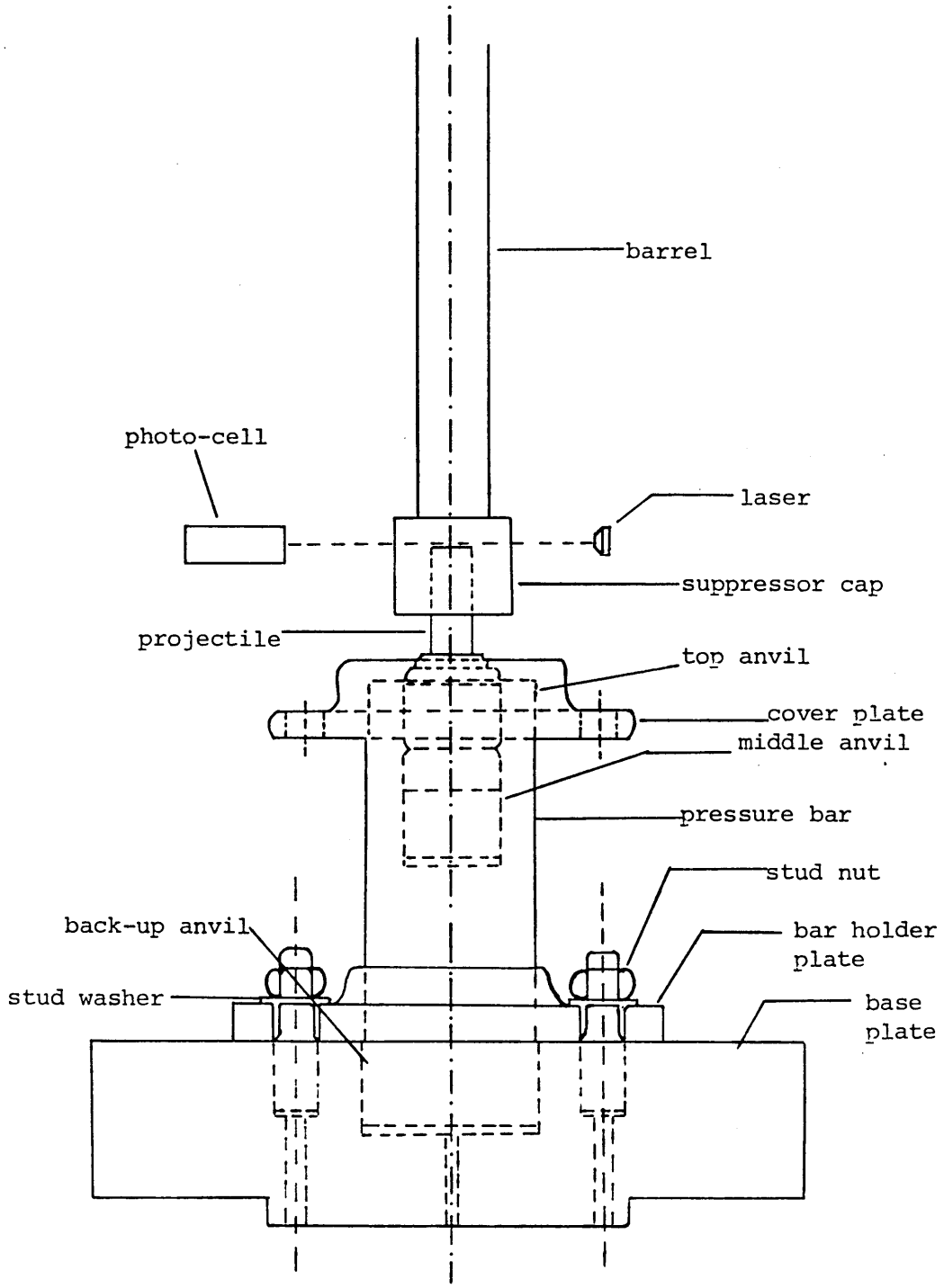

Fig [2.3[Anvil Unit, Barrel and Laser

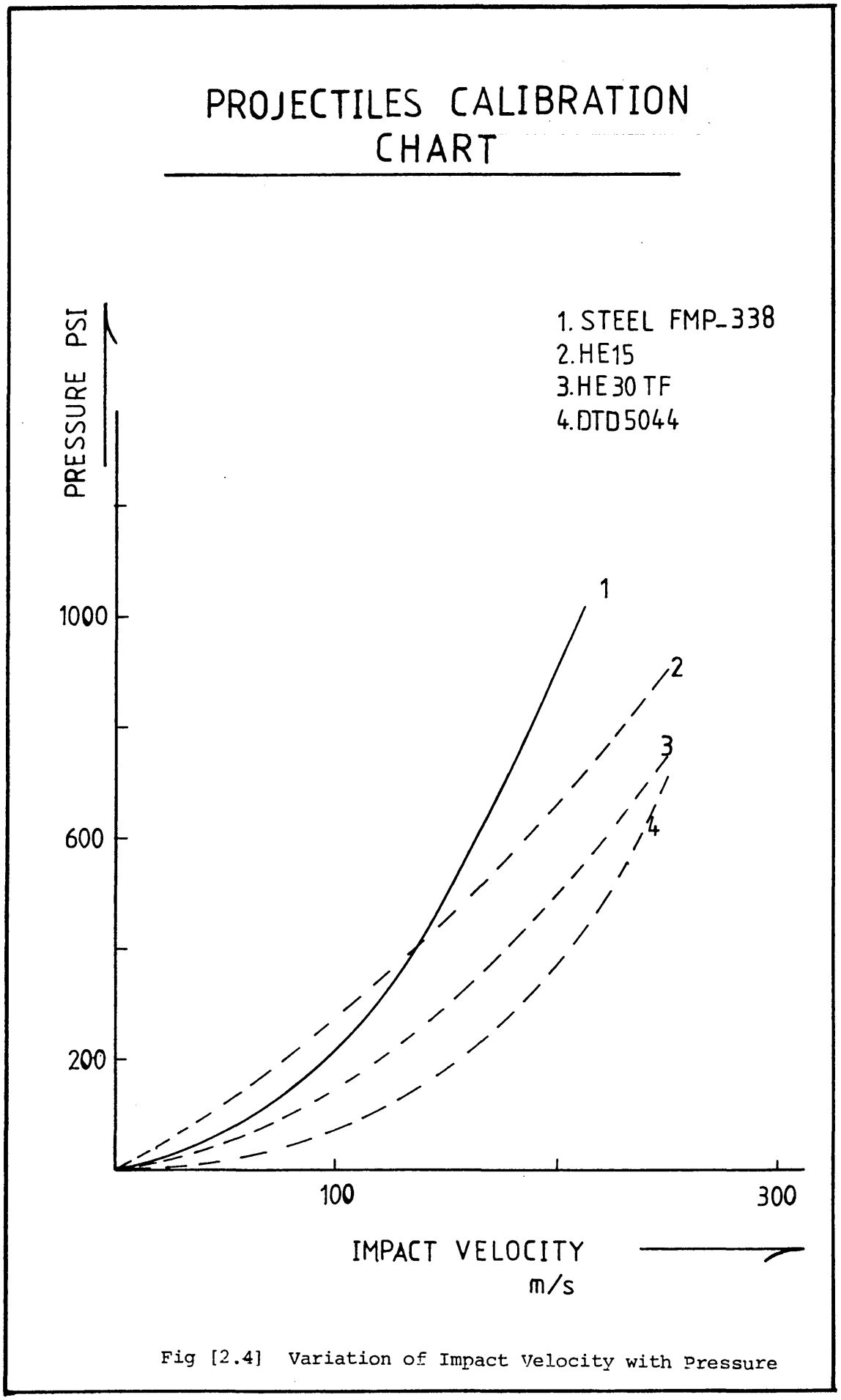

Fig [2.4] Variation of Impact Velocity with Pressure

Plate No [2.1] Experimental Set-Up

Plate No [2.1] Experimental Set-Up

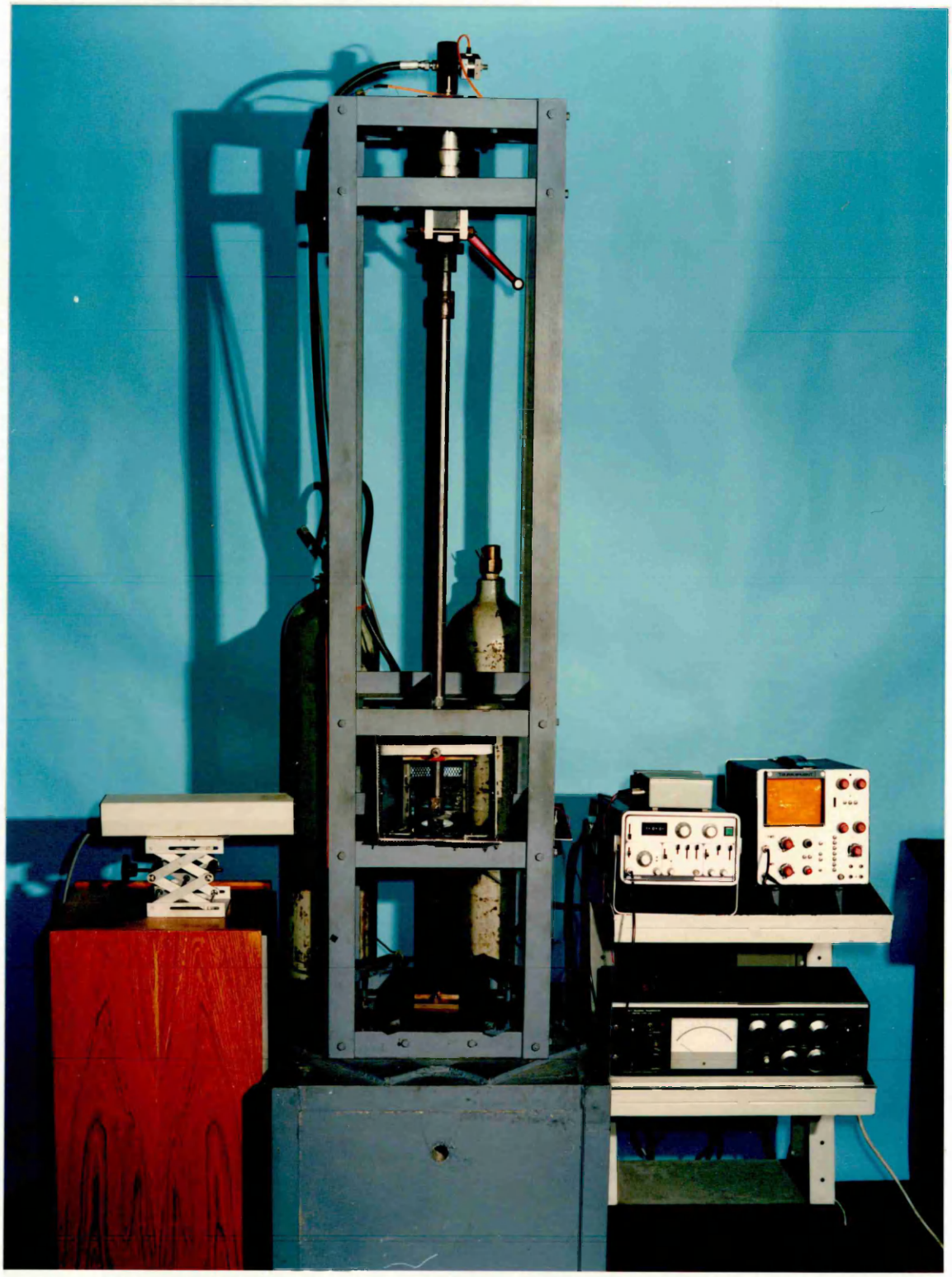

Undeformed Specimen
0% deformation

Dynamically Deformed
35% deformation

Statically Deformed
47% deformation

Plate No [2.2] HE15 Ring Test Specimens

Plate No [2.2] HE15 Ring Test Specimens

Undeformed Specimen
0% deformation

Deformed Specimen
32% deformation

Deformed Specimen
41% deformation

Material Chemical Composition (wt%)				
Tool Steel FMP-338	Structural Steel En-8	HE15 20MTF	HE30TF BS1474	DTD5044
C -2.05	C -0.41	Si-0.794	Si-1.4	Si-0.4
Mn-0.40	Mn-0.78	Fe-0.271	Fe-0.18	Fe-0.15
Si-0.30	Si-0.26	Mn-0.360	Mn-0.2	Mn-0.31
Cr-13.00	Ni-0.13	Zn-0.060	Zn-0.07	Zn-5.4
Fe-Rem	Mo-0.02	Cu-3.870	Cu-0.07	Cu-0.45
	Al-0.012	Mg-0.05	Mg-0.56	Mg-2.22
	Fe-Rem	Ni-0.02	Ni-0.01	Ni-0.02
		Ti<0.2	Ti<0.2	Ti<0.2
		Li<0.002	Li<0.002	Li<0.002
		Al - REM	Al - REM	Al - REM

Table [2.1] Materials Chemical Compositions

Material	Hardness No
FMP-338	800HV 30Kg
En-8	210.2HV 30Kg
HE15	137.7HV 20Kg
HE30TF	109.0HV 20Kg
DTD5044	179.1HV 20Kg

Objective lens = 2/3" for all tests

Table [2.2] Materials Vickers Hardness Nos.

Budenberg Gauge Tester Reading psi	Roband Digital Voltmeter volts
100	0.101
150	0.151
200	0.202
250	0.252
300	0.302
350	0.352
400	0.403
450	0.453
500	0.503
550	0.553
600	0.604
650	0.654
700	0.703
750	0.754
800	0.803
850	0.853
900	0.902
950	0.951
1000	1.001

Table [2.3] Calibration chart of air pressure versus voltmeter readings

CHAPTER THREE

3.0 Numerical Technique

3.1 Introduction

Materials strain rate behaviour is significant over a very wide range. Low strain rates 10^{-12} to 10^{-5} per second are generally associated with creep whilst the range between 10^{-4} to 10^{-2} per second is known as the quasi-static range. Both of these ranges are of great interest to design engineers and material scientists.

The next range is very important as far as metal deformation and structural loading are concerned and is called the dynamic or high strain rate range. In this range inertia effects become important and the temperature rises in the specimen during deformation must be considered. High strain rates of 10 to 10^5 per second are associated with mechanical loading from a moving mass or a chemical explosion. Any deformation analysis in this region must include strain rate as well as strain hardening and frictional effects.

Many experimental techniques have been proposed by researchers to determine stress-strain characteristics of materials at strain rates in excess of 10 per second during deformation. These purely experimental techniques become more sophisticated and expensive as strain rates increase.

This is one of the reasons for considering combined experimental and analytical techniques to determine stress-strain relationships at high strain rates. Taylor (38), conducted tests which

involved impinging flat-ended projectiles onto a rigid target to determine the dynamic yield stress. He used the momentum equation in his analytical work, assuming that radial inertia effects were negligible so that the stress can be considered constant over any cross-section along the projectile. He reported that the dynamic yield stress estimated by his technique was underestimated.

Wiffins (39) used the same technique as Taylor (38) to determine the dynamic stress of various metallic materials such as steel, duralumin, copper and lead. He investigated the effect of pre-straining the materials before testing, reporting that the technique was inaccurate at low and high impact velocities. The strain rate employed during his tests could not be measured, and was estimated, thus creating errors in his data.

Later, Hawkyard et al (40) also used a combined experimental and analytical technique. They deduced the mean dynamic yield strength of copper and mild steel from strain measurements on the "mushroomed" ends of flat ended projectiles after impact onto a flat rigid anvil. Their analytical work involved equating the kinetic energy at impact with the plastic work to give a mean dynamic yield strength. The assumptions of homogeneous deformation and the conversion of kinetic energy to plastic work, together with the neglect of shearing between adjacent sections in the projectile, inevitably introduced inaccuracy in their results.

However, Hawkyard (41) presented a new technique which basically employed a similar approach to Taylor's (38) but instead applied

an energy equilibrium equation across the plastic boundary. The outcome of this new technique was the ability to predict more accurately than others the deformation profile of the projectiles after impact. It was suggested that the inclusion of the radial inertia forces in the analysis would improve the predictions.

Subsequently Hashmi and Thompson (47) introduced a new experimental and theoretical technique to predict the profiles of projectiles after impact for given stress-strain relationships at high strain rates. In their work they replaced the projectile with a lumped parameter model which consisted of a number of concentrated masses, connected to each other by massless links. The equation of motion was then applied to each individual mass and a solution for the dynamic behaviour was obtained using a numerical technique, taking into account the strain hardening and strain rate effects.

Later, Hashmi (48) incorporated into the technique previously outlined in reference (47) the effects of material inertia and strain rate sensitivity. The outcome of this work was the ability to establish the strain rate dependent constitutive equation of materials at very high strain rates.

In the present study the technique developed over the years by Hashmi (48) was modified to incorporate the effects of temperature rise and radial inertia and used in conjunction with experimental data.

3.2 Numerical Technique for Computer Simulation of Deformations

Although numerous strain-rate laws have been proposed there appears to be no universally accepted law. With reference to the quasi-static stress-strain properties and in order to demonstrate the capability of the lumped parameter model approach to incorporate the effects of strain rate on deformation, the constitutive equation of the form below were used by Hashmi and Thompson (47):

$$\sigma d = \sigma s \left[1 + \left(\frac{|\dot{\varepsilon}|}{D}\right)^{1/P}\right] \qquad 3.1$$

where σd and σs are the dynamic and static flow stresses respectively, and D and P are constants of strain-rate sensitivity. This equation was chosen because of its simplicity and the availability of relevant data.

The equation maintains the overall shape of the static stress-strain curve, but shifts it vertically with strain rate and also assumes that the effect of strain rate is independent of strain. The finite-difference numerical technique was used to predict the strain and strain rate at any point along the length of the cylindrical test specimen being dynamically deformed and also to predict the final profile of specimen for given values of P and D. The technique assumes the following:

(i) The projectile (phase one) or billet (phase two) consists of a number of lines of concentrated masses connected to each other by massless links which have the same strength properties as the material (projectile or billet) undergoing deformation.

(ii) Uniform axial strain occurs in each individual link. For a projectile impinging onto a rigid anvil the axial strain varies slightly across the diameter from the axis to the surface (of the projectile) in the region near the anvil. Therefore accuracy will not be high in estimates relating to the lateral spread of the links in the mushroomed region close to the anvil.

(iii) The radial expansion of each connecting link is governed by the condition of volume constancy and there is no resistance to expansion from the neighbouring links.

However, in phase two, where tool steel projectiles are impacted onto small cylindrical billets, the deformation is homogeneous, ie. shearing does not take place between layers in the specimen. Temperature rise during deformation was also introduced to govern the stress during deformation.

The general equation for an element soon after it strikes the anvil can be derived by considering the internal and inertia forces acting on the element as in figure 3.1a and is given by

$$\frac{\partial N}{\partial s} - m\ddot{u} = 0 \qquad 3.2$$

where m is the mass per unit length.

Figure 3.1b shows forces between the masses and links of the lumped parameter model for a number of elemental lengths of the specimen. Figure 3.2a shows the specimen and its actual configuration just before deformation. Its equivalent lumped mass model is shown in figure 3.2b.

The finite-difference equation for the elemental length is given by

$$N_{i+1,j} - N_{i,j} - \Delta S_o m.\ddot{u}_{i,j} = 0 \qquad 3.3$$

Equation 3.3 applies to all the elemental lengths along the specimen and gives the instantaneous value of $u_{i,j+1}$ for any instant in time t_{j+1} when coupled with the following relationship between the acceleration and displacement in finite-difference notation.

$$u_{i,j+1} = \ddot{u}_{i,j} (\delta t)^2 + 2u_{i,j} - u_{i,j-1} \qquad 3.4$$

The time increment δt is defined by

$$\delta t = t_{j+1} - t_j \qquad 3.5$$

The change in length of the element $\delta(\Delta S)_{i,j+1}$ of the link occuring during the time interval δt is

$$\delta(\Delta S)_{i,j+1} = \Delta S_{i,j+1} - \Delta S_{i,j}$$

where

$$\Delta S_{i,j+1} = u_{i,j+1} - u_{i+1,j+1} \qquad 3.6$$

The increment of link length is then used to calculate the increment in strain given by $\delta\varepsilon_i = \delta(\Delta S)_{i,j+1}/\Delta S_{i,j+1}$

The strain rate is then given by $\dot{\varepsilon}_i = \delta\varepsilon_{i/\delta t}$ and the total strain is obtained as $\varepsilon_{i,j+1} = \varepsilon_{i,j} + \delta\varepsilon_{i,j+1}$.

Once the strain and strain rate in any link are known the stress is determined using the appropriate constitutive equation given by

$$\sigma_{i,j+1} = f(\varepsilon, \dot{\varepsilon}, T) \qquad 3.7$$

In order to incorporate elastic-plastic stress into the calculation the material of each link is assumed to be made up of a number of elastic perfectly plastic materials. The yield stress of each of these materials is given by the product of the elastic modulus and the corresponding plastic strain levels of

the polygonal stress-strain diagram illustrated in figure 3.3. This idealisation permits stress computations and unloading following an elastic path. See Appendix IX.

The yield stresses of the constituent material are thus given by

$$\sigma y_1 = \varepsilon_1 E_1,\ \sigma y_2 = \varepsilon_2 E_1 \text{ and } \sigma y_3 = \varepsilon_3 E_1$$

The cross-sectional areas of each of the constituent materials are given by

$$A_1 = A(E_1 - E_2)/E_1$$

$$A_2 = A(E_2 - E_3)/E_1$$

$$A_3 = A(E_3 - E_4)/E_1$$

where A is the cross-sectional area of the link. The stress in the link is then simply given by

$$\sigma_i = (A_1\sigma y_1 + A_2\sigma y_2 + A_3\sigma y_3)/A \qquad 3.8$$

The value of $\sigma_i,j+1$ is then modified to take into account the effect of friction and material inertia by use of the following equation which was derived from basic plasticity theory (71).

$$\sigma m_i = \sigma_i[1 + \frac{m_f R}{6} + \frac{3}{64}\frac{\rho v^2 R^2}{\sigma_i}] \qquad 3.9$$

for the links immediately in contact with the anvil or the projectile, and

$$\sigma m_i = \sigma_i[1 + \frac{3}{64}\frac{\rho v^2 R^2}{\sigma_i}] \qquad 3.10$$

For all other elements, where v is the constant velocity of deformation of the link during the time δt, R is the diameter to height ratio for the link and m_f is the friction factor which may vary from 0 to 1 depending on the frictional condition at the interface.

For low friction operation where $m_f \simeq 0$ equation 3.10 may be used for all links. The axial force $N_{i,j+1}$ in the link i is

then given by

$$N_{i,j+1} = A_{i,j+1} \cdot \overline{\sigma_m}_{i,j+1} \qquad 3.11$$

At the end of each time interval δt, the diameter of each link is calculated from the known cross-sectional area and the instantaneous profile of the projectile is obtained by joining the mid-diametral points of all links. The cycle of computation described is then repeated until plastic deformation ceases.

The constitutive equation 3.7 was based on the quasi-static stress-strain curves, and the strain rate sensitivity relationship given by equation 3.1. Appendices I and II contain the software for the finite-difference numerical technique employed in phase one and two respectively of the present work.

3.3 Temperature Rise during Deformation

During plastic deformation the energy consumed is transformed largely into heat while only a small proportion of that energy is used up in distorting the crystal structure of the material.

Temperature rises in a material during the deformation process affect material behaviour in two ways, (i) the change in flow stress with temperature at constant strain rate, and (ii) the change in strain rate with the temperature at constant stress. In reference (48) the heat generation during plastic deformation of the test specimen was ignored and the initial specimen temperature was taken to be the test temperature. The lack of correction for temperature changes during a test may lead to errors in estimating the flow stress of certain materials (eg aluminium and its alloys) undergoing deformation, especially in high strain rate tests involving large strains, where heat

transfer is reduced and temperature rise is considerable. Following the work by Holzer and Brown (17) the temperature rise ΔT has been calculated assuming that adiabatic conditions exist during high speed homogeneous deformation. Thus,

$$\Delta T = \frac{Z}{\rho s} \int_0^{\varepsilon_f} \sigma d\varepsilon \qquad 3.12$$

where ε_f is the final strain, σ the true stress, ε the true strain, ρ the density and s is the mean specific heat (although s increases with temperature, the increase is very small and negligible). The factor Z is the portion of the work of deformation appearing as heat.

Bishop (58) reported that the values of Z for aluminium alloys and steel were 0.955 and 0.865 respectively. A sample of this calculation is shown in Appendices III & VI, for HE15 aluminium alloy. Due to these temperature rises in the test specimen during deformation, its effect has been investigated thoroughly and introduced in the technique as discussed in Chapter Seven.

3.4 Friction during Deformation

Frictional effects are of importance both from the practical and theoretical point of view in all mechanical-working operations where the stock material is deformed in contact with rigid tools or dies. In many metal forming processes, lubricant is trapped between the tool and the work-piece and this reduces friction and often prevents seizure.

The coefficient of friction and the surface conditions of the deformed specimens or work-pieces are affected by the viscosity of lubricants, the speed of deformation and the size of the work-piece. It is widely accepted that hydrodynamic effects

play an important role in trapping lubricant, by squeezing a film of the lubricant between the tool and the work-piece. However, in slow speed compression the elastic deformation of the tool may have important effects not only on the shape of the end surface but also on the process of lubricant trapping.

In the cold working of metal, especially in the aluminium industry, lubrication is essential. For example in the case of cold rolling a high reduction per pass is desirable in order to reduce the number of passes needed for a given total reduction in thickness. An excessive reduction per pass is likely to affect the surface finish of the material owing to a local breakdown of the lubricant. A good lubricant will not break down easily and will therefore permit a high reduction per pass without affecting the surface finish.

In the present study, although lubricant (tallow-graphite) has been used during tests to minimise the friction effect, it is useful to show the extent of such an effect under dry conditions ie, without using tallow-graphite. The following analysis was reported and adopted by Haque (14) to correct his results since he conducted his tests under dry conditions. The analysis is also used in this investigation to show the extent of this effect and how the lubricant used minimises it.

The compressive flow stress using lubricant may be expressed as

$$\sigma s = Y[1 + \frac{2}{3} \mu \frac{r}{h}] \qquad 3.13$$

where

σ_s = quasi-static compressive flow stress using lubricant

Y = frictionless flow stress of specimen materials

r = current specimen radius (projectile mushroomed end in phase one and current radius of billet in phase two)

h = current specimen height

μ = coefficient of friction.

During a test the current value of r corresponding to a current height h was found using the volume of constancy. Tests were carried out quasi-statically for this purpose under dry and lubricated conditions with all specimens having the same aspect ratio (height/diameter). Now taking the coefficient of friction for graphite mixed with grease as 0.01 as reported by Watts and Ford (59), and using stress values from the quasi-static test, Y the frictionless flow stress can be calculated; hence the coefficient of friction μ_D, under dry quasi-static test can be found from equation 3.13 as

$$\mu_D = [\frac{\sigma_{sD}}{Y} - 1]/\frac{2}{3}\frac{r}{h} \qquad 3.14$$

where σ_{sD} is the quasi-static flow stress under dry conditions and r and h are as defined earlier. Typical calculations of this effect are shown in Appendix VII for phases one and two of the present investigation.

3.5 Radial Inertia during Deformation

One of the main problems encountered when experimentally investigating the mechanical behaviour of materials at high strain rates is associated with inertia effects. As the rate of loading is increased, the acceleration of any moving parts of the straining apparatus and the specimen material begins to require forces comparable with these necessary to deform the specimen.

It is often impossible to separate these inertia effects from the effects due to the physical properties of the material under investigation and at the highest rates of loading the inertia of the specimen itself will result in a non-uniform distribution of stress along its length. When a specimen (projectile or short cylindrical billet) is subjected to a fast (dynamic) compression between rigid platens, inertia forces would be present and the plastic yielding might be affected. The force, energy and power requirements are therefore different from those which may be predicted by the quasi-static test. Slater (60) reported that for velocities in excess of about 300 m/s elastic and plastic stress waves may be propagated which are able to travel up and down the specimen several times during the compression process. It can therefore be anticipated that the magnitudes of the axial force which may be detected at upper and lower platens will be different.

The analysis developed by Slater (60) was used in the present work in order to assess the inertia effect during the dynamic impact of projectiles and deformation of small cylindrical billets. It will be assumed that frictional resistance at interfaces is absent due to the use of lubricant and the deformation is homogeneous. Furthermore, the effects of stress wave propagation are considered to be insignificant because the impact velocities of the tests conducted in this study are in the range of 20-250 m/s. The axial force F, exerted on the cylindrical projectile or small billets is given by

$$F = \pi r^2 Y\left[1 + \frac{3}{16}\left(\frac{\rho V^2}{Y}\right)\left(\frac{r}{h}\right)^2\right] \qquad 3.15$$

where

r = current radius of specimen

h = current height of specimen

Y = current yield stress

ρ = density of the materials

V = impact velocity

Typical calculations of this effect are shown in Appendices IV and VI, for phases one and two of the present investigation.

3.6 Specimen Geometry

There is no definitive theory for the influence of specimen geometry on deformation. However, much information is available from researchers who have carried out work in this field investigating specimen length and diameter during static and dynamic compression tests.

Stress-strain properties can be obtained from specimens of different aspect ratios (h/d) undergoing compression tests assuming that the effect of friction is small. However, to achieve a good approximation to homogeneous deformation, large aspect ratios are desirable to minimise the effect of any frictional forces at the specimen-platen interface. However, large aspect ratios cause buckling during compression and to avoid this, aspect ratios should be as near to unity as possible. Small aspect ratios mean large diameters and consequently high friction unless a very efficient lubricant is used. For the tests specimens in phase two (small cylindrical billets) the aspect ratio was kept less than one and was maintained at 0.961 throughout the tests whilst friction effects were minimised using a lubricant.

Other sizes of billets (with aspect ratios less than one) were tested for the purpose of investigating the radial inertia and specimen size effect during deformation.

3.7 Plastic Wave Propagation during Deformation

Plastic wave propagation during impact deformation is of great interest to those who are involved in measuring loads during deformation processes. Many theories have been proposed resulting from experimental investigations carried out in this field.

However, in this study, no load was measured and consequently used in determining the strain rate sensitivity and hence stress wave propagation did not affect the results obtained by the present investigation.

3.8 Lumped Mass Model

In the present study the specimen was represented by a lumped mass model. The number of mass points was assumed to be ten throughout the work as shown in figure 3.2b. This was found to be sufficiently large without making excessive demands on computing time.

In order to verify the accuracy of the analysis, different numbers of mass points were considered. There was no indication that this affected results significantly though. This effect is shown in figures 3.4 and 3.5, taking HE15 aluminium alloy as example and using 10, 15, 20 elements during deformation.

It was convenient for computational purposes to consider the stress-strain properties of materials to be represented by a

number of connected linear lines as shown in figure 3.3; thus the lubricated quasi-static stress-strain curves of the materials were assumed to consist of four straight line segments from which stress and strain input data of the finite-difference numerical technique were extracted.

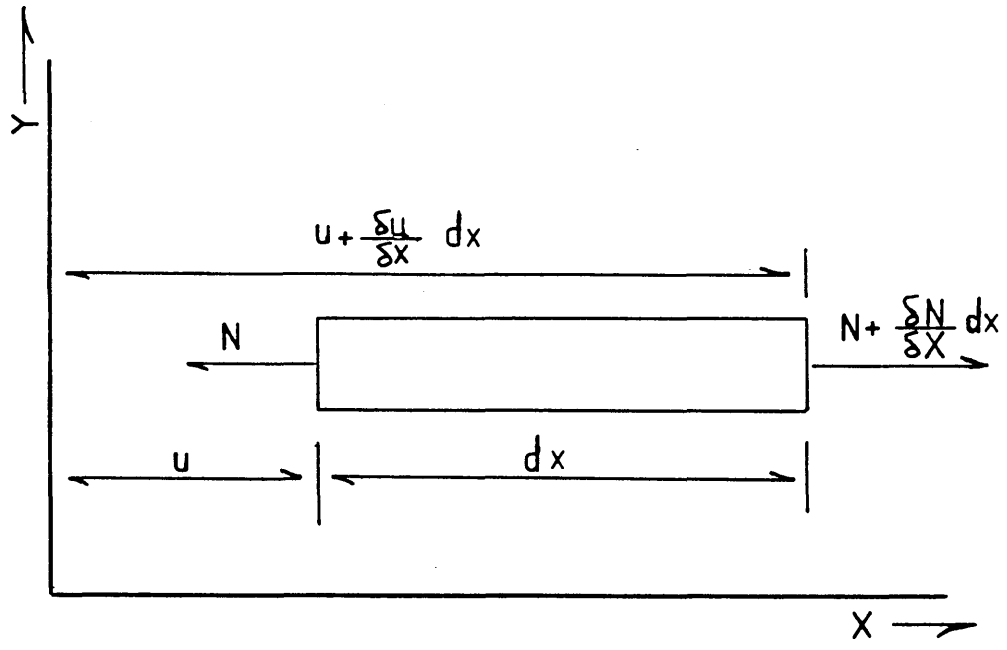

(a)

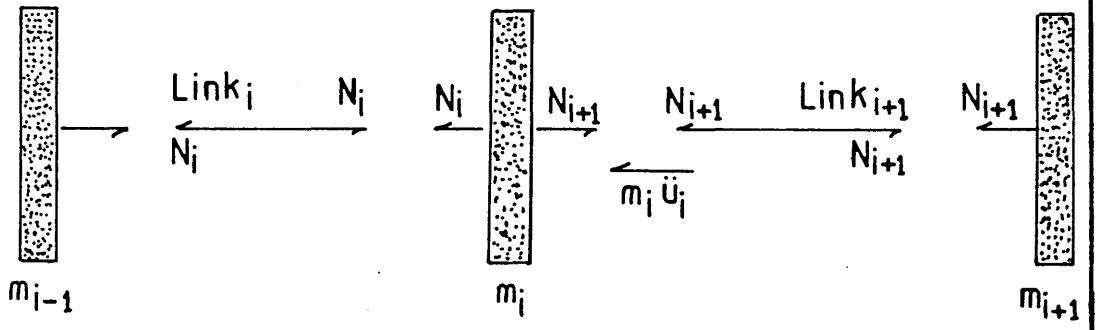

(b)

Fig [3.1] (a) Inertia forces acting on element

(b) Lumped Parameter Model

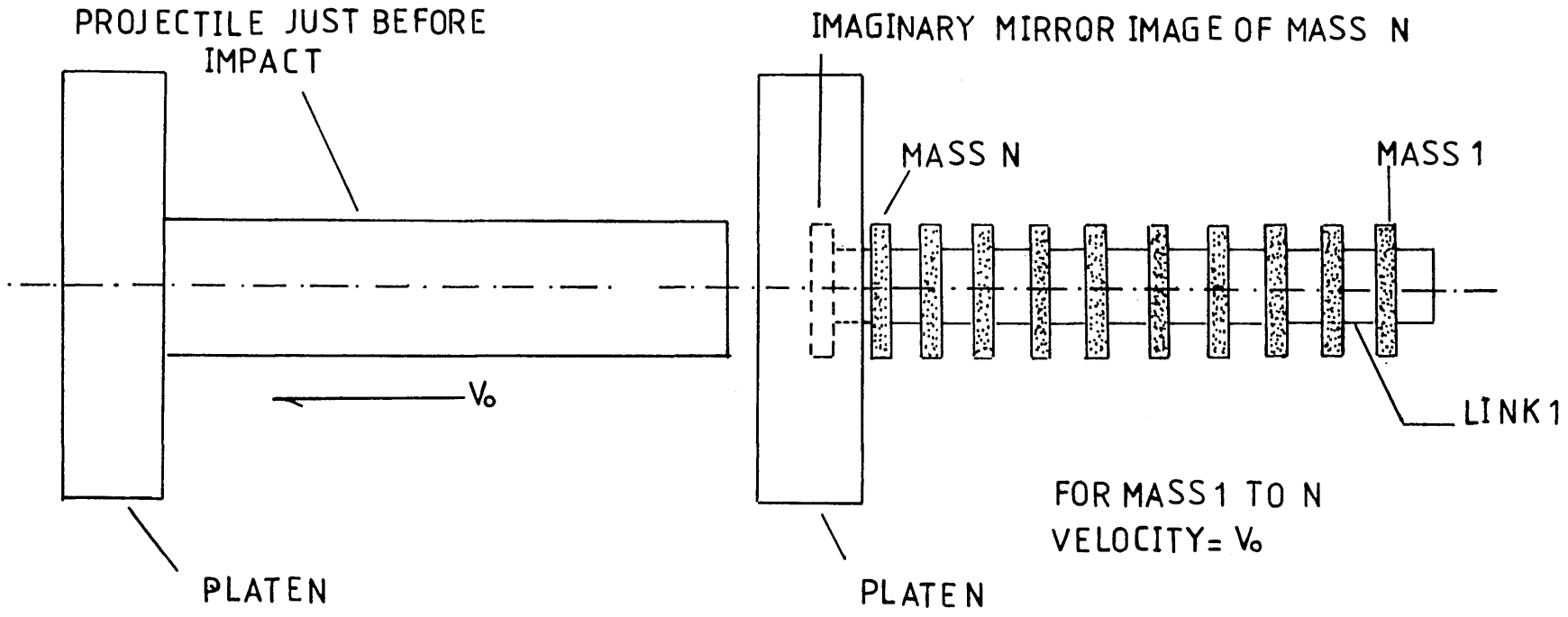

Fig [3.2] (a) Projectile Actual Configuration (b) Equivalent Lumped Masses

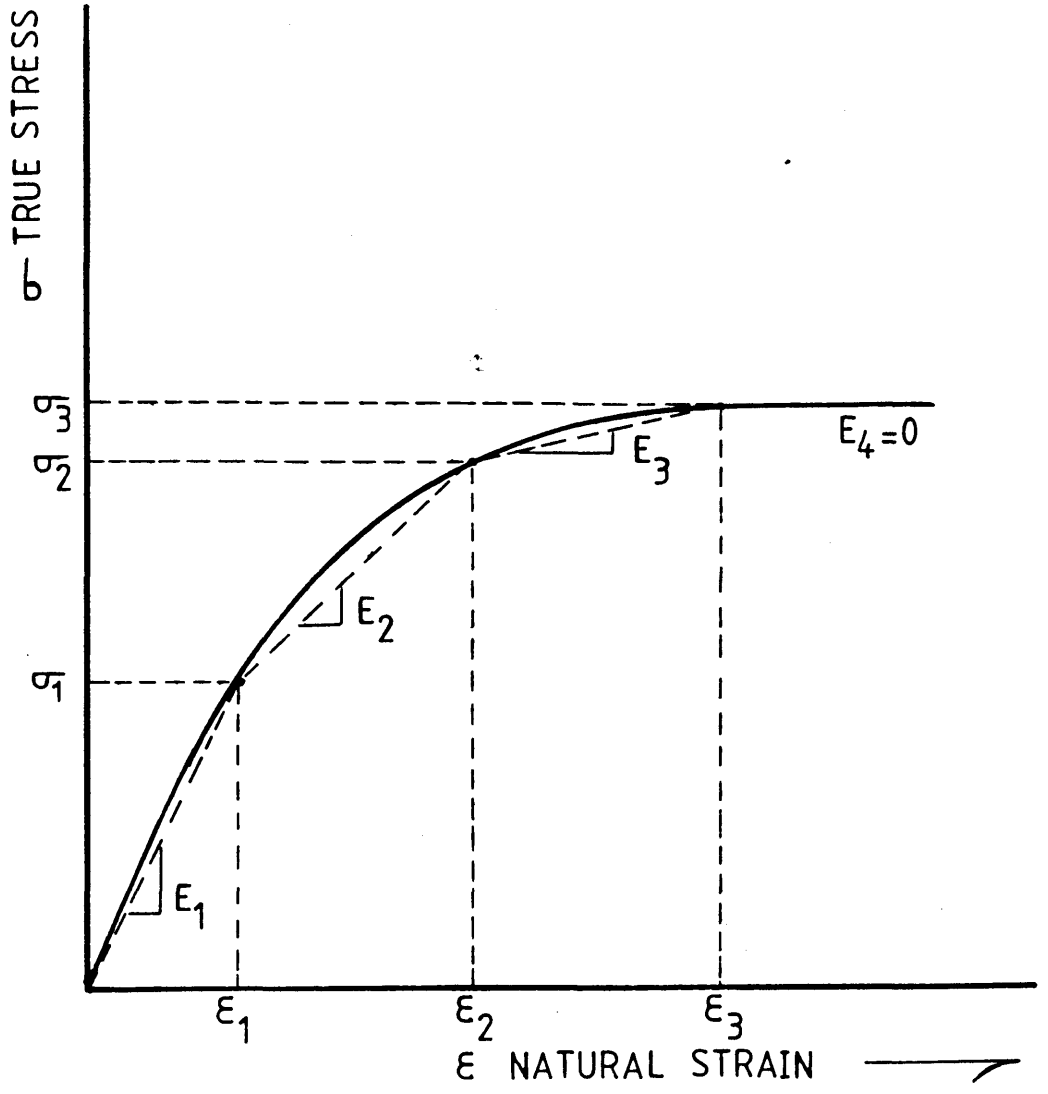

Fig [3.3[True stress-natural strain curve, linear lines elements

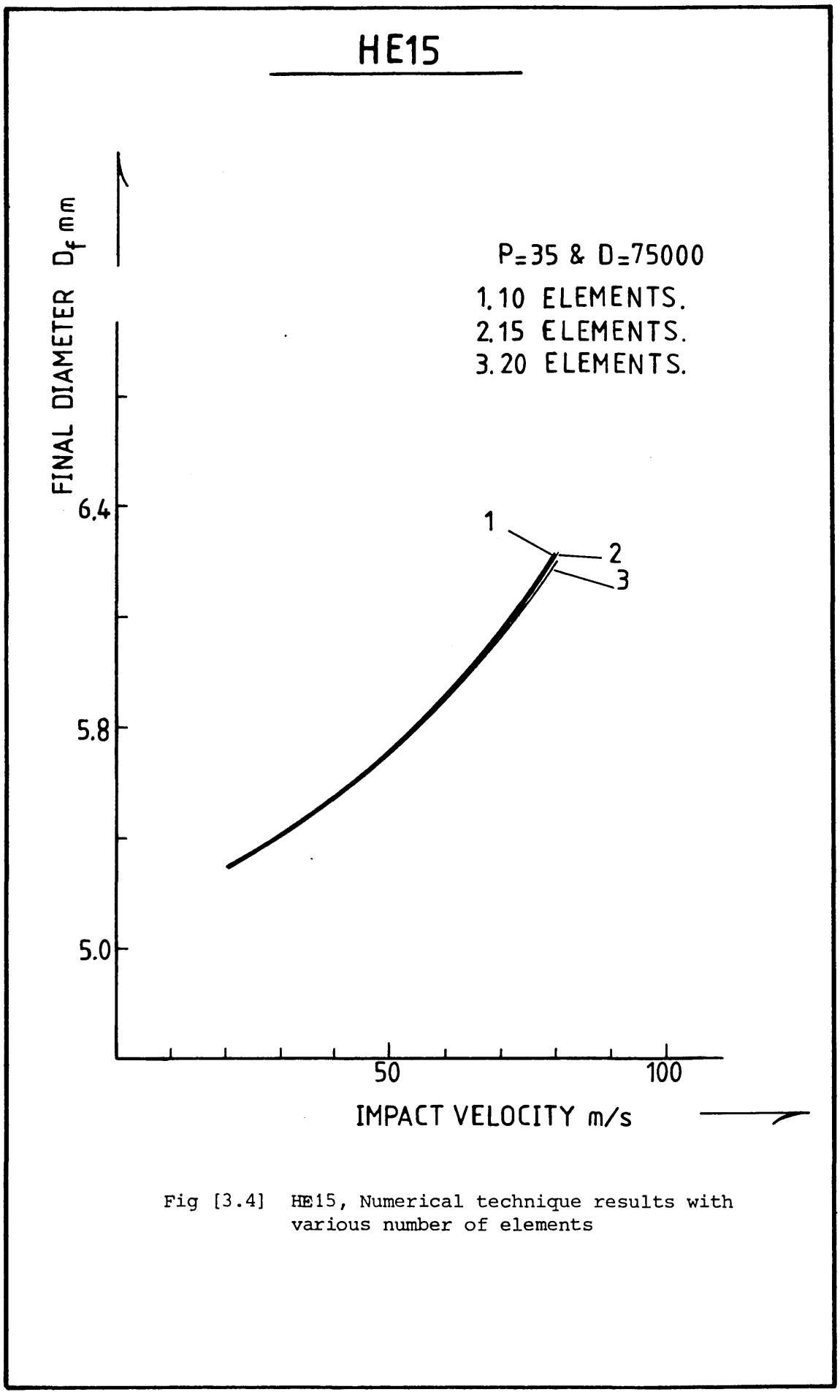

Fig [3.4] HE15, Numerical technique results with various number of elements

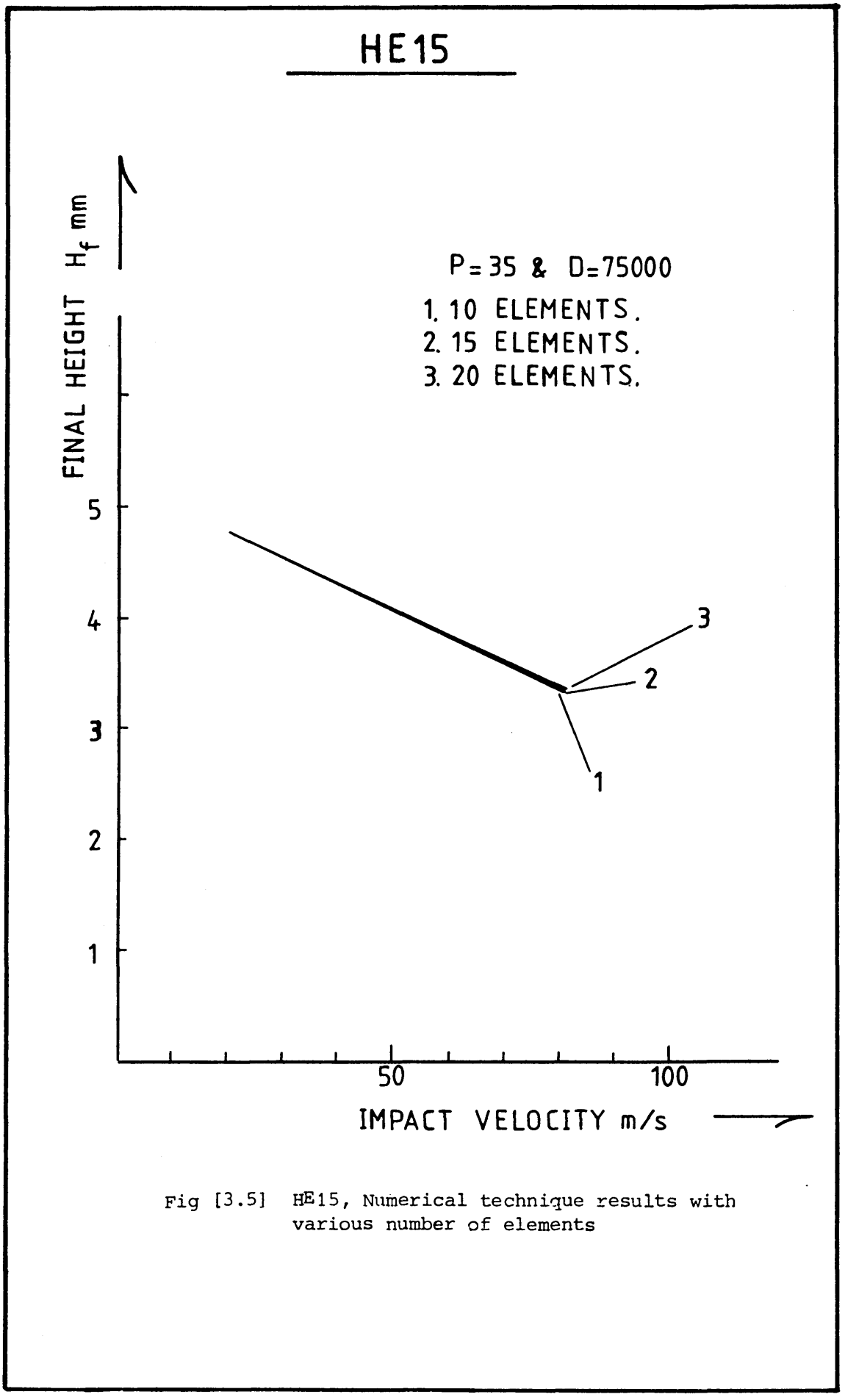

Fig [3.5] HE15, Numerical technique results with various number of elements

4.0 Phase One Experimental Results

4.1 Introduction

This experimental section of the present work, which is referred to as phase one, involves firing projectiles made of the three aluminium alloys HE15, HE30TF and DTD5044 onto a rigid anvil, as shown in Plate No 2, at different impact velocities.

Following the experimental procedure described in Chapter Two of the present work, the experimental results were processed in the following order:

(i) Quasi-static compression tests carried out on the three aluminium alloys and En-8 structural steel. The tests were conducted at a low constant strain rate of 3.70×10^{-3} per second.

(ii) High velocity impact (dynamic) tests, which were carried out on the three aluminium alloy materials in a cylindrical projectile form at high strain rates varying between 2.5×10^{4} to 1.25×10^{5} per second (maximum).

(iii) Construction of the stress-strain curves at high strain rates.

(v) Profiles of the deformed projectiles.

All the experimental work done in this phase was under lubricated conditions at room temperature, catering for radial inertia effect in the finite-difference numerical technique.

4.2 Quasi-Static Tests

The results of the quasi-static compression tests of the three aluminium alloys and En-8 steel are presented in figures 4.1 to

4.4. The figures show the true stress-natural strain curves of the four materials involved in the present work.

The construction of these curves was involved with plane compression tests of solid circular cylinders at a slow constant velocity of 0.5mm per minute. During each test on the circular cylinders the diameter increased from the initial value Do to the current value D. Similarly the height was reduced from an initial value Ho to the current value H. The fractional reduction R is given by

$$R = \frac{Ho - H}{Ho} = 1 - \left(\frac{H}{Ho}\right)$$

$$\frac{H}{Ho} = (1 - R)$$

The compressive natural strain is $\varepsilon = \ln\frac{Ho}{H} = \ln\left[\frac{1}{1 - R}\right]$. Since the stress $\sigma = \frac{F}{A}$ and the current area A is not known, it is possible to determine this area from the volume (v) which is constant. The compressive true stress at a current height and load can be calculated from the equation $= \frac{FH}{v}$. This enabled the determination of true stresses and their corresponding natural strains so that the curves shown in figures [4.1-4.4] could be constructed.

The trends of the quasi-static true stress-natural strain curves were parabolic in form and the effect of the lubricant usage can be observed from the difference between the dry and lubricated flow stresses. The En-8 steel showed the highest strength of the materials involved. However, DTD5044 showed a higher strength than the other two aluminium alloys HE15 and HE30TF.

4.3 High Velocity Impact (Dynamic) Tests

The high velocity impact tests were conducted to obtain the stress-strain characteristics of the three aluminium alloys at high strain rates. The impact velocities varied between 50 and 250 m/s achieving strain rates of 2.5×10^3 to 1.25×10^4 per second for each alloy. Plate No 3 shows deformed specimens of each aluminium alloy at different impact velocities.

For each test the final diameter (D_f) and final height (H_f) of the deformed mushroom shaped specimen was measured. After impact each deformed specimen was numbered, placed in a small envelope and labelled with its corresponding test number and impact velocity. The final diameter and height of the deformed specimens were measured by a Digimatic Micrometer. This equipment is a high precision electronic measuring micrometer which can store many readings in its memory. The micrometer has a facility which can provide the maximum, minimum and average of the readings stored in its memory.

Fifteen random readings around the circumference of the deformed projectile were taken at the maximum diameter, which has been in contact with the rigid anvil. The average of these readings was noted. A similar approach was adopted for the final height measurement and so the curves of D_f and H_f against impact velocity were constructed. Figures 4.5 to 4.10 show several selected test results plotted on the same graph in order to determine the scatter of the results and the trend of the curves. The average curves for the three aluminium alloys were represented by the continuous lines shown in these figures.

4.4 Determination of the Material Constants

With reference to the quasi-static stress-strain properties of the three aluminium alloys, a strain rate sensitivity equation of the form

$$\sigma D = \sigma s[1 + (\frac{/\dot{\varepsilon}/}{D})^{1/p}]$$

which has previously been suggested in references (47-48) was adopted. This equation does not cater for any change in the overall shape of the stress-strain curves for various strain rates and also assumes that the effect of strain rate is independent of strain. When the above equation is incorporated into the numerical technique for analysing the deformation of projectiles, it enables the final diameters, final heights and other parameters such as strain rates and strains to be determined at different intervals during deformation for a given impact velocity and material constants P and D. Arbitrary values of P and D parameters have been assigned and the final radius at the projectile-anvil interface together with the final height have been predicted theoretically for various impact velocities.

These predicted results (broken lines) were then plotted together with the experimental ones (solid lines) against impact velocity as shown in figures 4.11 to 4.16. The combination of P and D values was then modified in order to get the theoretically predicted curves to converge towards the experimental ones. When the theoretically predicted curves were as close a fit as possible to the experimental ones, the P and D values were taken to be the material constants. A considerable computational exercise was undertaken to achieve the degree of match shown in the figures.

The chosen best fit values of P and D for the three aluminium alloys were as follows:

Material	P	D
HE15	35	100
HE30TF	25	100
DTD5044	15	100

Finally it is worth mentioning that these values have been chosen on the basis of closest match between the theoretically predicted and the experimental curves for both final diameter and final height against impact velocity.

4.5 Construction and Characteristics of the Stress-Strain Curves at High Strain Rates

When the material constants P and D were established for each of the three aluminium alloys, the stress-strain curves for each of the aluminium alloys under consideration were determined for strain rates ranging from 2.5×10^3 to 1.25×10^4 per second Figures 4.17 to 4.19. The figures also contain the quasi-static curves for comparison. The high strain rate curves were obtained simply by using the proposed strain rate sensitivity equation 3.1 in conjunction with the static stress-strain curve and the values of P and D established earlier on in this chapter. The main aspect of this strain rate sensitivity equation is that it does not allow any change in the overall shape of the quasi-static stress-strain curve but does allow its position to shift depending on the strain rate. The stress radio $\sigma D/\sigma s$ (dynamic stress/static stress) against strain rate curves were established by simply rearranging the strain rate sensitivity equation. Thus stress ratio $\frac{\sigma D}{\sigma s} = [1 + (\frac{/\dot{\varepsilon}/}{D})^{1/p}]$.

Figures [4.20-4.22] show the variation of the stress ratio with strain rate for each material. It was found that these variations were as follows for a strain rate range between 2.5×10^3 to 1.25×10^4 per second.

Material	Stress Ratio Range
HE15	2.096 to 2.148
HE30TF	2.137 to 2.247
DTD5044	2.239 to 2.245

From the theoretical output data, true stress-strain rate variations were established. Figures 4.23 to 4.25 present these curves at strain rates varying from 2.5×10^3 to 1.25×10^4 per second and strains of 0.047-0.431.

4.6 Profiles of the Deformed Projectiles

After deformation, the final profile of the mushroom shaped projectiles were plotted. Typical deformed shapes are shown in Figures 4.26 to 4.34 at different selected impact velocities for the three aluminium alloys.

The main purpose of plotting the profiles after impact is to show the difference between the experimentally measured and the theoretically estimated profiles corresponding to the P and D values established in Section 4.4 for each material. The measurement of the profiles has been conducted using a Higler Universal Projector (shadowgraph) machine. This equipment enabled the shadow of the projectile to be enlarged 15 times so that the measurement of diameter at equal spacings and their corresponding heights could be obtained accurately. In this case measurements were taken at locations 1mm apart and the

profiles were plotted at different velocities. The dotted and continuous lines represent the theoretically estimated and the experimentally measured profiles respectively. The impact velocities were chosen to show the strength of the three aluminium alloys, indicated by the degree of deformation at various strain rates.

Finally, values of temperature rise, radial inertia and co-efficients of friction during deformation in this phase for the three aluminium alloys were obtained and displayed in Table 4.1. Typical calculations are presented in Appendices I, IV and VII.

4.7 Summary

Results of the experimental work done in phase one of the present study were presented in this chapter. The results highlight the following:

1 The quasi-static stress-strain characteristics of the three aluminium alloys, HE15, HE30TF, DTD5044 and En-8 steel, showing the effect of lubricant in reducing the stress during deformation.

2 High velocity impact (Dynamic) test results showing the true stress-natural strain characteristics of the three aluminium alloys under investigation at strain rates varying between 2.5×10^3 to 1.25×10^4 per second.

3 Material constants P and D in the strain rate sensitivity equation $\sigma D = \sigma s[1 + (\frac{/\dot{\varepsilon}/}{D})^{1/p}]$ were obtained for each of the aluminium alloys by matching the experimental results and the theoretically estimated ones obtained by the finite-difference numerical technique.

4 The variation of stress ratio with strain rate was demonstrated.

5 The deformation in this phase was found to be inhomogeneous and localised at the interface of the projectile-anvil section of the projectile.

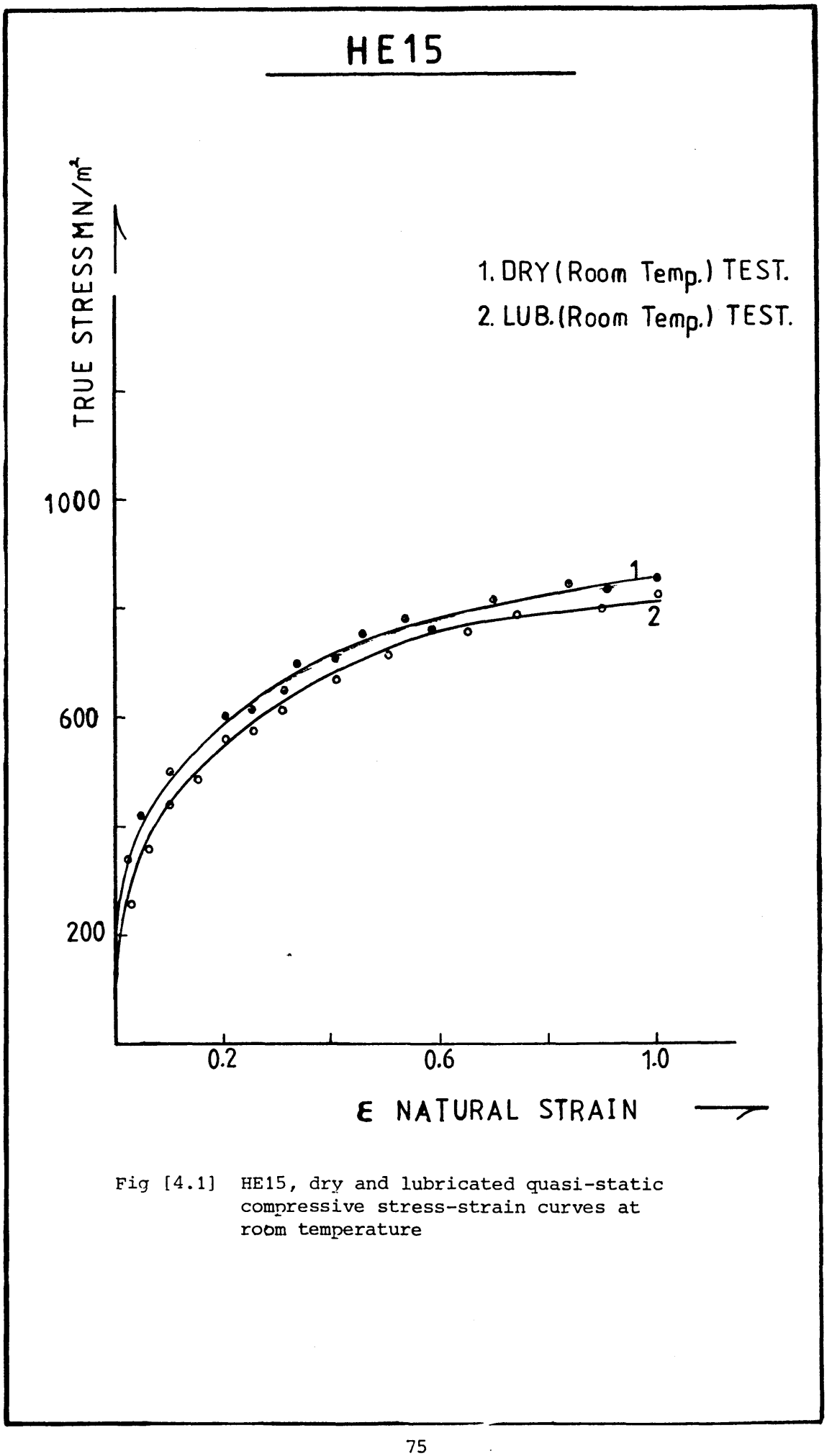

Fig [4.1] HE15, dry and lubricated quasi-static compressive stress-strain curves at room temperature

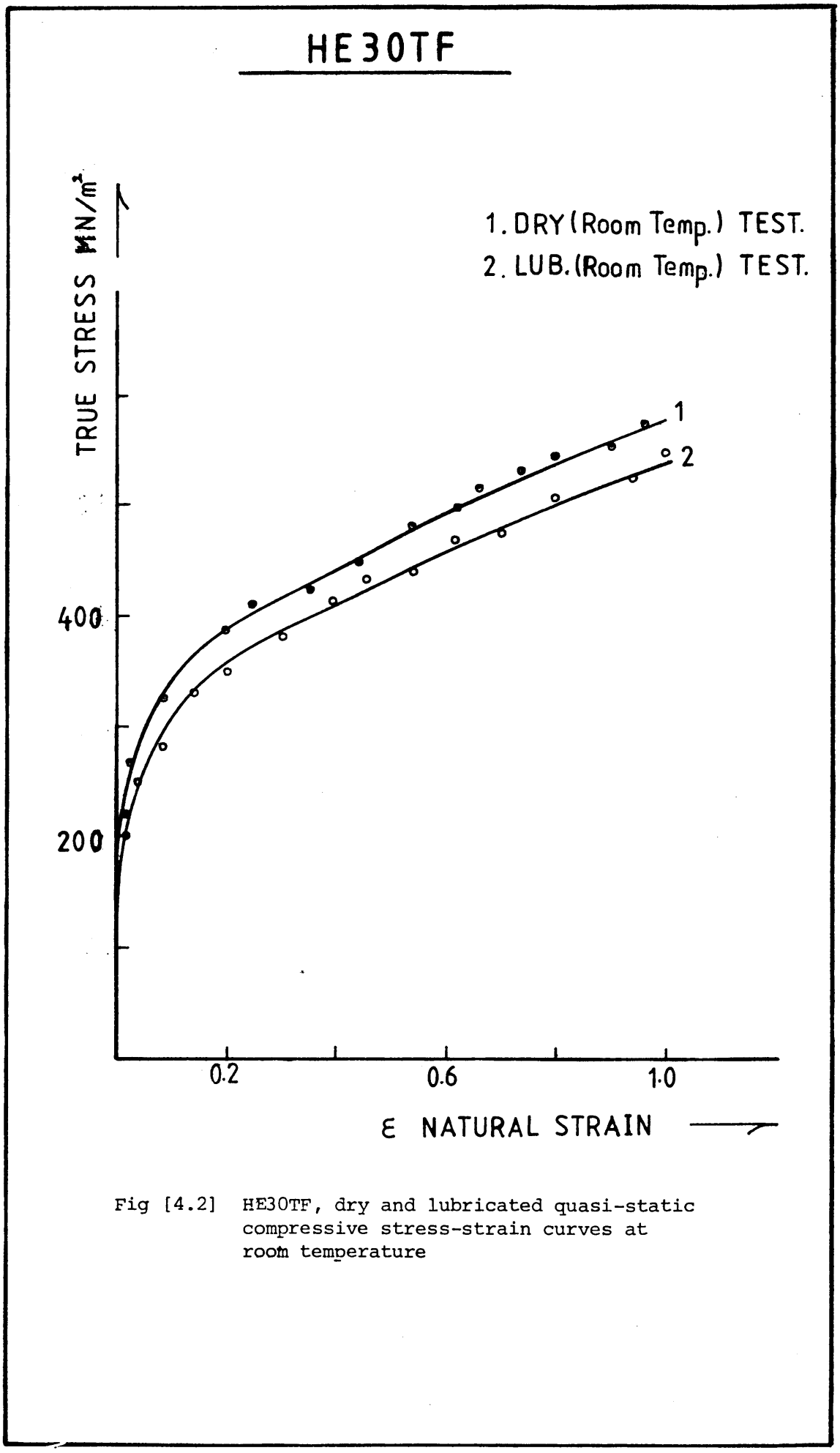

Fig [4.2] HE30TF, dry and lubricated quasi-static compressive stress-strain curves at room temperature

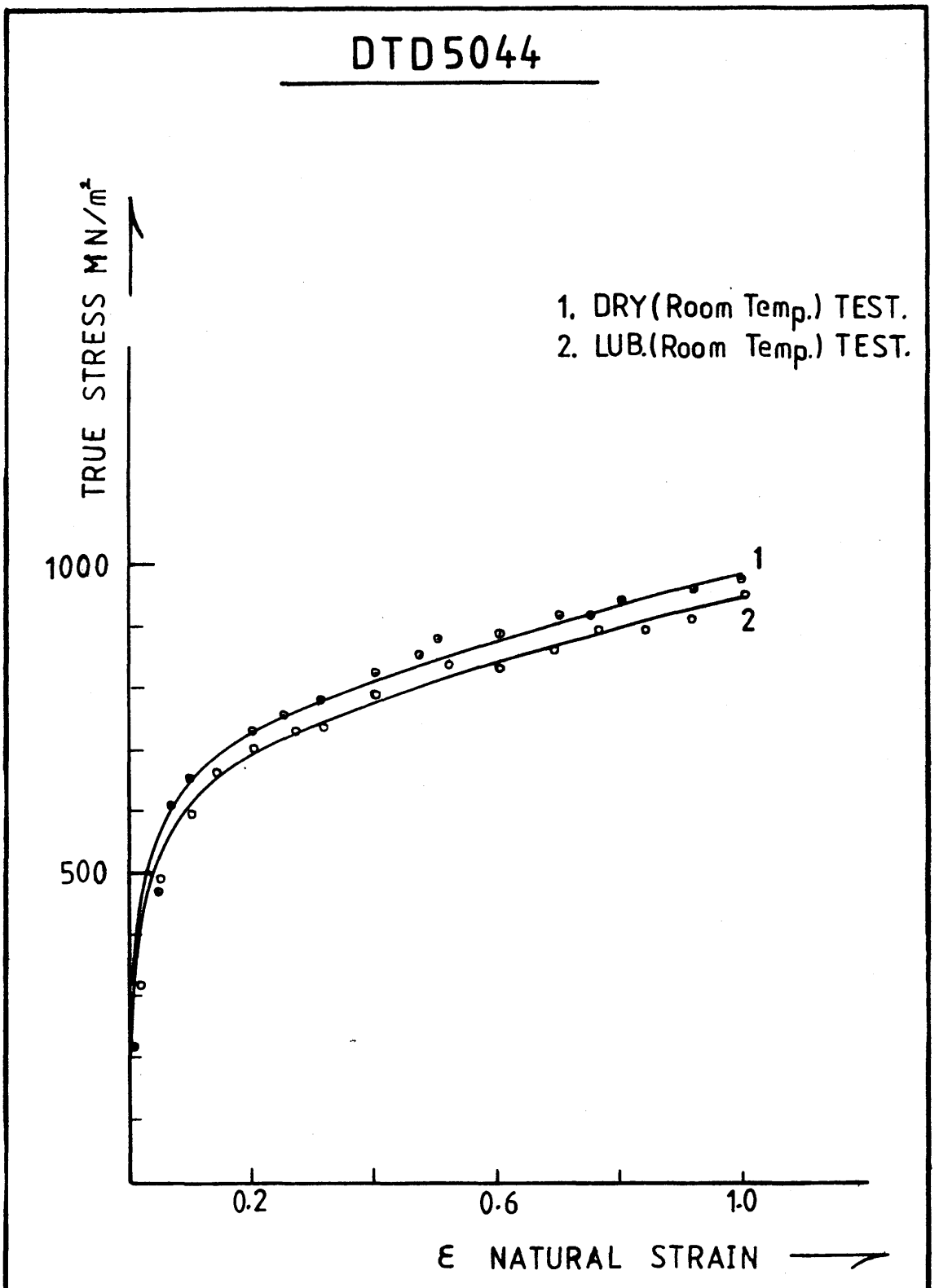

Fig [4.3] DTD5044, dry and lubricated quasi-static compressive stress-strain curves at room temperature

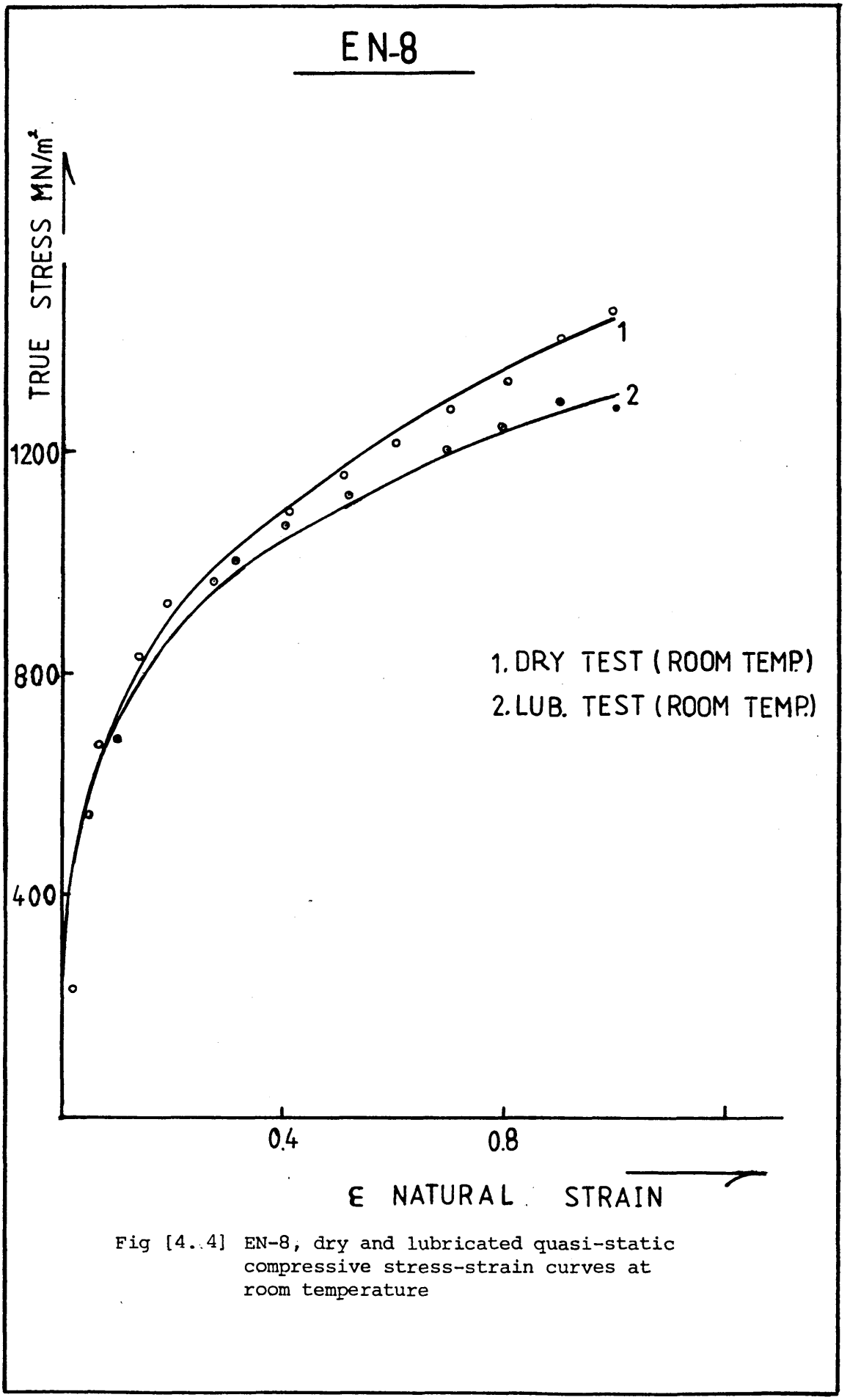

Fig [4.4] EN-8, dry and lubricated quasi-static compressive stress-strain curves at room temperature

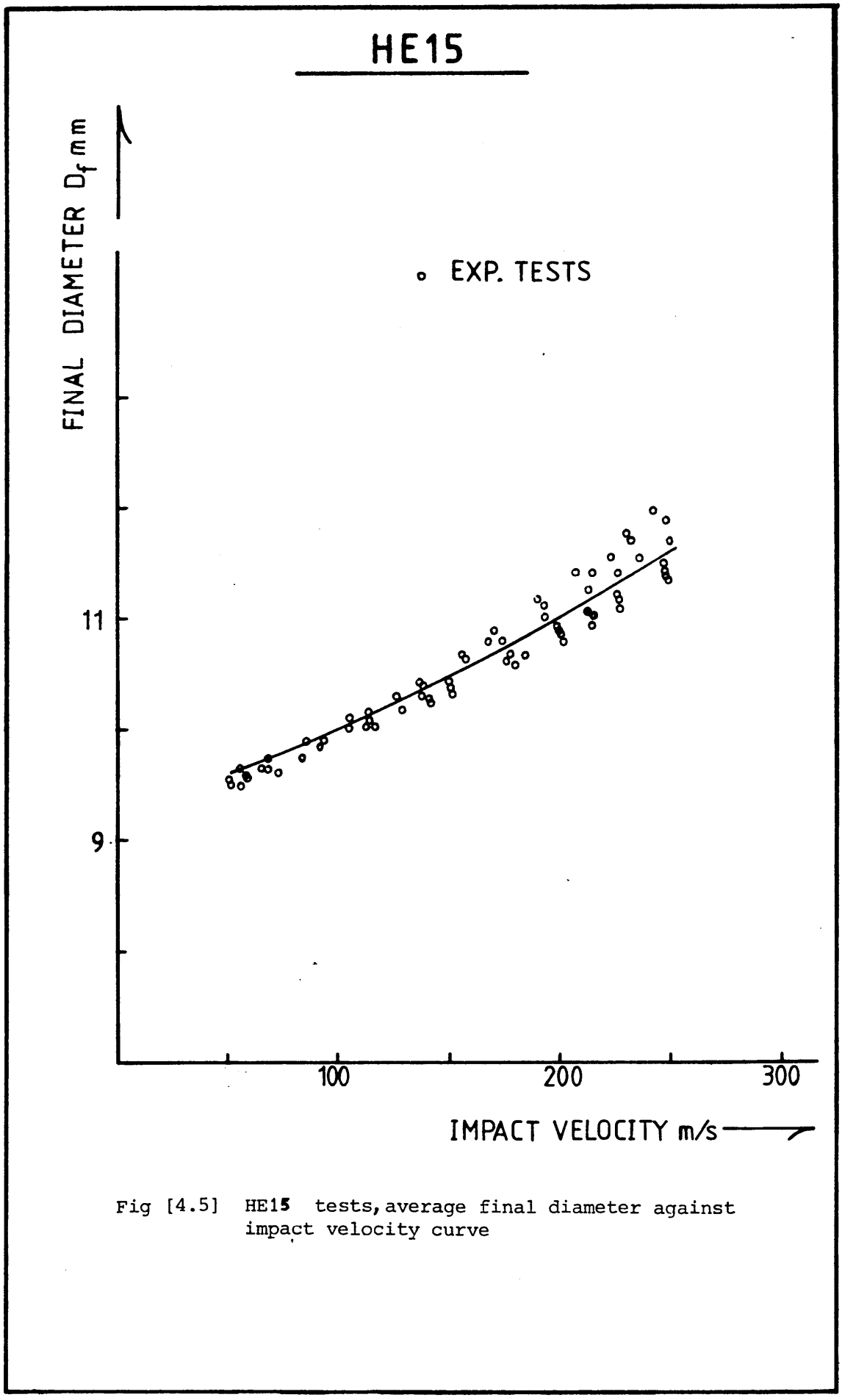

Fig [4.5] HE15 tests, average final diameter against impact velocity curve

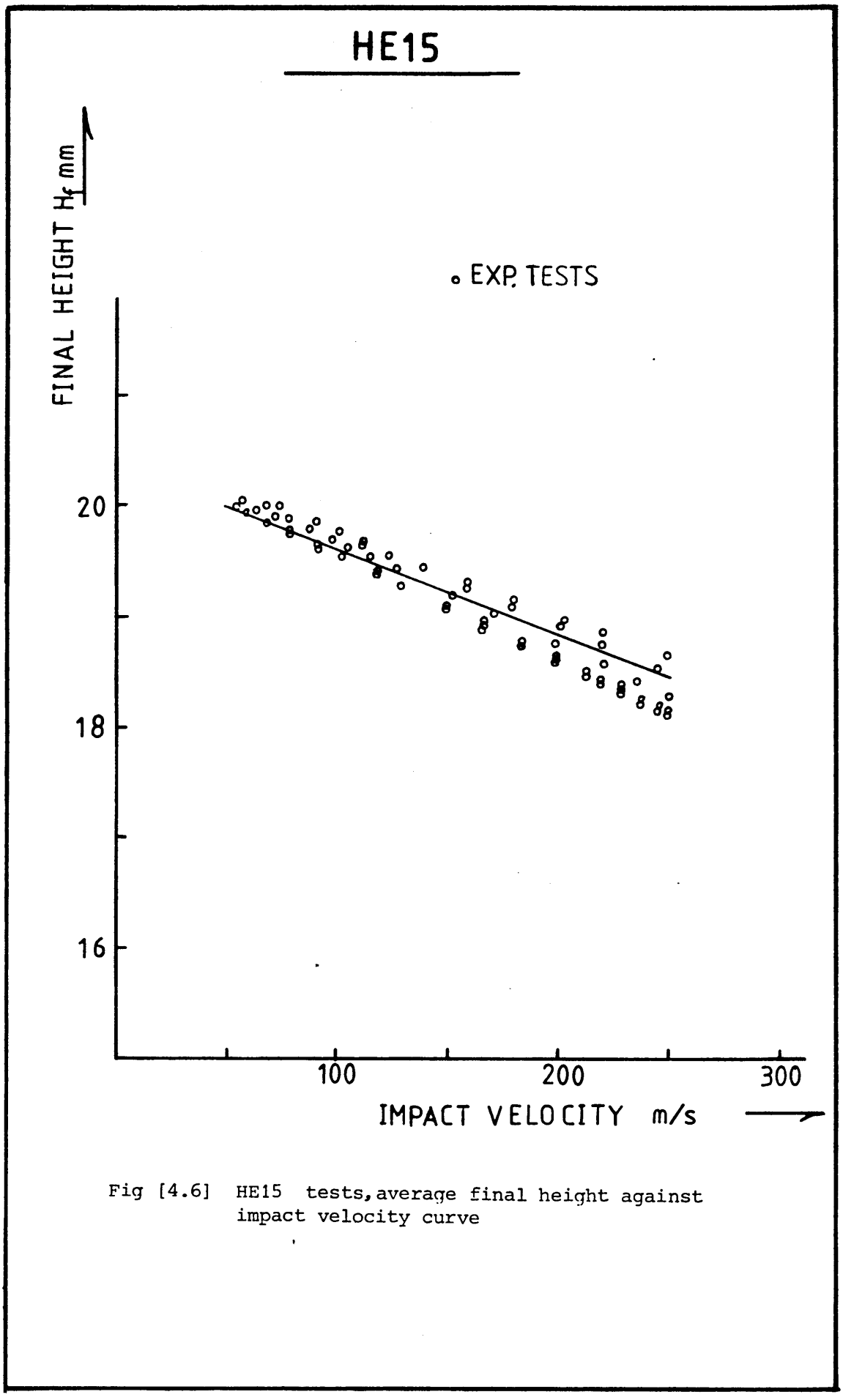

Fig [4.6] HE15 tests, average final height against impact velocity curve

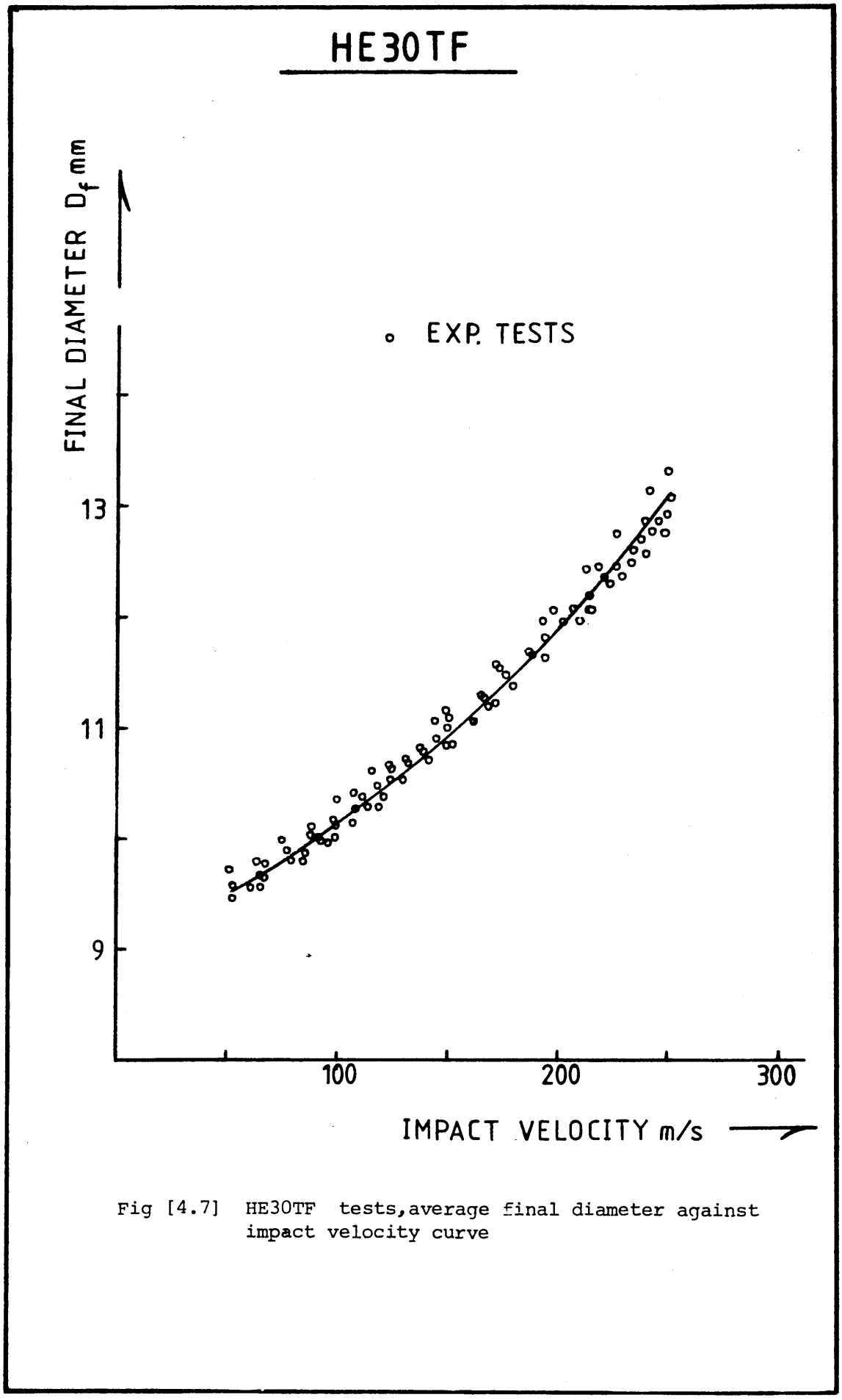

Fig [4.7] HE30TF tests, average final diameter against impact velocity curve

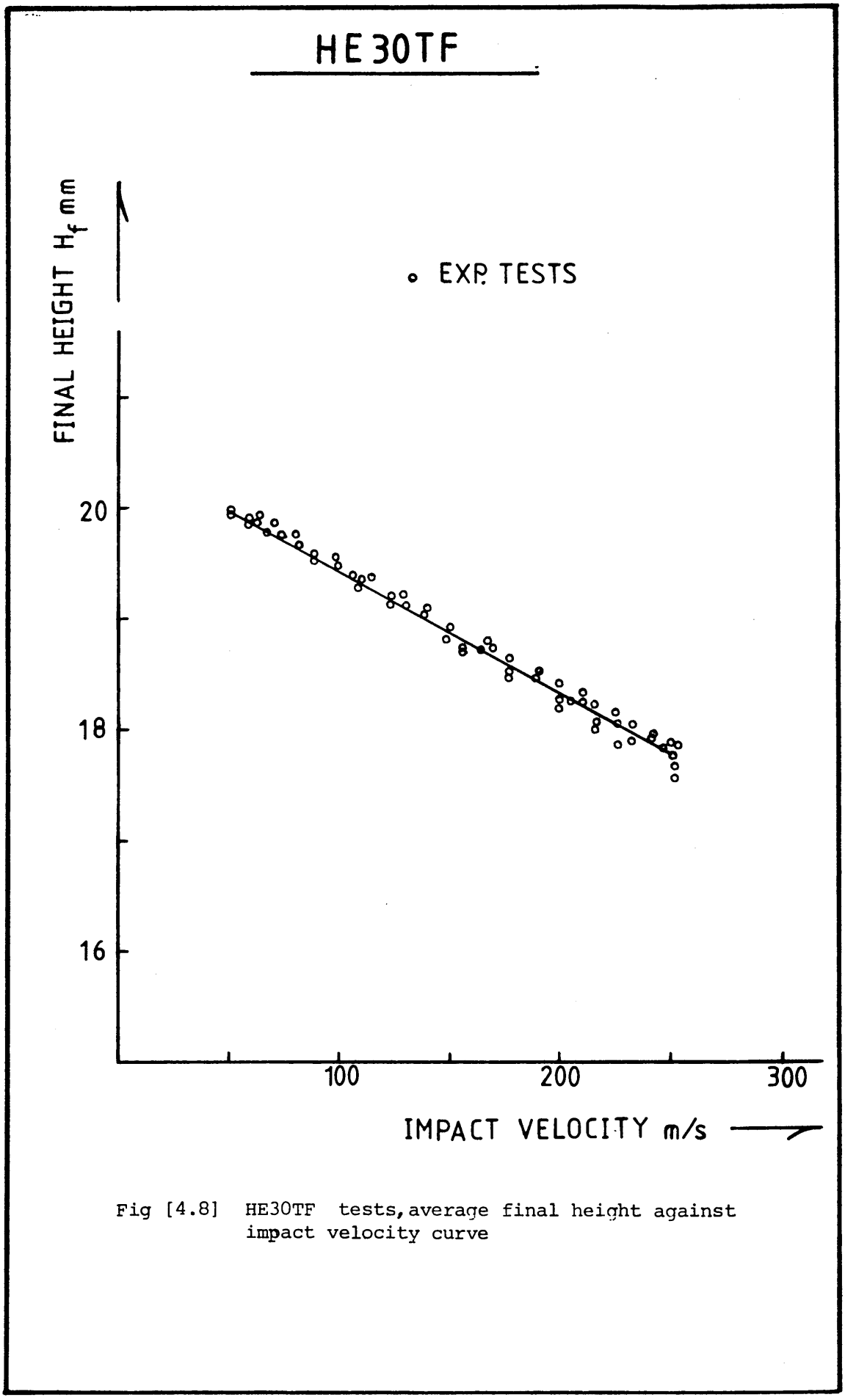

Fig [4.8] HE30TF tests, average final height against impact velocity curve

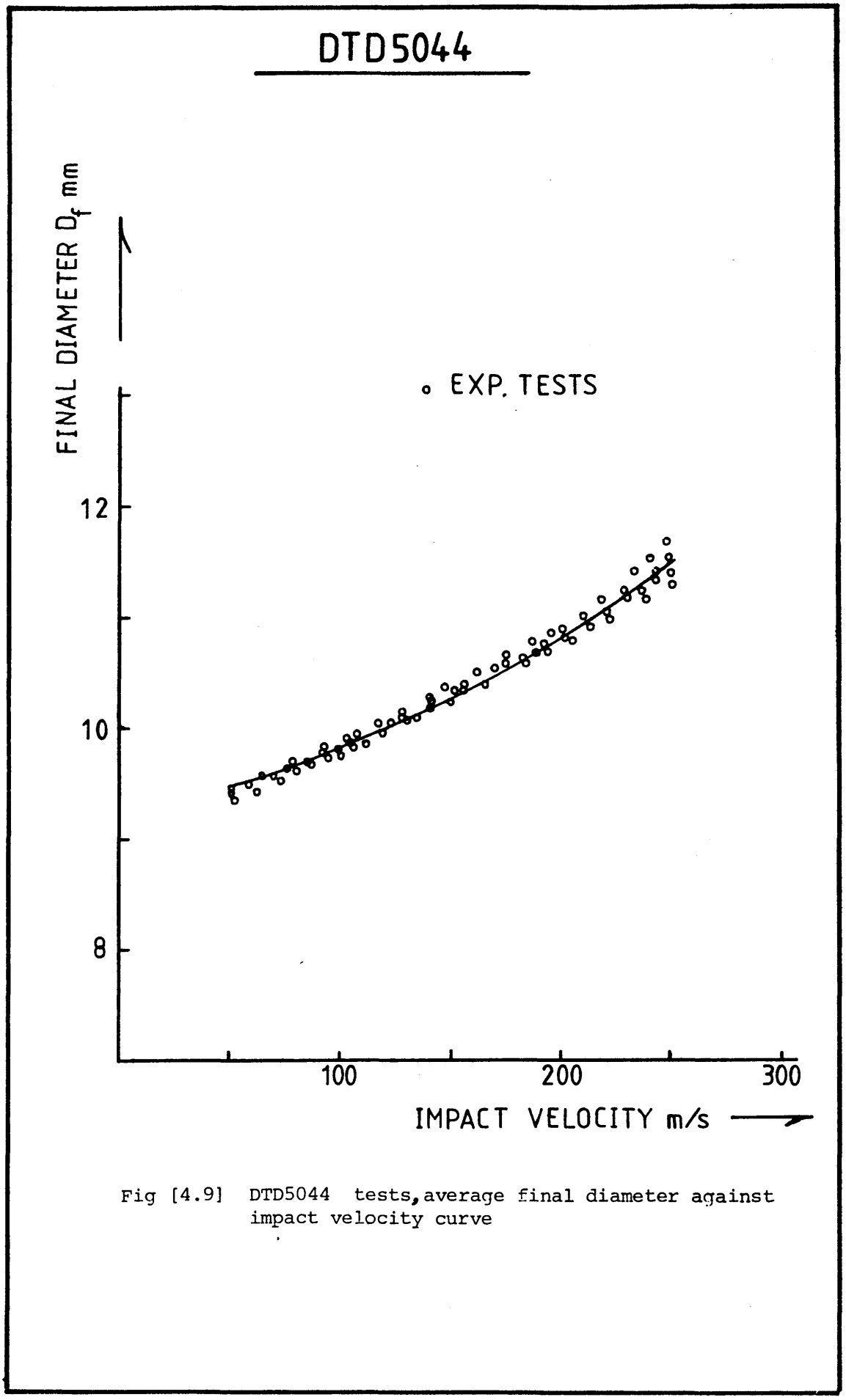

Fig [4.9] DTD5044 tests, average final diameter against impact velocity curve

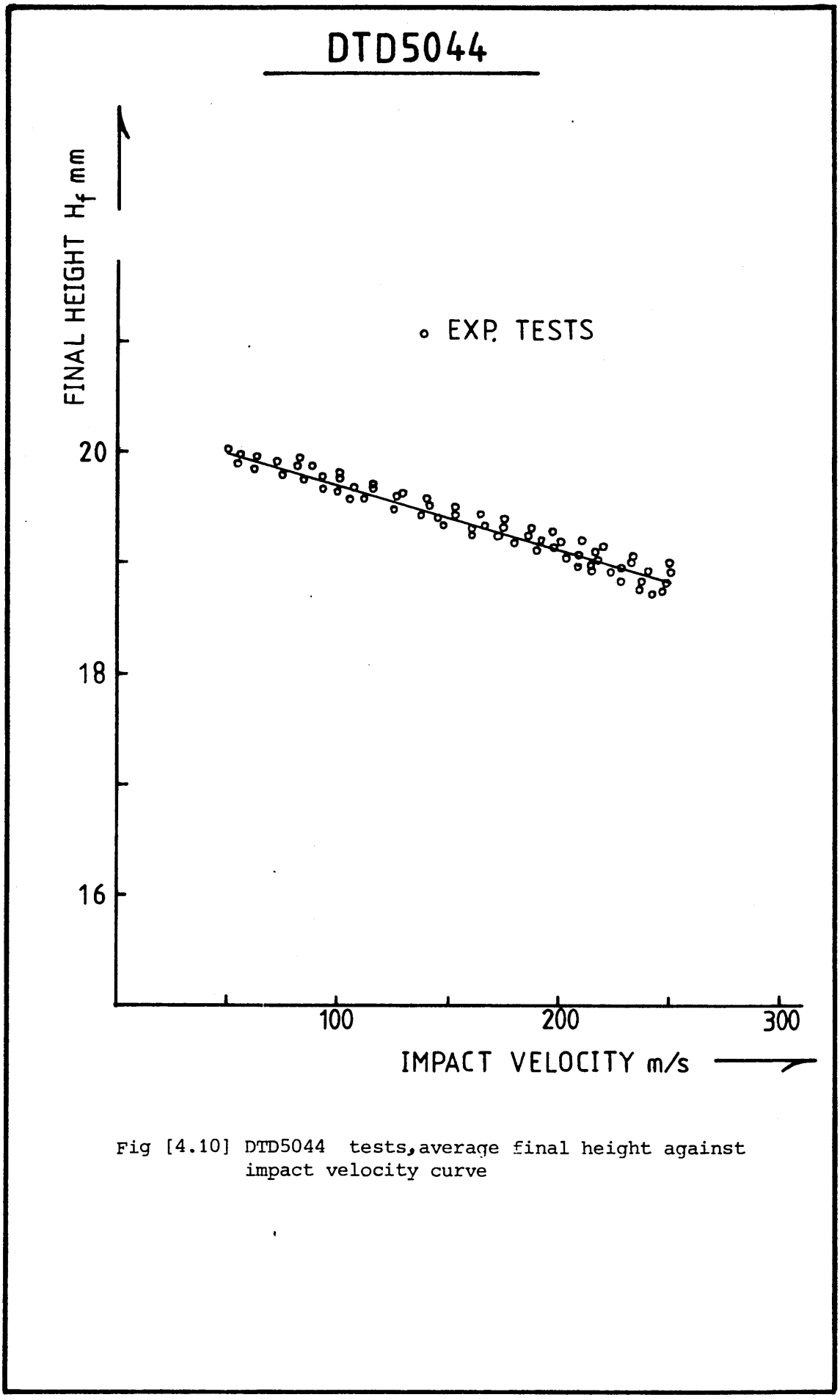

Fig [4.10] DTD5044 tests, average final height against impact velocity curve

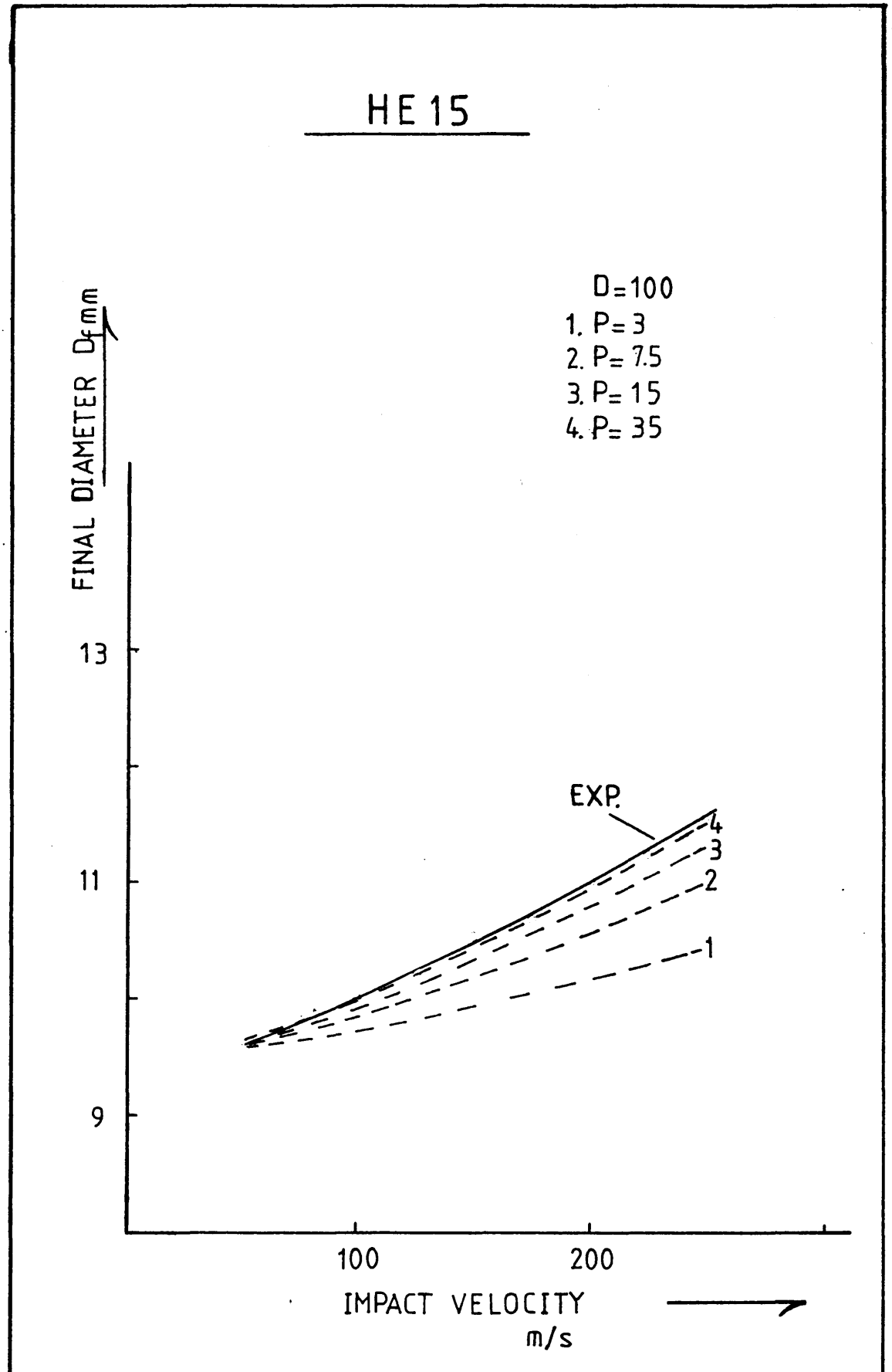

Fig [4.11] HE15, variation of final diameter with impact velocity for various P and D combinations

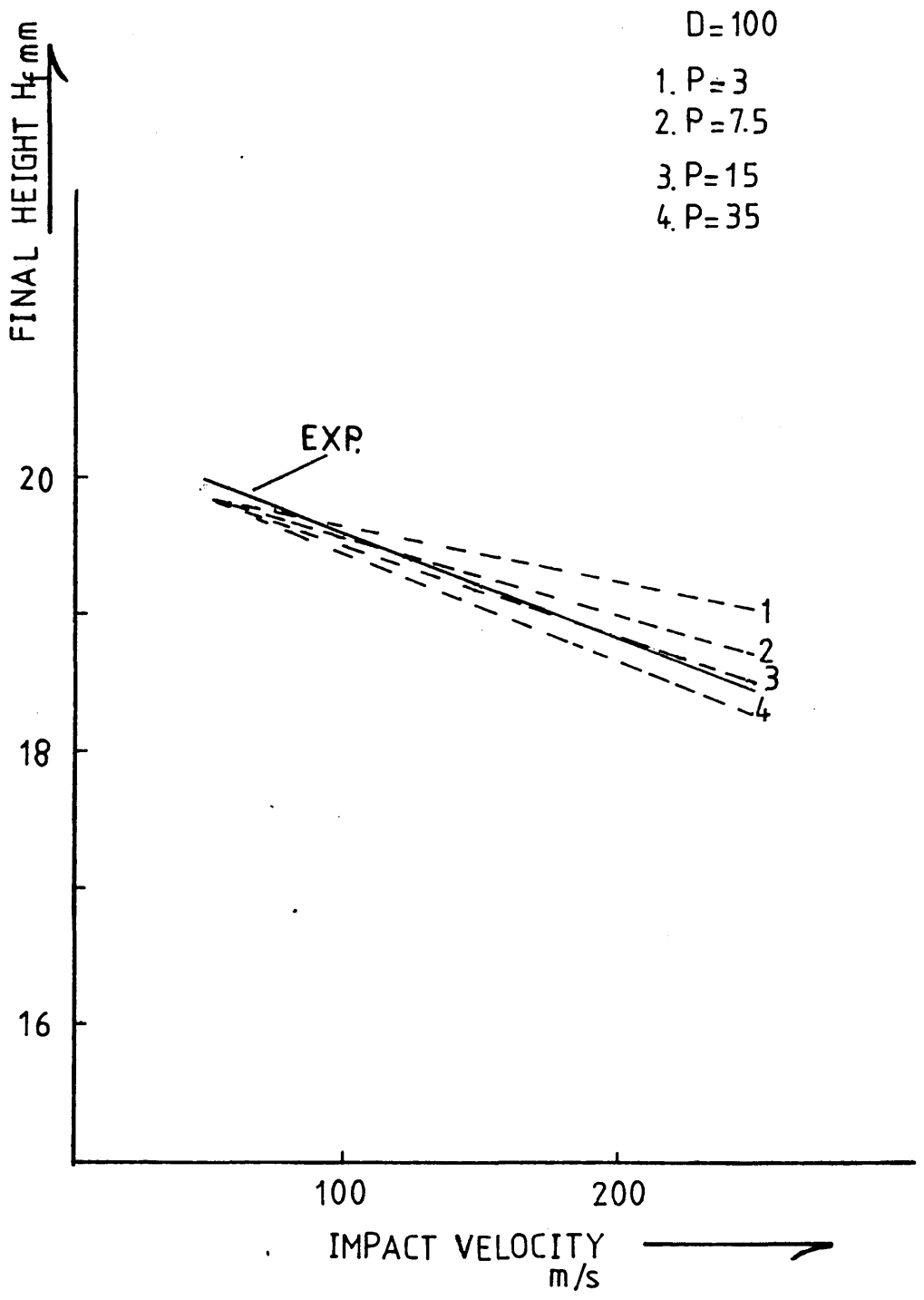

Fig [4.12] HE15, variation of final height with impact velocity for various P and D combinations

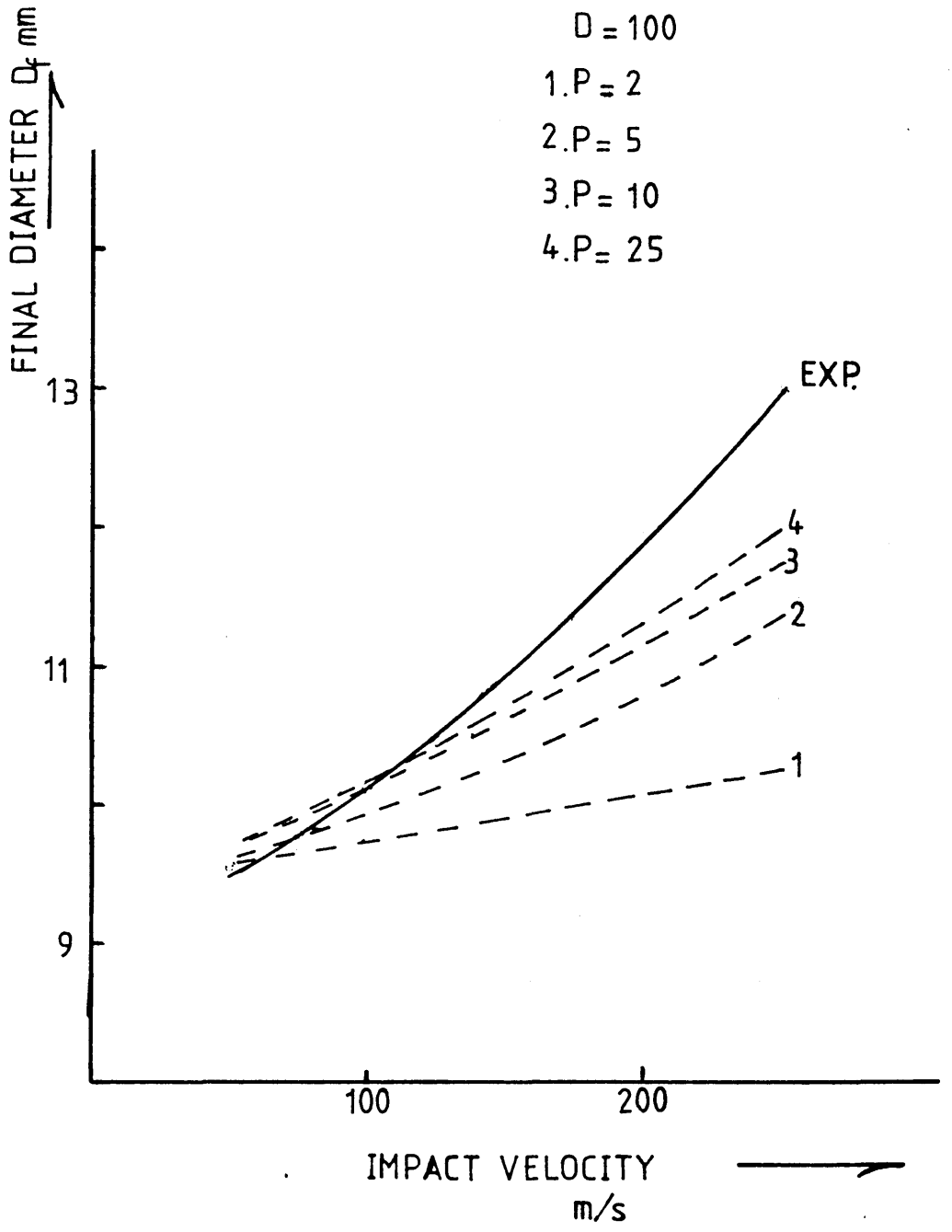

Fig [4.13] HE30TF, variation of final diameter with impact velocity for various P and D combinations

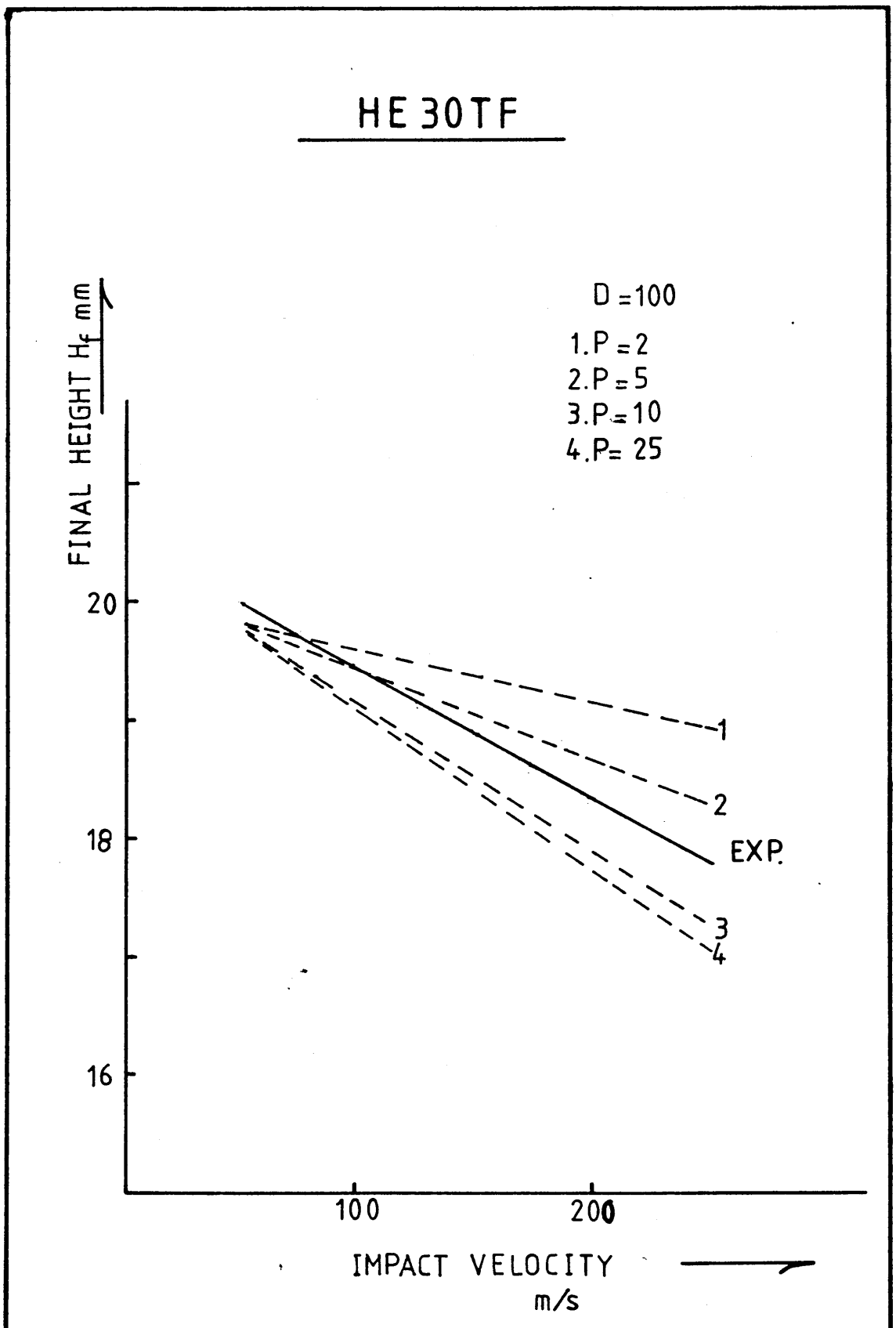

Fig [4.14] HE30TF, variation of final height with impact velocity for various P and D combinations

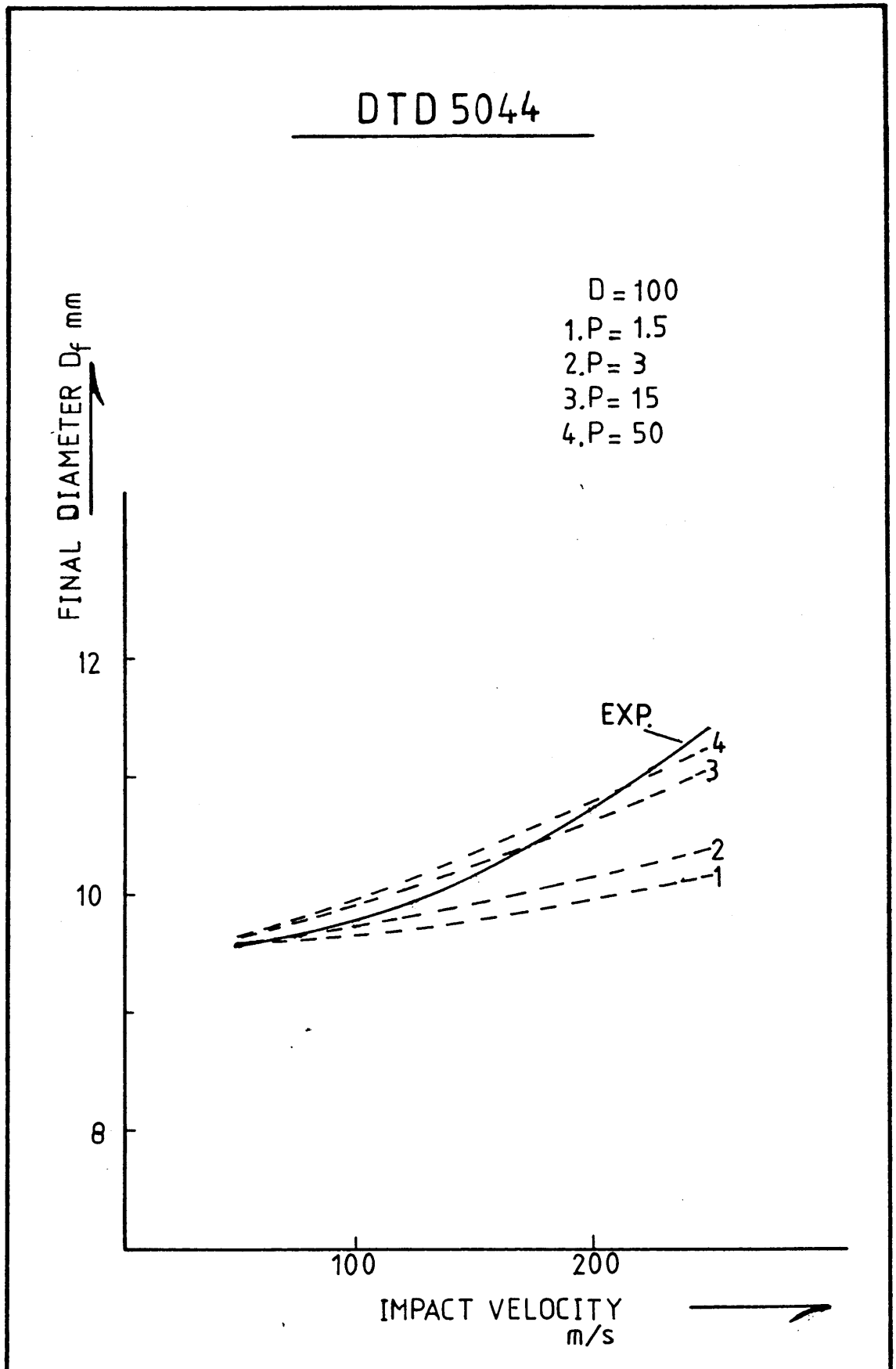

Fig [4.15] DTD5044, variation of final diameter with impact velocity for various P and D combinations

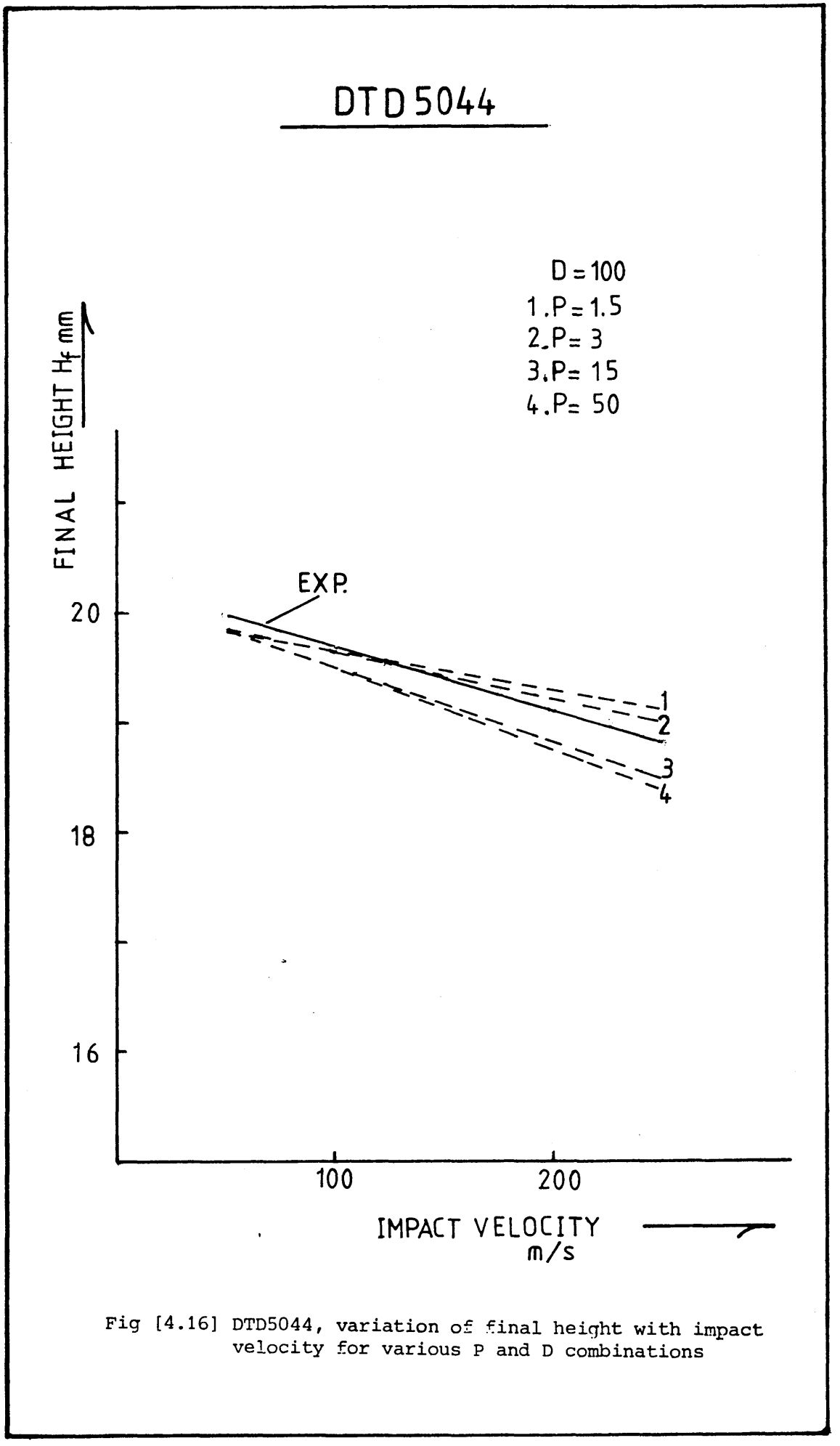

Fig [4.16] DTD5044, variation of final height with impact velocity for various P and D combinations

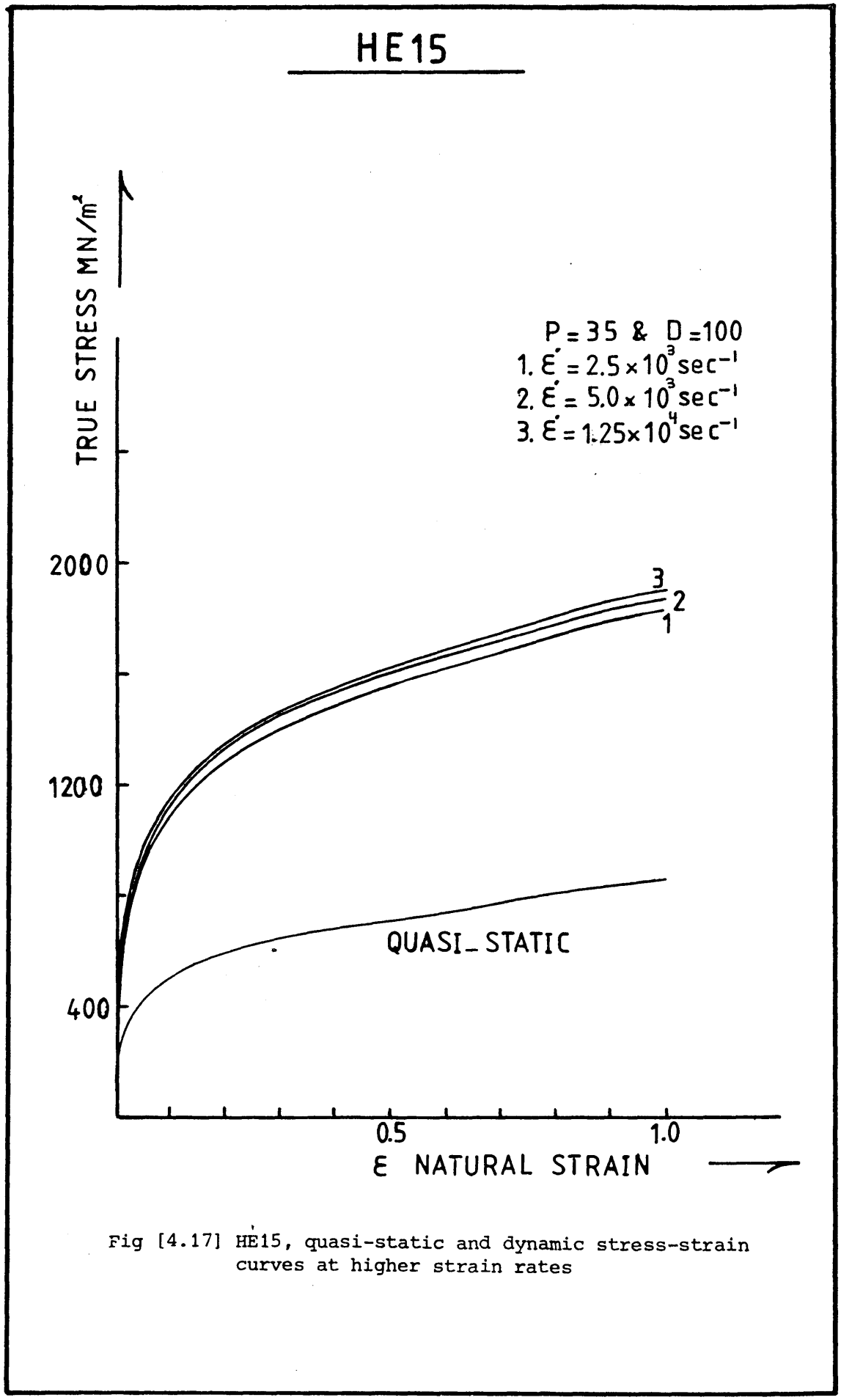

Fig [4.17] HE15, quasi-static and dynamic stress-strain curves at higher strain rates

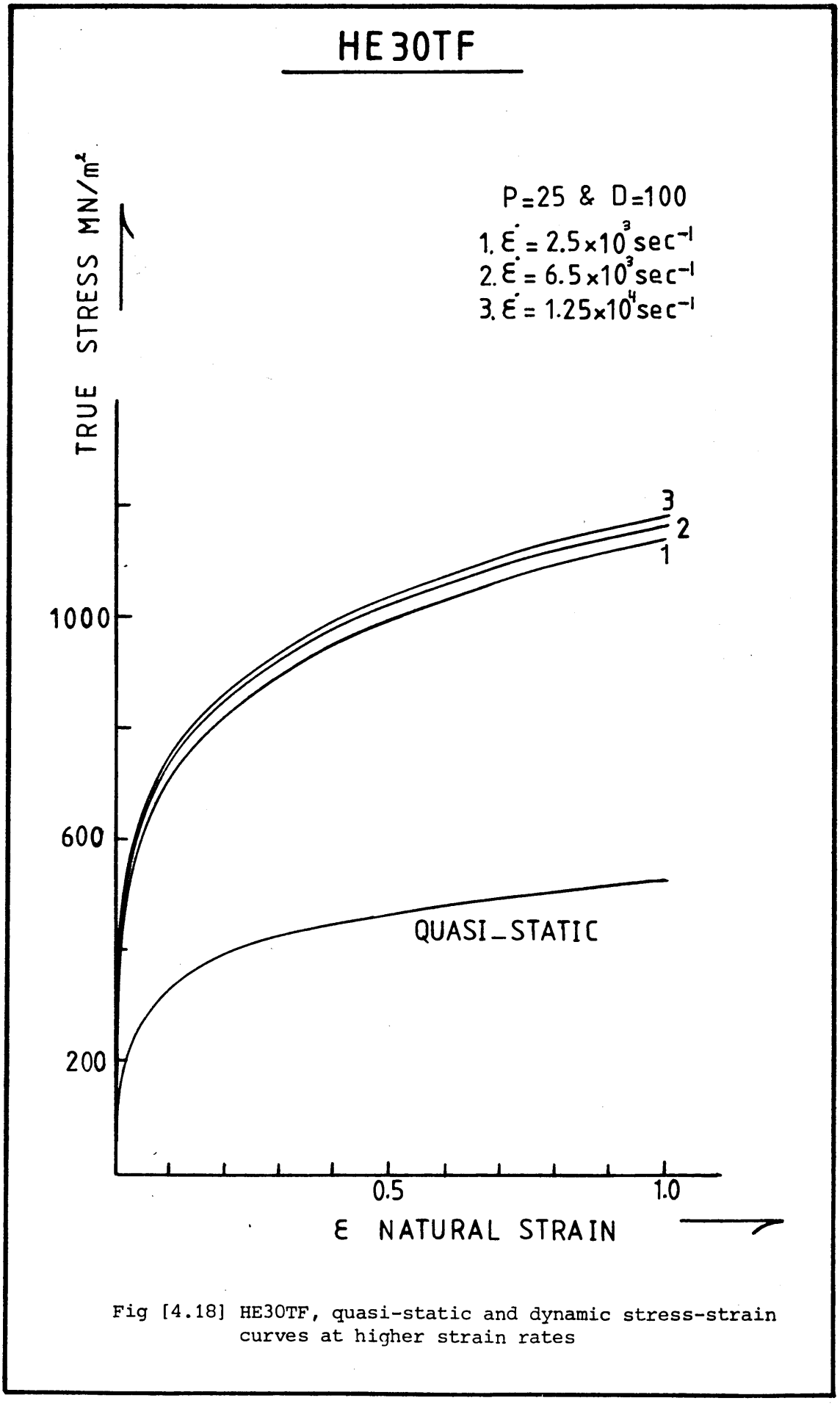

Fig [4.18] HE30TF, quasi-static and dynamic stress-strain curves at higher strain rates

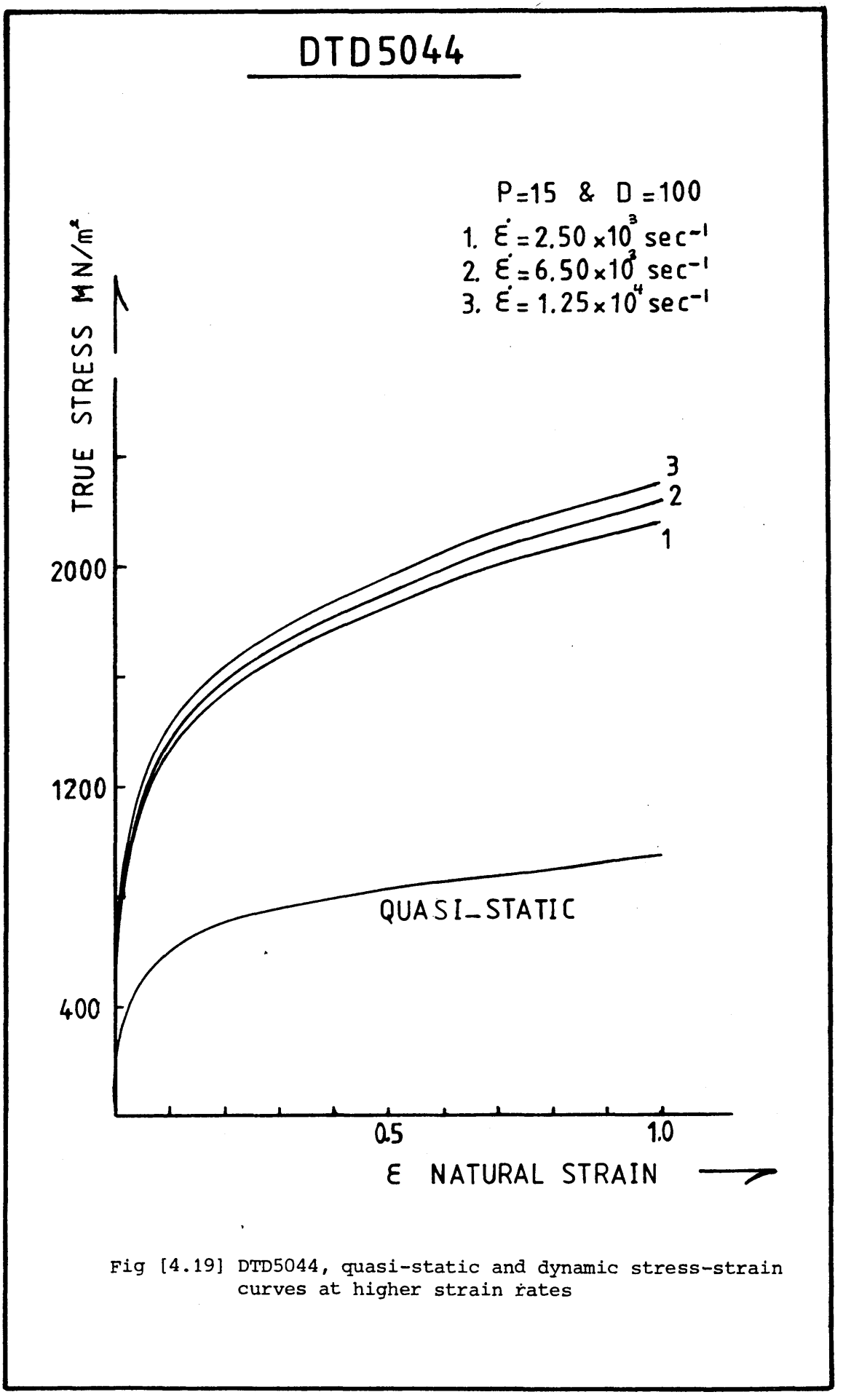

Fig [4.19] DTD5044, quasi-static and dynamic stress-strain curves at higher strain rates

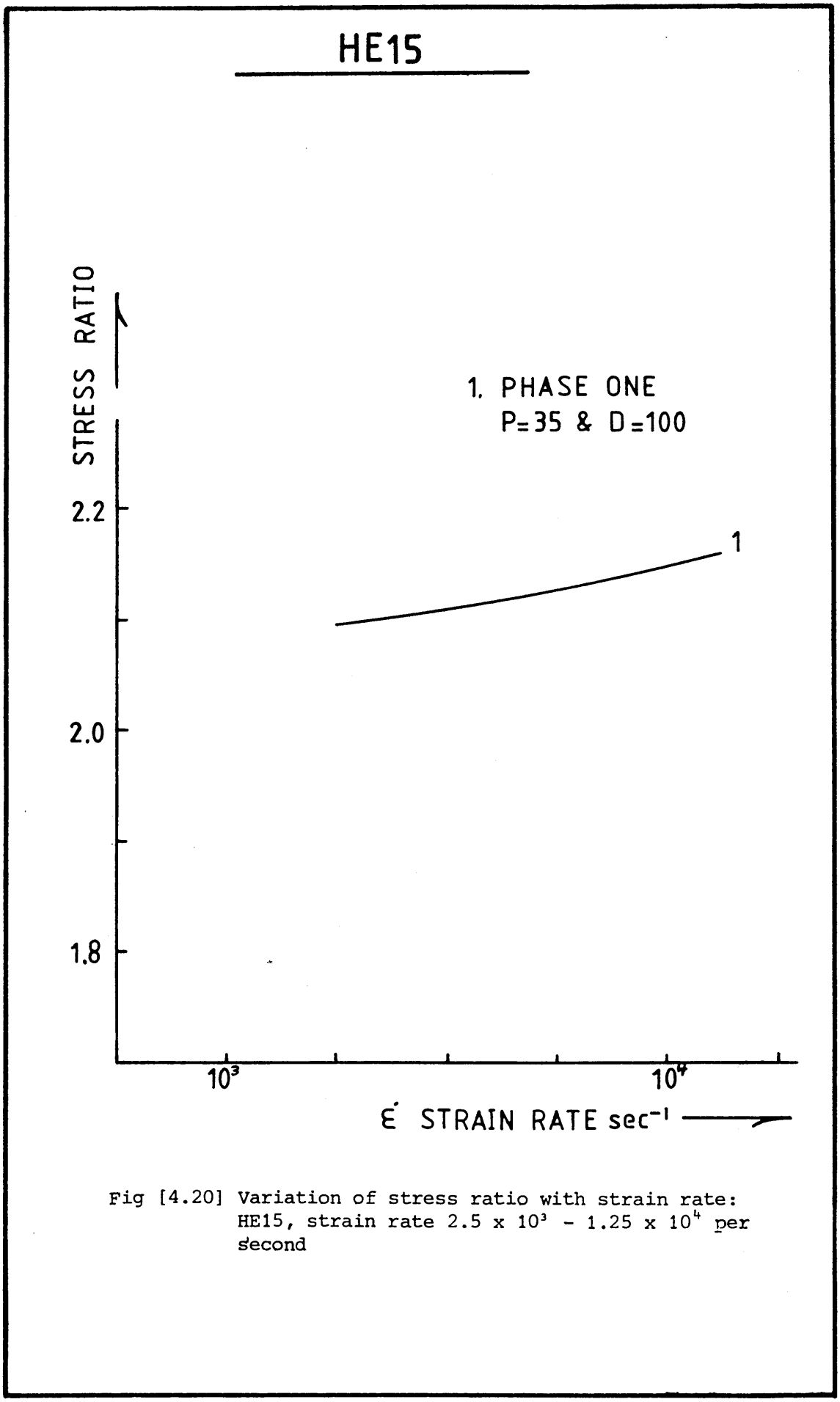

Fig [4.20] Variation of stress ratio with strain rate: HE15, strain rate 2.5×10^3 - 1.25×10^4 per second

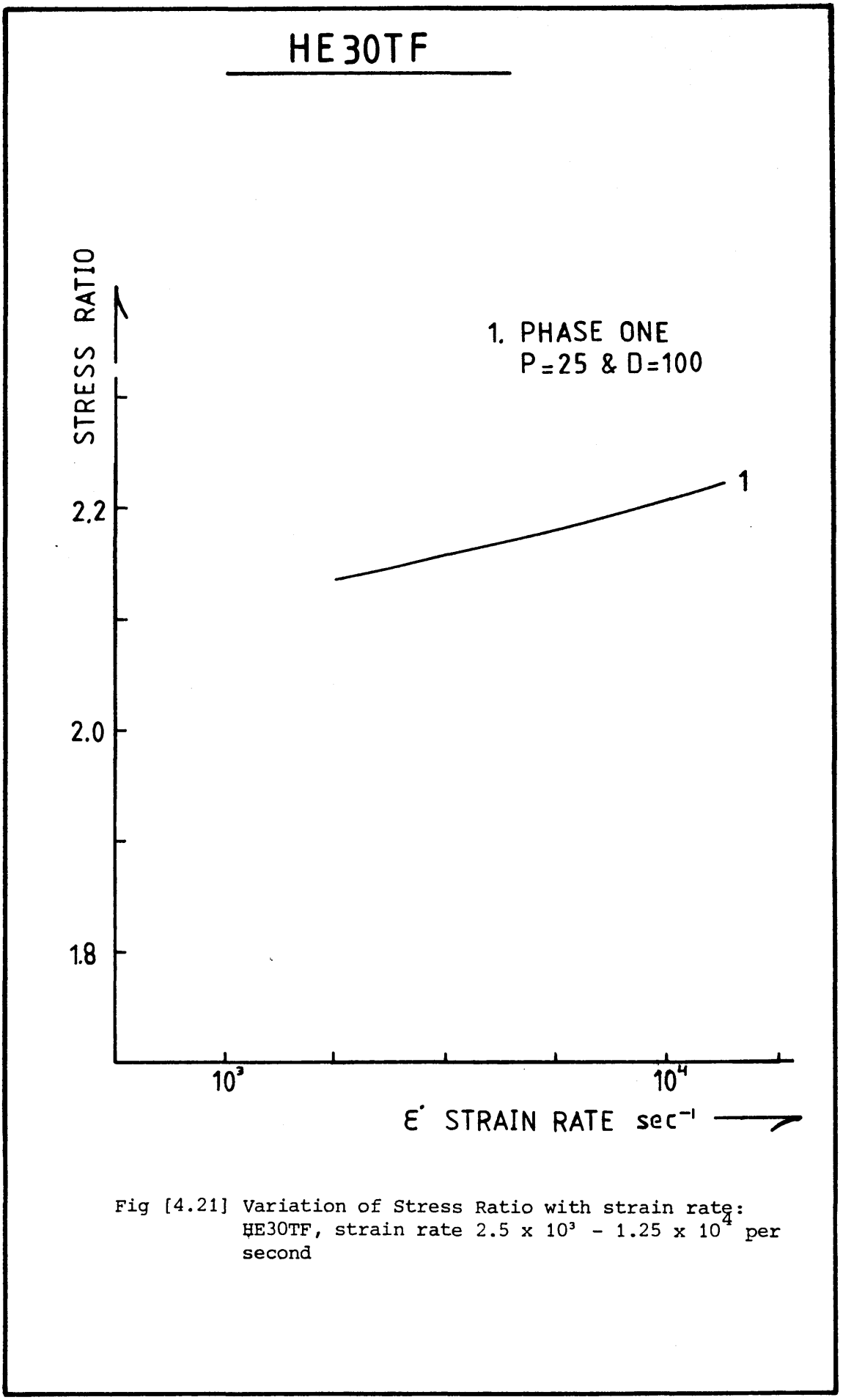

Fig [4.21] Variation of Stress Ratio with strain rate: HE30TF, strain rate 2.5×10^3 - 1.25×10^4 per second

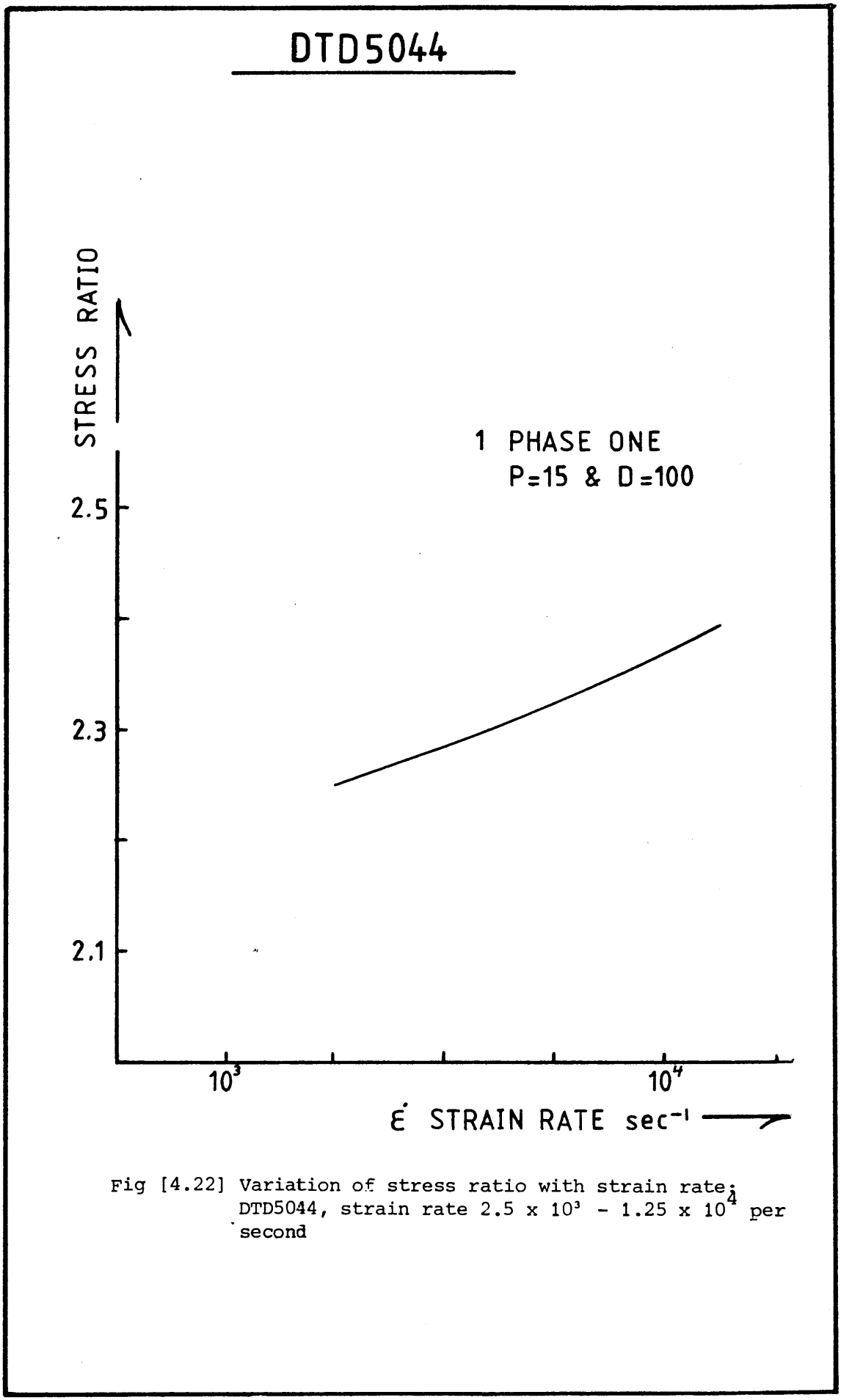

Fig [4.22] Variation of stress ratio with strain rate; DTD5044, strain rate 2.5 x 10^3 - 1.25 x 10^4 per second

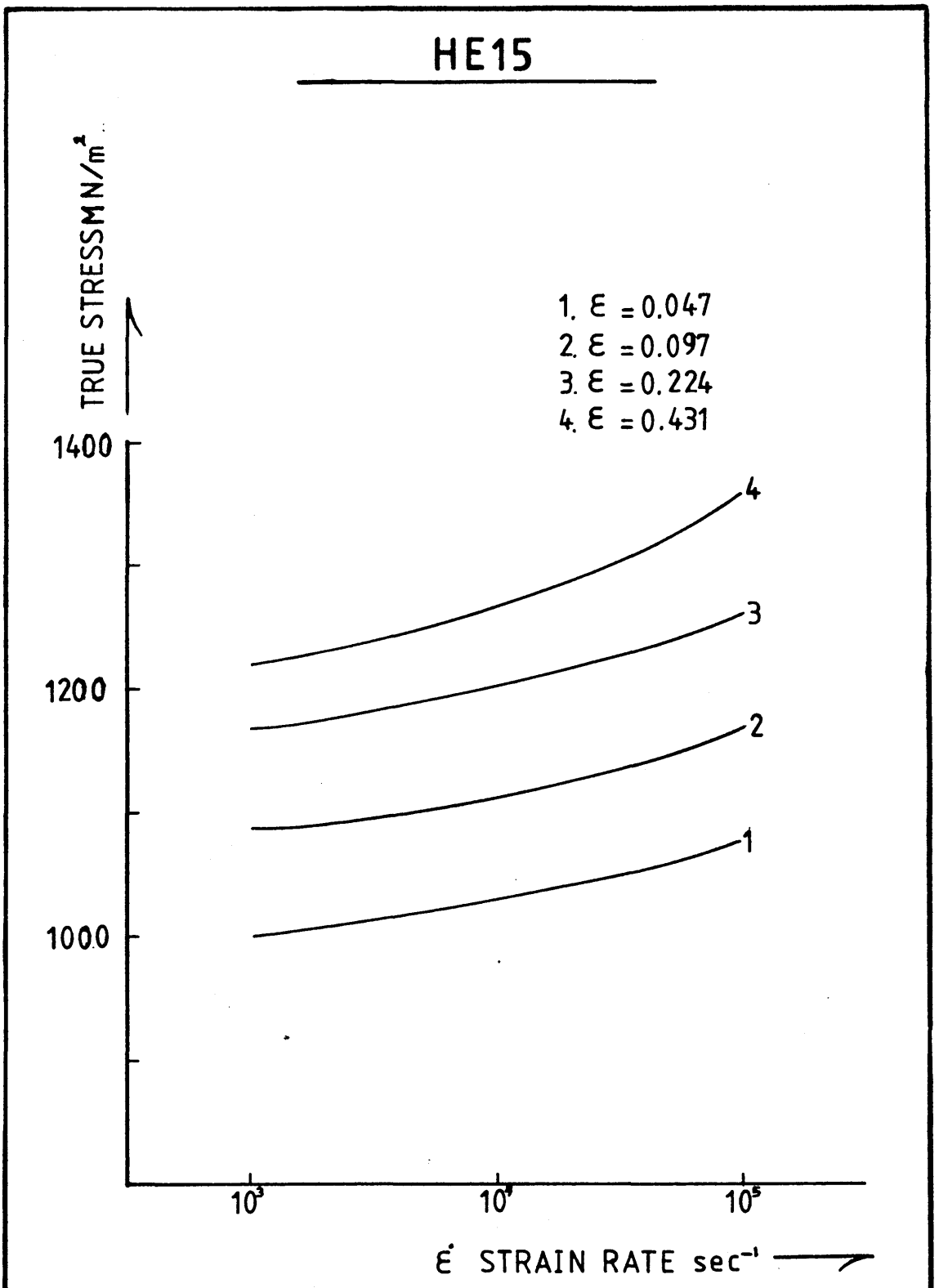

Fig [4.23] Theoretical variation of stress with strain rate at different strains for HE15

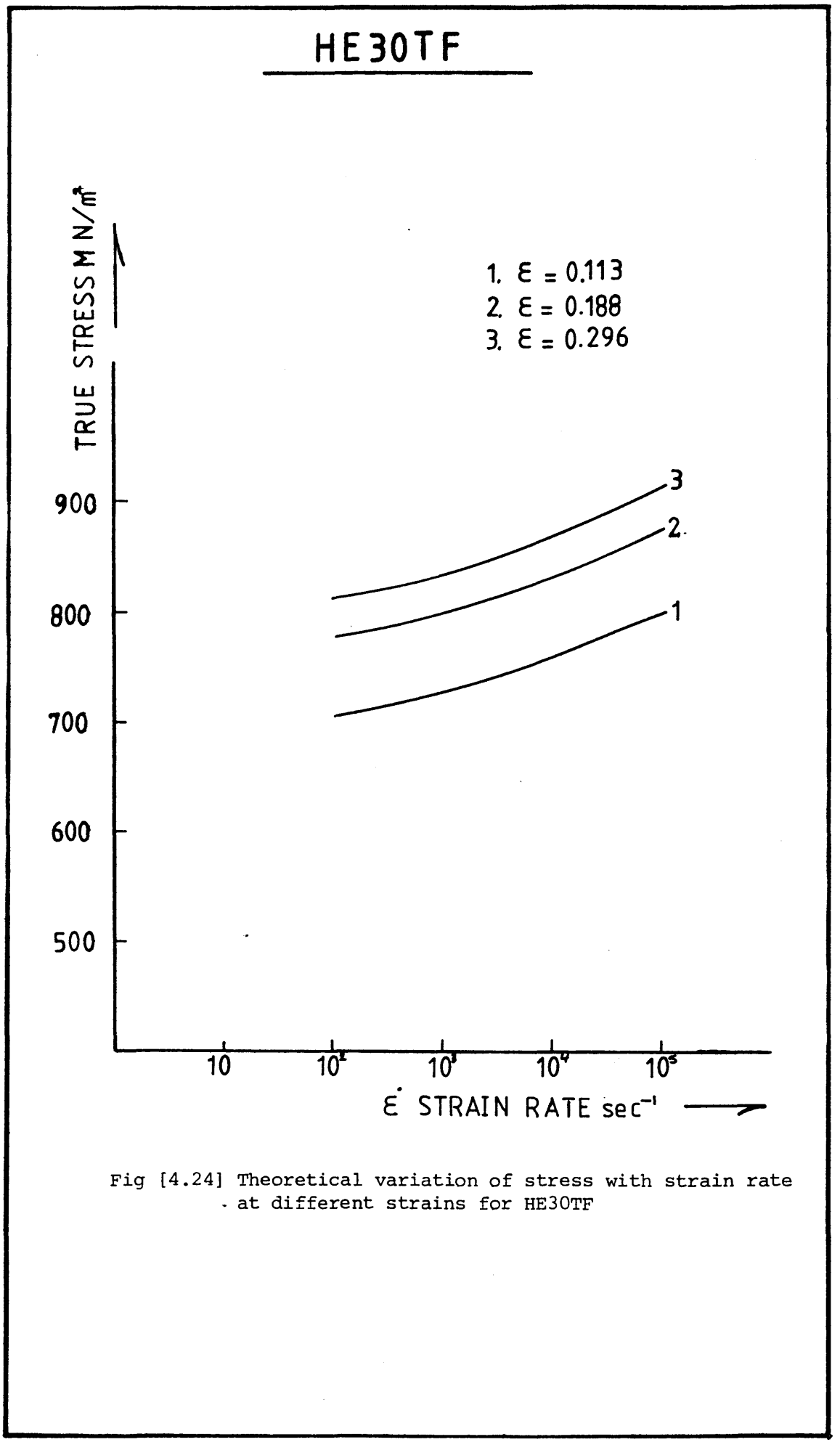

Fig [4.24] Theoretical variation of stress with strain rate at different strains for HE30TF

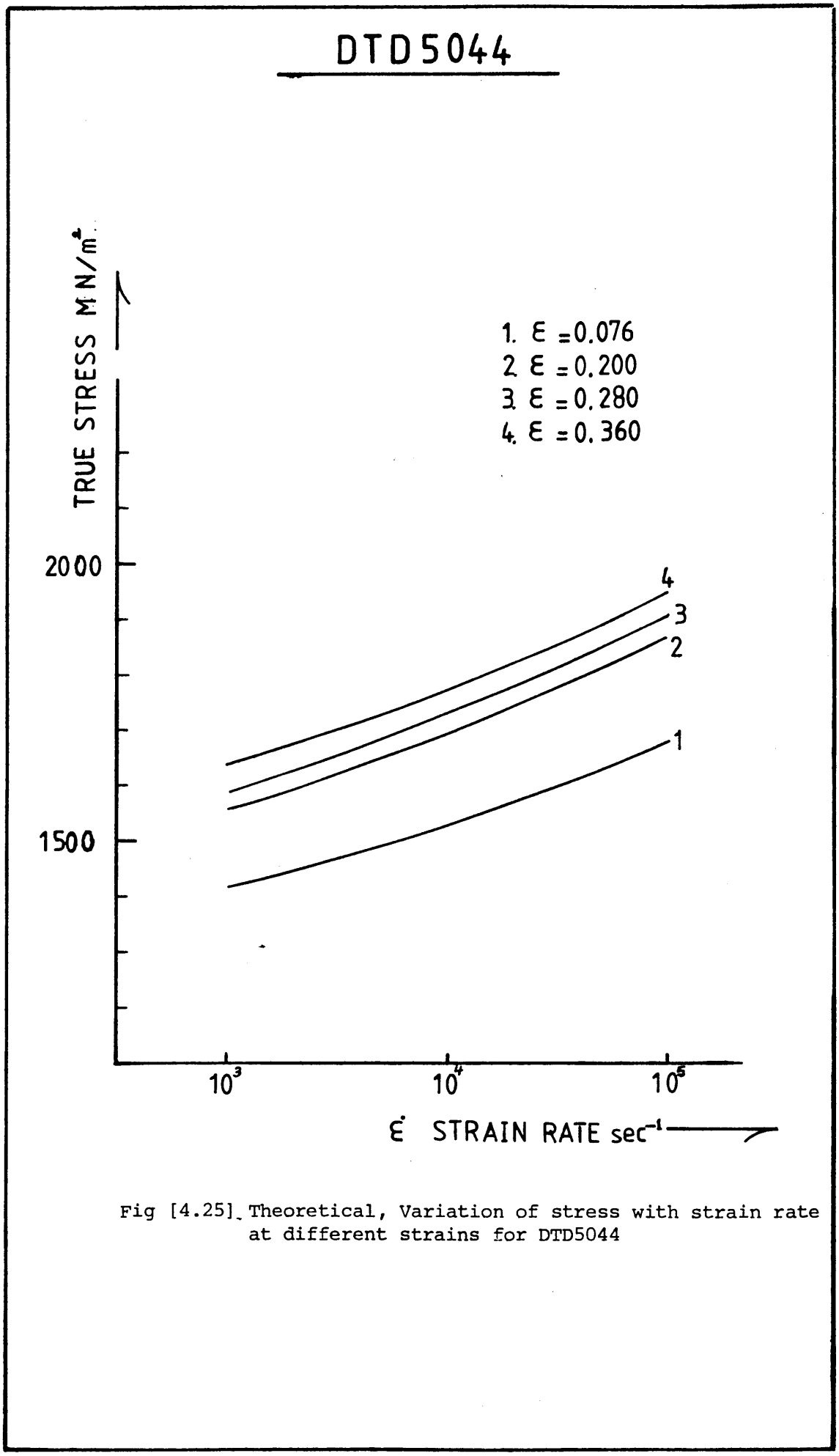

Fig [4.25] Theoretical, Variation of stress with strain rate at different strains for DTD5044

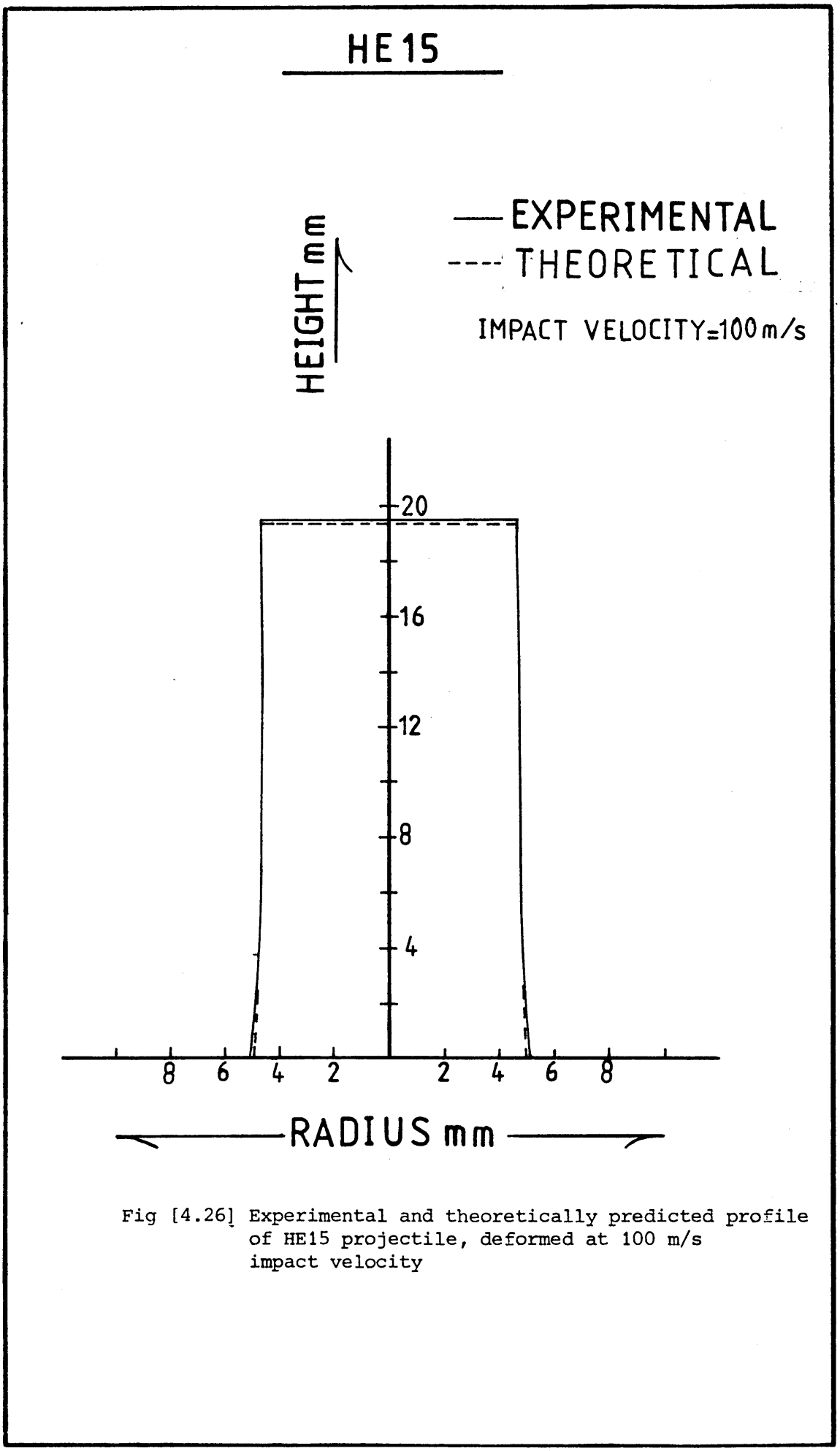

Fig [4.26] Experimental and theoretically predicted profile of HE15 projectile, deformed at 100 m/s impact velocity

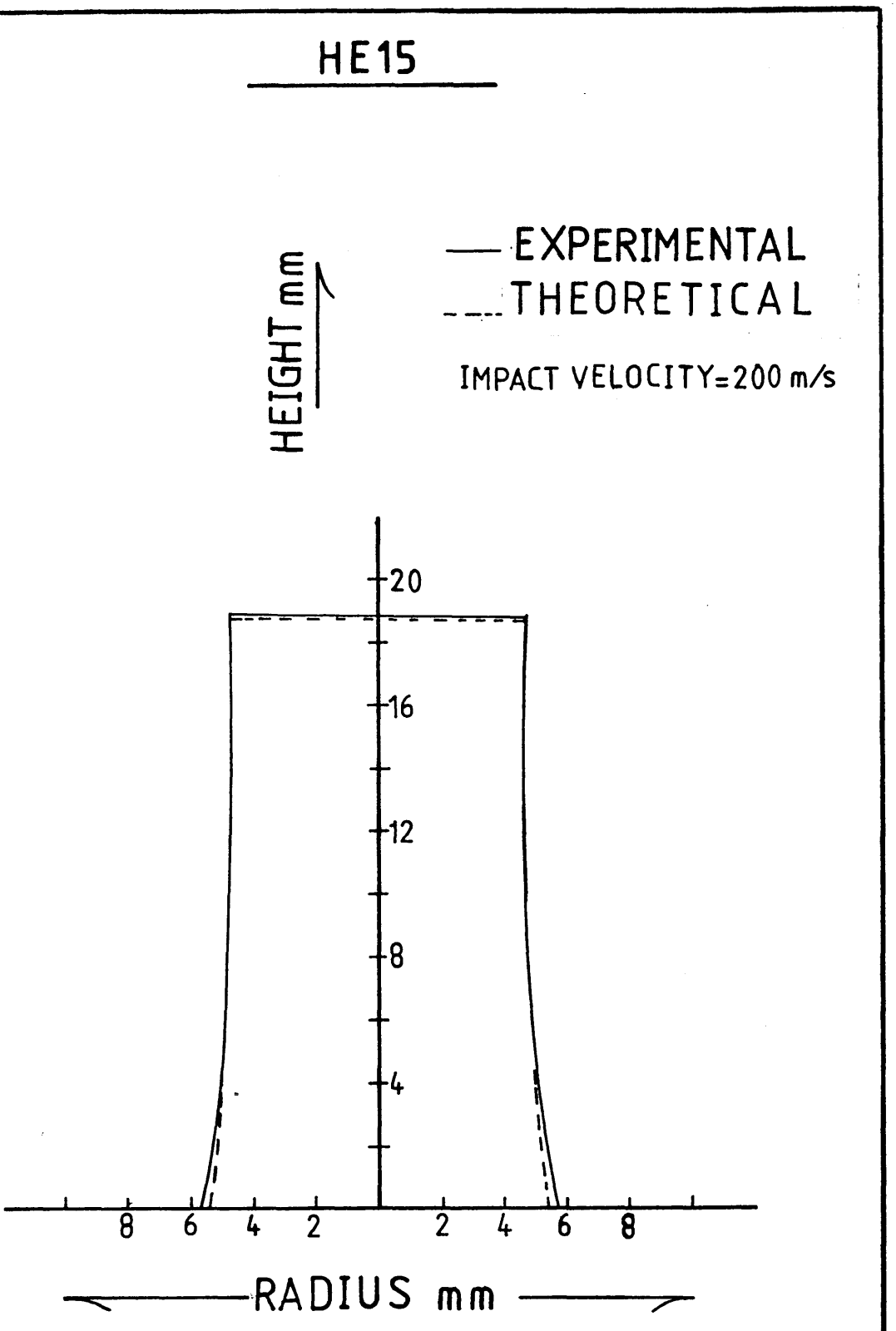

Fig [4.27] Experimental and theoretically predicted profile of HE15 projectile, deformed at 200 m/s impact velocity

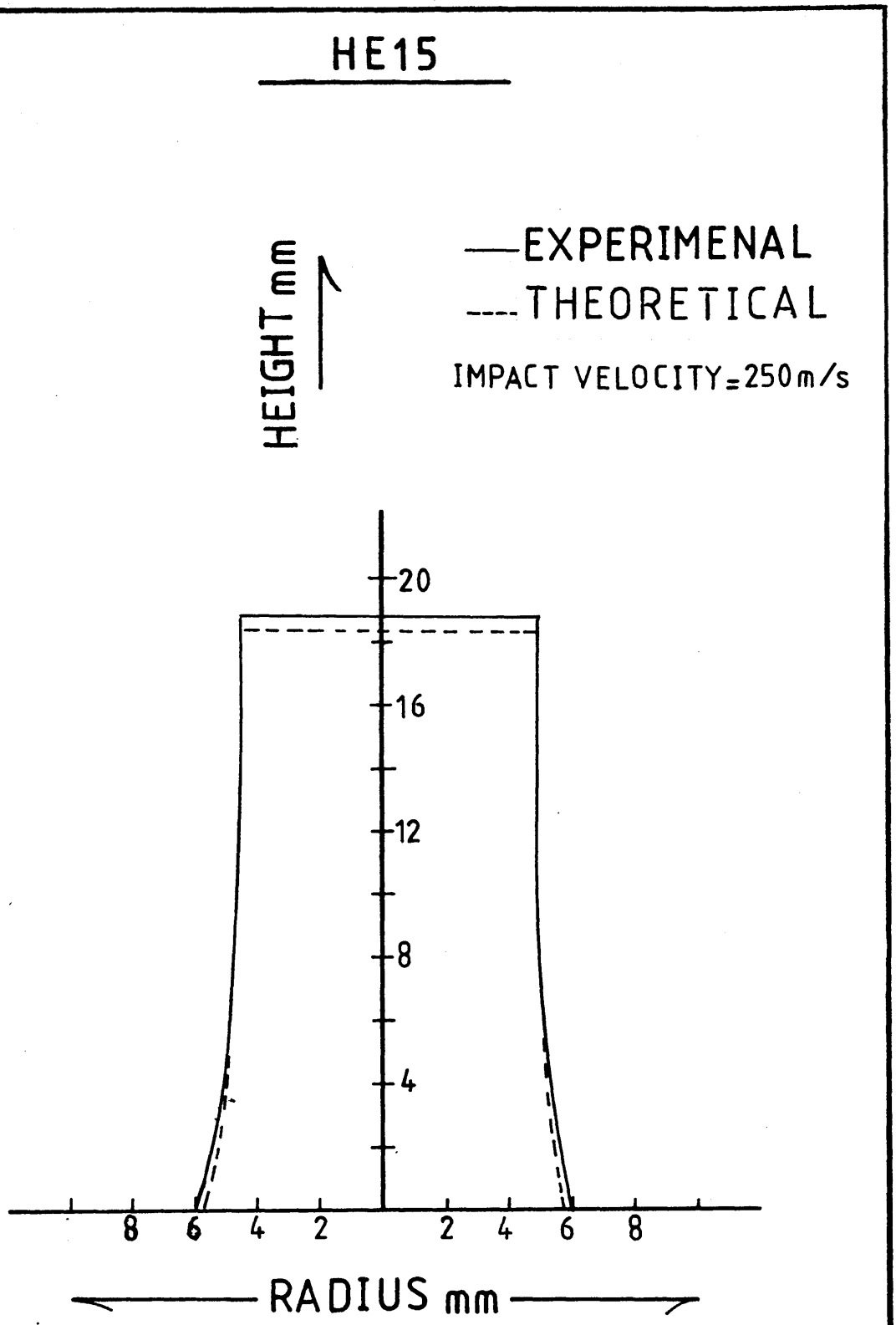

Fig [4.28] Experimental and theoretically predicted profile of HE15 projectile, deformed at 250 m/s impact velocity

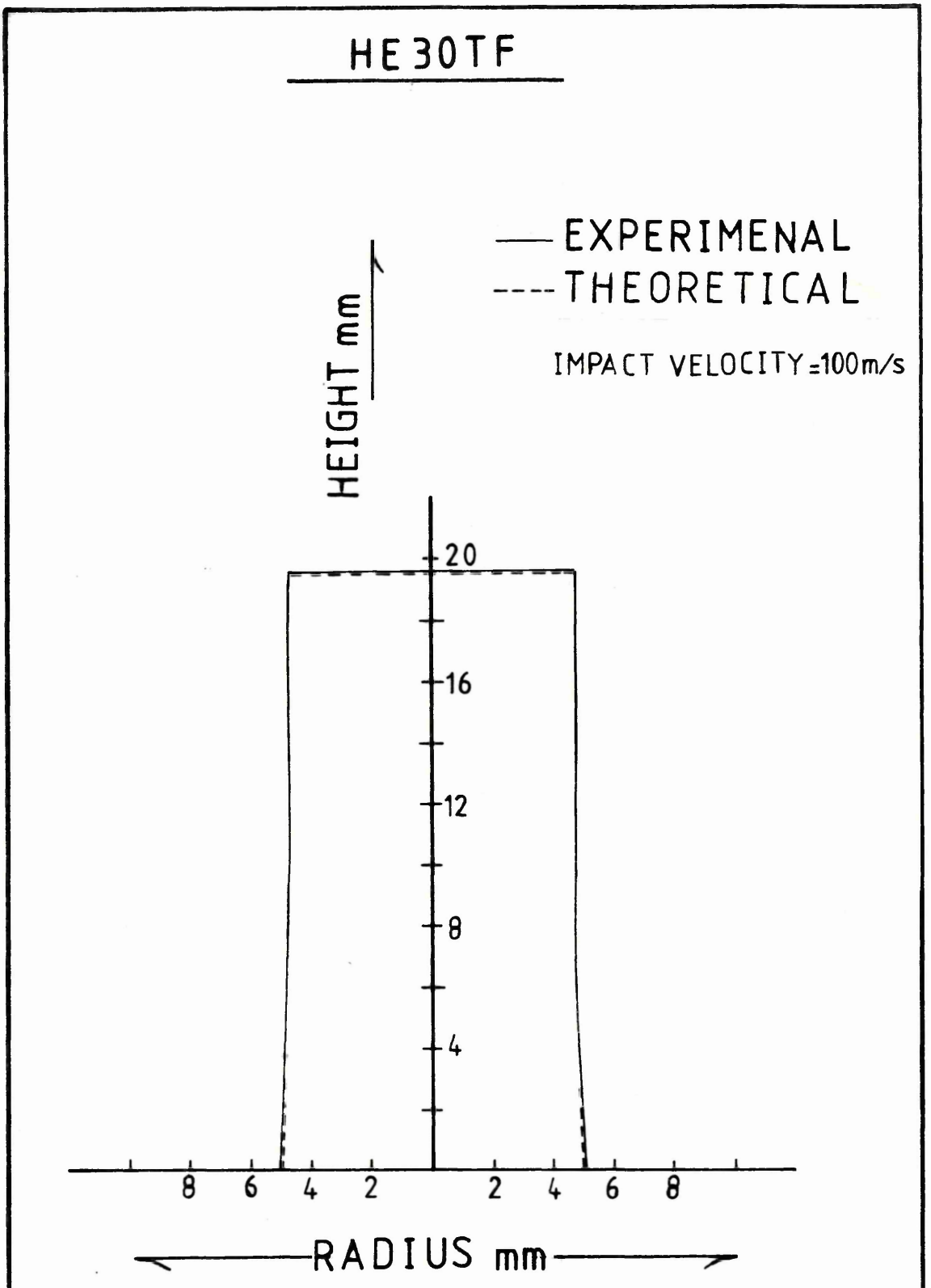

Fig [4.29] Experimental and theoretically predicted profile of HE30TF projectile, deformed at 100 m/s impact velocity

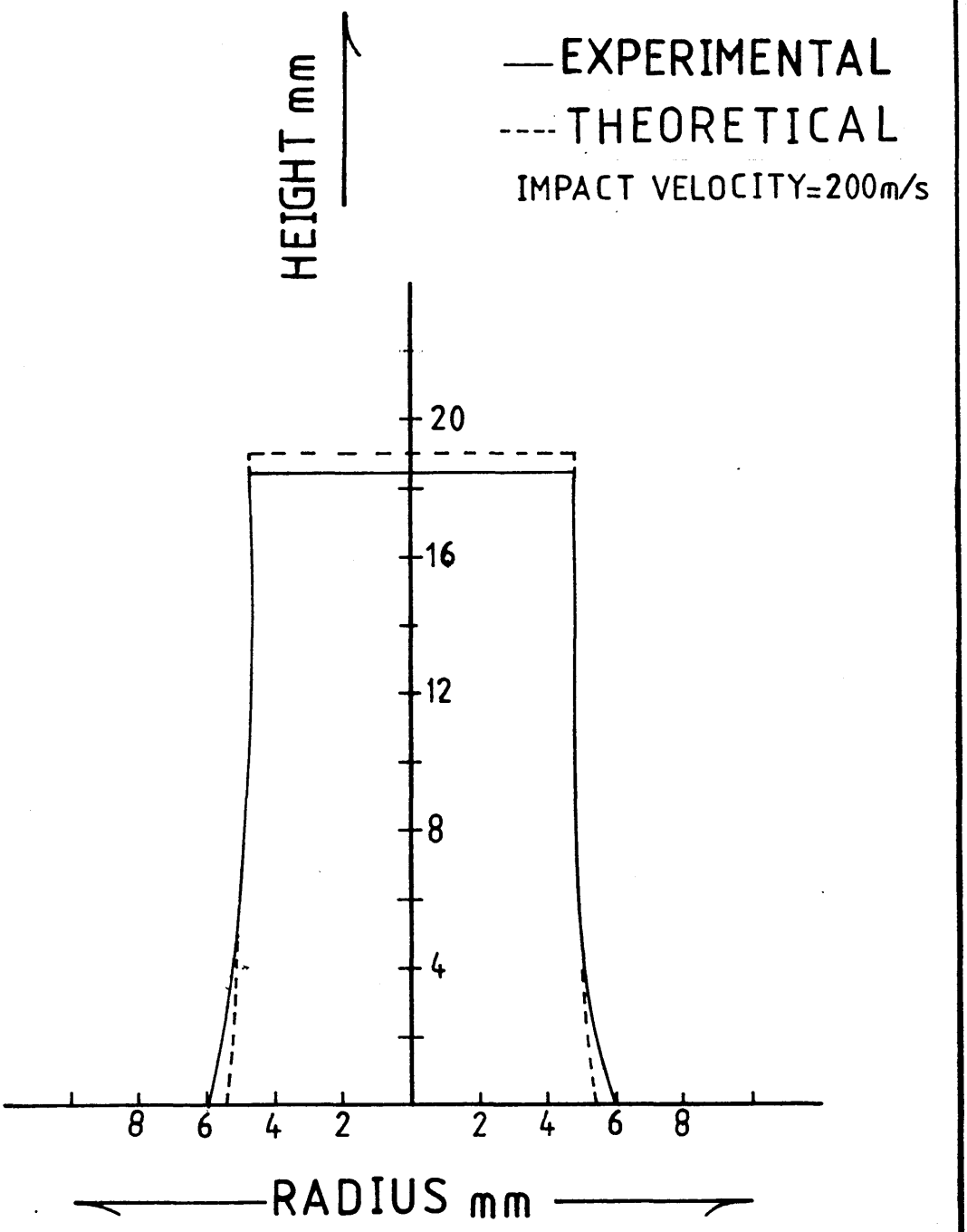

Fig [4.30]- Experimental and Theoretically predicted profile of HE30TF projectile, deformed at 200 m/s impact velocity

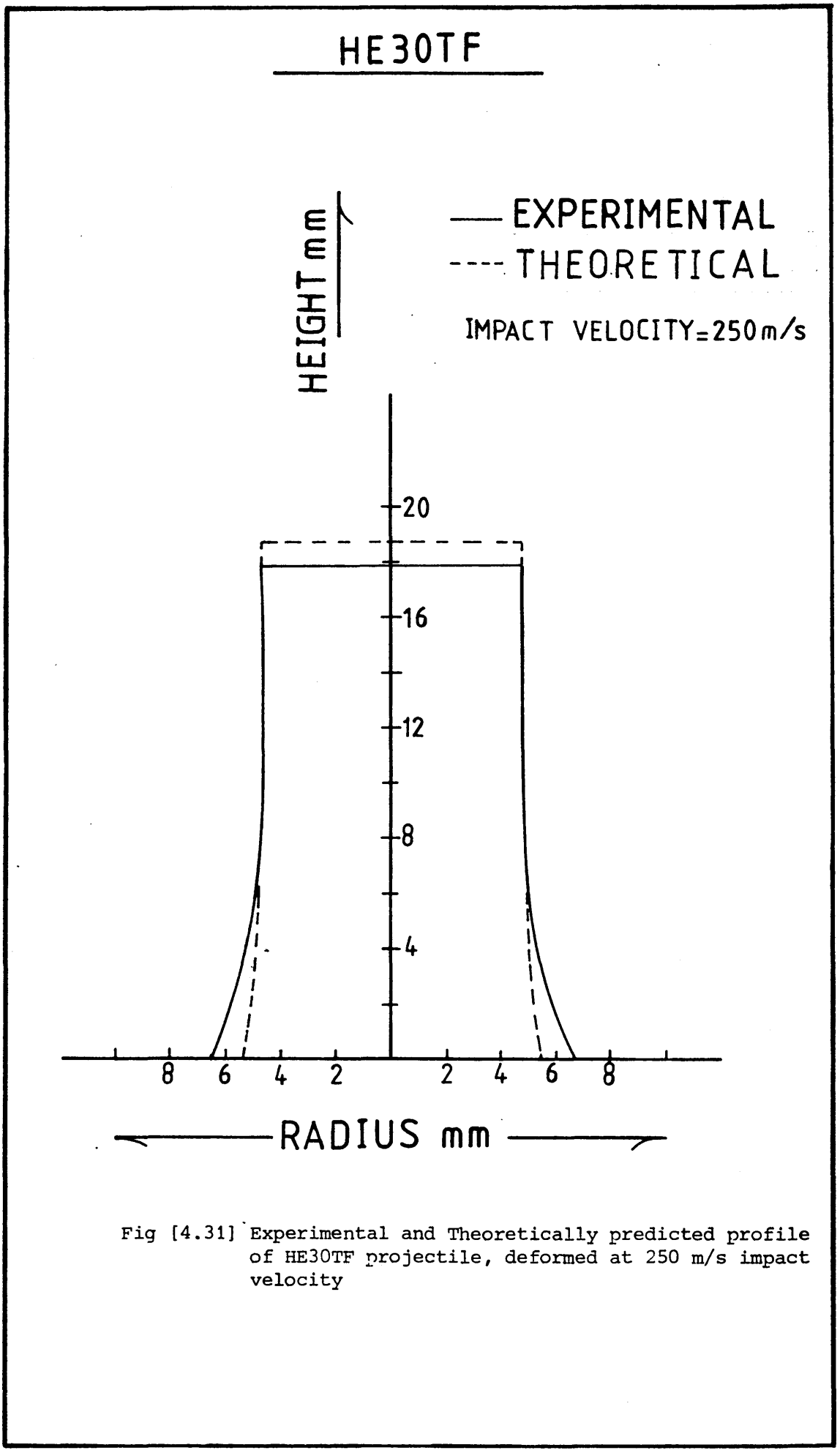

Fig [4.31] Experimental and Theoretically predicted profile of HE30TF projectile, deformed at 250 m/s impact velocity

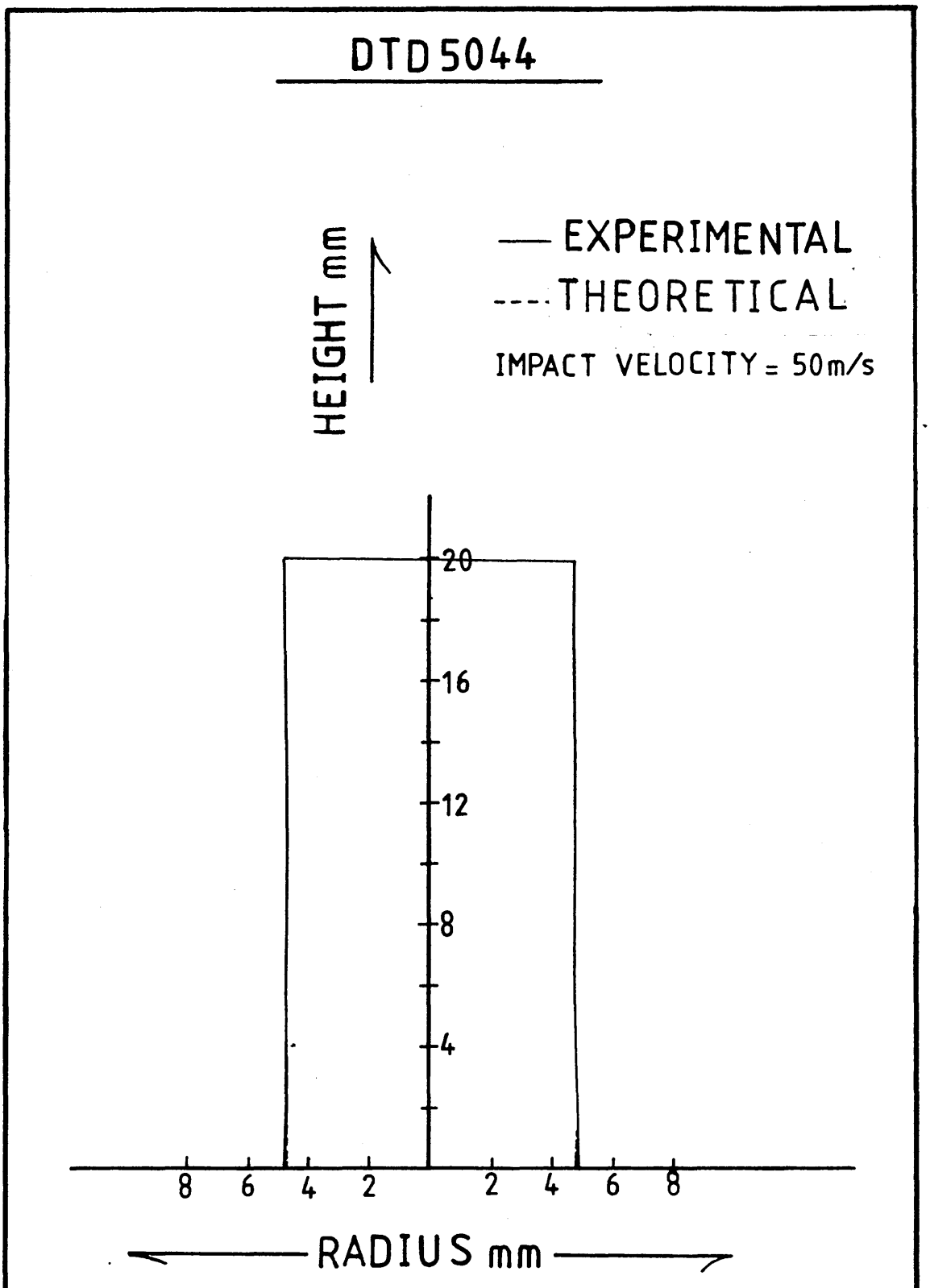

Fig [4.32] .Experimental and Theoretically predicted profile of DTD5044 projectile, deformed at 50 m/s impact velocity

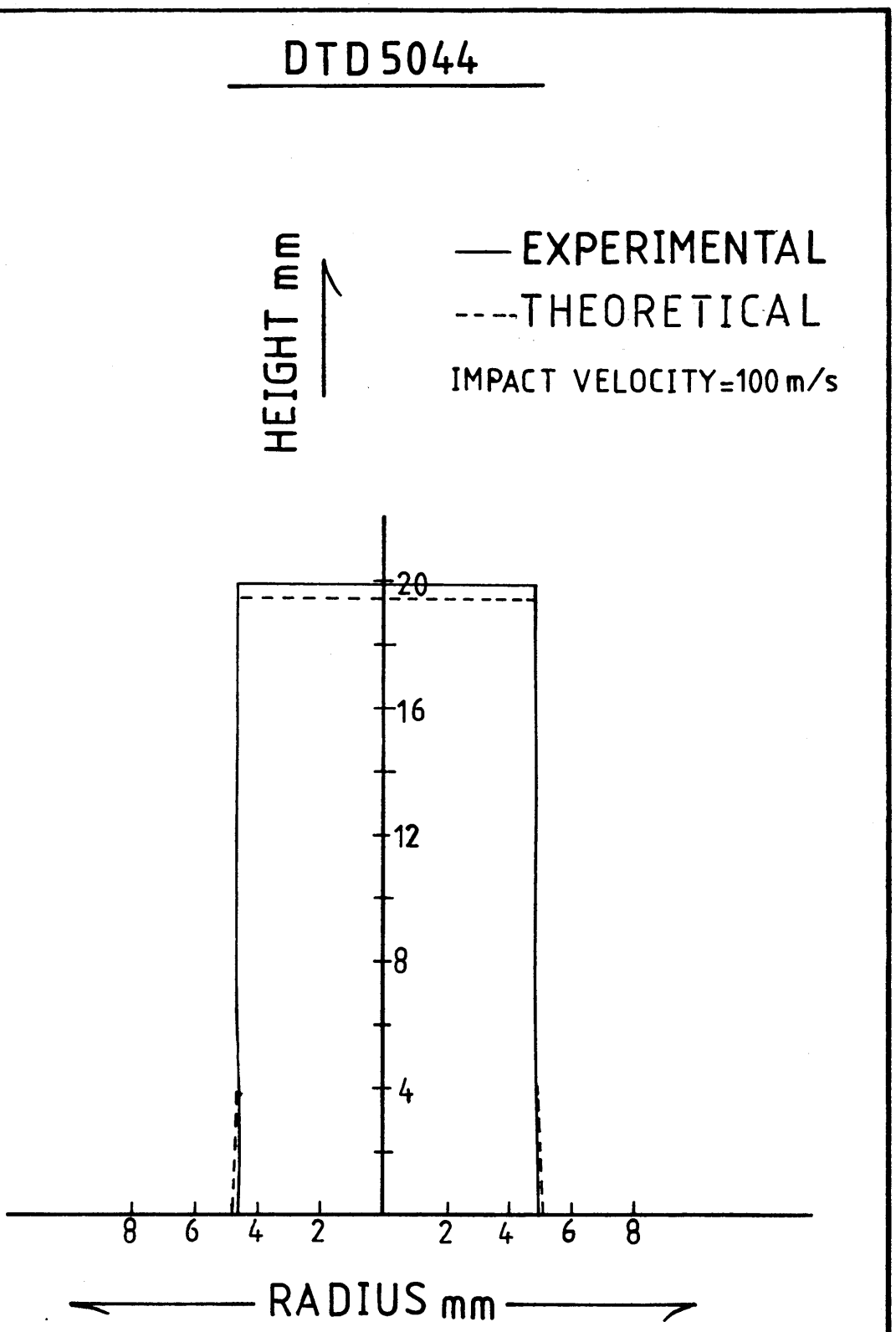

Fig [4.33] Experimental and Theoretically predicted profile of DTD5044 projectile, deformed at 100 m/s impact velocity

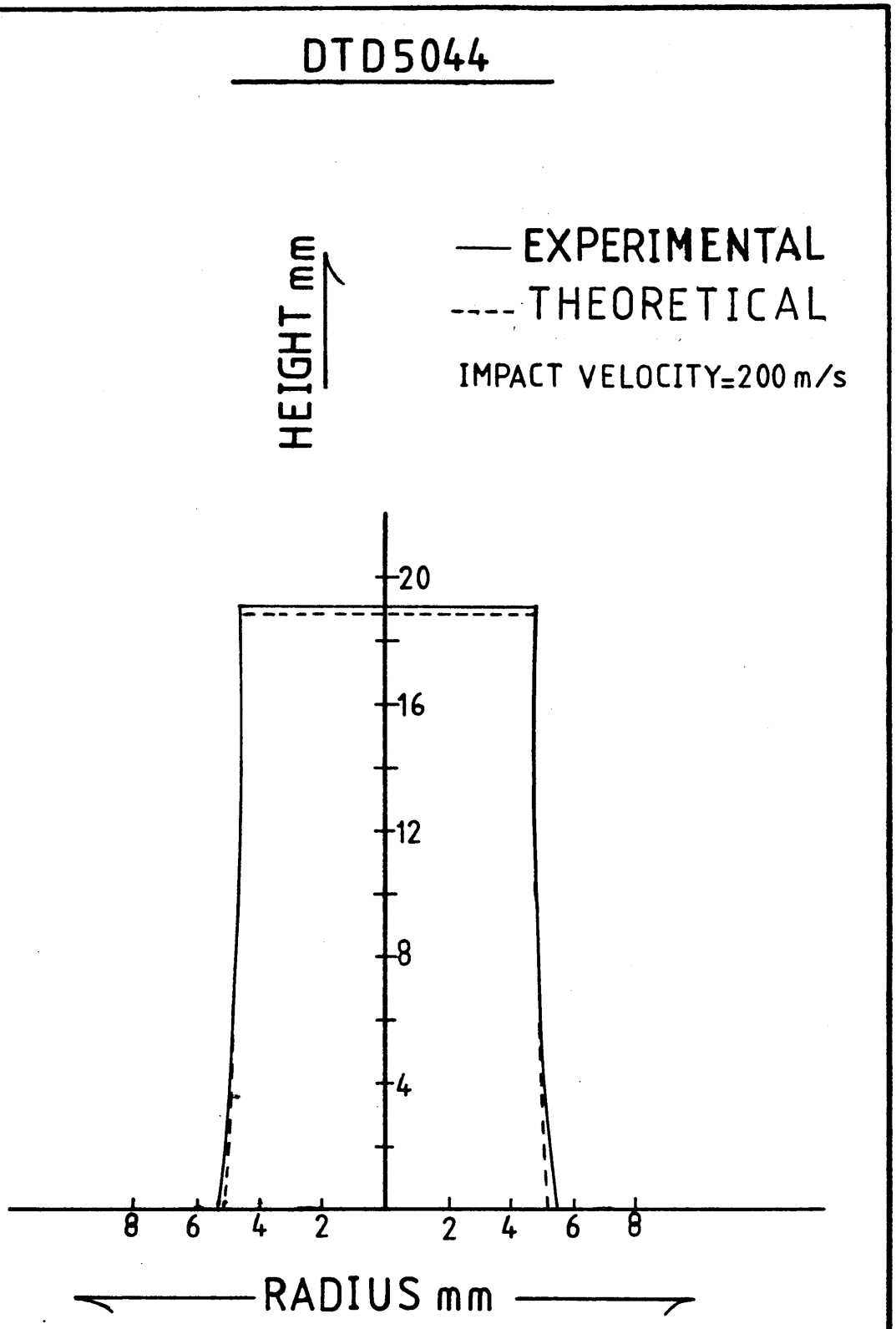

Fig [4.34] Experimental and Theoretically predicted profile of DTD5044 projectile, deformed at 200 m/s impact velocity

HE15

46.5 m/s 160 m/s 250 m/s

HE30TF

50 m/s 154 m/s 250 m/s

DTD5044

50 m/s 154 m/s 250 m/s

Plate No [4.2] Deformed projectiles at different impact velocities

HE15

46.5 m/s 160 m/s 250 m/s

HE30TF

50 m/s 154 m/s 250 m/s

DTD5044

50 m/s 154 m/s 250 m/s

Plate No [4.2] Deformed projectiles at different impact velocities

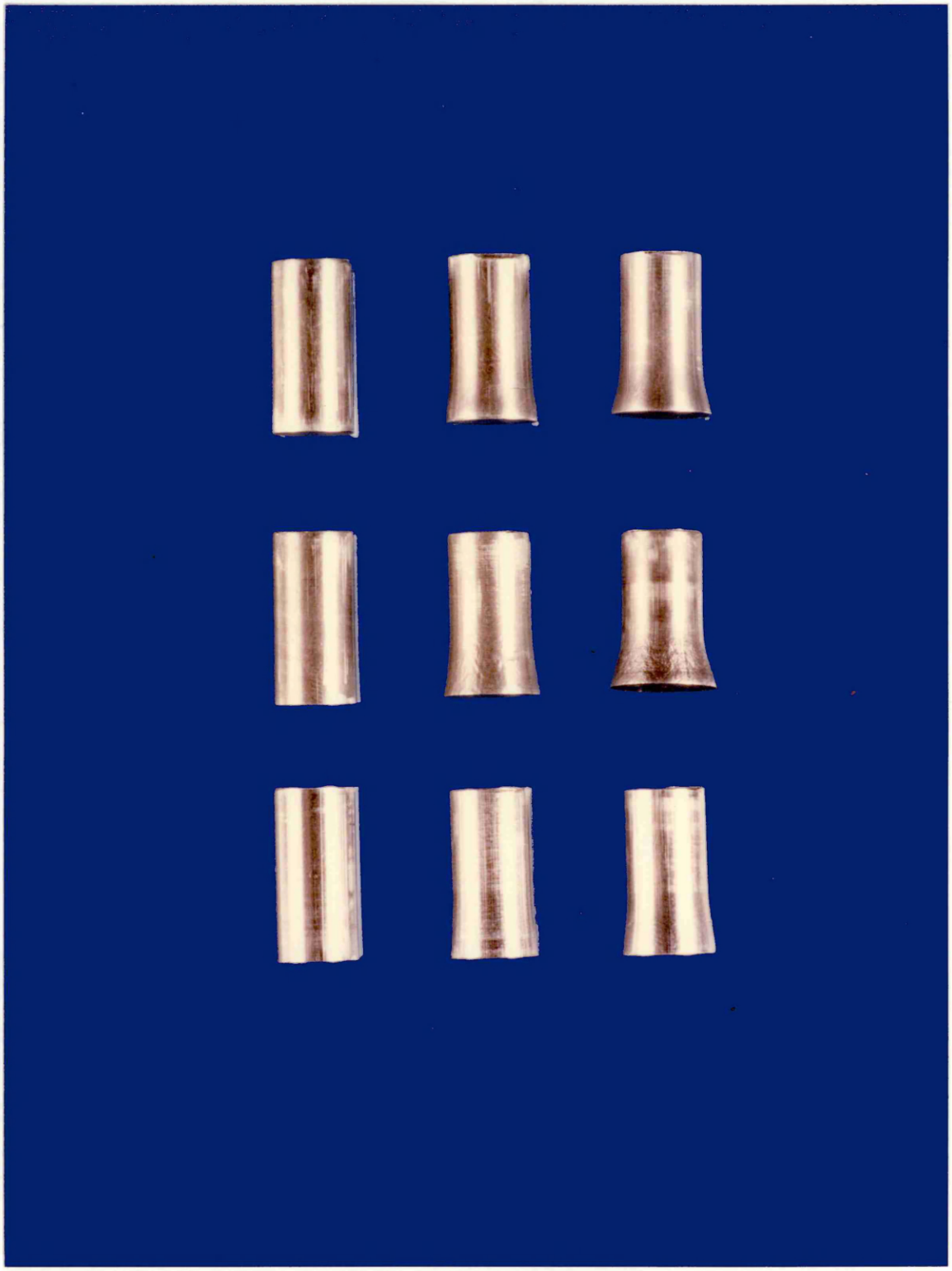

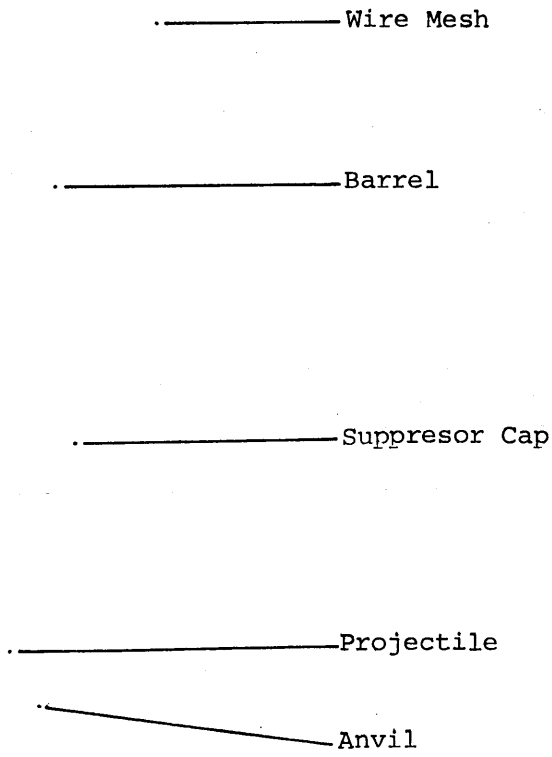

Plate No [4.1] Aluminium alloy projectile impinging onto a rigid anvil

Wire Mesh

Barrel

Suppressor Cap

Projectile

Anvil

Plate No [4.1] Aluminium alloy projectile impinging onto a rigid anvil

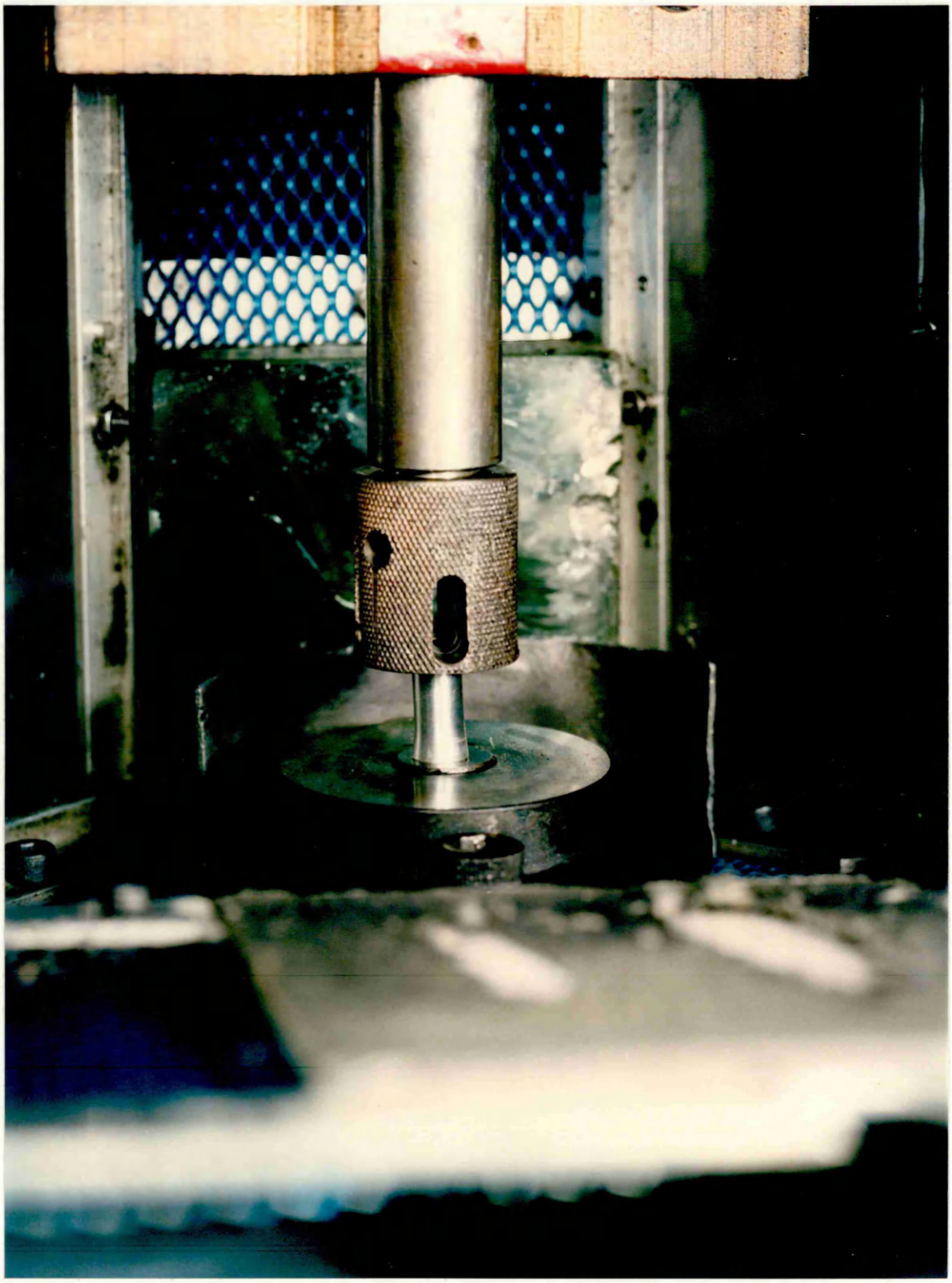

Materials		HE15	HE30TF	DTD5044
Maximum Temperature Rise °C		101.0	72.88	102.27
Radial Inertia Effect %	50 m/s	0.008	0.018	0.007
	250 m/s	0.329	0.6	0.28
Coefficient of Friction Under Dry Conditions		0.0622	0.055	0.0432

Table [4.1] Temperature Rise, Radial Inertia Effects and coefficients of friction for the three aluminium alloys

5.0 Phase Two Experimental Results

5.1 Introduction

Phase one test results, presented in Chapter Four, show that when aluminium alloy projectiles were impinged onto a rigid anvil, the deformation, characterised by the mushroom shaped deformed projectiles shown in figures 4.26 to 4.34, was inhomogeneous and localised. Only the first few elements of the projectiles which were in contact with the rigid anvil were deformed significantly whilst the rest were hardly deformed. Lubrication problems arose from the fact that only the rigid anvil surface was lubricated, thus affecting the temperature rise within the projectiles during deformation.

Due to these observations, a new method of testing was devised and adopted in the second phase of the study. The objectives of the new method were to obtain

(i) Homogeneous deformation.

(ii) Better and more effective lubrication conditions.

(iii) Uniform strain rates.

This was achieved by impacting heat treated FMP-338 tool steel projectiles onto small cylindrical billets made of HE15, HE30TF and DTD5044 aluminium alloys as shown in figure 5.1 and in Plate No 5.1. En-8 structural steel specimens were tested in the same manner at this stage of the study.

Homogeneous deformation was achieved by deforming the whole specimen in the absence of barrelling and buckling as shown in

Plate No 5.2 where deformed samples of HE15 are shown. Lubricant (Tallow-graphite 8/1 weight) was used extensively and effectively by lubricating the anvil surface and both sides of the billet, thus minimising the effect of friction. Higher strain rates were difficult to achieve when testing aluminium alloys as the small test billets fractured at strain rates exceeding 2 x 10^4 per second.

The experimental procedure used in the second phase of the study was described in Chapter Two. The results from the phase two tests were grouped as follows:

(i) High velocity (Dynamic) tests, which were carried out on small aluminium alloy and En-8 steel billets at high strain rates.

(ii) Final dimension measurements.

(iii) Determination of material constants.

(iv) Stress-strain characteristics at high strain rate.

(v) Ring Test.

All experimental work in this phase was performed under lubricated conditions at room temperature, catering for radial inertia effect in the finite-difference technique.

5.2 High Velocity (Dynamic) Impact Tests

This section contains the main body of the experimental results from phase two of the study. The tests involved impacting heat treated tool steel FMP-338 projectiles onto small billets made from HE15, HE30TF, DTD5044 aluminium alloys and En-8 structural steel.

The dimensions of these billets are 5.2mm initial diameter (d) and 5mm initial height (h) with an aspect ratio, h/d, less than

unity. Other billet sizes were tested in order to investigate the effect of specimen size. This will be discussed later in Chapter Six. A series of experimental tests were conducted involving more than 200 specimens for each material undergoing investigation. The results for each material are shown in figures 5.2 to 5.9. These results show the variation of final diameter (D_f) and final height (H_f) with impact velocity.

It is evident from these figures that the final diameter (D_f) tends to increase gradually with impact velocity, while the final height (H_f) decreases heavily with impact velocity. The figures also show the degree of variation between nominally identical tests for each material. The solid curves shown in figures 5.2 to 5.9 represents the mean of all the experimental points over the range of impact velocities. By varying the impact velocity of the FMP-338 tool steel projectiles, different strain rates were achieved. For the three aluminium alloys, the impact velocities were varied between 20 and 80 m/s, achieving strain rates of 4×10^3 to 1.6×10^4 per second. For the En-8 structural steel impact velocities between 30 and 110 m/s were used which produced strain rates of 6×10^3 to 2.2×10^4 per second.

However, as mentioned earlier, other billet sizes made from the aluminium alloys were tested, all with aspect ratios less than unity. Their initial diameters were 6.2, 7.2 and 7.7mm while their initial heights were 6.0, 7.0 and 7.5mm respectively. Larger sizes were considered but found to be unsuitable because of the projectile diameter of 9.52mm, while smaller sizes were considered as well but excessive compression and resulting

fracture proved to be a problem at high strain rates. Figures 5.10 to 5.15 show the variation of final diameter and height against their initial values at constant impact velocity. For each aluminium alloy, curves for three impact velocities are presented. The figures also indicate the extent of deformation and size effect under high strain rate compression.

5.3 Final Dimension Measurements

It was found that, provided sufficient lubricant was used in high speed compression, the billet deformed with negligible barrelling and homogeneous deformation was obtained.

However, in a number of specimens the deformation gave rise to minor undulations on the curved surface thus causing some difficulty, especially when measuring the diameter of deformed aluminium alloy billets. This was due to (a) grain growth when subjecting aluminium alloy materials to high strain rate deformation and (b) lubricant expansion across the flat surfaces of the billets was not as quick as the expansion of the materials thus causing friction and a rise in temperature.

In all cases a Digimatic Micrometer described in Section 4.3 was used to obtain the diameter and height measurements. An average of fifteen readings were taken for each billet before and after impact.

5.4 Determination of Material Strain Rate Sensitivity Constants

With reference to the quasi-statically determined stress-strain properties, a strain rate sensitivity equation of the form

$$\sigma D = \sigma s[1 + (/\dot{\varepsilon}/_{D})1/P_{]}$$

proposed and applied in Chapter Four, has also been used for

this phase of the investigation. It should be noted that this equation does not cater for any change in the overall shape of the stress-strain curve for various strain rates and also assumes that the effect of strain rate is independent of strain.

The above equation was then incorporated into the numerical technique for analysing the deformation of the billets. The technique provides predictions of final diameter and height for given impact velocities and known values of strain rate sensitivity constants P and D.

In Chapter Four it was shown that for phase one tests, the deformation was inhomogeneous and localised at the projectile-anvil interface. In this phase of the study, the billets were deformed approximately homogeneously under good lubrication condition resulting in a virtually uniform diameter along the length of the deformed specimen.

As a first step in the derivation P and D, arbitrary values of these parameters were assigned and final diameters and heights were predicted theoretically for various impact velocities. These results were then plotted against impact velocity and compared with those obtained experimentally. The experimentally obtained curves are the mean of a series of results presented in the previous section in Figures 5.2 to 5.9. The values of P and D were then systematically modified in order to get the theoretically predicted curves to converge towards their respective experimental ones as shown in Figures 5.16 to 5.23.

The values of P and D which produced the closest fit between the two sets of curves were then taken to be the material strain-

sensitivity constants. A selection of theoretical curves and the corresponding experimental ones can be seen in Figures 5.16 to 5.23. It can be seen from these figures that by increasing the value of D the curves of final diameter against impact velocity are shifted upwards whilst the linear relationship between final height and impact velocity are moved downwards.

Many combinations of P and D values were used for each material. The selected values shown in Figures 5.16 to 5.23 were presented to show the scope of such a computational exercise. The dashed lines are the theoretically predicted curves while the solid lines represent the curves obtained experimentally.

The accepted best fit constants for the materials investigated are tabulated as follows:

Material	P	D
HE15	35	75000
HE30TF	25	30000
DTD5044	15	100
En-8	7.5	80

It is essential to state that these values of P and D give the best compromise match between the experimental and theoretical results for final diameter and final height against impact velocity curves. A better fit cannot be achieved for say the final diameter curve without worsening the fit for the final height curve. The match could have been improved marginally by undertaking an extensive computational exercise but this was considered unnecessary.

5.5 Stress-Strain Characteristic at High Strain Rates

Having determined the strain rate sensitivity constants P and D for each material under test and knowing the corresponding quasi-static stress-strain curve, the stress-strain curves at higher strain rates (dynamic) can be obtained.

This was achieved by using the proposed strain rate sensitivity equation

$$\sigma D = \sigma s[1 + (\frac{/\dot{\varepsilon}/}{D})^{1/P}]$$

Figures 5.24 to 5.27 show the dynamic stress-strain curves at different strain rates together with the respective quasi-static curves for the four materials under investigation. Strain rates between 4×10^3 and 1.6×10^4 per second were achieved when testing the small cylindrical aluminium alloy billets. However, when testing the structural steel En-8 in the same manner strain rates between 6×10^3 and 2.2×10^4 per second were achieved. Only three values of strain rate have been shown for each material in figures 5.24 to 5.27. The figures show that there is little change in the general shape of the stress-strain curves. The main feature in using the proposed strain rate sensitivity equation is that it only moves the curves higher as the strain rate increases. The figures also show the effect of strain rate on the true stress.

Stress-strain rate curves were obtained theoretically at constant strain values varying between 0.016 and 0.250 and are shown in figures 5.28 to 5.31, for the aluminium alloys and En-8 steel. The stress ratio $\sigma D/\sigma s$ against strain rate curves are shown in figures 5.32 to 5.35. These figures show that different degrees of rate sensitivity are obtained for HE15 and HE30TF

when the two separate experimental methods are used. However, for DTD5044 no difference is suggested (this is by far the strongest of the three alloys).

Finally Table 5.1 shows the temperature rise, radial inertia effect and coefficient of friction under dry conditions during deformation. A typical calculation of these effects is shown in Appendices V, VI and VII respectively.

5.6 Ring Test

Tallow-graphite (8/1 by weight) was used as the lubricant throughout the present study. Although it has been recommended and used by other researchers, it was essential to justify its use and hence the ring test was carried out.

The specimens were prepared by drilling a small hole axially through the billets; HE15 aluminium alloy was used as an example to verify friction at low and high strain rates. The billets were lubricated and tested statically and dynamically using the Mayes press and the ballistic rig respectively. Under frictionless conditions the inside diameter of a drilled billet should increase in the same manner as a solid cylindrical specimen under deformation and may be calculated using the constant volume relationship. Comparison between this calculated inside diameter and that obtained experimentally gives a very good indication of the level of friction present.

A number of deformed drilled billets are shown in Plate No 2.2. Average results of several samples deformed in static and dynamic compression are shown in Table 5.2. It can be seen that although the degree of deformation for static and dynamic tests

differs, the percentage difference between the theoretical and experimental inside diameters are approximately the same. Both percentage difference values indicate a low level of friction during static and dynamic compression tests thus indicating the suitability of the lubricant used.

5.7 Summary

Results of the experimental work performed in phase two of the study are presented in this Chapter; the results highlight the following:

1 Homogeneous deformation at high strain rates.

2 High velocity impact (dynamic) tests were conducted to obtain the true stress-natural strain characteristics of the three aluminium alloys and En-8 steel at strain rates varying between 4×10^3 to 1.6×10^4 per second and 6×10^3 to 2.2×10^4 per second respectively.

3 Material constants P and D were obtained for the four materials:

Material	P	D
HE15	35	75000
HE30TF	25	30000
DTD5044	15	100
En-8	7.5	80

4 The variation of the stress ratio with strain rate was demonstrated.

5 The justification of the use of tallow-graphite (8/1 by weight) as a lubricant was demonstrated by means of the ring test at low and high strain rates.

6 Results of temperature rise, radial inertia and co-efficient of friction (under dry dynamic conditions) were obtained.

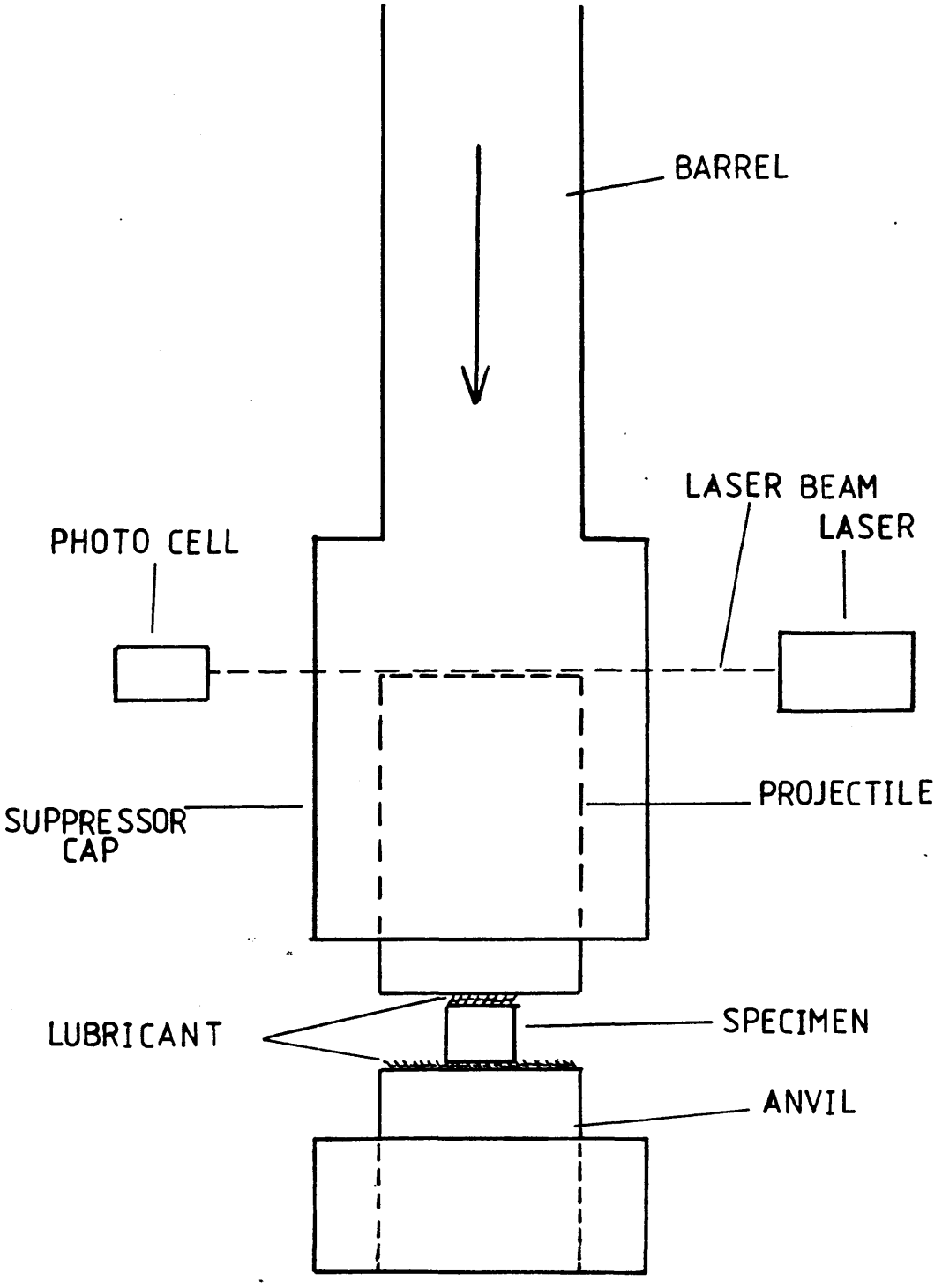

Fig [5.1] Anvil, Shooting Barrel and Measuring Equipment Arrangement

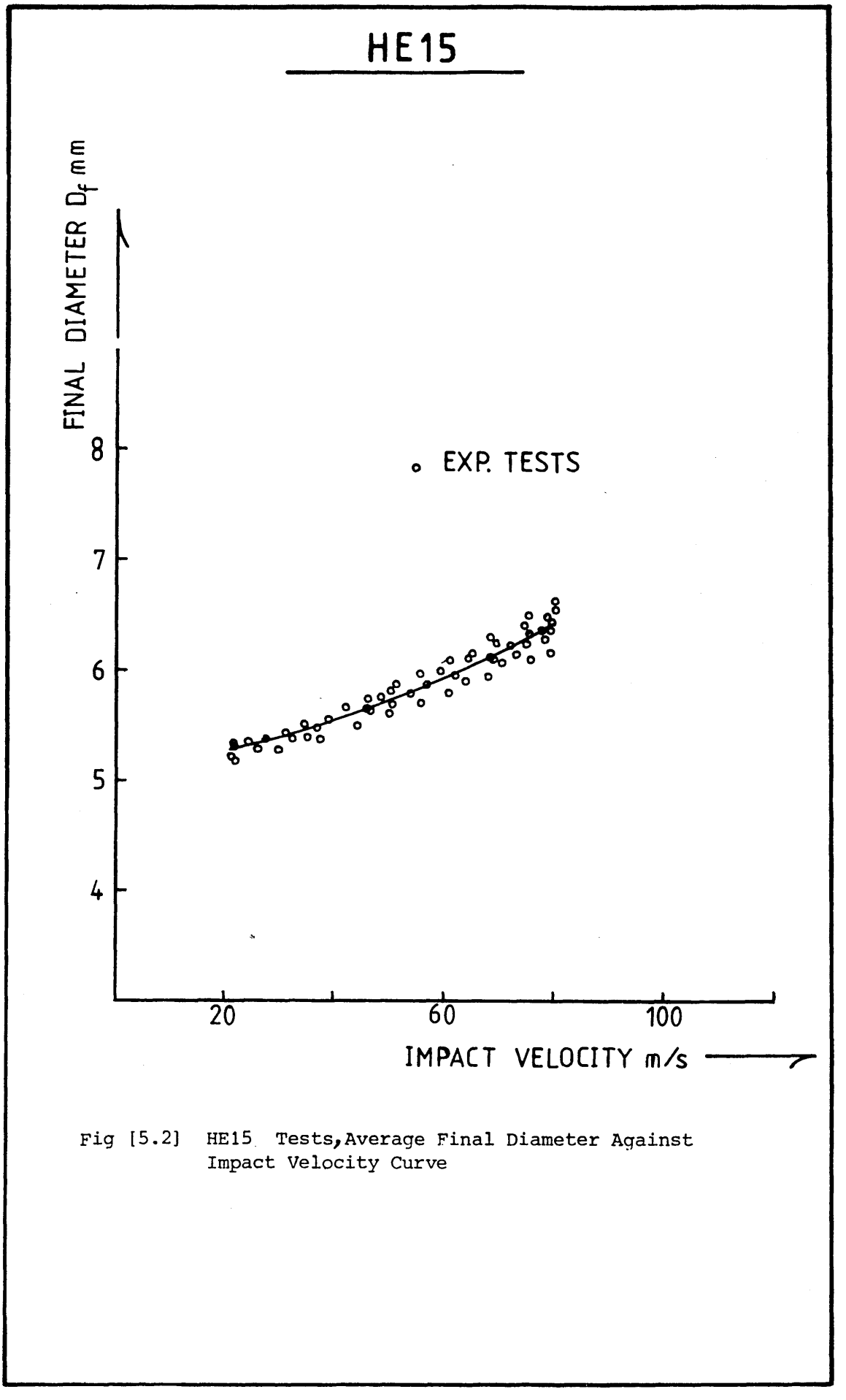

Fig [5.2] HE15 Tests, Average Final Diameter Against Impact Velocity Curve

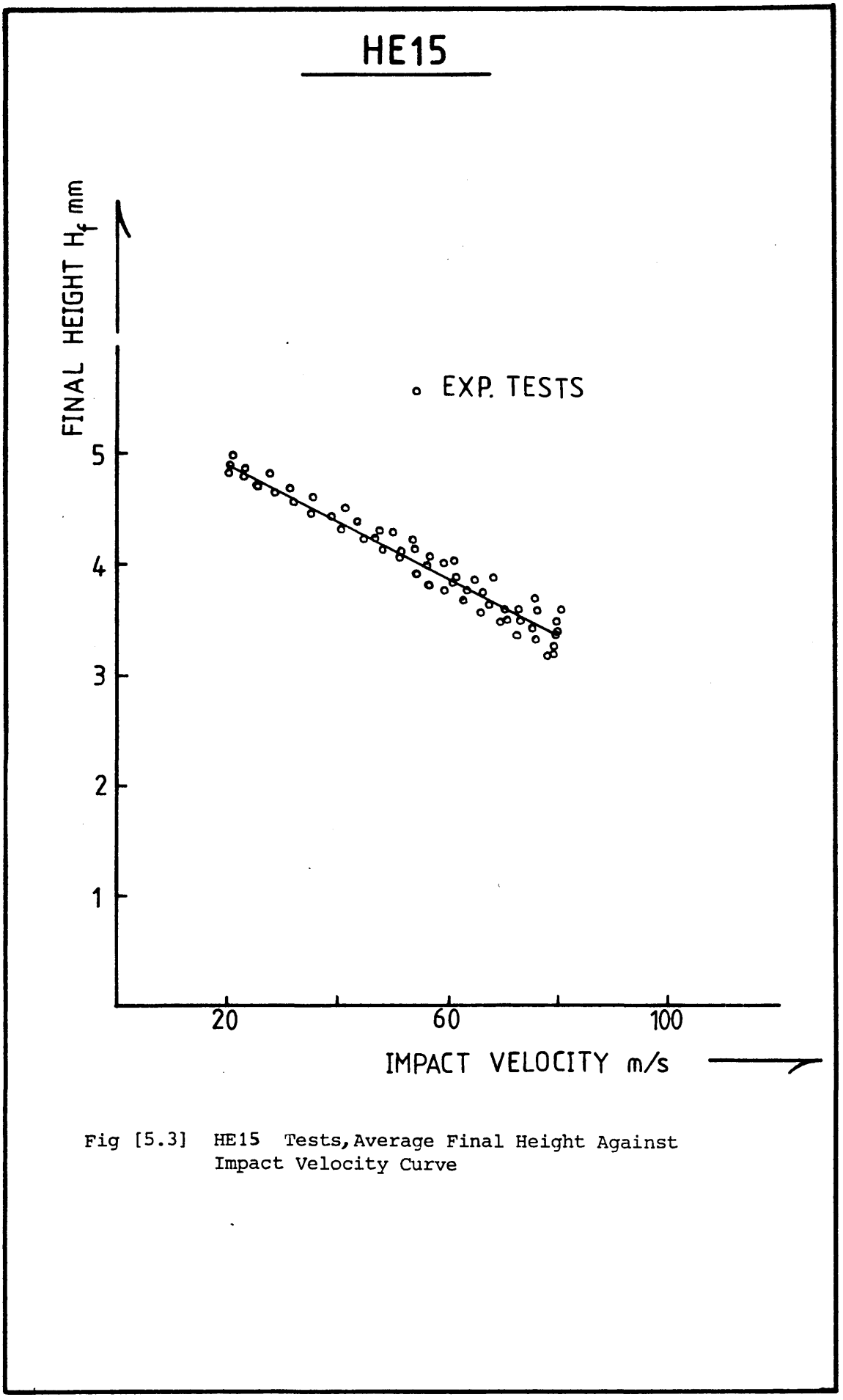

Fig [5.3] HE15 Tests, Average Final Height Against Impact Velocity Curve

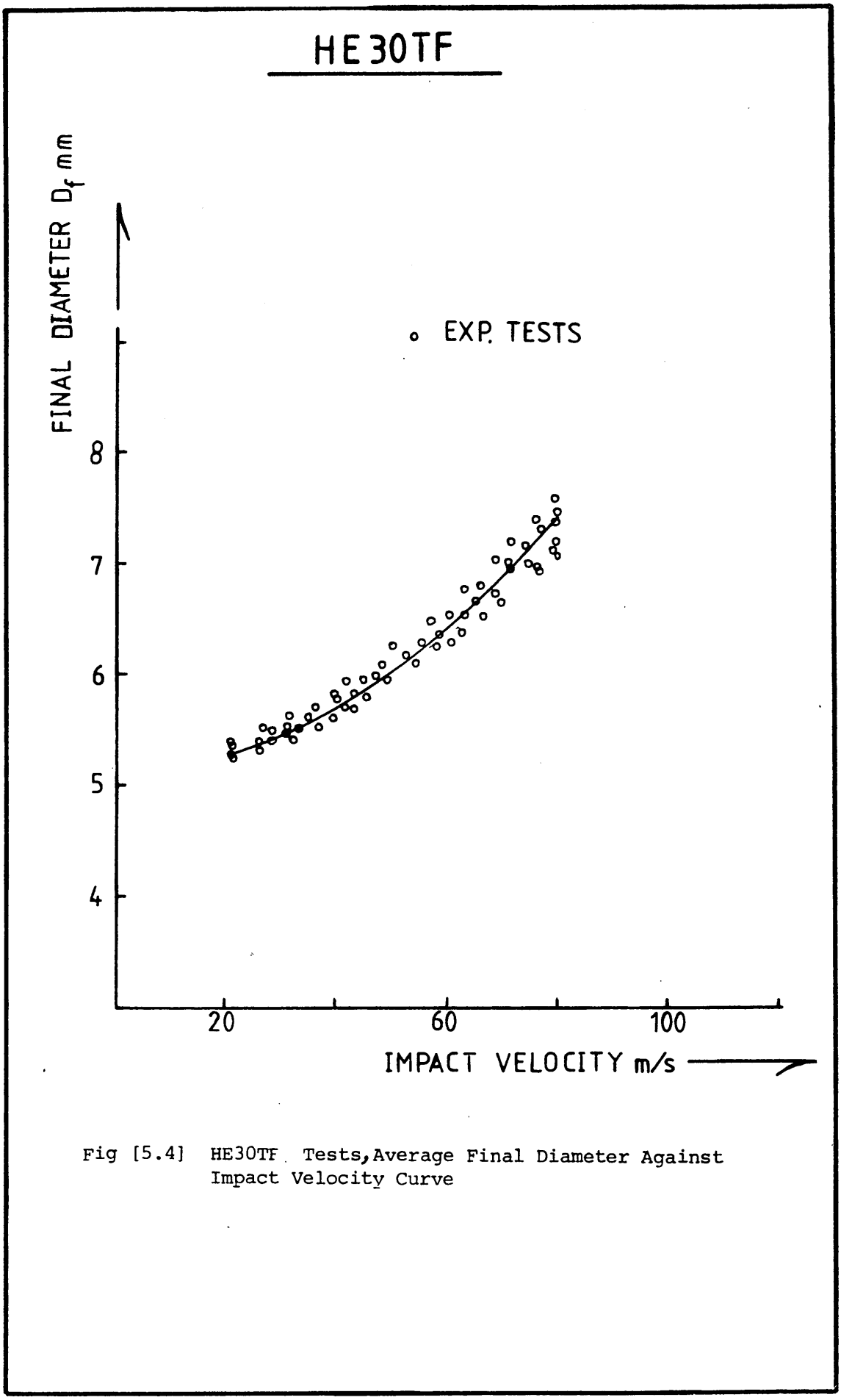

Fig [5.4] HE30TF Tests, Average Final Diameter Against Impact Velocity Curve

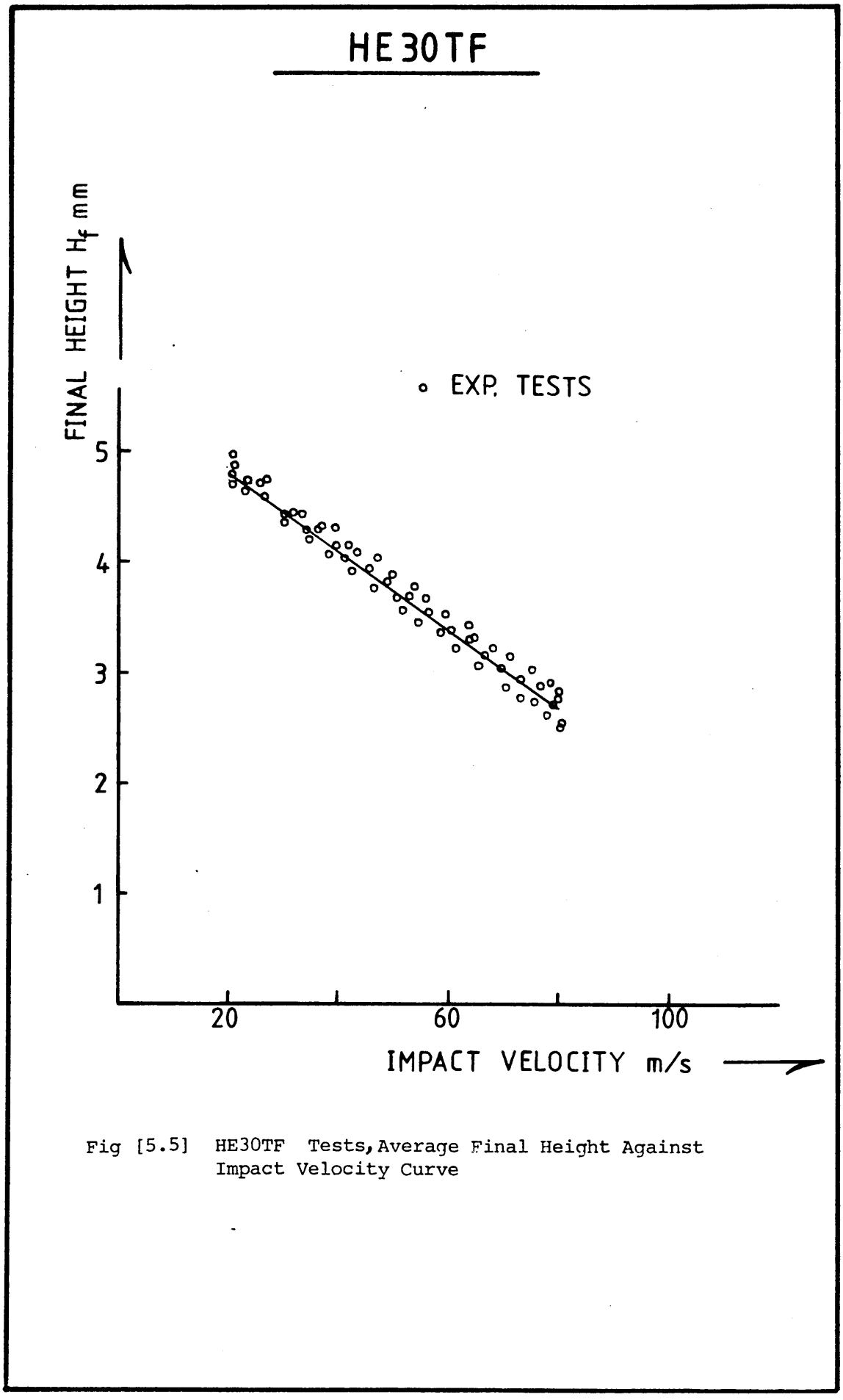

Fig [5.5] HE30TF Tests, Average Final Height Against Impact Velocity Curve

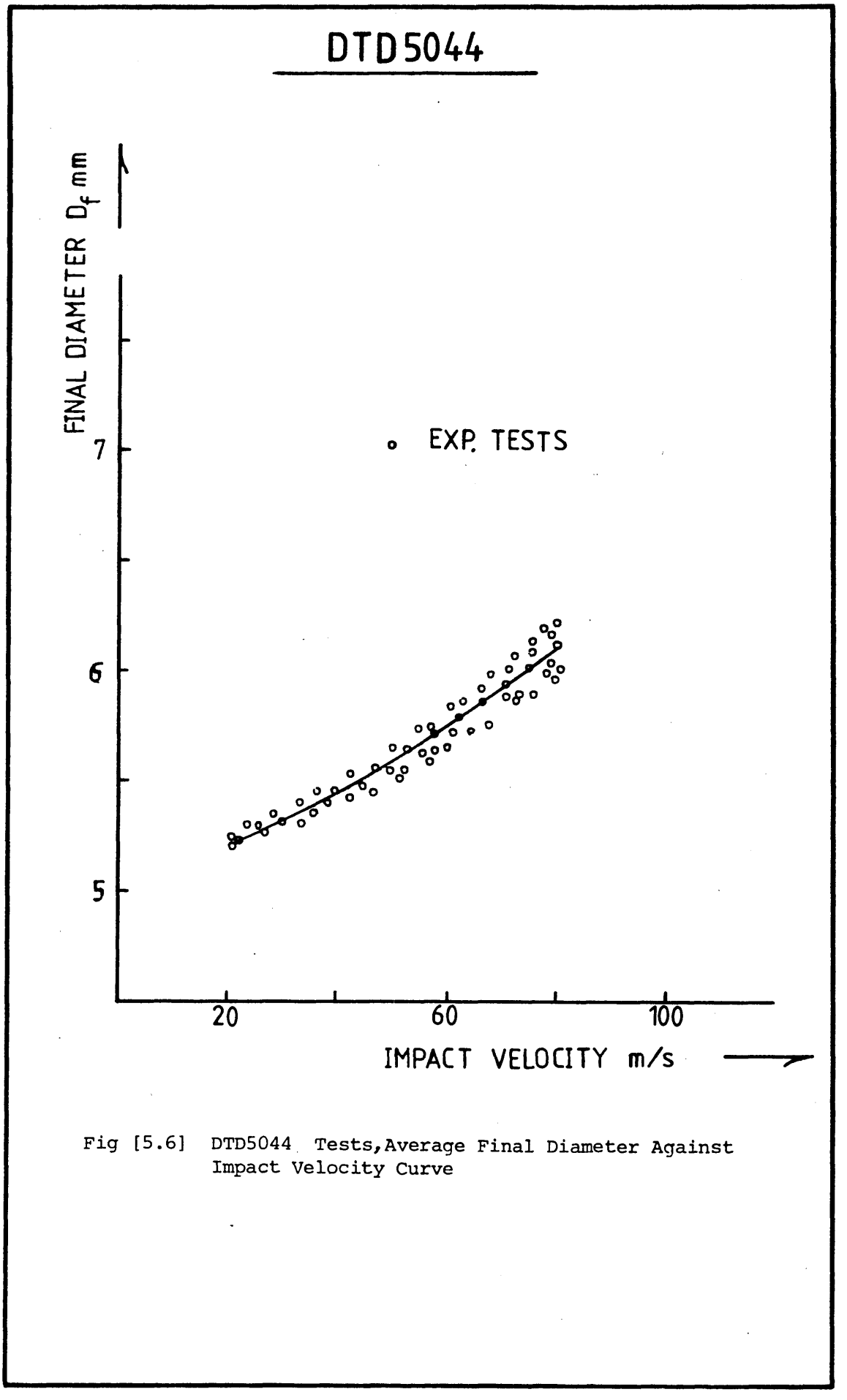

Fig [5.6] DTD5044 Tests, Average Final Diameter Against Impact Velocity Curve

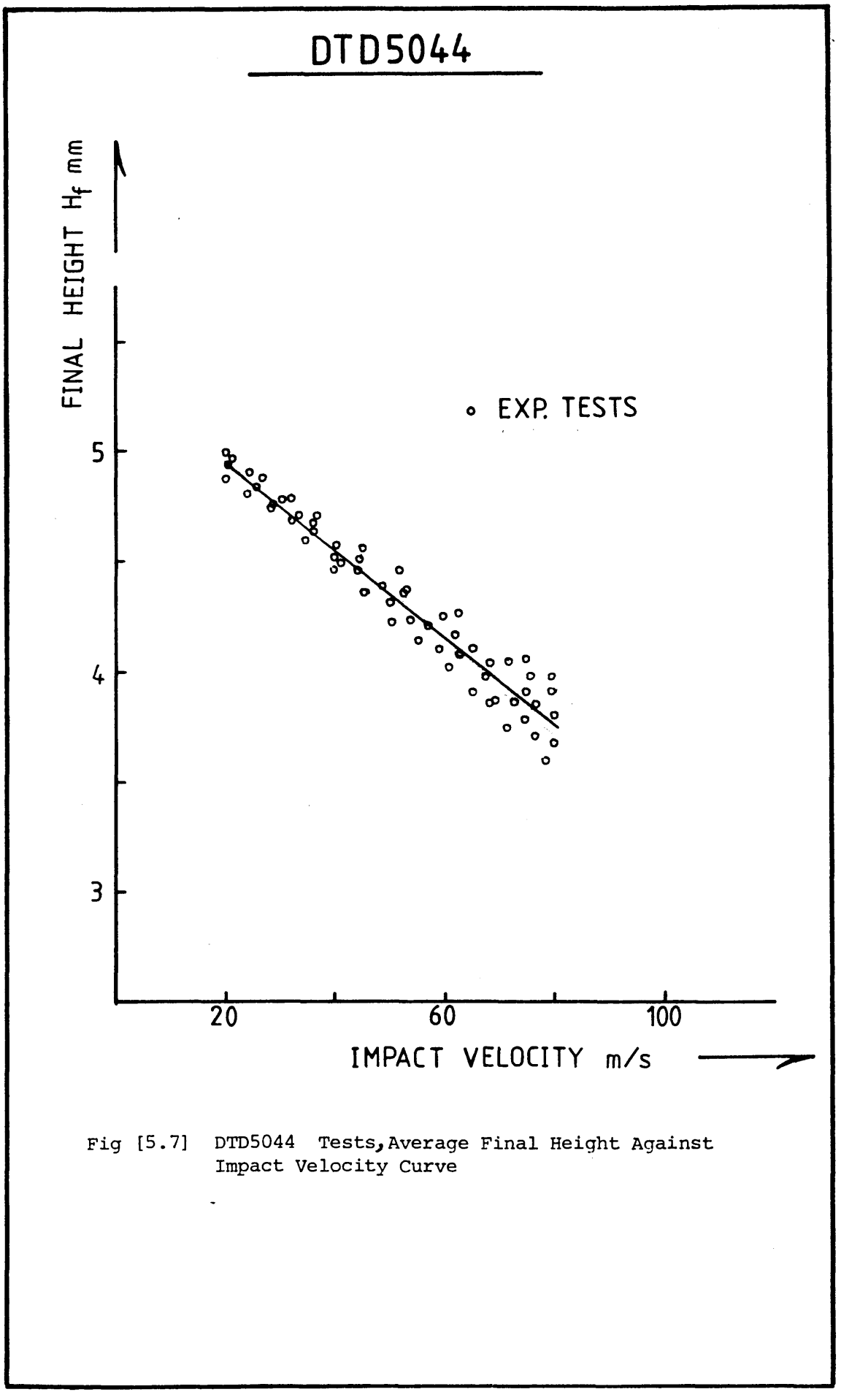

Fig [5.7] DTD5044 Tests, Average Final Height Against Impact Velocity Curve

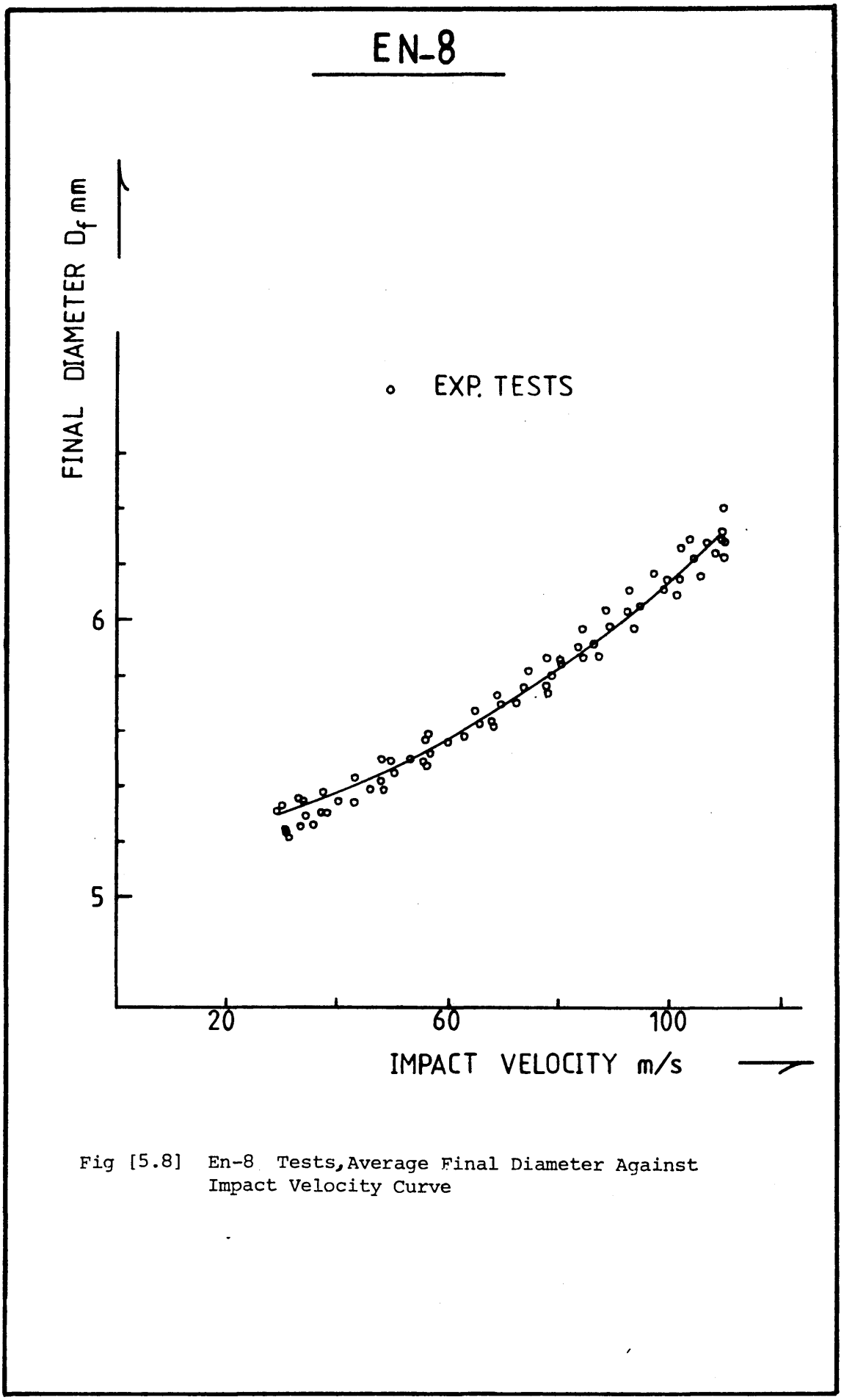

Fig [5.8] En-8 Tests, Average Final Diameter Against Impact Velocity Curve

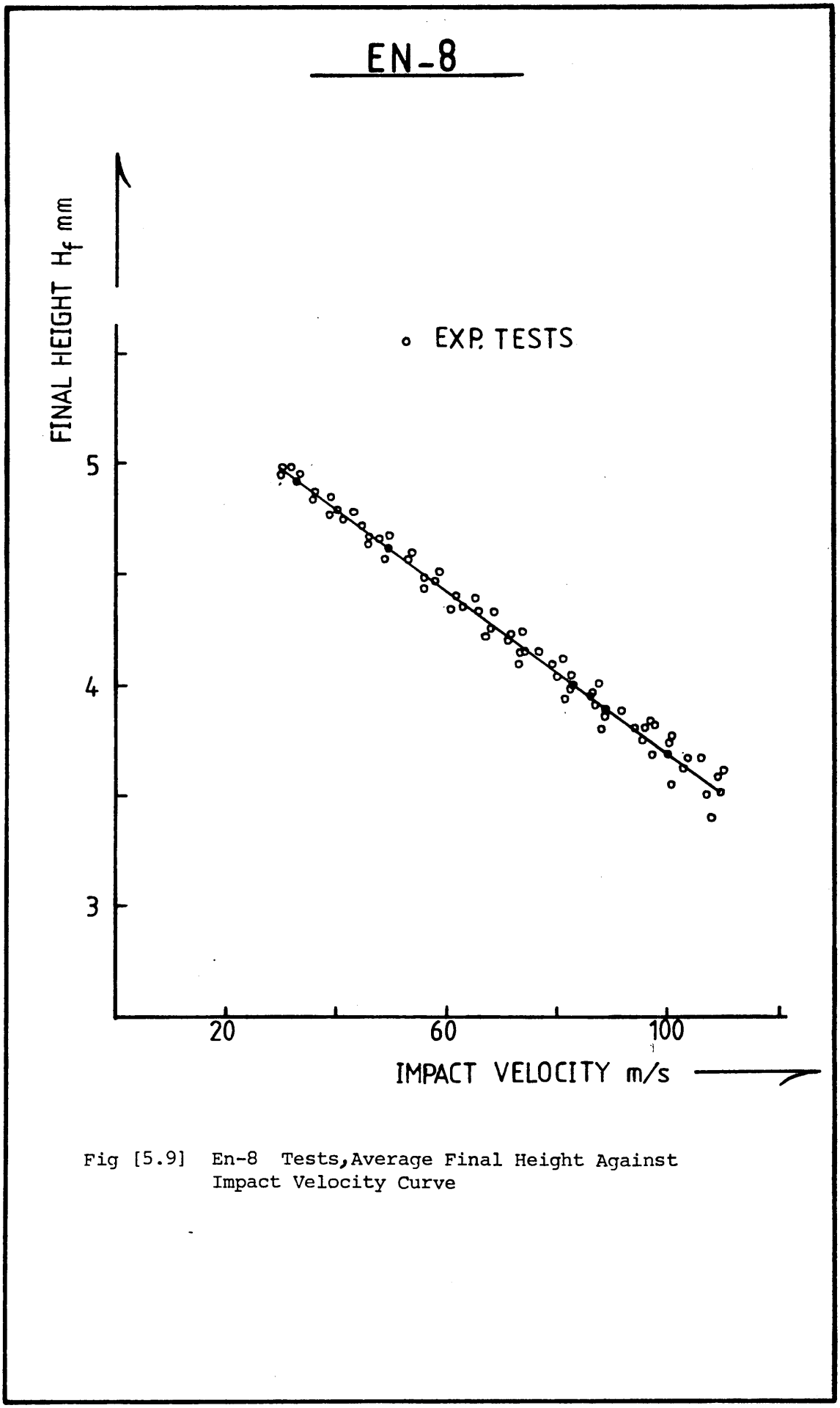

Fig [5.9] En-8 Tests, Average Final Height Against Impact Velocity Curve

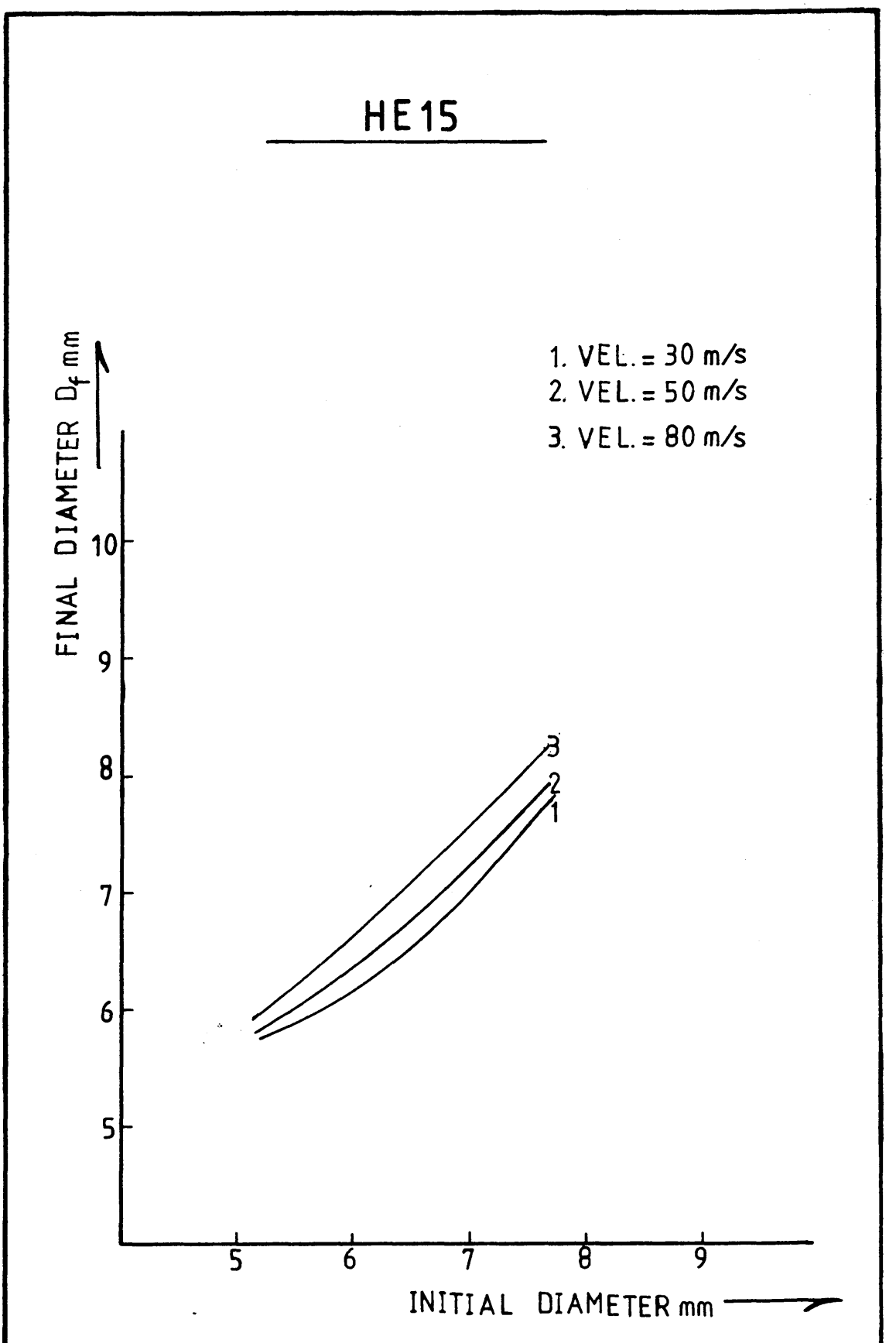

Fig [5.10] HE15, Variation of Final Diameters with Initial Ones at Different Impact Velocities

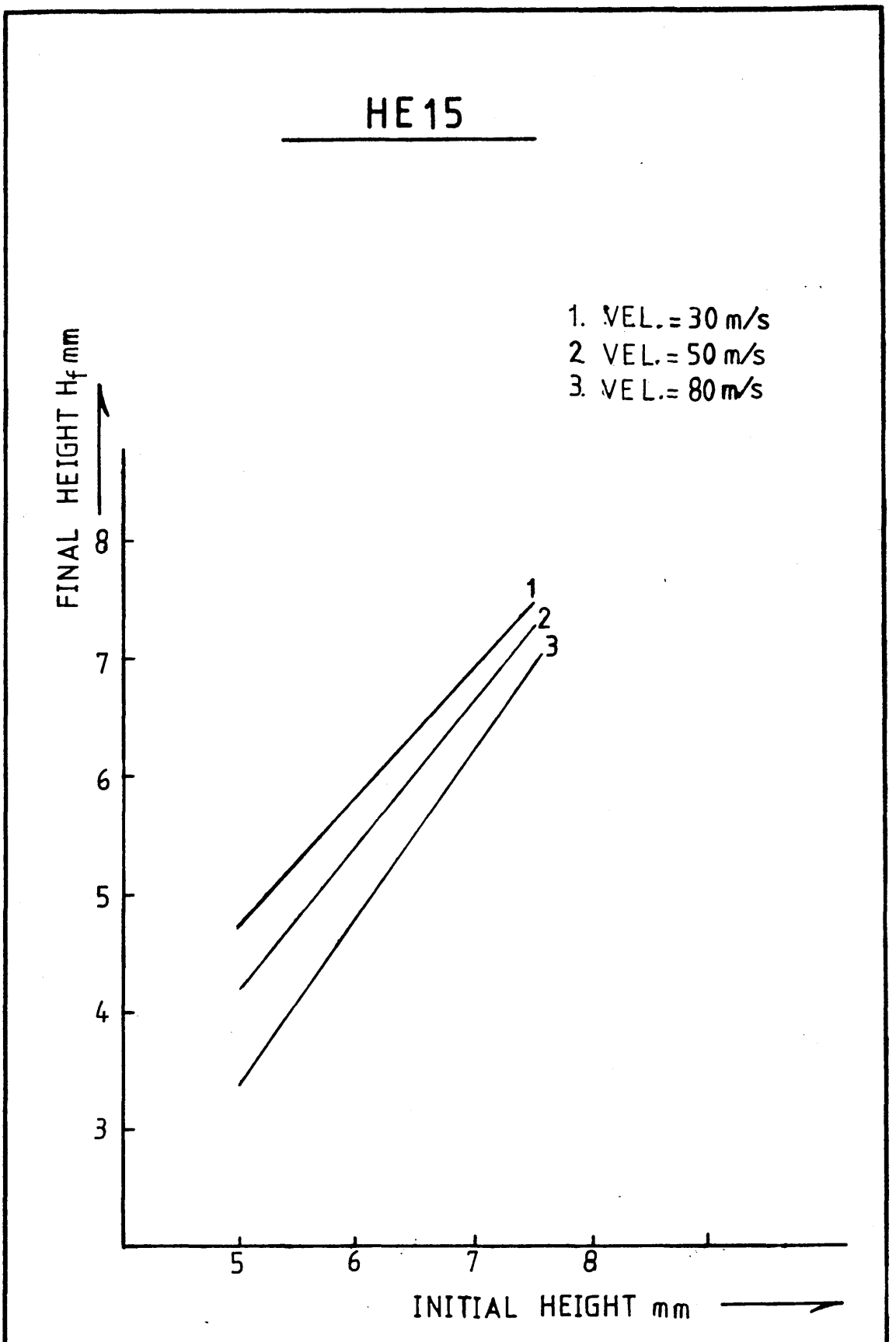

Fig [5.11] HE15, Variation of Final Heights with Initial Ones at Different Impact Velocities

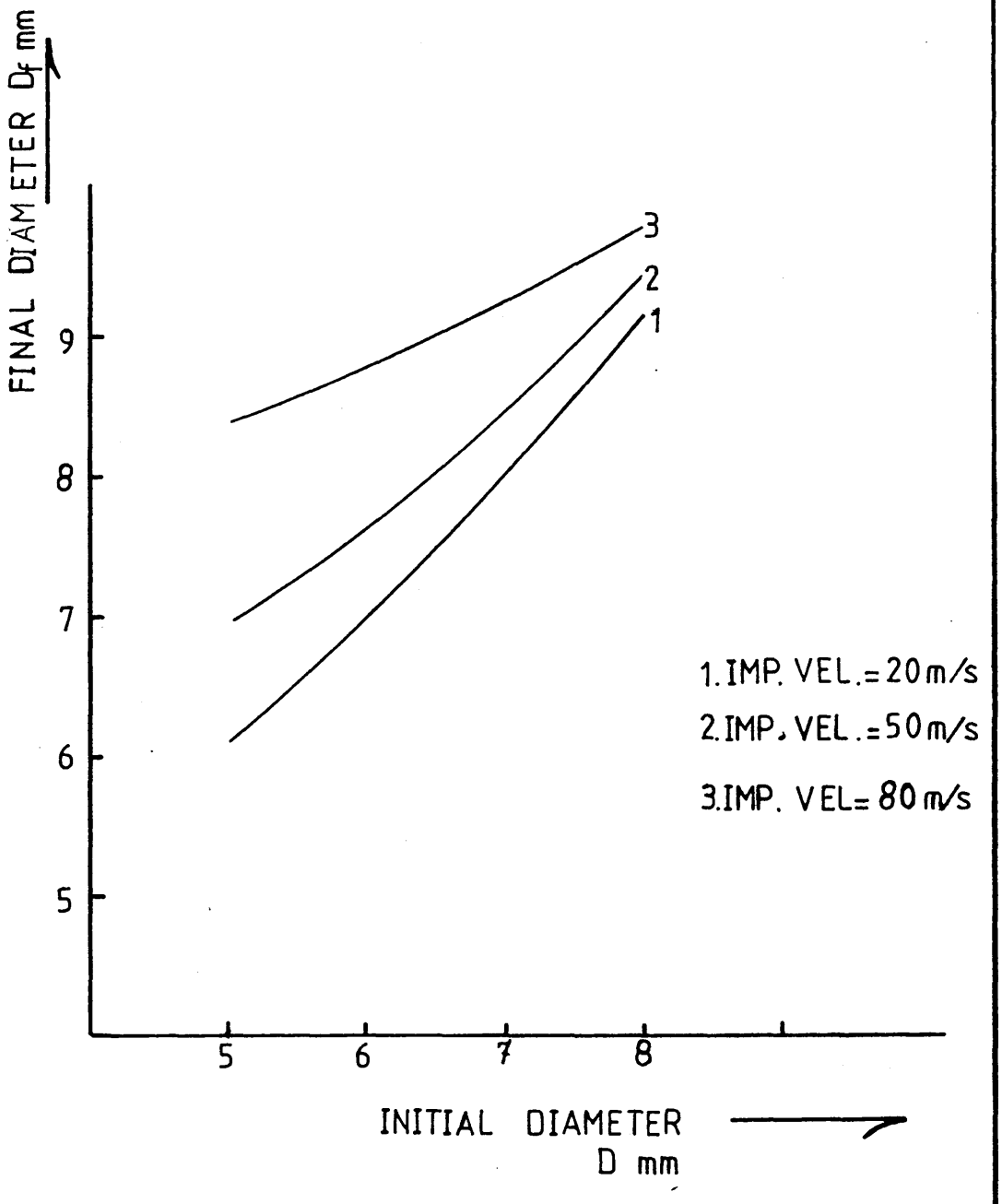

Fig [5.12] HE30TF, Variation of Final Diameters with Initial Ones at Different Impact Velocities

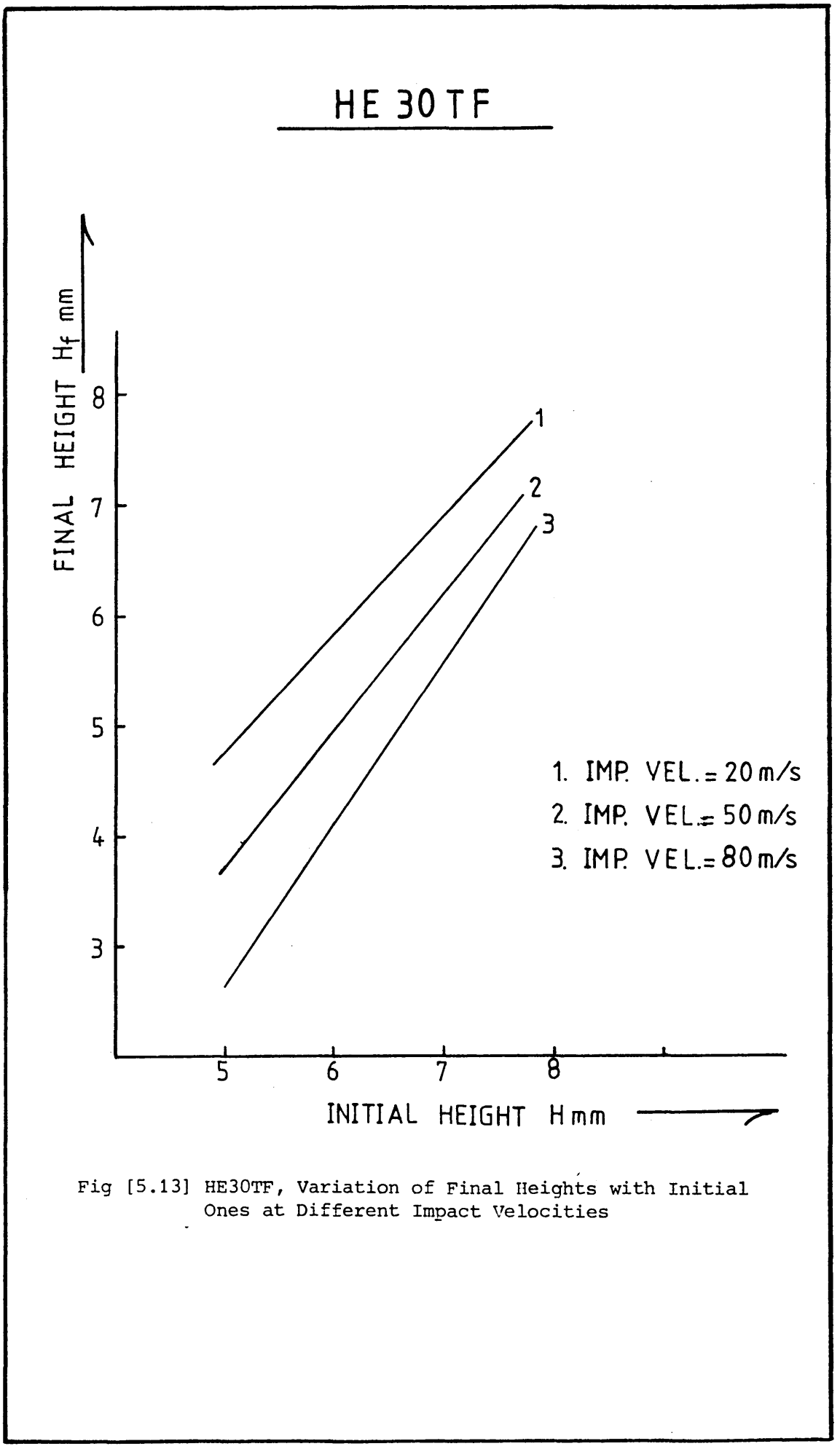

Fig [5.13] HE30TF, Variation of Final Heights with Initial Ones at Different Impact Velocities

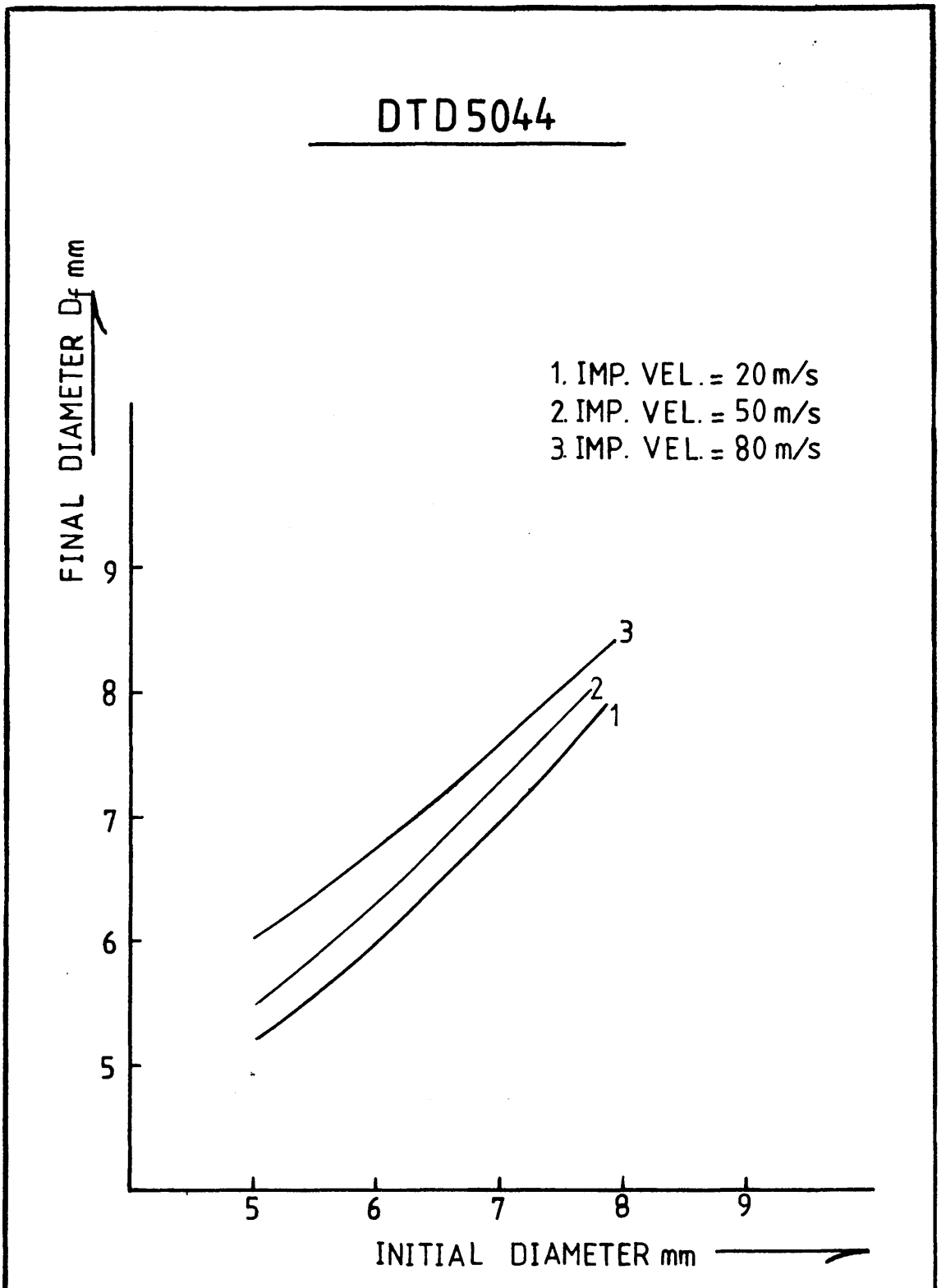

Fig [5.14] DTD5044, Variation of Final Diameters with Initial Ones at Different Impact Velocities

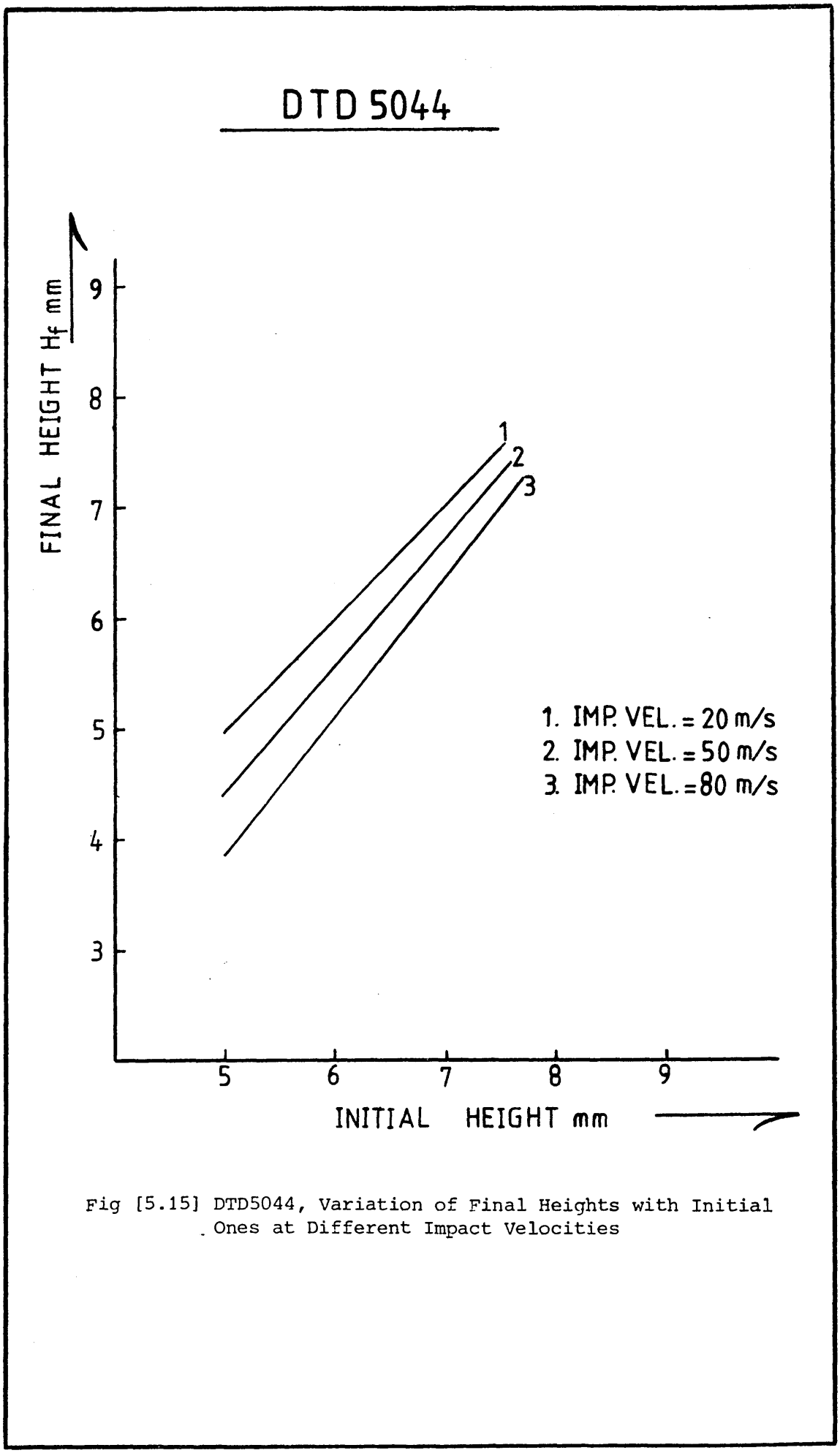

Fig [5.15] DTD5044, Variation of Final Heights with Initial Ones at Different Impact Velocities

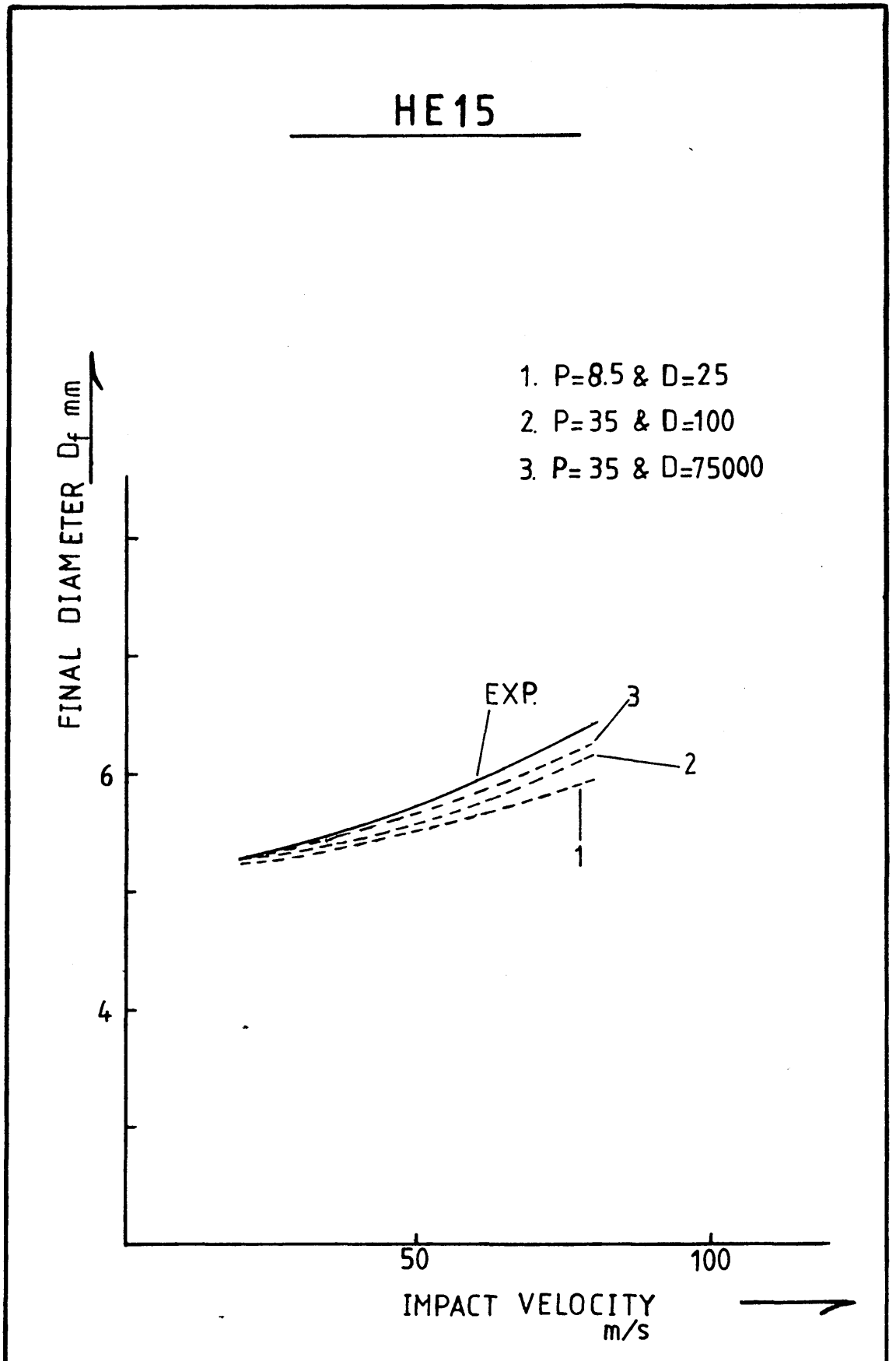

Fig [5.16] HE15, Variation of Final Diameter with Impact Velocity for Various P and D Combinations

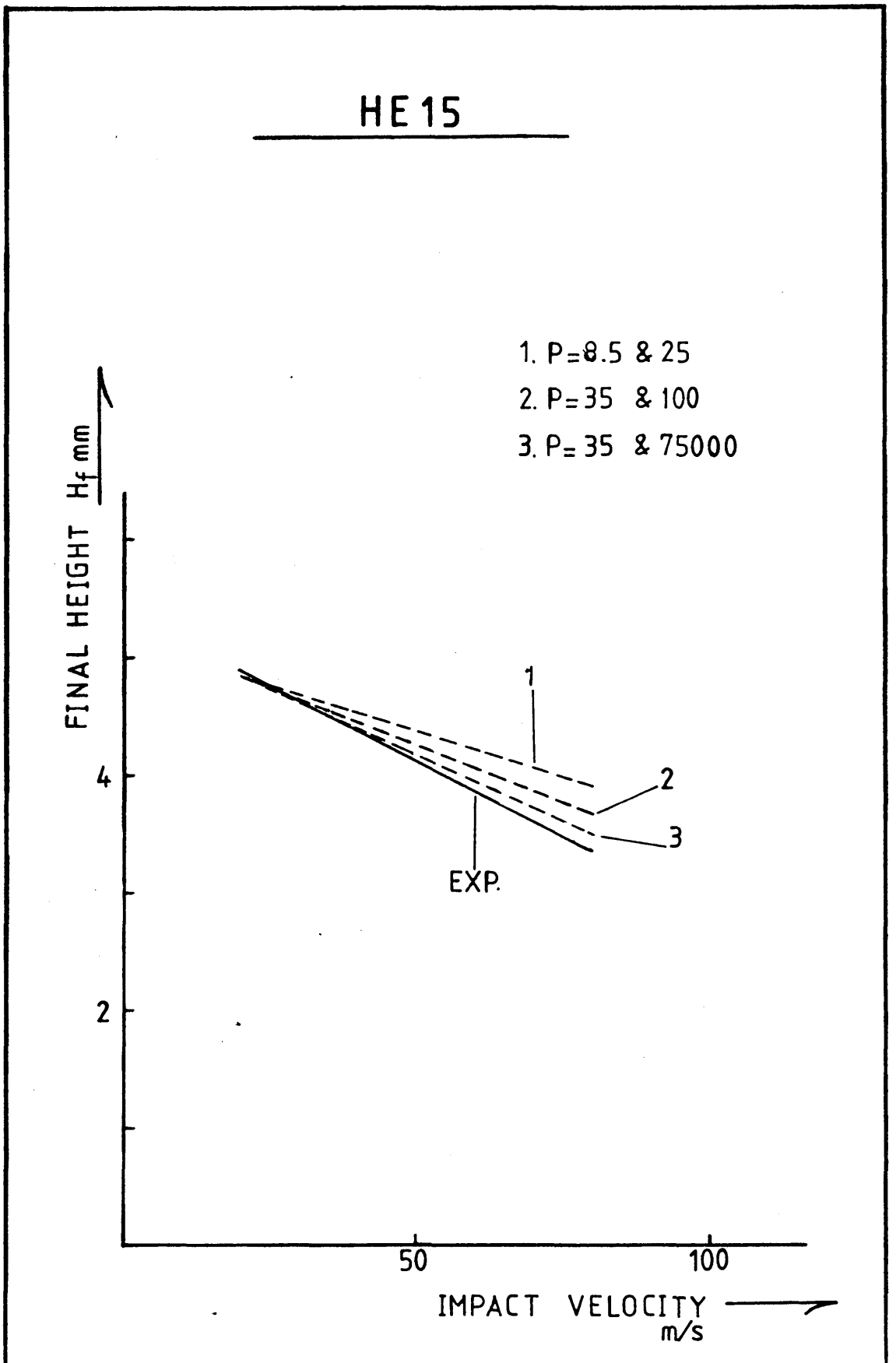

Fig [5.17] HE15, Variation of Final Height with Impact Velocity for Various P and D Combinations

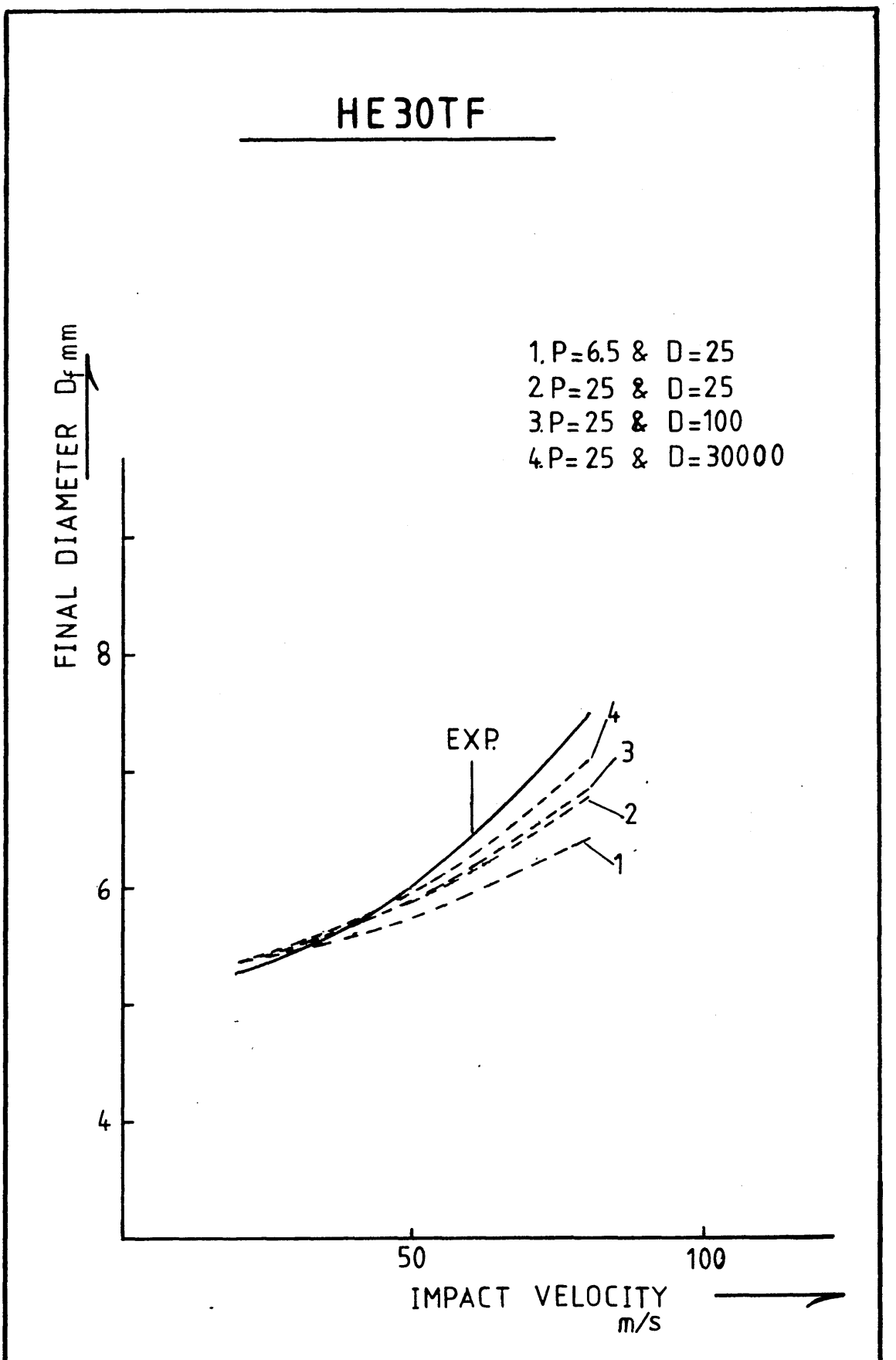

Fig [5.18] HE30TF, Variation of Final Diameter with Impact Velocity for Various P and D Combinations

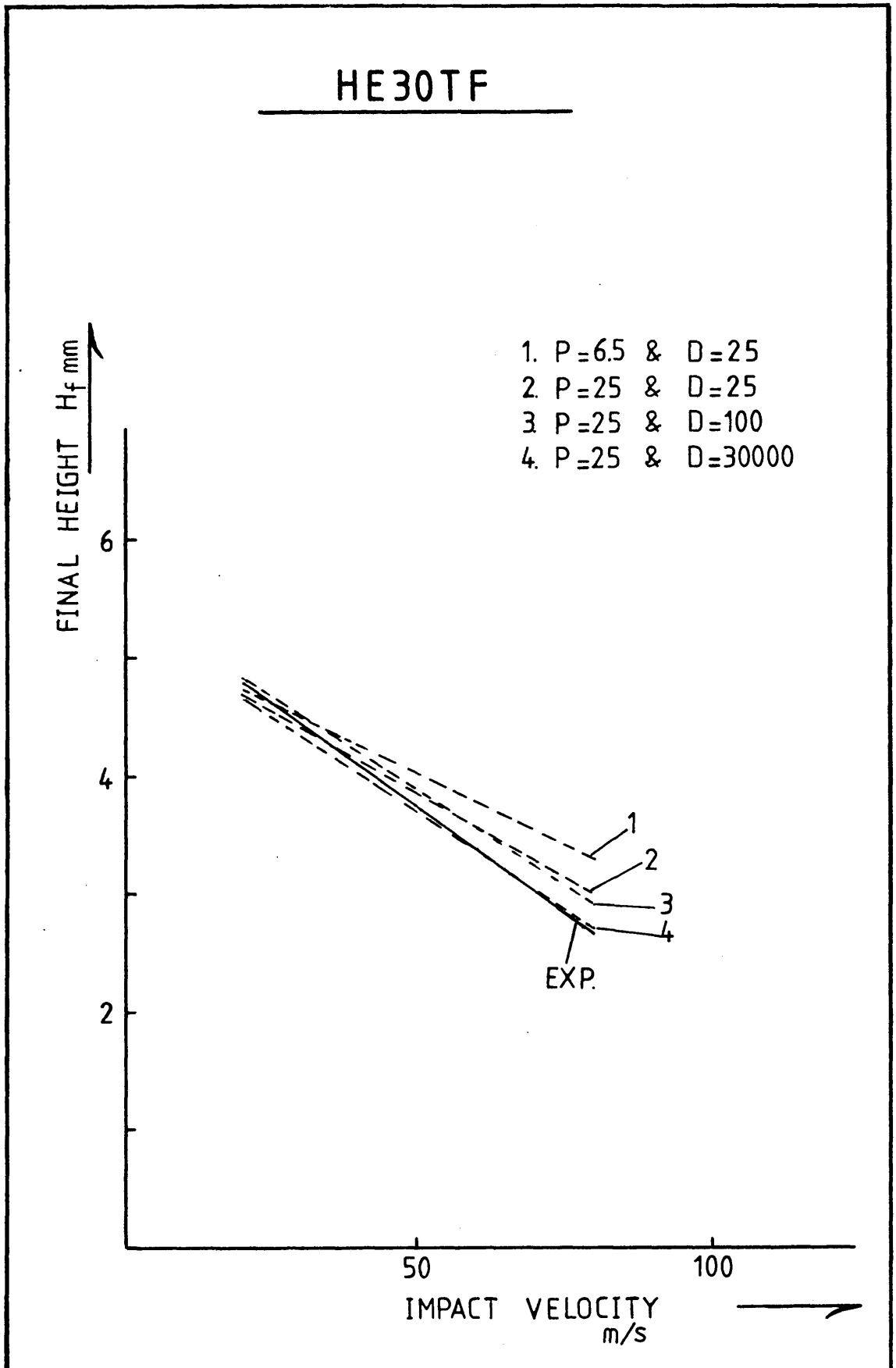

Fig [5.19] HE30TF, Variation of Final Height with Impact Velocity for Various P and D Combinations

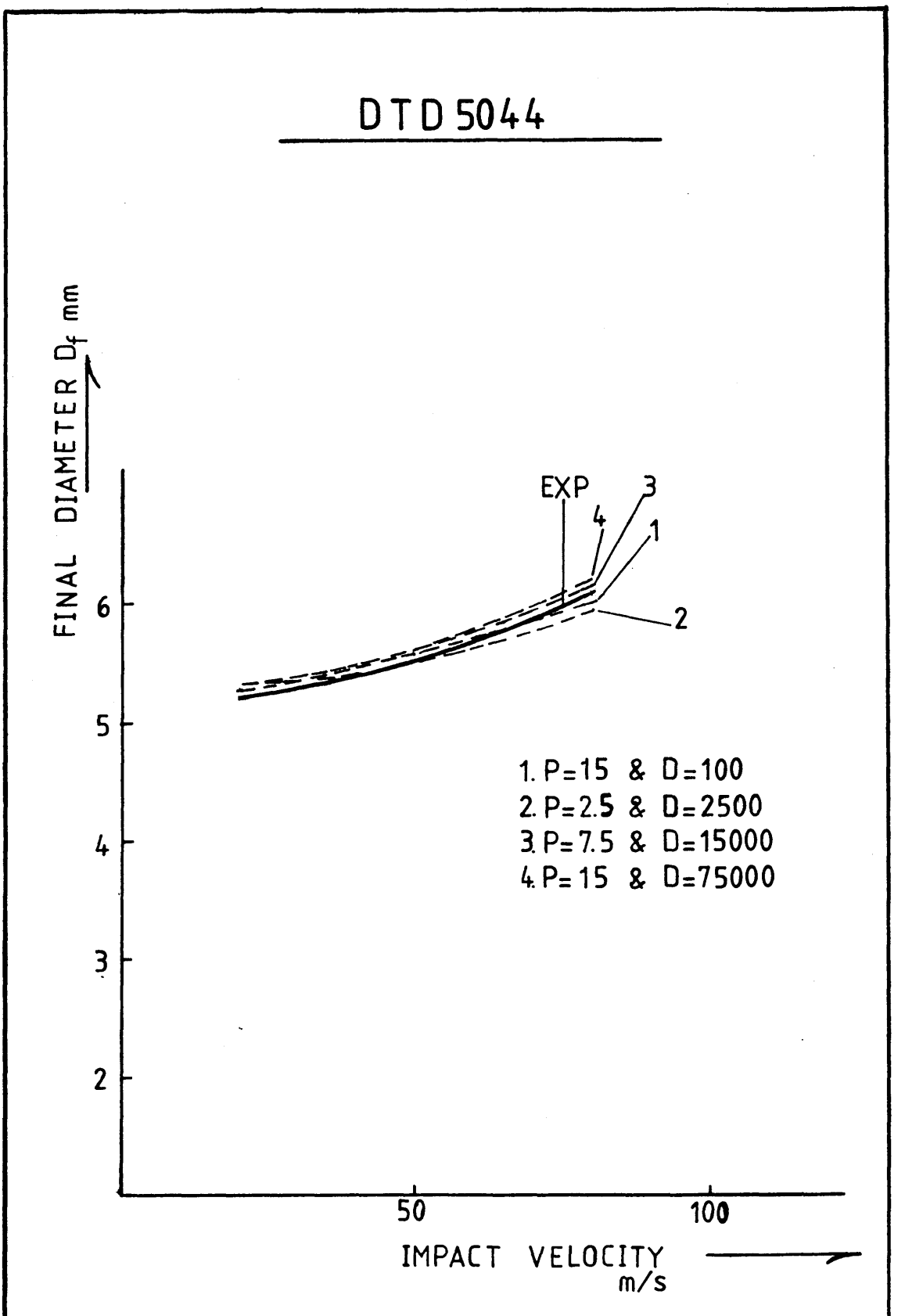

Fig [5.20] DTD5044, Variation of Final Diameter with Impact Velocity for Various P and D Combinations

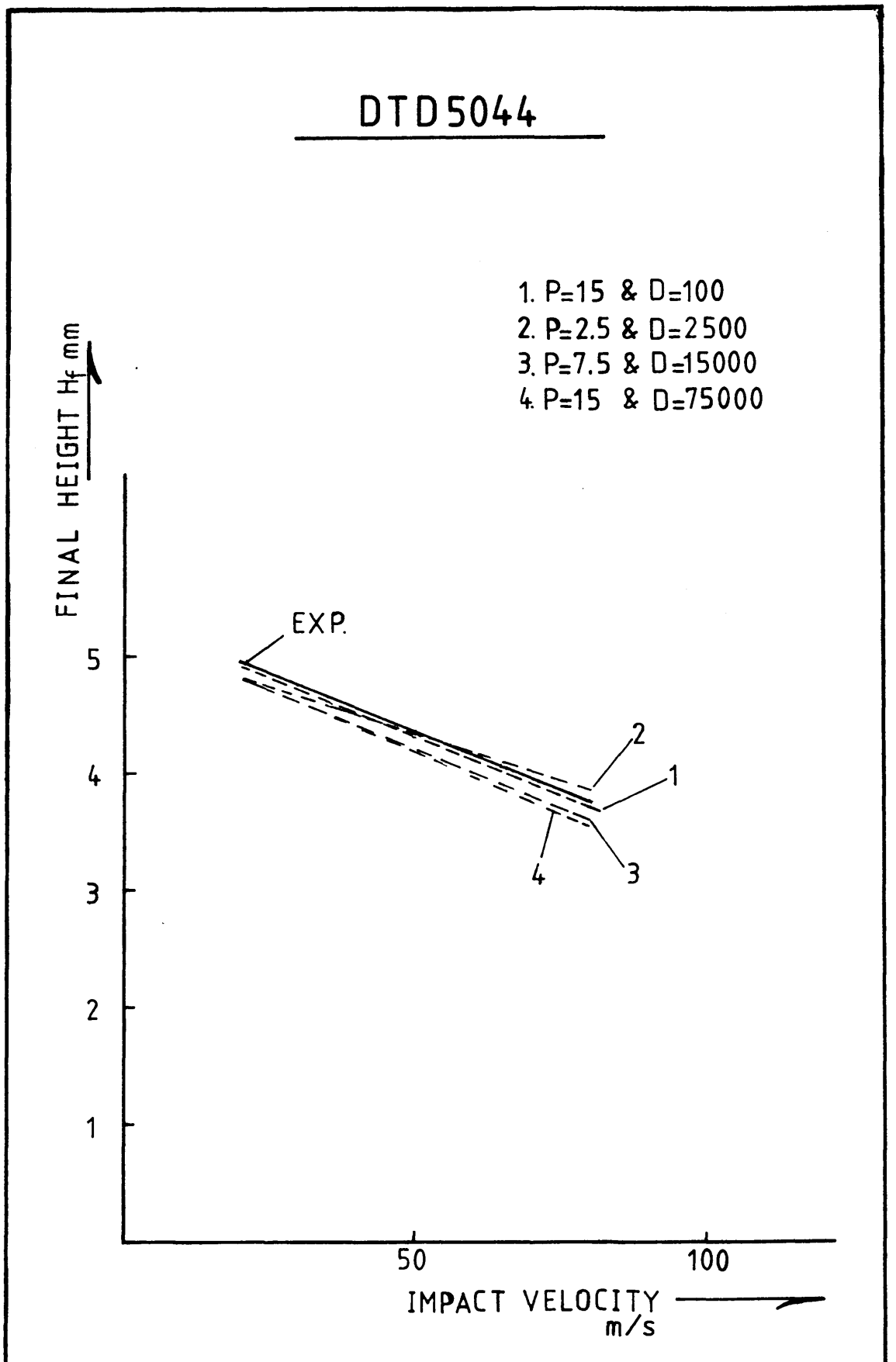

Fig [5.21] DTD5044, Variation of Final Height with Impact Velocity for Various P and D Combinations

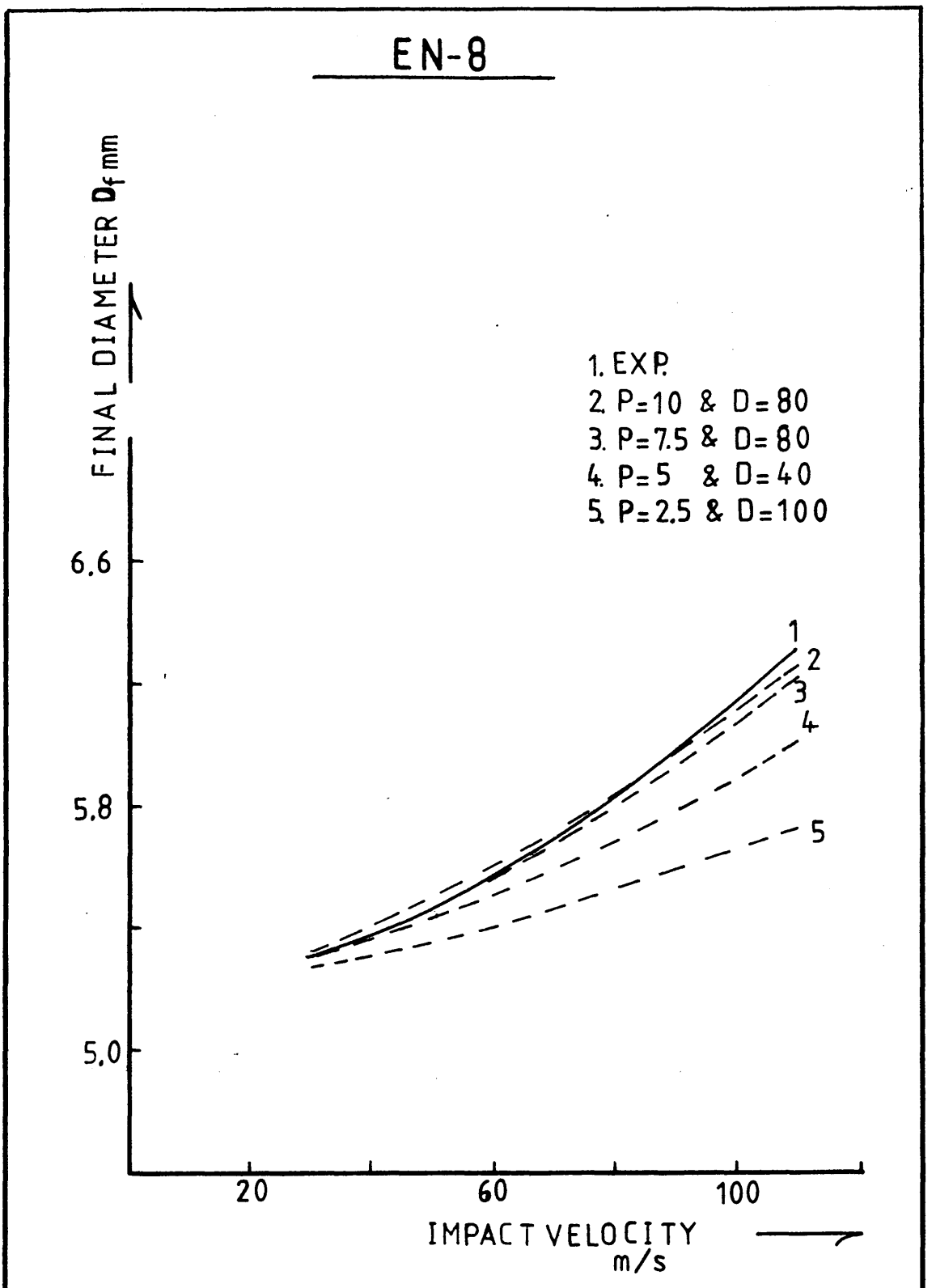

Fig [5.22] En-8, Variation of Final Diameter with Impact Velocity for Various P and D Combinations

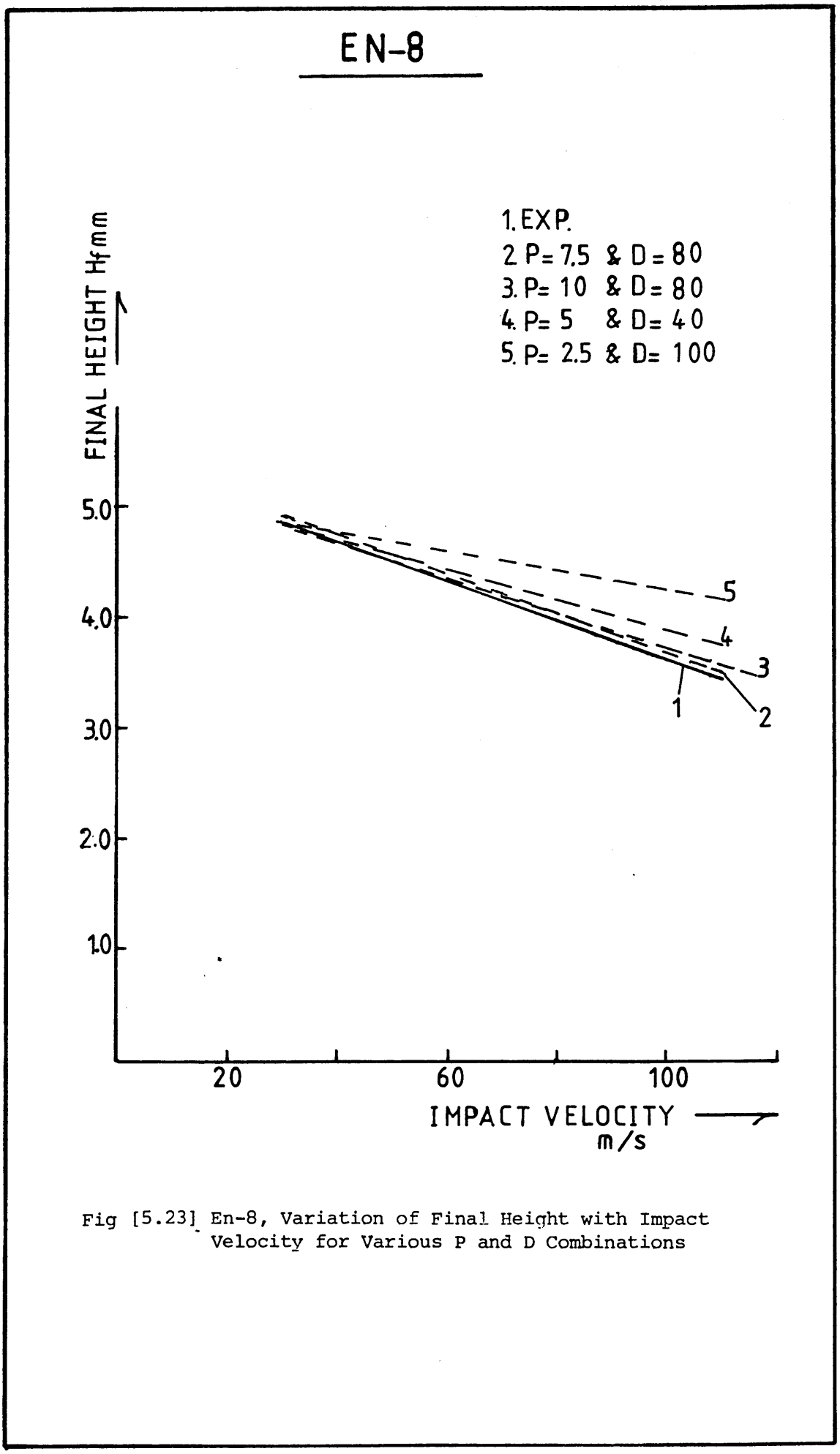

Fig [5.23] En-8, Variation of Final Height with Impact Velocity for Various P and D Combinations

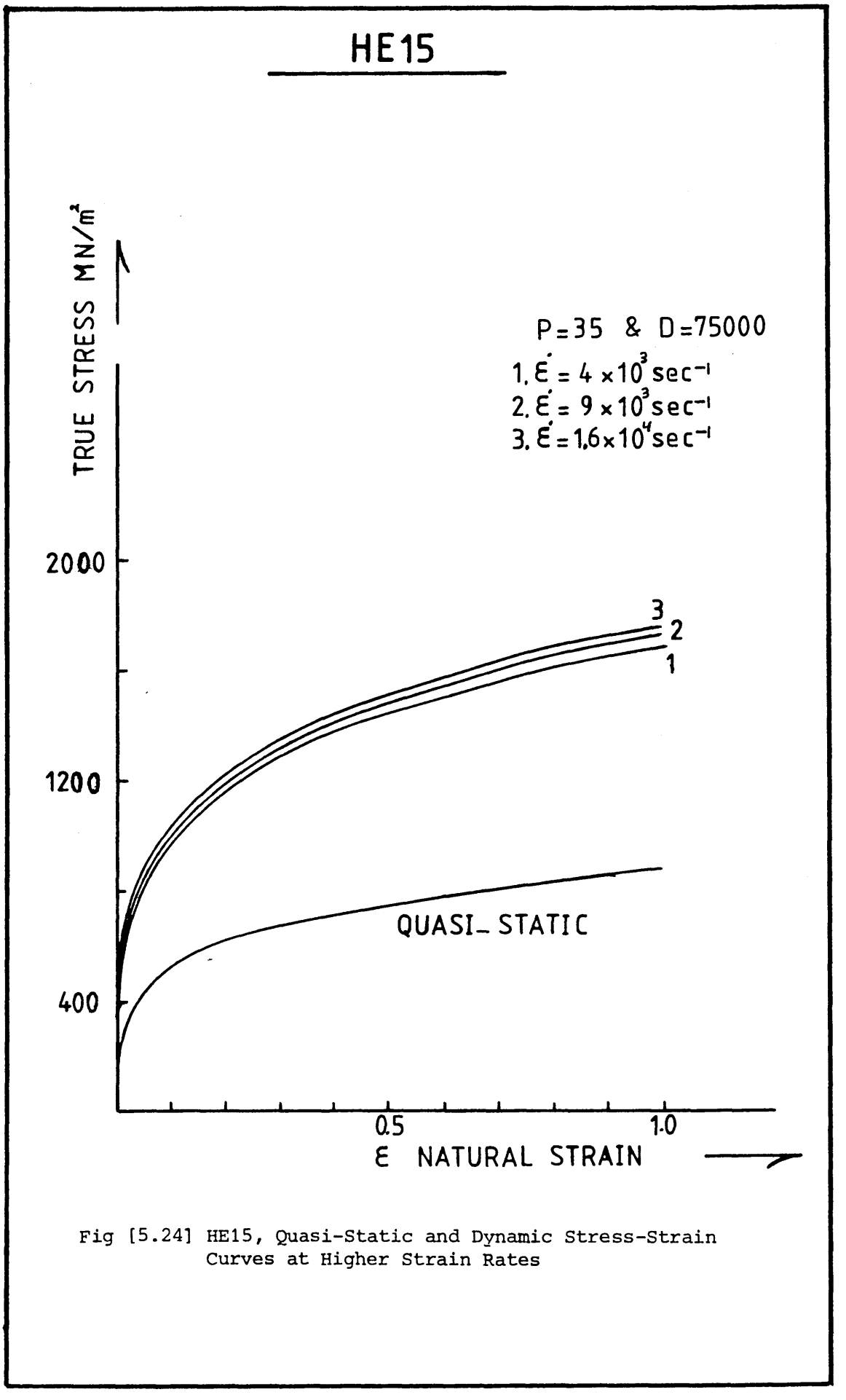

Fig [5.24] HE15, Quasi-Static and Dynamic Stress-Strain Curves at Higher Strain Rates

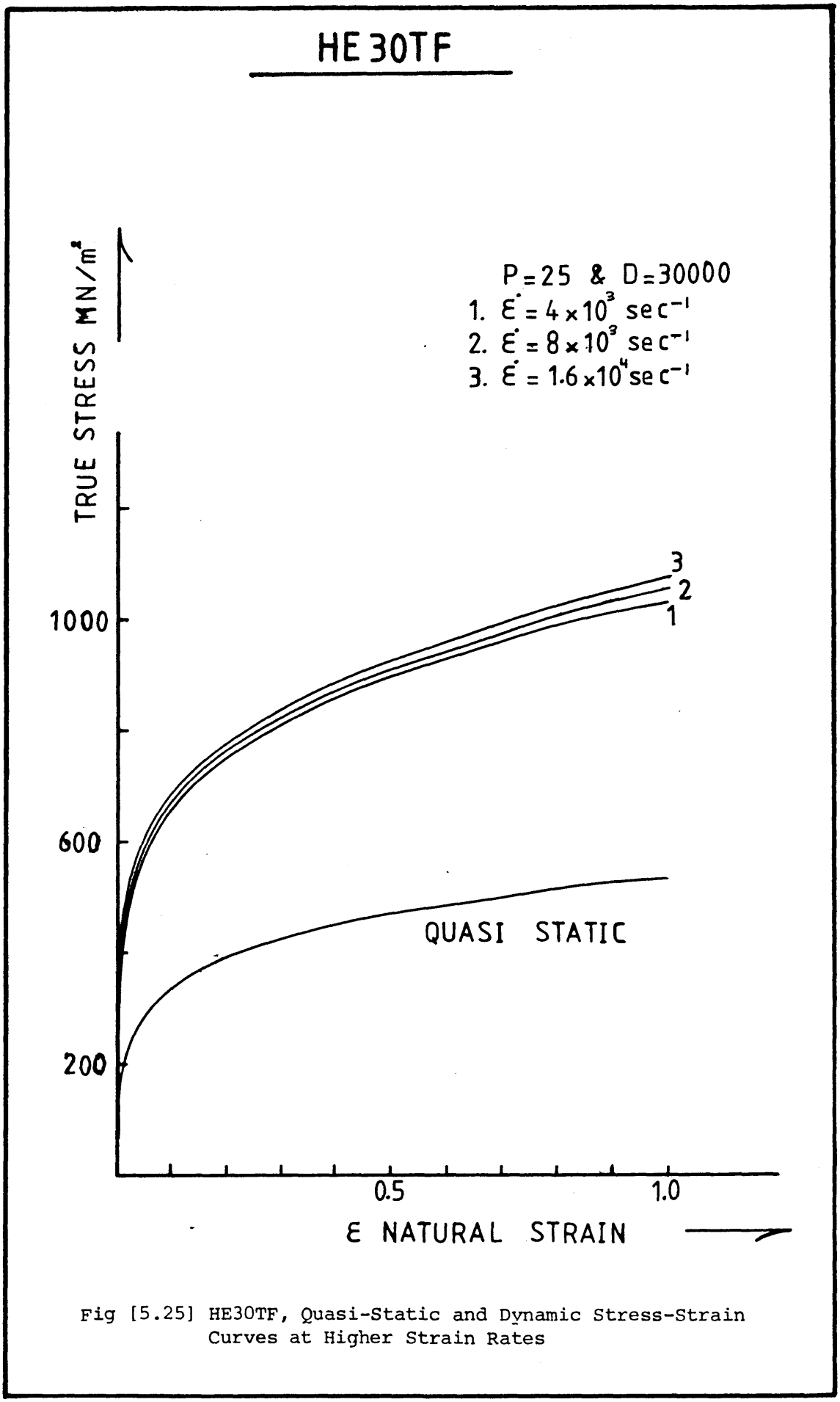

Fig [5.25] HE30TF, Quasi-Static and Dynamic Stress-Strain Curves at Higher Strain Rates

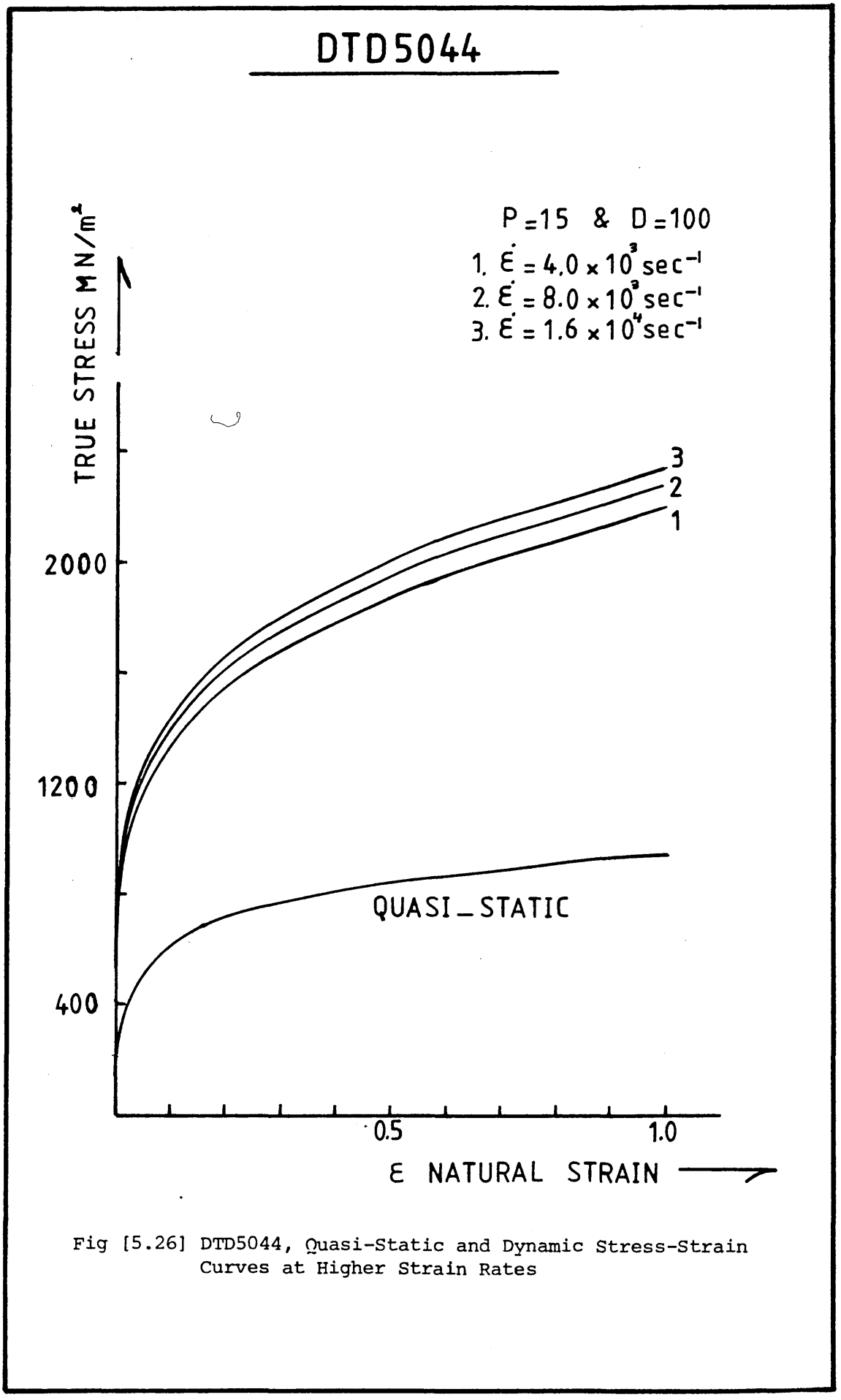

Fig [5.26] DTD5044, Quasi-Static and Dynamic Stress-Strain Curves at Higher Strain Rates

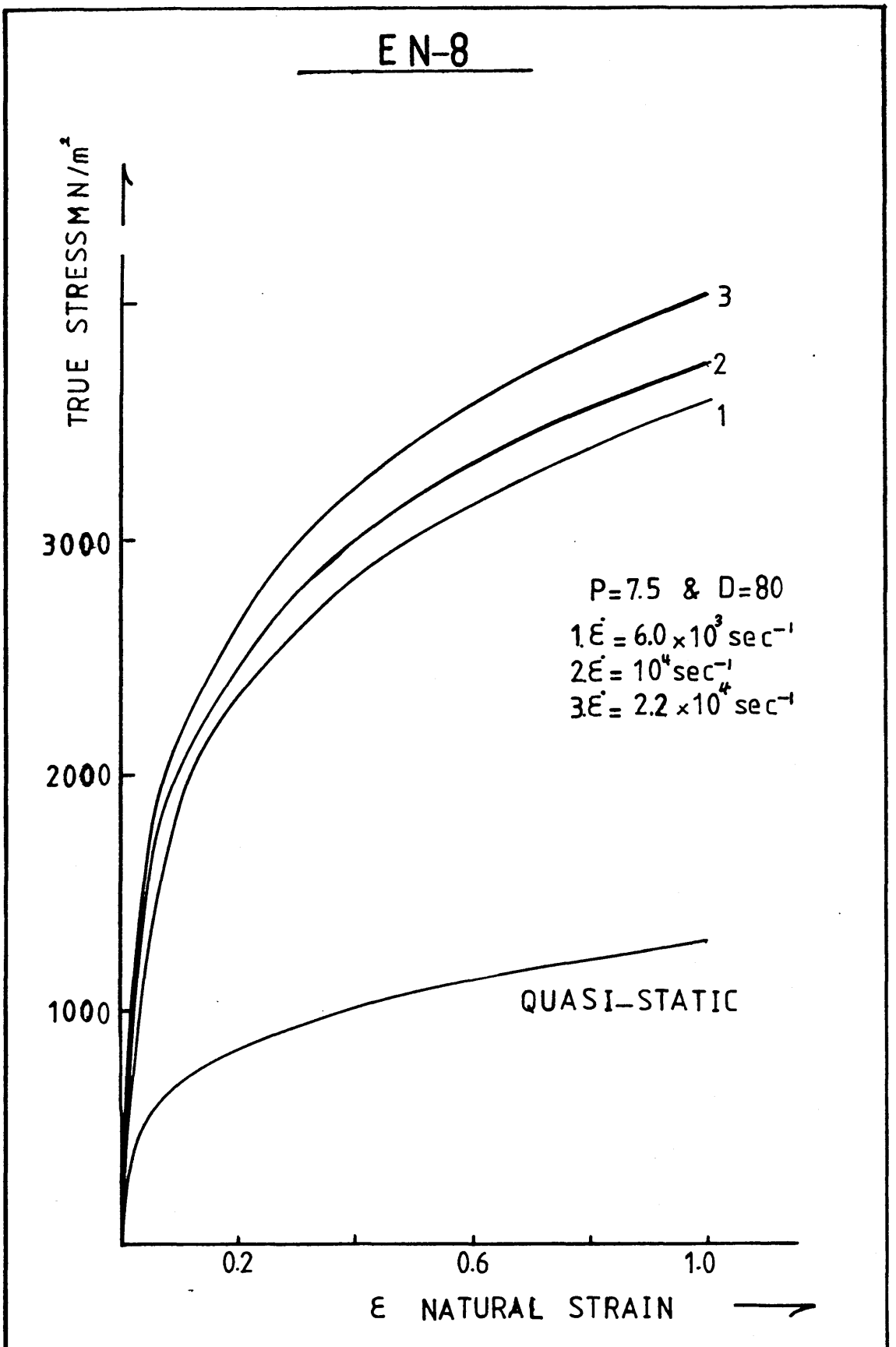

Fig [5.27] En-8, Quasi-Static and Dynamic Stress-Strain Curves at Higher Strain Rates

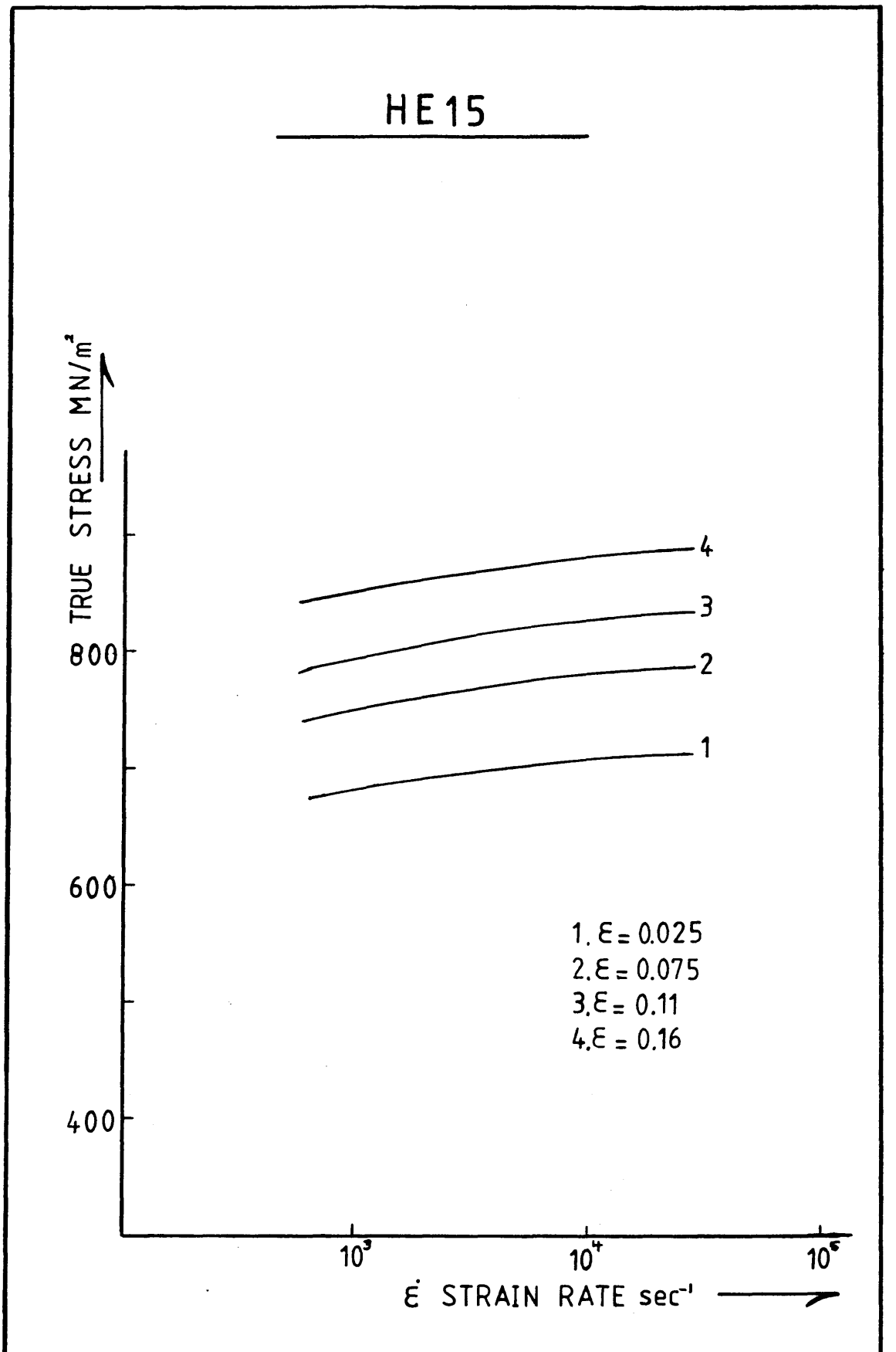

Fig [5.28] Theoretical Variation of Stress with Strain Rate at Different Strains for HE15

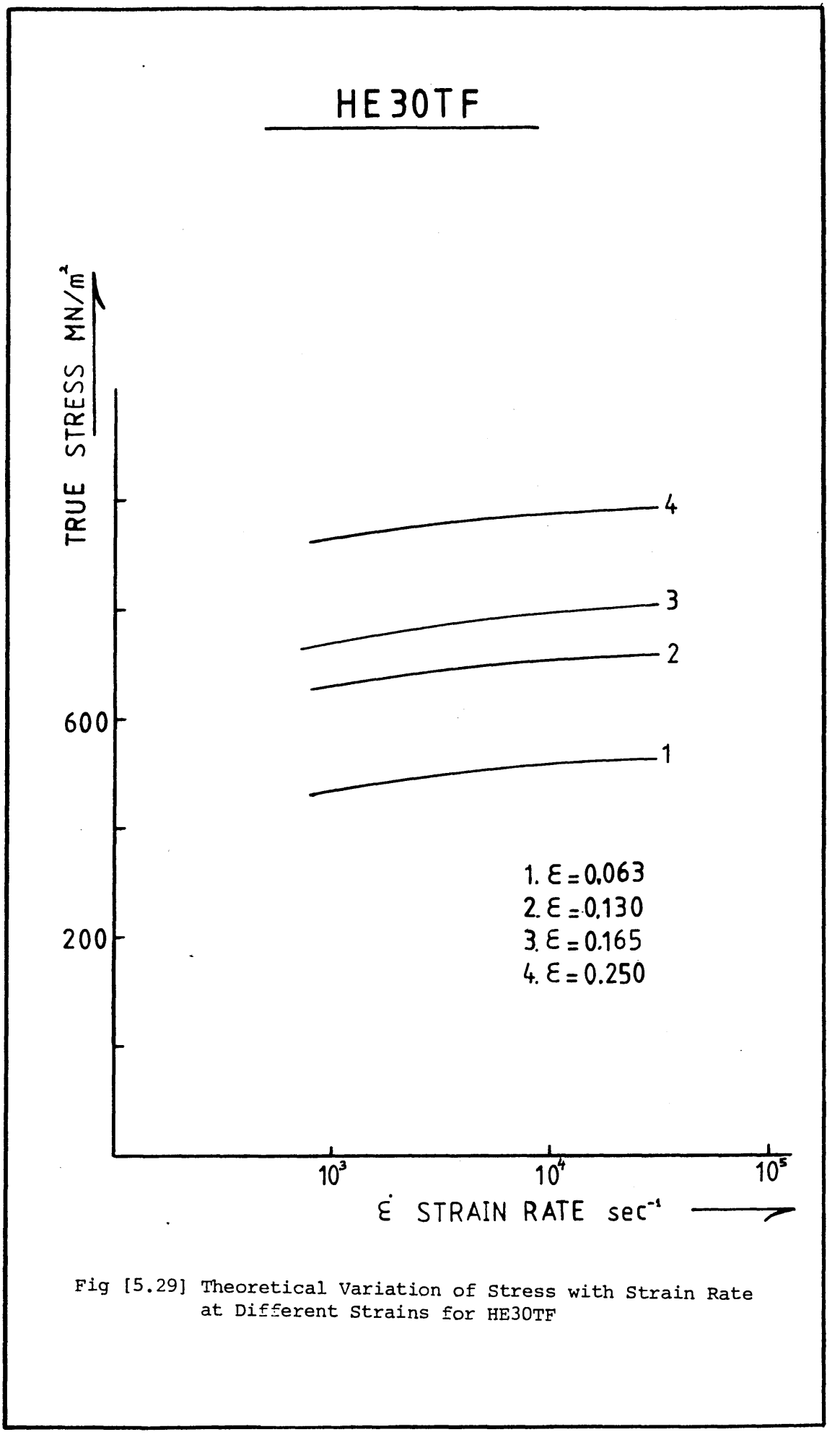

Fig [5.29] Theoretical Variation of Stress with Strain Rate at Different Strains for HE30TF

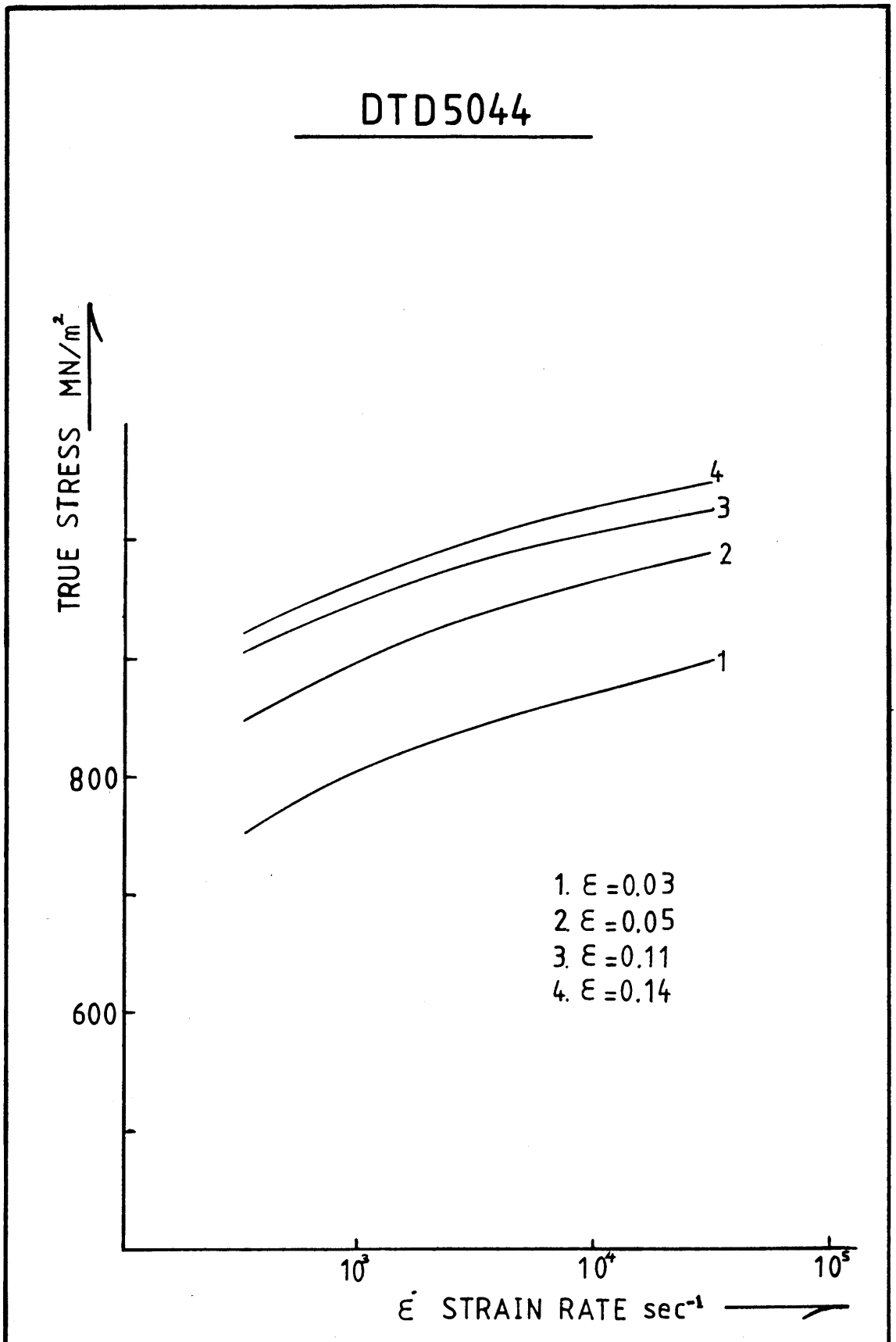

Fig [5.30] Theoretical Variation of Stress with Strain Rate at Different Strains for DTD5044

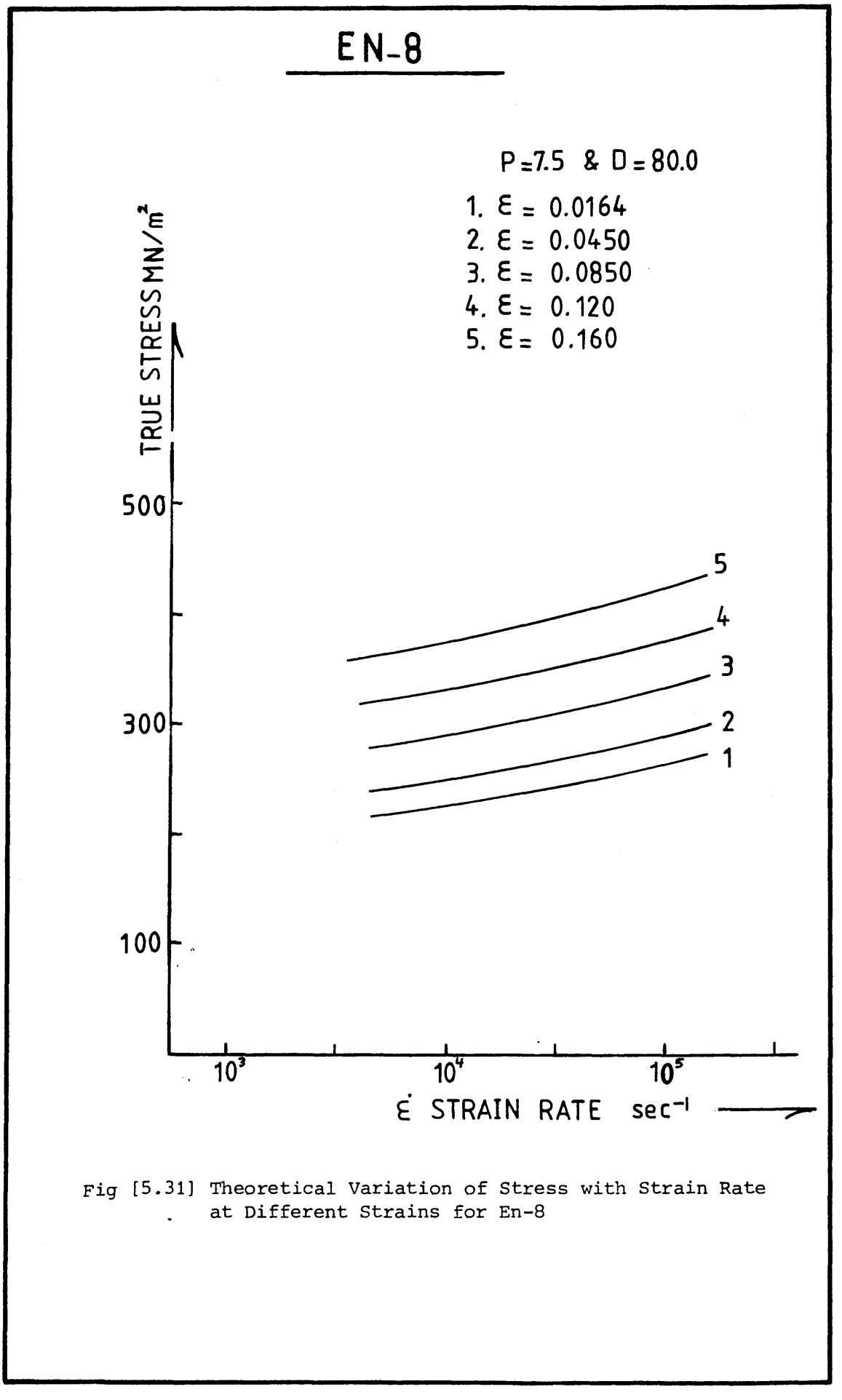

Fig [5.31] Theoretical Variation of Stress with Strain Rate at Different Strains for En-8

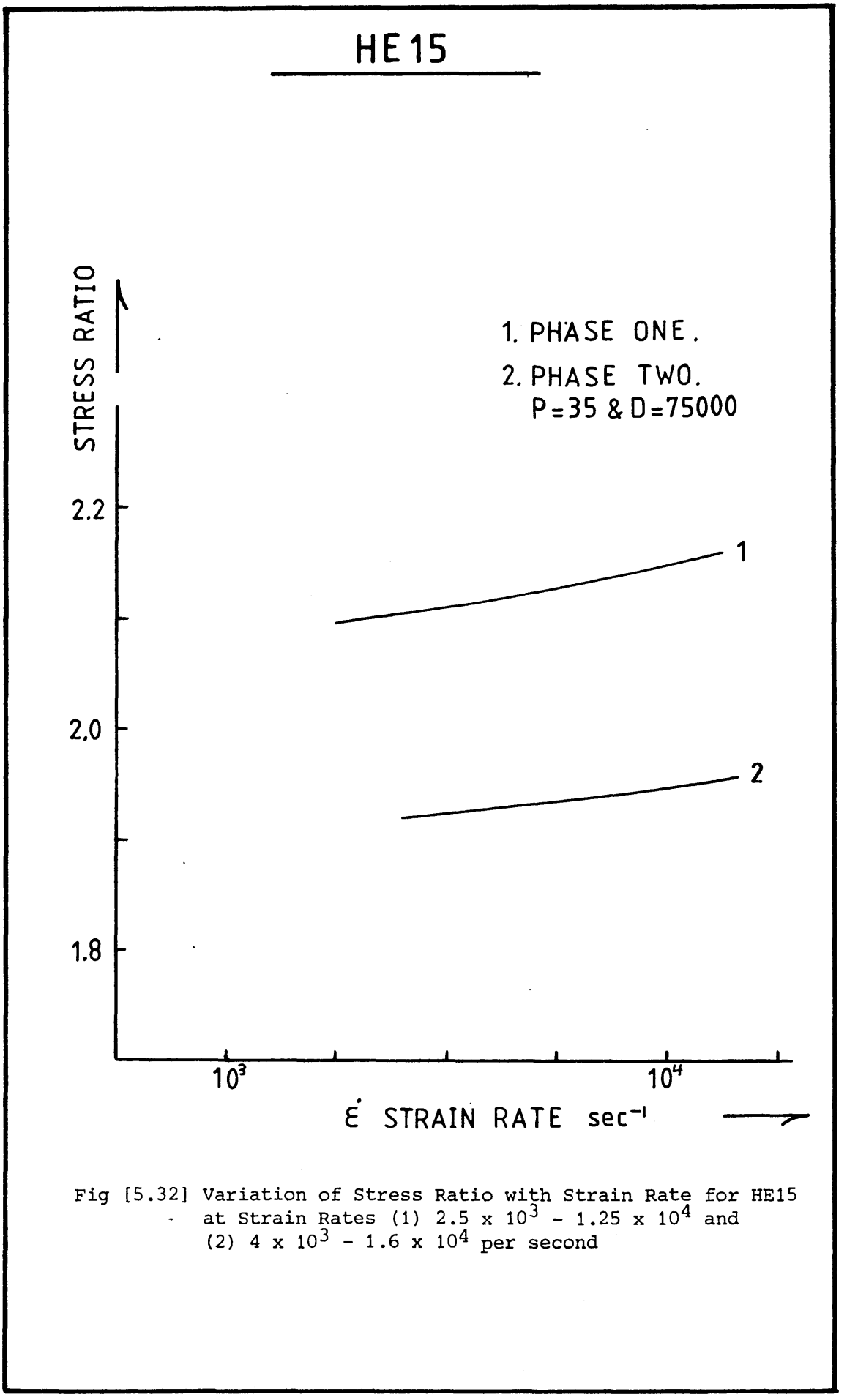

Fig [5.32] Variation of Stress Ratio with Strain Rate for HE15 at Strain Rates (1) $2.5 \times 10^3 - 1.25 \times 10^4$ and (2) $4 \times 10^3 - 1.6 \times 10^4$ per second

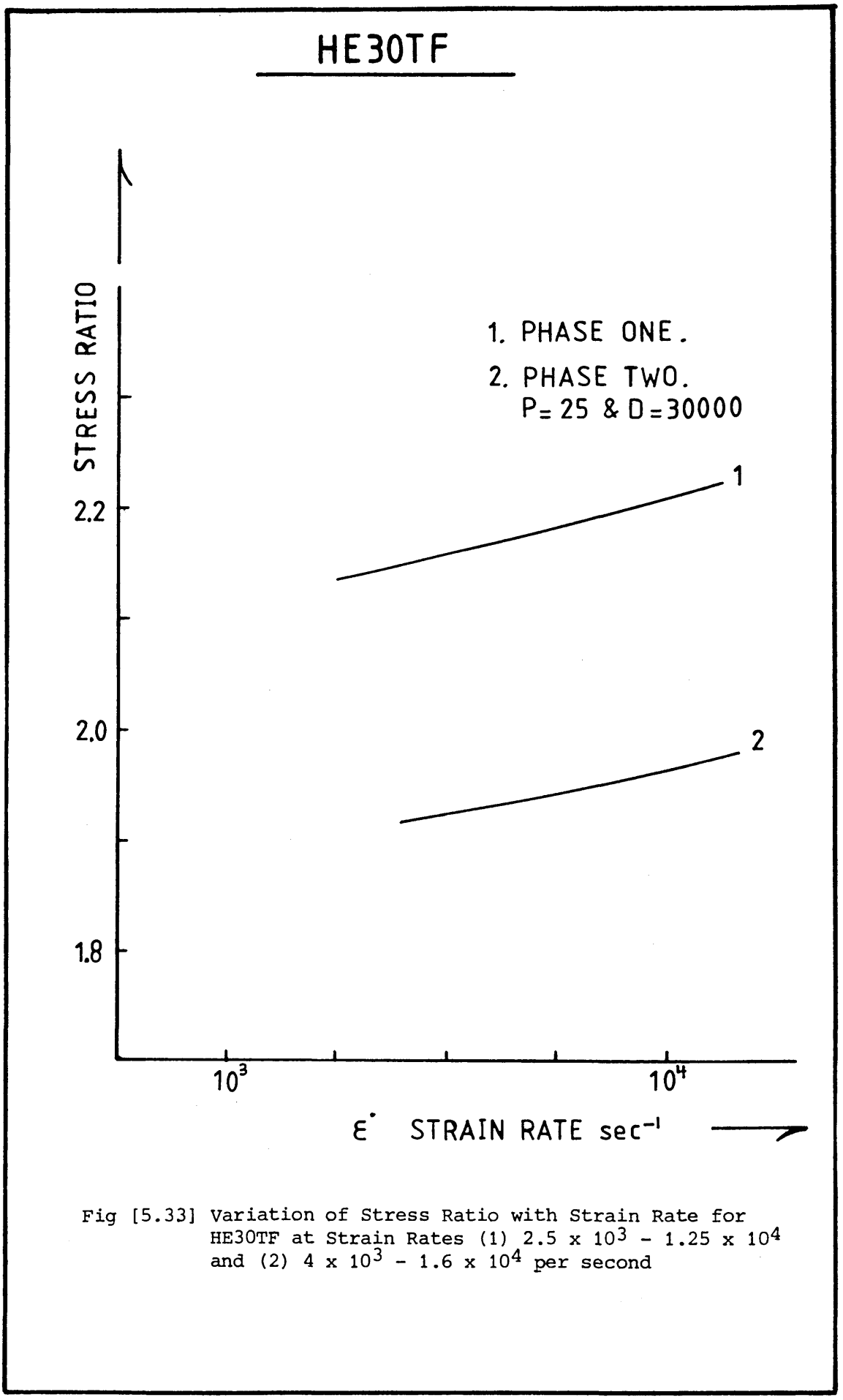

Fig [5.33] Variation of Stress Ratio with Strain Rate for HE30TF at Strain Rates (1) $2.5 \times 10^3 - 1.25 \times 10^4$ and (2) $4 \times 10^3 - 1.6 \times 10^4$ per second

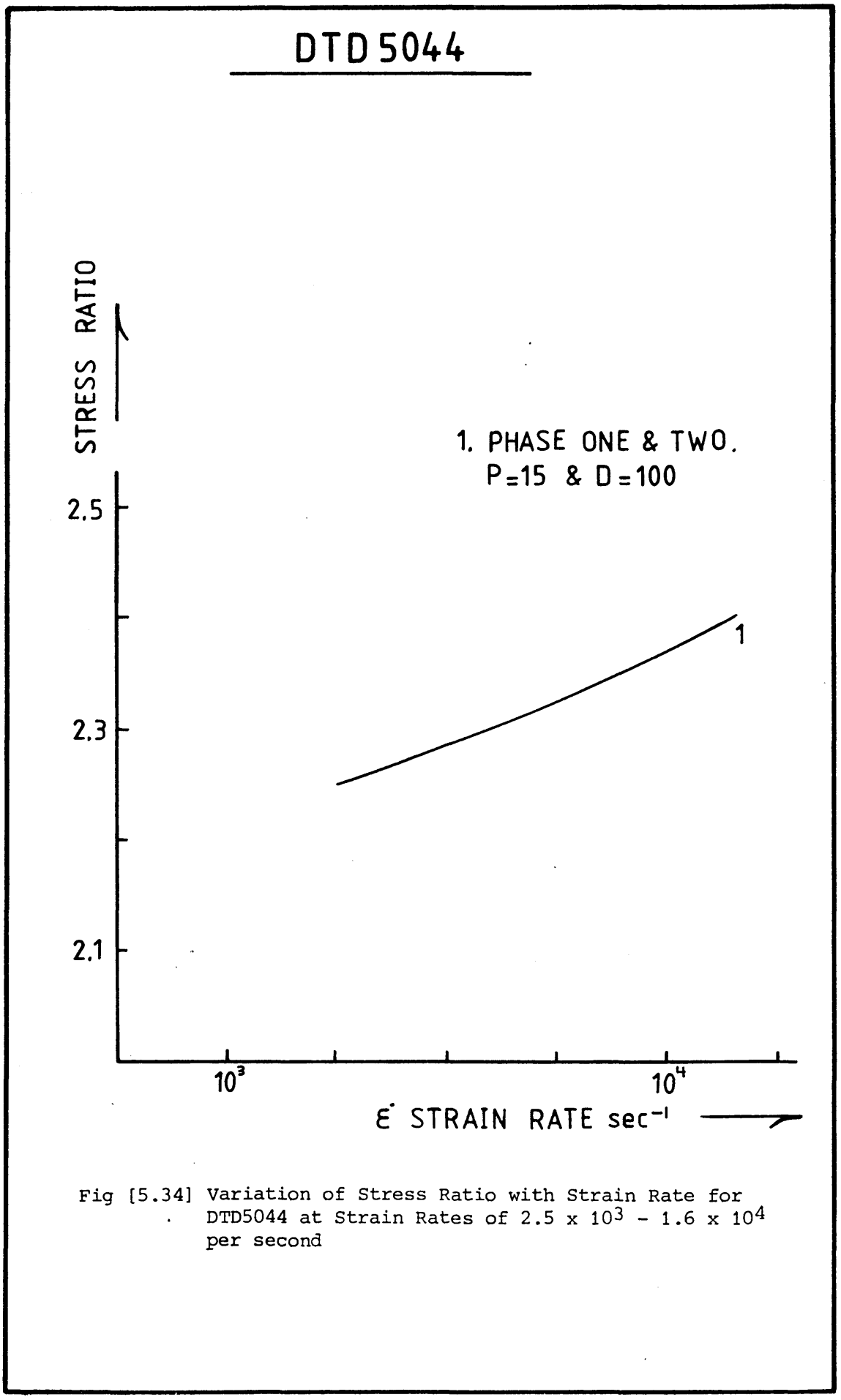

Fig [5.34] Variation of Stress Ratio with Strain Rate for DTD5044 at Strain Rates of 2.5×10^3 - 1.6×10^4 per second

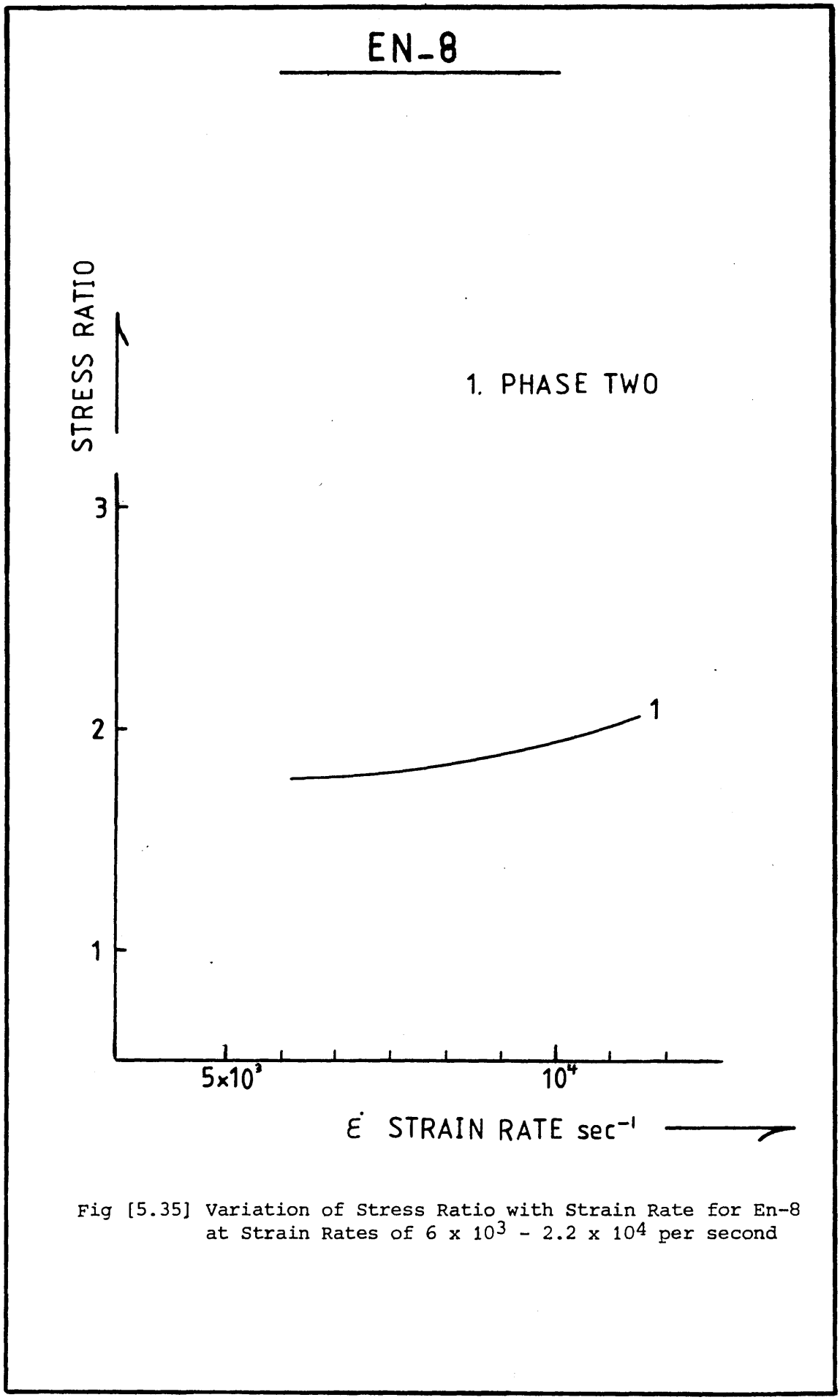

Fig [5.35] Variation of Stress Ratio with Strain Rate for En-8 at Strain Rates of 6 x 10^3 - 2.2 x 10^4 per second

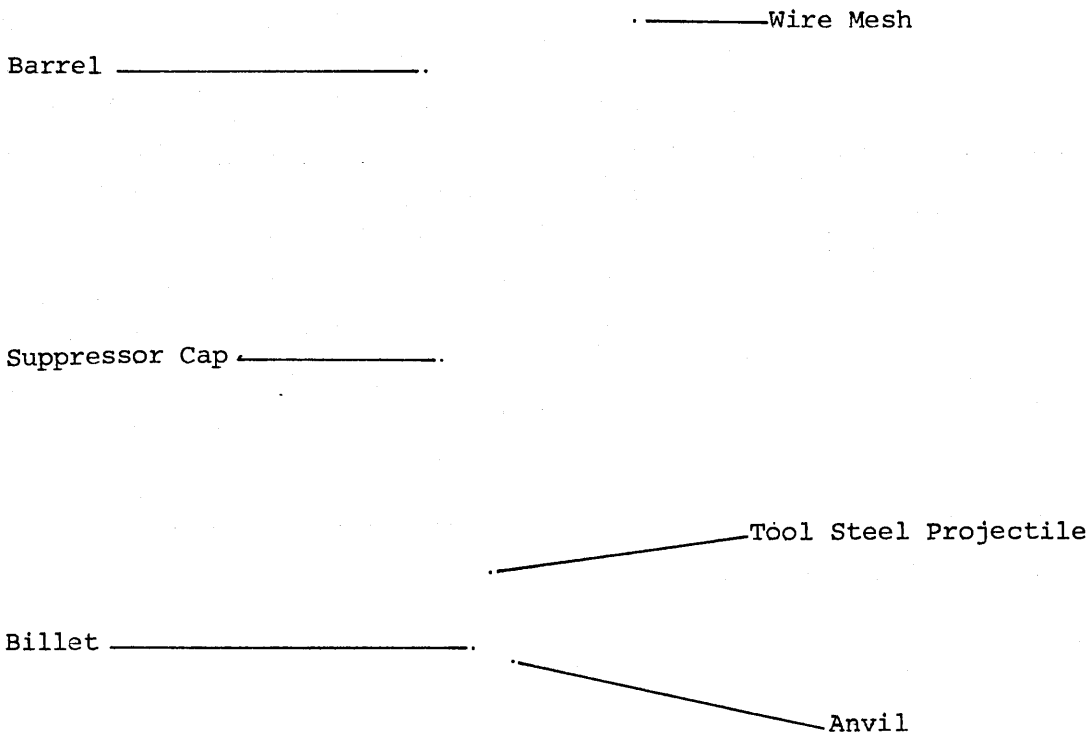

Plate No [5.1] Tool steel projectile impacting onto a small billet placed on a rigid anvil

Plate No [5.1] Tool steel projectile impacting onto a small billet placed on a rigid anvil

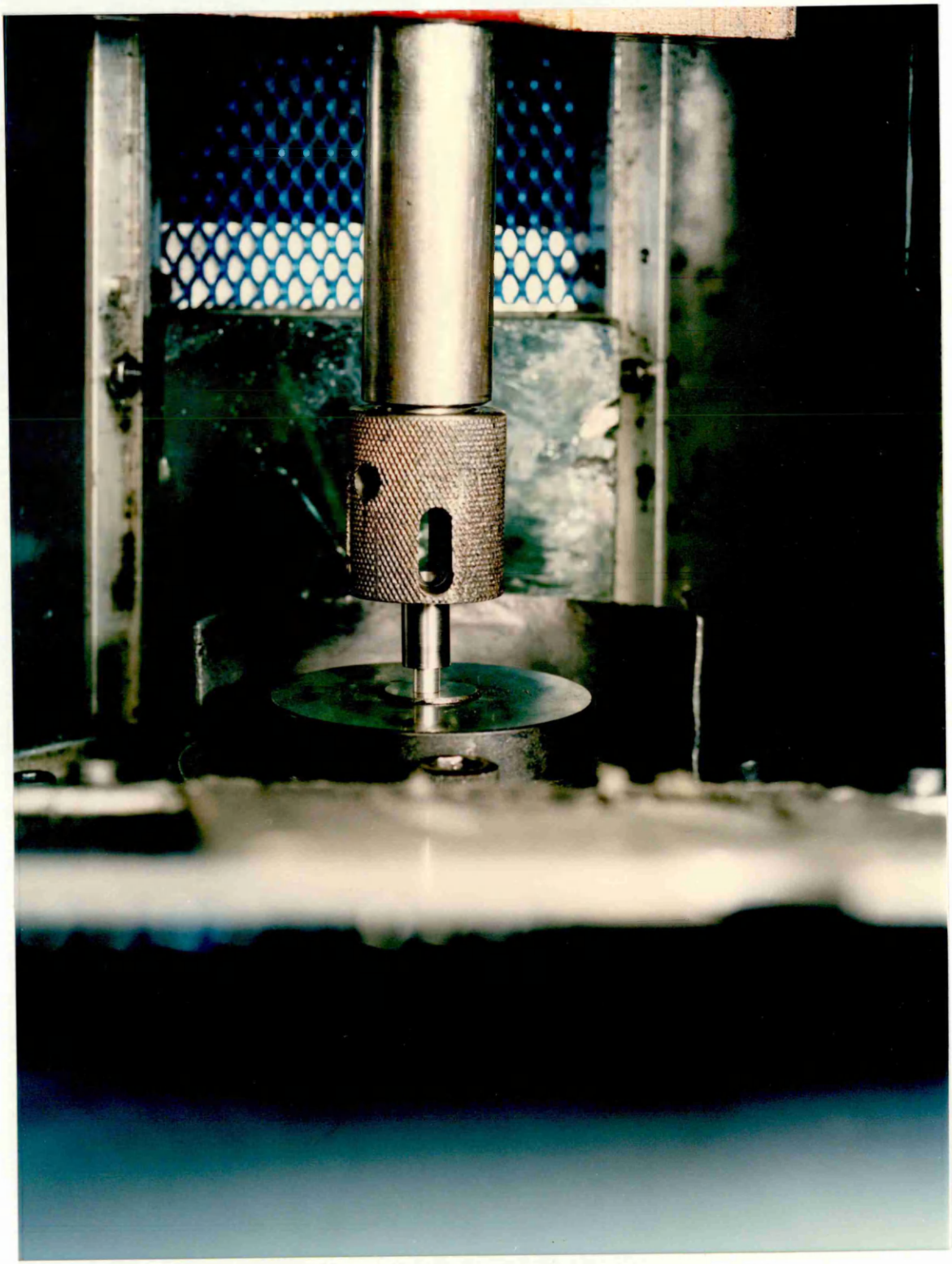

79.16 m/s

47.5 m/s

20 m/s

Plate No [5.2] HE15, Deformed billets at different impact velocities

Plate No [5.2] HE15, Deformed billets at different impact velocities

50 m/s

144.2 m/s

191.61 m/s

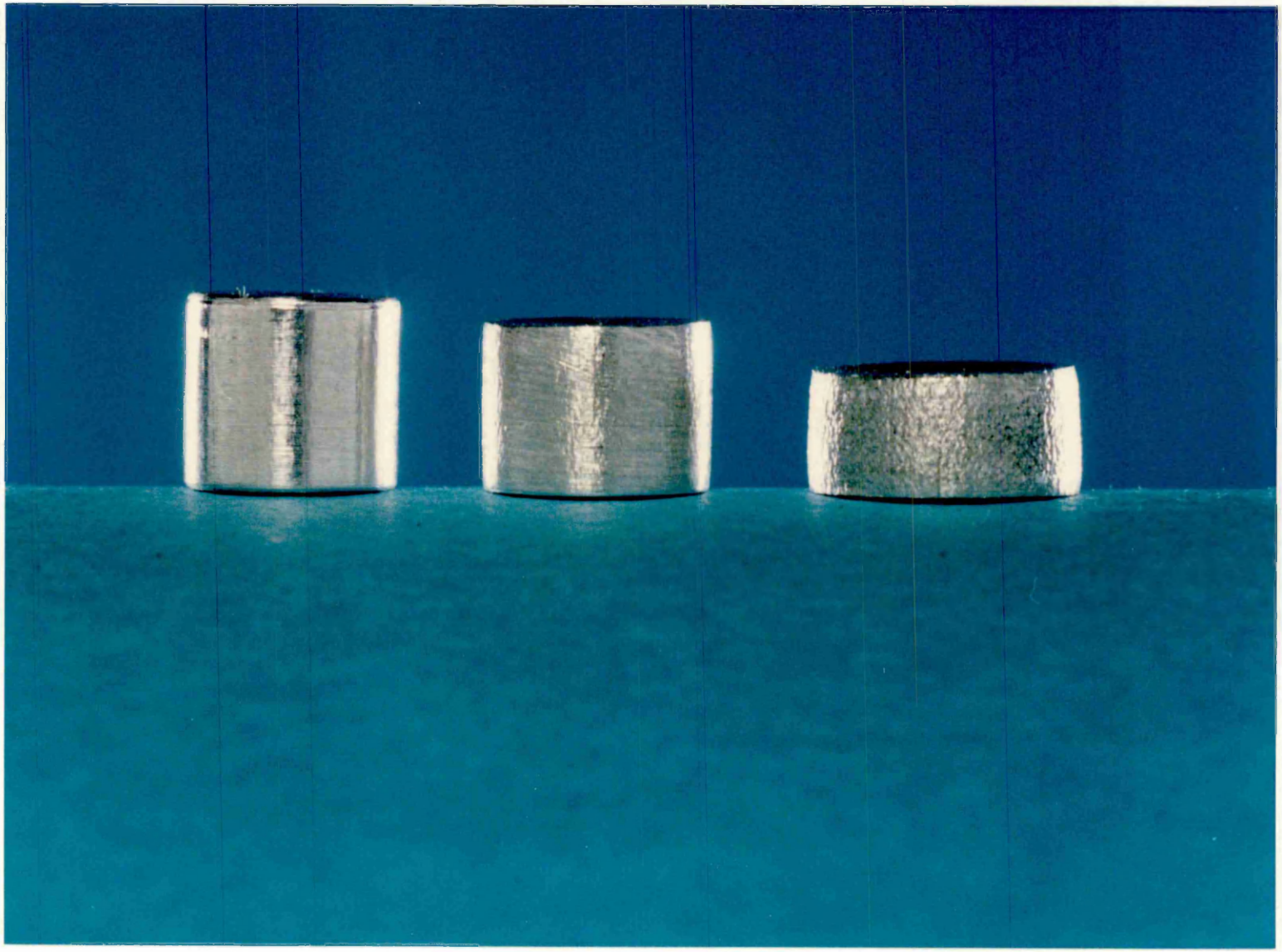

Materials		HE15	HE30TF	DTD5044	En-8
Maximum temperature rise °C		140.8	137.24	162.7	166.0
Radial Inertia Effect %	20 m/s	0.008	0.226	0.006	
	80 m/s	0.32	1.05	0.184	
	30 m/s				0.037
	110 m/s				1.5
Coefficient of Friction in dry conditions		0.0622	0.055	0.0432	0.0317

Table 5.1 Temperature Rise, Radial Inertia and Coefficient of friction effect

Initial Inside Diameter mm	Strain Rate sec^{-1}	Deformation %	Theoretical Inside Diameter mm	Experimental Inside Diameter mm	Percentage Difference
1.7	static 5×10^{-3}	54.38	2.325	2.268	2.45%
1.7	Dynamic 1.7×10^{4}	35.22	2.112	2.0558	2.66%

Table 5.2 Ring Test Results

6.0 The Effect of Temperature Rise and Strain History on Deformation

6.1 Introduction

The temperature rise in a material undergoing high strain rate deformation may be significant and should be taken into account in processing the results due to its effect on the flow stress. The plastic deformation of materials is characterised by irreversible strains. The plastic work of deformation largely appears in the form of heat energy and so an increase in the temperature of the metal may occur. At room temperature slow speed deformation (quasi-static), the effects of this increase in temperature do not appear to be significant.

However, for some materials there will be certain test temperature and strain rate for which a net gain in temperature will take place. In this event the flow stress of the metal would be expected to decrease with increasing temperature.

The effect of radial inertia has been discussed and calculated previously in chapter three and shown in tables 4.1 and 5.1 for the two test phases. The effect of this contribution is not very significant and has been shown in this study to be less than 2 per cent.

The temperature rise affects the rheology of the aluminium alloys more than that of the steel at room temperature. About 95.5 per cent of the plastic work is transformed into temperature for an aluminium alloy and 86.5 per cent for steel as reported in reference (58).

In this chapter (phase three of the present study), the effect of temperature rise during deformation will be taken into account, incorporating the effect in the finite-difference numerical technique used in phase two to predict the material strain rate sensitivity constants P and D based on data taken from the quasi-static stress-strain curves.

6.2 Quasi-Static Compression Tests at Elevated Temperatures

6.2.1 Description of Equipment

A substantial rise in temperature occurred during the high strain rate deformation of the billets. Since this rise may affect the material properties and characteristics during deformation, it was essential to perform quasi-static compression tests at elevated temperature.

A Mayes Press was used for conducting quasi-static compression tests on small cylindrical billets made from HE15, HE30TF and DTD5044 aluminium alloys and En-8 steel at different elevated temperatures of up to 250°C. Plate No 6.1 shows the tests set up. The press is a servo hydraulic testing machine offering a range of tensile-compressive loading with a maximum load of 100KN. The Mayes Press was equipped with a water cooled hydraulic pump for application of load. It is also equipped with a hot chamber (furnace) to heat the test specimen to the desired temperature before conducting the compression test.

It was essential to manufacture a die which could be fitted to the press ram and anvil parts as shown in

figure 6.1. The figure also shows the specimen between the die platens and the thermocouples attached to the surfaces as near as possible to the specimen. The die was made of En-47 steel with material chemical composition by wt% given in the table below.

C	Mn	Si	S	P	Ni	Cr	Mo	V
0.435	0.760	0.265	0.02	0.007	0.200	1.05	0.025	0.265

The En-47 was hardened, by heating to 865°C, oil quenched and tempered to 410°C. En-47 steel was used because of its high strength at room and elevated temperatures. Its hardenability characteristics are superior to plain carbon steels and its high yield strength are adequate for high load conditions.

The die consists of two platens, machined from a 33.5mm as received round bar. The platens were each threaded, so they could be screwed into the ram and anvil parts of the press. A round undercut was machined into each platen so that it could carry most of the load during compression rather than the thread itself. A detailed drawing of the die is shown in figure 6.2. The Mayes Press was controlled through a control panel as shown in plate No 6.2. The compression velocity (strain rate) and the furnace temperature were also controlled through the same panel. The press was also connected to an X-Y plotter, as shown in plate No 6.3 which plots load on the Y-axis and reduction in height on the X-axis.

6.2.2 Calibration of Thermocouples and Furnace

Difficulty was experienced in bonding the thermocouples to the small cylindrical specimen undergoing compression. An alternative was to bond two thermocouples of the copper-constantan type to the flat surfaces of the upper and lower platens as shown in plate No 6.4. The positions of the thermocouples were chosen to be as close as possible to the billet which was usually situated in the centre. The adhesive used to bond the thermocouples to the steel surface was Autostick 1000, a high temperature adhesive with a ceramic base.

The two thermocouples were then connected to a junction box which was connected to a Comark electronic thermometer which offers various temperature ranges. Because the dimensions of the billets were small, especially the height which separates the two platens, it was possible to minimise the difference in temperature reading between the two thermocouples to less than 4°C at any stage. This was done by adjusting the furnace zones.

The furnace has three zones, upper zone Z_1, middle zone Z_2 and lower zone Z_3 as shown in plate No 6.4. The furnace was calibrated by placing a billet between the ram and anvil of the press with the furnace closed. Figure (6.3) shows the calibration graph regarding temperature, time and divisions on the control knob. The setting of the zones for each stage of heating the specimen is shown in the table below.

Stage	Temperature °C	Z_1	Z_2	Z_3
1	20-55	1.0	2.0	10.0
2	55-250	3.0	2.0	10.0
3	250-300	4.0	2.0	10.0

The graph shown in figure 6.3 represents the average reading of the two thermocouples which is approximately the temperature of the test billet undergoing the compression process.

6.2.3 Quasi-Static Test Procedure

Small cylindrical billets were machined to size from as received round bars of the test materials and then finely ground and polished. The dimensions of the billets were 5.2mm in diameter and 5.0mm in height, with an aspect ratio of 0.96. When a billet was ready for testing both of its flat surfaces, together with the ram and anvil surfaces, were lubricated with tallow-graphite. The billet was then placed on the centre of the anvil and the ram was moved down to touch the upper surface of the billet; this was done visually. The furnace was then closed, switched on and the zones adjusted depending on the desired test temperature. When the desired temperature was reached, the compression process was commenced.

The load against reduction in height graph was plotted on the X-Y plotter connected to the Mayes Press control panel.

6.2.4 Tests Results

Quasi-static tests were carried out at low strain rate of 3.7×10^{-3} per second and elevated temperature varying between 20°C (Room Temperature) and 250°C as shown in figures 6.4 to 6.7. Unlubricated (Dry) and lubricated tests were carried out at room temperature as well.

The quasi-static stress-strain curves for the three aluminium alloys showed a substantial decrease in the flow stress as the temperature increased. However, figure 6.7 which presents the quasi-static stress-strain curves for En-8 structural steel at temperatures from 20°C to 250°C, shows that there was no significant change in the flow stress for this range of temperature.

6.3 Construction of General Constitutive Equations

6.3.1 Introduction

In the previous section 6.2 of this chapter, the quasi-static stress-strain curves at different elevated temperatures up to 250°C were obtained. Input data for the finite-difference numerical technique were previously (in phase one and two) obtained from the quasi-static stress-strain curves at room temperature. However, because of the rise in temperature during deformation, and its effect on the stress-strain curves (especially the flow stress), it was essential to find a general temperature dependent constitutive equation for each of the three aluminium alloys over a range of temperatures between 20-250°C.

The general temperature dependent constitutive equation should describe stress, strain and their relationship with temperature in the elastic and plastic range.

6.3.2 Construction of Stress, Strain and Temperature Dependent Constitutive Equations

The following equation reported by Dorn (67) was used to describe the stress-strain curves illustrated in figures (6.4 to 6.7) for the three aluminium alloys

$$\varepsilon = \frac{\sigma}{Eo} + \left(\frac{\sigma}{\sigma o}\right)^{n} \qquad (6.1)$$

where

ε = total strain being the sum of the elastic strain ε_e and the plastic strain ε_p.

σ = stress.

Eo, σo, n = temperature dependent constants.

Equation 6.1 was found to give a close fit to the experimental data and was easy to handle in the computational procedure. The constants Eo, σo and n are the main parameters which have to be determined for each material over a range of temperature. For each curve in figures 6.4 to 6.7, these parameters were determined by using computer software employing the least square method of curve fitting.

The method converts the curves into a sequence of lines using a logarithmic representation. After Eo, σo and n were found for a certain temperature a visual and numerical check was conducted on the experimental and estimated data. Finally the Eo, σo and n data for a material over a range of temperatures were combined

together and converted by trial and error into one general constitutive equation describing stress, strain and temperature corresponding to the static compression test range.

The following expressions for the parameters σo, Eo and n were constructed relating to temperature (T)°C over the temperature range 20°C-250°C.

$\sigma o = 10^3 MN/m^2$

$Eo = GN/m^2$

(a) For HE15

(i) $\sigma o = 0.885 - \frac{9.4T^2}{10^6}$

(ii) $Eo = 10.22 - 0.111T$

(iii) $n = 4.5$ if $T < 140°C$

(iv) $n = \frac{8.6T^2}{10^4} - 0.268T + 25.18$ if $T > 140$ and $< 250°C$

(b) For HE30TF

(i) $\sigma o = 0.609 - \frac{1.7T}{10^3}$

(ii) $Eo = 7.08 - \frac{6.53T}{10^3}$

(iii) $n = 1/0.244 - \frac{7.76T}{10^4}$

(c) For DTD5044

(i) $\sigma o = 0.97 - \frac{1.123T^2}{10^5}$

(ii) $Eo = 33.26e^{\frac{-7.12T}{10^3}}$

(iii) $n = 4.293T^{\frac{5.01}{10^2}}$

(d) For En-8 steel

Since for En-8 steel the flow stress is not affected appreciably by temperature in the temperature range of 20°C-250°C, the following were found

(i) $\sigma o = 1.30$

(ii) $Eo = 15$

(iii) $n = 5$

However since $\varepsilon = \frac{\sigma}{Eo} + (\frac{\sigma}{\sigma o})^n$

$$\varepsilon - \frac{\sigma}{Eo} = (\frac{\sigma}{\sigma o})^n$$

$$\sigma = \sigma o(\varepsilon - \frac{\sigma}{Eo})^{1/n}$$

Since σ/Eo is very small compared to any value of strain beyond elastic limit

$$\sigma = \sigma s = \sigma o \varepsilon^{1/n}$$

Therefore the static flow stress for any of the four materials can be determined at any temperature up to 250°C if the strain is known. The strain rate sensitivity equation

$$\sigma D = \sigma s[1 + (\frac{/\dot{\varepsilon}/}{D})^{1/P}]$$

can now be expressed as

$$\sigma_D = \sigma_o \varepsilon^{1/n}[1 + (\frac{/\dot{\varepsilon}/}{D})^{1/P}] \qquad (6.2)$$

Equation 6.2 is the new strain rate sensitivity constitutive equation catering for the temperature rise effect during deformation.

6.4 Modified Results Catering for Radial Inertia and Temperature Rise during Deformation

After the introduction of temperature rise and radial inertia effects into the finite-difference numerical technique employed in phase one and two of the present study, the final diameter and height against impact velocity curves were modified and consequently the material constants P and D changed. The results are presented as follows.

1 Modified ballistic compression of small billets (phase two) test results.

2 Impact velocity and temperature rise during deformation (phase two).

3 Modified projectile (phase one) test results.

4 Ballistic compression test results of different billet sizes.

6.4.1 Modified Ballistic Compression of Small Billets (Phase Two) Test Results

The experimental final diameter and height against impact velocity curves for HE15, HE30TF, DTD5044 and En-8 presented previously in figures 5.16 to 5.23 were again used in this part of the study (phase three).

The theoretical results modified to include temperature effects are shown in figures 6.8 to 6.15. The continuous curves represent the experimental results, while the dotted ones represent the theoretical results obtained using the finite-difference numerical technique. For the three aluminium alloys and En-8 steel, strain rates between 4×10^3 to 1.6×10^4 per second and 6×10^3 to 2.2×10^4 per second respectively were covered. Several combinations of P and D values were used to approach the closest fit of experimental and theoretical for each material.

The values of P and D for all the four materials are shown in the table below.

Material	P	D
HE15	35	75000
HE30TF	75	30000
DTD5044	4	2500
En-8	15	80

These new values of P and D (for each material) were then used in equation 6.1 to obtain the stress-strain curves at different strain rates (higher than the quasi-static one) as shown in figures 6.16 to 6.19. The strain rates presented in these figures are only those within the range involved during the experimental work.

Figures 6.20 to 6.23 show the variation of stress ratio with strain rate for all four materials tested in each of the three phases. This was done in order to show how the relationship is affected by homogeneity, radial inertia and temperature rise during deformation. Finally figures 6.24 to 6.25 show the stress ratio against strain rate curves for the three aluminium alloys and En-8 steel in compression with other work done in this field.

6.4.2 Temperature Rise and Impact Velocity

The theoretical temperature rise in the specimen during deformation was assumed to be adiabatic during the homogeneous deformation. HE15 alloy was used as an example in this section. From the output data of the finite-difference numerical technique the temperature rise along each element in the specimen at different deformation levels was plotted as shown in figure 6.26.

Figure 6.27 shows the relationship between the maximum temperature rise and impact velocity during deformation. These relationships were found to be as follows in the temperature range 20-250°C.

1. For HE15

$$T = 16.32e^{0.287V}$$

where T is the maximum rise in temperature in degree C corresponding to a certain impact velocity V m/s.

2. For HE30TF

$$T = 15.4e^{0.03V}$$

3. For DTD5044

$$T = V/0.77 - \frac{3.66V}{10^3}$$

4. For En-8

$$T = 17.58e^{\frac{2.128V}{10^2}}$$

6.4.3 Modified Projectiles (Phase One) Tests Results

The experimental results for the three aluminium alloys presented in phase one were used in this section. Temperature rise (T) and radial inertia (I) effects were introduced into the finite-difference numerical technique used in phase one of the present work. The final diameter and final height against impact velocity curve are presented in figures 6.28 to 6.33 using P and D values obtained in phases one and three of the present study. The figures also show the effect of several different combinations of radial inertia and temperature rise on the curves (eg T - I, indicates inclusion of temperature rise effect and exclusion of radial inertia effect) consequently altering the material constants P and D.

6.4.4 Ballistic Compression Test Results of Different Billet Sizes

The purpose of this section is to investigate specimen size effects and how temperature rise and radial inertia may influence the results. Different sizes of billets made from the three aluminium alloys were deformed dynamically using the same experimental procedure as in phase two. These tests were restricted to the aluminium alloys.

The initial diameters (Do) varied between 5.2 and 7.7mm while initial height (Ho) varied between 5 and 7.5mm keeping the aspect ratio Ho/Do less than one. Other sizes were considered but abandoned because of the limited diameter of the tool steel projectile. The finite-difference numerical technique used in phase three was employed, catering for radial inertia (I) and temperature rise (T) during deformation. The material constants P and D used in this section were the same as those reported in section 6.4.1.

Figures 6.34 to 6.57 show the variation of final diameter (D_f) and final height (H_f) of the deformed billets with impact velocity at strain rates varying between 4×10^3 and 1.6×10^4 per second. The figures also show the effect of different combinations of radial inertia (I) and temperature rise (T) on the curves.

6.4.5 Strain History Tests

This section was introduced in order to investigate the strain history effect on the material constants obtained

by the finite-difference numerical technique reported in section 6.4.1 and consequently the effect on the deformation process.

Billets, 5.2mm in diameter and 5mm in height were pre-strained statically at a strain rate of 2×10^{-3} per second. HE15, HE30TF, DTD5044 and En-8 were pre-strained statistically to 19.4%, 19.2%, 19.8% and 19.7% respecttively. The pre-strained billets were then deformed dynamically on the ballistic rig at different impact velocities.

Figures 6.58 to 6.65 show the final diameter and final height against impact velocity curves. The continuous line represents the experimental results while the dotted line is the theoretical result obtained using the materials constants P and D established in section 6.4.1. The range of impact velocities varied from 20 to 80 m/s and 30 to 110 m/s resulting in strain rates of 4×10^{3} to 1.6×10^{4} per second and 6×10^{3} to 2.2×10^{4} per second for the three aluminium alloys and En-8 steel respectively.

In order to obtain very close agreement between the experimental and theoretical results for the pre-strained specimen either new values of P and D have to be determined or pre-straining aspects have to be incorporated in the computational technique if the P and D values established from the as received specimens are used.

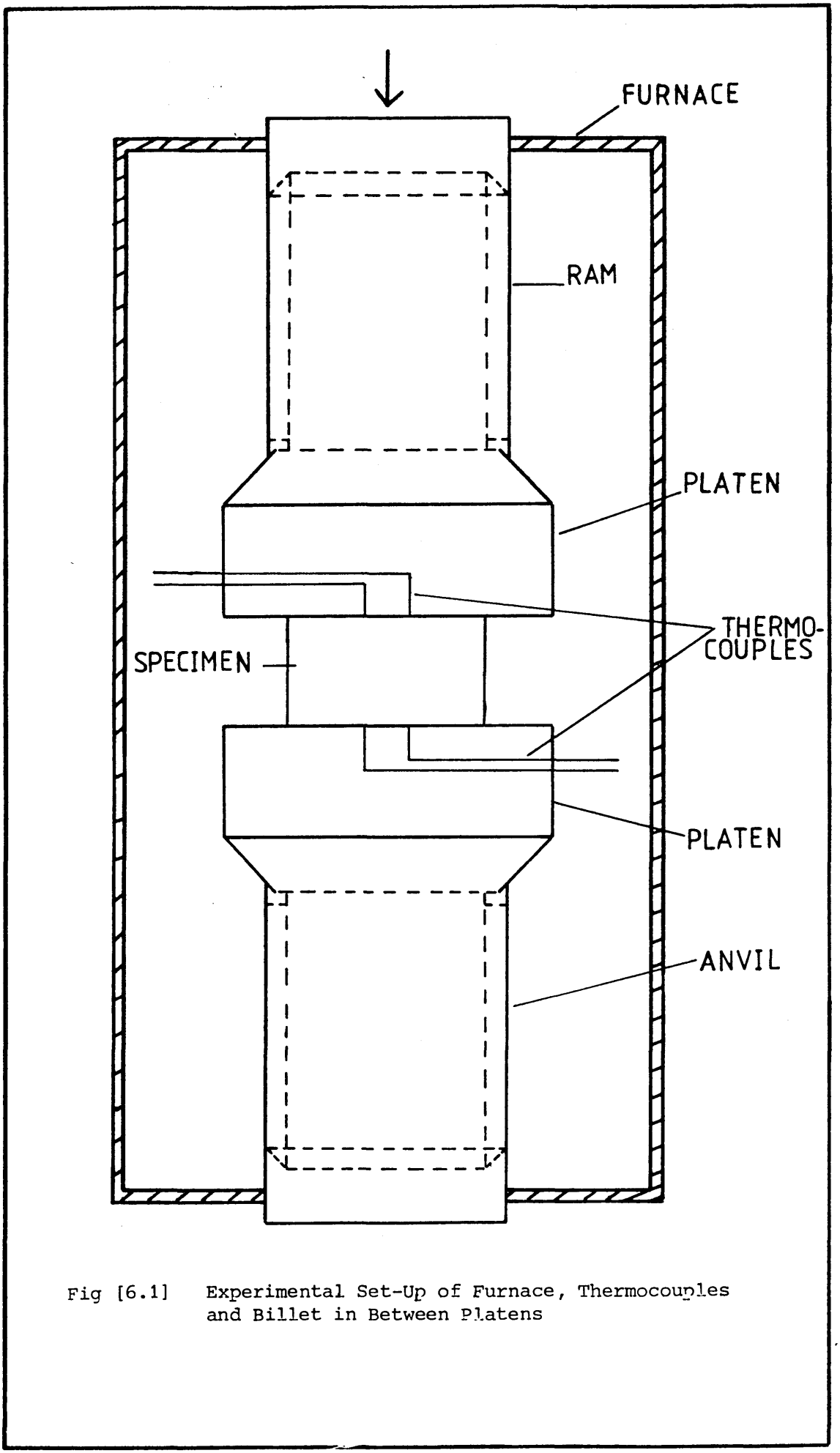

Fig [6.1] Experimental Set-Up of Furnace, Thermocouples and Billet in Between Platens

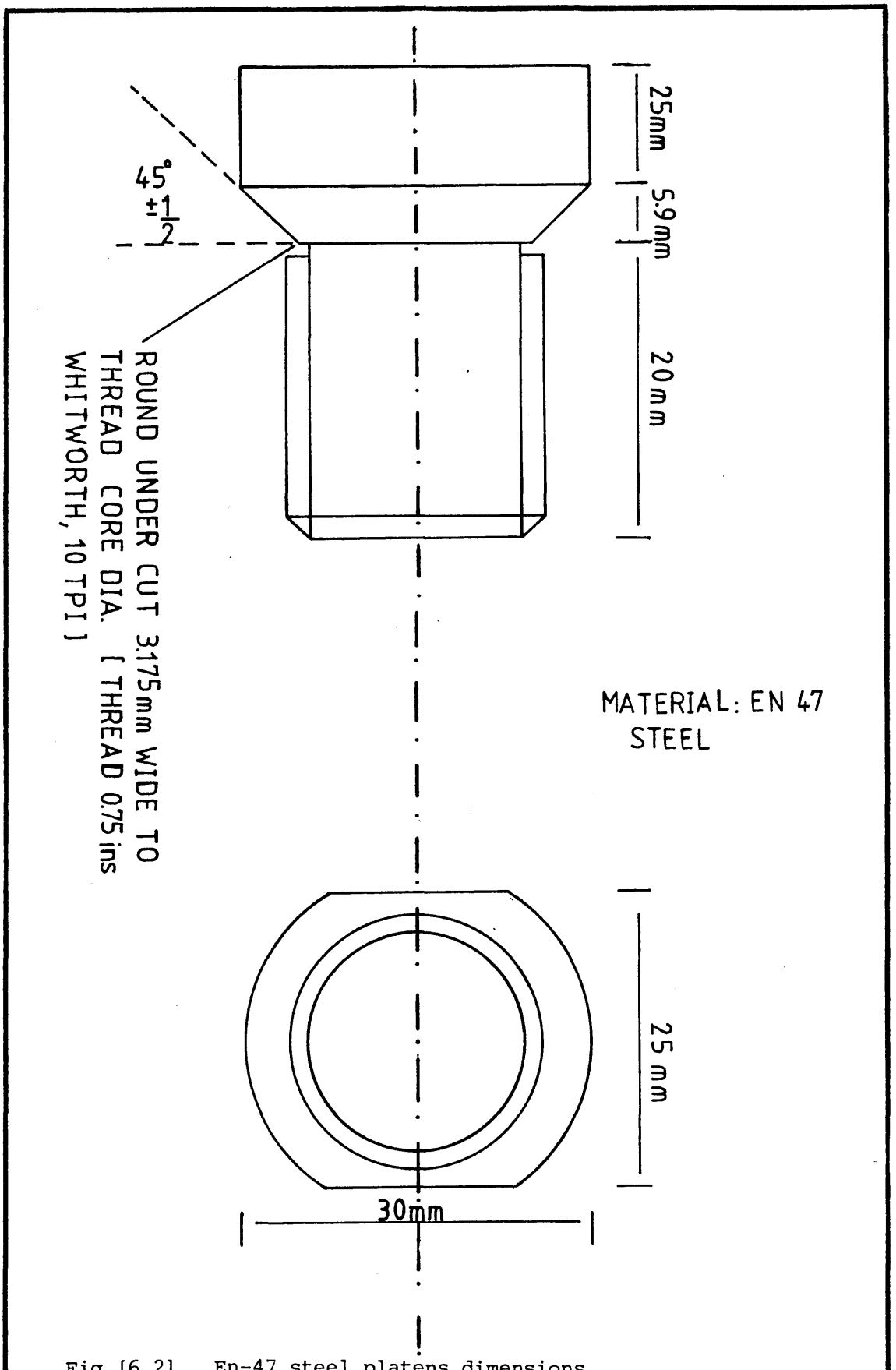

Fig [6.2] En-47 steel platens dimensions

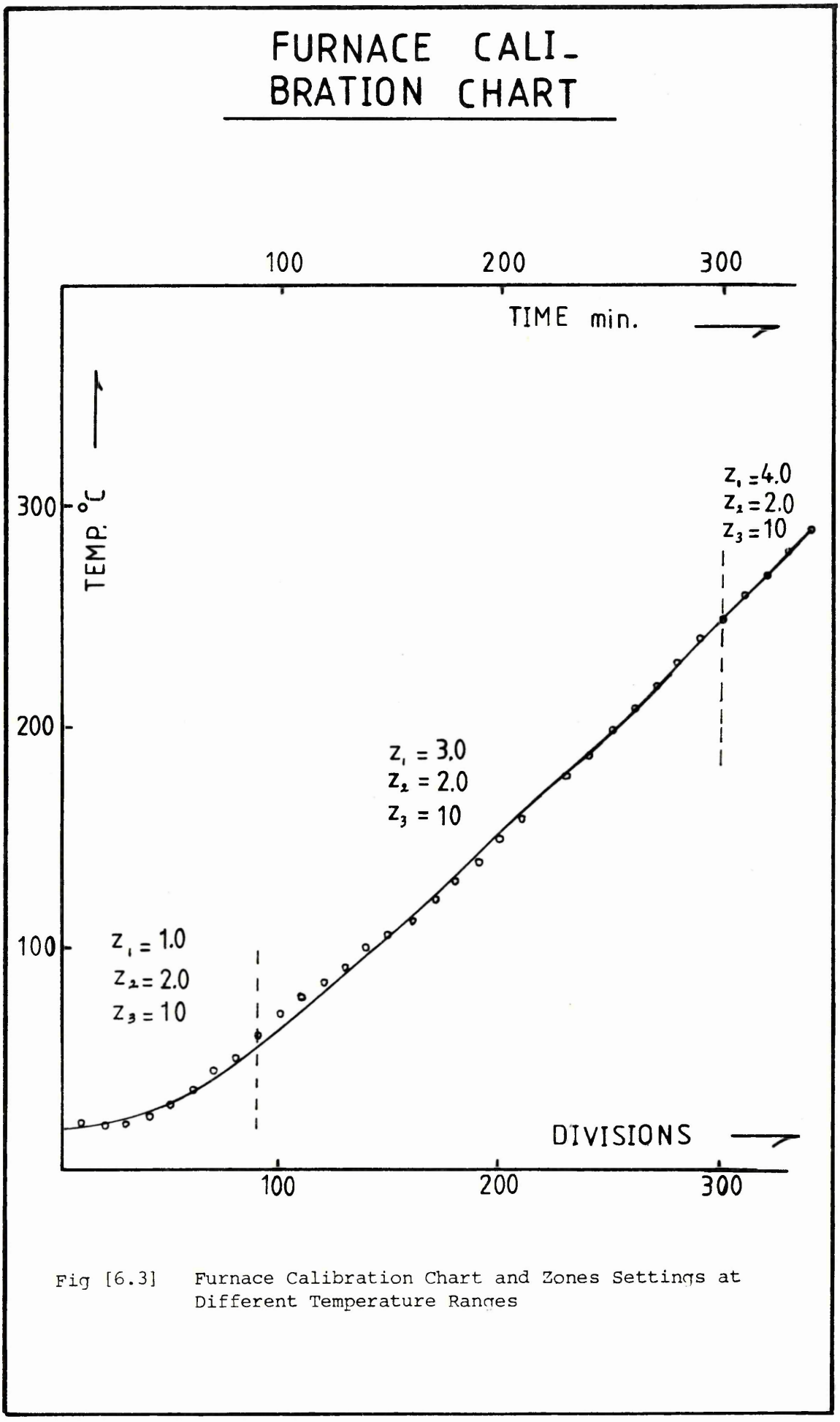

Fig [6.3] Furnace Calibration Chart and Zones Settings at Different Temperature Ranges

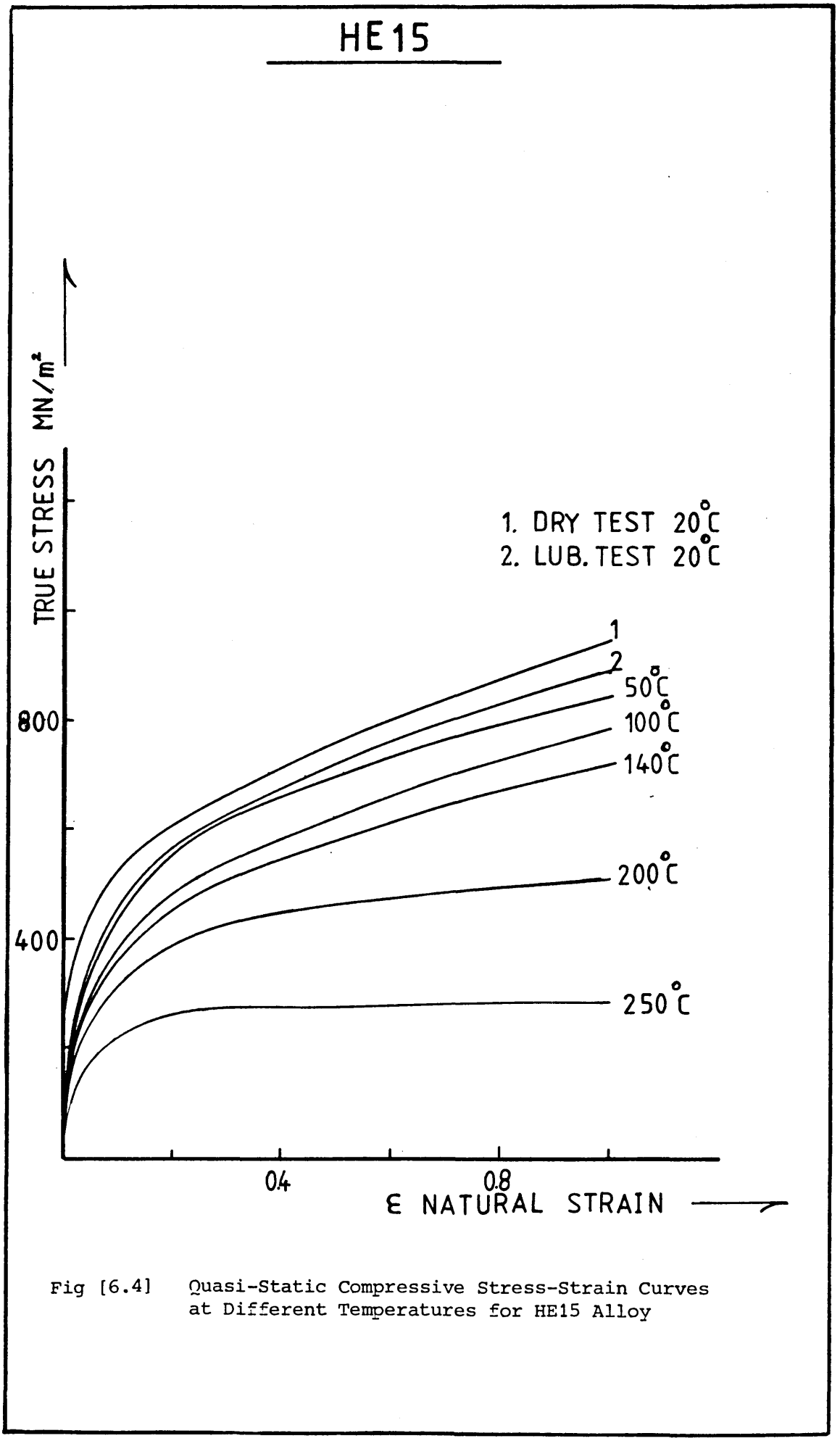

Fig [6.4] Quasi-Static Compressive Stress-Strain Curves at Different Temperatures for HE15 Alloy

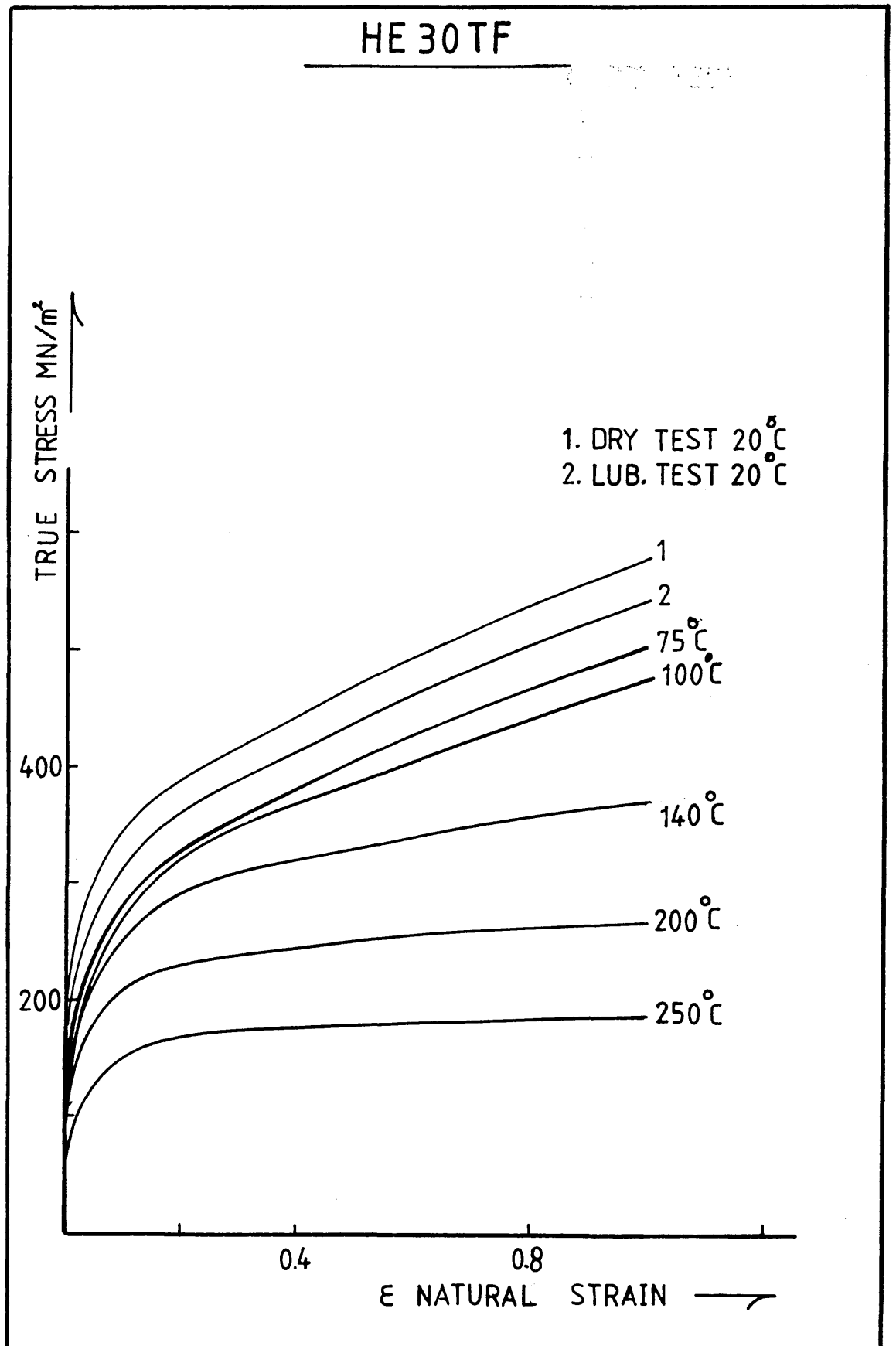

Fig [6.5] Quasi-Static Compressive Stress-Strain Curves at Different Temperatures for HE30TF Alloy

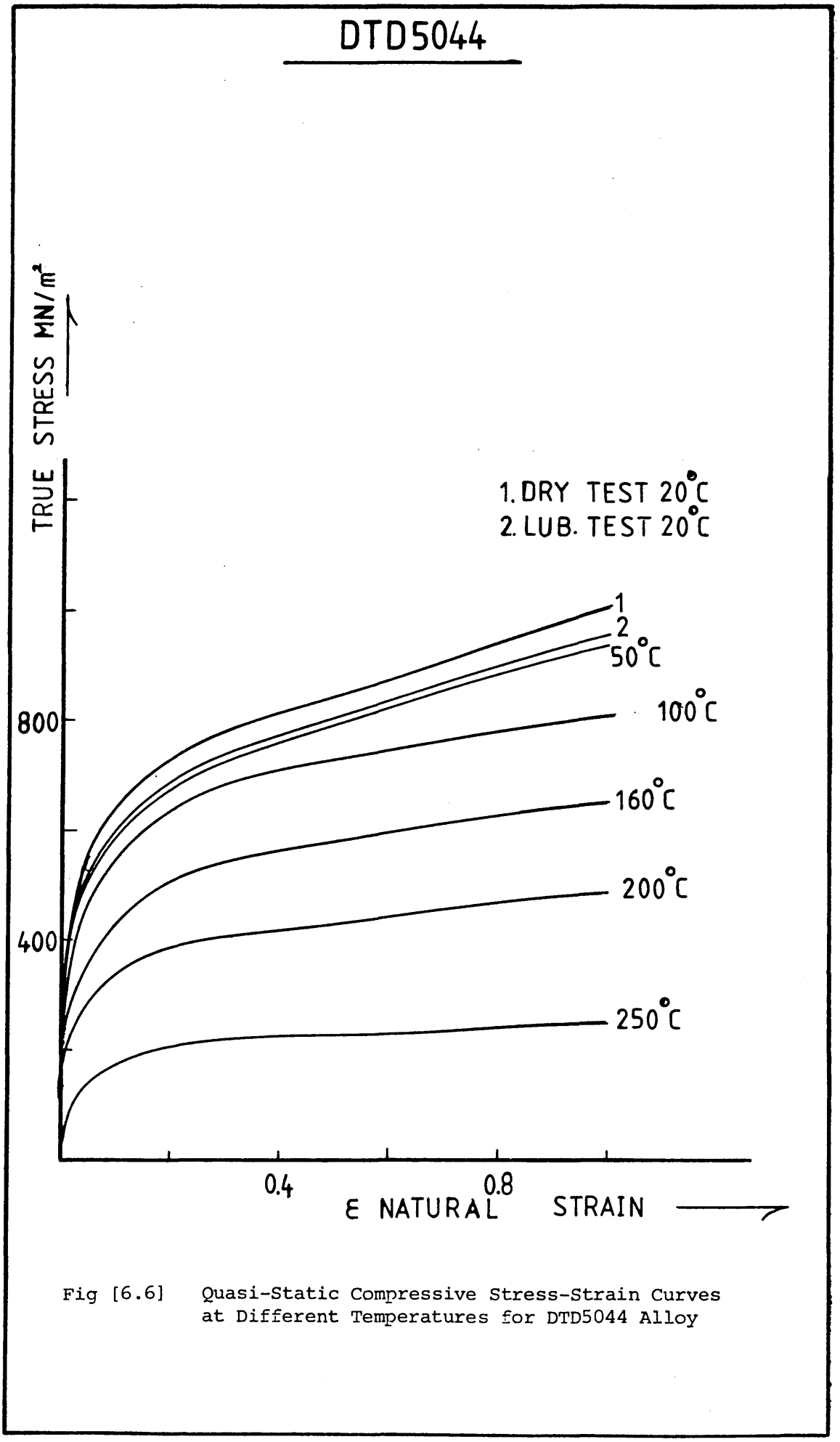

Fig [6.6] Quasi-Static Compressive Stress-Strain Curves at Different Temperatures for DTD5044 Alloy

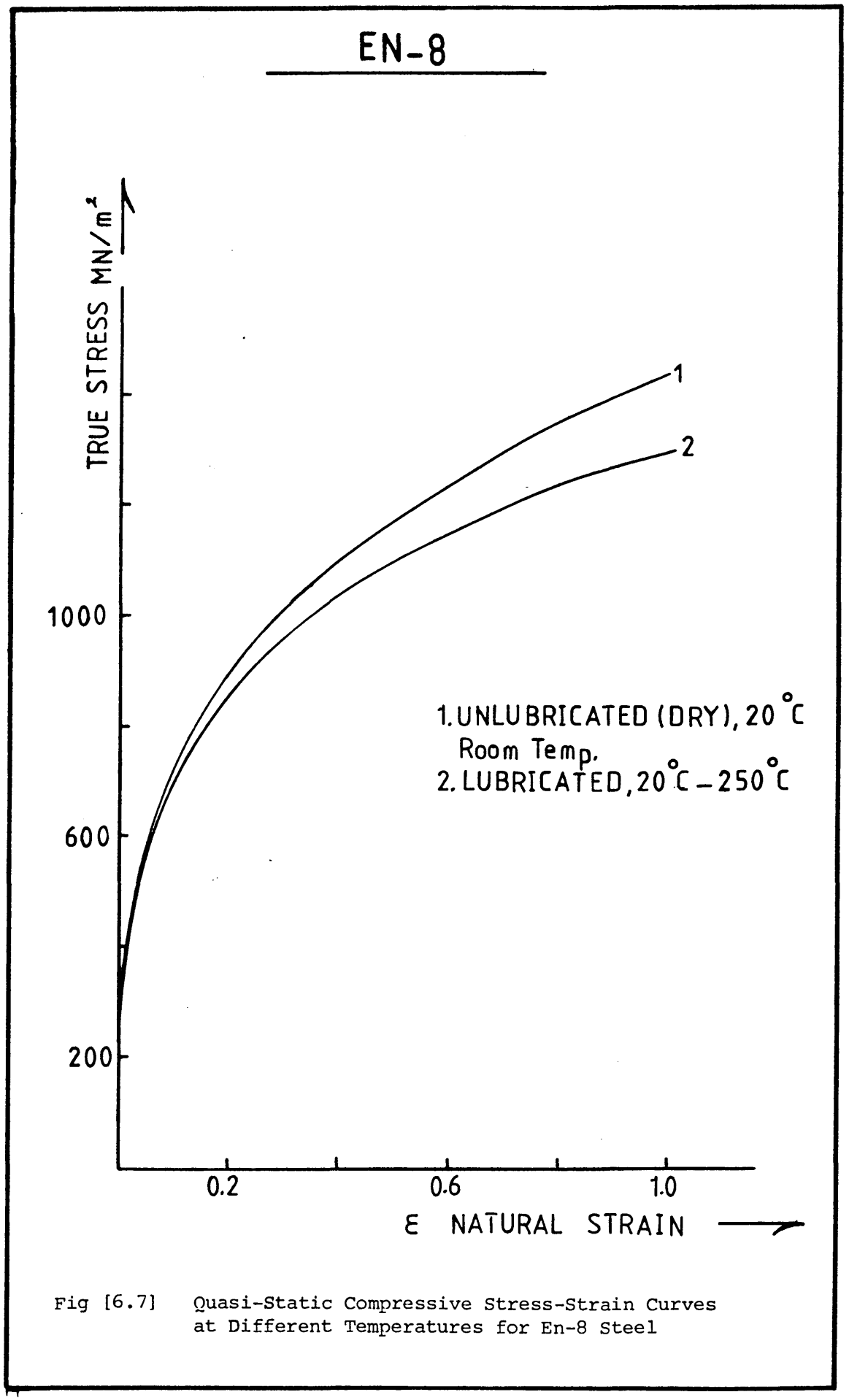

Fig [6.7] Quasi-Static Compressive Stress-Strain Curves at Different Temperatures for En-8 Steel

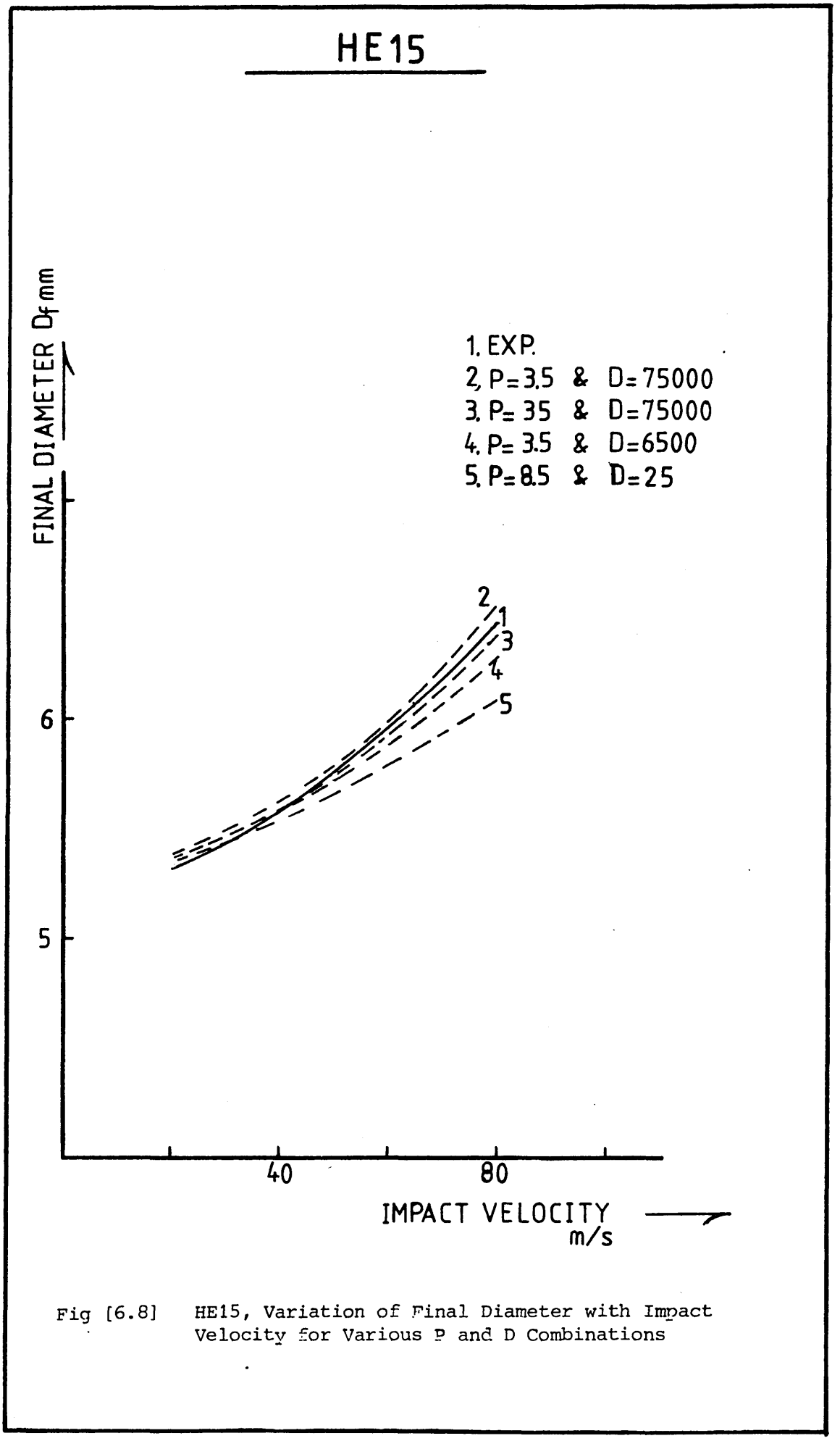

Fig [6.8] HE15, Variation of Final Diameter with Impact Velocity for Various P and D Combinations

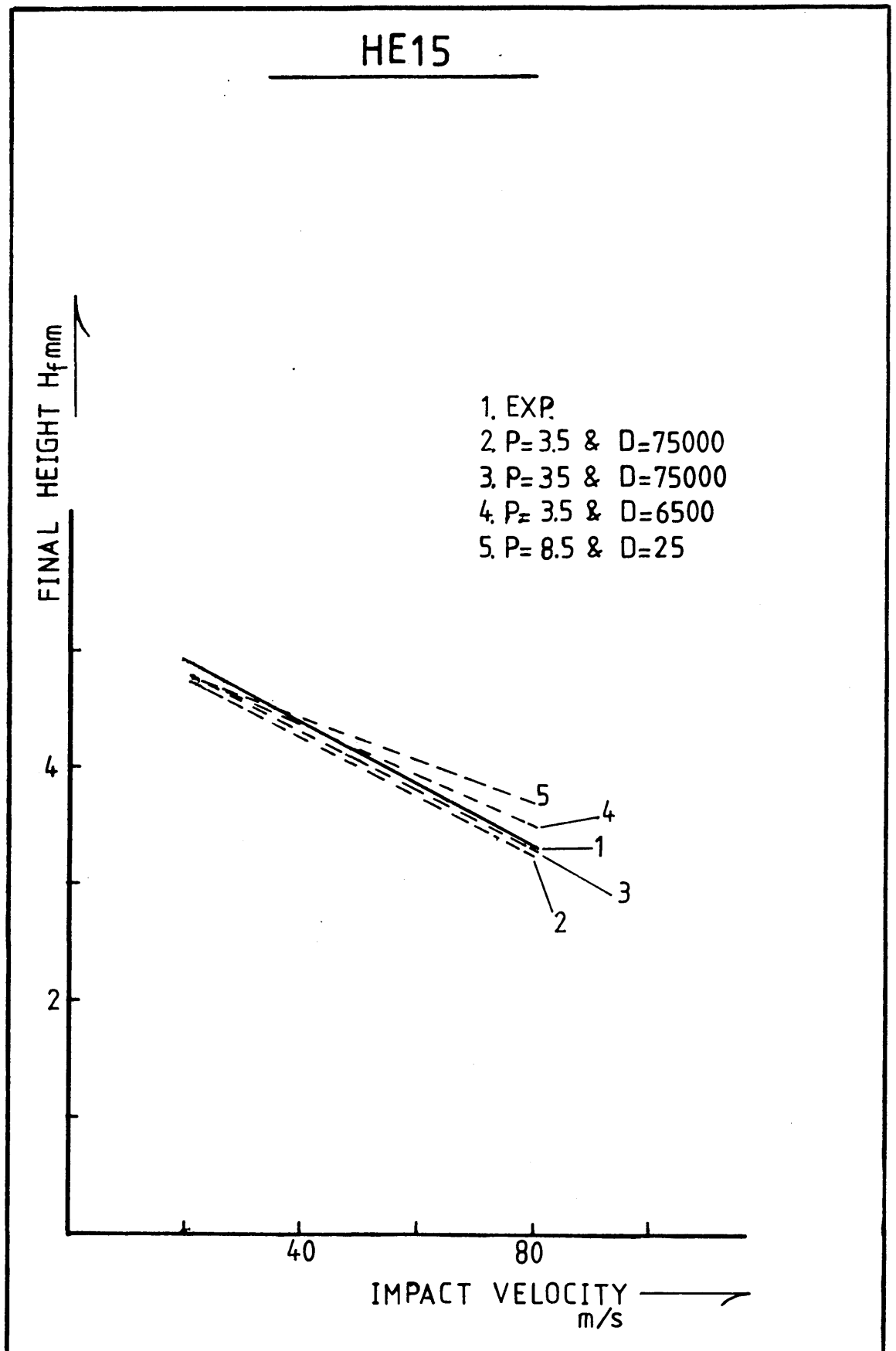

Fig [6.9] HE15, Variation of Final Height with Impact Velocity for Various P and D Combinations

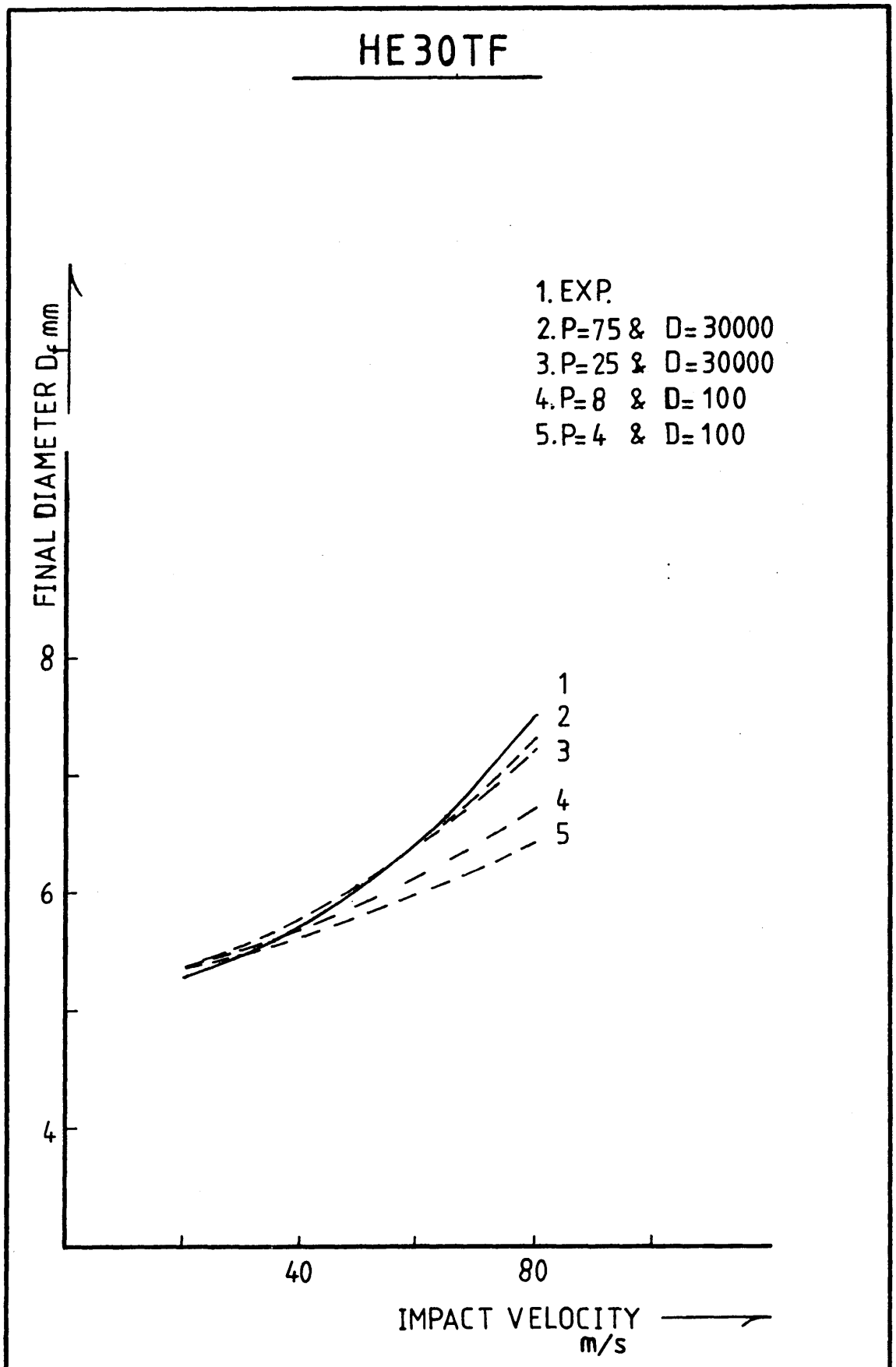

Fig [6.10] HE30TF, Variation of Final Diameter with Impact Velocity for Various P and D Combinations

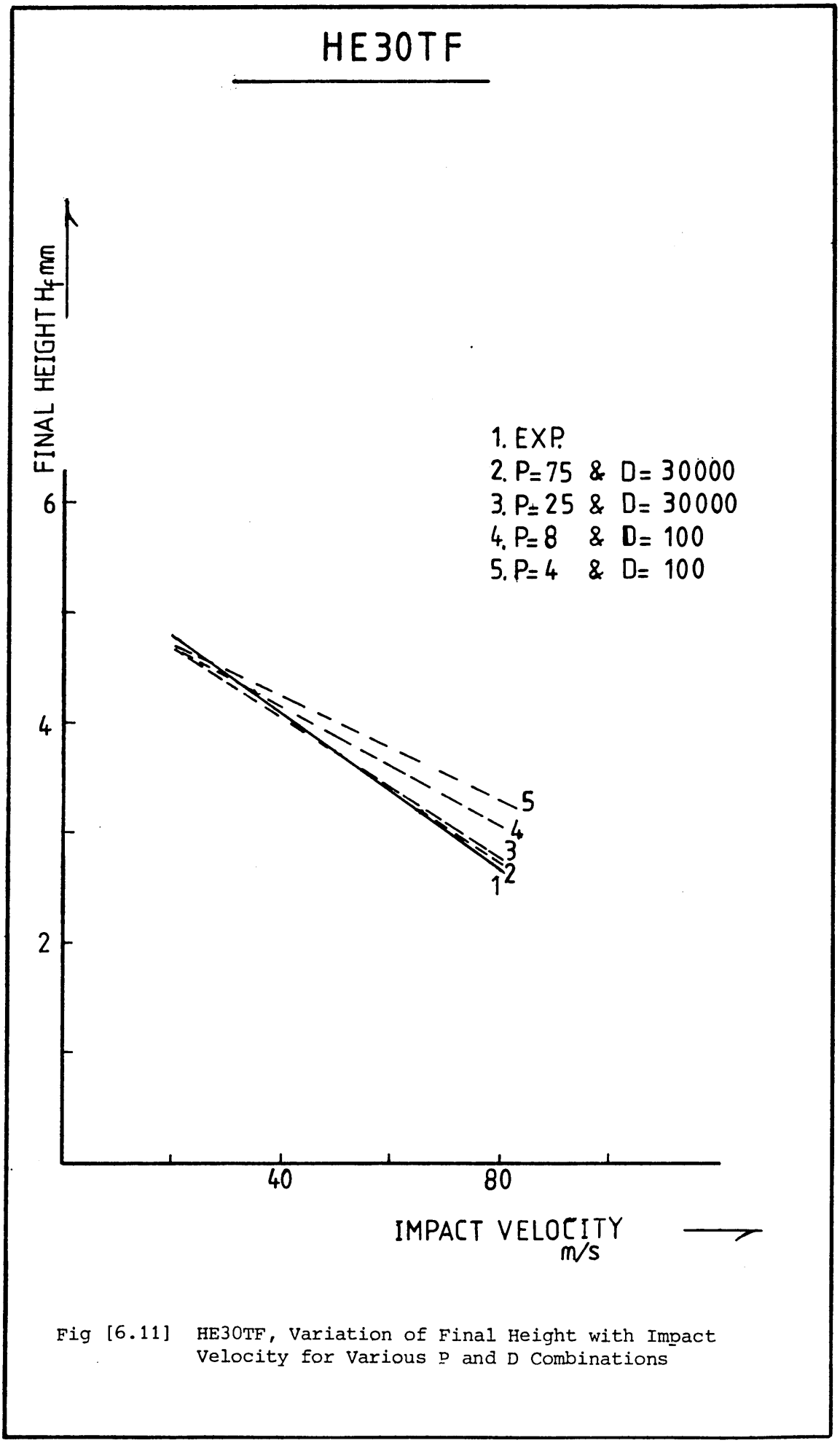

Fig [6.11] HE30TF, Variation of Final Height with Impact Velocity for Various P and D Combinations

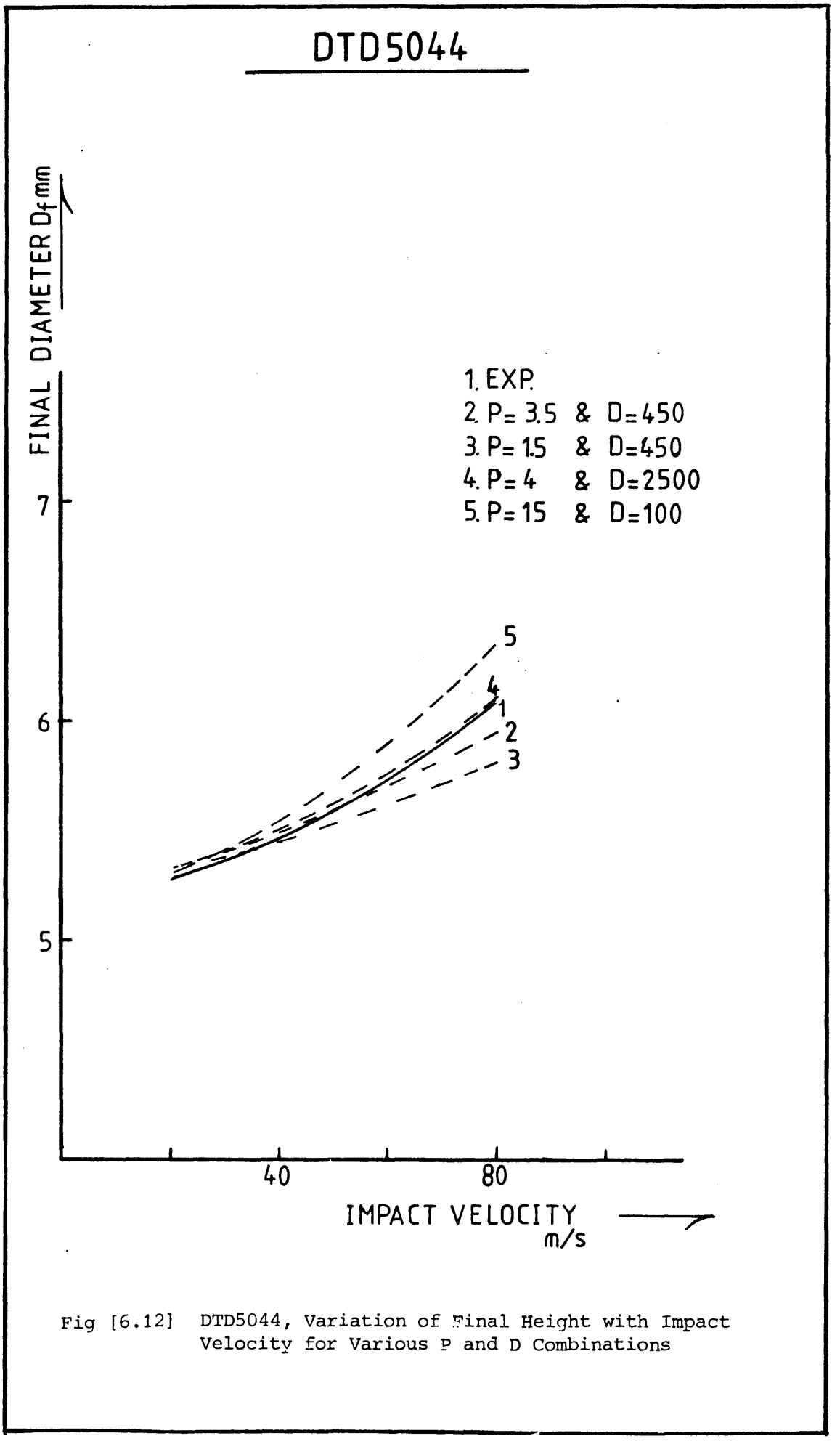

Fig [6.12] DTD5044, Variation of Final Height with Impact Velocity for Various P and D Combinations

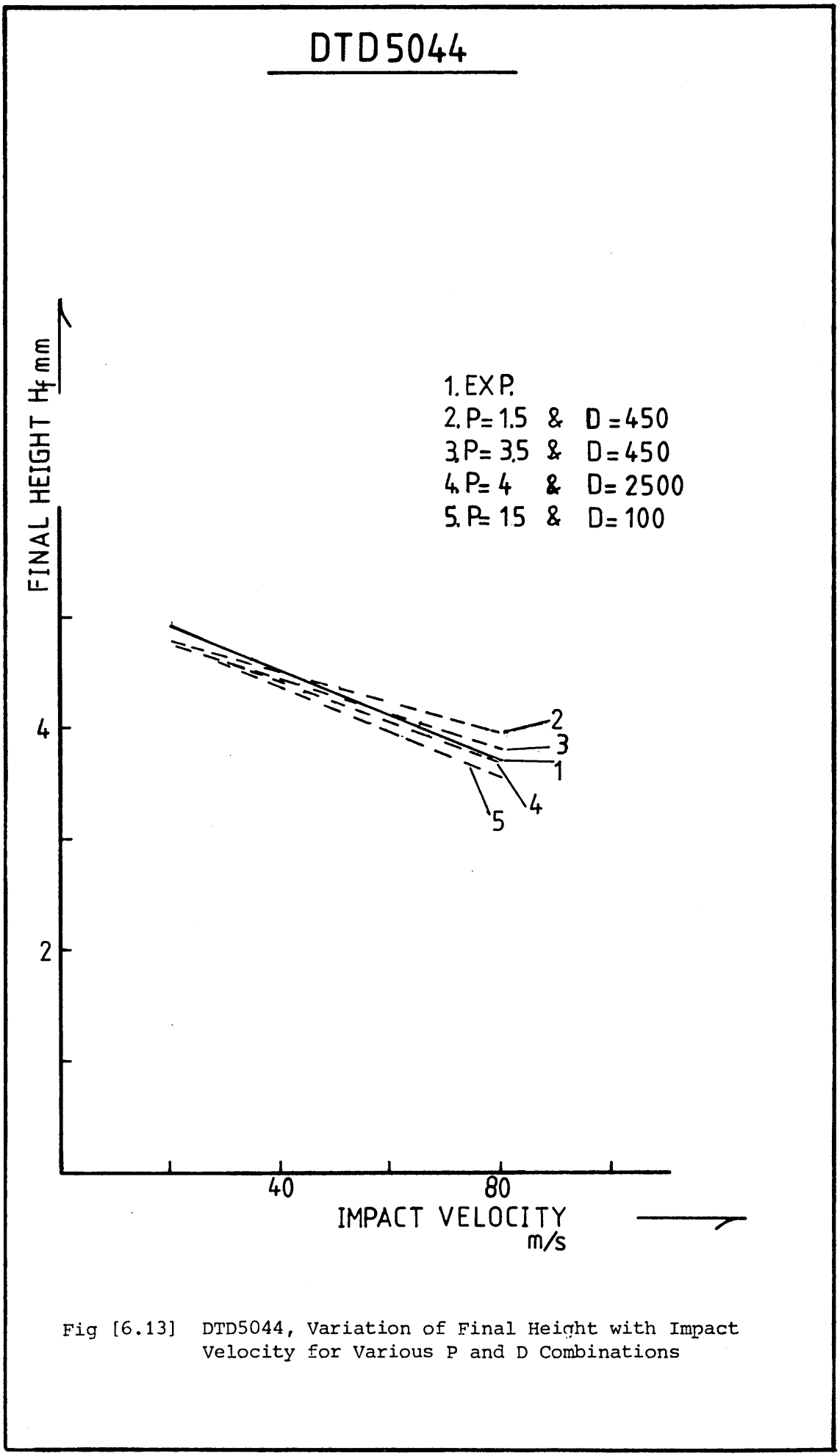

Fig [6.13] DTD5044, Variation of Final Height with Impact Velocity for Various P and D Combinations

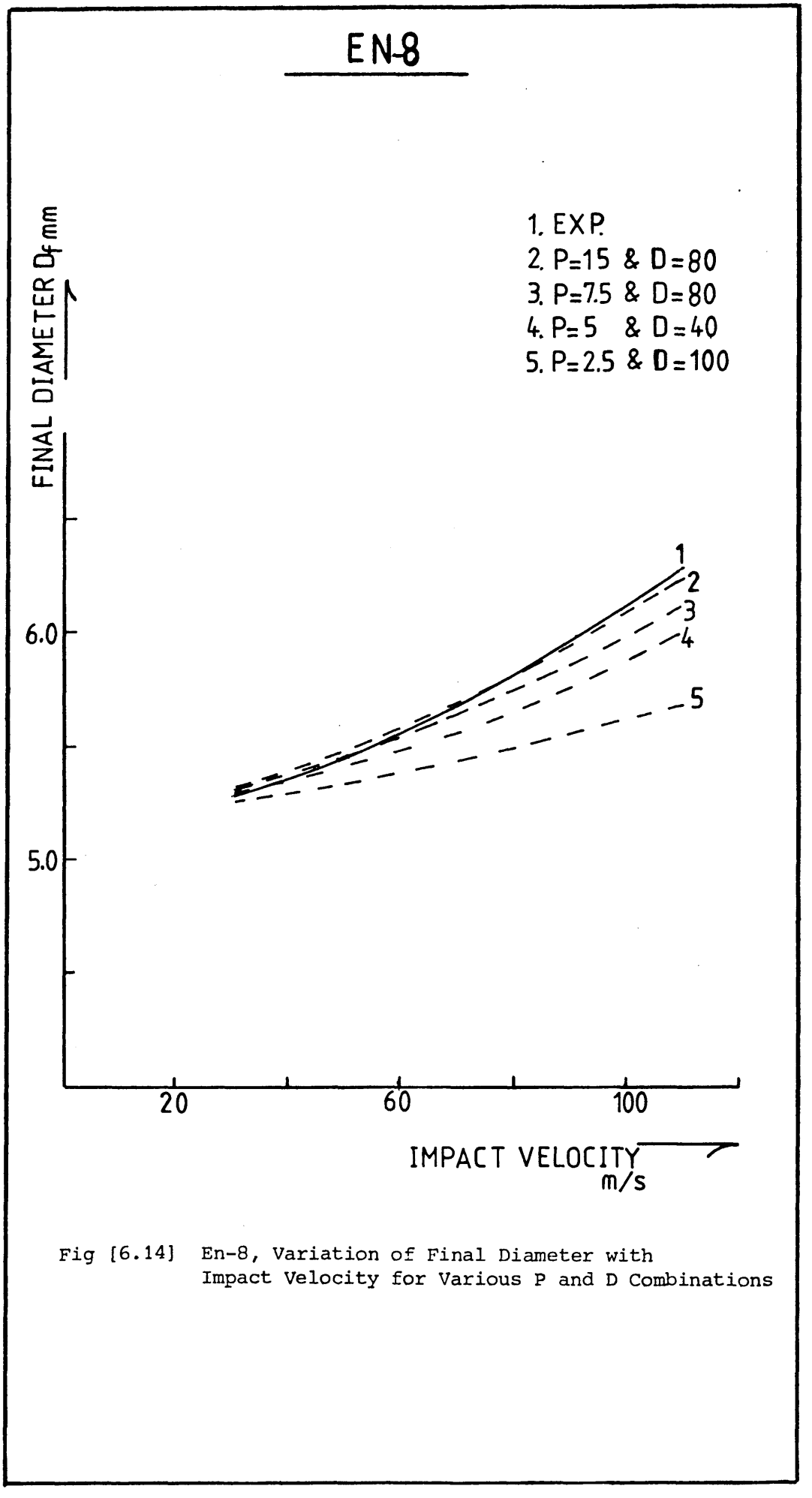

Fig [6.14] En-8, Variation of Final Diameter with Impact Velocity for Various P and D Combinations

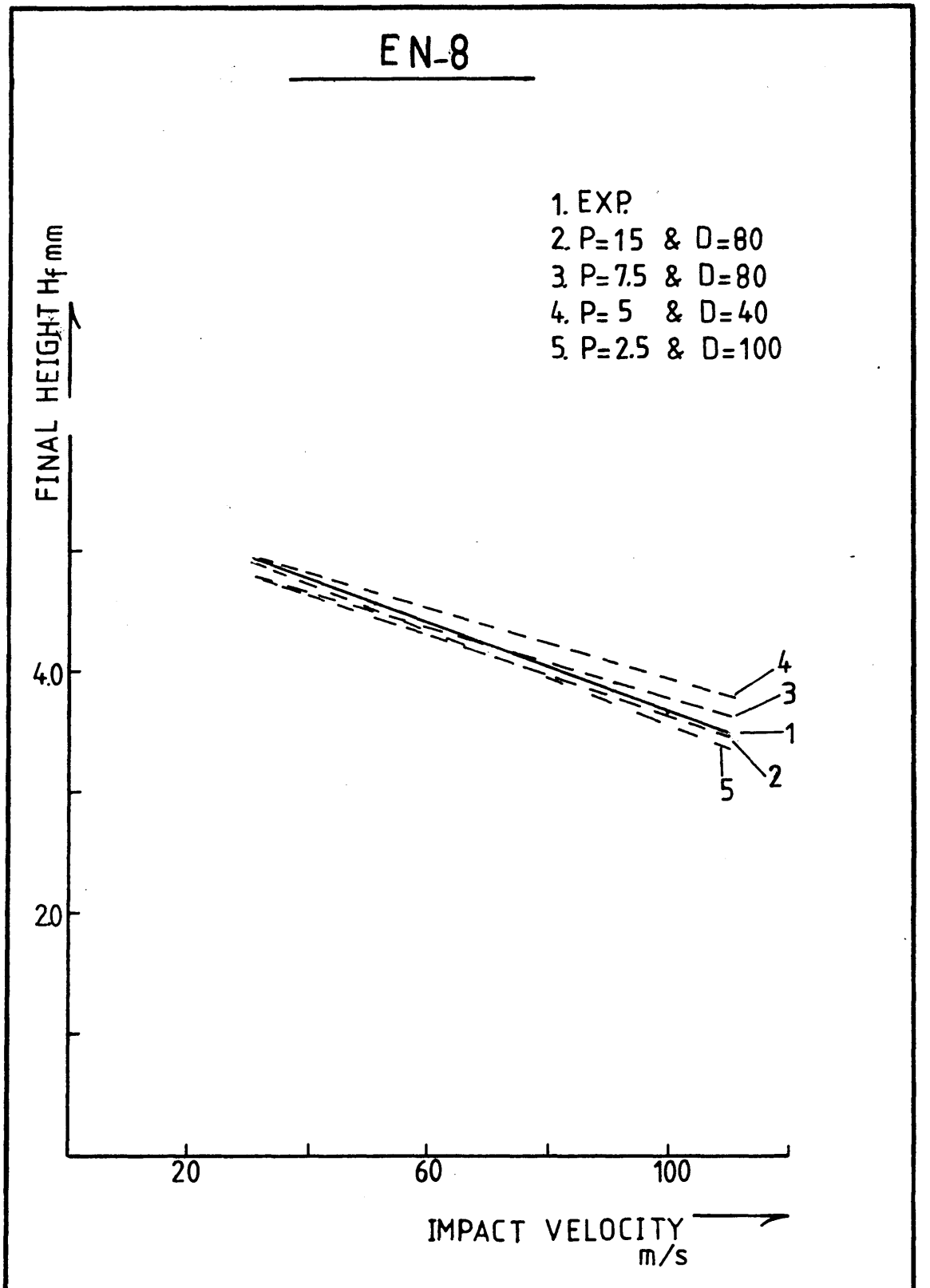

Fig [6.15] En-8, Variation of Final Height with Impact Velocity for Various P and D Combinations

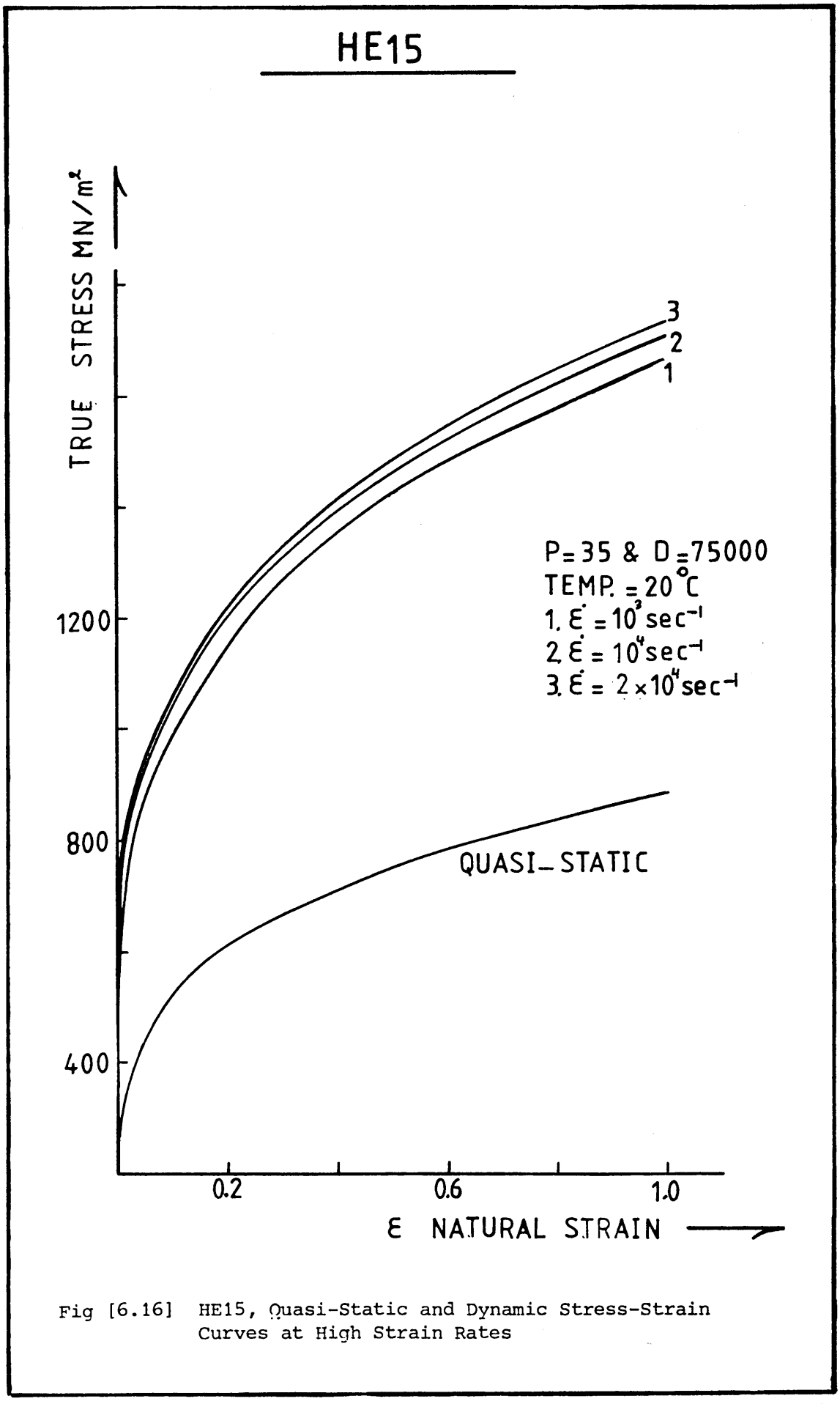

Fig [6.16] HE15, Quasi-Static and Dynamic Stress-Strain Curves at High Strain Rates

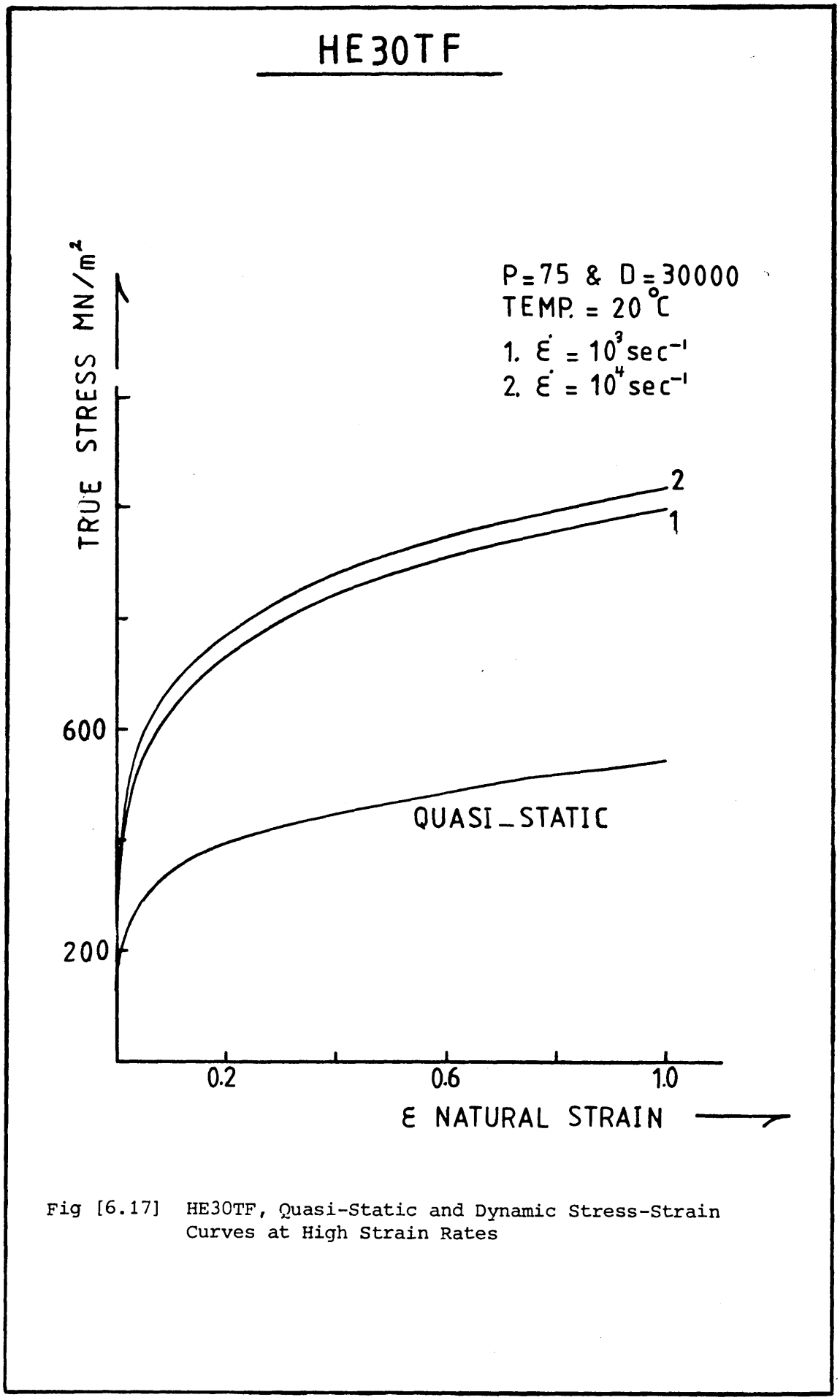

Fig [6.17] HE30TF, Quasi-Static and Dynamic Stress-Strain Curves at High Strain Rates

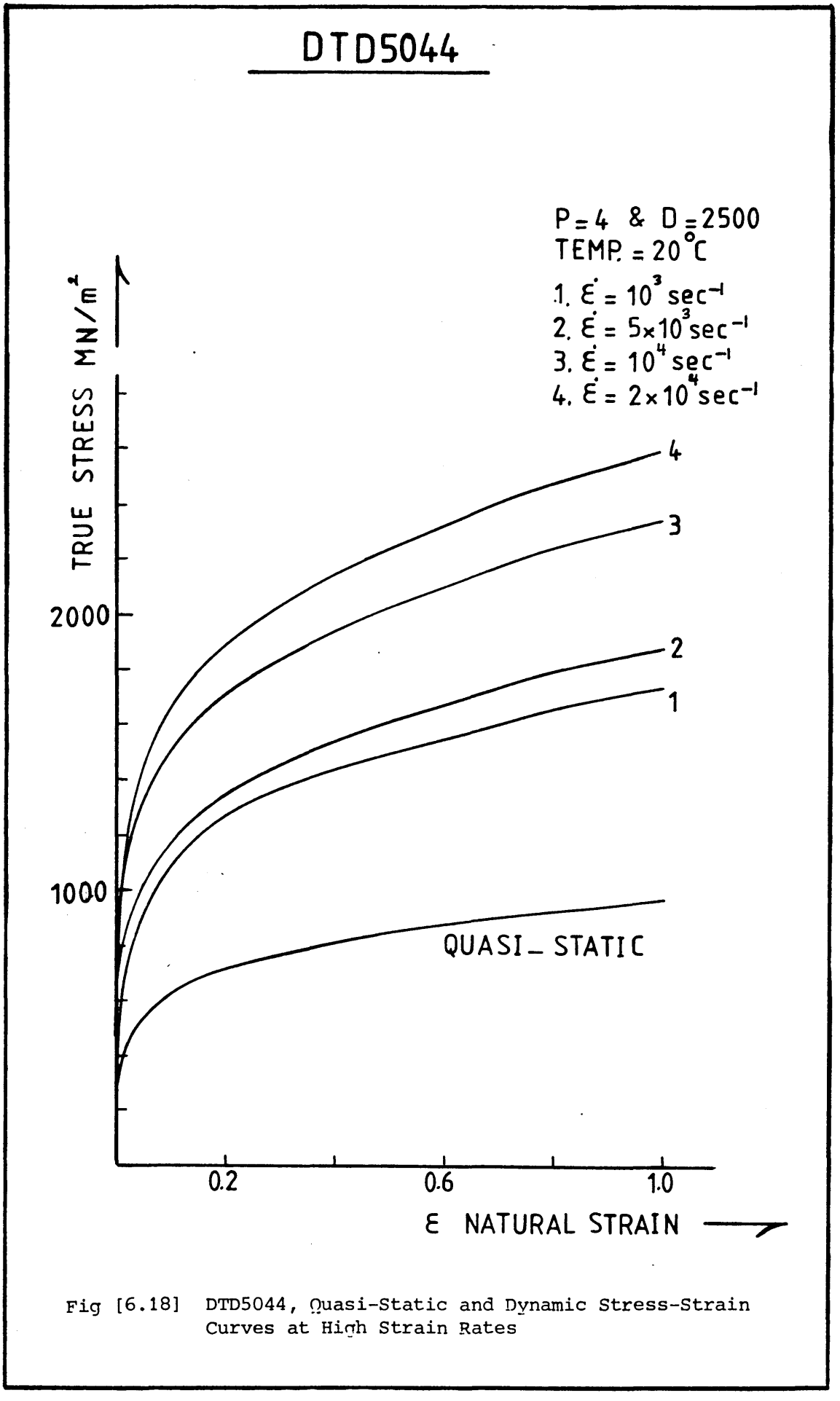

Fig [6.18] DTD5044, Quasi-Static and Dynamic Stress-Strain Curves at High Strain Rates

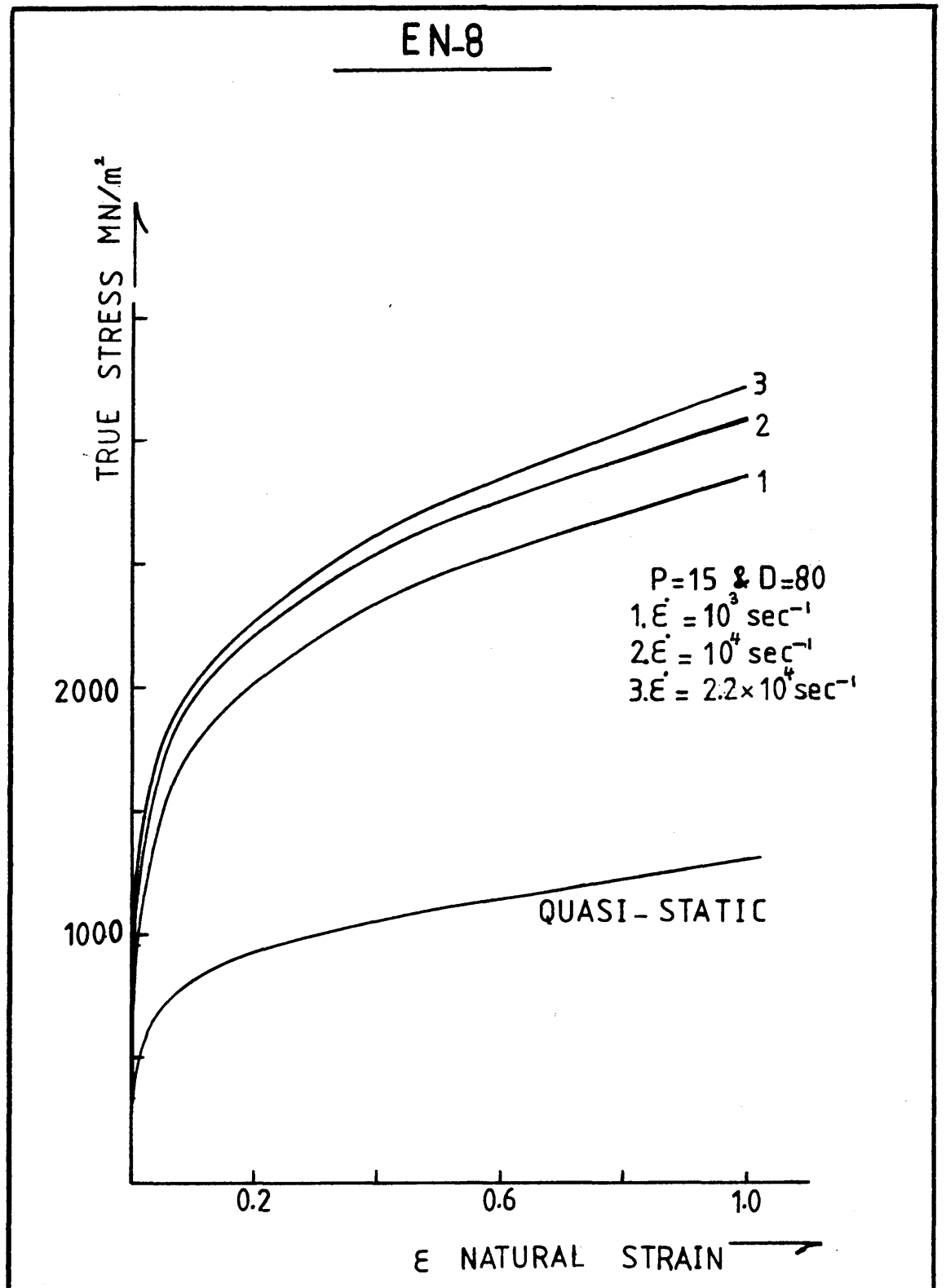

Fig [6.19] En-8, Quasi-Static and Dynamic Stress-Strain Curves at High Strain Rates

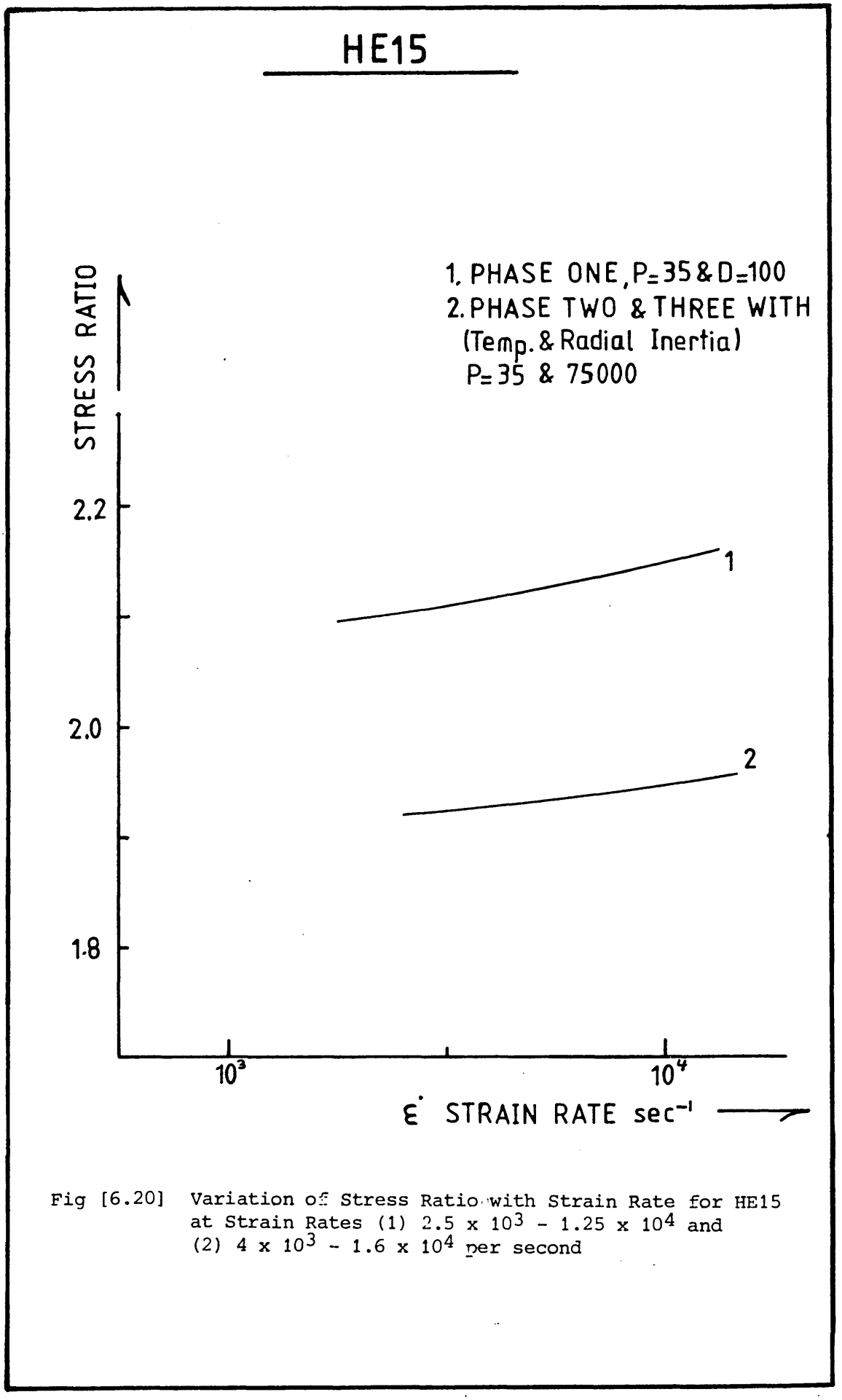

Fig [6.20] Variation of Stress Ratio with Strain Rate for HE15 at Strain Rates (1) $2.5 \times 10^3 - 1.25 \times 10^4$ and (2) $4 \times 10^3 - 1.6 \times 10^4$ per second

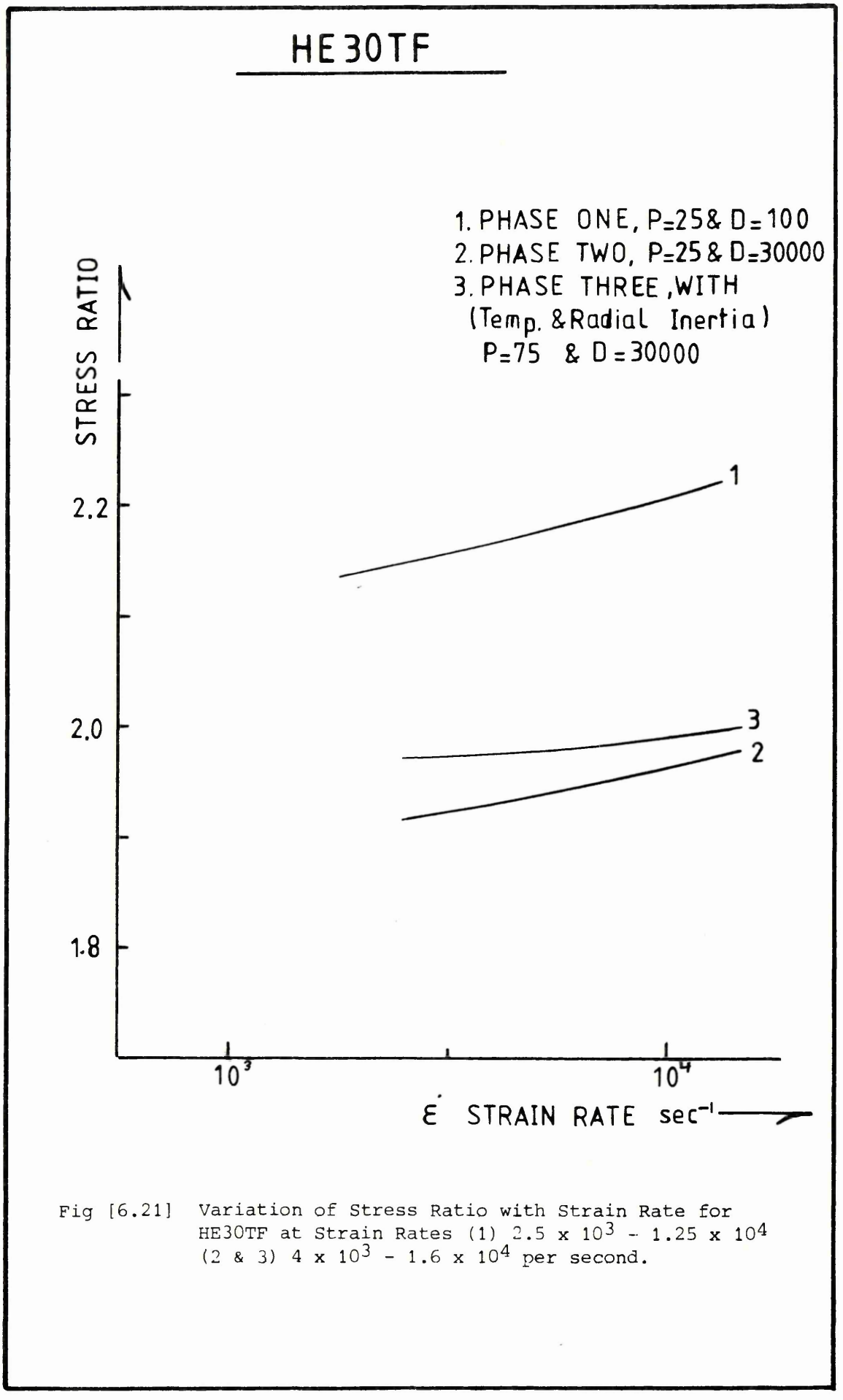

Fig [6.21] Variation of Stress Ratio with Strain Rate for HE30TF at Strain Rates (1) 2.5×10^3 - 1.25×10^4 (2 & 3) 4×10^3 - 1.6×10^4 per second.

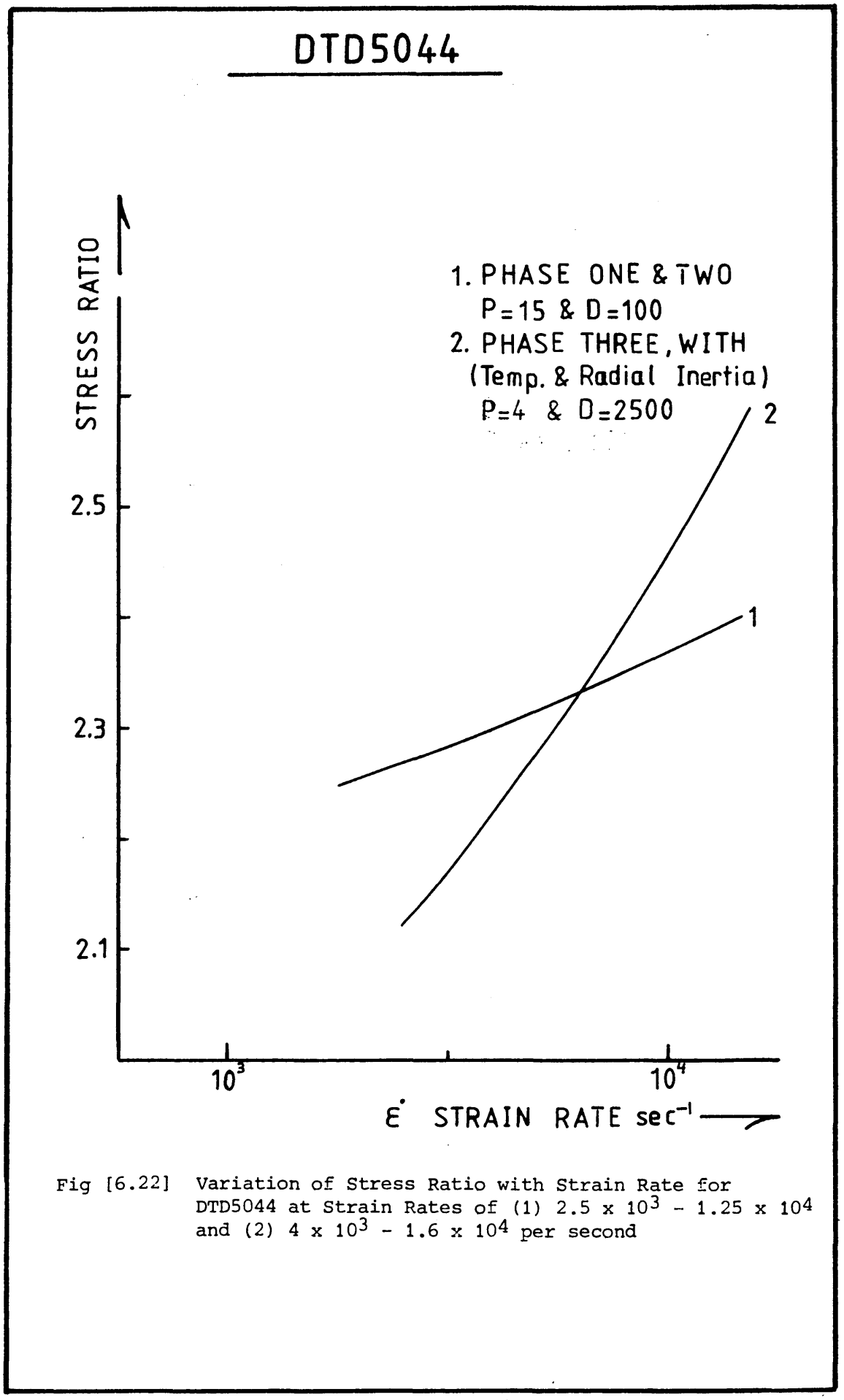

Fig [6.22] Variation of Stress Ratio with Strain Rate for DTD5044 at Strain Rates of (1) $2.5 \times 10^3 - 1.25 \times 10^4$ and (2) $4 \times 10^3 - 1.6 \times 10^4$ per second

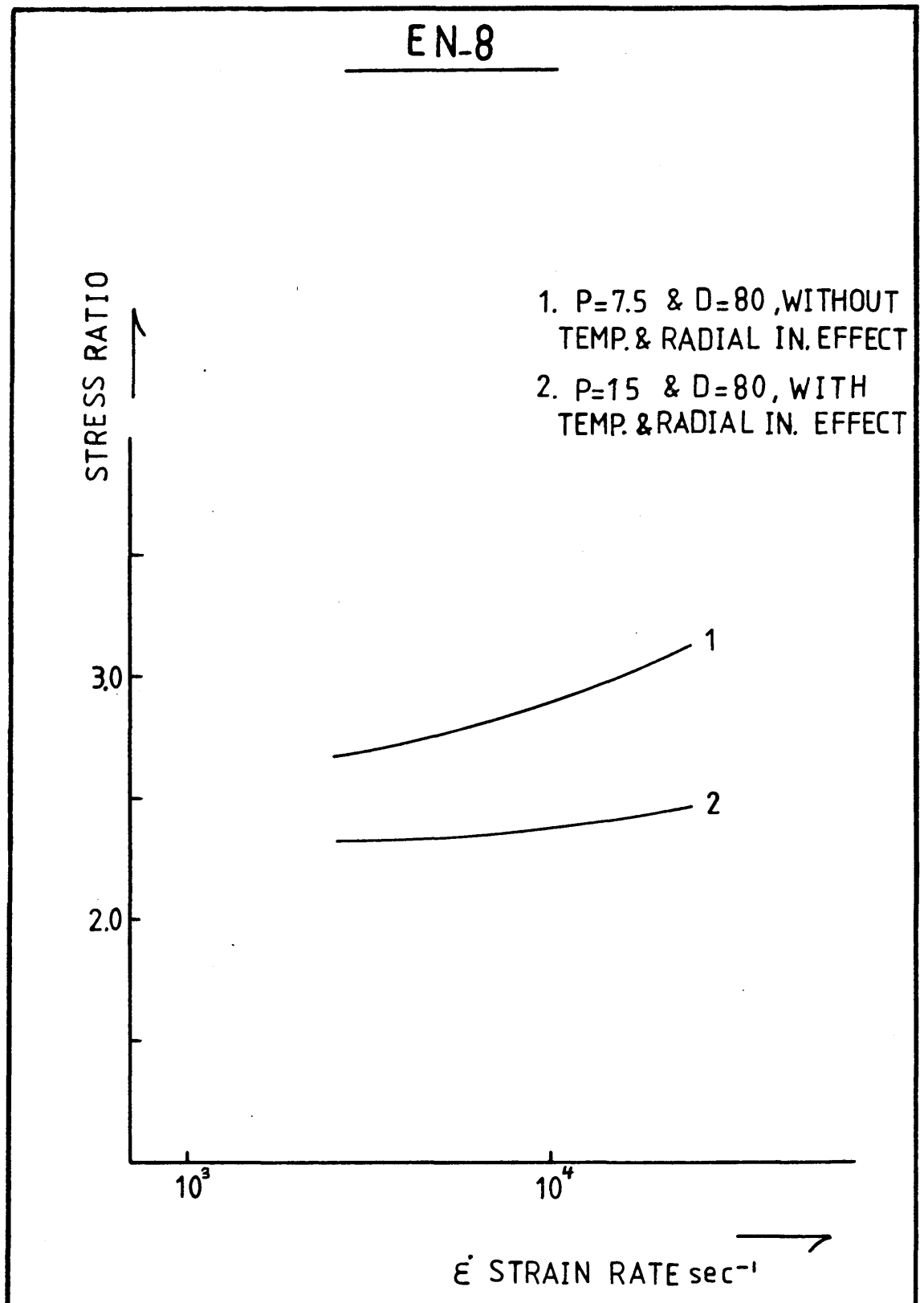

Fig [6.23] Variation of Stress Ratio with Strain Rate for En-8 at Strain Rates (1 & 2) 6 x 10^3 - 2.2 x 10^4 per second

ALUMINIUM ALLOYS

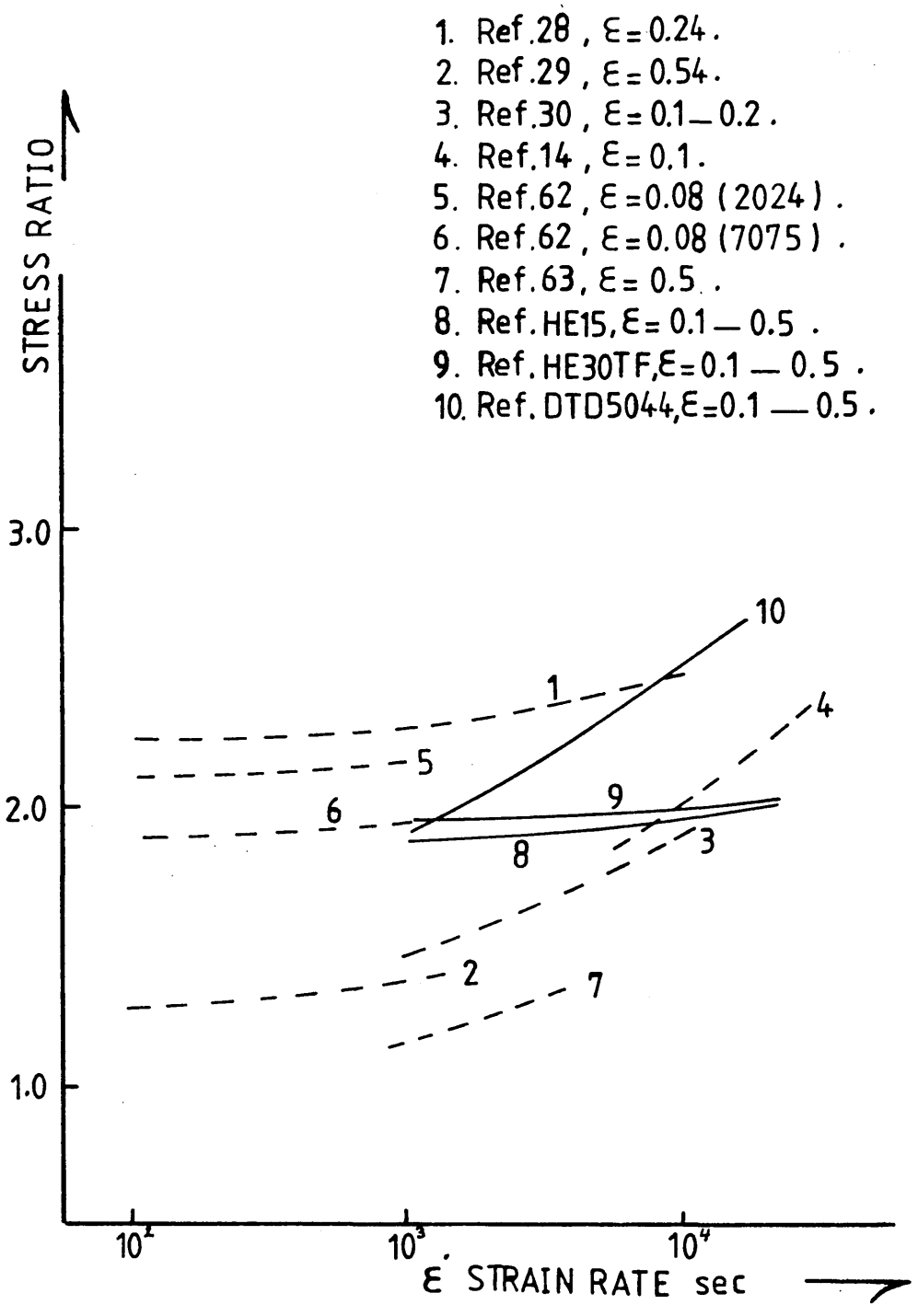

Fig [6.24] Comparison of Stress Ratio against Strain Rate Curves with Similar Work Done by Others

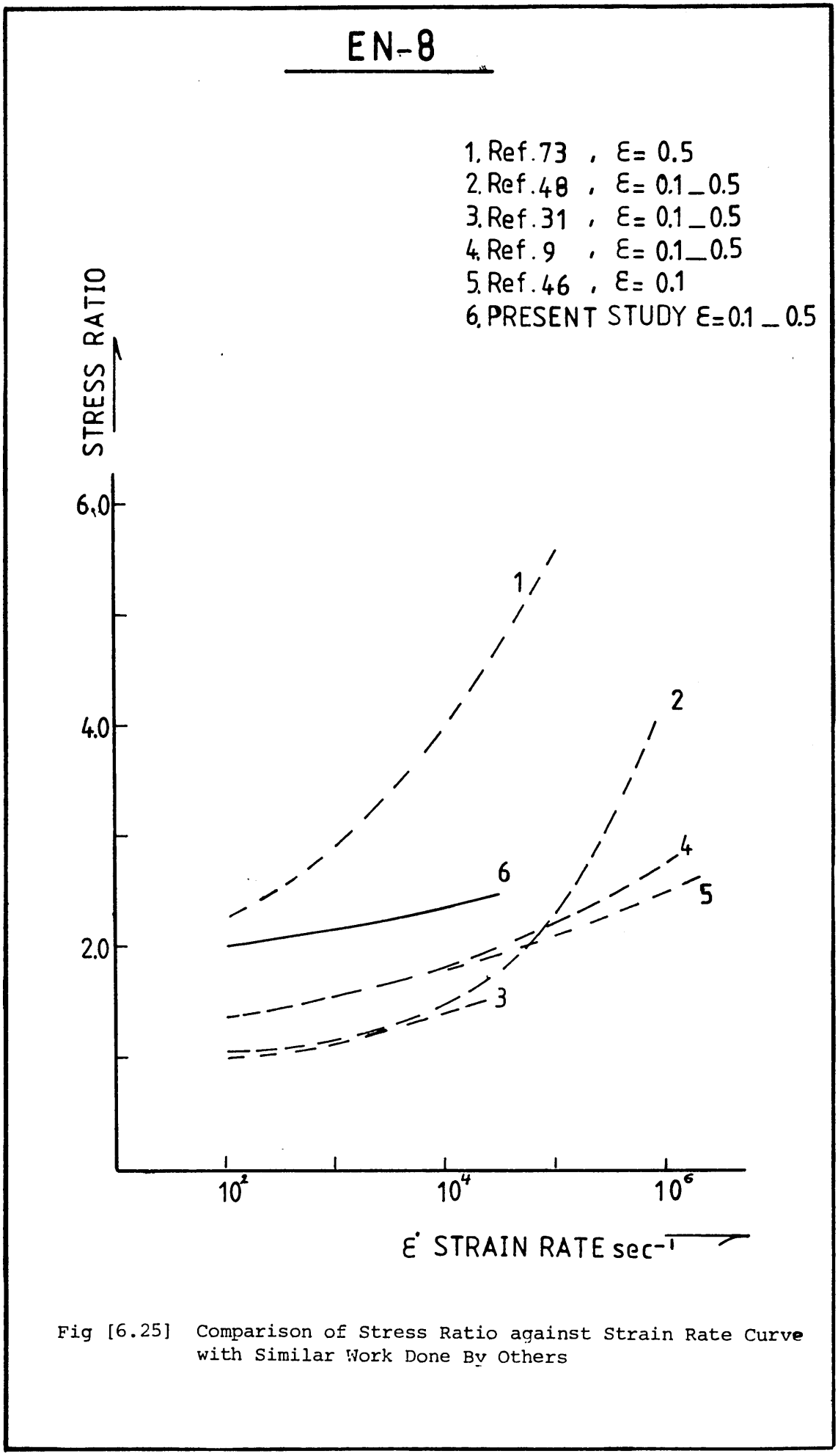

Fig [6.25] Comparison of Stress Ratio against Strain Rate Curve with Similar Work Done By Others

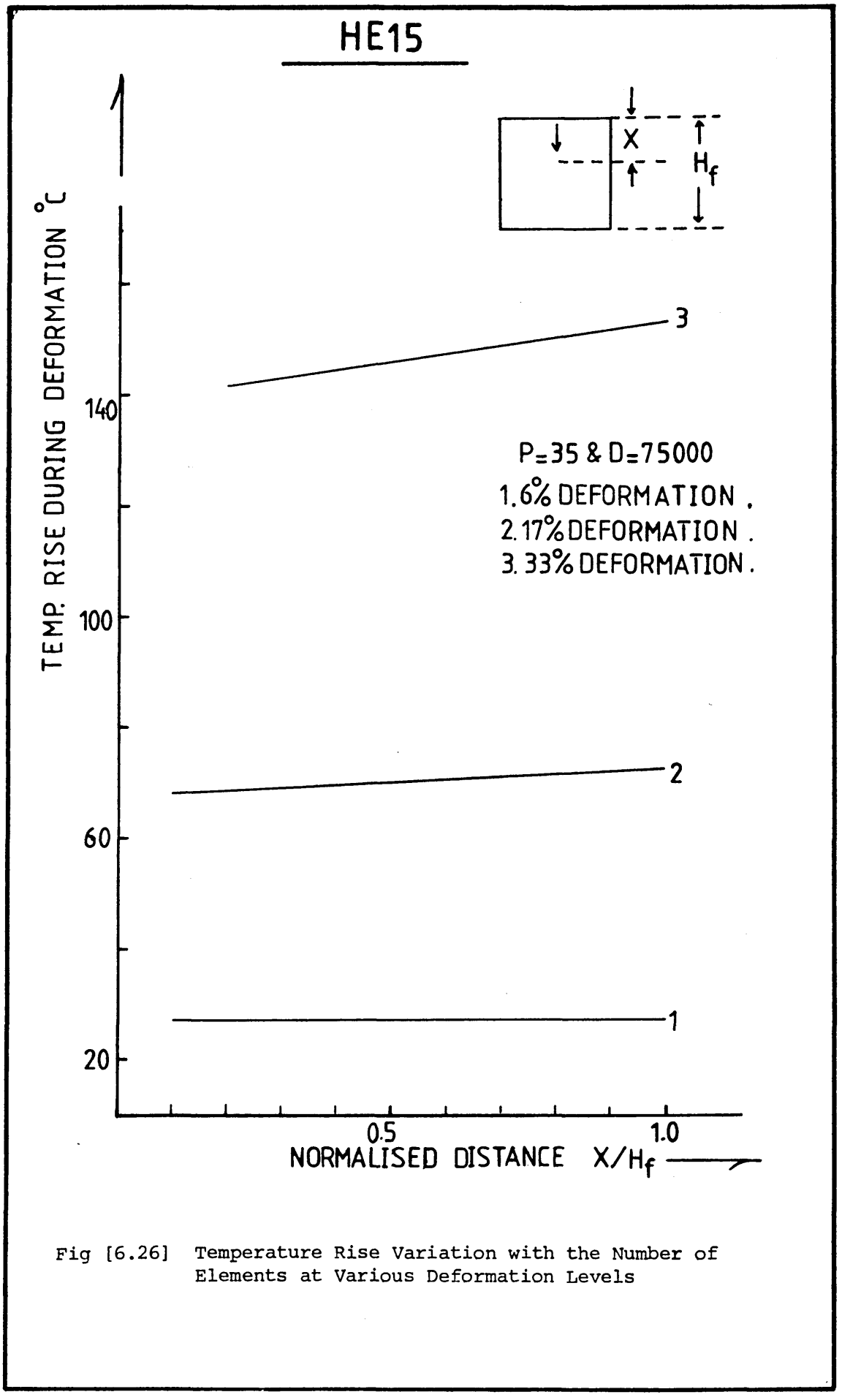

Fig [6.26] Temperature Rise Variation with the Number of Elements at Various Deformation Levels

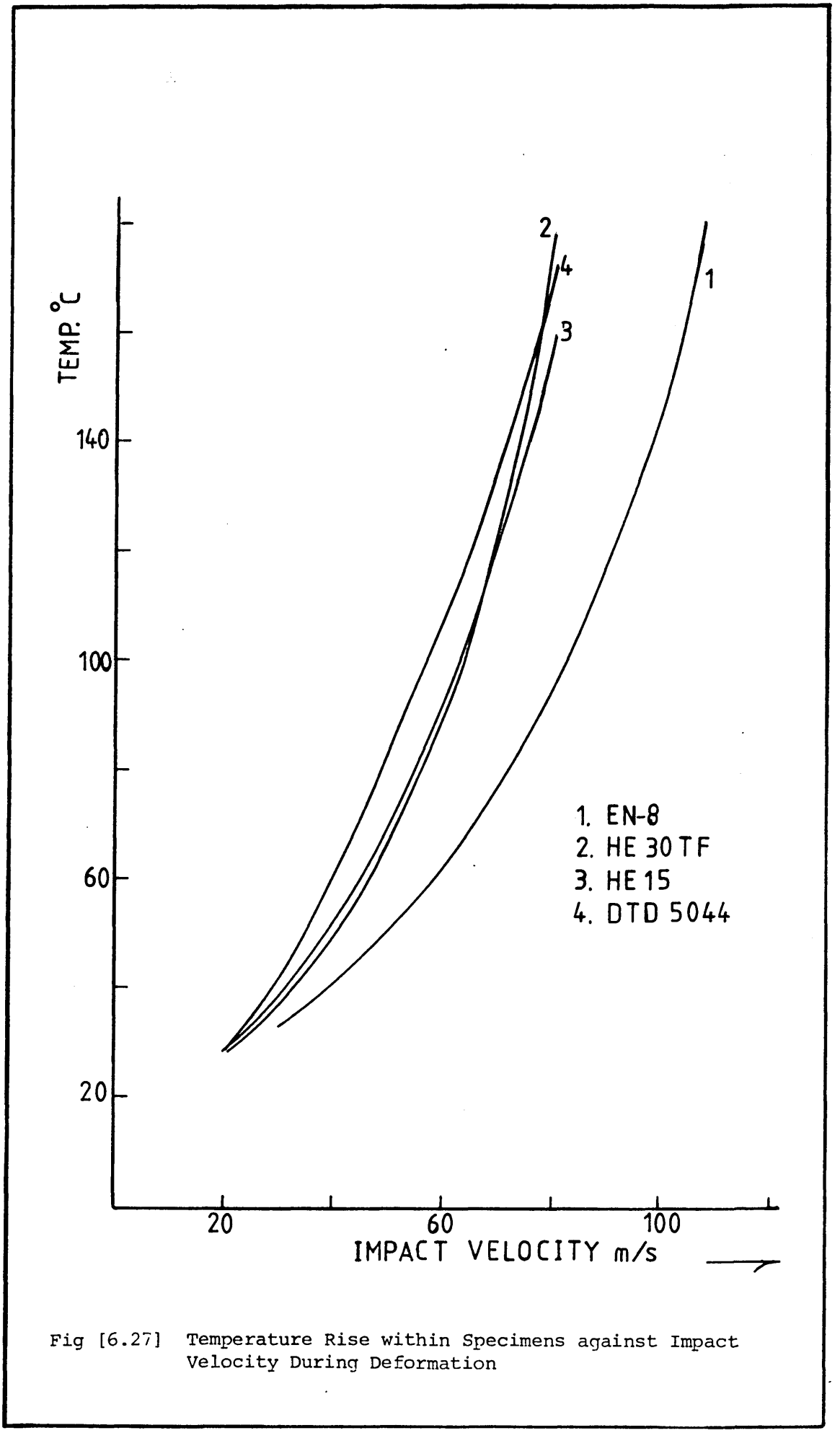

Fig [6.27] Temperature Rise within Specimens against Impact Velocity During Deformation

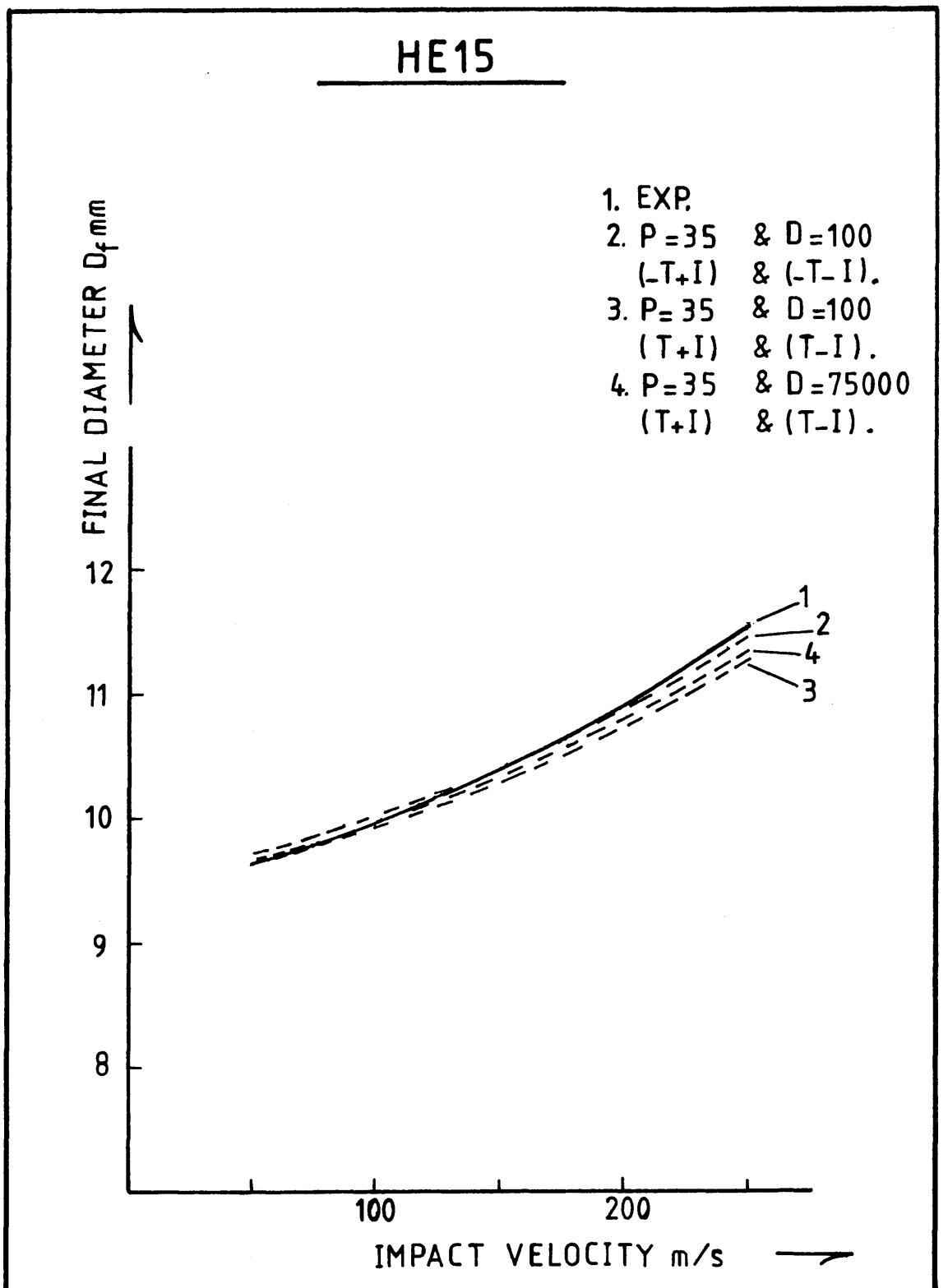

Fig [6.28] HE15, Variation of Final Diameter with Impact Velocity at Various P and D Combinations and Different Conditions

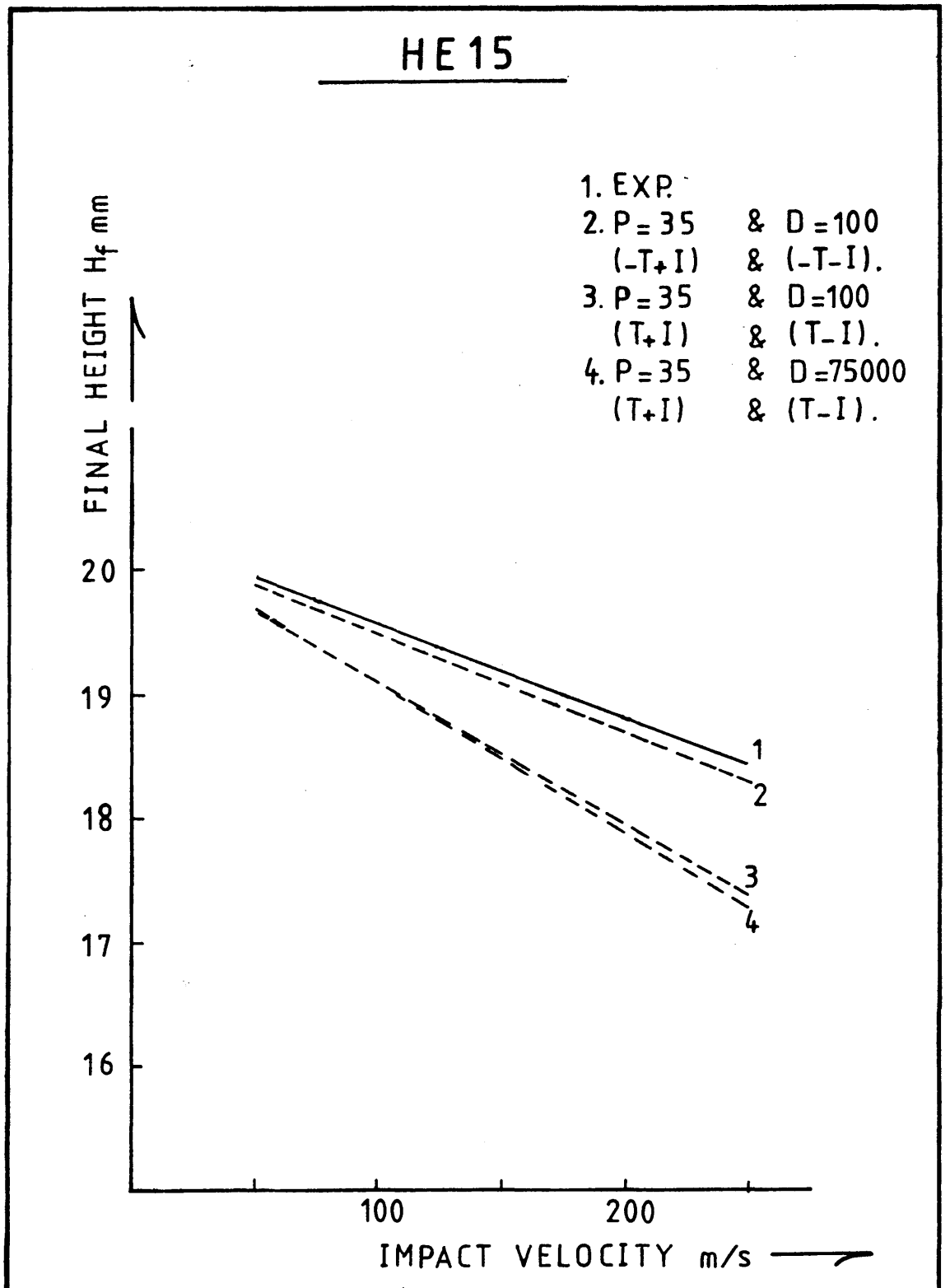

Fig [6.29] HE15, Variation of Final Height with Impact Velocity at Various P and D Combinations and Different Conditions

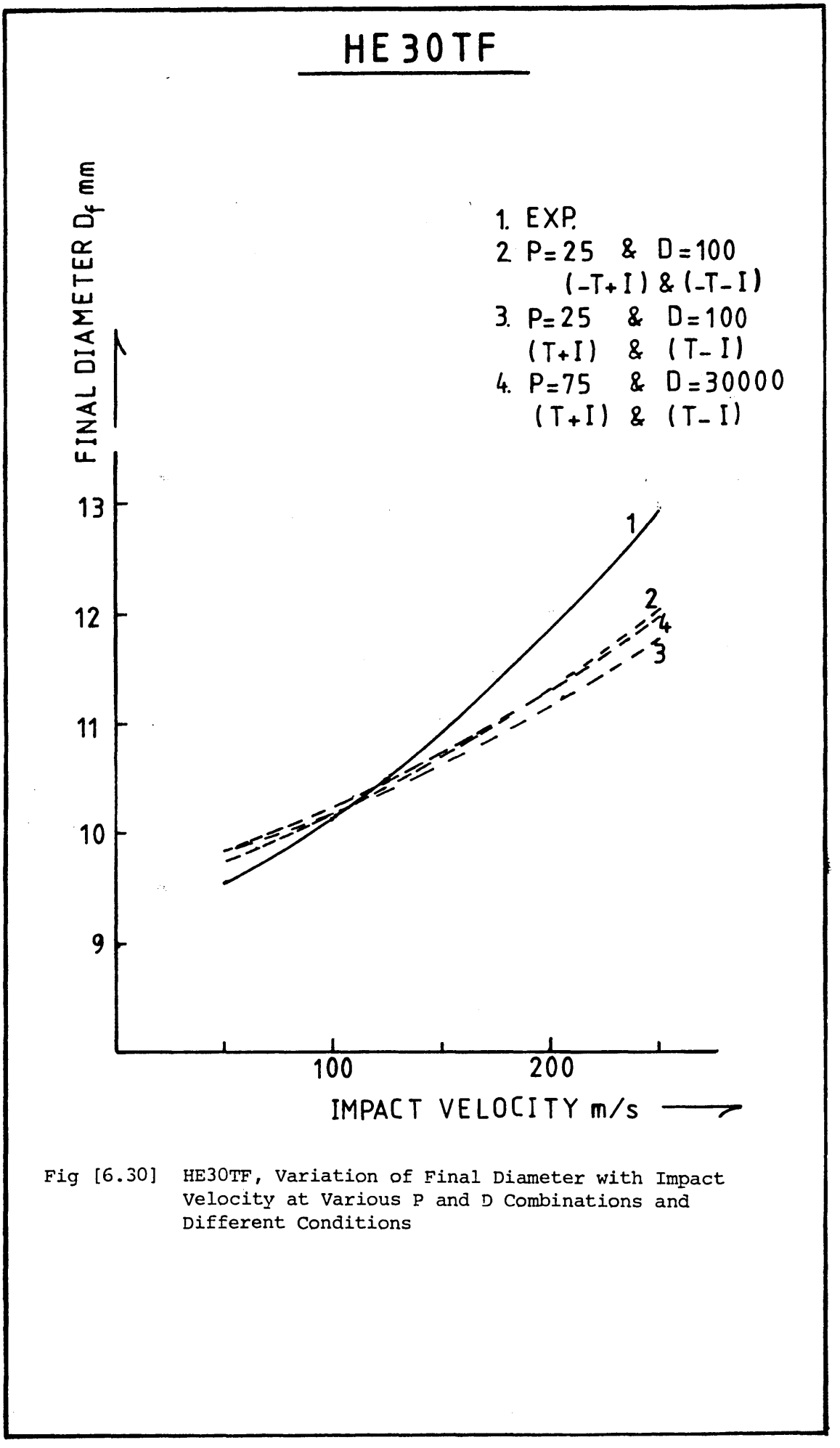

Fig [6.30] HE30TF, Variation of Final Diameter with Impact Velocity at Various P and D Combinations and Different Conditions

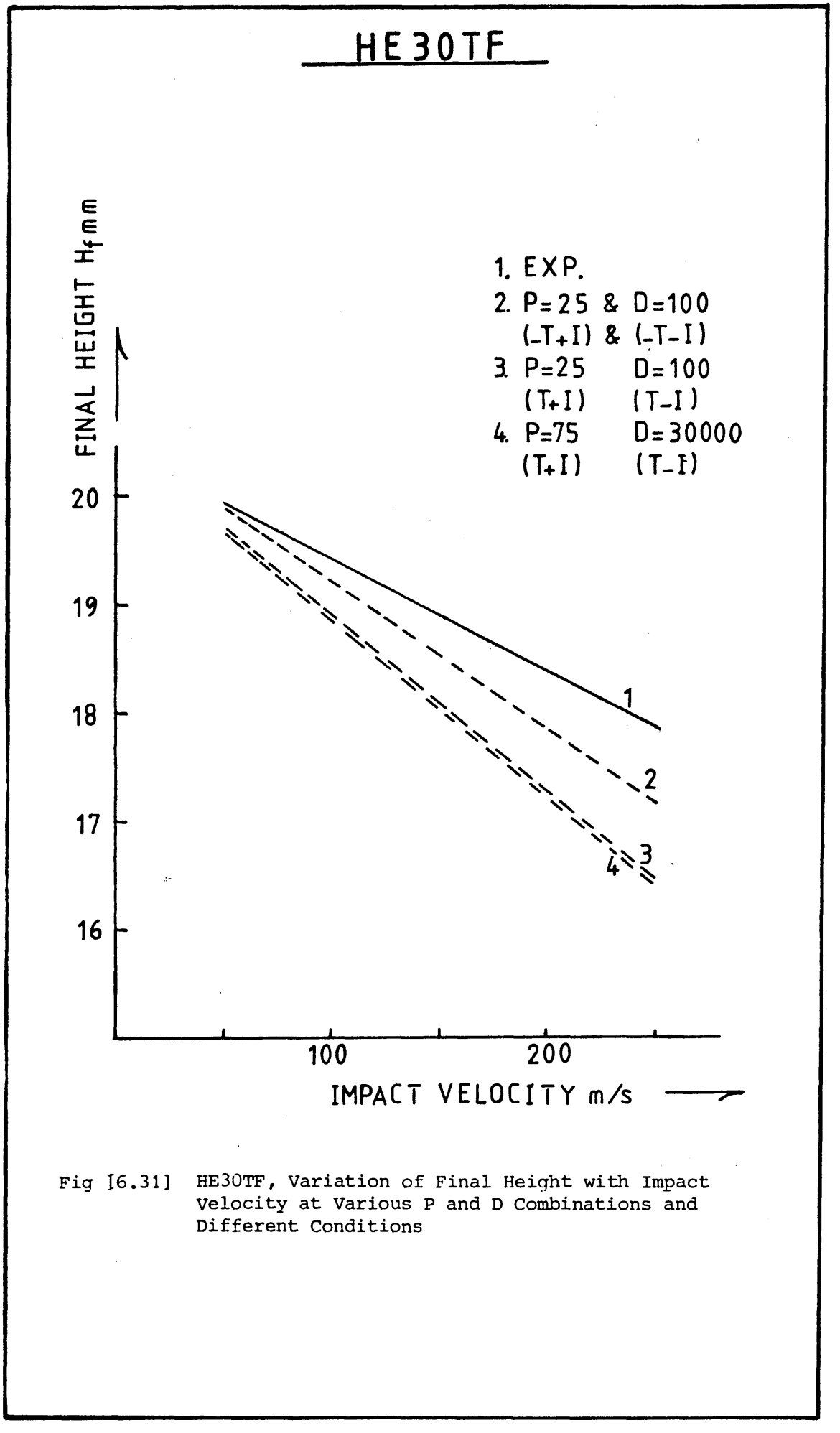

Fig [6.31] HE30TF, Variation of Final Height with Impact Velocity at Various P and D Combinations and Different Conditions

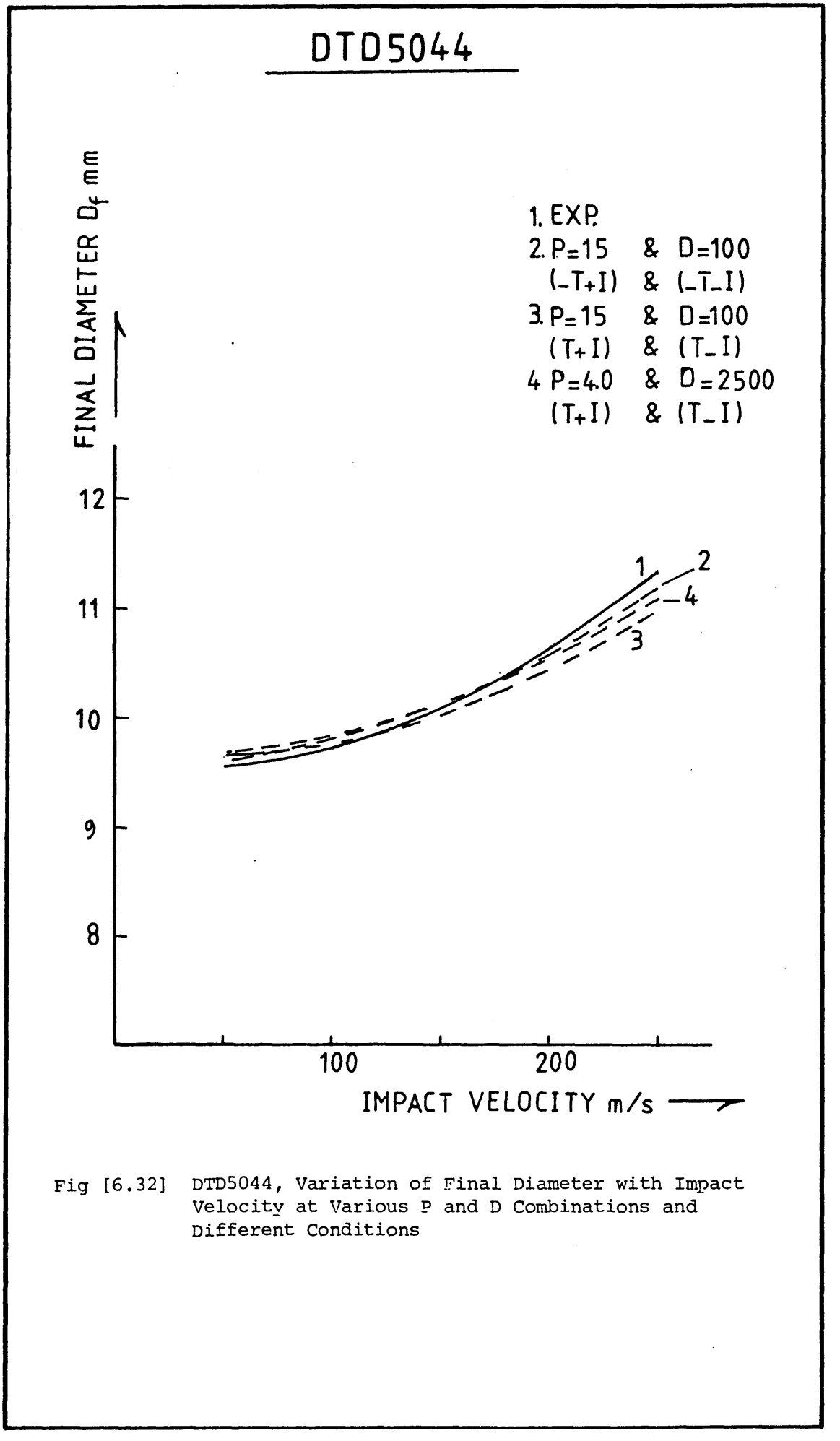

Fig [6.32] DTD5044, Variation of Final Diameter with Impact Velocity at Various P and D Combinations and Different Conditions

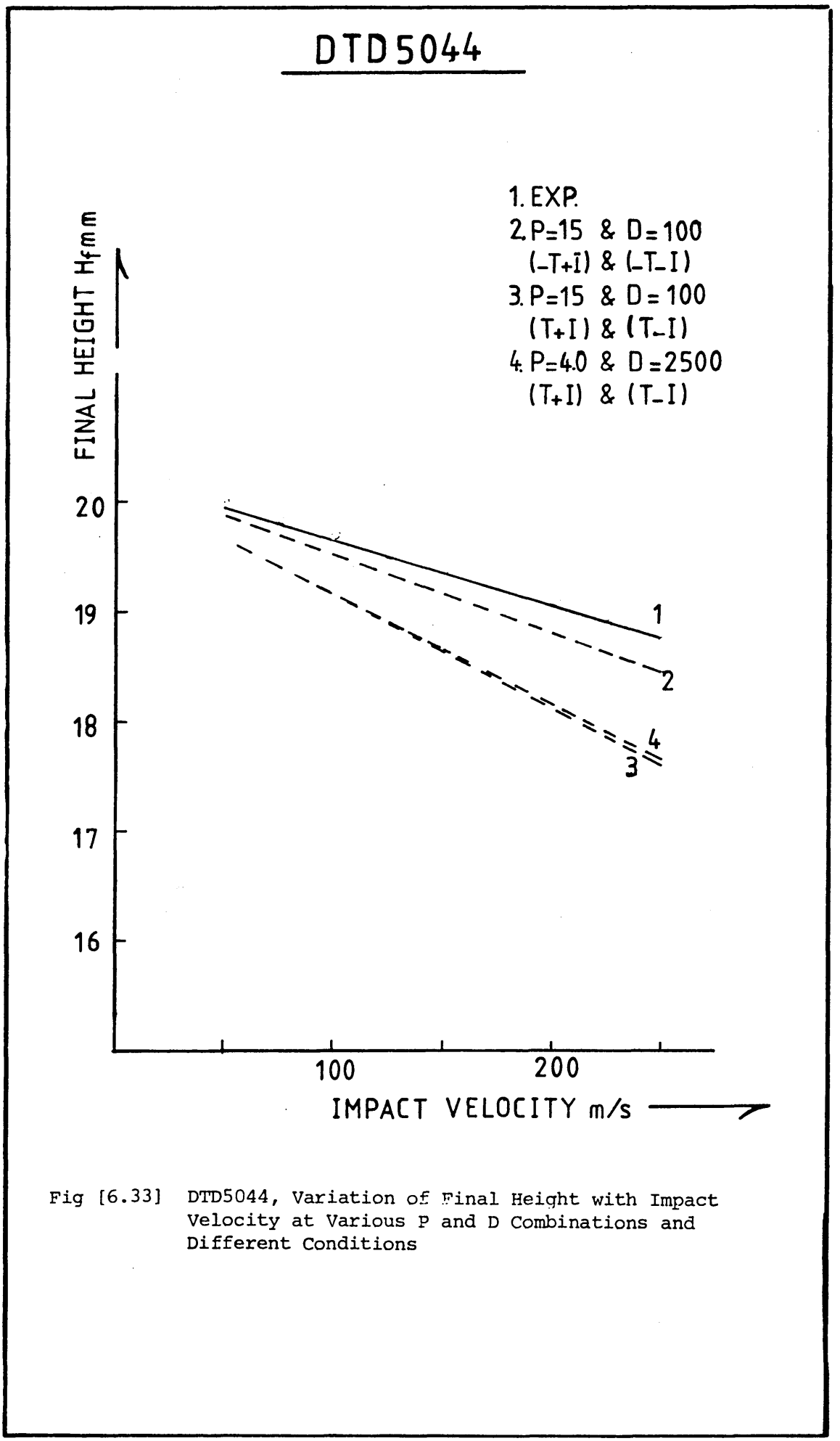

Fig [6.33] DTD5044, Variation of Final Height with Impact Velocity at Various P and D Combinations and Different Conditions

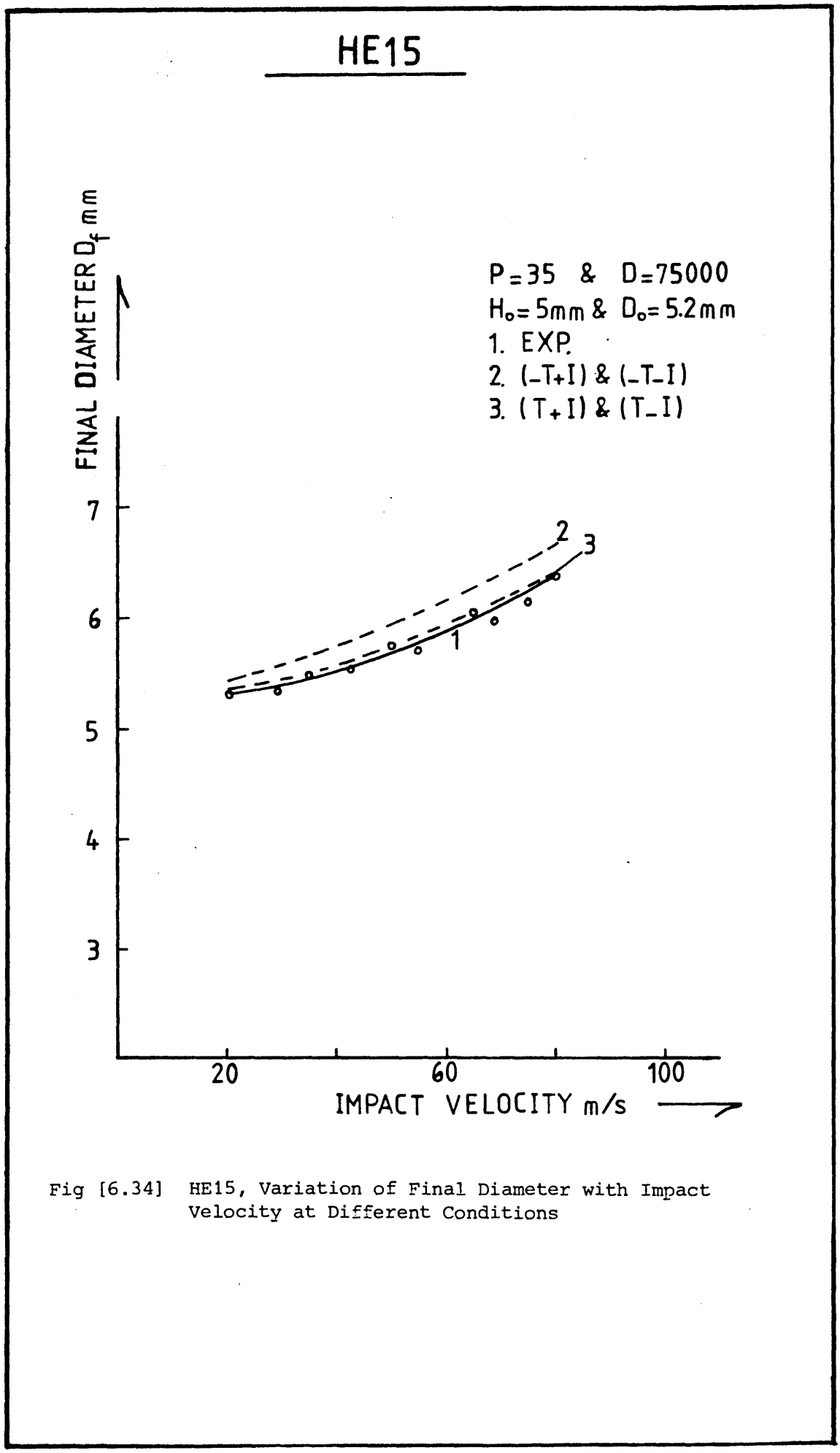

Fig [6.34] HE15, Variation of Final Diameter with Impact Velocity at Different Conditions

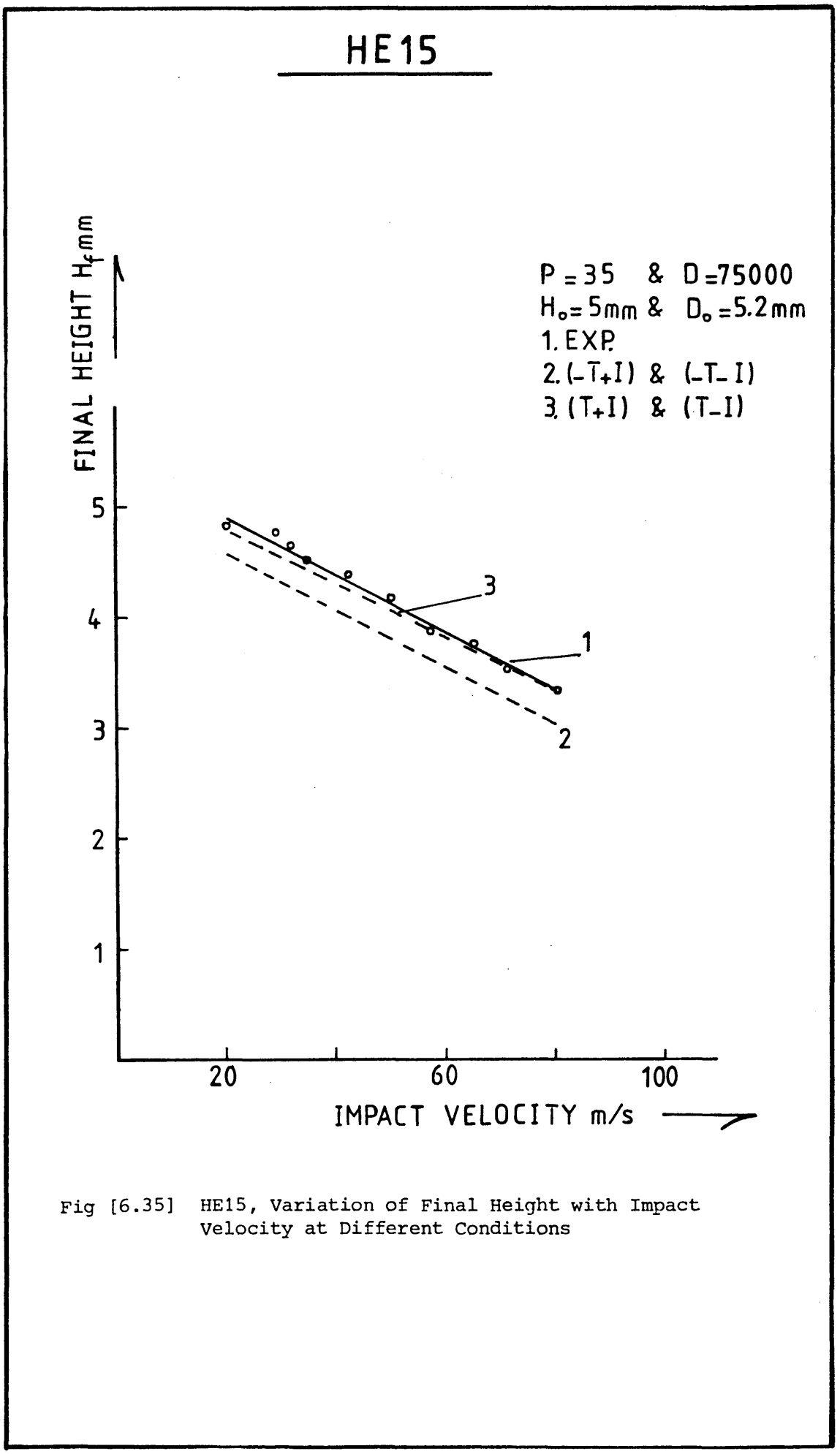

Fig [6.35] HE15, Variation of Final Height with Impact Velocity at Different Conditions

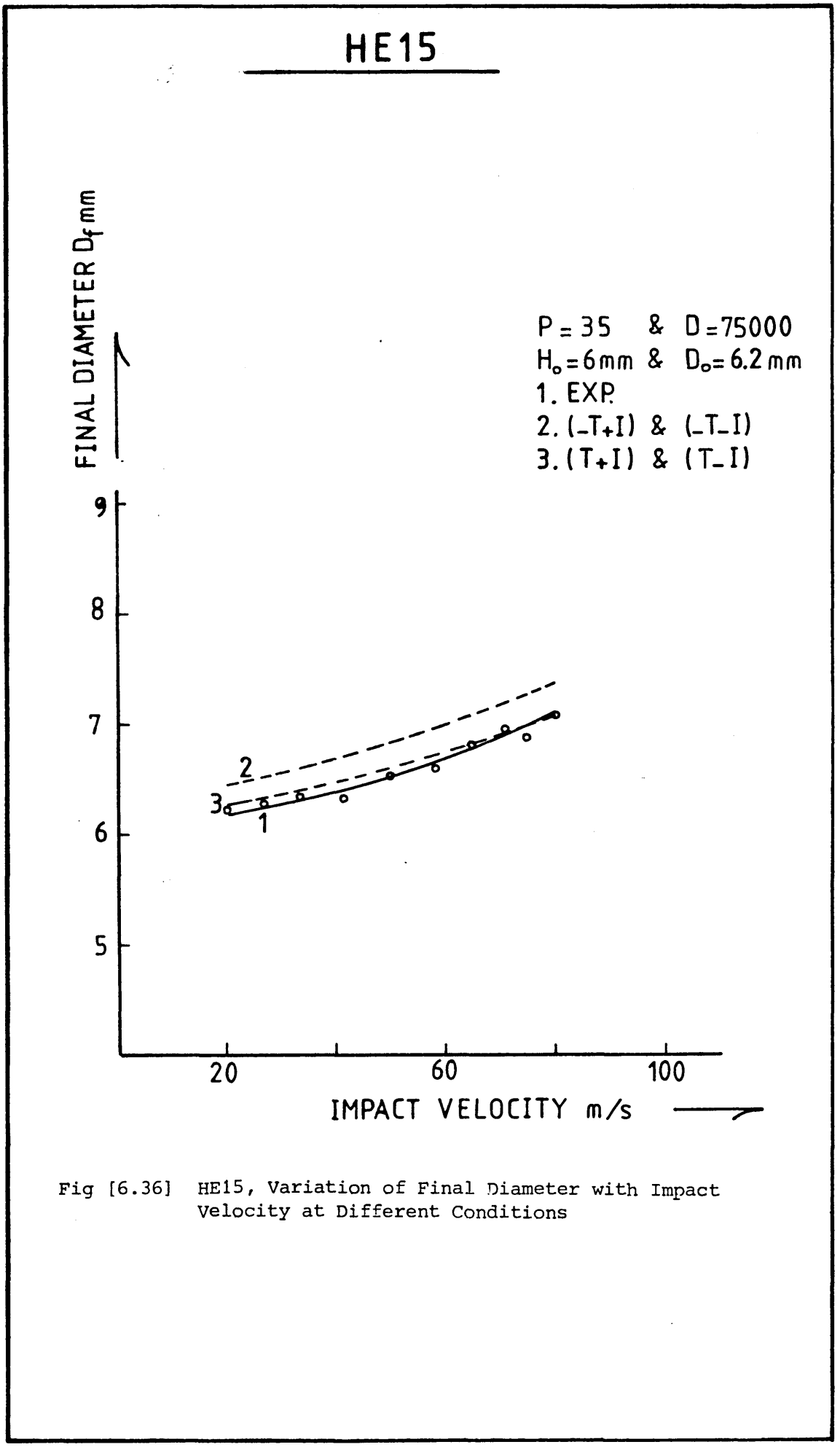

Fig [6.36] HE15, Variation of Final Diameter with Impact Velocity at Different Conditions

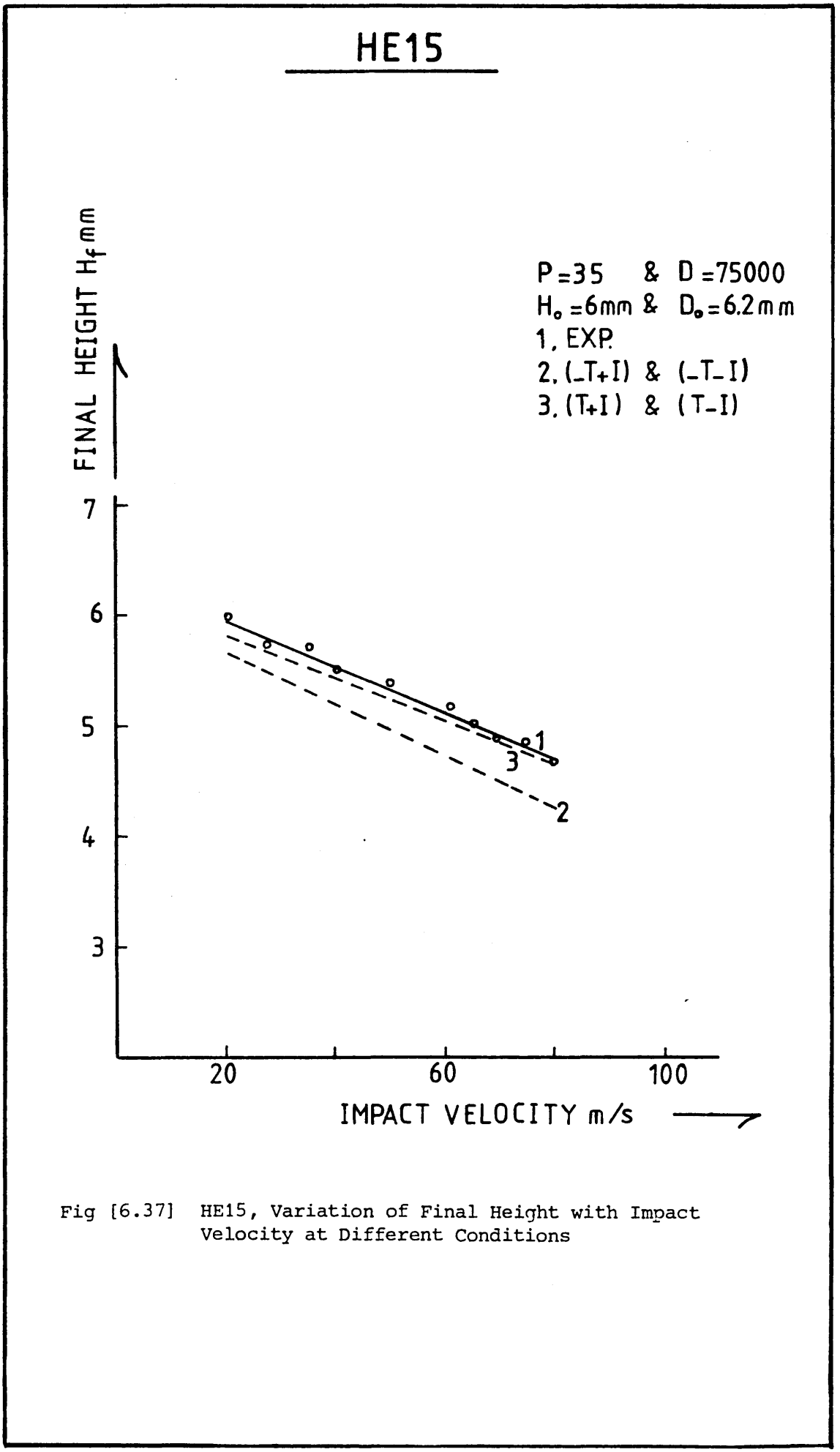

Fig [6.37] HE15, Variation of Final Height with Impact Velocity at Different Conditions

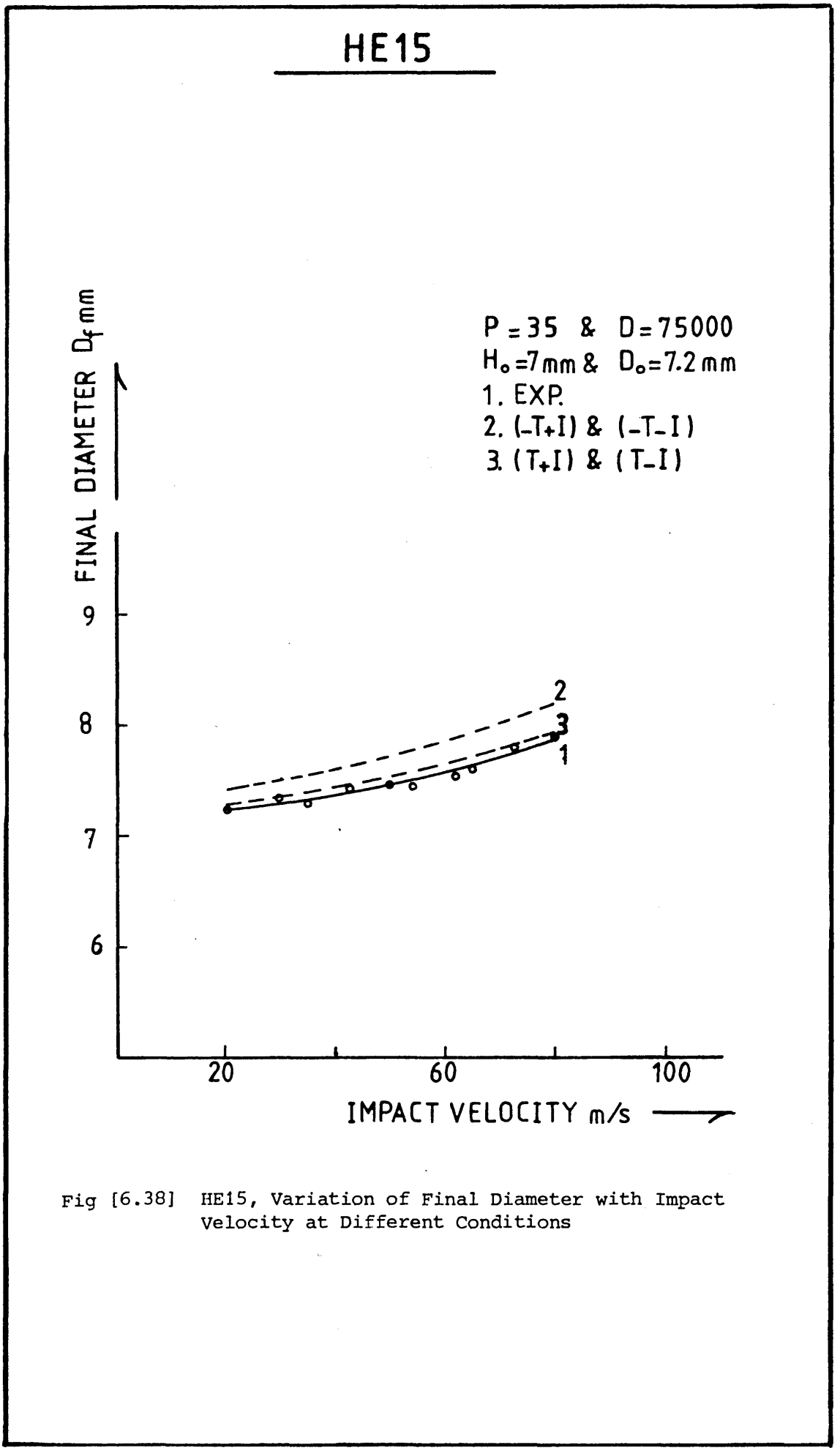

Fig [6.38] HE15, Variation of Final Diameter with Impact Velocity at Different Conditions

HE15

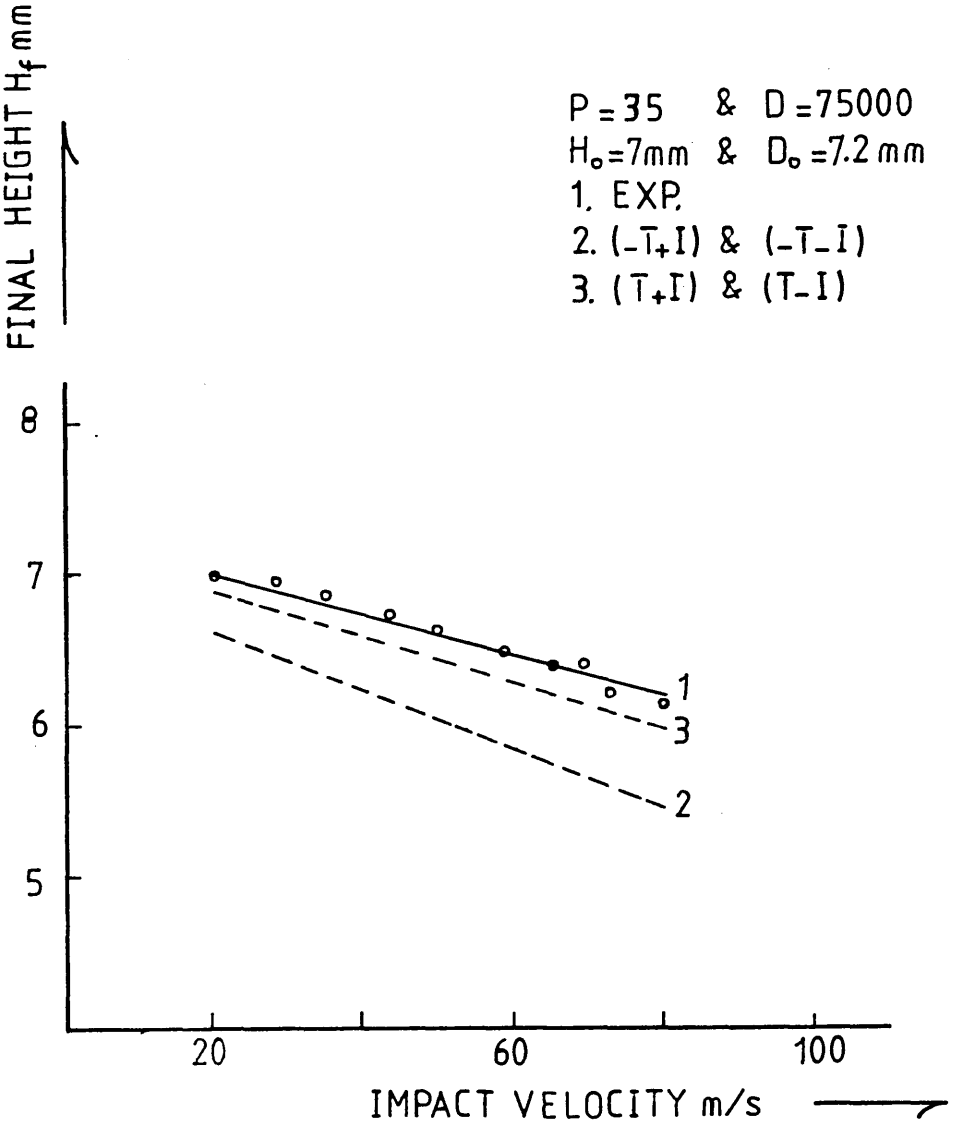

Fig [6.39] HE15, Variation of Final Height with Impact Velocity at Different Conditions

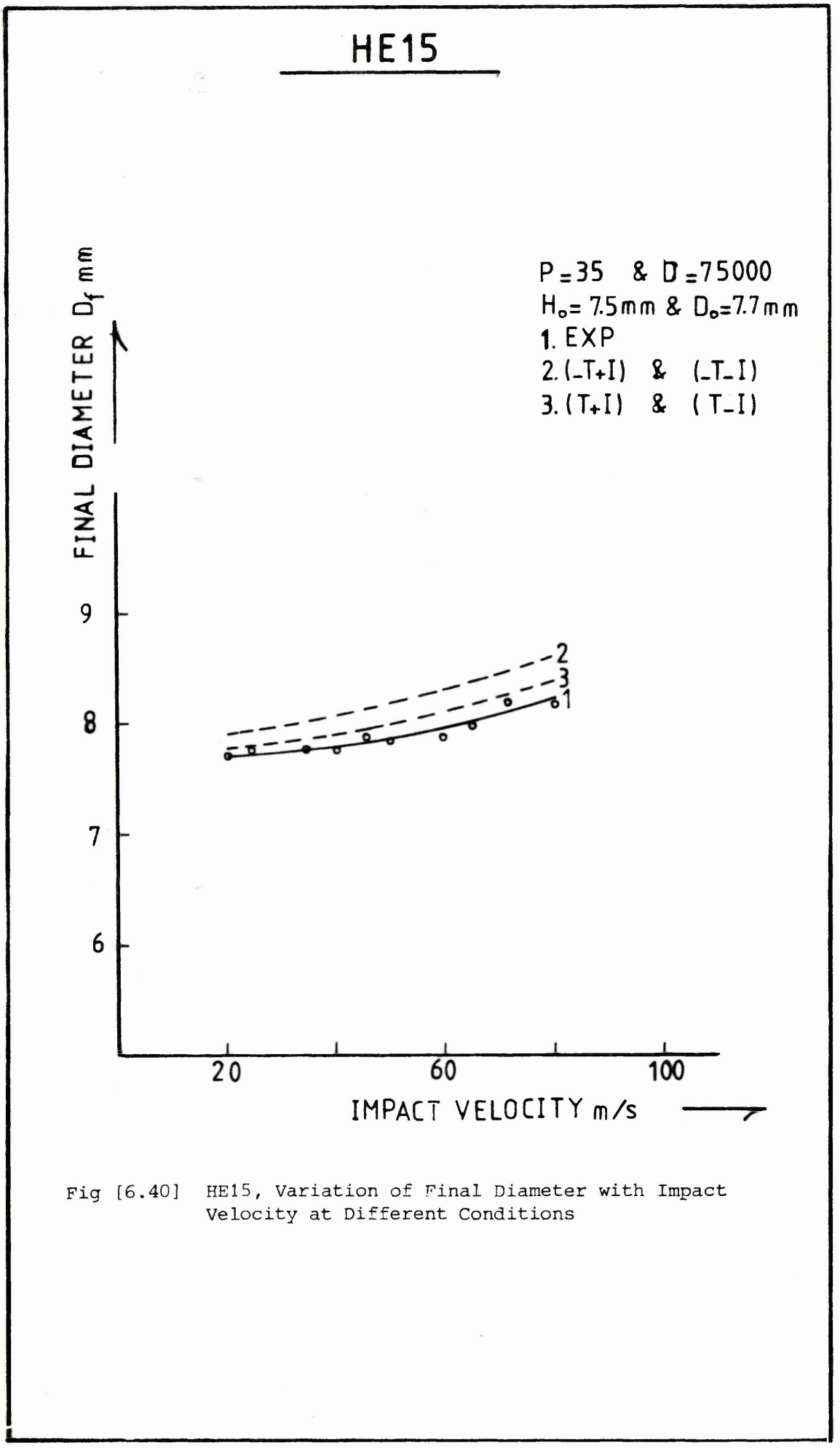

Fig [6.40] HE15, Variation of Final Diameter with Impact Velocity at Different Conditions

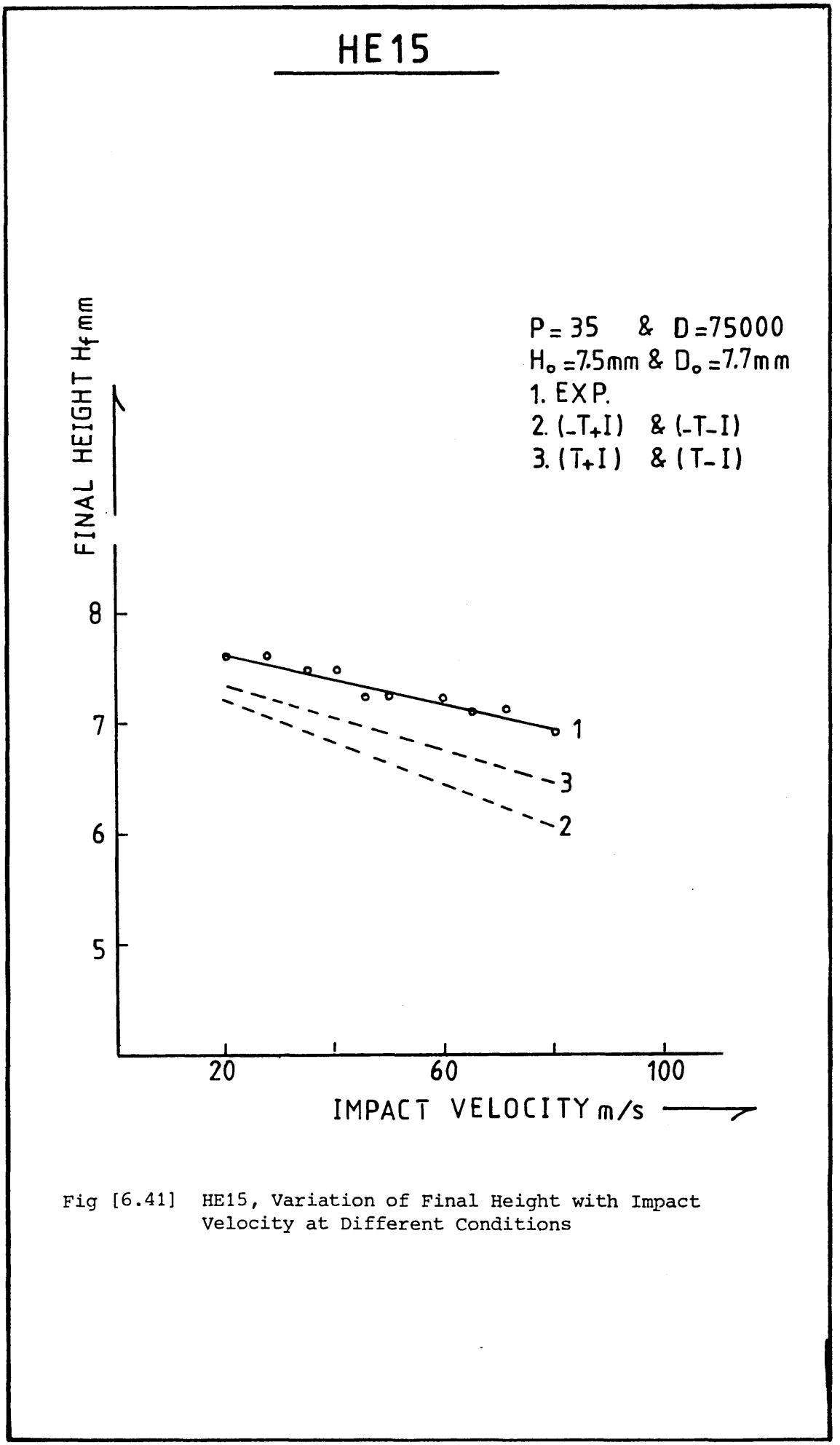

Fig [6.41] HE15, Variation of Final Height with Impact Velocity at Different Conditions

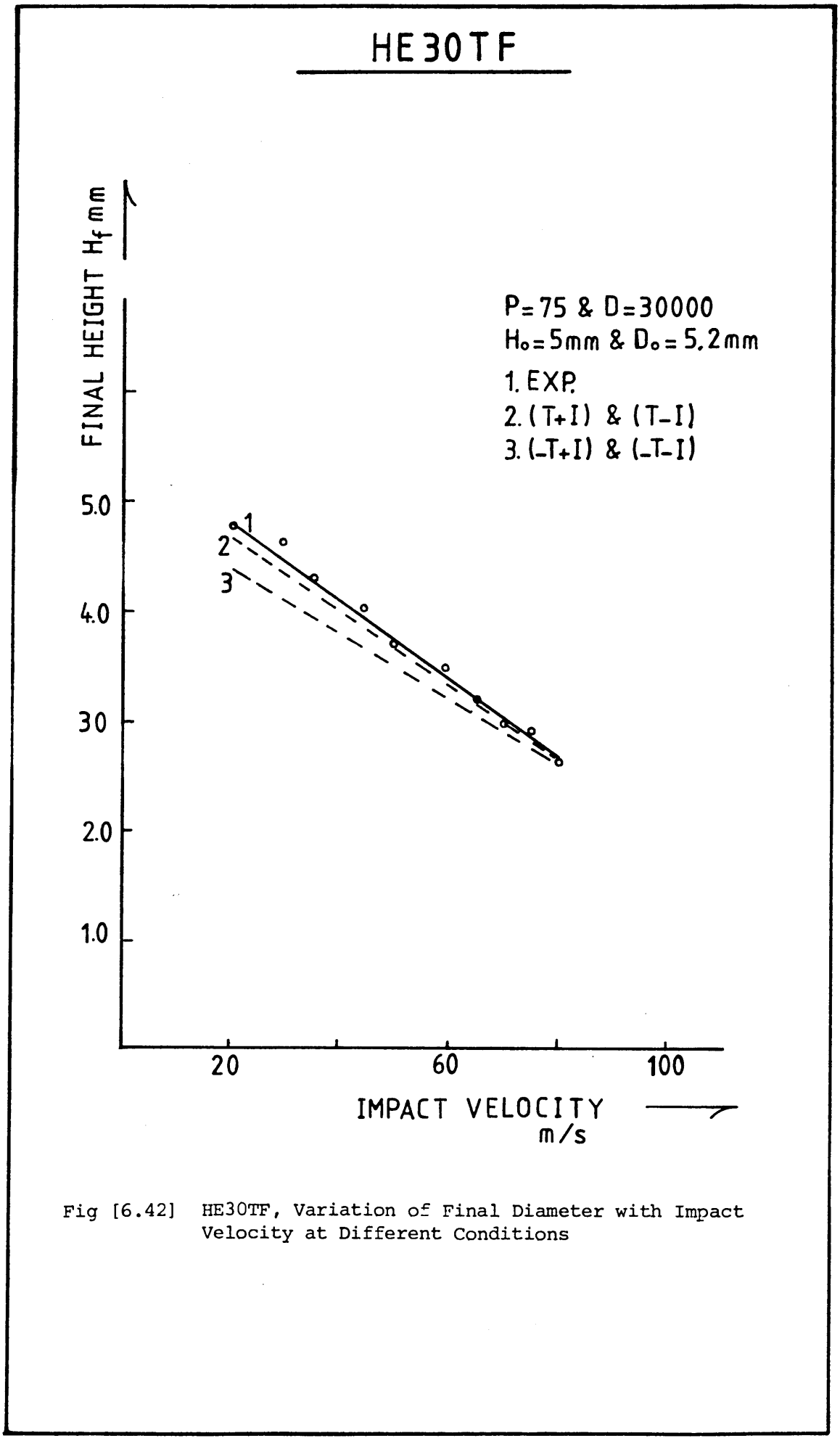

Fig [6.42] HE30TF, Variation of Final Diameter with Impact Velocity at Different Conditions

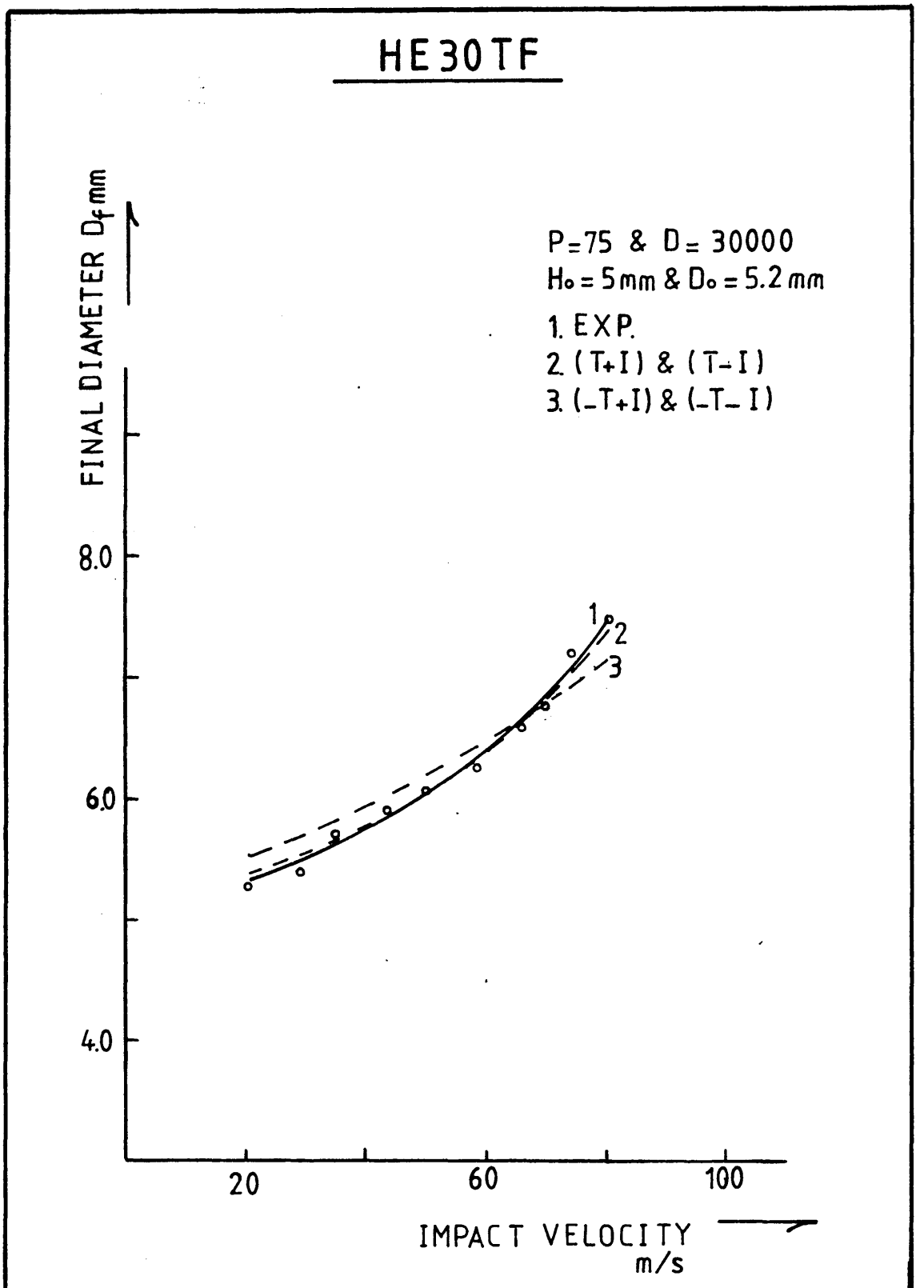

Fig [6.43] HE30TF, Variation of Final Height with Impact Velocity at Different Conditions

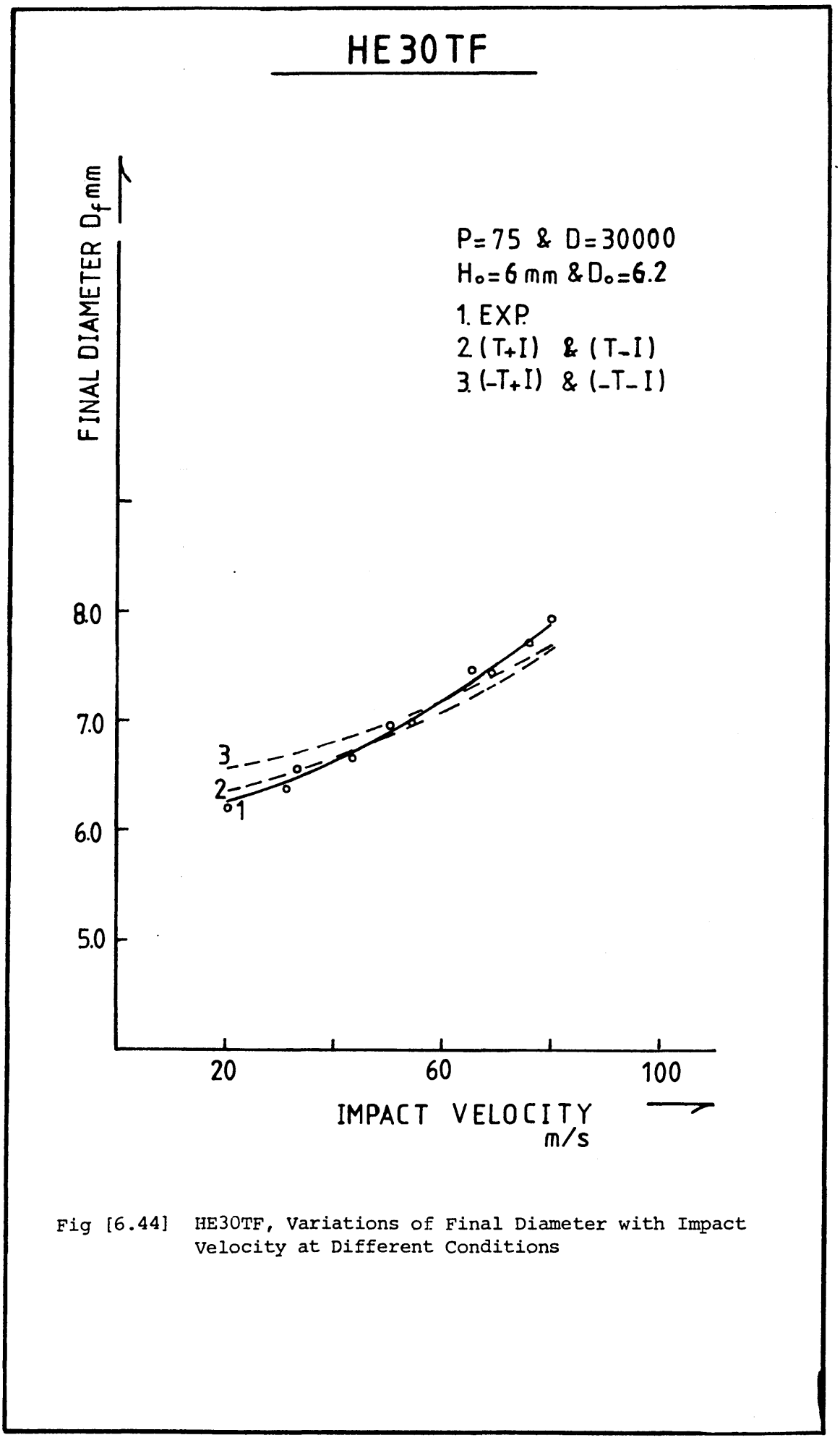

Fig [6.44] HE30TF, Variations of Final Diameter with Impact Velocity at Different Conditions

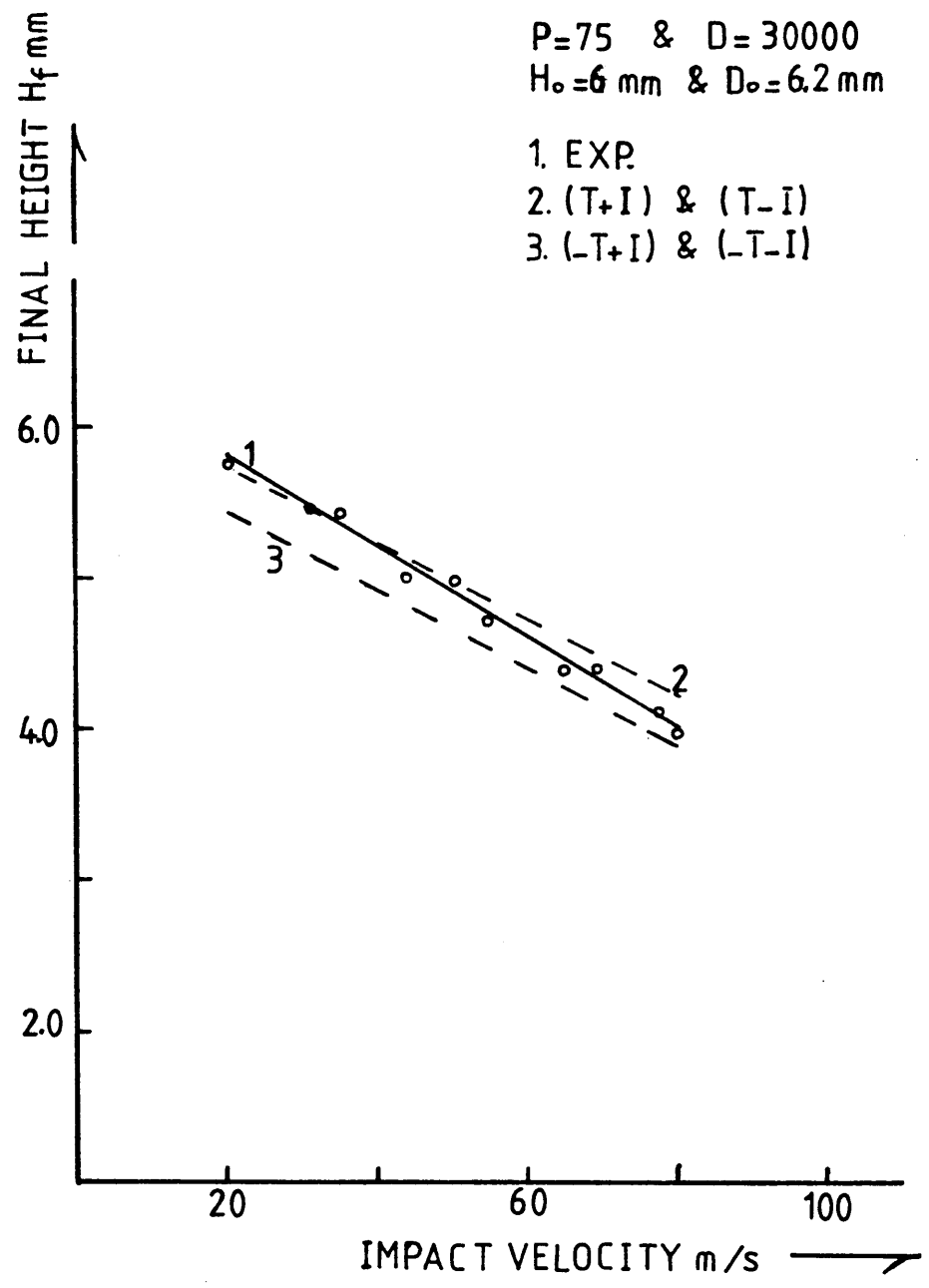

Fig [6.45] HE30TF, Variation of Final Height with Impact Velocity at Different Conditions

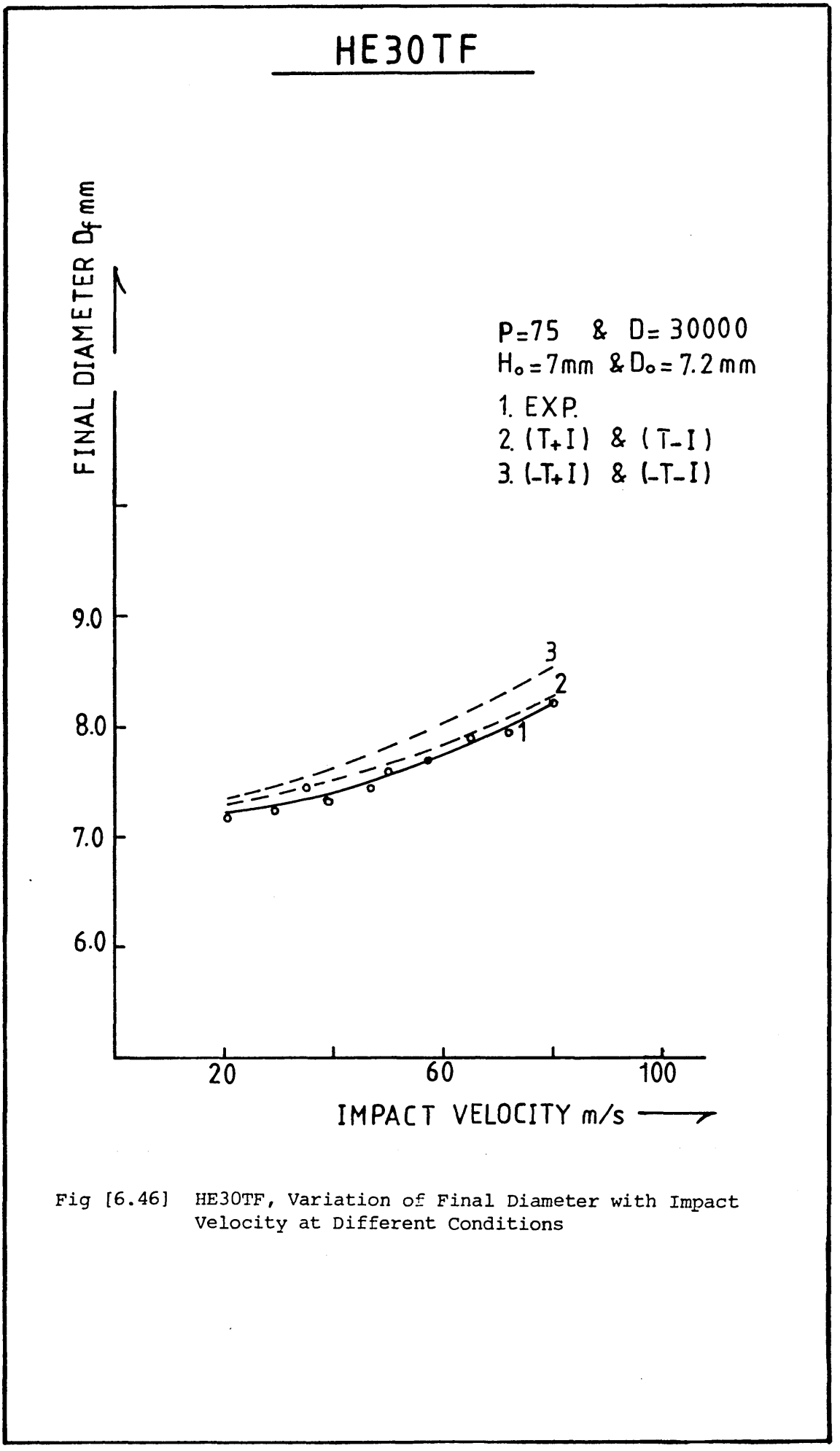

Fig [6.46] HE30TF, Variation of Final Diameter with Impact Velocity at Different Conditions

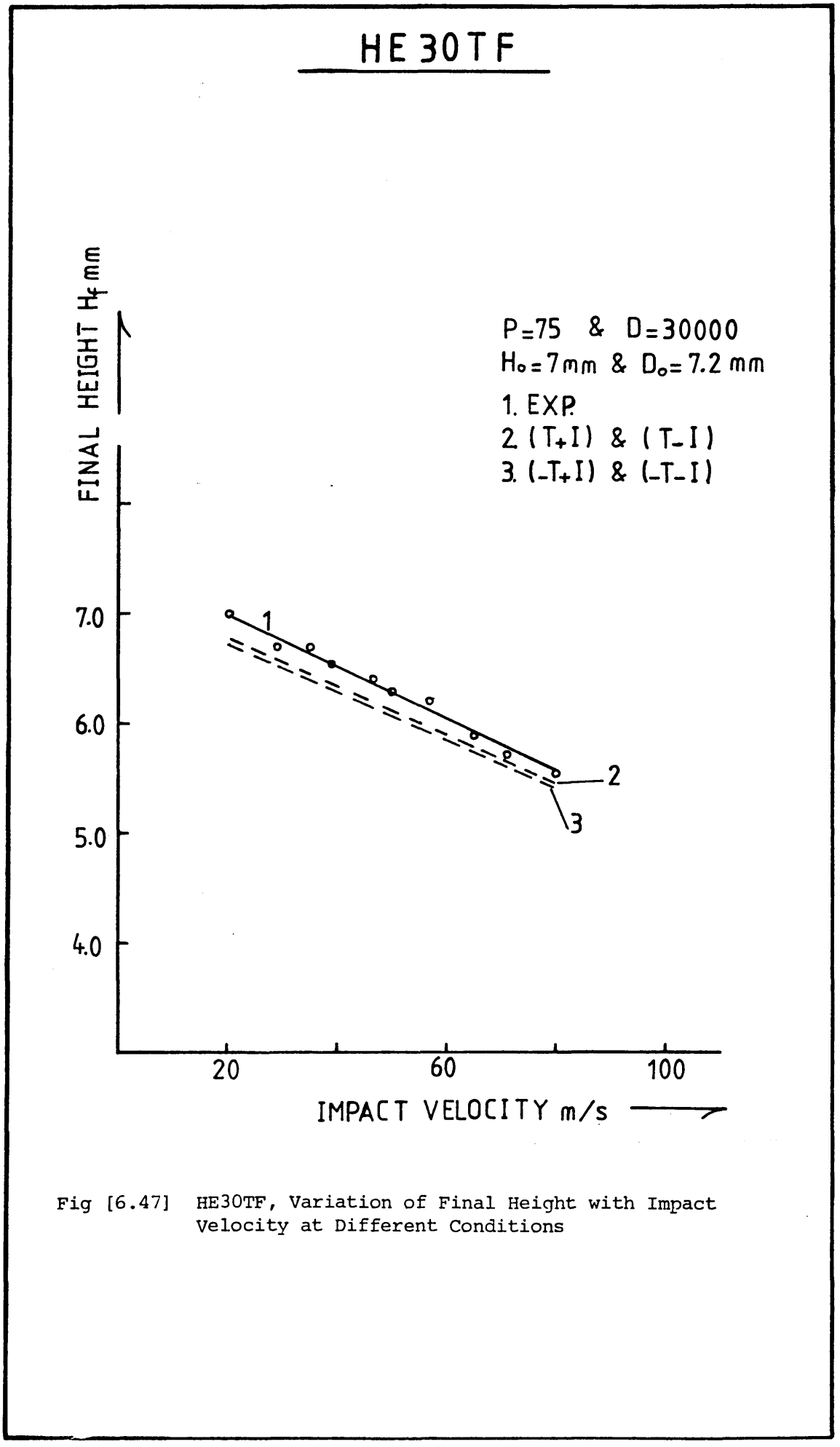

Fig [6.47] HE30TF, Variation of Final Height with Impact Velocity at Different Conditions

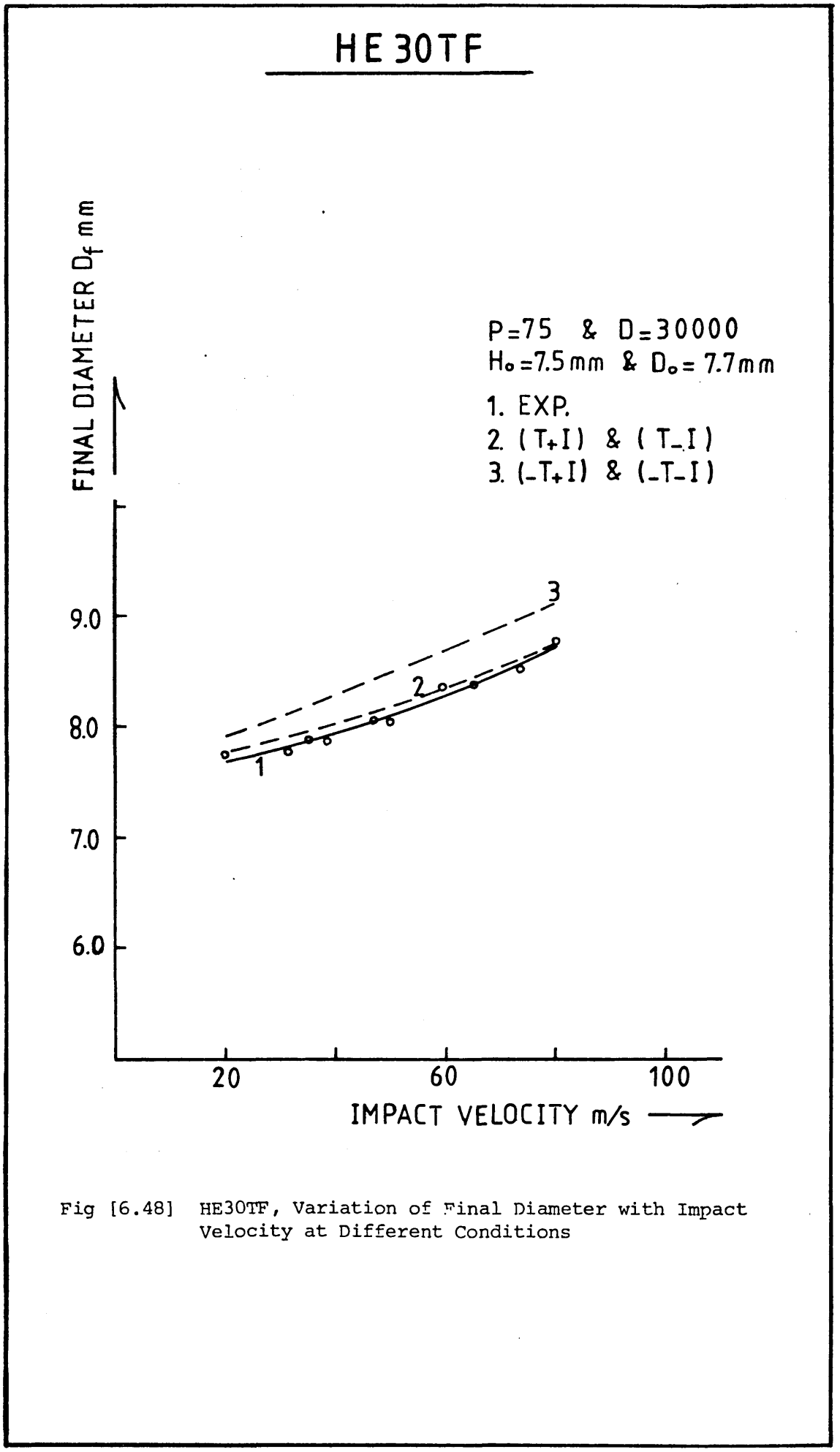

Fig [6.48] HE30TF, Variation of Final Diameter with Impact Velocity at Different Conditions

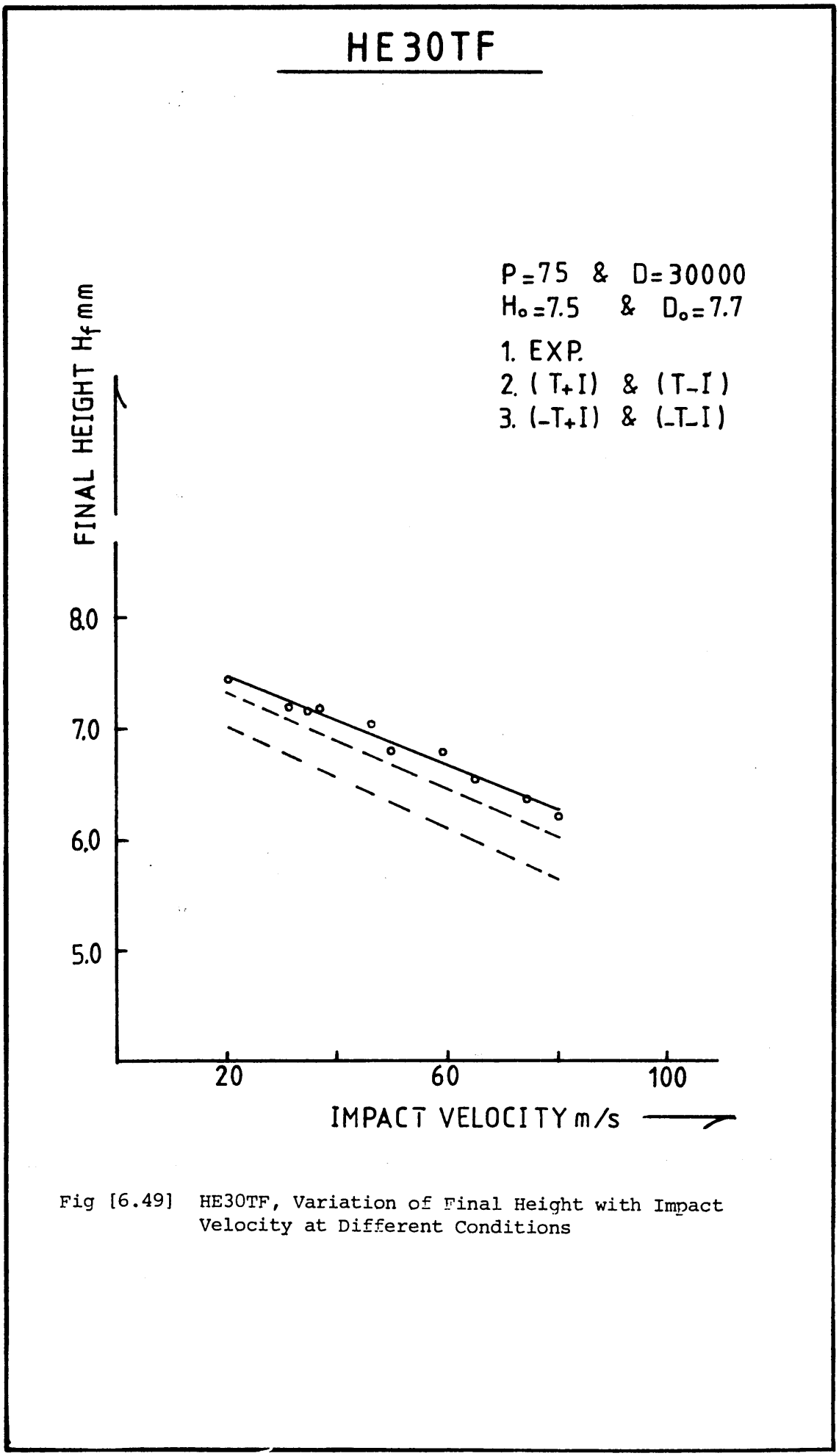

Fig [6.49] HE30TF, Variation of Final Height with Impact Velocity at Different Conditions

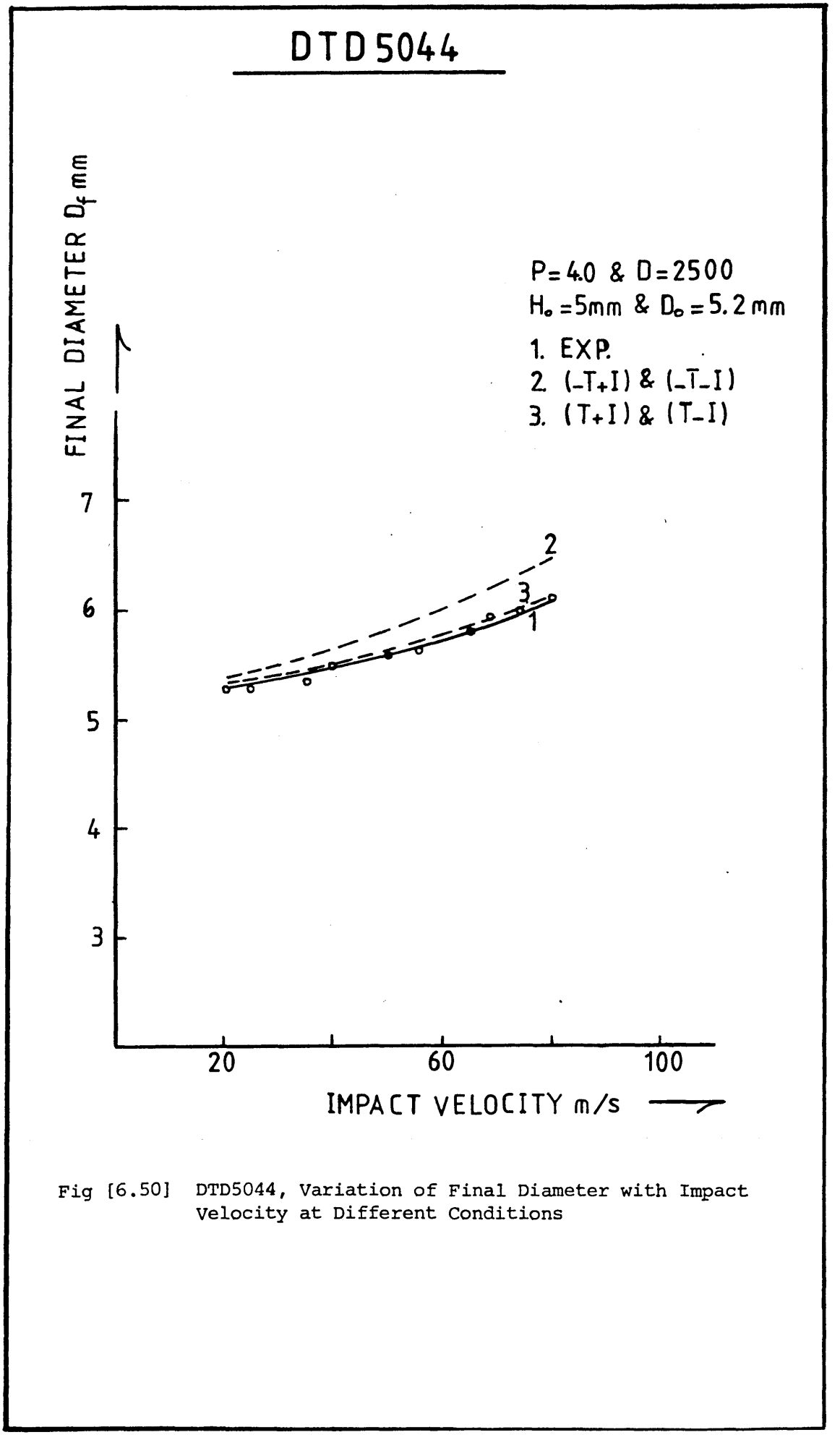

Fig [6.50] DTD5044, Variation of Final Diameter with Impact Velocity at Different Conditions

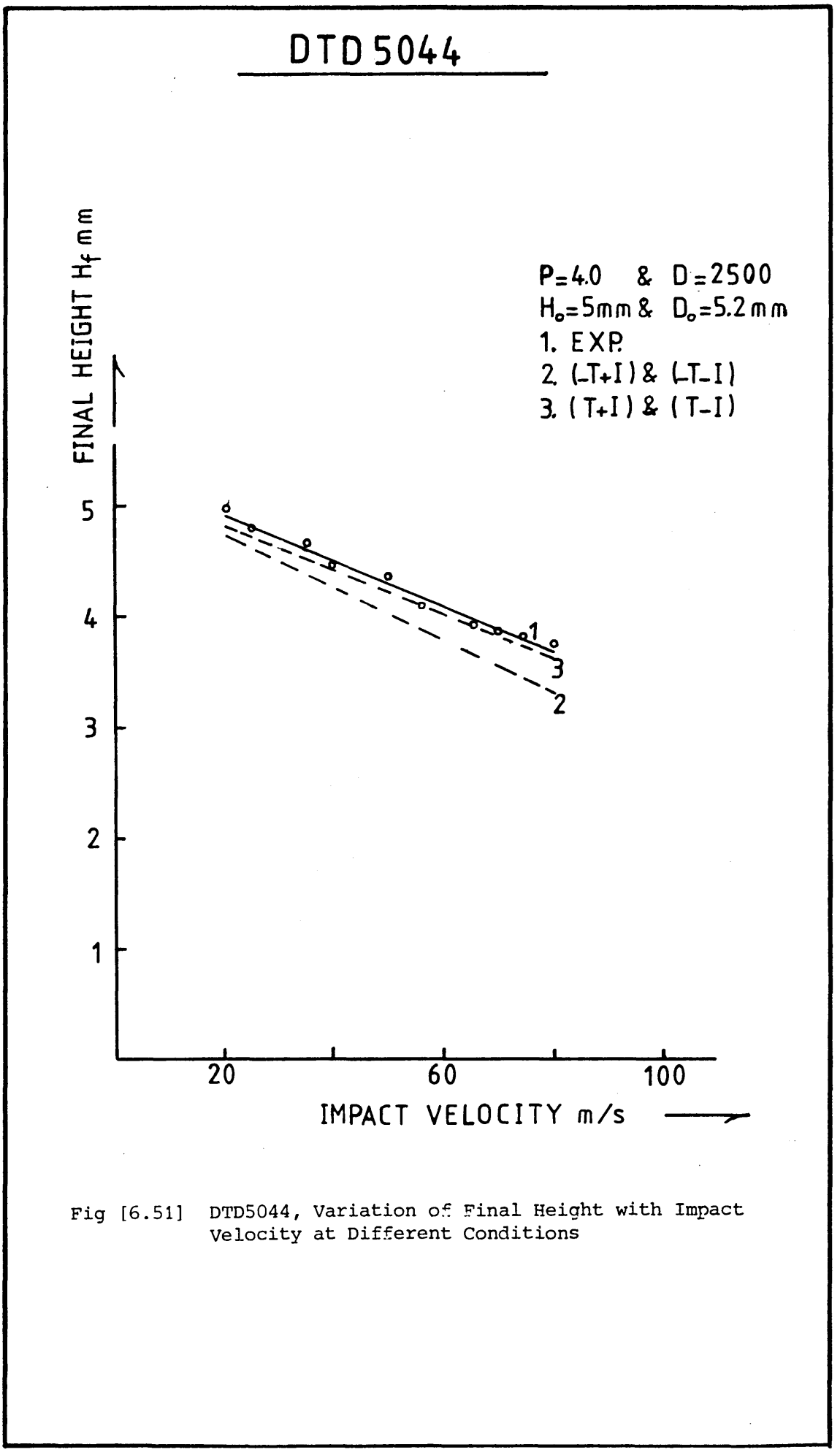

Fig [6.51] DTD5044, Variation of Final Height with Impact Velocity at Different Conditions

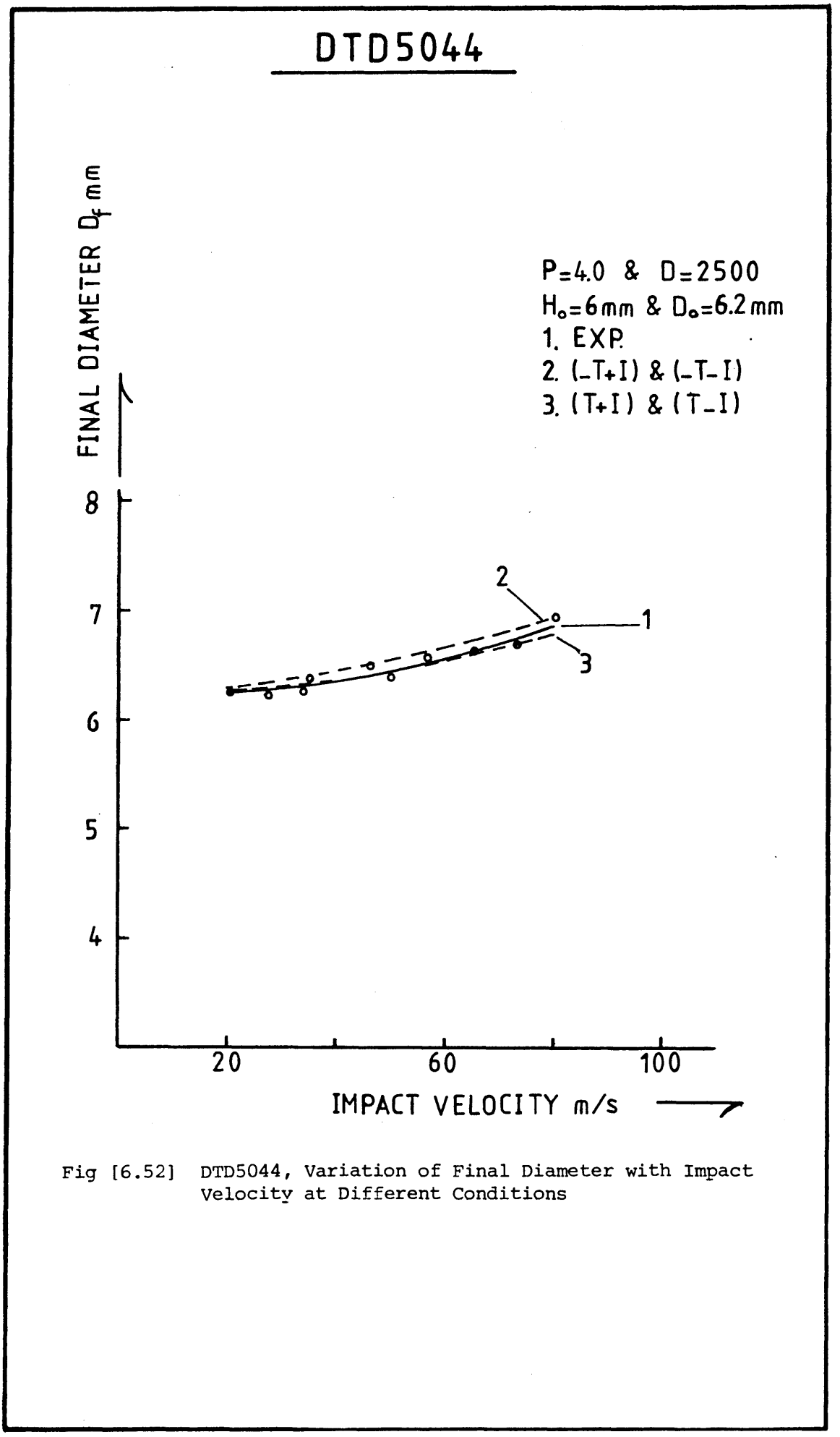

Fig [6.52] DTD5044, Variation of Final Diameter with Impact Velocity at Different Conditions

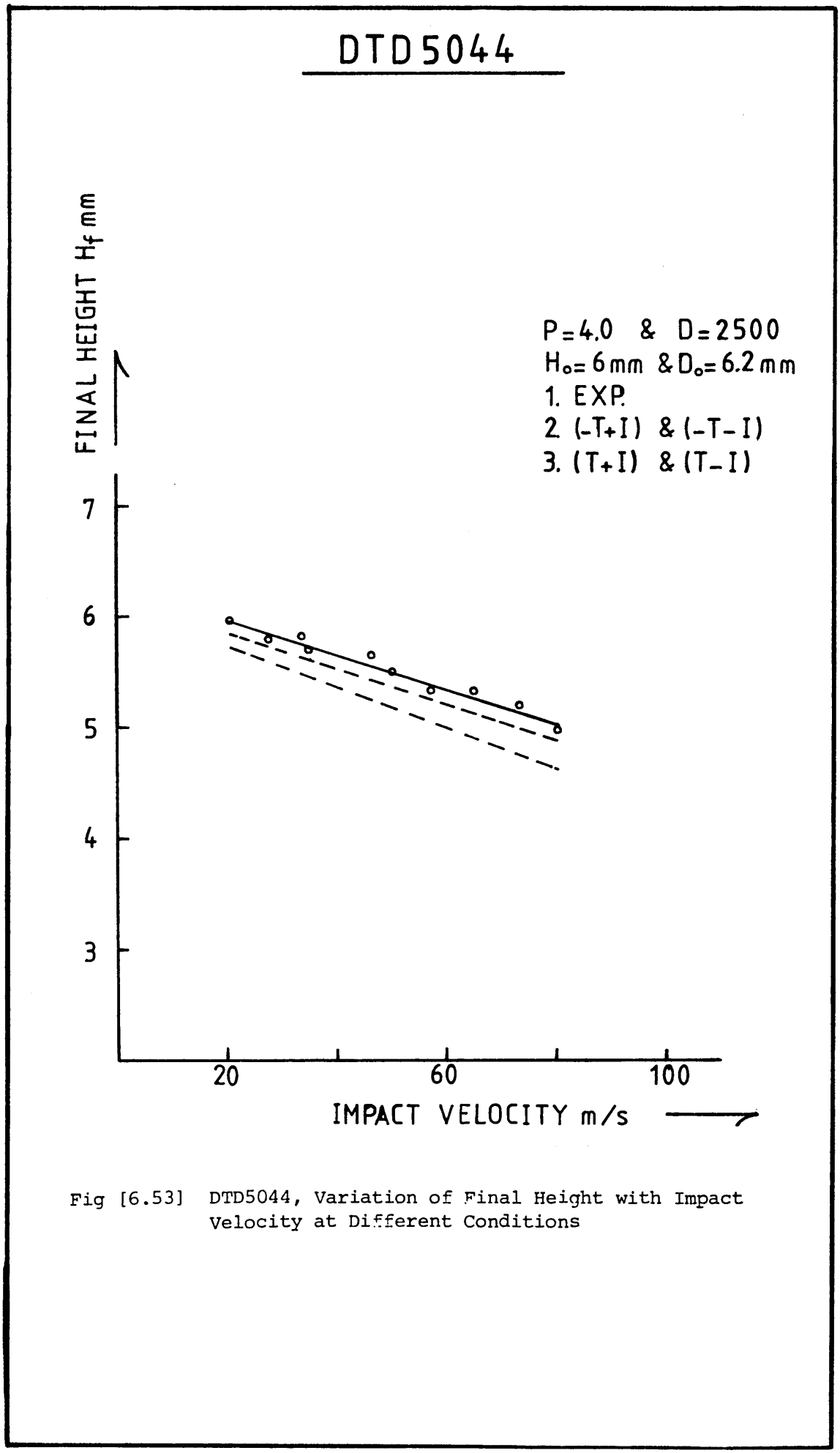

Fig [6.53] DTD5044, Variation of Final Height with Impact Velocity at Different Conditions

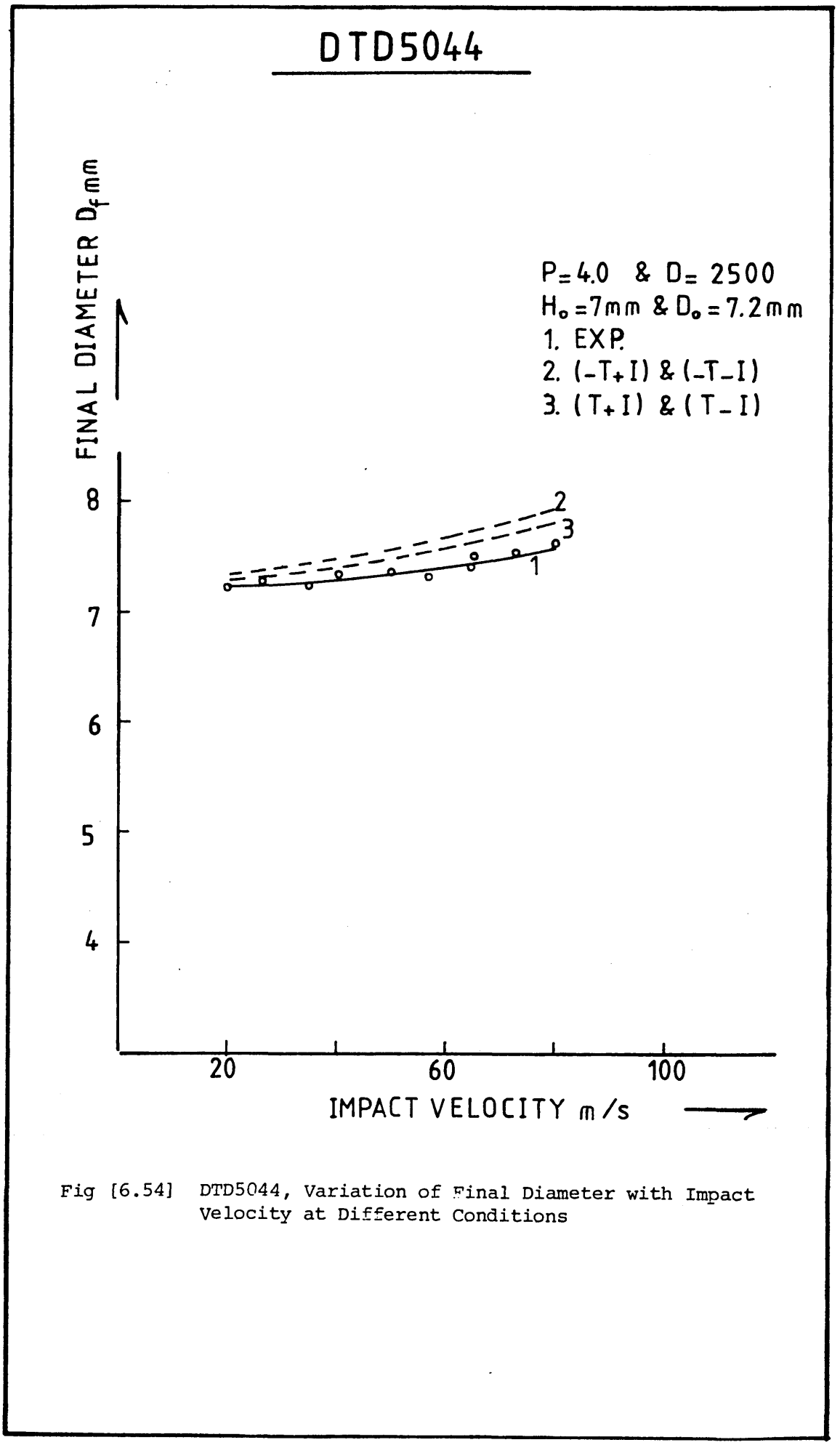

Fig [6.54] DTD5044, Variation of Final Diameter with Impact Velocity at Different Conditions

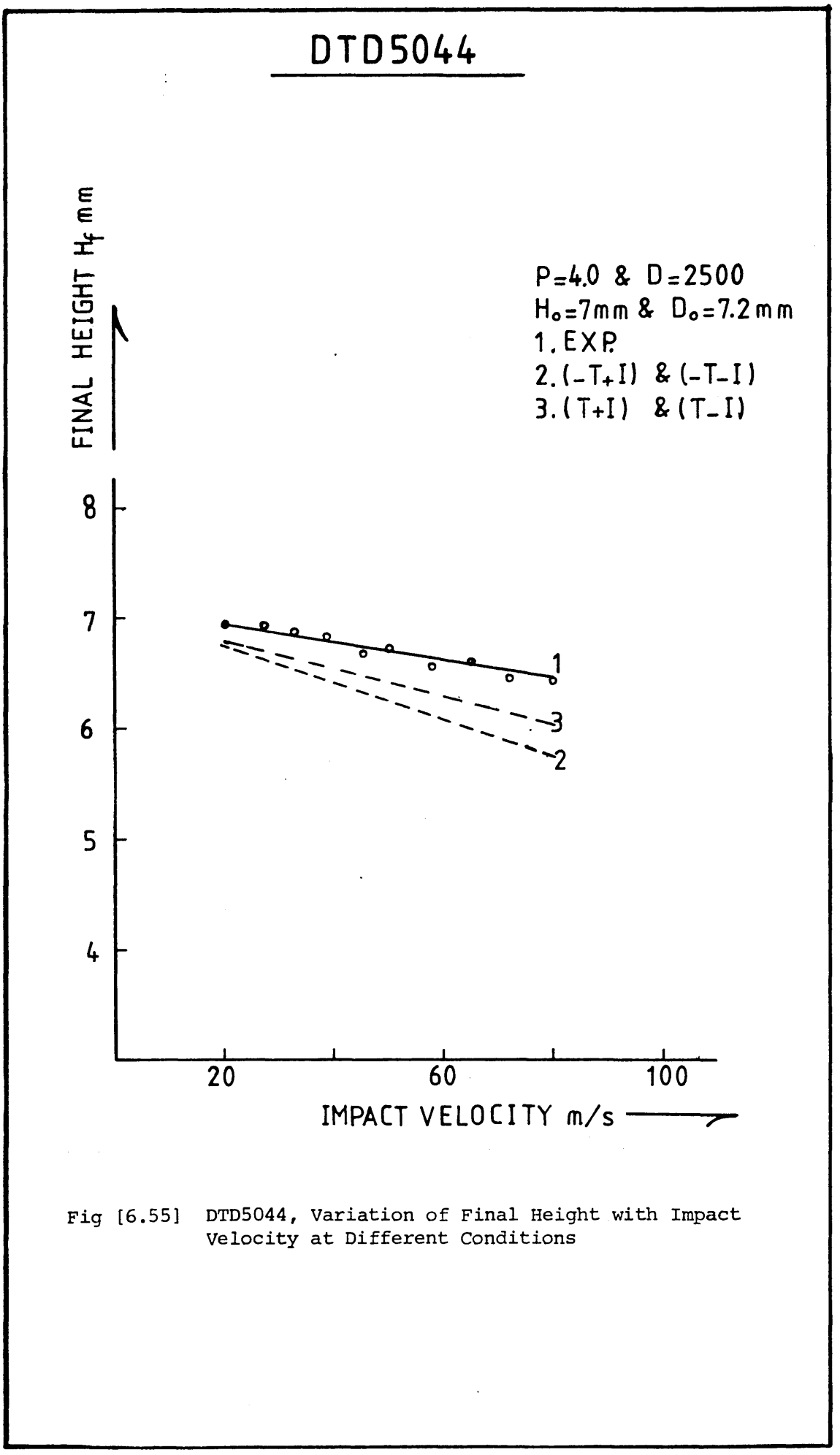

Fig [6.55] DTD5044, Variation of Final Height with Impact Velocity at Different Conditions

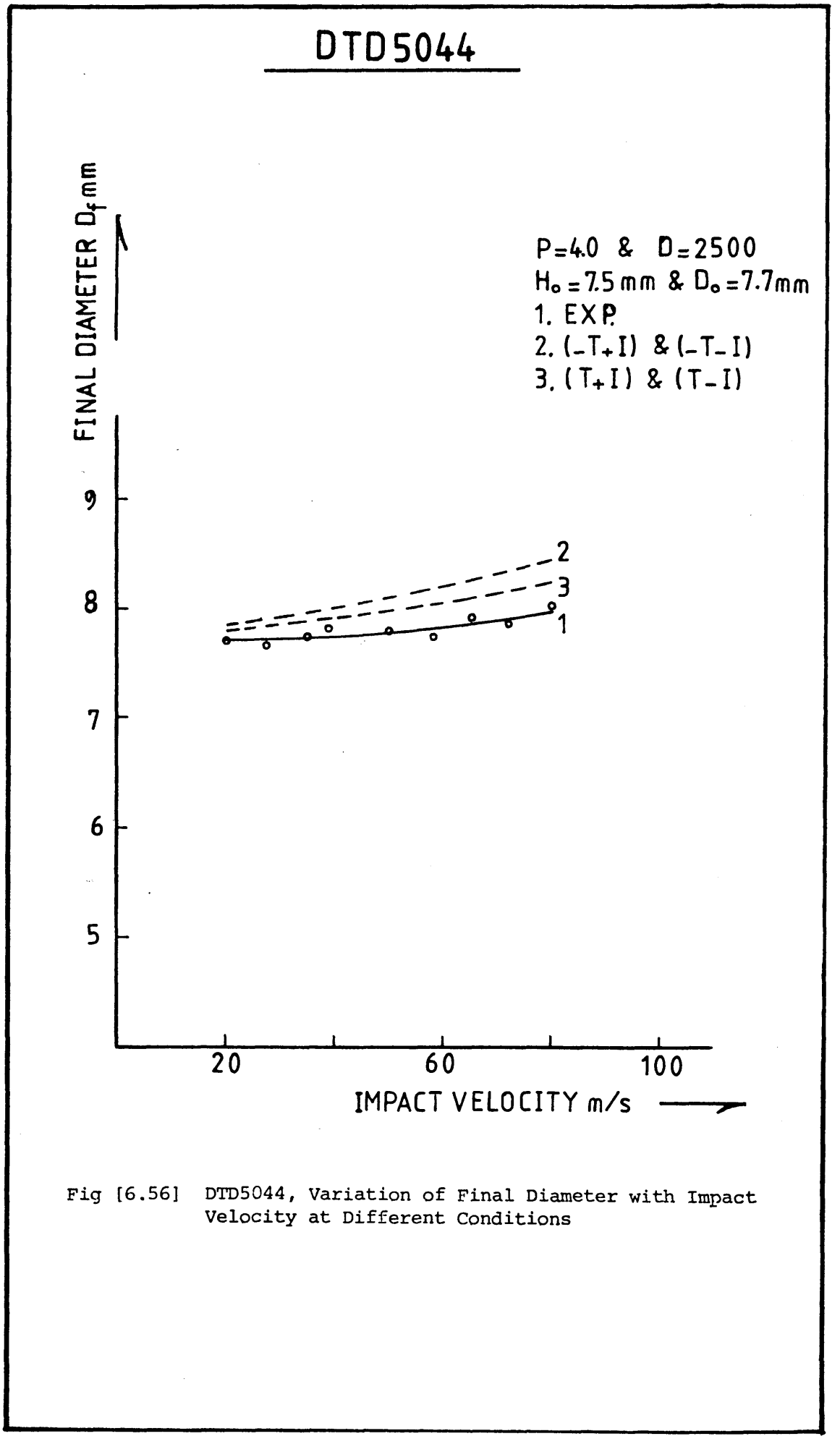

Fig [6.56] DTD5044, Variation of Final Diameter with Impact Velocity at Different Conditions

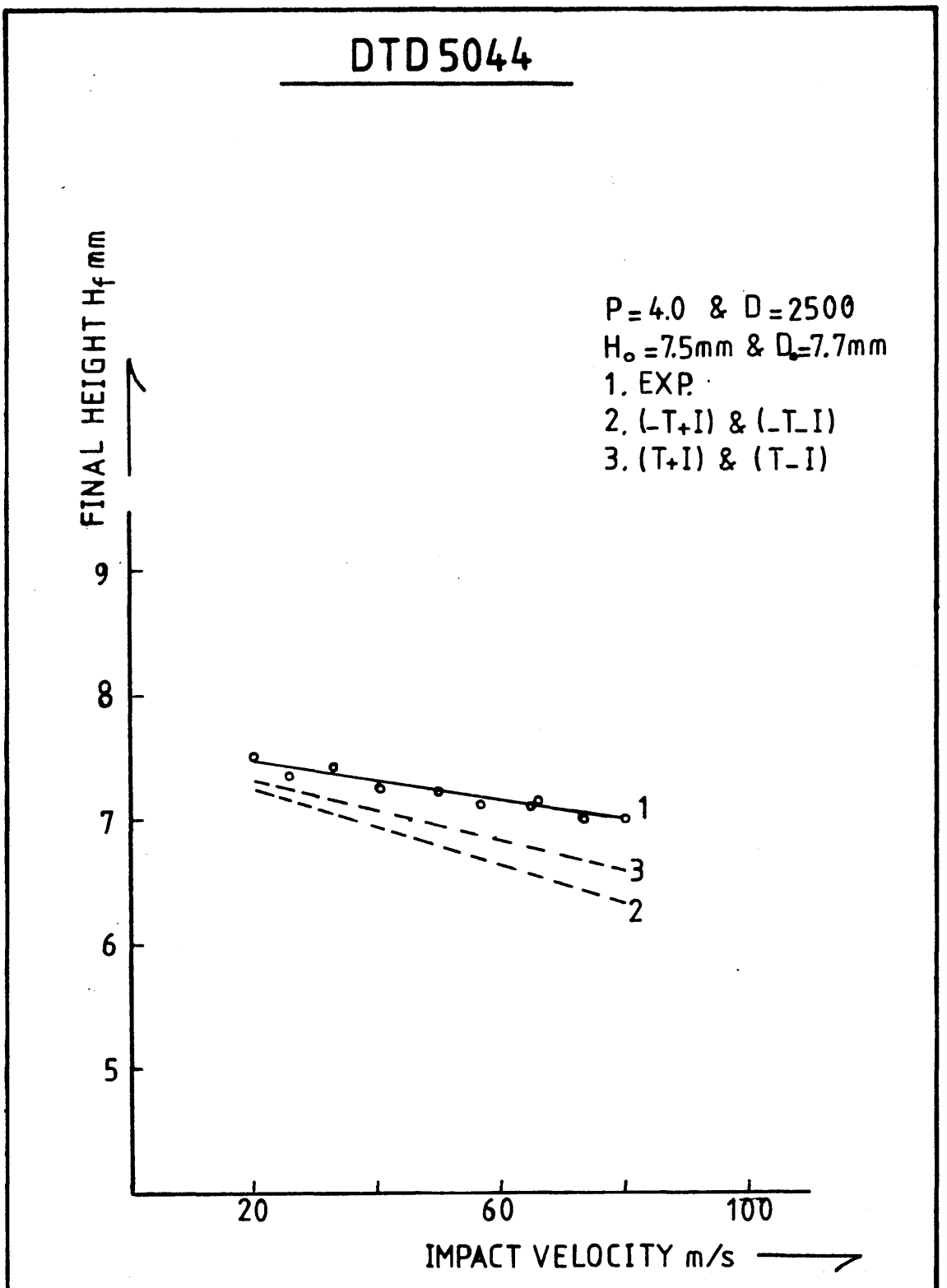

Fig [6.57] DTD5044, Variation of Final Height with Impact Velocity at Different Conditions

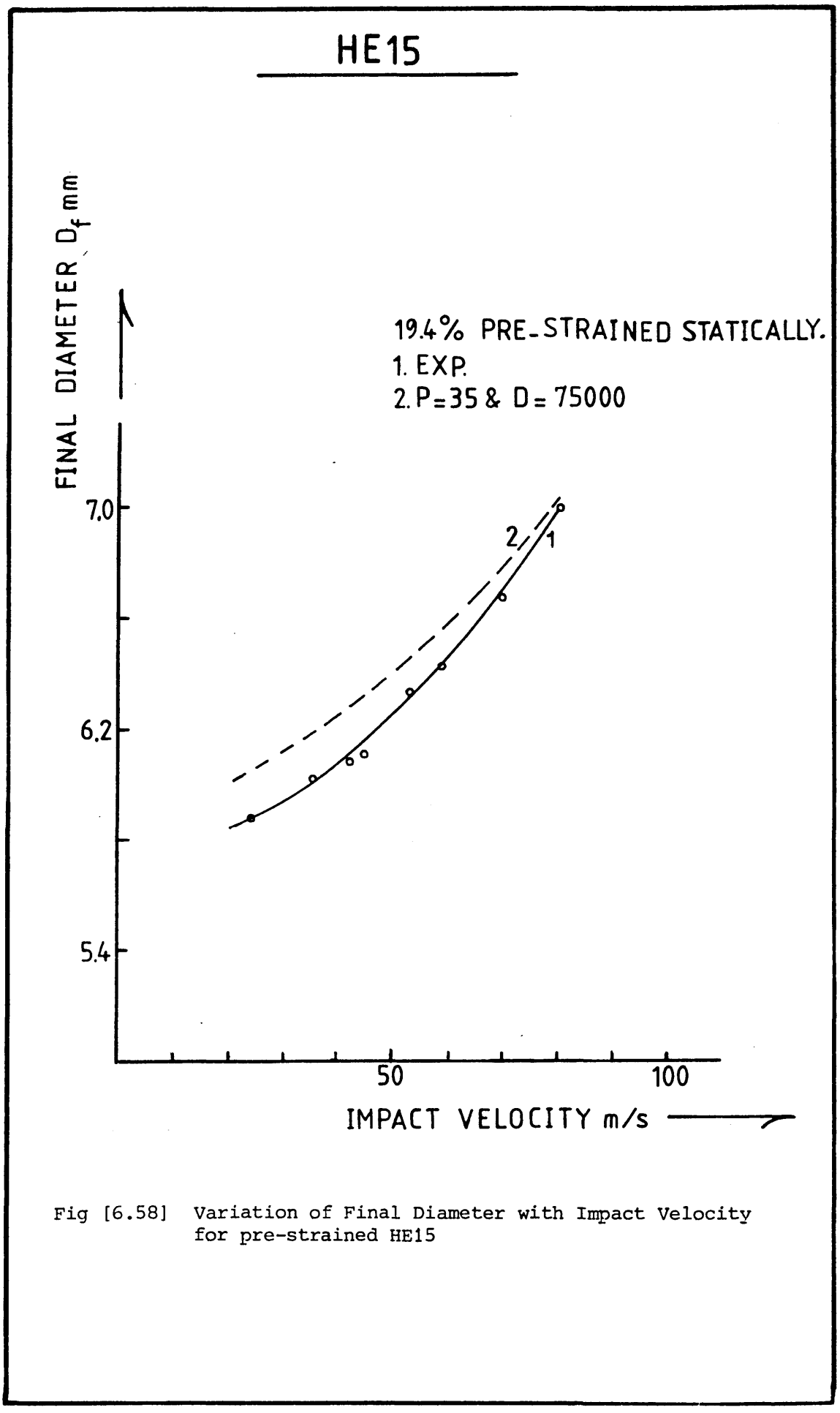

Fig [6.58] Variation of Final Diameter with Impact Velocity for pre-strained HE15

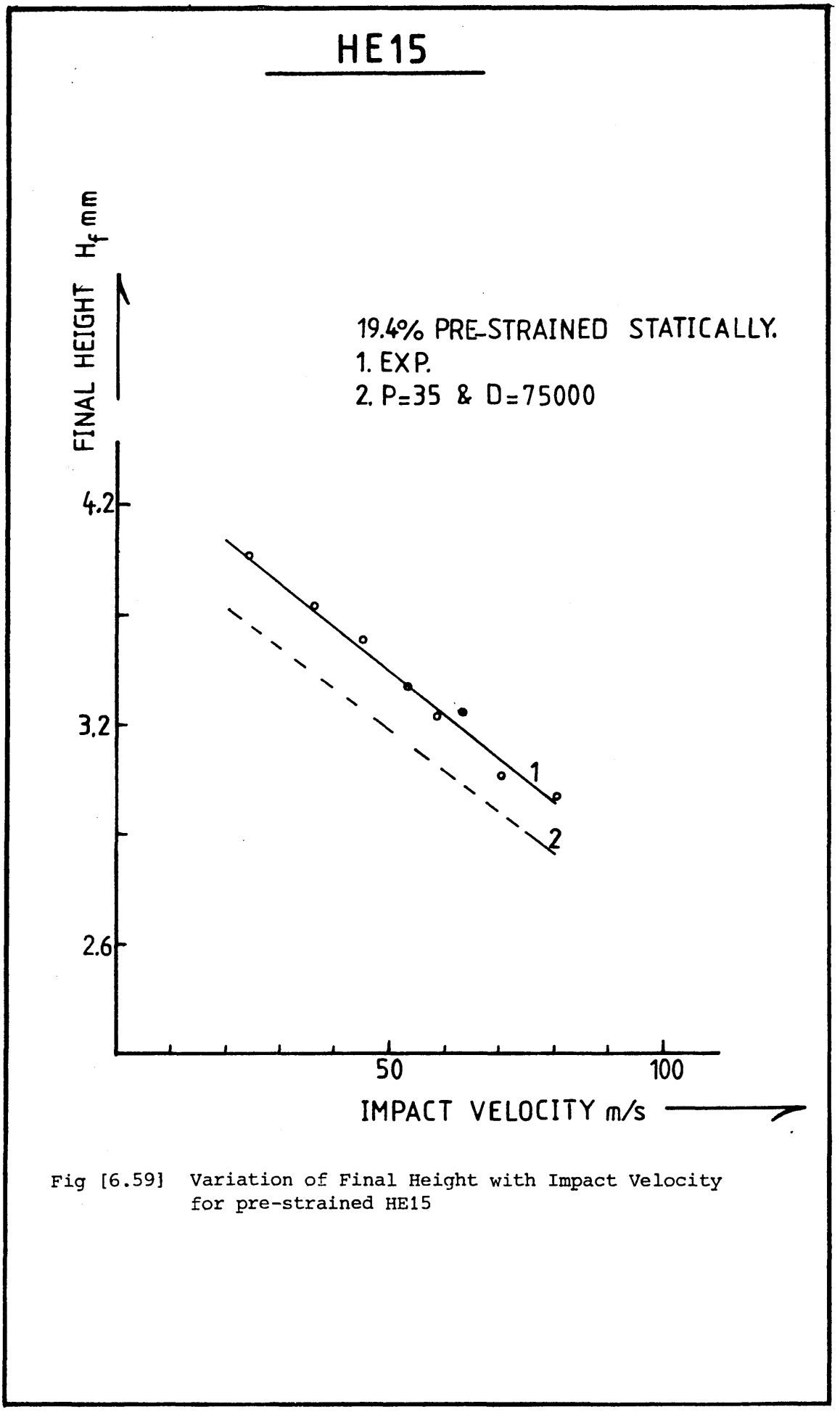

Fig [6.59] Variation of Final Height with Impact Velocity for pre-strained HE15

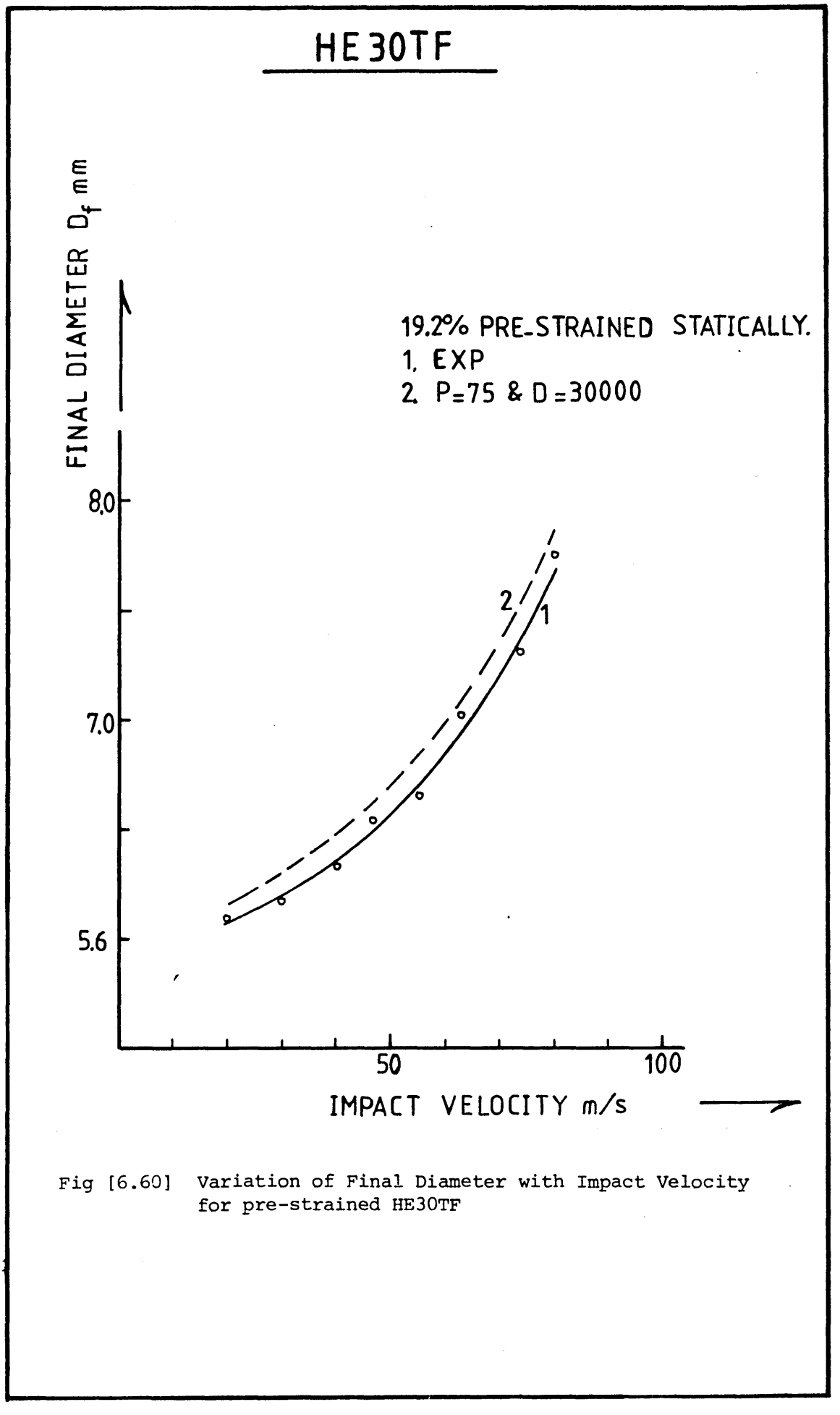

Fig [6.60] Variation of Final Diameter with Impact Velocity for pre-strained HE30TF

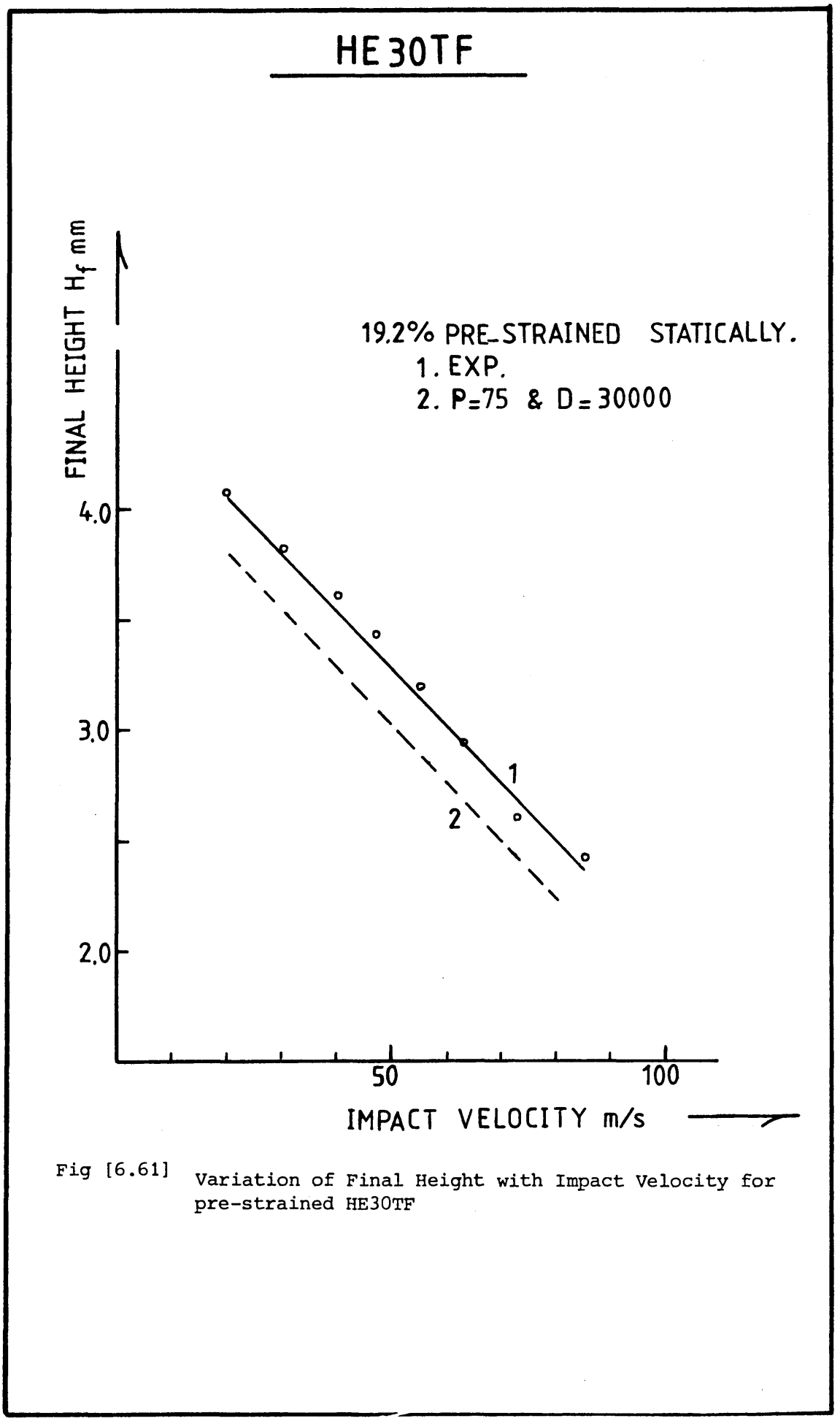

Fig [6.61] Variation of Final Height with Impact Velocity for pre-strained HE30TF

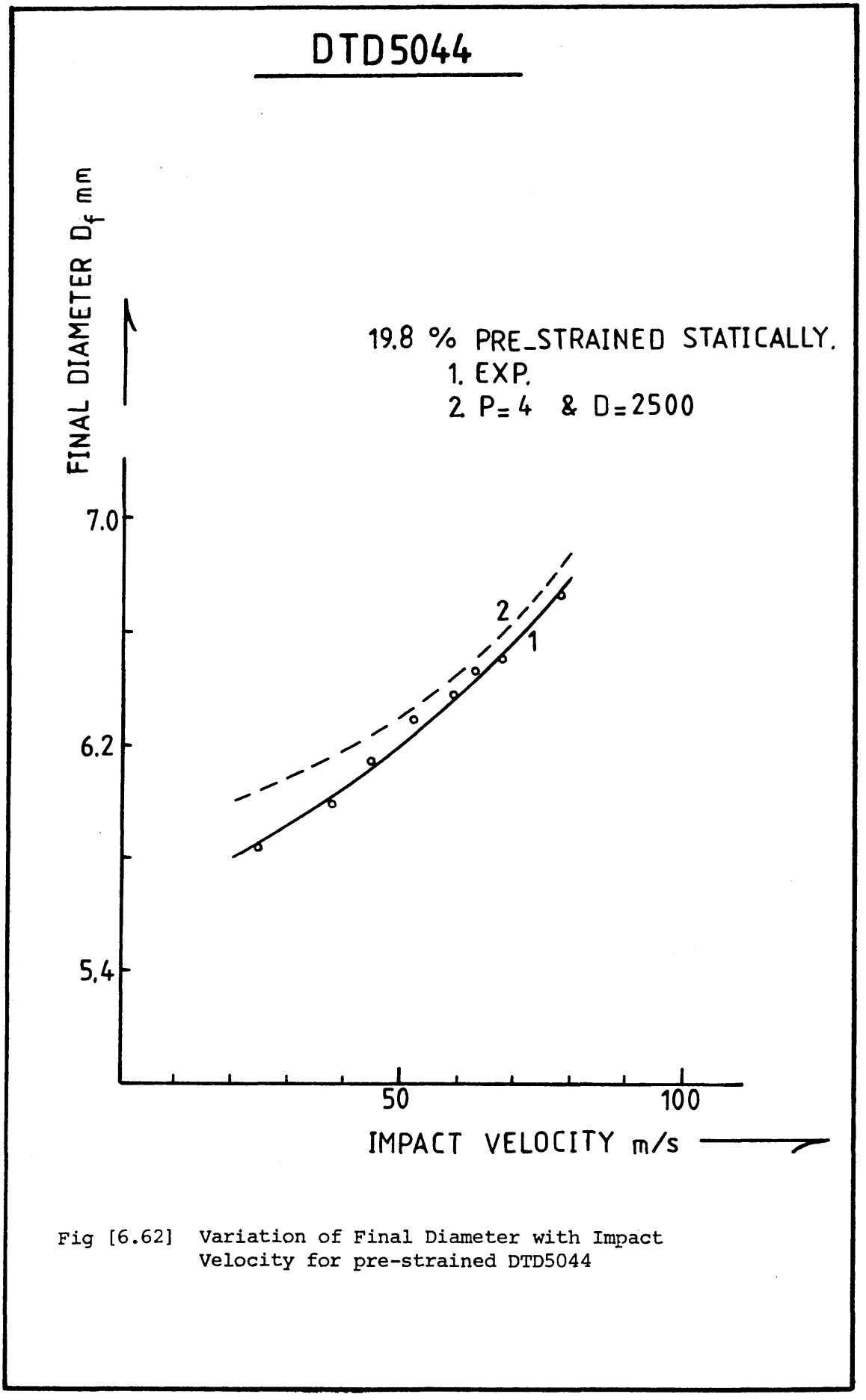

Fig [6.62] Variation of Final Diameter with Impact Velocity for pre-strained DTD5044

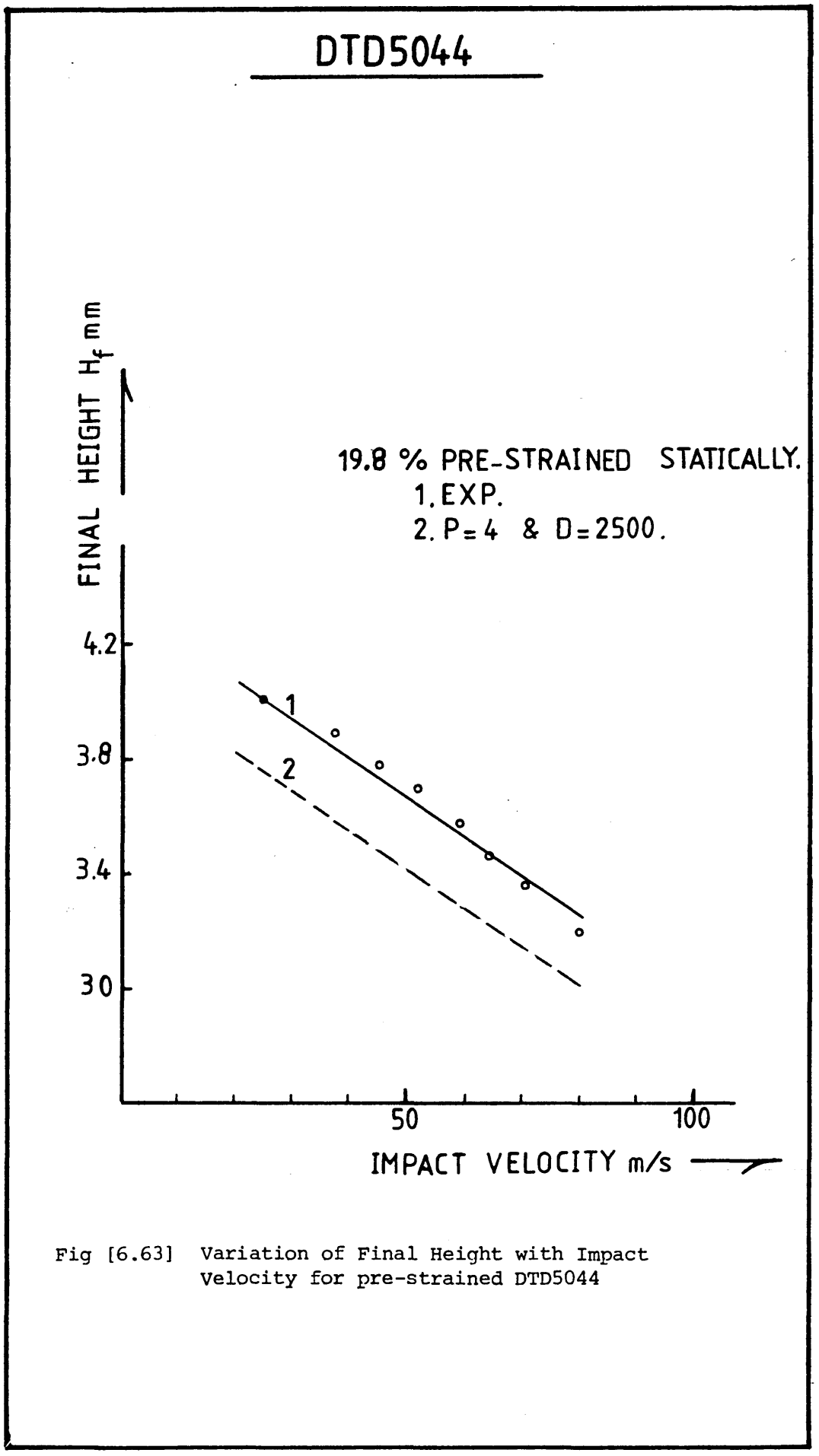

Fig [6.63] Variation of Final Height with Impact Velocity for pre-strained DTD5044

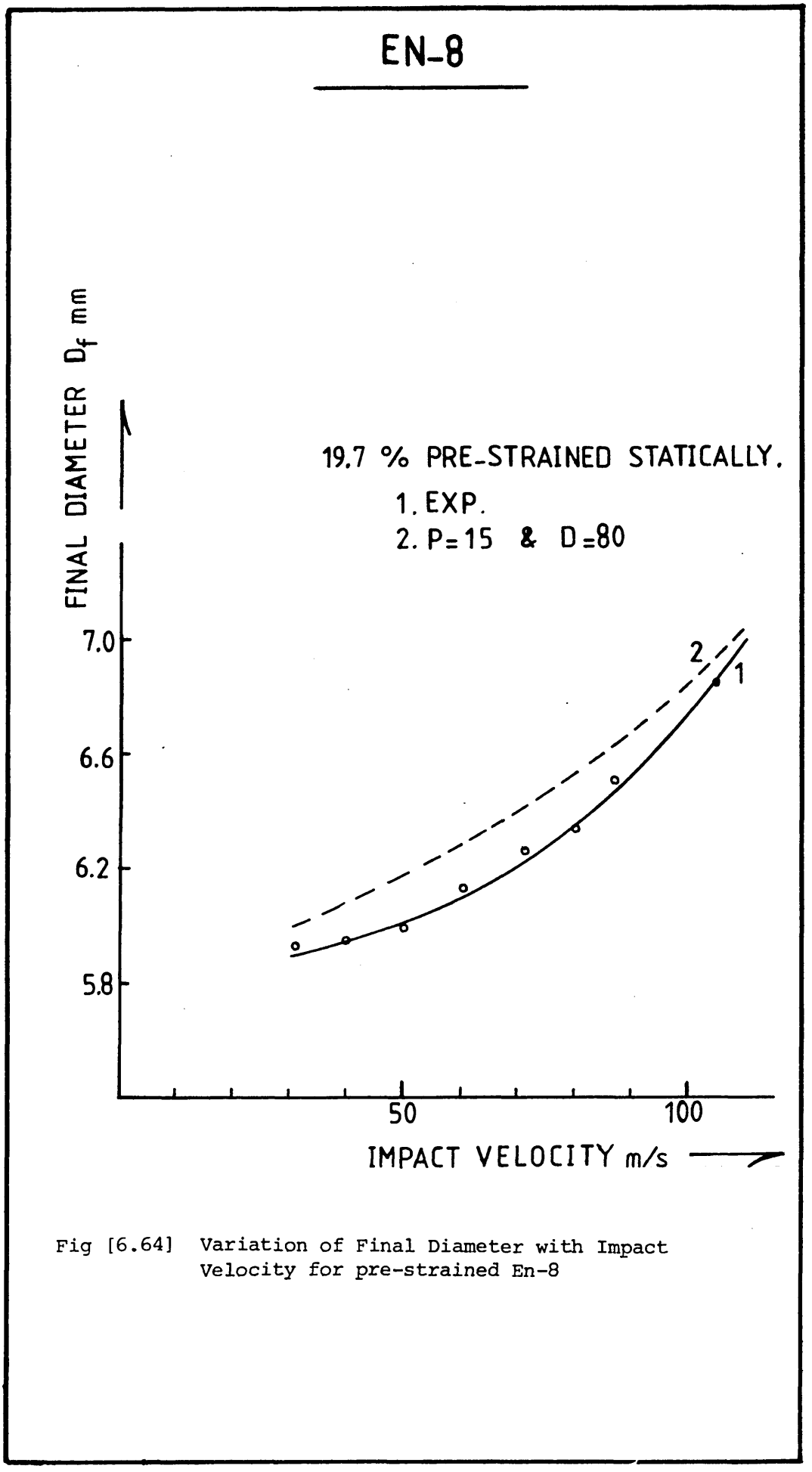

Fig [6.64] Variation of Final Diameter with Impact Velocity for pre-strained En-8

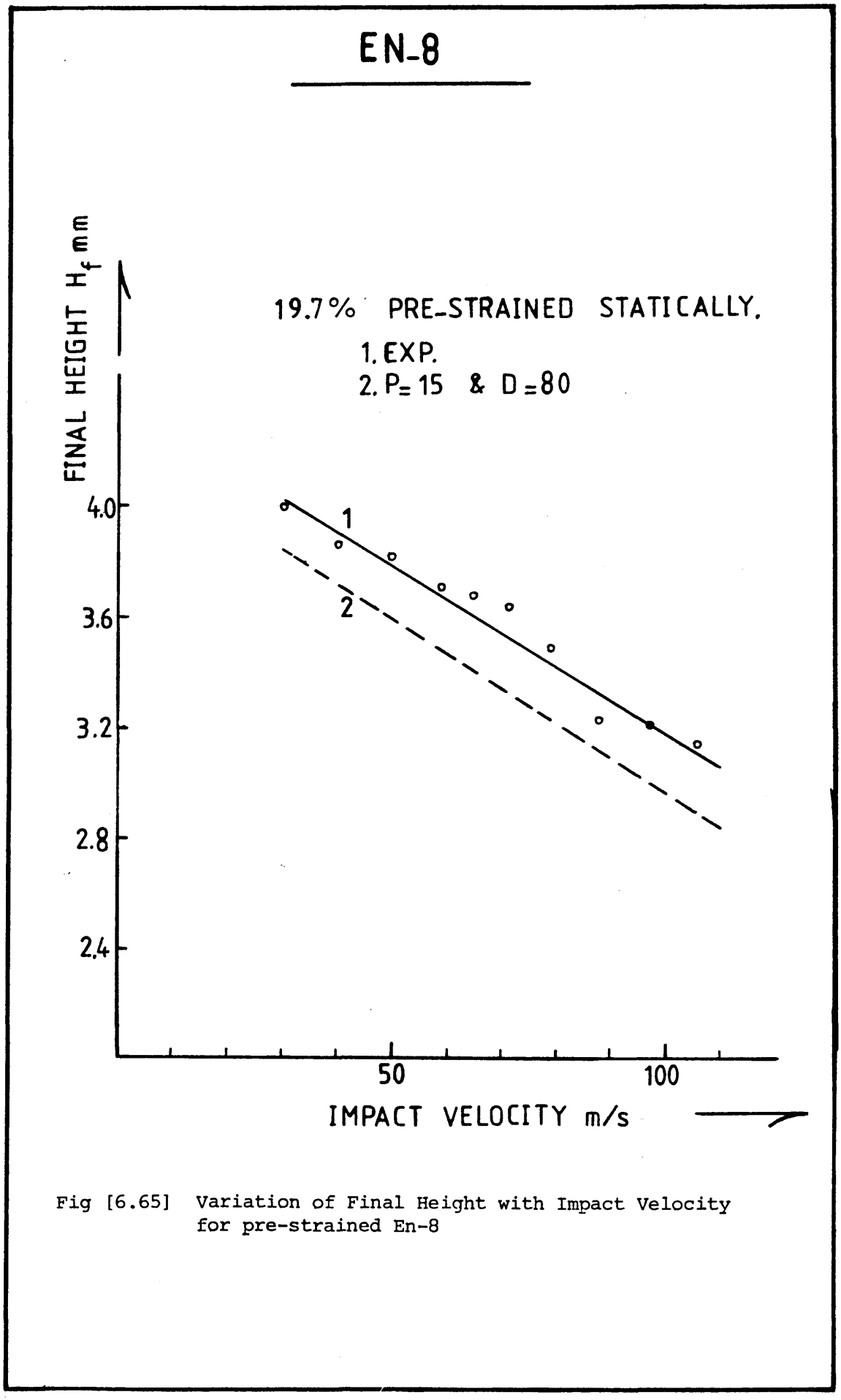

Fig [6.65] Variation of Final Height with Impact Velocity for pre-strained En-8

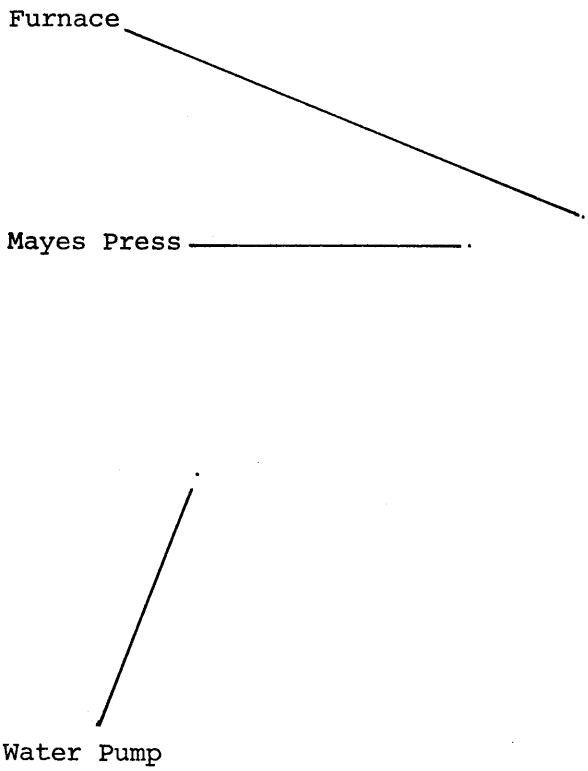

Plate No [6.1] Mayes press and cooling water pump

Plate No [6.1] Mayes press and cooling water pump

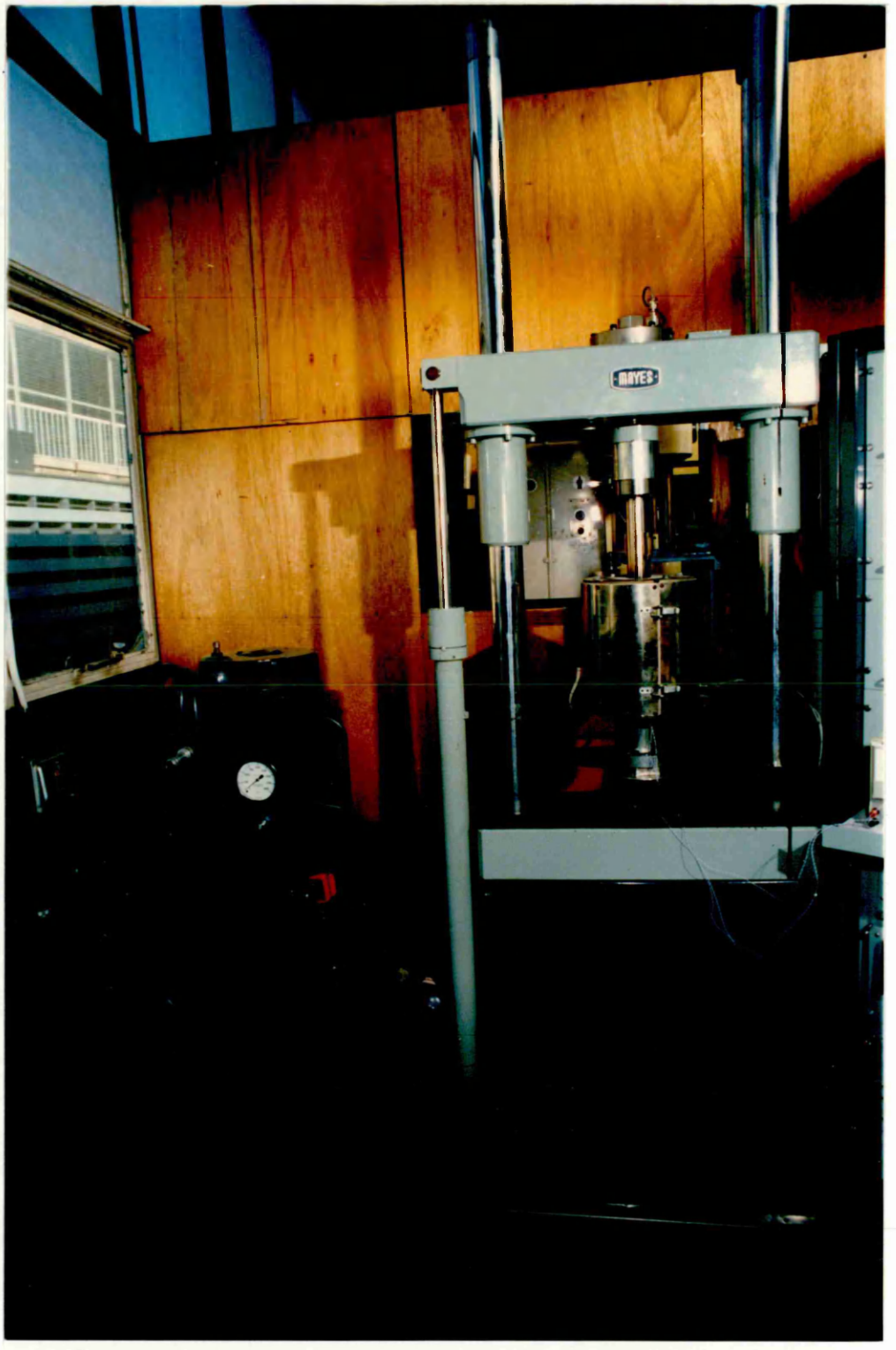
MAYES

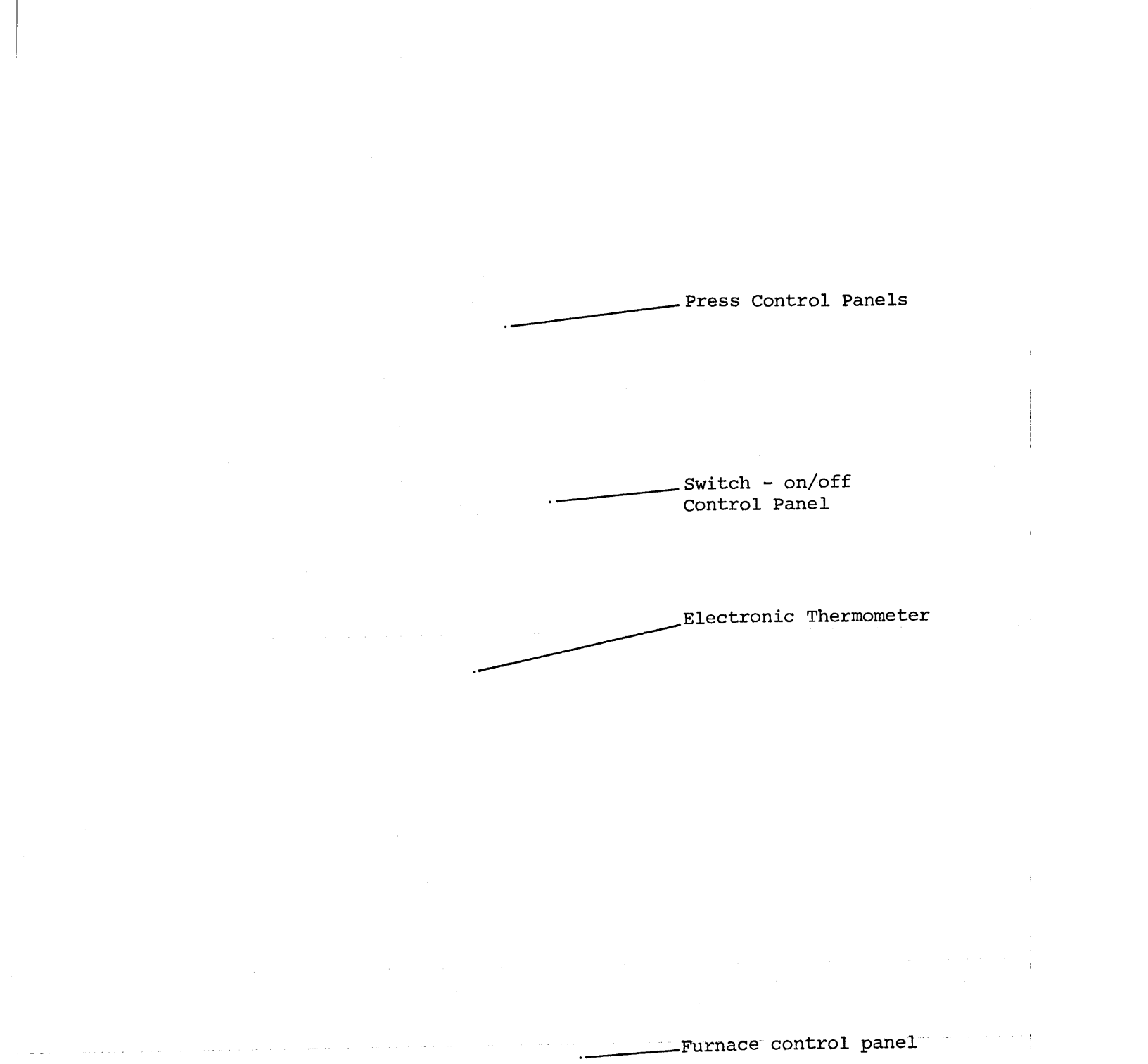

Plate No [6.2] Mayes press and furnace control panels

Press Control Panels

Switch - on/off
Control Panel

Electronic Thermometer

Furnace control panel

Plate No [6.2] Mayes press and furnace control panels

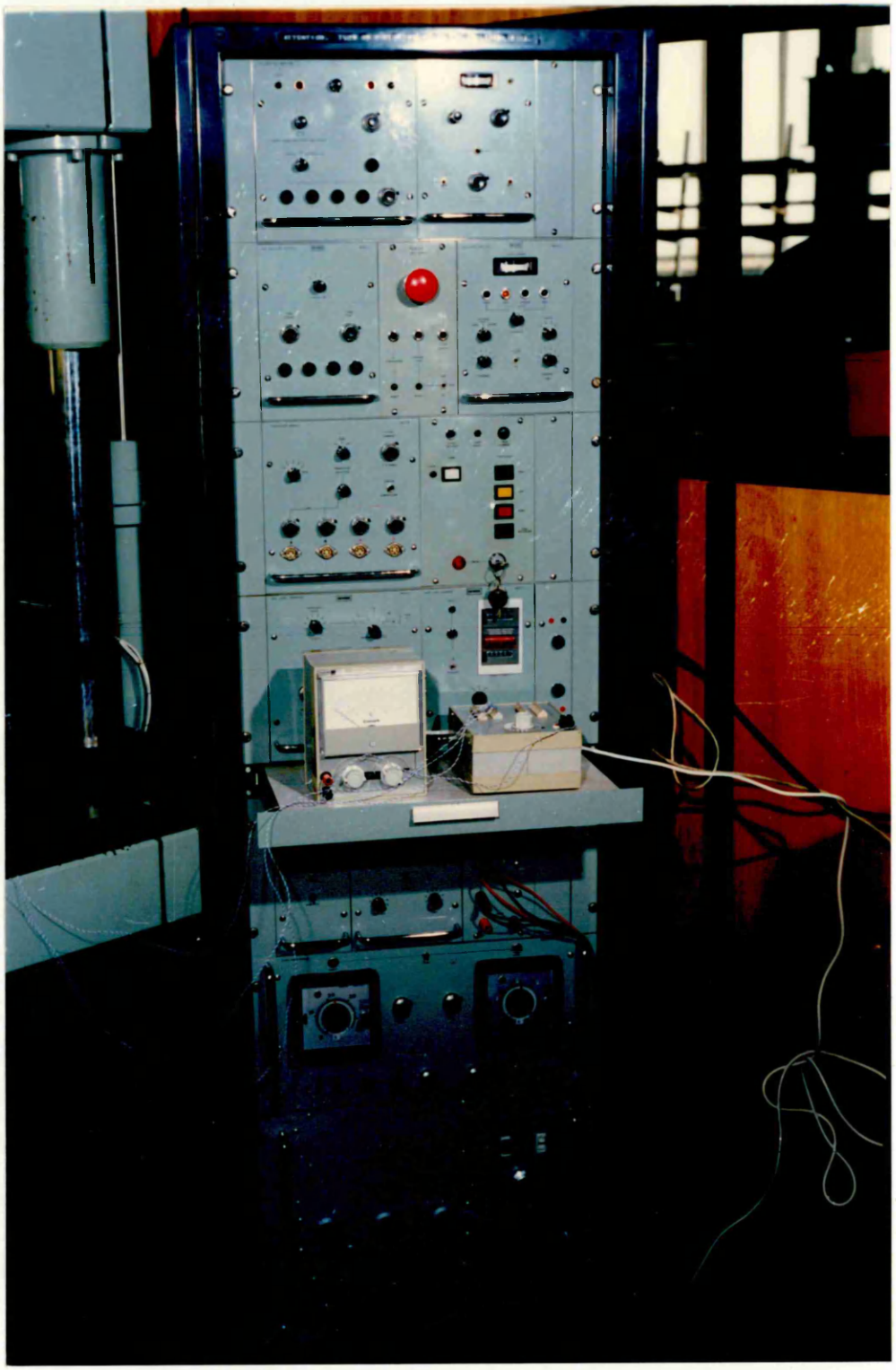

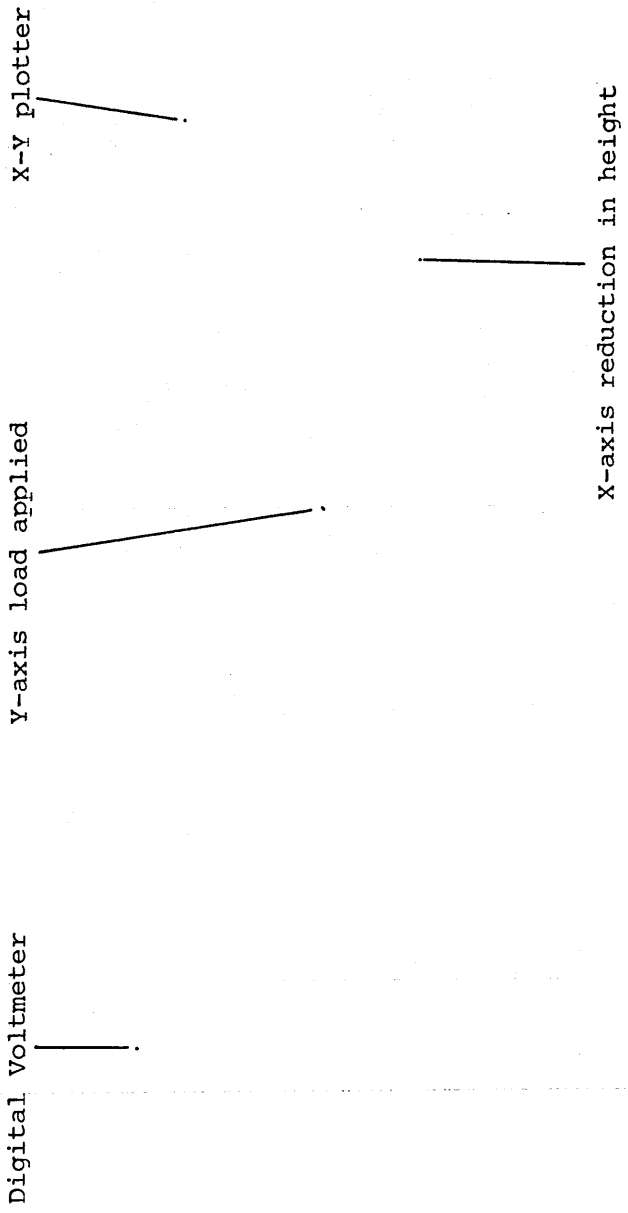

Plate No [6.3] Digital voltmeter and X-Y plotter

Plate No [6.3] Digital voltmeter and X-Y plotter

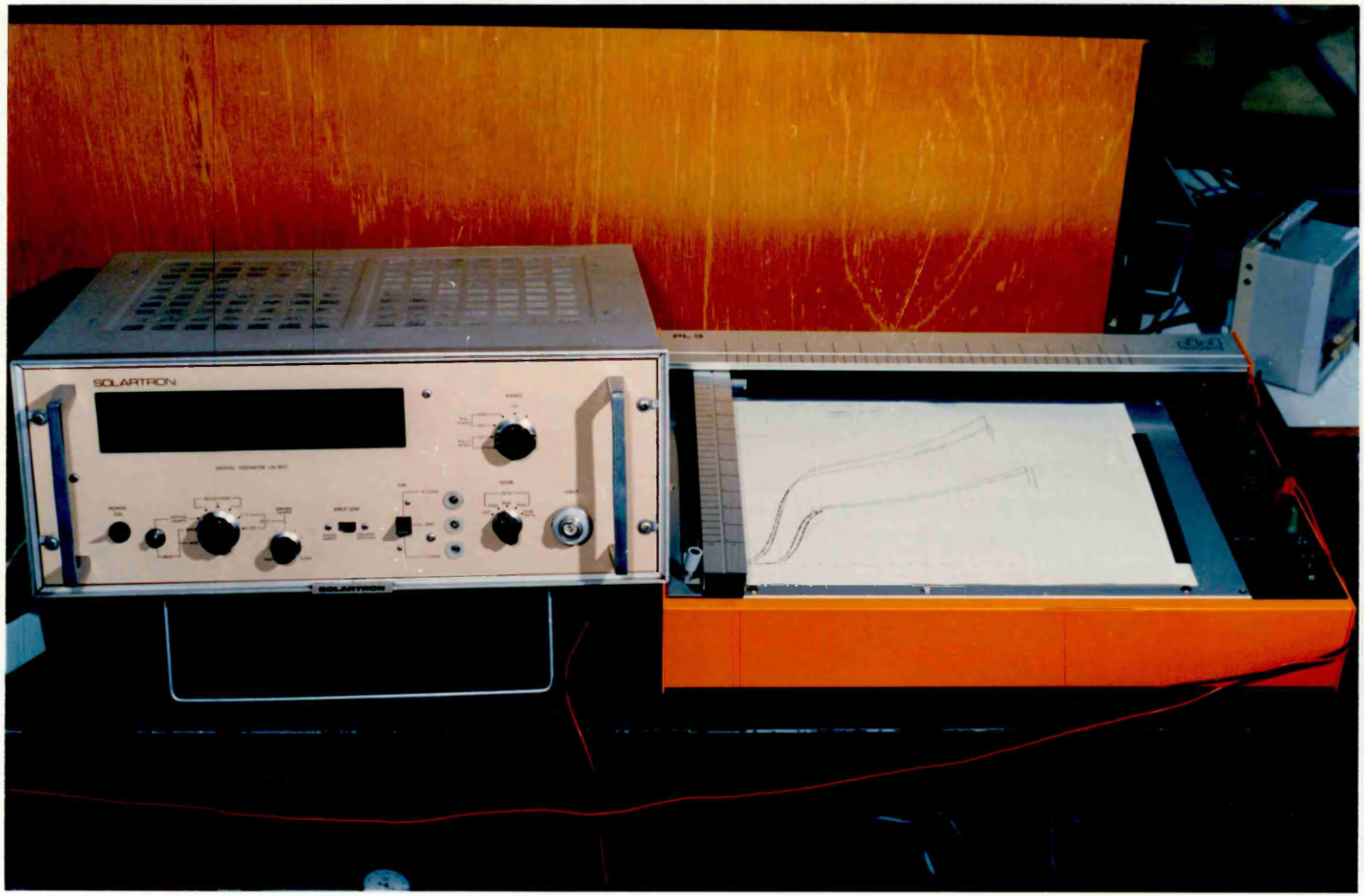
SOLARTRON
SOLARTRON

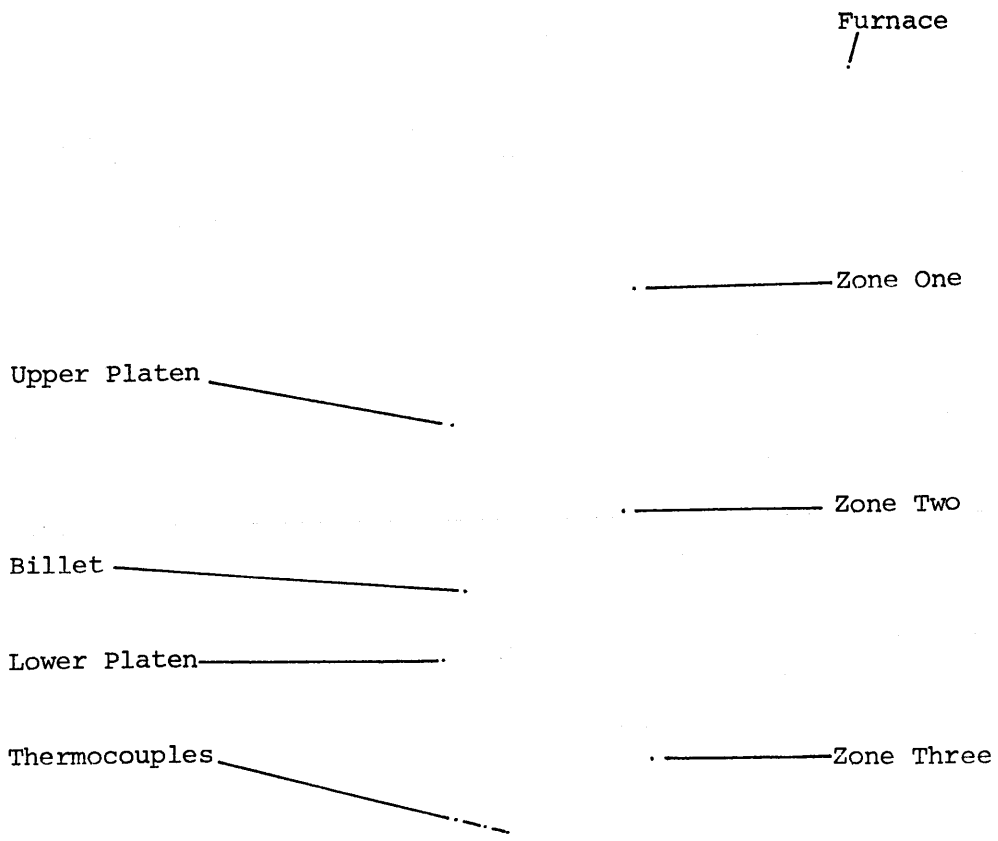

Plate No [6.4] Furnace zones, compression platens, thermocouples and billet arrangement

Plate No [6.4] Furnace zones, compression platens, thermocouples and billet arrangement

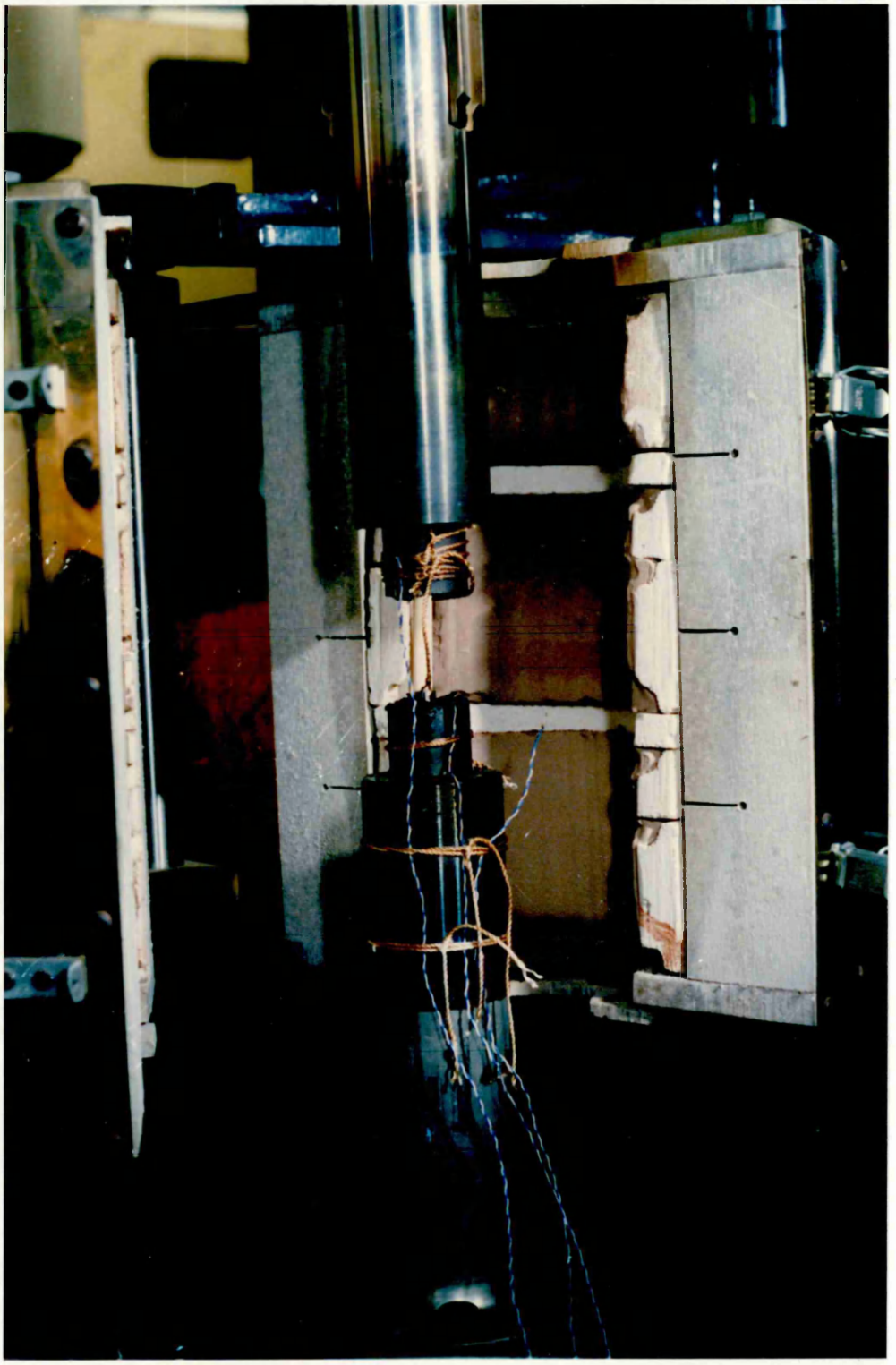

CHAPTER SEVEN

7.0 Discussion of Results

7.1 Introduction

The present work is mainly involved in developing a technique for processing experimental data in order to determine the stress-strain properties of metals and alloys undergoing deformation at high strain rates.

In order to establish the technique a number of preliminary tests were conducted in phase one of the present investigation and the results presented in chapter four. The main purpose of these preliminary results was to establish test conditions, obtain a comparison of the techniques with those of other researchers and act as an introduction to the main investigation, phases two and three, presented in chapters five and six. The results of all these tests are discussed in the following sub-sections.

7.2 Quasi-Static Stress-Strain Characteristics

The stress-strain characteristics of HE15, HE30TF, DTD5044 aluminium alloys and En-8 steel were investigated at the low strain rate of 3.7×10^{-3} per second. These characteristics were extensively studied over a temperature range of 20 to 250°C as explained in sections 4.2 and 6.2 with their relevant figures 4.1 to 4.4 and 6.4 to 6.7. These show that stresses under lubricated conditions were about 4 to 8 per cent lower in value than those obtained under dry conditions.

It was found that the quasi-static flow stress of DTD5044 is higher than those for HE15 and HE30TF. This was also reported by Baily and Singer (65) when they tested a Duralumin-type alloy containing 4.2 per cent copper and an aluminium alloy containing 5.7 per cent zinc. It was also found for the three aluminium alloys that for a given strain the stress values at room temperature were higher than those obtained at elevated temperatures. Stress decreases as temperature increases provided the strain rate remains constant. This was observed previously by Hockett (51) when he tested commercially pure (1100) aluminium in compression over a wide range of constant strain rates varying from 0.1 to 200 per second and temperatures between -50°C and 400°C. Samanta (54) tested aluminium at a strain rate of 6.6×10^{-2} per second and over a temperature range of 250-550°C reporting a decrease in flow stress as temperature increased. Chiddister and Malvern (55) observed the same characteristic when testing annealed (1100) F aluminium at temperatures varying from 30 to 550°C at constant strain rates. The decrease in flow stress with increasing temperature is due to the fact that recovery, recrystallisation and grain growth are thermally activated processes which lead to a reduction in the flow stress.

It was also observed in the present investigation that there were negligible changes in stress values for the En-8 steel at temperatures ranging from 20 to 250°C, as shown in figure 6.7. Haque and Hashmi (46) have also reported that the stress values for En-8 steel at 235°C are just about equal to those obtained at room temperature. This is understandable, since the

recrystallisation temperature is around 1000°C for steels. Dean and Sturgess (56) tested En-8 at temperatures varying between 600 and 1200°C, reporting that an increased flow stress accompanies either a reduction in temperature or an increase in strain rate. This does not affect the present investigation since the highest test temperature was 250°C.

It is also well known that ductility is very low for a low carbon steel at temperatures between 100°C and 300°C. This ductility range is known as the blue-brittle range which is a dynamic strain ageing effect, due to diffusion of carbon and nitrogen atoms to dislocations during straining at the above mentioned temperatures. It is a phenomenon associated with ferrite, and thus it might be expected to occur more in low carbon steel than in En-8 steel as in this case.

7.3 Dynamic Stress-Strain Characteristics

From the dynamic stress-strain curves presented in the three phases, figures 4.17 to 4.19, 5.24 to 5.27 and 6.16 to 6.19 of the present study, it was found that the dynamic stress-strain curves show similar trends to the static ones. This is not surprising, since the same rate sensitivity equation has been used in the numerical technique with different values of the constants P and D. It was also observed that the dynamic stress is always higher than the quasi-static one, being about 2.5 times for strain rates of the order of 10^4 per second (figures 6.16 to 6.19). Yoshida and Nagata (30) reported the same trends when they conducted compression tests on polycrystalline aluminium (99% purity) at room temperature and strain rates between 10^2 and 8×10^3 per second.

Lindholm and Yeakley (33) also reported the same behaviour when they conducted compression tests on high purity aluminium at strain rates of up to 5 x 10^2 per second. Hockett (51) conducted compression tests on aluminium over a wide range of strain rates ranging from 0.1 to 2 x 10^2 per second at constant temperatures of -50 to 400°C reporting that an increase in flow stress with an increase in strain rate occurred. Holt et al (62) tested aluminium alloys, with similar copper and zinc contents to HE15 and DTD5044 respectively, in compression at constant strain rates ranging from 10^{-3} to 10^3 per second. They reported an increase in the flow stress with increase in strain rate, as did Samanta (68) when he conducted tests on face centred aluminium.

For En-8 structural steel results from the present study, as shown in figure 6.19, also indicate an increase in the flow stress with increasing strain rate, eg at a strain rate of 2.2 x 10^4 per second the stress corresponding to a strain of 0.5 was about 2750 MN/m². Holzer and Brown (17) reported similar results for mild steel and medium carbon steel when undergoing compression tests at strain rates between 10^{-3} and 10^3 per second; so did Woodward and Brown (31) when testing mild steel at strain rates of up to 10^4 per second. Later on Haque and Hashmi (46) reported a similar trend for En-8 steel undergoing high strain rate impact compression tests of up to 10^5 per second.

The stress ratio (dynamic to static stress ratio's) values obtained in the present study at strain rates between 4 x 10^3 and 1.6 x 10^4 per second for HE15, HE30TF and DTD5044 aluminium

alloys varied from 1.92 to 1.95, 1.97 to 1.99 and 2.12 to 2.59 respectively. It is observed that stress ratio values for DTD5044 are higher than those for the other two alloys due to its higher strength. This has caused separation between the stress-strain curves at high strain rates as shown in figure 6.18 compared with figures 6.16 and 6.17.

Figure 6.24 shows the variation of stress ratio with strain rate obtained in the present study and by different investigators. There is a general tendency for stress ratio to increase with strain rate, this feature being particularly prominent for DTD5044. Lindholm (28) when testing aluminium at strain rates between 10^2 and 10^4 per second obtained stress ratios between 2.225 and 2.375 indicating that errors might have arisen from load readings due to the use of strain gauges, stress wave propagation and from not including radial inertia, temperature rise and strain rate variation. In the present study no load readings were involved and the temperature rise, radial inertia and strain rate effects were catered for.

Bodner (64) also reported stress ratios of 3.11 to 3.46 for aluminium at strain rates ranging from 10^3 to 10^4 per second. Later, Haque (14) achieved homogeneous deformation by impacting tool steel projectiles onto small cylindrical billets. The stress ratio values obtained in this investigation for HE30TF at strain rates ranging from 6.7×10^3 to 3.3×10^4 per second differ from those obtained in the present study for the same material, as shown in figure 6.24 curve 4 compared with curve 9. Haque's stress ratios were higher than those obtained in the present study due to the fact that he obtained his results by

analysing deformation from high speed photographs and did not cater for temperature rise in the material during deformation.

For En-8 steel, values obtained for the stress ratios at strain rates of 6×10^3 to 2.2×10^4 per second compare favourably with other investigators values as shown in figure 6.25. Hashmi (48) has tested mild steel in high strain rate compression tests of up to 10^5 per second. His stress ratio values were lower than the values obtained in the present study due to inhomogeneity and localised deformation, as shown in figure 6.35 curve 2 compared with curve 6. Haque and Hashmi (46) subsequently employed homogeneous deformation tests. However, their values were still lower due to analysing deformation from high speed photographs and not catering for temperature rise, as shown in figure 6.25.

7.4 Temperature Rise During Deformation

The results presented in table 4.1 during deformation were obtained from experimental data as shown in Appendix III. Although in this case deformation was inhomogeneous, the same method was adopted to produce results presented in table 5.1 for homogeneous deformation as shown in Appendix V.

The maximum temperature rise was obtained at maximum impact velocities of 80 m/s and 110 m/s for the three aluminium alloys and En-8 steel respectively. The results were obtained at strains of 35%, 60%, 29% and 31.6% for HE15, HE30TF, DTD5044 and En-8 steel respectively.

Haque (14) assumed in his investigation that for En-8 steel the temperature within the specimen during deformation at a strain

level of 15% did not change appreciably from the initial test temperature and so ignored this effect. He justified his assumption by reference to work done by Holzer and Brown (17). This might be the case for En-8 steel where the recrystallisation temperature is high. It was found in the present study that there was no change in flow stress when conducting quasi-static compression tests on En-8 steel at temperatures between 20°C and 250°C as shown in figure 6.7. However a modest change in temperature during the deformation of the aluminium alloys did affect their flow stresses, figures 6.4 to 6.6.

A number of solutions have been suggested by Lahoti and Altan (50), Mohitpour and Lengyel (69) for the temperature distribution in axisymmetric compression but their results are in disagreement. It was reported in reference (50) that the temperature rise at the specimen-die interface decreases with increasing friction, while according to reference (69) the opposite effect occurs. Reference (50) reported that the temperature within the specimen during deformation is much greater than that at the interface while reference (69) reported the opposite, indicating inhomogenity in deformation.

In the present investigation an approximately uniform temperature distribution was achieved and consequently homogeneous deformation was obtained. Figure 6.26 shows that the difference in temperature between the centre and both ends of HE15 specimen was approximately 3.5°C which is small enough to cause negligible material inhomogenity within the specimen.

The temperature rises during dynamic deformation have been calculated using the equation reported by Holzer and Brown (17)

for the aluminium alloy and En-8 steel. Under homogeneous and adiabatic conditions the rises in temperature for HE15, HE30TF, DTD5044 and En-8 were 141, 137, 163 and 166°C respectively. Haque (14) reported a rise of 62°C for En-8 steel at a strain of 14.75% and a strain rate of 10^5 per second. In the present study it was found that the maximum rise in temperature for En-8 steel at 31.6% strain and an average strain rate of 2.167×10^3 per second was 166°C. Samanta (53) reported a rise in temperature between 60 and 70°C for steel at a strain rate of 4.3×10^2 per second. Wallace (8) also reported a 155°C rise in temperature during the extrusion of 99.7% aluminium at a strain rate of 5.7×10^3 per second which agrees approximately with the temperature rise obtained in the present study as shown in table 5.1. The results shown in table 5.1 were obtained at strain rates of 7.15×10^3, 3.66×10^3, 1.023×10^3 and 4.334×10^3 per second for HE15, HE30TF, DTD5044 and En-8 respectively.

7.5 Radial Inertia Effect

In the present study the radial inertia effect during the high strain rate compression tests was investigated. To assess this effect during the fast compression of cylindrical billets, it is to be assumed (60) that frictional resistance at the billet-anvil and projectile interfaces is absent and that the deformation is homogeneous. Furthermore the effect of stress wave propagation is considered to be insignificant at compression velocities in the range 10 to 300 m/s.

In phase two of the present study the deformation was homogeneous (chapter five) and lubricant was used in all tests to minimise friction as shown by ring test, table 5.2. The other

feature of the present investigation is that the compression velocities varied between 50 and 250, 20 and 110 in phases one and two respectively. Under these conditions the stress wave propagation effect is negligible. Reference (60) reported this to be the case for velocities less than 300 m/s. The specimens used were very small and so the transit time for the stress waves is very short and equilibrium is rapidly established.

The method introduced by Slater (60) was adopted in the present investigation and the results are presented in table 5.1 (see Appendix VI). The radial inertia contribution to stress for HE15, HE30TF and DTD5044 varied from 0.008% to 0.034%, 0.226% to 1.05% and 0.006% to 0.184% respectively corresponding to strain rates range of 4×10^3 to 1.64×10^4 per second over a strain range of 0.1 to 0.5. For En-8 steel it was found that the radial inertia contribution was 0.037% to 1.5% corresponding to strain rate range of 6×10^3 to 2.2×10^4 per second and over a strain range of 0.1 to 0.5.

Haque (14) reported that the radial inertia contribution to the total force for En-8 steel is 0.08% to 9.7% corresponding to strain rates of 10^3 and 10^5 per second. He also used the method reported by Slater (60) and considered this effect to be negligible. Holzer and Brown (17), stated that if radial inertia was significant it would lead to a much larger separation of the stress-strain curves in the high strain rate region and this was not observed in their work. This effect has not been observed in the present work, figures 6.16 to 6.19.

Hashmi and Islam (49) considered the material inertia effect when they conducted high strain rate ballistic tests on railway

steel, at strain rates ranging from 10^4 to 6 x 10^4 per second and natural strains between 10% to 40%. They reported that this effect was quite small and ignored it. Later on Hashmi and Haque (72) found that this effect varied between 0.06% to 2% at strain rates of 6.6 x 10^3 and 3.3 x 10^4 per second respectively over a strain of 10% for an aluminium alloy.

However, Maiden and Green (37), when testing aluminium alloys, found the inertia contribution was about 10% at strain rates of 10^4 per second and considered it negligible. Samanta (54) reported that for constant strain rate experiments with aluminium, the contribution from radial inertia would be minimal for specimen with r/h = 2.3, where r is the radius and h is the height of specimen at strain rate of up to 2.2 x 10^3. However, when using aluminium specimens with ratio r/h = 0.5 which is similar to the ratio used in the present work, he reported inertia corrections of 0.05% and 0.03% at strains of 20% and 50% respectively and strain rate of 2.2 x 10^3 per second.

Davis and Hunter (61) reported that in order to minimise the radial inertia effect at strain rates between 10^3 and 10^4 per second a ratio of r/h = 1.0 was required. Maiden and Green (37) reported a required ratio of r/h = 0.375 for similar results as (61). Haque and Hashmi (46) used r/h = 0.5 for the lower strain rate of 7.3 x 10^3 per second and r/h = 2 for the high strain rate of 9 x 10^4 per second.

In the present study the ratio r/h was kept $\simeq$ 0.5 and therefore from the above discussion, it is reasonable to claim that the specimen dimensions were satisfactory in minimising the radial

inertia effect. Finally, although a correction for the radial inertia effect was made by introducing it into the finite-difference technique the contribution was found to be very small and so did not affect the results shown in figures 6.28 to 6.57.

7.6 Friction Effect

The contribution of friction to stress during static and dynamic compression tests is generally considered to be a major source of error, especially for large deformations. In the present study, although coefficients of friction were calculated under dry conditions, tallow-graphite (8/1 by weight) was used as a lubricant to minimise this effect. The tallow was mixed with the graphite to make it easy for spreading on anvil and specimen.

Male et al (21) recommended graphite as a lubricant at high temperatures; they also added that graphite will fail as a lubricant when it is heated with stock materials above 300°C. In the present work the temperatures reached during the quasi-static compression tests, figures 6.4 to 6.7, and the rise in temperature within the specimens during dynamic deformation, as reported in table 5.1 (see Appendix VII), did not exceed 250°C. Baily et al (23) recommended graphite and molybdenum disulphide.

Based on the work done by Osakada (20), it was reasonable to assume in the present work, during the initial stages of deformation, that the friction mechanism remained similar in all tests. However, the friction distribution in high speed compression tests is considered by Holzer and Brown (17) to be uneven, due to the uneven rise in temperature. Mohitpour et al

(69) and Lahoti et al (50) considered an even friction distribution in high speed compression tests. This is why their results differ completely from those in reference (17). Takahoshi and Alexander (22) reported an increase in friction (in incremental loading tests) at the high stresses associated with large deformation in aluminium and mild steel.

In the present study both the static and dynamic compression tests were assumed to have a uniform friction distribution. In high speed compression, although the temperature distribution was adiabatic, the exact nature of the friction behaviour was difficult to assess due to the complex mechanism with which the topography of the contacting surfaces changed as the deformation progressed. The coefficient of friction under dynamic conditions was found to be very low, table 5.1, hence no attempt was made to correct the results.

In addition, ring tests were conducted on one of the materials involved, using tallow-graphite, under static and dynamic conditions to demonstrate the effectiveness of the lubricant. In both static and dynamic compression tests the inside diameter of the specimens increased approximately equally although not as much as from constant volume predictions for totally frictionless conditions. The percentage difference between experimental and theoretical inside diameters for static and dynamic tests were 2.5% and 3.7% respectively. This indicates a slight increase in the friction coefficient as strain rate increases; this was reported previously by Male et al (21).

The friction coefficients in the present study varied between 0.032 and 0.062 for the four materials tested. Hashmi and Haque (72) also reported an average coefficient of friction of 0.08 for aluminium tested at high strain rate. Haque and Hashmi (46) reported a value of 0.14 - 0.15 when using tallow-graphite as lubricant for high strain rate compression tests on En-8 steel and corrected their results accordingly. Similar observations were made by Samanta (52) who found that the coefficient of friction was about 0.145 for a 40% reduction of specimen when r/h = 1.0, where r and h are the radius and length of specimen respectively. Finally the coefficient of friction values reported in the present study fits approximately within values obtained by Dean and Sturgess (56). Their values for steels varied from 0.05 to 0.15 for strain rates of up to 2.5×10^3 per second. They also reported that friction is generally lower for higher deformation speeds which is compatible with results obtained in the present study.

7.7 Specimen Geometry

In the present investigation, different values of strain rate were obtained by changing the impact velocity of the projectile and also by using different specimen sizes. It was possible to use smaller billets, but this was abandoned due to fracture occurring at high strain rates in the aluminium alloy materials. Larger sizes of billets were therefore tested but the maximum size was restricted by the projectile diameter.

The aspect ratio h/d (where h is the length and d is the diameter) was kept less than unity to avoid barrelling and buckling during deformation. However slight barrelling was observed at high strain rates for large strains as shown in

plate No 5.2. Typically the diameter varied by about 3%. Gorham et al (70) have stated that the absence of barrelling is not necessarily a sensitive or reliable indicator of homogeneous deformation. Haque (14) conducted tests on En-8 steel billets with aspect ratios of 0.92 and 0.428 for medium and high strain rates respectively, reporting that no barrelling or buckling occurred. Friction due to the small aspect ratio was minimised by the use of tallow-graphite as lubricant, which proved to be adequate and effective as shown in the ring test results, table 5.2.

Gunasekera et al (12) reported that larger aspect ratio specimens are desirable to minimise frictional effect, however to avoid buckling they kept their aspect ratio to 1.5. They reported that the suitable combination of lubricant thickness and specimen diameter can reduce barrelling at high strain rate. Gorham (70) also indicated that the combination of lubricant and surface condition can reduce barrelling. Kramer (13) reported a change in flow stress with specimen diameter at low strain rates and explained that it was due directly to the increase in the surface layer stress.

Hauser and Brown (17) used different aspect ratios reporting that barrelling is highly dependent on the h/d ratio and that the stress increases as h/d decreases. However, when they kept the diameter constant the dependence of stress on the aspect ratio was reduced at low as well as high strain rates. Excessive barrelling at high strain rates may cause errors in estimating the stress. Although only slight barrelling was observed in the present study, the final diameter readings were taken from the average of many readings in order to minimise any error.

Haque (14) reported slight barrelling when h/d was larger than unity. This was observed at high strain rates in the present study although the aspect ratio was kept less than unity. Finally different billet sizes of the three aluminium alloys were deformed at high strain rates, figures 6.34 to 6.57, showing a small difference in results using the same material constants determined for each material in chapter six. This can be explained as the combined effect of both billet size and friction effects.

7.8 Deformation History

High strain rate compression tests were conducted on the aluminium alloys and En-8 steel in the as received material condition. Although no pre-straining was involved in the main part of the study, it was essential to investigate the effect of pre-straining on the characteristics and behaviour of materials at high strain rates. Specimens made of the four materials were pre-strained statically to approximately 20% in compression, and then tested in compression at high strain rates up to 2.2×10^4 per second, figures 6.58 to 6.65. These figures show a substantial difference between the theoretically determined curves and the experimental ones, when the material constants P and D for the as received material determined in chapter six were used. This indicates a change in the values of the materials constants due to pre-straining before dynamically testing. It has been observed that the total deformation was smaller for the pre-strained specimens than for those in the as received condition at the same strain rates.

Haque (14) pre-strained En-8 steel specimens to 20% and 40% before conducting high strain compression tests on them. He reported that the higher the pre-straining, the harder the material and consequently the range of constant strain rate for a given velocity of projectile is shorter. This was observed in the present study, figures 6.58 to 6.65, where the shift in curves indicate a decrease in the material constant D required to cause the theoretical curve to approach the experimental one. The decrease in the required value of D indicates that the material strength increased due to the hardening effect which is a direct result of pre-straining, consequently the quasi-static flow stress is larger for pre-strained material than for as received material.

Yoshida and Nagata (30) tested pre-strained polycrystalline aluminium at high strain rates of up to 8×10^3 per second. They reported that the flow stress of specimens which have been given a certain amount of deformation varies depending on the strain rate history during deformation. This suggests that the flow stress depends not only on the instantaneous strain and strain rate but also on the strain rate history of the specimen.

Woodward and Brown (31) observed the same features when they conducted compression tests on mild steel at strain rates of up to 10^4 per second. They reported that mild steel in the as received condition showed a marked increase in flow stress at high strain rates and that pre-straining reduced this phenomenon. Lindholm (34) observed similar trends when testing pre-loaded aluminium at high strain rates of up to 10^3 per second, reporting that the prior strain rate history of loading

has a significant effect on the magnitude of the flow stress. He also added that materials deformed to the same strain are different in structure if the deformation is produced statically or dynamically.

7.9 Strain Rate Sensitivity

The stress-strain characteristics for the three aluminium alloys and En-8 steel were obtained at strain rates of 4×10^3 to 1.6×10^4 and 6×10^3 to 2.2×10^4 per second respectively. It was observed from the results obtained in phase three (chapter six) of the present study, that both the flow stress and stress ratio increases with strain rate, figures 6.16 to 6.23. Stress ratio values varied from 1.92 to 1.957, 1.974 to 1.992 and 2.124 to 2.59 for HE15, HE30TF and DTD5044 respectively at strain rates of 4×10^3 to 1.6×10^4 per second and strains ranging from 0.1 to 0.5.

The stress ratio for En-8 varied between 2.333 and 2.454 at strain rates varying between 6×10^3 and 2.2×10^4 per second and strains ranging from 0.1 - 0.5. Haque (14) reported stress ratio values of 1.9 to 2.3 for HE30TF and 1.8 to 2.5 for En-8 steel at strain rates of 6.7×10^3 to 3.3×10^4 and 10^3 to 10^5 per second respectively. His results were over estimated for HE30TF aluminium alloy due to the fact that he ignored the temperature rise effect during deformation.

However, with En-8 steel the temperature rise within the specimen during deformation has a negligible effect on the flow stress; the explanation for the discrepancy in stress ratios could be the pre-straining technique used in reference (14) and

error involved in processing the experimentally obtained deformation time histories of the specimens.

Holzer and Brown (17) tested mild steel and a medium carbon steel at strain rates of 10^{-3} to 10^{4} per second, reporting an increase in true stress as strain rate increases. They also indicated that over a strain rate range of 5×10^{2} to 1.5×10^{3} per second there was a slight decrease in the trend of the flow stress to increase due to the temperature effect and softening. Woodward and Brown (31) tested as received mild steel at strain rates of 10^{-3} to 10^{4} per second, reporting an increase in initial flow stress at high strain rates (thus showing a strain rate sensitivity). Haque and Hashmi (46), when subjecting En-8 steel to strain rates of 10^{3} to 10^{5} per second up to strains of 50%, reported that En-8 steel showed a strong strain rate sensitivity. This strain rate sensitivity for the En-8 steel was observed to be similar in the present study, figure 6.19.

Yoshida and Nagata (30) subjected polycrystalline aluminium to strain rates of 10^{2} to 2×10^{3} per second, reporting that the dynamic stress is always higher than the static one thus showing a strain rate dependence. Samanta (55) observed that strain rate has a much greater effect at high temperature when he subjected aluminium to strain rates of 6.6×10^{-2} to 2.2×10^{3} per second. Haque (14) also reported a strong strain rate sensitivity for HE30TF aluminium alloy at strain rates of 6.7×10^{3} to 3.3×10^{4} per second. In the present study the two aluminium alloys HE15 and HE30TF showed a moderate strain rate sensitivity, figures 6.16 and 6.17 respectively, while DTD5044 showed a strong strain rate sensitivity due to its higher strength, figure 6.18.

Maiden and Green (37) subjected 7075-T6 aluminium alloy (which has the same zinc content as DTD5044) to strain rates of 10^{-3} to 10^{4} per second during their tests. They reported in their preliminary work that it is not sensitive to strain rates at least up to a strain rate of 10^{3} per second. Holt et al (62) subjected 7075-T6, 7075-0and 2024-T6, 2024-0 aluminium alloys (2024 alloys have the same copper content as HE15) to strain rates up to 10^{3} per second. They reported that both alloys in the 0 temper state are sensitive to strain rate and that the sensitivity decreases as the alloying elements are increased. References (37) and (62) both showed a small sensitivity in the T6 temper condition. This may be due to the dislocation movement being controlled by coherent precipitates. Antonio (66) also reported that the 7075-0 aluminium alloy showed a strain rate sensitivity at low strain rates of 10^{-5} to 10^{-1} per second. As observed in the present study, figure 6.18, DTD5044 showed a moderate strain rate sensitivity at strain rates of 10^{3} per second and a strong one at strain rates higher than 10^{3} per second.

A comparison of the stress ratio-strain rate relationship for several investigators is presented in figures 6.24 and 6.25 for the aluminium alloys and En-8 steel respectively. The figures show that the strain rate sensitivity of the aluminium alloys and En-8 steel determined in the present study compares favourably with previously reported work.

Finally, it is worth mentioning that the strain rate sensitivity equation 3.1 is also valid at strain rates smaller than those obtained in the present study for the four materials involved.

7.10 Comparison between Phases One, Two and Three

Phase one of the present work was involved with impinging projectiles made of HE15, HE30TF and DTD5044 aluminium alloys onto a rigid anvil. A finite-difference numerical technique developed by Hashmi (48) was used to obtain the stress-strain characteristics of the materials involved at high strain rates. Although the technique took into account the material inertia, strain hardening and strain rate sensitivity, it ignored inhomogeneity and temperature rise within the specimen during deformation. Friction was investigated and lubricant was used but not effectively.

Localised deformation occurred only in the small portion of the projectile adjacent to the rigid anvil, while the remainder of the projectile had little deformation. Temperature rise during deformation within the specimen, which can effect the flow stress of the material, and friction forces which can create errors in data were not taken into account.

Due to the factors mentioned above, phase two was introduced, achieving homogeneous deformation by a different experimental method and using a modified finite-difference numerical technique. This was done by impinging a heat treated tool steel projectile onto small cylindrical billets. More effective lubrication was used to minimise the friction forces, although slight barrelling still occurred at high strain rates. The effectiveness of the lubricant was proved by the ring test results. Haque and Hashmi (46) used a similar experimental method which involved recording deformation time histories using an image convertor (IMACON) camera. This caused errors in estimating loads and the temperature rise effect was ignored.

Phase three of the present work was a combination of phase two together with the effects of temperature rise within the specimen, specimen size and deformation history. The final values of the material constants P and D obtained in this phase were determined by the finite-difference numerical technique catering for strain hardening, strain rate sensitivity, radial inertia, temperature rise and friction. The P and D constants varied from one phase to another for some materials.

(a) Phase One

Material	P	D
HE15	35	100
HE30TF	25	100
DTD5044	15	100

(b) Phase Two

Material	P	D
HE15	35	75000
HE30TF	25	30000
DTD5044	15	100
En-8	7.5	80

(c) Phase Three

Material	P	D
HE15	35	75000
HE30TF	75	30000
DTD5044	4	2500
En-8	15	80

In phase one (chapter four) the values obtained for the aluminium alloys indicated a moderate strain rate sensitivity at strain rates ranging from 2.5×10^3 to 1.25×10^4 per second, figures 4.20 to 4.22.

However, in phase two (chapter five) the P and D constants obtained for HE15 and HE30TF were different from those in phase one indicating again a moderate strain rate sensitivity at strain rates varying between 4×10^3 and 1.6×10^4 per second, figures 5.32 to 5.34. For DTD5044 aluminium alloy the constants P and D remained the same as in phase one due to its high strength. En-8 steel, figure 5.35, showed a strong strain rate sensitivity over the strain rate range 6×10^3 to 2.2×10^4 per second.

In phase three (chapter six) of the present study, different values of the constants P and D were obtained for all materials except HE15 aluminium alloy, figure 6.16. Both HE15 and HE30TF aluminium alloys showed more strain rate sensitivity than in phase one. However DTD5044, figure 6.18, showed a strong strain rate sensitivity in this phase due to its higher rise in temperature during deformation than the other two aluminium alloys.

For En-8 steel the constants P and D were different from phase two, figure 6.19. Although the temperature rise within the specimens during deformation did not affect the flow stress significantly, new values were obtained. This can be explained as a slight improvement in the computational exercise and the small change due to the temperature effect.

8.0 Conclusions and Suggestions for Future Work

8.1 Conclusions

The following conclusions were drawn from the experimental and theoretical work carried out in the present study for HE15, HE30TF, DTD5044 aluminium alloys and En-8 structural steel over a strain range up to about 50 per cent.

1 A method using high speed compression testing in conjunction with a finite-difference numerical technique has been successfully used to determine materials properties at high strain rates. The technique takes into account the material strain hardening, strain rate sensitivity and temperature rise during deformation.

2 The quasi-static stress-strain characteristics of the three aluminium alloys and En-8 steel were obtained at room temperature and elevated temperatures of up to 250°C. It was found that for the aluminium alloys the flow stress decreases with increasing temperature, while it remained the same for the En-8 steel over this range of temperature.

3 Inhomogeneity occurred in phase one tests due to localised deformation occurring only in the first few elements of the projectile end (where it has been in contact with the rigid anvil) while the other end remained undeformed.

4 The phase one high speed compression testing approach was modified in phase two to achieve homogeneous deformation. The finite-difference numerical technique was also modified to allow for the new test procedure.

5 The temperature rise within the specimen during deformation was considered important and hence introduced into the new modified technique. It was found that it affects the materials constants and consequently the flow stress.

6 The radial inertia force and its contribution to the flow stress for each material was investigated. Its effect was found to be negligible.

7 Ring tests were conducted at static and dynamic strain rates, proving that the lubricant used was suitable and effective in minimising friction under static and dynamic test conditions.

8 The new modified approach and technique (phase three) enabled the determination of strain rate sensitivity constants P and D in the flow equation

$$\sigma_D = \sigma_s \left[1 + \left(\frac{|\dot{\varepsilon}|}{D}\right)^{1/P}\right]$$

for the four materials at room temperature as follows:

Material	P	D
HE15	35	75000
HE30TF	75	30000
DTD5044	4.0	2500
En-8	15	80

9 The aluminium alloy DTD5044 and En-8 steel were found to have a strong strain rate sensitivity at strain rates from 4×10^3 to 1.6×10^4 and 6×10^3 to 2.2×10^4 per second respectively. HE15 and HE30TF aluminium alloys were found to have a moderate strain rate sensitivity over a strain rate range of 4×10^3 to 1.6×10^4 per second.

10 A comparison of the strain rate sensitivity, in the form of the stress ratio - strain rate relationship for the four materials, while other researchers work showed that the results obtained were consistent with previous studies.

11 In order to investigate the effect of specimen size, different billet sizes were used keeping the aspect ratio h/d less than unity. It has been shown that aspect ratio has an effect on results during high strain rate impact tests by altering the materials constants. This is due to friction and rise in temperature which affects the flow stress.

12 Deformation history was investigated in the present work. It was shown that for a specimen which has been given a certain amount of pre-straining before being dynamically tested, the flow stress changes and is dependent on strain history. This was observed from changes which occurred to the materials constants P and D.

8.2 Suggestions for Further Work

Several factors have been considered in the present work which affect deformation. Some have been investigated thoroughly, others have not due to the limited scope of the study and the time available. More information could be obtained as follows.

1 The stress-strain characteristics of materials at high strain rates and at sub-zero and elevated temperatures. This involves cooling or heating the material before statically and dynamically deforming specimens and establishing a relationship between strain rate, stress

and strain over a wide range of temperatures. The results of the present study only apply at room temperature.

2 The effect of specimen size needs to be investigated thoroughly. Different aspect ratios (h/d) need to be considered (in conjunction with friction) by increasing the specimen diameter, although at present it is restricted on the existing rig by the projectile size.

3 Deformation history also needs to be investigated thoroughly. Static and Dynamic pre-straining before deforming dynamically can be conducted to establish the dependence of the flow stress on strain history and its effect on deformation at high strain rates.

4 Other materials can be tested to obtain their properties at high strain rates and so form a material data base.

5 The effect of any elastic deflection of the anvil (although negligible) was not incorporated in the numerical technique. This should be taken into account by modifying the present technique.

REFERENCES

1 Woodward, A R, "Future Uses of Aluminium Alloys", Proc Instn Mech Engrs, Vol 194, 85, 1980.

2 Woodward, A R, "Future Uses of Aluminium Alloys", The Metallurgist and Materials Technologist, Vol 16, 20, January 1984.

3 Hyatt, M V, "New Aluminium Aircraft Alloys For The 1980s", Boeing Materials Technology, Boeing Commercial Airplane Company, Seattle, Washington.

4 Staley, J T, "Aluminium Alloy and Process Developments for Aerospace", Metal Engineering Quarterly, 52, May 1976.

5 Pugh, H L I D and Watkins, M T, "Some Strain-Rate Effects in Drop-Forging Tests", Proceeding of Conferemce on Properties of Materials at High Rates of Strain, 1956, pp 122-127.

6 Dowling, A R; Harding, J and Campbell, J D, "The Dynamic Punching of Metals", Journal of Institute of Metals, Vol 98, pp 215-24, 1970.

7 Green, S J; Langan, J J; Leasia, J D and Yang, W H, "Materials Properties, Including Strain-Rate Effects as Related to Sheet Metal Forming", Metallurgical Transactions, Vol 2, pp 1813-20, July 1971.

8 Wallace, J F, "Adiabatic Deformation in Impact Extrusion", Journal of the Institute of Metals, Vol 90, pp 38-41, 1961-62.

9 Oxley, P L B and Stevenson, M G, "Measuring Stress/Strain Properties at Very High Strain Rates Using a Machining Test", Journal of the Institute of Metals, Vol 95, pp 308-13, 1967.

10 Christopherson, D G and Parsons, B, "The Effect of High Strain-Rate in Strip-Rolling", Proceeding of Conf on Properties of Materials at High Rates of Strain, 1957, pp 115-21.

11 Bittans, K and Whitton, P W, "High Strain-Rate Investigations, with Particular Reference to Stress/Strain Characteristics", International Metallurgical Reviews, Vol 17, pp 66-75, 1972.

12 Gunasekera, J S; Havronek, J and Littlejohn, M H, "The Effect of Specimen Size on Stress-Strain Behaviour in Compression", Transactions of the ASME, Vol 104, pp 274-79, 1982.

13 Kramer, I R, "The Effect of Specimen Diameter on the Flow Stress of Aluminium", Transactions of the Metallurgical Society of AIME, Vol 239, pp 1754-58, Nov 1967.

14 Haque, M M, "Stress-Strain Properties and Microstructure Change in Metal Deformed at Strain Rates of up to 10^4 per second", PhD Thesis, Sheffield City Polytechnic, Sheffield, UK, 1983.

REFERENCES (cont)

15 Hauser, F E, "Techniques of Measuring Stress-Strain Relations at High Strain Rates", Experimental Mechanics, pp 395-402, August 1966.

16 Dharan, C K H and Hauser, F E, "Determination of Stress-Strain Characteristics at Very High Strain Rates", Experimental Mechanics, pp 370-76, Sept 1970.

17 Holzer, A J and Brown, R H, "Mechanical Behaviour of Metals in Dynamic Compression", Transactions of the ASME, pp 238-46, Vol 101, July 1979.

18 McQueen, H J and Hockett, J E, "Microstructure of Aluminium Compressed at Various Rates and Temperatures", Metallurgical Transactions, Vol 1, pp 2997-3004, Nov 1970.

19 Lloyd, D J, "Deformations of Fine-Grained Aluminium Alloys", Metal Science, pp 193-98, May 1980.

20 Osakada, K, "A Mechanism of Lubricant Trapping in Slow Speed Compression", Inst J Mech Sci, Vol 19, pp 413-421, 1977.

21 Male, A T and Cockcroft, M G, "A Method for the Determination of the Coefficient of Friction of Metals under Conditions of Bulk Plastic Deformation", Journal of the Institute of Metals, Vol 93, pp 38-45, 1964-65.

22 Takahashi, H and Alexander, J M, "Friction in Plain-Strain Compression Test", Journal of the Institute of Metals, Vol 90, pp 72-79, 1961-62.

23 Baily, J A and Singer, Professor A R E, "The Determination of the Coefficient of Friction at Elevated Temperatures Using a Plain-Strain Compression Test", Journal of the Institute of Metals, Vol 92, pp 378-80, 1963-64.

24 Clark, D S, "The Influence of Impact Velocity on the Tensile Characteristics of Some Aircraft Metals and Alloys", Nat Adv Ctee for Aeronautics, TN No 868, Oct 1942.

25 Duffy, J, "A Dynamic Plastic Deformation of Metals", A Review Materials Laboratory, Wright-Patterson Air Force Base, Ohio 45433, Report No AFWAL-TR-82-4024, October 1982.

26 Eleiche, A M, "A Literature Survey of Combined Effect of Strain Rate and Elevated Temperature of the Mechanical Properties of Metals", 1972, Air Force Materials, Lab Tech Report 72-125, Wright-Patterson Air Force Base, Ohio.

27 Ripperger, E A, "Dynamic Plastic Behaviour of Aluminium, Copper and Iron", Behaviour of Materials under Dynamic Loading, Winter Annual Meeting of the ASME, Chicago, Illinois, Tuesday, 9 Nov 1965, Edited by Norris J Huffington Jr, pp 62-80.

28 Lindholm, U S, "Dynamic Deformation of Metals", Behaviour of Metals under Dynamic Loading, Winter Annual Meeting of the ASME, Chicago, Illinois, Tuesday 9 Nov 1965, Edited by Norris J Huffington Jr, pp 42-61.

29 Lengyel, B and Mohitpour, M, "Dynamic Stress/Strain Data to Large Strains", Journal of the Institute of Metals, Vol 100, pp 1-5, 1972.

30 Yoshida, S and Nagata, N, "Deformation of Polycrystalline Aluminium at High Strain Rates", Transactions of National Research Institute for Metals, Vol 9, pp 20-28, 1967.

31 Woodward, R L and Brown, Professor R H, "Dynamic Stress-Strain Properties of a Steel and a Brass at Strain Rates up to 10^4 per second", Proc Instn Mech Engrs, Vol 189, pp 107-115, 1975.

32 Bell, J F, "An Experimental Diffraction Grating Study of the Quasi-Static Hypothesis of the Split Hopkinson Bar Experiment", J Mech Phys Solids, 1966, Vol 14, pp 309-327.

33 Lindholm, U S and Yeakley, L M, "Dynamic Deformation of Single and Polycrystalline Aluminium", J Mech Phys Solids, 1965, Vol 13, pp 41-53.

34 Lindholm, U S, "Some Experiments with Split Hopkinson Pressure Bar", J Mech Phys Solids, 1964, Vol 12, pp 315-335.

35 Wingrove, A L, "A Device for Measuring Strain-Time Relationships in Compression at Quasi-Static and Dynamic Strain Rates", J Physics E, Vol 4, pp 873-875, 1971.

36 Wulf, G L and Richardson, G T, "The Measurement of Dynamic Stress-Strain Relationship at Very High Strain", J Physics E, Vol 7, pp 167-169, 1974.

37 Maiden, C J and Green, S J, "Compressive Strain Rate Tests on Six Selected Materials at Strain Rates from 10^{-3} to 10^4 in/in/sec", Transactions of the ASME, pp 496-504, Sept 1966.

38 Taylor, G I, "The Use of Flat-Ended Projectiles for Determining Dynamic Yield Stress", Proc R Soc, Vol 194, pp 289-299, 1948.

39 Wiffens, A C, "The Use of Flat Ended Projectiles for Determining Dynamic Yield Stress", Proc R Soc, Vol 194, 00 300-322, 1948.

40 Hawkyard, J B; Eaton, D and Johnson, W, "The Mean Dynamic Yield Strength of Copper and Low Carbon Steel at Elevated Temperatures from Measurements of the "Mushrooming" of Flat-Ended Projectiles", Int J Mech Sci, 1968, Vol 10, pp 929-948.

41 Hawkyard, J B, "A Theory for the Mushrooming of Flat-Ended Projectiles Impinging on a Flat Rigid Anvil, Using Energy Consideration", Int J Mech Sci, 1969, Vol 11, pp 313-333.

42 Balendra, R and Travis, F W, "An Examination of the Double-Frustum Phenomenon in the Mushrooming of Cylindrical Projectiles upon High-Speed Impact with a Rigid Anvil", Int J Mech Sci, 1971, pp 495-505.

43 Ghosh, S K, "On the Repeated Impact of Short Metal Cylinders", J of Mechanical Working Technology, Vol 7, pp 339-354, 1983.

44 Hutchins, I M and O'Brien, T J, "Normal Impact of Metal Projectiles Against A Rigid Target at Low Velocities", Int J Mech Sci, Vol 23, pp 255-261, 1981.

45 Gorham, D A, "Measurement of Stress-Strain Properties of Strong Metals at Very High Rates of Strain", Inst Phys Conf Ser No 47, Chapter 1, 1979.

46 Haque, M M and Hashmi, M S J, "Stress-Strain Properties of Structural Steel at Strain Rates of up to 10^5 per second at Sub-Zero, Room and High Temperatures", Mechanics of Materials Vol 3, pp 245-256, 1984.

47 Hashmi, M S J and Thompson, P J, "A Numerical Method of Analysis for the Mushrooming of Flat-Ended Projectiles Impinging on a Flat Rigid Anvil", Int J Mech Sci, Vol 19, pp 273-283, 1977.

48 Hashmi, M S J, "Strain Rate Sensitivity of a Mild Steel at Room Temperature and Strain Rates of up to 10^5 s^{-1}, J of Strain Analysis, Vol 15, No 4, 1980.

49 Hashmi, M S J and Islam, M N, "Stress-Strain Properties of Railway Steel at Strain Rates of up to 10^5 per second", Transactions of the 8th International Conference on Structural Mechanics in Reactor Technology, Vol L, pp 397-402, August 19-23, 1985.

50 Lahotiand, G D and Altan, T, "Prediction of Temperature Distribution in Axisymmetric Compression and Torsion", Journal of Engineering Materials and Technology, pp 113-120, April 1975, Transactions of the ASME.

51 Hockett, J E, "On Relating the Flow Stress of Aluminium to Strain, Strain Rate and Temperature", Transactions of the Metallurgical Sociaty of AIME, Vol 239, pp 968-976, July 1967.

52 Barya, G L; Johnson, W and Slater, R A C, "The Dynamic Compression of Circular Cylinders of Super-Pure Aluminium at Elevated Temperatures", Int J Mech Sci, 1965, Vol 7, pp 621-645.

53 Samanta, S K, "Resistance to Dynamic Compression of Low-Carbon Steel and Alloy Steels at Elevated Temperatures and at High Strain-Rates", Int J Mech Sci, 1968, Vol 10, pp 613-636.

54 Samanta, S K, "Dynamic Deformation of Aluminium and Copper at Elevated Temperatures", J Mech Phys Solids, 1971, Vol 19, pp 117-135.

55 Chiddister, J L and Malvern, L E, "Compression-Impact Testing of Aluminium at Elevated Temperatures", Experimental Mechanics, pp 81-90, April 1963.

56 Dean, T A and Sturgess, C E N, "Stress-Strain Characteristics of Various Steels over a Wide Range of Strain-Rates and Temperatures", Proc Instn Mech Engrs 1973, Vol 187, pp 523-533.

57 Alder, J F and Phillips, V A, "The Effect of Strain Rate and Temperature on the Resistance of Aluminium, Copper and Steel to Compression", Journal of the Institute of Metals, Vol 83, pp 80-86, 1954-55.

58 Bishop, J F W, "An Approximate Method for Determining the Temperatures Reached in Steady Motion Problems of Plane Plastic Strain", Quart Journ Mech and Applied Math, Vol 9, Pt 2, 1956, pp 236-245.

59 Watts, A B and Ford, Professor H, "An Experimental Investigation of the Yielding of Strip between Smooth Dies", The Institution of Mech Engrs, Proceeding 1B, pp 448-453, 1952-53.

60 Slater, R A C, "Engineering Plasticity", Macmillan Press Ltd, London, 1977, pp 134-171 and 266-273.

61 Davies, E D and Hunter, S C, "The Dynamic Compression Testing of Solids by the Method of the Split Hopkinson Pressure Bar", J Mech Phys Solids, 1963, Vol 11, pp 155-179.

62 Holt, D L; Babcock, S G; Green, S J and Maiden, C J, "The Strain-Rate Dependence of the Flow Stress in Some Aluminium Alloys", Transactions of the ASM, Vol 60, pp 152-158, 1967.

63 Komes, C H and Ripperger, E A, "Strain Rate Effects in Cold Worked High-Purity Aluminium", J Mech Phys Solids, 1966, Vol 14, pp 75-88.

64 Bodner, S R, "Strain Rate Effects in Dynamic Loading of Structures", Behaviour of Materials under Dynamic Loading, Winter Annual Meeting of the ASME, Chicago, Illinois, Nov 9 1965, Edited by Norris J Huffington Jr, pp 93-105.

65 Bailey, J A and Singer, Professor A R E, "Effect of Strain Rate and Temperature on the Resistance to Deformation of Aluminium, Two Aluminium Alloys and Lead", J of the Institute of Metals, Vol 92, pp 404-408, 1963-64.

66 D'Antonio, C R; Maciag, R J; Mukherjee, K and Fischer, G J, "The Effect of Strain Rate and Temperature on the Flow Stress of 7075 Aluminium", Transactions of the Metallurgical Society of AIME, Vol 242, pp 2295-2297, Nov 1968.

67 Dorn, J E, "Mechanical Behaviour of Materials at Elevated Temperatures", pp 1-8 and 183-197, McGraw-Hill Book Company Inc, 1961.

68 Samanta, S K, "Effect of Strain Rate on Compressive Strength of Tool Steel at Elevated Temperatures", Iron and Steel Institute, Publicon 108, London Scisson C, 122, 1968.

69 Mohitpour, M and Langyel, B, "Temperature Rise in the High Speed Compression of Right Cylindrical Billets", Proc 2nd North American Metal Working Conf, Soc Manuf Engnrs, 48, 1974.

70 Gorham, D A; Pope, P H and Cox, O, "Sources of Error in High Strain Rate Compression Tests", Proceeding of Third Conference on Mechanical Properties of Materials at High Rates of Strain, 9-12 April 1984, pp 151-158.

71 Johnson, W, "Impact Strength of Materials", Edward Arnold (Publishers) Limited, 1972.

72 Hashmi, M S J and Haque, M M, "High Strain Rate Properties of an Aluminium Alloy and High Purity Copper at Room Temperature", International Symposium on Intense Dynamic Loading and its Effects, Beijing, Peoples Republic of China, June 1986, pp 637-647.

73 Manjoine, M J, "Influence of Rate of Strain and Temperature on Yield Stresses of Mild Steel", J of Applied Mechanics, Vol 11, pp 211-218, Dec 1944.

BIBLIOGRAPHY

1 Glanville-Jones, R, "Progress in High-Energy-Rate Forging", Journal of the Institute of Metals, Vol 97, pp 257-70, 1969.

2 Cook, P M, "True Stress-Strain Curves for Steel in Compression at High Temperatures and Strain Rates, for Application to the Calculation of Load and Torque in Hot Rolling", Proceeding of Conf on Properties of Materials at High Rates of Strain, 1957, pp 86-97.

3 Jonas, J J; Sellars, C M and Tegart, W J, "Strength and Structure under Hot-Working Conditions", Metallurgical Reviews, Review 130, pp 1-24, 1969.

4 Johnson, W, "Application Processes involving High Strain Rates", Inst Phys Conf Ser No 47, Chapter 4, pp 337-357, 1979.

5 Ayres, R A and Wenner, M L, "Strain and Strain-Rate Hardening Effects in Punch Stretching of 5182-0 Aluminium at Elevated Temperatures", Metallurgical Transactions A, Vol 10A, pp 41-46, January 1979.

6 Ostermann, F, "Improved Fatigue Resistance of Al-Zn-Mg-Cu (7075) Alloys through Thermomechanical Processing", Metallurgical Transactions, Vol 2, pp 2897-2902, October 1971.

7 Pond, R B and Class, C M, "Crystallographic Aspects of High Velocity Deformation of Aluminium Single Crystal", Proceeding of Conference on Response of Metals at High Velocity Deformation, edited by P G Sharman and V F Zackay, 1961, New York, pp 145-160.

8 Keller, F, "Metallography of Aluminium Alloys", Proceeding of Conference on Response of Metals at High Velocity Deformation, edited by P G Sharman and V F Zackay, 1961, New York, pp 93-127.

9 Guminski, R D and Willis, J, "Development of Cold-Rolling Lubricants for Aluminium Alloys", Journal of the Institute of Metals, Vol 88, pp 481-92, 1959-1960.

10 Butter, L H, "The Effect of Interposed Lubricants on the Surface Deformation of Metals during Plastic Working", Journal of the Institute of Metals, Vol 88, pp 337-43, 1959-60.

11 Malvern, L E, "Experimental Studies of Strain-Rate Effects and Plastic-Wave Propagation in Annealed Aluminium", Behaviour of Materials under Dynamic Loading, Winter Annual Meeting of the ASME, Chicago, Illinois, Tuesday Nov 9 1965, Edited by Norris J Huffington Jr, pp 81-92.

12 Chalupnik, J D and Ripperger, E A, "Dynamic Deformation of Metals under High Hydrostatic Pressure", Experimental Mechanics, pp 547-54, Nov 1966.

13 Lloyd, D J, "The Stress-Strain Behaviour of Aluminium Alloys at Large Strains", Scripta Metallurgica, Vol 11, pp 297-300, 1977.

14 Sharpe, W N Jr and Hoge, K G, "Specimen Strain Measurement in the Split-Hopkinson-Pressure-Bar Experiment", Experimental Mechanics, pp 570-574, Dec 1972.

15 Ogawa, K, "Impact Tension Compression Test by Using a Split-Hopkinson Bar", Experimental Mechanics, pp 81-86, June 1984.

16 Carrington, W E and Gayler, M, "Changes in Microstructure caused by Deformation under Impact at High-Striking Velocities", Proc R Soc, Vol 194, pp 323-331, 1948.

17 Campbell, J D, "An Investigation of the Plastic Behaviour of Metal Rods subjected to Longitudinal Impact", J of the Mechanics and Physics of Solids, 1953, Vol 1, pp 113-123.

18 Habib, E T, "A Method of Making High-Speed Compression Tests on Small Copper Cylinders", Journal of Applied Mechanics, pp 248-255, Sept 1948.

19 Arnold, R R and Parker, R J, "Resistance to Deformation of Aluminium and Some Aluminium Alloys", J of the Institute of Metals, Vol 88, pp 255-259, 1959-60.

20 Watson, H Jr and Ripperger, E A, "Dynamic Stress-Strain Characteristics of Metals at Elevated Temperatures", Experimental Mechanics, pp 289-295, July 1969.

21 Cuplan, E A and Arrowsmith, D J, "The Chemical Polishing of Aluminium", Transactions of the Institute of Metal Finishing, 1973, Vol 51, pp 17-21.

22 Farren, W S and Taylor, G I, "The Heat Developed during Plastic Extension of Metals", Proc Royal Soc, Series A, Vol 107, pp 422-451, 1925.

23 Kolsky, H, "An Investigation of the Mechanical Properties of Materials at Very High Rates of Loading", Proceeding of Physical Society, London, England, Vol 62, pp 676-700, 1949.

24 Hauser, F E; Simmons, J A and Dorn, J E, "Strain Rate Effects in Plastic Wave Propagation", Proceeding of Conference on Response of Metals to High Velocity Deformation, edited by P H Sharman and V F Zackay, New York, 1961, pp 93-114.

25 Immarigeon, J-P A and Jonas, J J, "Flow Stress and Substructural Change During the Transient Deformation of Armco Iron and Silicon Steel, Acta Metallurgica, Vol 19, pp 1053-1061, Oct 1971.

26 Rosen, A and Border, S R, "The Influence of Strain Rate and Strain Ageing on the Flow Stress of Commercially-Pure Aluminium", J Mech Phys Solids, 1967, Vol 15, pp 47-62.

27 Nassef, G A; Suery, M and El-Ashram, A, "Superplastic Behaviour During Compression of As-Cast Al-Cu Entectic Alloy", Metals Technology, Vol 9, pp 355-359, Sept 1982.

28 Zukas, J; Nicholas, T; Swift, H F; Greszczuk, L B and Curran, D R, "Material Behaviour at High Strain Rates", Impact Dynamics, pp 277-288 and 308-325, A Wiley - Interscience Publication, New York, 1982.

29 Hoge, K G, "Influence of Strain Rate on Mechanical Properties of 6061-TE Aluminium under Uniaxial and Biaxial State of Stress", Experimental Mechanics, pp 204-211, April 1966.

30 Davis, R G and Magee, C L, "The Effect of Strain-Rate Upon the Tensile Deformation of Materials", J of Engineering Materials and Technology Transactions of the ASME, pp 151-155, April 1975.

31 Billington, E W and Brissenden, C, "Mechanical Properties of Various Polymeric Solids Tested in Compression", Int J Mech Sci, Pergamon Press, 1971, Vol 13, pp 531-545.

32 Slater, R A C; Johnson, W and Aku, S Y, "Experiments in the Fast Upsetting of Short Pure Lead Cylinders and Tintative Analysis", Int J Mech Sci, Pergamon Press, 1968, Vol 10, pp 169-186.

33 Sundararajan, G and Shewman, P G, "The Use of Dynamic Impact Experiments in the Determination of the Strain Rate Sensitivity of Metals and Alloys", Acta Metall, Vol 31, pp 101-109, 1983.

34 Cottrell, A H, "Deformation of Solids at High Rates of Strain", Proceeding of Conf on Properties of Materials at High Rates of Strain, 1957, pp 1-22.

35 Wulf, G L, "The High Strain Rate Compression of 7039 Aluminium", Int J Mech, Vol 20, 609-615, Pergamon Press Ltd, 1978.

36 Johnson, J E; Wood, D S and Clark, D S, "Dynamic Stress-Strain Relations for Annealed 2S Aluminium Under Compression Impact", J of Applied Mechanics, pp 523-529, Dec 1953.

37 Senseny, P E; Duffy, J and Hawley, R H, "Experiments on Strain Rate History and Temperature Effects During the Plastic Deformation of Close-Packed Metals", J Applied Mechanics, Vol 45, pp 60-66, March 1978, Transactions of the ASME.

38 Hayashi, T; Yamamura, H and Okano, S, "Temperature Measurement of Metals Under High Velocity Deformation", Procs 20th Japan Cong on Mat Res Soc at Mat Sci, Kyoto, Japan, pp 94-98, 1977.

39 Trozera, T A; Sherby, O D and Dorn, J E, "Effect of Strain Rate Temperature on the Plastic Deformation of High Purity Aluminium", Transactions of the ASM, Vol 49, pp 173-188, 1957.

40 Bailey, J A, "The Plane Strain Forging of Aluminium and an Aluminium Alloy at Low Strain Rates and Elevated Temperatures", Int J Mech Sci, Pergamon Press, 1969, Vol 11, pp 491-507.

41 Baily, J A; Haas, S L and Shah, M K, "Effect of Strain-Rate and Temperature on the Resistance to Torsional Deformation of Several Aluminium Alloys", Int J Mech Sci, Pergamon Press, 1972, Vol 14, pp 735-754.

42 Bell, J F, "Single, Temperature-Dependent Stress-Strain Law for the Dynamic Plastic Deformation of Annealed Face-Centred Cubic Metals", J of Applied Physics, Vol 34, No 1, pp 134-141, Jan 1963.

43 Tanner, R I and Johnson, W, "Temperature Distribution in Some Fast Metal-Working Operations", Int J Mech Sci, Pergamon Press, 1960, Vol 1, pp 28-44.

44 Samanta, S K, "On Relating the Flow Stress of Aluminium and Copper to Strain, Strain-Rate and Temperature", Int J Mech Sci, Pergamon Press, 1969, Vol 11, pp 433-453.

```
C       THE FOLLOWING COMPUTER PROGRAM SIMULATE AND ANALYIS THE
C       DEFORMATION PROCESS OF A CIRCULAR CYLINDRICAL PROJICTILE
C       IMPACTING AGINST A RIGID ANVIL.
C       EFFECTS OF TEMPERATURE RISE DURING DEFORMATION,RADIAL
C       INERTIA,STRAIN HARDENING,STRAIN RATE SENSITIVITY ARE
C       CATERED FOR.
        IMPLICIT REAL * 8 (A-H,O-Z)                                          TLP00002
        COMMON V,DV,W,DW,DELTS,DDS,DT,SINT,COST,BIGN,E,EPSIL,SIGMA,          TLP00003
       1BIGR,SNO,ARR,AFL,ASFL,SN,DIA,TIME,DELTSO,CINETO,C1,C2,C3,C4,         TLP00004
       2C5,C6,C7,T,STN,DIAO,BIGRO,PI,DELTAT,EM,EPSM,SIGMM,SIGMO,             TLP00005
       3RHO,TEMP,N,N1,N2,NFL,NSFL,J,N3                                       TLP00006
        DIMENSION V(22),DV(22),W(22),DW(22),DELTS(22),DDS(22),               TLP00007
       1DT(22),SINT(22),COST(22),BIGN(22),E(5),EPSIL(5),SIGMA(5),            TLP00008
       2BIGR(22),SNO(5),ARR(5,22),AFL(5,22),ASFL(5,6,22),                    TLP00009
       3SN(5,6,22),DIA(22),STN(22),STNRT(22),C1(22),                         TLP00010
       4EM(5,22),EPSM(5,22),SIGMM(5,22),SIGMO(22),TEMP(22)                   TLP00011
        READ(1,1) N,NFL,NSFL,M,M1,M2,BIGRO,RHO,DELTAT,D,P,VINITO,BIGL,PI,    TLP00012
       1(EPSIL(L),SIGMA(L),L=1,NSFL)                                         TLP00013
      1 FORMAT(6I5/(4E18.8))                                                 TLP00014
        N1=N+1                                                               TLP00015
        N2=N                                                                 TLP00016
        DELTSO=BIGL/FLOAT(N)                                                 TLP00017
        DELT=DELTSO/2.                                                       TLP00018
        DO 2 I=1,N1                                                          TLP00019
        BIGR(I)=BIGRO                                                        TLP00020
      2 CONTINUE                                                             TLP00021
        E(1)=SIGMA(1)/EPSIL(1)                                               TLP00022
        C2=DELTAT**2/RHO/BIGRO**2/PI/DELTSO                                  TLP00023
        C3=E(1)/DELTSO                                                       TLP00024
        C4=C2*2.                                                             TLP00025
        IF(D)10,12,11                                                        TLP00026
     11 C5=1./P                                                              TLP00027
        C6=1./D/DELTAT/E(1)                                                  TLP00028
        GO TO 13                                                             TLP00029
```

```
 12 C5=1.                                                                TLP00030
    C6=0.                                                                TLP00031
 13 IF(NSFL-1)210,16,14                                                  TLP00032
 14 DO 15 L=2,NSFL                                                       TLP00033
    E(L)=(SIGMA(L)-SIGMA(L-1))/(EPSIL(L)-EPSIL(L-1))                     TLP00034
 15 CONTINUE                                                             TLP00035
 16 E(NSFL+1)=0.                                                         TLP00036
    FLONFL=NFL                                                           TLP00037
    DO 3 I=1,N1                                                          TLP00038
    T=BIGR(I)/FLONFL                                                     TLP00039
    DO 4 K=1,NFL                                                         TLP00040
    ARR(K,I)=FLOAT(K+K-1)*T/2.                                           TLP00041
    AFL(K,I)=2.*PI*ARR(K,I)*T                                            TLP00042
  4 CONTINUE                                                             TLP00043
  3 CONTINUE                                                             TLP00044
    DO 17 I=1,N1                                                         TLP00045
    DO 18 K=1,NFL                                                        TLP00046
    DO 19 L=1,NSFL                                                       TLP00047
    ASFL(L,K,I)=AFL(K,I)*(E(L)-E(L+1))/E(1)                              TLP00048
 19 CONTINUE                                                             TLP00049
 18 CONTINUE                                                             TLP00050
 17 CONTINUE                                                             TLP00051
    DO 20 L=1,NSFL                                                       TLP00052
    SNO(L)=E(1)*EPSIL(L)                                                 TLP00053
 20 CONTINUE                                                             TLP00054
    DO 210 I1=1,5                                                        TLP00055
    M1=5                                                                 TLP00056
    M2=80                                                                TLP00057
    VDOTO=50000.0                                                        TLP00058
    VDOTO=VDOTO+FLOAT(I1-1)*50000.0                                      TLP00059
    WRITE(6,300) N,NFL,NSFL,M,BIGRO,RHO,DELTAT,D,P,VDOTO,BIGL,           TLP00060
   1(L,EPSIL(L),SIGMA(L),L=1,NSFL)                                       TLP00061
300 FORMAT(5H0 N= ,I5,6H NFL= ,I5,7H NSFL= ,I5,5H  M= ,I5/9H  BIGRO= ,   TLP00062
   1D18.8,7H  RHO= ,D18.8,10H  DELTAT= ,D18.8,5H  D= ,D18.8/5H  P= ,D1TLP00063
   28.8,11H  VDOTO= ,D18.8,6H  BIGL= ,D18.8/39H0  L  EPSIL TLP00064
   3  SIGMA/(I5,2D18.8))                                                TLP00065
```

```
      J=0                                                                    TLP00066
      TIME=0.                                                                TLP00067
      DO 50 I=1,N1                                                           TLP00068
      V(I)=DELT*FLOAT(I+I-1)                                                 TLP00069
      DV(I)=0.                                                               TLP00070
      W(I)=0.                                                                TLP00071
      DW(I)=0.                                                               TLP00072
      TEMP(I)=20.                                                            TLP00073
      BIGR(I)=BIGRO                                                          TLP00074
      STNRT(I)=0.0                                                           TLP00075
      DELTS(I)=DELTSO                                                        TLP00076
      SINT(I)=0.                                                             TLP00077
      COST(I)=1.                                                             TLP00078
      BIGN(I)=0.                                                             TLP00079
      C1(I)=E(1)/DELTS(I)                                                    TLP00080
      DO 40 K=1,NFL                                                          TLP00081
      DO 39 L=1,NSFL                                                         TLP00082
      SN(L,K,I)=0.                                                           TLP00083
   39 CONTINUE                                                               TLP00084
   40 CONTINUE                                                               TLP00085
   50 CONTINUE                                                               TLP00086
      DO 55 I=1,N1                                                           TLP00087
      DO 60 L=1,NSFL                                                         TLP00088
      SIGMM(L,I)=SIGMA(L)                                                    TLP00089
      EPSM(L,I)=EPSIL(L)                                                     TLP00090
   60 CONTINUE                                                               TLP00091
   55 CONTINUE                                                               TLP00092
      DO 62 I=1,N1                                                           TLP00093
      DO 63 L=1,NSFL                                                         TLP00094
      EM(1,I)=E(1)                                                           TLP00095
   63 CONTINUE                                                               TLP00096
   62 CONTINUE                                                               TLP00097
      DO 65 I=1,N1                                                           TLP00098
      DO 70 L=1,NSFL                                                         TLP00099
      EM(L,I)=(SIGMM(L,I)-SIGMM((L-1),I))/(EPSM(L,I)-EPSM((L-1),I))          TLP00100
```

```
 70 CONTINUE                                                        TLP00101
    EM((NSPL+1),I)=0.                                               TLP00102
 65 CONTINUE                                                        TLP00103
    DO 80 I=1,N                                                     TLP00104
    DV(I)=DELTAT*VDOTO                                              TLP00105
 80 CONTINUE                                                        TLP00106
    CALL PRINT                                                      TLP00107
    BIGN(1)=0.                                                      TLP00108
120 J=J+1                                                           TLP00109
    DO 90 I=1,N1                                                    TLP00110
    C1(I)=E(1)/DELTS(I)                                             TLP00111
 90 CONTINUE                                                        TLP00112
    IF(BIGN(N1)-1.)129,129,150                                      TLP00113
129 IF((V(10)-V(1))-0.40)150,150,130                                TLP00114
150 TIME=DELTAT*FLOAT(J)                                            TLP00115
    CALL PRINT                                                      TLP00116
    GO TO 210                                                       TLP00117
130 DDS(N+1)=-2.*DV(N)                                              TLP00118
    V(N+1)=V(N+1)-DV(N)                                             TLP00119
    DDS(1)=0.                                                       TLP00120
    CALL STRAIN                                                     TLP00121
    CALL TEMPER                                                     TLP00122
    CALL STRESS                                                     TLP00123
    CALL EQUILI                                                     TLP00124
    IF(J-M1)120,140,210                                             TLP00125
140 M1=M1+M2                                                        TLP00126
    TIME=DELTAT*FLOAT(J)                                            TLP00127
    CALL PRINT                                                      TLP00128
    IF(J-M)120,210,210                                              TLP00129
210 CONTINUE                                                        TLP00130
    CALL EXIT                                                       TLP00131
    STOP                                                            TLP00132
    END                                                             TLP00133
```

```
      SUBROUTINE STRAIN                                                 TLP00134
      IMPLICIT REAL * 8 (A-H,O-Z)                                       TLP00135
      COMMON V,DV,W,DW,DELTS,DDS,DT,SINT,COST,BIGN,E,EPSIL,SIGMA,       TLP00136
     1BIGR,SNO,ARR,AFL,ASFL,SN,DIA,TIME,DELTSO,CINETO,C1,C2,C3,C4,      TLP00137
     2C5,C6,C7,T,STN,DIAO,BIGRO,PI,DELTAT,EM,EPSM,SIGMM,SIGMO,          TLP00138
     3RHO,TEMP,N,N1,N2,NFL,NSFL,J,N3                                    TLP00139
      DIMENSION V(22),DV(22),W(22),DW(22),DELTS(22),DDS(22),            TLP00140
     1DT(22),SINT(22),COST(22),BIGN(22),E(5),EPSIL(5),SIGMA(5),         TLP00141
     2BIGR(22),SNO(5),ARR(5,22),AFL(5,22),ASFL(5,6,22),                 TLP00142
     3SN(5,6,22),DIA(22),STN(22),STNRT(22),C1(22),                      TLP00143
     4EM(5,22),EPSM(5,22),SIGMM(5,22),SIGMO(22),TEMP(22)                TLP00144
      DO 10 I=2,N                                                       TLP00145
      DELDV=DV(I)-DV(I-1)                                               TLP00146
      DELDW=DW(I)-DW(I-1)                                               TLP00147
      DDS(I)=DELDV*COST(I)+DELDW*SINT(I)                                TLP00148
      DT(I)=(DELDW*COST(I)-DELDV*SINT(I))/DELTS(I)                      TLP00149
      SINTI=SINT(I)                                                     TLP00150
      SINT(I)=SINTI+COST(I)*DT(I)                                       TLP00151
      COST(I)=COST(I)-SINTI*DT(I)                                       TLP00152
   10 CONTINUE                                                          TLP00153
      DO 30 I=1,N                                                       TLP00154
      V(I)=V(I)+DV(I)                                                   TLP00155
      W(I)=W(I)+DW(I)                                                   TLP00156
   30 CONTINUE                                                          TLP00157
      DO 40 I=1,N1                                                      TLP00158
      DELTS(I)=DELTS(I)+DDS(I)                                          TLP00159
      IF(DELTS(I)-0.01*DELTSO)31,32,32                                  TLP00160
   31 DELTS(I)=0.01*DELTSO                                              TLP00161
   32 BIGR(I)=(DABS(DELTSO*BIGRO**2/DELTS(I)))**0.5                     TLP00162
      FLONFL=NFL                                                        TLP00163
      T=BIGR(I)/FLONFL                                                  TLP00164
      DO 50 K=1,NFL                                                     TLP00165
      ARR(K,I)=FLOAT(K+K-1)*T/2.                                        TLP00166
      AFL(K,I)=2.*PI*ARR(K,I)*T                                         TLP00167
```

```
      DO 60 L=1,NSFL                                                    TLP00168
      ASFL(I,K,I)=AFL(K,I)*(EM(L,I)-EM((L+1),I))/E(1)
   60 CONTINUE                                                          TLP00170
   50 CONTINUE                                                          TLP00171
   40 CONTINUE                                                          TLP00172
      RETURN                                                            TLP00173
      END                                                               TLP00174
      SUBROUTINE STRESS                                                 TLP00175
      IMPLICIT REAL * 8 (A-H,O-Z)                                       TLP00176
      COMMON V,DV,W,DW,DELTS,DDS,DT,SINT,COST,BIGN,E,EPSIL,SIGMA,       TLP00177
     1BIGR,SNO,ARR,AFL,ASFL,SN,DIA,TIME,DELTSO,CINETO,C1,C2,C3,C4,      TLP00178
     2C5,C6,C7,T,STN,DIAO,BIGRO,PI,DELTAT,EM,EPSM,SIGMM,SIGMO,          TLP00179
     RHO,TEMP,N,N1,N2,NFL,NSFL,J,N3                                     TLP00180
      DIMENSION V(22),DV(22),W(22),DW(22),DELTS(22),DDS(22),            TLP00181
     1DT(22),SINT(22),COST(22),BIGN(22),E(5),EPSIL(5),SIGMA(5),         TLP00182
     2BIGR(22),SNO(5),ARR(5,22),AFL(5,22),ASFL(5,6,22),SN(5,6,22),      TLP00183
     3DIA(22),STN(22),STRNT(22),C1(22),                                 TLP00184
     4EM(5,22),EPSM(5,22),SIGMM(5,22),SIGMO(22),TEMP(22)                TLP00185
      SUM=0.                                                            TLP00186
      DO 1 I=2,N1                                                       TLP00187
      SUM=SUM+DELTS(I)                                                  TLP00188
    1 CONTINUE                                                          TLP00189
      DO 100 I=2,N1                                                     TLP00190
      SNDS=C1(I)*DDS(I)                                                 TLP00191
      BIGN(I)=0.                                                        TLP00192
      DO 90 K=1,NFL                                                     TLP00193
      FN=0.                                                             TLP00194
      DO 80 L=1,NSFL                                                    TLP00195
      SN(L,K,I)=SN(L,K,I)+SNDS                                          TLP00196
      IF(SN(L,K,I)-SNO(L))30,70,11                                      TLP00197
   11 SNY=SNO(L)*(1.+(C6*DABS(SNDS))**(C5)                              TLP00198
      IF(SN(L,K,I)-SNY)70,70,20                                         TLP00199
   20 SN(L,K,I)=SNY                                                     TLP00200
      GO TO 70                                                          TLP00201
   30 IF(SN(L,K,I)+SNO(L))31,70,70                                      TLP00202
```

```
 31 SNY=SNO(L)*(1.+(C6*DABS(SNDS))**C5)                                  TLP00203
    IF(SN(L,K,I)+SNY)40,70,70                                            TLP00204
 40 SN(L,K,I)=-SNY                                                       TLP00205
 70 FN=FN+SN(L,K,I)*ASFL(L,K,I)                                          TLP00206
 80 CONTINUE                                                             TLP00207
    FN=FN+3.*RHO*(DDS(I)/DELTAT)**2*(BIGR(I)**2                          TLP00208
   1-ARR(K,I)**2)/8./DELTS(I)**2/1000.0                                  TLP00209
  5 BIGN(I)=BIGN(I)+FN                                                   TLP00215
 90 CONTINUE                                                             TLP00216
100 CONTINUE                                                             TLP00217
    RETURN                                                               TLP00218
    END                                                                  TLP00219
    SUBROUTINE EQUILI                                                    TLP00220
    IMPLICIT REAL * 8 (A-H,O-Z)                                          TLP00221
    COMMON V,DV,W,DW,DELTS,DDS,DT,SINT,COST,BIGN,E,EPSIL,SIGMA,          TLP00222
   1BIGR,SNO,ARR,AFL,ASFL,SN,DIA,TIME,DELTSO,CINETO,C1,C2,C3,C4,         TLP00223
   2C5,C6,C7,T,STN,DIAO,BIGRO,PI,DELTAT,EM,EPSM,SIGMM,SIGMO,             TLP00224
   3RHO,TEMP,N,N1,N2,NFL,NSFL,J,N3                                       TLP00225
    DIMENSION V(22),DV(22),W(22),DW(22),DELTS(22),DDS(22),               TLP00226
   1DT(22),SINT(22),COST(22),BIGN(22),E(5),EPSIL(5),SIGMA(5),            TLP00227
   2BIGR(22),SNO(5),ARR(5,22),AFL(5,22),ASFL(5,6,22),SN(5,6,22),         TLP00228
   3DIA(22),STN(22),STNRT(22),C1(22),                                    TLP00229
   4EM(5,22),EPSM(5,22),SIGMM(5,22),SIGMO(22),TEMP(22)                   TLP00230
    DO 20 I=1,N                                                          TLP00231
    DV(I)=DV( )+C2*1000.0*(BIGN(I+1)*COST(I+1)-BIGN(I)*COST(I))          TLP00232
    DW(I)=DW(I)+C2*1000.0*(BIGN(I+1)*SINT(I+1)-BIGN(I)*SINT(I))          TLP00233
 20 CONTINUE                                                             TLP00234
    RETURN                                                               TLP00235
    END                                                                  TLP00236
    SUBROUTINE TEMPER                                                    TLP00237
    IMPLICIT REAL * 8 (A-H,O-Z)                                          TLP00238
    COMMON V,DV,W,DW,DELTS,DDS,DT,SINT,COST,BIGN,E,EPSIL,SIGMA,          TLP00239
   1BIGR,SNO,ARR,AFL,ASFL,SN,DIA,TIME,DELTSO,CINETO,C1,C2,C3,C4,         TLP00240
   2C5,C6,C7,T,STN,DIAO,BIGRO,PI,DELTAT,EM,EPSM,SIGMM,SIGMO,             TLP00241
   3RHO,TEMP,N,N1,N2,NFL,NSFL,J,N3                                       TLP00242
```

```
      DIMENSION V(22),DV(22),W(22),DW(22),DELTS(22),DDS(22),
     1DT(22),SINT(22),COST(22),BIGN(22),E(5),EPSIL(5),SIGMA(5),
     2BIGR(22),SNO(5),ARR(5,22),AFL(5,22),ASFL(5,6,22),
     3SN(5,6,22),DIA(22),STN(22),STNRT(22),CL(22),
     4EM(5,22),EPSM(5,22),SIGMM(5,22),SIGMO(22),TEMP(22)
      DO 10 I=1,N1
      TW=(DABS(DDS(I)*BIGN(I))/(PI*(BIGR(I)**2)*DELTS(I)))
      TEMP(I)=(TW*0.955/(RHO*875.E+3))+TEMP(I)
10    CONTINUE
      DO 40 I=1,N1
      SIGMO(I)=((0.885-(9.4E-6)*(TEMP(I)**2))*1000.0
      C7=0.222
      DO 50 L=2,NSFL
      SIGMM(L,I)=SIGMO(I)*EPSM(L,I)**C7
50    CONTINUE
40    CONTINUE
      DO 60 I=1,N1
      DO 70 L=2,NSFL
      EM(L,I)=(SIGMM(L,I)-SIGMM((L-1),I))/(EPSM(L,I)-EPSM((L-1),I))
70    CONTINUE
      EM((NSFL+1),I)=0.
60    CONTINUE
      RETURN
      END
      SUBROUTINE PRINT
      IMPLICIT REAL * 8 (A-H,O-Z)
      COMMON V,DV,W,DW,DELTS,DDS,DT,SINT,COST,BIGN,E,EPSIL,SIGMA,
     1BIGR,SNO,ARR,AFL,ASFL,SN,DIA,TIME,DELTSO,CINETO,C1,C2,C3,C4,
     2C5,C6,C7,T,STN,DIAO,BIGRO,PI,DELTAT,EM,EPSM,SIGMM,SIGMO,
     3RHO,TEMP,N,N1,N2,NFL,NSFL,J,N3
      DIMENSION V(22),DV(22),W(22),DW(22),DELTS(22),DDS(22),
     1DT(22),SINT(22),COST(22),BIGN(22),E(5),EPSIL(5),SIGMA(5),
     2BIGR(22),SNO(5),ARR(5,22),AFL(5,22),ASFL(5,6,22),SN(5,6,22),
```

```
C      THE FOLLOWING COMPUTER PROGRAM SIMULATE AND ANALYIS THE
C      DEFORMATION PROCESS OF A SMALL CIRCULAR CYLINDRICAL
C      BILLET PLACED ON A RIGID ANVIL,BY IMPINGING A TOOL
C      STEEL PROJECTILE ONTO IT.
C      EFFECTS OF TEMPERATURE RISE DURING DEFORMATION,RADIAL INERTIA,
C      STRAIN HARDENING,STRAIN RATE SENSITIVITY ARE CATERED FOR.
       IMPLICIT REAL * 8 (A-H,O-Z)                                          TPR00002
       COMMON V,DV,W,DW,DELTS,DDS,DT,SINT,COST,BIGN,E,EPSIL,SIGMA,          TPR00003
      1BIGR,SNO,ARR,AFL,ASFL,SN,DIA,TIME,DELTSO,CINETO,H,C1,C2,C3,          TPR00004
      2C4,C5,C6,C7,C8,T,STN,DIAO,BIGRO,PI,DELTAT,RADIN,FMU1,FMU2,           TPR00005
      3STNRT,EM,EPSM,SIGMM,SIGMO,RHO,TEMP,C9,N,N1,N2,NFL,NSFL,J,N3          TPR00006
       DIMENSION V(22),DV(22),W(22),DW(22),DELTS(22),DDS(22),DT(22),        TPR00007
      1SINT(22),COST(22),BIGN(22),E(5),EPSIL(5),SIGMA(5),BIGR(22),          TPR00008
      2SNO(4),ARR(5,22),AFL(5,22),ASFL(4,6,22),SN(4,6,22),DIA(22),          TPR00009
      3STN(22),STNRT(22),C1(22),EM(5,22),EPSM(5,22),                        TPR00010
      4SIGMM(5,22),SIGMO(22),TEMP(22)                                       TPR00011
       READ(1,1) N,NFL,NSFL,M,M1,M2,BIGRO,RHO,DELTAT,D,P,VOOTO,BIGL,PI,     TPR00012
      1(EPSIL(L),SIGMA(L),L=1,NSFL)                                         TPR00013
     1 FORMAT(6I5/(4D18.8))                                                 TPR00014
       N1=N+1                                                               TPR00015
       N2=N                                                                 TPR00016
       FMU1=0.00                                                            TPR00017
       FMU2=0.00                                                            TPR00018
       DELTSO=BIGL/FLOAT(N)                                                 TPR00019
       DELT=DELTSO/2.                                                       TPR00020
       DO 2 I=1,N1                                                          TPR00021
       BIGR(I)=BIGRO                                                        TPR00022
     2 CONTINUE                                                             TPR00023
       E(1)=SIGMA(1)/EPSIL(1)                                               TPR00024
       C3=E(1)/DELTSO                                                       TPR00025
       C2=DELTAT**2/RHO/BIGRO**2/PI/DELTSO                                  TPR00026
       C4=C2*2.                                                             TPR00027
       C7=(DELTAT**2)/((RHO*(BIGRO**2)*PI*DELTSO)+0.0102)                   TPR00028
       C8=C7*2.                                                             TPR00029
```

```
      IF(D)210,12,11                                                    TPR00030
   11 C5=L./F                                                           TPR00031
      C6=1./D/DELTAT/E(1)                                               TPR00032
      GO TO 13                                                          TPR00033
   12 C5=1.                                                             TPR00034
      C6=0.                                                             TPR00035
   13 IF(NSFL-1)210,16,14                                               TPR00036
   14 DO 15 L=2,NSFL                                                    TPR00037
      E(L)=(SIGMA(L)-SIGMA(L-1))/(EPSIL(L)-EPSIL(L-1))                  TPR00038
   15 CONTINUE                                                          TPR00039
   16 E(NSFL+1)=0.                                                      TPR00040
      FLONFL=NFL                                                        TPR00041
      DO 3 I=1,N1                                                       TPR00042
      T=BIGR(I)/FLONFL                                                  TPR00043
      DO 4 K=1,NFL                                                      TPR00044
      ARR(K,I)=FLOAT(K+K-1)*T/2.                                        TPR00045
      AFL(K,I)=2.*PI*ARR(K,I)*T                                         TPR00046
    4 CONTINUE                                                          TPR00047
    3 CONTINUE                                                          TPR00048
      DO 17 I=1,N1                                                      TPR00049
      DO 18 K=1,NFL                                                     TPR00050
      DO 19 L=1,NSFL                                                    TPR00051
      ASFL(L,K,I)=AFL(K,I)*(E(L)-E(L+1))/E(1)                           TPR00052
   19 CONTINUE                                                          TPR00053
   18 CONTINUE                                                          TPR00054
   17 CONTINUE                                                          TPR00055
      DO 20 L=1,NSFL                                                    TPR00056
      SNO(L)=E(1)*EPSIL(L)                                              TPR00057
   20 CONTINUE                                                          TPR00058
      DO 210 I1=1,5                                                     TPR00059
      M1=50                                                             TPR00060
      M2=1000                                                           TPR00061
      VDOTO=30000.0                                                     TPR00062
      VDOTO=VDOTO+FLOAT(I1-1)*20000.0                                   TPR00063
```

```
      WRITE(6,300) N,NFL,NSFL,M,BIGRO,RHO,DELTAT,D,P,VDOTO,BIGL,          TPR00064
     1(L,EPSIL(L),SIGMA(L),L=1,NSFL)                                      TPR00065
  300 FORMAT(5H0 N= ,I5,6H NFL= ,I5,7H NSFL= ,I5,5H  M= ,I5/9H  BIGRO= ,TPR00066
     1D18.8,7H  RHO= ,D18.8,10H  DELTAT= ,D18.8,5H  D= ,D18.8/5H  P= ,D1TPR00067
     28.8,11H    VDOTO= ,D18.8,8H  BIGL= ,D18.8/39H0     L          EPSIL TPR00068
     3              SIGMA/(I5,2D18.8))                                    TPR00069
      J=0                                                                 TPR00070
      TIME=0.                                                             TPR00071
      DO 50 I=1,N1                                                        TPR00072
      V(I)=DELT*FLOAT(I+I-1)                                              TPR00073
      DV(I)=0.                                                            TPR00074
      W(I)=0.                                                             TPR00075
      DW(I)=0.                                                            TPR00076
      TEMP(I)=20.                                                         TPR00077
      DELTS(I)=DELTSO                                                     TPR00078
      SINT(I)=0.                                                          TPR00079
      COST(I)=1.                                                          TPR00080
      BIGN(I)=0.                                                          TPR00081
      C1(I)=E(1)/DELTS(I)                                                 TPR00082
      DO 40 K=1,NFL                                                       TPR00083
      DO 39 L=1,NSFL                                                      TPR00084
      SN(L,K,I)=0.                                                        TPR00085
   39 CONTINUE                                                            TPR00086
   40 CONTINUE                                                            TPR00087
   50 CONTINUE                                                            TPR00088
      DO 55 I=1,N1                                                        TPR00089
      DO 60 L=1,NSFL                                                      TPR00090
      SIGMM(L,I)=SIGMA(L)                                                 TPR00091
      EPSM(L,I)=EPSIL(L)                                                  TPR00092
   60 CONTINUE                                                            TPR00093
   55 CONTINUE                                                            TPR00094
      DO 62 I=1,N1                                                        TPR00095
      DO 63 L=1,NSFL                                                      TPR00096
      EM(1,L)=E(1)                                                        TPR00097
   63 CONTINUE                                                            TPR00098
```

```
 62 CONTINUE                                                                TPR00099
    DO 65 I=1,N1                                                            TPR00100
    DO 70 L=1,NSFL                                                          TPR00101
    EM(L,I)=(SIGMM(L,I)-SIGMM((L-1),I))/(EPSM(L,I)-EPSM((L-1),I))           TPR00102
 70 CONTINUE                                                                TPR00103
    EM((NSFL+1),I)=0.                                                       TPR00104
 65 CONTINUE                                                                TPR00105
    DO 80 I=1,1                                                             TPR00106
    DV(I)=DELTAT*VDOTO                                                      TPR00107
 80 CONTINUE                                                                TPR00108
    CALL PRINT                                                              TPR00109
    BIGN(1)=0.                                                              TPR00110
120 J=J+1                                                                   TPR00111
    DO 90 I=1,N1                                                            TPR00112
    C1(I)=E(1)/DELTS(I)                                                     TPR00113
 90 CONTINUE                                                                TPR00114
    IF(BIGN(2)-1.)129,129,150                                               TPR00115
129 IF((V(10)-V(1))-0.40)150,150,130                                        TPR00116
150 TIME=DELTAT*FLOAT(J)                                                    TPR00117
    CALL PRINT                                                              TPR00118
    GO TO 210                                                               TPR00119
130 DDS(N+1)=-2.*DV(N)                                                      TPR00120
    V(N+1)=V(N+1)-DV(N)                                                     TPR00121
    DDS(1)=0.                                                               TPR00122
    CALL STRAIN                                                             TPR00128
    CALL TEMPER                                                             TPR00129
    CALL STRESS                                                             TPR00130
    CALL EQUILI                                                             TPR00131
    IF(J-M1) 20,140,210                                                     TPR00136
140 M1=M1+M2                                                                TPR00137
    TIME=DELTAT*FLOAT(J)                                                    TPR00138
    CALL PRINT                                                              TPR00139
    IF(J-M)120,210,210                                                      TPR00140
210 CONTINUE                                                                TPR00141
    CALL EXIT                                                               TPR00142
```

```
      STOP                                                              TPR00143
      END                                                               TPR00144
      SUBROUTINE STRAIN                                                 TPR00145
      IMPLICIT REAL * 8 (A-H,O-Z)                                       TPR00146
      COMMON V,DV,W,DW,DELTS,DDS,DT,SINT,COST,BIGN,E,EPSIL,SIGMA,       TPR00147
     1BIGR,SNO,ARR,AFL,ASFL,SN,DIA,TIME,DELTSO,CINETO,H,C1,C2,C3,       TPR00148
     2C4,C5,C6,C7,C8,T,STN,DIAO,BIGRO,PI,DELTAT,RADIN,FMU1,FMU2,        TPR00149
     3STNRT,EM,EPSM,SIGMN,SIGMO,RHO,TEMP,C9,N,N1,N2,NFL,NSFL,J,N3       TPR00150
      DIMENSION V(22),DV(22),W(22),DW(22),DELTS(22),DDS(22),DT(22),     TPR00151
     1SINT(22),COST(22),BIGN(22),E(5),EPSIL(5),SIGMA(5),BIGR(22),       TPR00152
     2SNO(4),ARR(5,22),AFL(5,22),ASFL(4,6,22),SN(4,6,22),DIA(22),       TPR00153
     3STN(22),STNRT(22),C1(22),EM(5,22),EPSM(5,22),                     TPR00154
     4SIGMM(5,22),SIGMO(22),TEMP(22)                                    TPR00155
      DO 10 I=2,N                                                       TPR00156
      DELDV=DV(I)-DV(I-1)                                               TPR00157
      DELDW=DW(I)-DW(I-1)                                               TPR00158
      DDS(I)=DELDV*COST(I)+DELDW*SINT(I)                                TPR00159
      DT(I)=(DELDW*COST(I)-DELDV*SINT(I))/DELTS(I)                      TPR00160
      SINTI=SINT(I)                                                     TPR00161
      SINT(I)=SINTI+COST(I)*DT(I)                                       TPR00162
      COST(I)=COST(I)-SINTI*DT(I)                                       TPR00163
   10 CONTINUE                                                          TPR00164
      DO 30 I=1,N                                                       TPR00165
      V(I)=V(I)+DV(I)                                                   TPR00166
      W(I)=W(I)+DW(I)                                                   TPR00167
   30 CONTINUE                                                          TPR00168
      DO 40 I=1,N1                                                      TPR00169
      DELTS(I)=DELTS(I)+DDS(I)                                          TPR00170
      IF(DELTS(I)-0.01*DELTSO)31,32,32                                  TPR00171
   31 DELTS(I)=0.01*DELTSO                                              TPR00172
   32 BIGR(I)=(DABS(DELTSO*BIGRO**2/DELTS(I)))**0.5                     TPR00173
      FLONFL=NFL                                                        TPR00174
      T=BIGR(I)/FLONFL                                                  TPR00175
      DO 50 K=1,NFL                                                     TPR00176
      ARR(K,I)=FLOAT(K+K-1)*T/2.                                        TPR00177
```

```
      AFL(K,I)=2.*PI*ARR(K,I)*T                                          TPR00178
      DO 60 L=1,NSFL                                                     TPR00179
      ASFL(L,K,I)=AFL(K,I)*(EM(L,I)-EM((L+1),I))/E(1)                    TPR00180
   60 CONTINUE                                                           TPR00181
   50 CONTINUE                                                           TPR00182
   40 CONTINUE                                                           TPR00183
      RETURN                                                             TPR00184
      END                                                                TPR00185
      SUBROUTINE STRESS                                                  TPR00186
      IMPLICIT REAL * 8 (A-H,O-Z)                                        TPR00187
      COMMON V,DV,W,DW,DELTS,DDS,DT,SINT,COST,BIGN,F,EPSIL,SIGMA,        TPR00188
     1BIGR,SNO,ARR,AFL,ASFL,SN,DIA,TIME,DELTSO,CINETO,H,C1,C2,C3,        TPR00189
     2C4,C5,C6,C7,C8,T,STN,DIAO,BIGRO,PI,DELTAT,RADIN,FMU1,FMU2,         TPR00190
     3STNRT,EM,EPSM,SIGMM,SIGMO,RHO,TEMP,C9,N,N1,N2,NFL,NSFL,J,N3       TPR00191
      DIMENSION V(22),DV(22),W(22),DW(22),DELTS(22),DDS(22),DT(22),      TPR00192
     1SINT(22),COST(22),BIGN(22),E(5),EPSIL(5),SIGMA(5),BIGR(22),        TPR00193
     2SNO(4),ARR(5,22),AFL(5,22),ASFL(4,6,22),SN(4,6,22),DIA(22),        TPR00194
     3STN(22),STNRT(22),C1(22),EM(5,22),EPSM(5,22),                      TPR00195
     4SIGMM(5,22),SIGMO(22),TEMP(22)                                     TPR00196
      SUM=0.                                                             TPR00197
      DO 1 I=2,N1                                                        TPR00198
      SUM=SUM+DELTS(I)                                                   TPR00199
    1 CONTINUE                                                           TPR00200
      DO 100 I=2,N1                                                      TPR00201
      SNDS=C1(I)*DDS(I)                                                  TPR00202
      BIGN(I)=0.                                                         TPR00203
      DO 90 K=1,NFL                                                      TPR00204
      FN=0.                                                              TPR00205
      DO 80 L=1,NSFL                                                     TPR00206
      SN(L,K,I)=SN(L,K,I)+SNDS                                           TPR00207
      IF(SN(L,K,I)-SNO(L))30,70,11                                       TPR00208
   11 SNY=SNO(L)*(1.+(C6*DABS(SNDS))**C5)                                TPR00209
      IF(SN(L,K,I)-SNY)70,70,20                                          TPR00210
   20 SN(L,K,I)=SNY                                                      TPR00211
      GO TO 70                                                           TPR00212
```

```
 30 IF(SN(L,K,I)+SNO(L))31,70,70                                    TPR00213
 31 SNY=SNO(L)*(1.+(C6*DABS(SNDS))**C5)                             TPR00214
    IF(SN(L,K,I)+SNY)40,70,70                                       TPR00215
 40 SN(L,K,I)=-SNY                                                  TPR00216
 70 RADIN=SN(L,K,I)                                                 TPR00217
    RADIN=RADIN-3.*RHO*(DDS(I)/DELTAT)**2*(BIGR(I)**2
   1-ARR(K,I)**2)/8./DELTS(I)**2/1000.0
    IF(I-2)2,3,2                                                    TPR00218
  2 IF(I-11)5,4,5                                                   TPR00219
  3 RADIN=RADIN*(1.+2.*FMU1*(BIGR(I)-ARR(K,I))/SUM)                 TPR00220
    GO TO 5                                                         TPR00221
  4 RADIN=RADIN*(1.+2.*FMU2*(BIGR(I)-ARR(K,I))/SUM)                 TPR00222
  5 FN=FN+RADIN*ASFL(L,K,I)                                         TPR00223
 80 CONTINUE                                                        TPR00224
    BIGN(I)=BIGN(I)+FN                                              TPR00225
 90 CONTINUE                                                        TPR00226
100 CONTINUE                                                        TPR00227
    BIGN(1)=0.                                                      TPR00228
    RETURN                                                          TPR00229
    END                                                             TPR00230
    SUBROUTINE EQUILI                                               TPR00231
    IMPLICIT REAL * 8 (A-H,O-Z)                                     TPR00232
    COMMON V,DV,W,DW,DELTS,DDS,DT,SINT,COST,BIGN,E,EPSIL,SIGMA,     TPR00233
   1BIGR,SNO,ARR,AFL,ASFL,SN,DIA,TIME,DELTSO,CINETO,H,C1,C2,C3,     TPR00234
   2C4,C5,C6,C7,C8,T,STN,DIAO,BIGRO,PI,DELTAT,RADIN,FMU1,FMU2,      TPR00235
   3STNRT,EM,EPSM,SIGMM,SIGMO,RHO,TEMP,C9,N,N1,N2,NFL,NSFL,J,N3     TPR00236
    DIMENSION V(22),DV(22),W(22),DW(22),DELTS(22),DDS(22),DT(22),   TPR00237
   1SINT(22),COST(22),BIGN(22),E(5),EPSIL(5),SIGMA(5),BIGR(22),     TPR00238
   2SNO(4),ARR(5,22),AFL(5,22),ASFL(4,6,22),SN(4,6,22),DIA(22),     TPR00239
   3STN(22),STNRT(22),C1(22),EM(5,22),EPSM(5,22),                   TPR00240
   4SIGMM(5,22),SIGMO(22),TEMP(22)                                  TPR00241
    DO 20 I=1,N                                                     TPR00242
    IF(I-1)17,15,17                                                 TPR00243
 15 DV(I)=DV(I)+C7*(BIGN(I+1)*COST(I+1)-BIGN(I)*COST(I))*1000.0     TPR00244
    DW(I)=DW(I)+C7*(BIGN(I+1)*SINT(I+1)-BIGN(J)*SINT(I))*1000.0     TPR00245
```

```
      GO TO 20                                                          TPR00246
   17 DV(I)=DV(I)+C2*(BIGN(I+1)*COST(I+1)-BIGN(I)*COST(I))*1000.0       TPR00247
      DW(I)=DW(I)+C2*(BIGN(I+1)*SINT(I+1)-BIGN(I)*SINT(I))*1000.0       TPR00248
   20 CONTINUE                                                          TPR00249
      CINET=0.                                                          TPR00250
      DO 30 I=2,N                                                       TPR00251
      CINET=CINET+DV(I)**2+DW(I)**2                                     TPR00252
   30 CONTINUE                                                          TPR00253
      CINET=CINET/C4+(DV(1)**2+DW(1)**2)/C8                             TPR00254
      RETURN                                                            TPR00255
      END                                                               TPR00256
      SUBROUTINE TEMPER                                                 TPR00257
      IMPLICIT REAL * 8 (A-H,O-Z)                                       TPR00258
      COMMON V,DV,W,DW,DELTS,DDS,DT,SINT,COST,BIGN,E,EPSIL,SIGMA,       TPR00259
     1BIGR,SNO,ARR,AFL,ASFL,SN,DIA,TIME,DELTSO,CINETO,H,C1,C2,C3,       TPR00260
     2C4,C5,C6,C7,C8,T,STN,DIAO,BIGRO,PI,DELTAT,RADIN,FMU1,FMU2,        TPR00261
     3STNRT,EM,EPSM,SIGMM,SIGMO,RHO,TEMP,C9,N,N1,N2,NFL,NSFL,J,N3       TPR00262
      DIMENSION V(22),DV(22),W(22),DW(22),DELTS(22),DDS(22),DT(22),     TPR00263
     1SINT(22),COST(22),BIGN(22),E(5),EPSIL(5),SIGMA(5),BIGR(22),       TPR00264
     2SNO(4),ARR(5,22),AFL(5,22),ASFL(4,6,22),SN(4,6,22),DIA(22),       TPR00265
     3STN(22),STNRT(22),C1(22),EM(5,22),EPSM(5,22),                     TPR00266
     4SIGMM(5,22),SIGMO(22),TEMP(22)                                    TPR00267
      DO 10 I=1,N1                                                      TPR00268
      TW=(DABS(DDS(I)*BIGN(I))/(PI*(BIGR(I)**2)*DELTS(I)))              TPR00269
      TEMP(I)=(TW*0.955/(RHO*875.E+3))+TEMP(I)                          TPR00270
   10 CONTINUE                                                          TPR00271
      DO 40 I=1,N1                                                      TPR00272
      SIGMO(I)=1300.0
      C9=0.2
      DO 50 L=2,NSFL                                                    TPR00275
      SIGMM(L,I)=SIGMO(I)*EPSM(L,I)**C9                                 TPR00276
   50 CONTINUE                                                          TPR00277
```

```
40 CONTINUE                                                              TPR00278
   DO 60 I=1,N1                                                          TPR00279
   DO 70 L=2,NSFL                                                        TPR00280
   EM(L,I)=(SIGMM(L,I)-SIGMM((L-1),I))/(EPSM(L,I)-EPSM((L-1),I))         TPR00281
70 CONTINUE                                                              TPR00282
   EM((NSFL+1),I)=0.                                                     TPR00283
60 CONTINUE                                                              TPR00284
   RETURN                                                                TPR00285
   END                                                                   TPR00286
   SUBROUTINE PRINT                                                      TPR00287
   IMPLICIT REAL * 8 (A-H,O-Z)                                           TPR00288
   COMMON V,DV,W,DW,DELTS,DDS,DT,SINT,COST,BIGN,E,EPSIL,SIGMA,           TPR00289
  1BIGR,SNO,ARR,AFL,ASFL,SN,DIA,TIME,DELTSO,CINETO,H,C1,C2,C3,           TPR00290
  2C4,C5,C6,C7,C8,T,STN,DIAO,BIGRO,PI,DELTAT,RADIN,FMU1,FMU2,            TPR00291
  3STNRT,EM,EPSM,SIGMM,SIGMO,RHO,TEMP,C9,N,N1,N2,NFL,NSFL,J,N3           TPR00292
   DIMENSION V(22),DV(22),W(22),DW(22),DELTS(22),DDS(22),DT(22),         TPR00293
  1SINT(22),COST(22),BIGN(22),E(5),EPSIL(5),SIGMA(5),BIGR(22),           TPR00294
  2SNO(4),ARR(5,22),AFL(5,22),ASFL(4,6,22),SN(4,6,22),DIA(22),           TPR00295
  3STN(22),STNRT(22),C1(22),EM(5,22),EPSM(5,22),                         TPR00296
  4SIGMM(5,22),SIGMO(22),TEMP(22)                                        TPR00297
   CINET=0.                                                              TPR00298
   DO 10 I=2,N                                                           TPR00299
   CINET=CINET+DV(I)**2+DW(I)**2                                         TPR00300
10 CONTINUE                                                              TPR00301
   CINET=CINET/C4                                                        TPR00302
   CINET=CINET+(DV(1)**2+DW(1)**2)/C8                                    TPR00303
   FLAST=0.                                                              TPR00304
   IF(J)30,20,30                                                         TPR00305
20 PLAST=0.                                                              TPR00306
   CINETO=CINET                                                          TPR00307
   GO TO 70                                                              TPR00308
30 DO 60 L=1,NSFL                                                        TPR00309
   SUM=0.                                                                TPR00310
   DO 50 I=1,N                                                           TPR00311
   DO 40 K=1,NFL                                                         TPR00312
```

```
      SUM=SUM+(SN(L,K,I)**2)*ASFL(L,K,I)                                TPR00313
   40 CONTINUE                                                          TPR00314
   50 CONTINUE                                                          TPR00315
      ELAST=ELAST+SUM                                                   TPR00316
   60 CONTINUE                                                          TPR00317
      ELAST=ELAST/C3/2.                                                 TPR00318
      PLAST=CINET0-CINET-ELAST                                          TPR00319
   70 DO 80 I=1,N1                                                      TPR00320
      STN(I)=DLOG(DELTS(I)/DELTS0)                                      TPR00321
      STNRT(I)=DDS(I)/DELTS0/DELTAT                                     TPR00322
   80 CONTINUE                                                          TPR00323
      WRITE(6,90) J,TIME,CINET,ELAST,PLAST,                             TPR00324
     1(I,V(I),TEMP(I),BIGN(I),STN(I),BIGR(I),STNRT(I),I=1,N1)           TPR00325
   90 FORMAT(9H0      J= ,I5,8H  TIME= ,D12.5,11H  KINETIC= ,D12.5,11H  DTPR00326
     1LASTIC= ,D12.5,11H  PLASTIC= ,D12.5/80H0    I        V              TEMPTPR00327
     2          N             STRAIN         RADIUS       STNRT/(I6,6D14.5))TPR00328
      RETURN                                                            TPR00329
      END                                                               TPR00330
```

APPENDIX III

PHASE ONE : (Aluminium Alloy Projectile Impacting against a Rigid Anvil)

Material: HE15
Specific Heat S = 875J/Kg°C
Density ρ = 2806 Kg/m³

From theoretical results P = 35 and D = 100
At Impact Velocity of 250 m/s : From theoretical results at element number 10 as shown in Figure AIII.1,
the mean strain rate

$$\dot{\varepsilon}_{mean} = \frac{0.8017 \times 10^4 + 0.00}{2} = 0.4 \times 10^4 \text{ per second}$$

corresponding to strain $\varepsilon = 0.2416$

$$\Delta T = \frac{0.955}{S}.A, \text{ where } A = \int_0^{\varepsilon_f} \sigma d\varepsilon$$

Total area under the true stress-natural strain curve at a strain rate of 0.4×10^4 per second and strain of 0.2416 = 645m²

Now 100 MN/m² x 0.2416 = 24.16 MN/m²
For 100 MN/m² Area = 5 x 12 = 60 mm²
Since 60 mm² represents 24.16 MN/m²
1 mm² represents $\frac{24.16}{60}$ MN/m²

$\therefore$ 645 represents $\frac{24.16}{60} \times 645 = 259.72$ MN/m²

$\therefore$ A = 259.72 MN/m² = 259.72×10^6 N/m²

Maximum temperature rise $T = \frac{0.955 \times 259.72 \times 10^6}{2806 \times 875} = 101°C$

at mean strain rate of 0.4×10^4 per second.

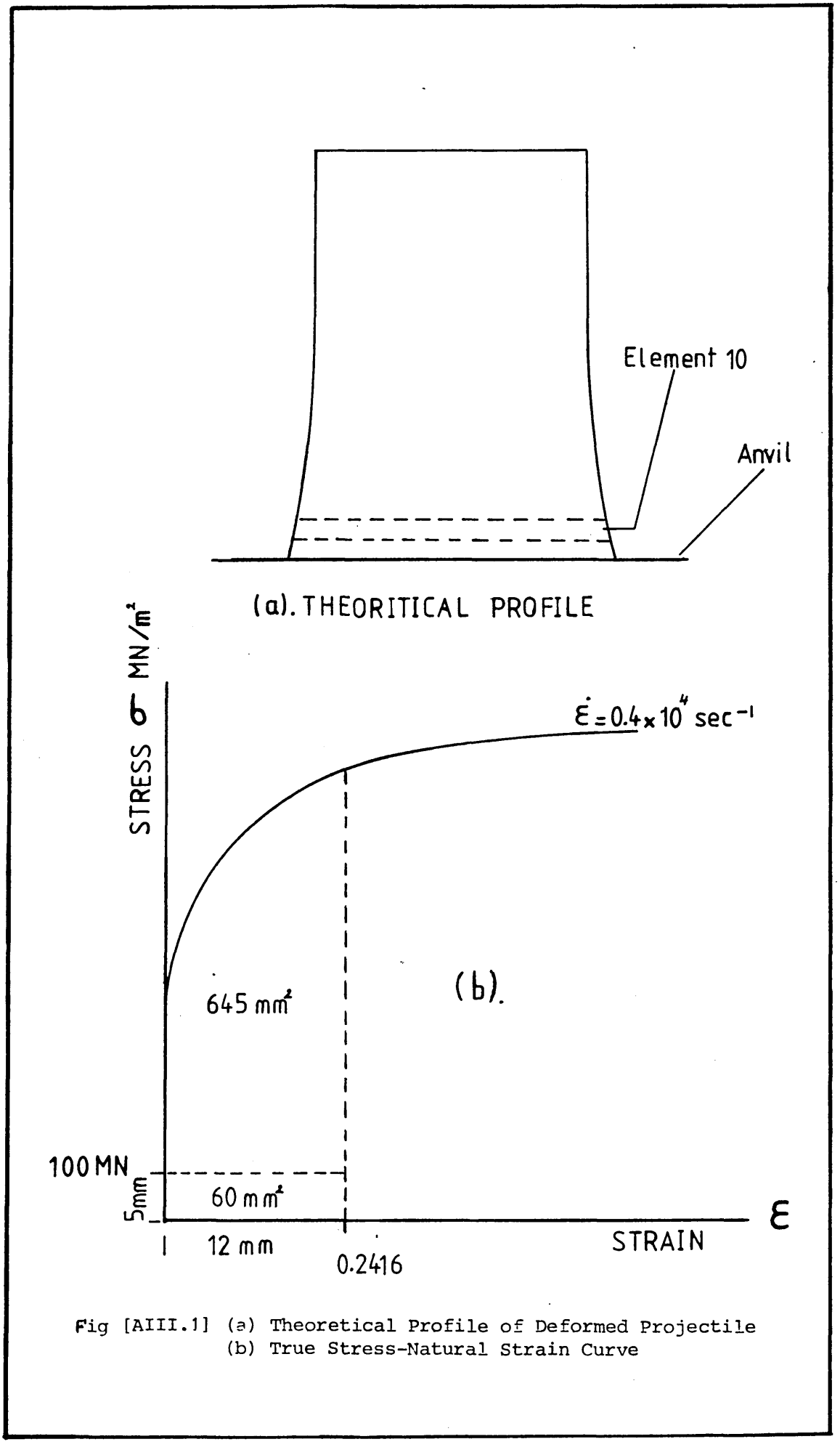

Fig [AIII.1] (a) Theoretical Profile of Deformed Projectile
(b) True Stress-Natural Strain Curve

APPENDIX IV

PHASE ONE : (Aluminium Alloy Projectile Impacting against a Rigid Anvil)

Material : HE15

Total Force, $F = \Pi r^2 Y + \Pi r^2 Y I$

$$I = \frac{3}{16} \rho \frac{V^2}{Y} \left(\frac{r}{h}\right)^2$$

$$\therefore \text{ Inertia effect} = \frac{\Pi r^2 Y I}{\Pi r^2 Y (1 + I)} = \frac{I}{1 + I}$$

P = 35 and D = 100

From theoretical results at element number 10 at impact velocity of 50 m/s

$\varepsilon = 0.011$ and $\dot{\varepsilon}_{mean} = 0.93 \times 10^3$ per second

Y = yield stress = 900 N/m^2 at 0.2% strain

$\rho = 2806$ Kg/m^3

$Y = 9 \times 10^8$ Kg/s^2m

r_o = initial radius = 4.76 mm

ho = initial height = 20 mm

$$\varepsilon = \text{Ln} \frac{ho}{h} \text{ where h = current height}$$

$$\frac{ho}{h} = e^{0.011}$$

$$\therefore h = 20 \times e^{-0.011} = 19.78 \text{ mm}$$

From constant volume $\Pi r_o^2 ho = \Pi r^2 h$

$$\therefore r = \sqrt{\frac{r_o^2 \times ho}{h}} = \sqrt{\frac{(4.76)^2 \times 20}{19.78}}$$

$$r = 4.786 \text{ mm}$$

$$\left(\frac{r}{h}\right)^2 = \left(\frac{4.786}{19.78}\right)^2 = 0.0586$$

$$I = \frac{3}{16} \times 2806 \times \frac{(50)^2}{9 \times 10^8} \times 0.0586 = 0.0086 \times 10^{-2}$$

The inertia effect $\frac{I}{I + 1} = \frac{0.008 \times 10^{-2}}{1 + 0.008 \times 10^{-2}} \times 100 = 0.079\%$

at an impact velocity of 50 m/s

At impact velocity of 250 m/s, $\dot{\varepsilon}_{mean} = 0.4 \times 10^4$ and $\varepsilon = 0.2416$

$Y = 1.16 \times 10^9$ N/m^2

$Y = 1.16 \times 10^9$ Kg/s^2m

$$h = 20e^{-0.2416} = 16.0707 \text{ mm}$$

$$r = \sqrt{\frac{(4.76)^2 \times 20}{15.0707}} = 5.37 \text{ mm}$$

$$\left(\frac{r}{h}\right)^2 = \left(\frac{5.37}{15.0707}\right)^2 = 0.117$$

$$I = \frac{3}{16} \times (250)^2 \times \frac{1}{1.16 \times 10^9} \times 0.117 \times 2806 = 0.0033$$

The inertia effect $\frac{I}{1 + I} = \frac{0.0033}{1 + 0.0033} \times 100 = 0.329\%$

at an impact velocity of 250 m/s

APPENDIX V

PHASE TWO : (Tool Steel Projectile Impinging onto a Small Cylindrical Billet)

Material : HE15
Specific Heat S = 875J/Kg°C
Density ρ = 2806 Kg/m^3

From theoretical results P = 35 and D = 75000
At impact velocity of 80 m/s:
From theoretical results, the maximum strain rate $\dot{\varepsilon}_{max} = 0.7146 \times 10^4$ per second corresponding to strain $\varepsilon = 0.3535$

$$\Delta T = \frac{0.955.A}{\rho S}, \text{ where } A = \int_0^{\varepsilon_f} \sigma d\varepsilon$$

Total area under the true stress-natural strain curve at a strain rate of 0.7146×10^4 per second and strain of 0.3535 = 921.6 mm^2

Now 100 MN/m^2 x 0.3535 = 35.35 MN/m^2
For 100 MN/m^2 Area = 5 x 18 = 90 mm^2

Since 90 mm^2 represents 35.35 MN/m^2

921.6 mm^2 represents $\frac{35.35 \times 921.6}{90}$ = 362.0 MN/m^2

$\therefore$ A = 362.0 MN/m^2 = 362.0×10^6 N/m^2

Maximum temperature rise $\Delta T = \frac{0.955 \times 362.0 \times 10^6}{2806 \times 875} = 140.8°C$

at maximum strain rate of 0.7146×10^4

APPENDIX VI

PHASE TWO : (Tool Steel Projectile Impinging onto a Small Cylindrical Billet)

Material : HE15

Total Force, $F = \Pi r^2 Y + \Pi r^2 Y I$

$$I = \frac{3}{16} \frac{V^2}{Y} \left(\frac{r}{h}\right)^2$$

.. Inertia effect $= \dfrac{\Pi r^2 Y I}{\Pi r^2 Y (1 + I)} = \dfrac{I}{1 + I}$

P = 35, D = 75000

From theoretical results at impact velocity 20 m/s

$\dot{\varepsilon}_{max} = 0.229 \times 10^4$ per second and $\varepsilon = 0.03283$

Y = 745 MN/m² at 0.2% strain

$\rho = 2806$ Kg/m³

$Y = 7.45 \times 10^8$ Kg/s²m

r_o initial radius = 2.6 mm

ho initial height = 5.0 mm

$\varepsilon = \text{Ln} \dfrac{ho}{h}$ where h = current height

$$\frac{ho}{h} = e^{0.03282}$$

.. $h = 5 \times e^{-0.03283} = 4.8385$ mm

From constant volume $\Pi r_o^2 ho = \Pi r^2 h$

.. $r = \sqrt{\dfrac{r_o^2 \times ho}{h}} = \sqrt{\dfrac{(2.6)^2 \times 5.0}{4.8385}} = 2.643$ mm

$$\left(\frac{r}{h}\right)^2 = \left(\frac{2.643}{4.8385}\right)^2 = 0.2984$$

$$I = \frac{3}{16} \times 2806 \times (20)^2 \times \frac{0.2984}{7.45 \times 10} = 0.00008$$

The inertia effect $\dfrac{I}{1 + I} = \dfrac{0.008 \times 10^{-2}}{1 + 0.008 \times 10^{-2}} \times 100 = 0.0079\%$ at

impact velocity of 20 m/s

At impact velocity of 80 m/s., $\dot{\varepsilon}_{max} = 0.7146 \times 10^4$ per second and $\varepsilon = 0.3535$

Y = 820 MN/m²

$Y = 8.2 \times 10^8$ Kg/s²m

$h = 5.0\ e^{-0.3535} = 3.511$ mm

$$r = \sqrt{\frac{(2.6)^2 \times 5.0}{3.511}} = 3.103 \text{ mm}$$

$$\left(\frac{r}{h}\right)^2 = \left(\frac{3.103}{3.511}\right)^2 = 0.7811$$

$$I = \frac{3}{16} \times (80)^2 \times 2806 \times \frac{0.7811}{8.2 \times 10^8} = 0.00321$$

The inertia effect $\frac{I}{1 + I} = \frac{0.00321}{1 + 0.00321} \times 100 = 0.319\%$ at

an impact velocity of 80 m/s

APPENDIX VII

PHASE ONE and TWO

Material : HE15

The coefficient of friction μ_D during dry quasi-static compression test found by

$$\mu_D = [\sigma sD - 1]/\frac{2}{3}\frac{r}{h}$$

where $Y = \sigma s/[1 + \frac{2}{3}\mu\frac{r}{h}]$

Now, from quasi-static test
Initial radius of specimen = 2.6 mm
Initial height of specimen = 5 mm

From dry test the current height and radius at strain 0.511 were found to be 1.83 mm and 3.97 mm respectively

Frictionless flow stress = 727 MN/m²

$\mu = 0.01$

$\frac{r}{h} = \frac{3.97}{1.83} = 2.168$

$Y = 727/1 + \frac{2}{3} \times 2.168 \times 0.01 = 716.8$ MN/m²

$\sigma s_D = 781$ MN/m² at dry condition

$\therefore \mu_D = [\frac{781}{716.8} - 1]/\frac{2}{3} \times 2.168 = 0.0622$ at room temperature

HIGH STRAIN RATE PROPERTIES OF ALUMINIUM ALLOYS AT ROOM TEMPERATURE

M S J Hashmi* T N M Al-Haddid+ and T D Campbell+

SUMMARY

High strain rate compression tests were carried out on three aluminium alloys, HE30TF, HE15 and DTD5044 by impacting tool steel projectiles onto small billets of cylindrical shape and aspect ratio of about 1.0.

Dynamic stress-strain properties of these alloys at room temperature and strain rates of up to 1.6×10^4 per second over a strain of about 50 per cent were determined by a new technique.

This technique takes into account the effects of radial inertia and temperature rise during deformation. Tallow in graphite was used as a lubricant to minimise the frictional effects. The technique is suggested to be relatively inexpensive and simple but efficient for determining high strain rate properties of materials.

- - - - - - - - -

* School of Mechanical Engineering NIHE Dublin, Ireland.

+ Department of Mechanical and Production Engineering, Sheffield City Polytechnic, Sheffield, England.

INTRODUCTION

With the advent of computer aided design and analysis of engineering components, the need for accurate data on material properties has increased significantly in the recent years. High strain rate behaviour of materials is important in process design where high rates of strain are experienced such as machining and high energy rate forming. High strain rate influences the strength and flow property of the material and hence affects the cutting and forming forces involved (1-5).

Many researchers have investigated high strain rate, the behaviour and properties of metals and alloys undergoing deformation and suggested that strain rate has significant effect on material strength and hence on the load required to cause deformation.

Haque (6), while determining high strain rate properties of a number of metals, kept the aspect ratio of the specimen less than one to avoid buckling and barrelling.

Radial and lateral inertia forces were investigated by Holzer and Brown (7), who indicated that radial forces influence the mechanical behaviour at high strain rates. They also looked into the effect of temperature rise during deformation and reported that in general an increase in flow stress with the strain rate takes place despite the increase in temperature of the specimen during testing.

The effects of friction and lubricants have been investigated in reference (8), where it has been suggested that friction may cause errors in static and dynamic compression and that the use of wrong lubricant would cause high friction leading to barrelling and inaccurate results.

A number of techniques have been developed such as ballistic compression tests and Hopkinson's pressure bar for determining stress-strain relationship at high strain rates and experiments have been carried out on different materials (9, 10).

Hashmi (9) used a finite-difference numerical technique in conjunction with experimental results to determine the high strain rate properties of a number of metals. In his investigation he used an air gun to propel projectiles which impacted against a rigid anvil and established the dynamic stress-strain characteristics of mild steel for strain rates of up to 10^5 sec^{-1}.

A number of other investigators used free flight impact devices (11-15), and others used the Split Hopkins pressure bar and its modified versions for high strain rate tests. Yoshida and Nagata (16) reported that for aluminium the dynamic flow stress is always higher than the static one thus showing rate dependence.

In the present study high speed compression of small cylindrical billets was achieved by means of a tool steel projectile in the same manner as has been used in reference (6). However, instead of using the deformation history recorded by means of an expensive IMACON camera, only the final dimensions of the specimen were used. A finite different numerical approach was then employed to predict these parameters for a range of impact speeds and for assumed values of the constants of a constitutive equation.

EXPERIMENTAL DETAILS

(a) Preparation of projectiles, anvil and test specimens:-

The projectiles and the anvil were machined from tool steel type FMP338 and heat treated to increase the hardness. Tables 1 and 2 show the chemical composition and hardness numbers respectively of the steel projectiles and the three aluminium alloys.

TABLE 1

Material Chemical Composition (WT %)			
Tool Steel FMP338	HE15 (2014TF)	BS1474 (HE30TF)	DTD5044
C-2.05	Si-0.794	Si-1.4	Zn-5.4
Mn-0.40	Fe-0.271	Fe-0.18	Si-0.4
Si-0.30	Mn-0.36	Mn-0.2	Fe-0.15
Cr-13.00	Zn-0.06	Zn-0.07	Mn-0.31
Fe-Rem	Cu-3.87	Cu-0.07	Cu-0.45
	Mg-0.05	Mg-0.56	Mg-2.22
	Ni-0.02	Ni-0.01	Ni-0.02
	Ti<0.2	Ti<0.2	Ti<0.2
	Li<0.002	Li<0.002	Li<0.002

TABLE 2

Material	HV	Hardness No
HE15	20	137.7
HE30TF	20	109
DTD5044	20	179.1
FMP338	30	800

The ballistic projectile was machined to size of 19 mm in height and 9.52 mm in diameter and the compression specimens were machined to size from as received aluminium alloys. The dimensions of the specimens were kept to 5 mm in height and 5.2 mm in diameter keeping the aspect ratio less than one to avoid buckling and barrelling during deformation.

All the specimens, ballistic projectiles and the anvil were finely ground and polished resulting in mirror finish.

Experimental Procedure and Processing of Results

Before carrying out each test the specimen was lubricated on both flat faces with Tallow-Graphite (8/1 weight) and placed on the anvil which was also lubricated with the same lubricant. The projectile was then propelled by air pressure through a barrel onto the specimen. Just before impact the projectile cuts a laser beam and the time interval during which the laser beam was interrupted was recorded using a CRO. Knowing the length of the projectile and the time it took to clear the path as shown in Fig 1 the impact speed was determined.

The deformed specimen was removed and its final height and diameter were recorded. In excess of 300 specimens were used for each alloy to construct graphs of final height and diameter versus impact velocity. A finite-difference numerical technique was then applied to theoretically predict the final height and diameter of the specimen at different velocities using only the quasi-static stress strain properties and assumed values of the constants of a constitutive equation of the form $\sigma_d = \sigma_s \left[1 + \left(\frac{|\dot{\varepsilon}|}{D}\right)^{1/P}\right]$ where P and D are

constants. These constants were changed in a systematic manner until the closest fit is obtained between the theoretically predicted and experimentally obtained curves.

Temperature Rise during Deformation

In the present study, the temperature rise, ΔT, during deformation was estimated by considering the plastic work done according to Bishop (17) and Holzer and Brown (7) as

$$\Delta T = \frac{0.955}{\rho s} \int_{0}^{\varepsilon f} \sigma f d\varepsilon$$

where ρ is the density in Kg/M^3, εf is the final strain, σ is the true stress, s is the mean specific heat, and ε is the true strain. The factor 0.955 suggested by Bishop (17) is the portion of deformation work converted to heat energy and S is the specific heat. Using the above equation the maximum temperature rise of about 160°C was suggested when a DTD5044 specimen was deformed with a projectile impacting at 80 m/s giving rise to maximum initial strain rate of 1.6 x 10^4 sec^{-1}. HE15 and HE30TF specimens tested under similar conditions temperature rises of about 140°C and 137°C were suggested. In view of these estimated rises it was considered important to include the temperature effect in this study. Quasi-static compression tests were carried out at temperatures ranging from room 20°C to 250°C for all three alloys.

The following constitutive equation for all three alloys was then suggested relating stress strain, work hardening index, Youngs Modulus and temperature for 20°C-250°C range of temperatures using the equation originally stated in reference (29).

$$\varepsilon = \frac{\sigma o}{Eo} + \left(\frac{\sigma}{\sigma o}\right)^n$$

where σo and Eo and n are temperature dependent constants. The following equations were constructed relating these constants with temperature T°C:-

where $\sigma o = 10^3 MN/m^2$

$Eo = GN/m^2$

(i) DTD5044 $\sigma o = 0.97 - 1.123 \times 10^{-5} T^2$

$Eo = 33.26\ e^{-7.12\ T/10^3}$

$n = 7.293T^{5.01/10^2}$

(ii) HE15 $\sigma o = 0.885 - 9.4 \times 10^{-6} T^2$

$Eo = 10.22 - 0.111T$

$n = 4.5$ if Temperature $\leqslant$ 140°C

and $n = \frac{8.64T^2}{10^4} - 0.268T + 25.18$ if T $\geqslant$ 140°C to 250°C

(iii) HE30TF $\sigma o = 0.609 - 1.7T/10^3$

$Eo = 7.08 - 6.53T/10^3$

$n = 1/(0.244 - 7.76T/10^4)$

These equations were then incorporated in the numerical technique in order to account for the temperature rise during deformation. The computed results in terms of the variation of final diameter and height of specimens with impact velocity are compared with those obtained experimentally as shown in Figs 2 to 7. For each alloy, the theoretical curves correspond to sets of p and D values for which the agreement is reasonably close. The set of p and D values for which the agreement is closest is then accepted as the constants governing the proposed constitutive equation for this particular material. For example, in Fig 2, the theoretical curve corresponding to p and D values of 35 and 75,000 respectively show the closest agreement with the experimental curve shown in solid line.

The degree of agreement might have been improved slightly in each case by extensive additional computational exercise but was thought unnecessary, since any improvement would be only marginal.

The sets of acceptable values of p and D ascertained in this manner for all three alloys are given in Table 3.

TABLE 3

Material	p	D
HE15	35	75,000
HE30TF	75	30,000
DTD5044	4	2,500

The stress strain curves shown in Figs 8 to 10 are those obtained under quasi-static test at temperatures of up to 250°C for the three alloys. The temperature dependent constitutive equations for quasi-static stress-strain properties given in previous section are based on curves in these figures.

Figs 11 to 13 show the dynamic stress-strain curves corresponding to a number of strain rates for the three aluminium alloys tested at room temperature. The quasi-statically obtained stress-strain curves are also shown in these figures for comparison. In constructing the dynamic stress-strain curves the p and D values given in Table 3 have been used for each material.

There are a number of important aspects which need to be discussed in support of the proposed method of determining dynamic stress strain properties of metallic alloys.

Radial Inertia

It is now well accepted that under dynamic loading condition the specimen requires higher stress to deform larger specimens of the same material. This is due to the fact that a proportion of this stress is used up to generate radial kinetic energy. For heavier material and larger specimen this stress enhancement can be considerable. For smaller specimens and lighter material this effect is often demonstrated to be insignificant and hence negligible (6). Maiden and Green (19) reported that inertia effect can be as high as 10 per cent at strain rates of 10^4 per second. In this work, the inertia effect has been accounted for by means of the equation (6),

$$\sigma = Y \left[1 + \frac{3}{16} \rho \frac{V^2}{Y} \left(\frac{r}{h}\right)^2 \right]$$

where r is the current radius, h is the current height, ρ is the density and V is the impact speed. Y is the current flow stress of the material. The numerical calculations are carried out at small but discrete time intervals during which V and Y can be assumed to remain constant. The extent of the effect of radial inertia calculated using the above equation for tests giving rise to strain rates of 4×10^3 and 1.4×10^4 per second is found to vary between 1 to 10 per cent. The higher figure relates to HE30TF alloy.

Interface Friction

Interface friction can affect the stress level required to deform a specimen in compression mode. This effect can, however, be minimised

by the use of efficient lubricant. In the present work, tallow in graphite was used to lubricate all the interfacing areas. The resulting frictional contribution was estimated to be less than 5 per cent under extreme loading conditions and hence was not accounted for. The low friction condition produced virtually homogenous deformation and hence insignificant barrelling was observed in the deformed specimens.

Temperature Rise

During plastic deformation the plastic work manifests in terms of increase in temperature of the specimen. This rise in temperature can have significant effect for alloys having lower melting temperature, especially under high speed loading situations where virtually adiabatic conditions prevail. Estimation for the alloys showed that temperature rise of up to 160°C occur. The stress strain property of aluminium alloys is quite sensitive to such level of temperature variation. It was therefore thought that inclusion of temperature effect during numerical calculation was imperative and hence temperature dependent quasi-static constitutive equations were established before proceeding to determine the dynamic stress-strain properties. The works reported in references 7, 17 and 28 confirm the level of temperature rises estimated in this study and reinforce the need for the incorporation of temperature effect in dynamic testing.

Rate Sensitivity of Strain Hardening

In recent years it has been suggested that strain rate sensitivity of metallic alloys depend on the strain rate history (20). This implies that if two specimens, prepared from the same material, are initially deformed to a certain strain level at two different strain rates and

then both specimens are deformed further at the same strain rate then the stress levels for the second part of the deformation will not be the same for both specimens. The degree of such discrepancy will depend on the type of material and for the same material on the strain and strain rate histories. In essence, this means that in putting forward any constitutive equation describing strain rate sensitivity of a material, its strain rate must be specified.

The strain rate properties established using the present experimental numerical technique would thus be for the as received aluminium alloys and hence particular to the strain and strain rate histories of the supply materials. It can, however, be safely suggested that these data will not give an under estimation of the rate sensitivity of these materials most likely to be used by the designers in conditions similar to those reported here.

In order to compare the results from this study with those reported in the literature the stress ratio against strain rate curves have been plotted in Fig 14. This figure shows that HE15 and HE30TF aluminium alloys demonstrate similar degree of rate sensitivity which is fairly constant for strain rates of between 10^3 to 10^4 per second. Holt et al (21) reported in their work results for 2024 aluminium alloy with 4.5 per cent copper content represented by curve number 6 in Fig 14 which at strain rates ranging between 10^2 to 10^3 per second shows approximately same degree of rate sensitivity as HE15 represented by curve number 8 at strain rates ranging between 10^3 to 10^4. The copper content in the HE15 is considerably less than that in 2024 alloy. The curve number 5 represents results for 7075 aluminium alloy with 5.6 per cent Zn content, also reported in reference (21) which shows higher rate sensitivity than HE15 and HE30TF alloys even at strain rates lower by an order of magnitude.

The DTD5044 aluminium alloy demonstrates rate sensitivity which is rather different in that the stress ratio increases from about 2.0 at strain rate of 10^3 per second to about 2.5 at strain rate of 10^4 per second. The trend is similar to that reported in reference (6) for aluminium structural alloy, although the level of sensitivity is reached at much lower strain rates.

The results from references 15, 16 and 22 are under-estimation of the rate sensitivity observed in this study although for different aluminium alloys.

Conclusions

A pseudo-experimental technique has been used to determine strain rate sensitivity of HE15, HE30TF and DTD5044 aluminium alloys at room temperatures and at strain rates ranging from 10^3 to 10^4 per second.

Effects of radial inertia and temperature rise due to plastic deformation has been accounted for in this technique. The effect of friction has been neglected in view of the fact that a very low co-efficient of friction lubricant was used during testing.

A stress ratio of about 2 was suggested for HE15 and HE30TF alloys over the range of strain rate. For DTD5044 alloy it changes from about 2 to 10^3 per second to about 2.5 at 10^4 per second.

REFERENCES

1 K Bittans and P W Witton, "High Strain Rate Investigation, with particular references to stress/strain characteristics", International Metallurgical Reviews - 1972, vol 17, pp 66-75.

2 E A Ripperger, "Dynamic Plastic Behaviour of Aluminium, Copper and Iron", Behaviour of materials under dynamic loading, Winter Annual Meeting of ASME, Tuesday, 9 November 1965, pp 62-80. Edited by Norris J Huffington Jr.

3 V Lindholm, "Dynamic Deformation of Metals", Behaviour of materials under dynamic loading, Winter Annual Meeting of ASME, Tuesday, 9 November 1965, pp 42-61. Edited by Norris J Huffington Jr.

4 H D Pugh, M T Watkins, "Some Strain Rate Effects in Drop-Forging Tests", Proceeding of Conference on Properties of Material at High Rates of Strain, 1957, pp 122-12.

5 D Christoperson, B Parsons, "The Effect of High Strain-Rate in Strip-Rolling", Proceeding of Conference on Properties of Material at High Rates of Strain, 1957, pp 115-121.

6 M M Haque, "Stress-Strain Properties and Microstructural Change in Metal Deformed at Strain Rates up to 10^5 per second, Sheffield City Polytechnic, 1983, PhD Thesis.

7 A J Holzer, R H Brown, "Mechanical Behaviour of Metals in Dynamic Compression". Transactions of ASME, July 1979, vol 101, pp 238-246.

8 R D Guminski, J Willis, "Development of Cold Rolling Lubricants for Aluminium Alloys", Journal of Inst of Metals 1959-60, vol 88, pp 481-492.

9 M S J Hashmi, "Strain Rate Sensitivity of a Mild Steel at Room Temperature and Strain Rates up to 10^5 sec^{-1}", Journal of Strain Analysis, vol 15, 1980, pp 201-207.

10 J L Chiddister and L E Malvern, "Compression-Impact Testing of Aluminium at Elevated Temperatures", Experimental Mechanics, April 1963, pp 81-90.

11 C K H Dharan and F E Houser, "Determination of Stress-Strain Characteristics at very high Strain Rates", Experimental Mechanics, Sept 1970, pp 370-76.

12 H Watson Jr and E A Ripperger, "Dynamic Stress-Strain Characteristics of Metals at Elevated Temperatures", Experimental Mechanics, July 1969, pp 289-295.

13 Kenneth G Hoge, "Influence of Strain Rate on Mechanical Properties of 6061-T6 Aluminium under Uniaxial and Biaxial States of Stress", Experimental Mechanics, April 1966, pp 204-211.

14 Frank E Houser, "Techniques for Measuring Stress-Strain Relationships at High Strain Rates", Experimental Mechanics, August 1966, pp 395-402.

15 B Lengyel and M Mohitpour, "Dynamic Stress/Strain Data to Large Strains", J of the Inst of Metals, 1972, vol 100, pp 1-5.

16 S Yoshida, N Nagata, "Deformation of Polyarystalline Aluminium High Strain Rates", Transactions of National Research Institute for Metals 1967, vol 9, pp 20-28.

17 J F Bishop, "An approximate method for determining the temperature reached in steady motion problems of plane plastic strain", Quarterly, J of Mechanics and Applied Mathematics, vol 9, 1956, pp 236-46.

18 F R Shanley, "General Introduction", Mechanical Behaviour of Materials at Elevated Temperatures, Edited by John Dorn, McGraw-Hill Book Company Inc, 1961, New York, pp 1-8.

19 C J Maiden, S J Green, "Compression Strain Rate Tests on Six Selected Materials at Strain Rates from 10^{-3} to 10^{4} in/in/sec, Transaction of the ASME Sept 1966, pp 496-504.

20 J R Klepaczko and C Y Chiem, "On rate sensitivity of f.c.c. metals, instantaneous rate sensitivity and rate sensitivity of strain hardening", J Mech Phys Solids, vol 34, no 1, pp 29-54, 1986.

21 D L Holt et al, "The Strain Dependence of the Flow Stress in some Aluminium Alloys", Transactions of ASM, 1967, vol 60, pp 152-59.

22 C H Karnes and E A Ripperger, "Strain Rate Effects in Cold Worked High-Purity Aluminium", J Mech Phys Solids, 1966, vol 14, pp 75-88.

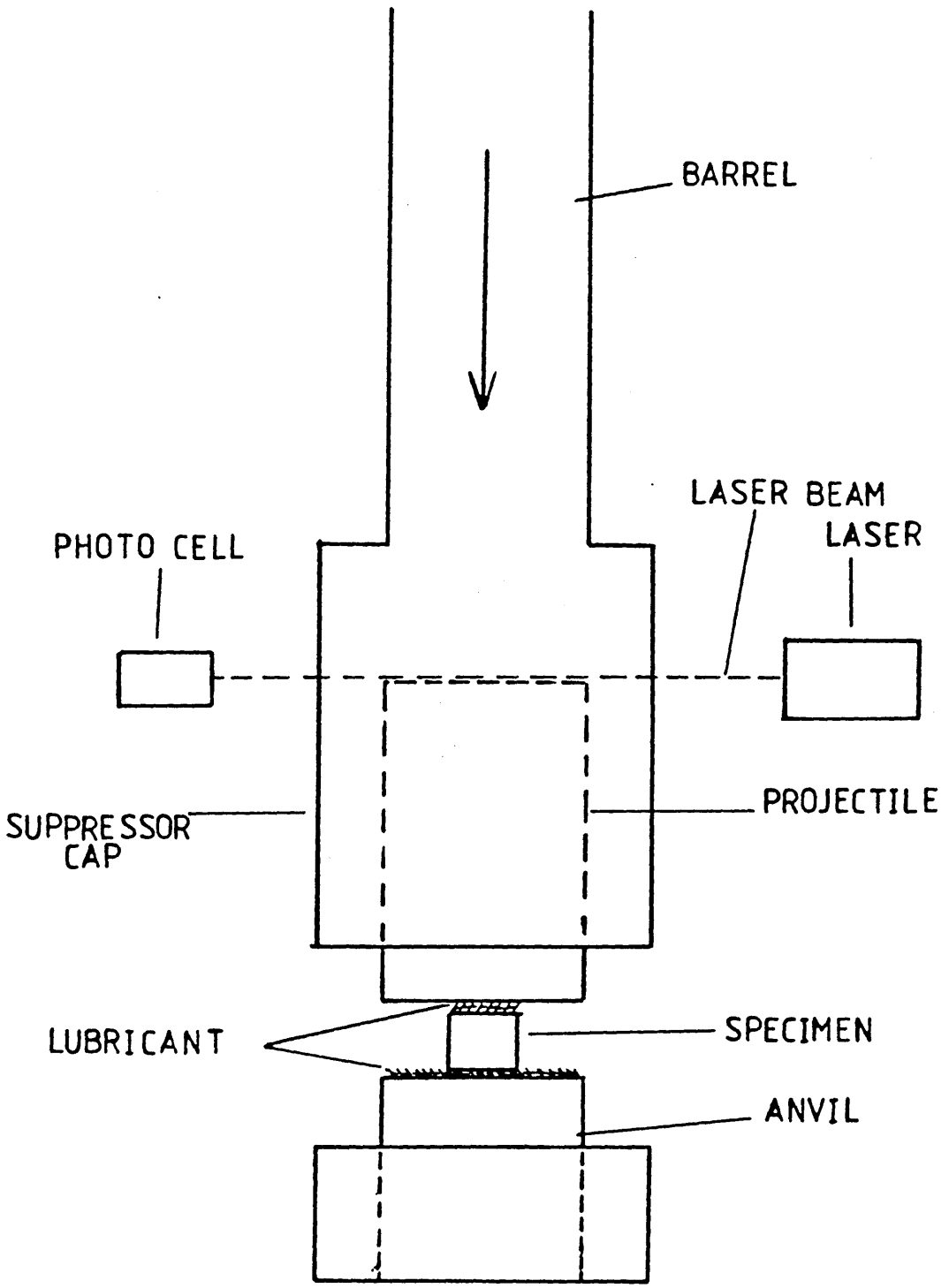

FIG [1] Anvil, shooting barrel and measuring equipment arrangement

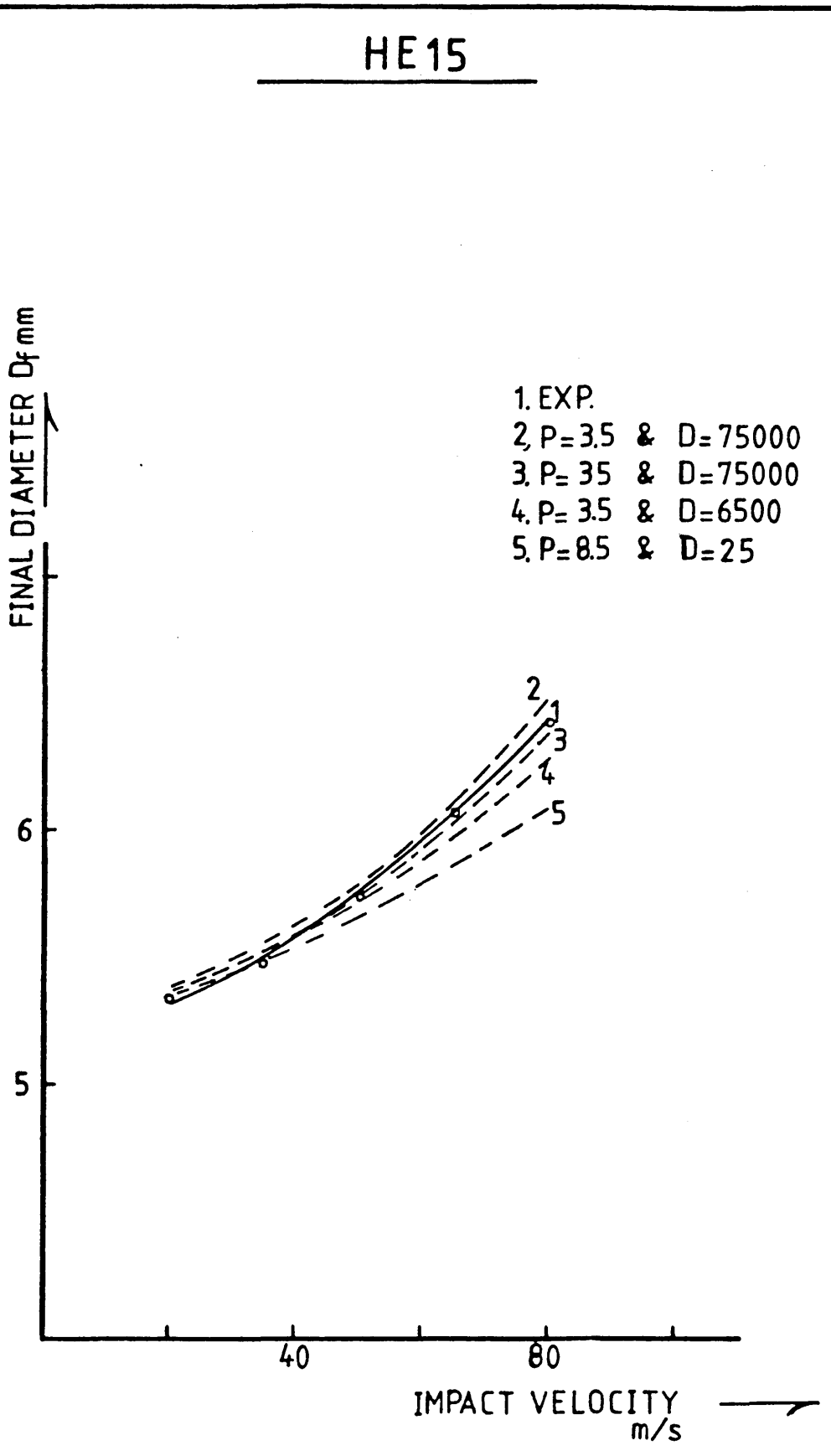

Fig [2], Variation of final diameter with impact velocity for various P and D combinations.

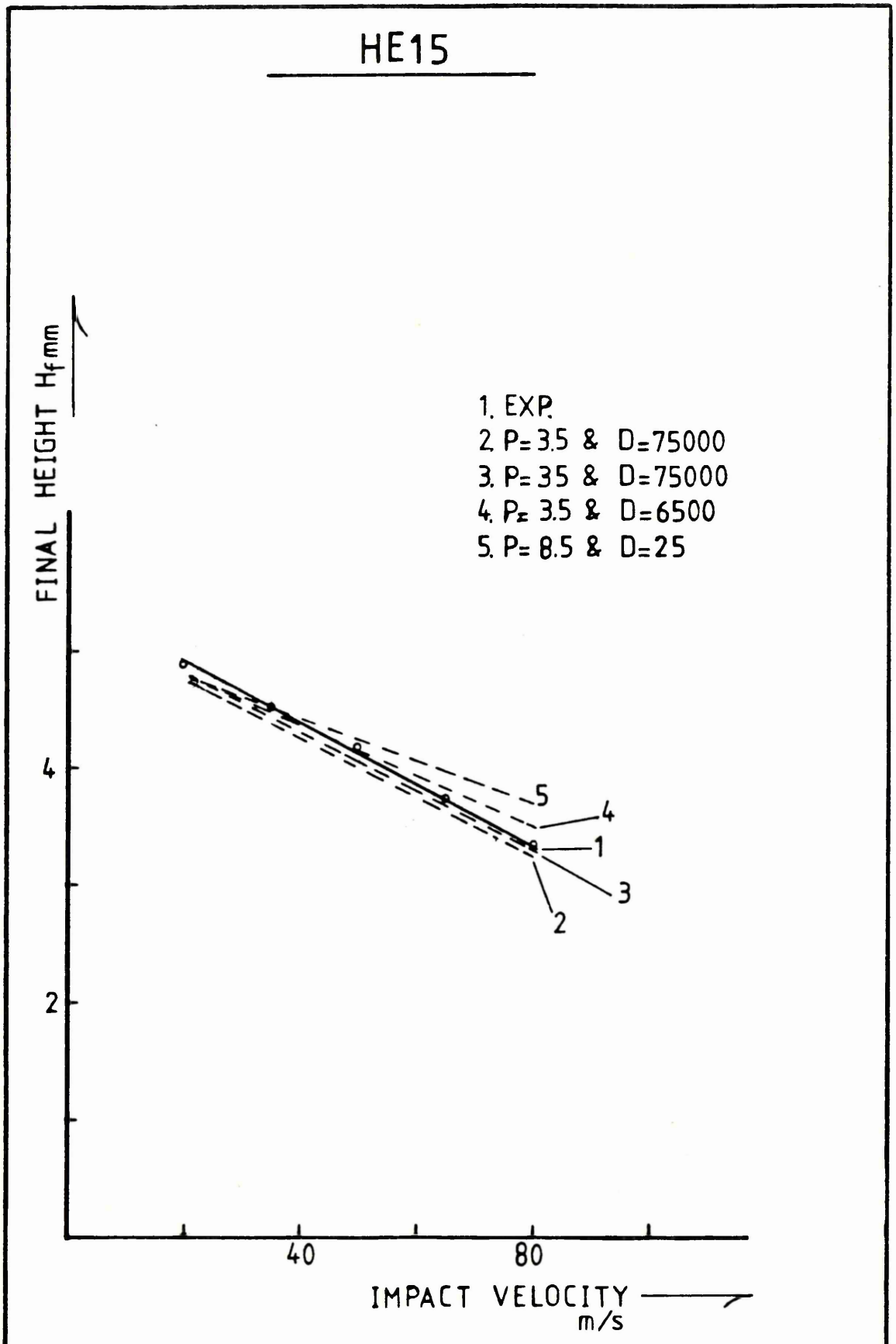

Fig [3], Variation of final height with impact velocity for various P and D combinations

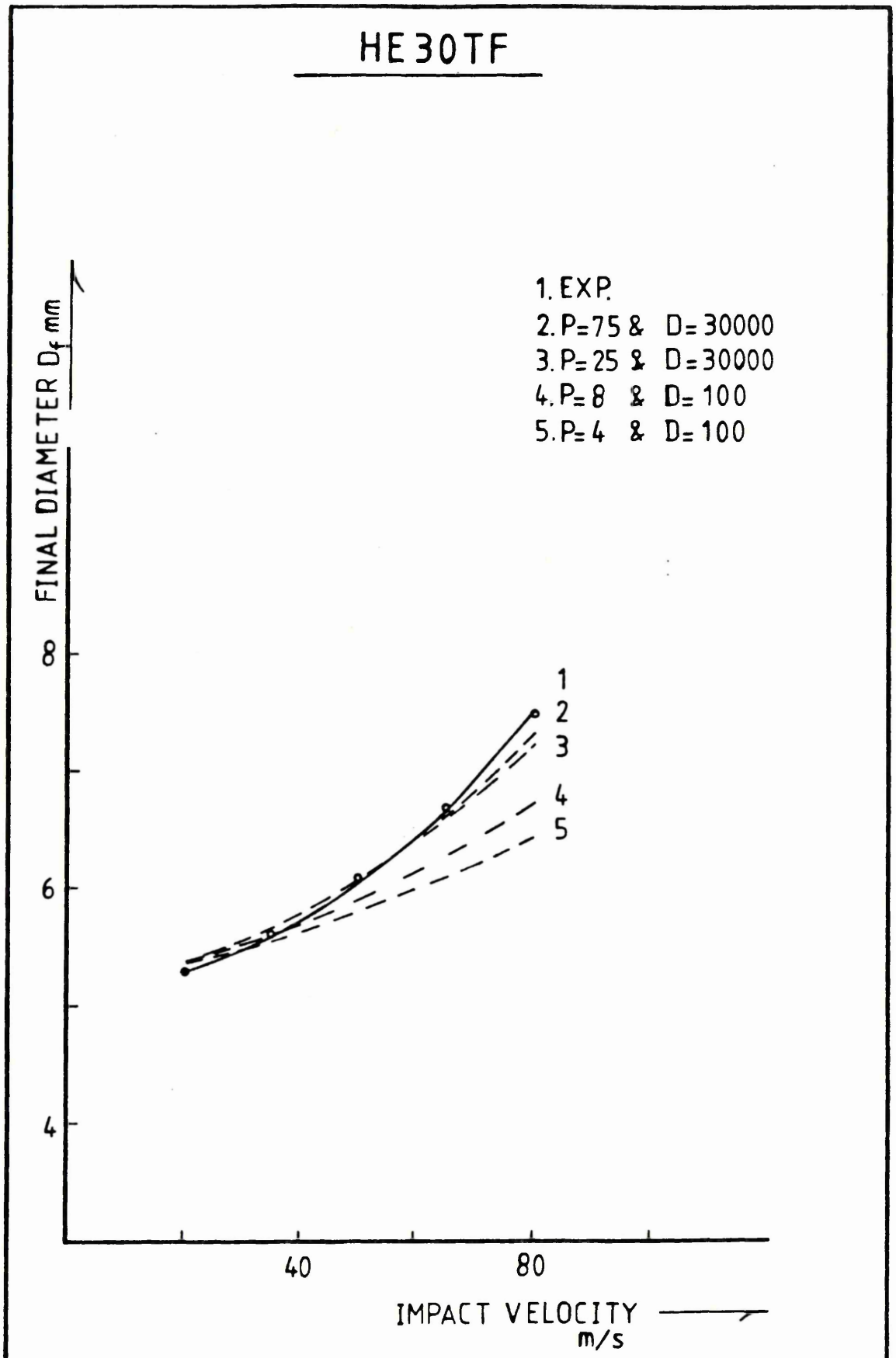

Fig [4], Variation of final diameter with impact velocities for various P and D combinations

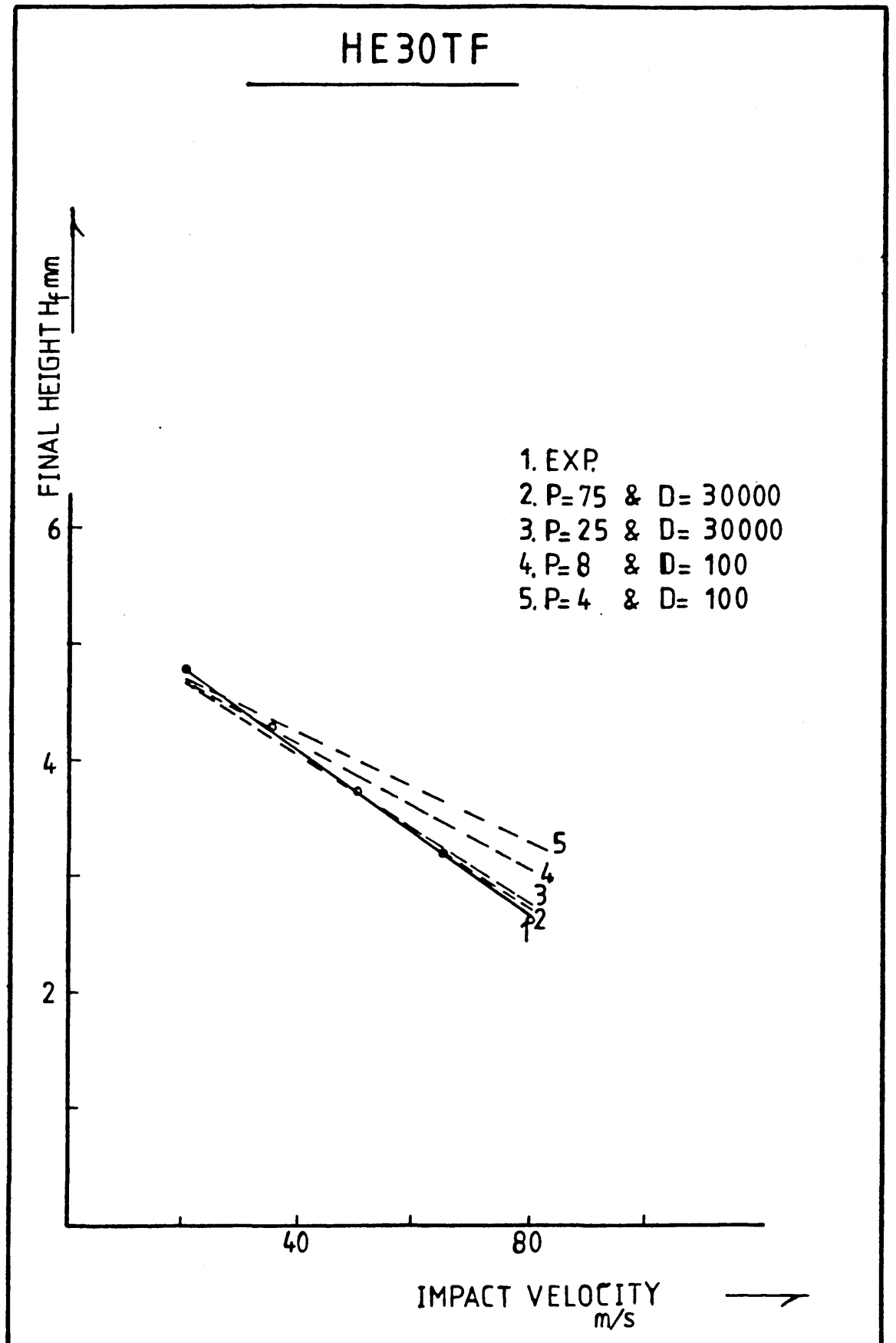

Fig [5], Variation of final height with impact velocity for various P and D combinations.

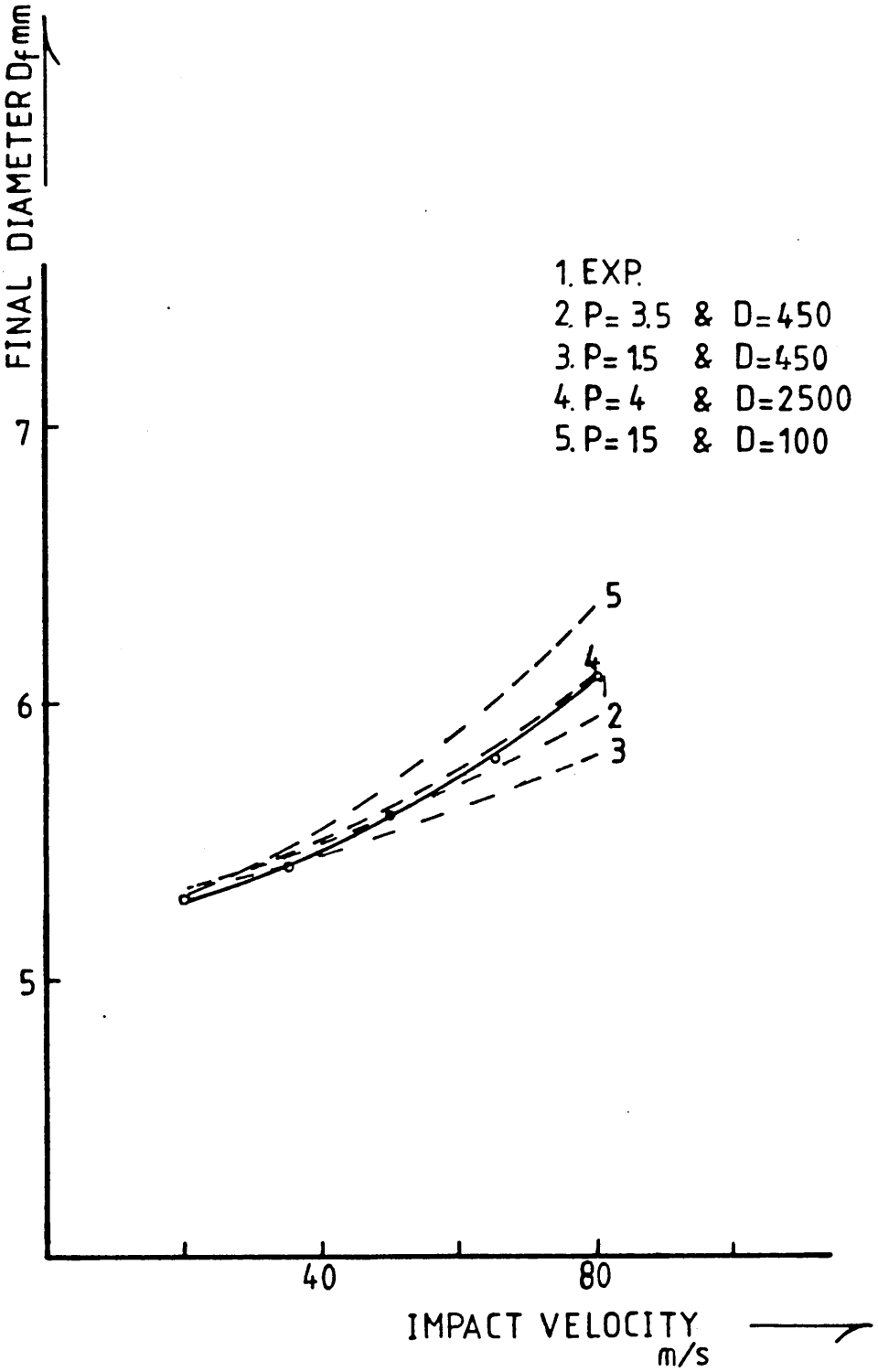

Fig [6], Variation of final diameter with impact velocities for various P and D combinations.

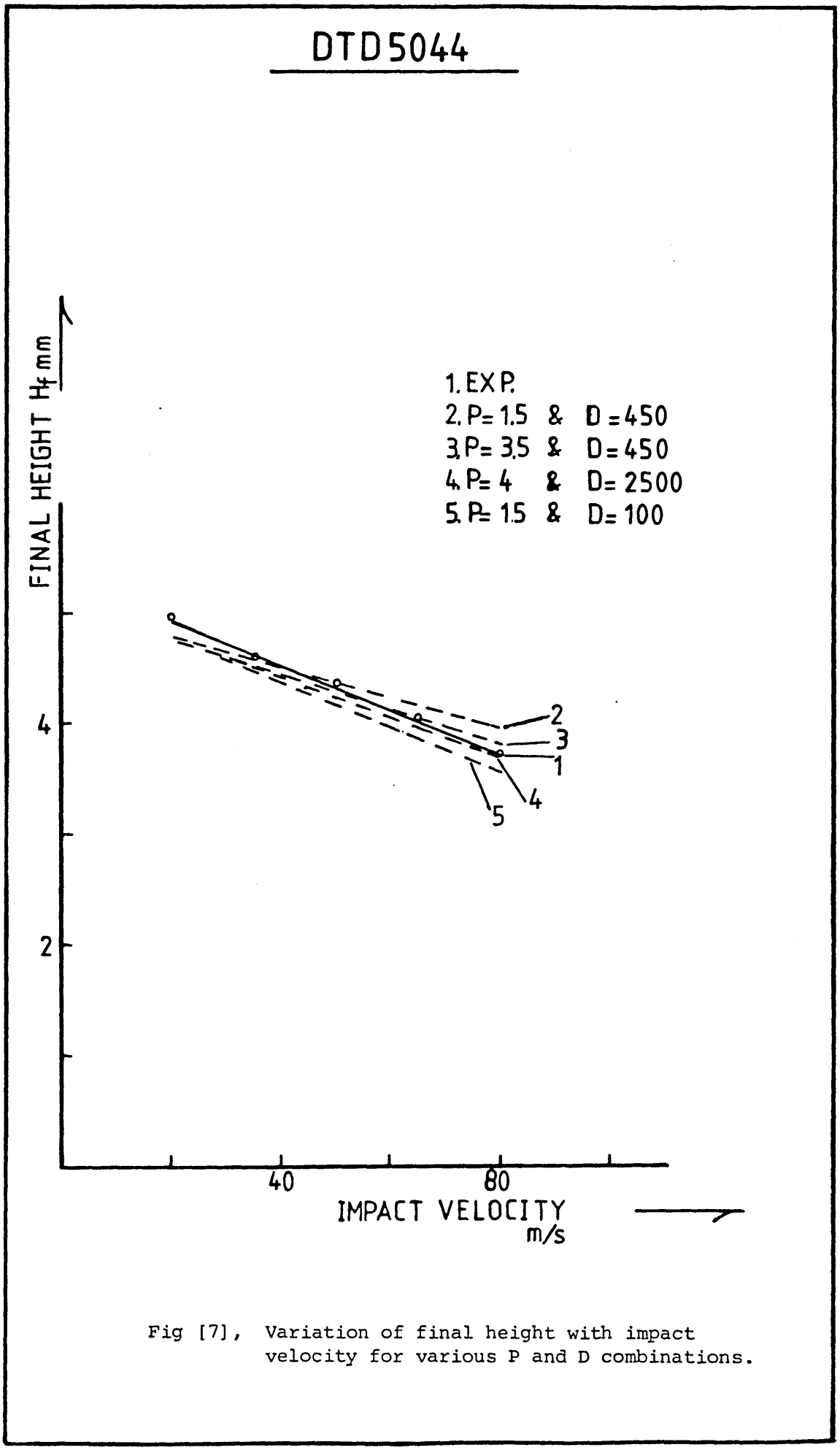

Fig [7], Variation of final height with impact velocity for various P and D combinations.

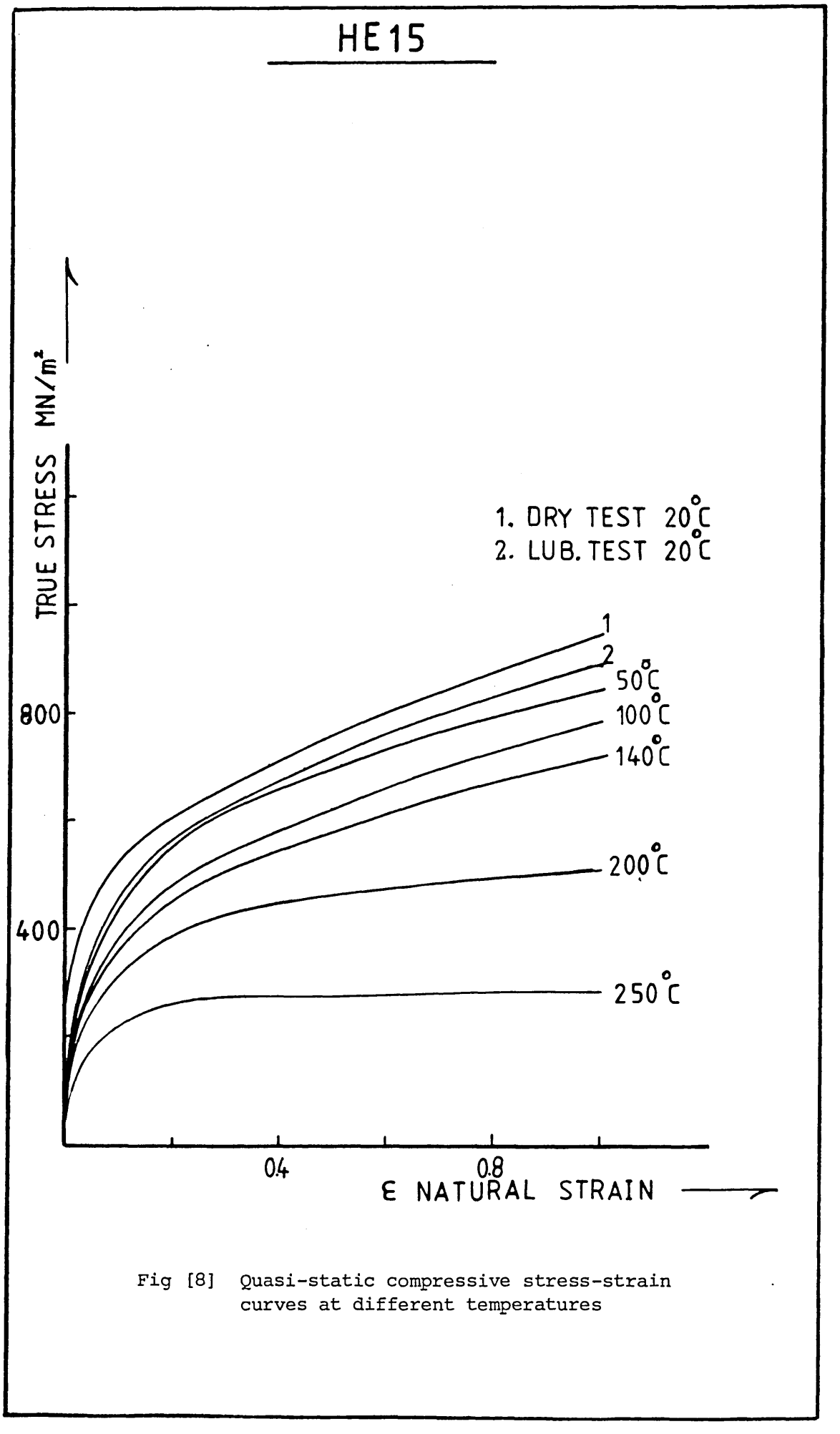

Fig [8] Quasi-static compressive stress-strain curves at different temperatures

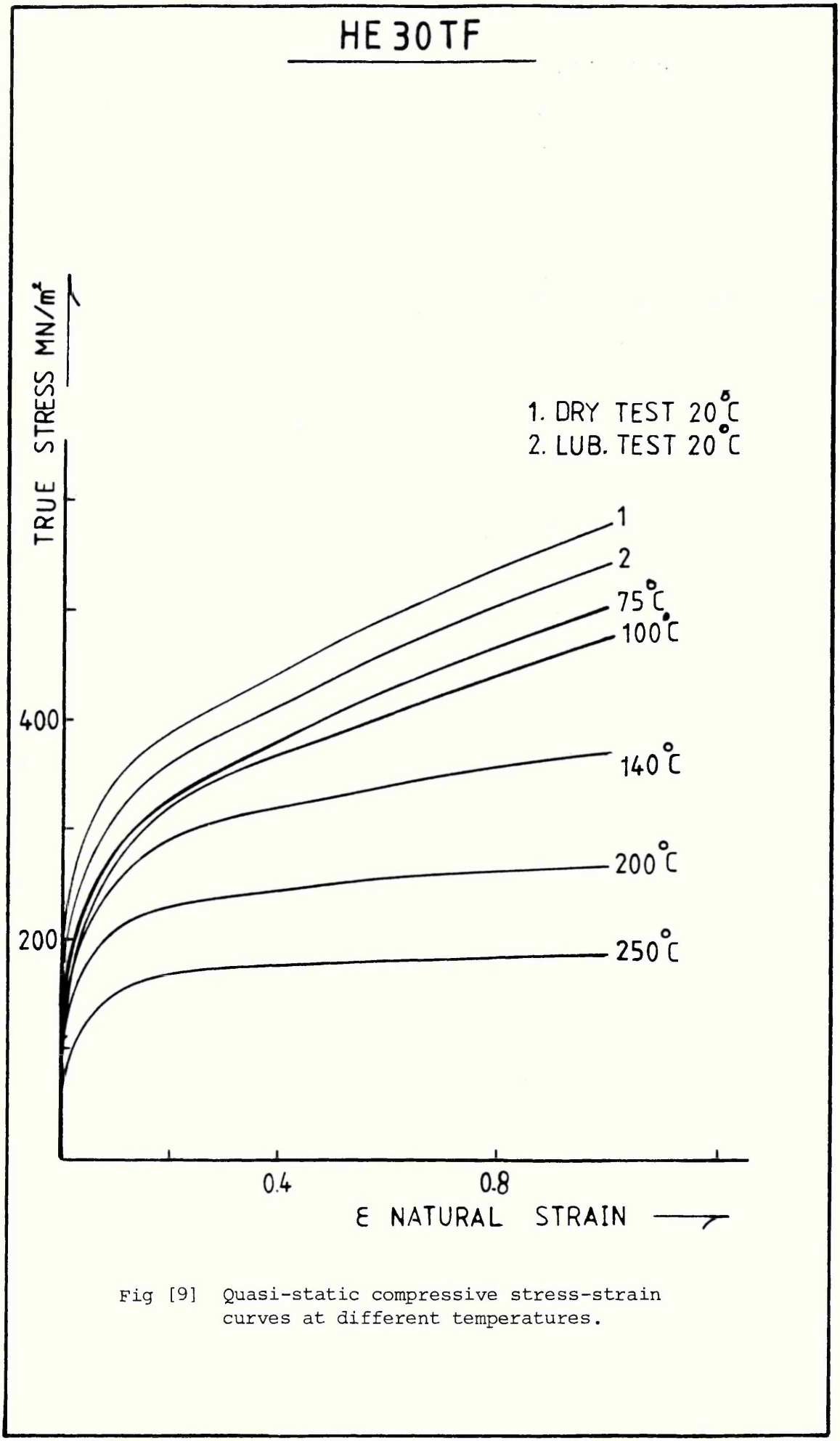

Fig [9] Quasi-static compressive stress-strain curves at different temperatures.

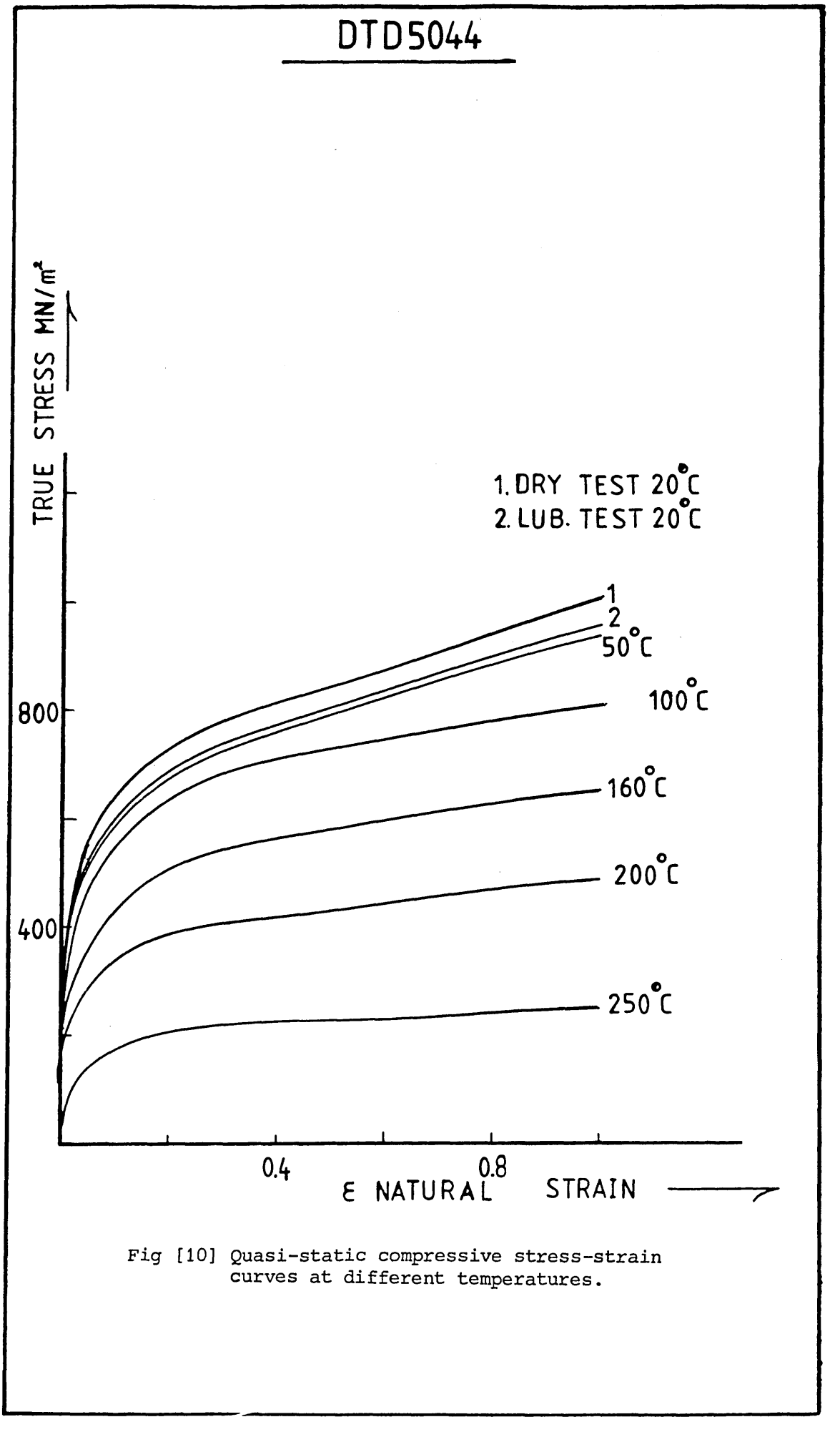

Fig [10] Quasi-static compressive stress-strain curves at different temperatures.

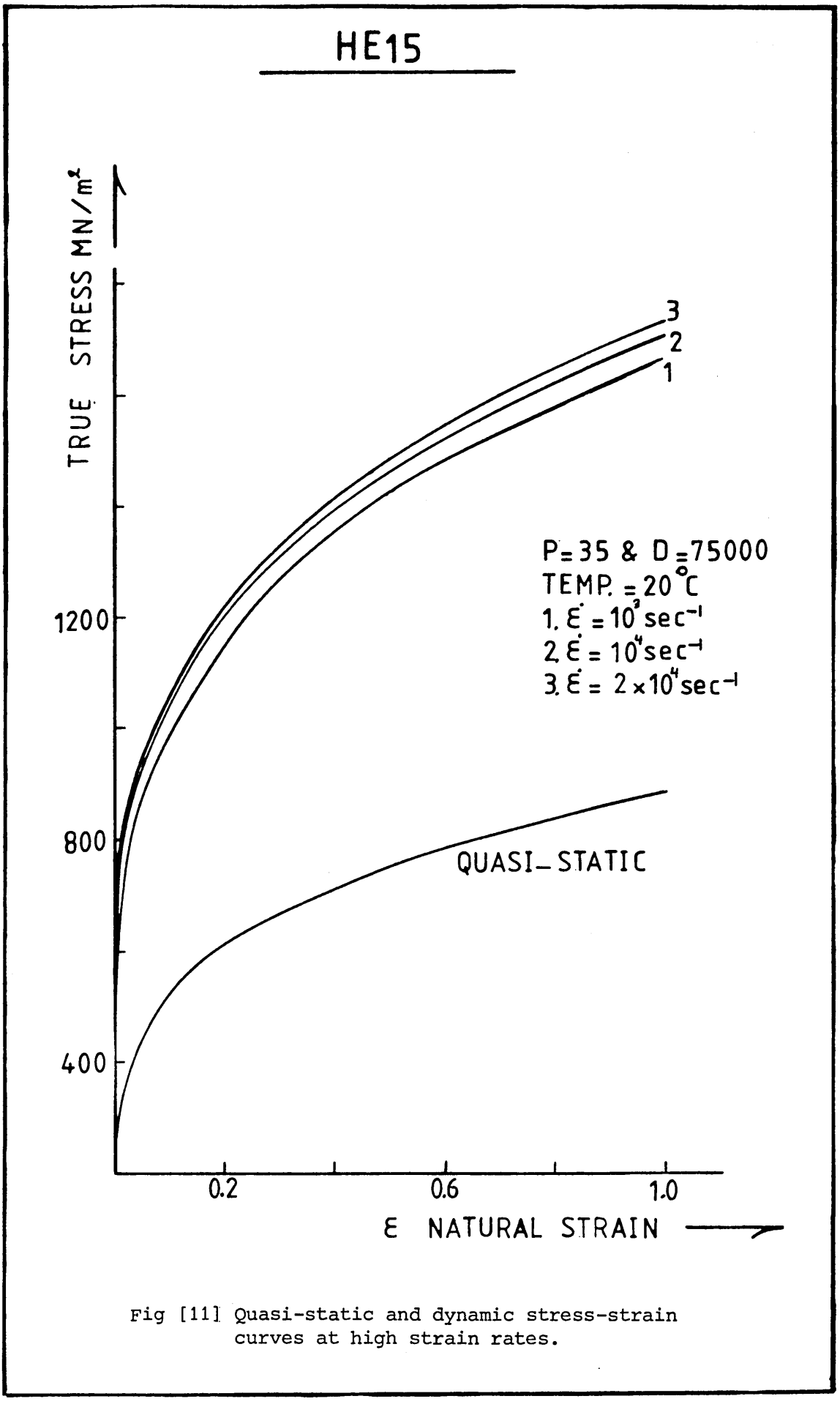

Fig [11] Quasi-static and dynamic stress-strain curves at high strain rates.

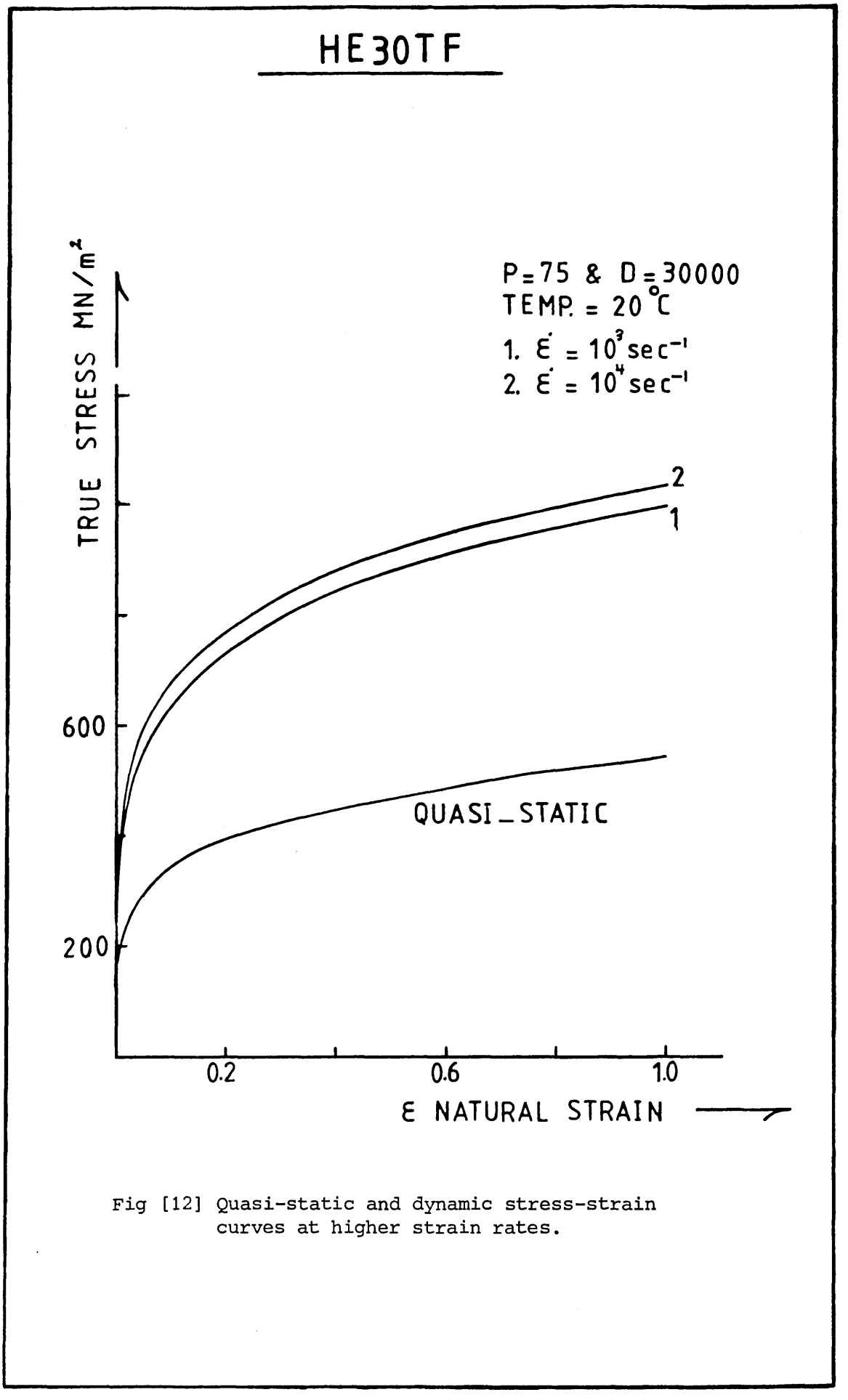

Fig [12] Quasi-static and dynamic stress-strain curves at higher strain rates.

DTD5044

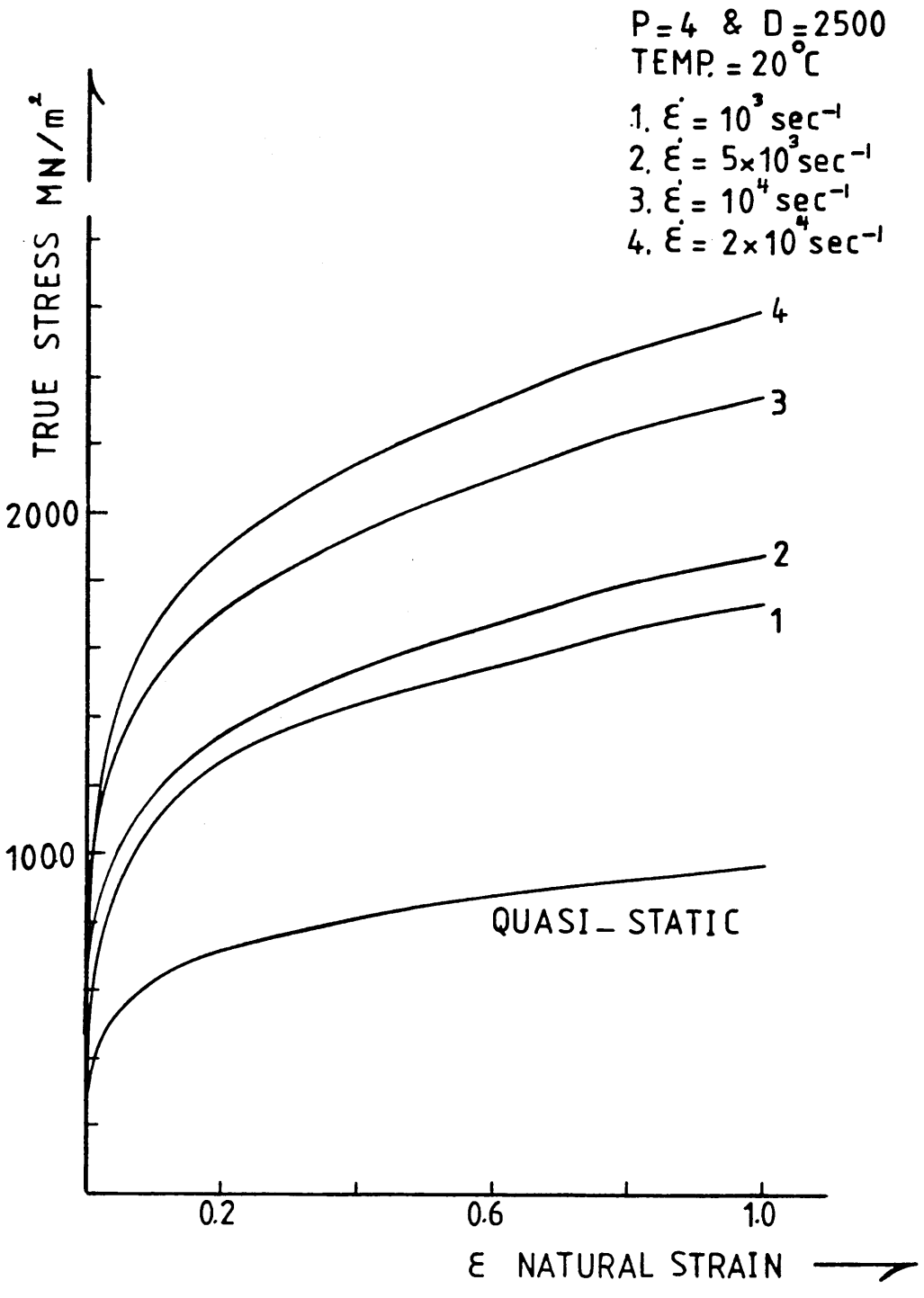

Fig [13] Quasi-static and dynamic stress-strain curves at higher strain rates.

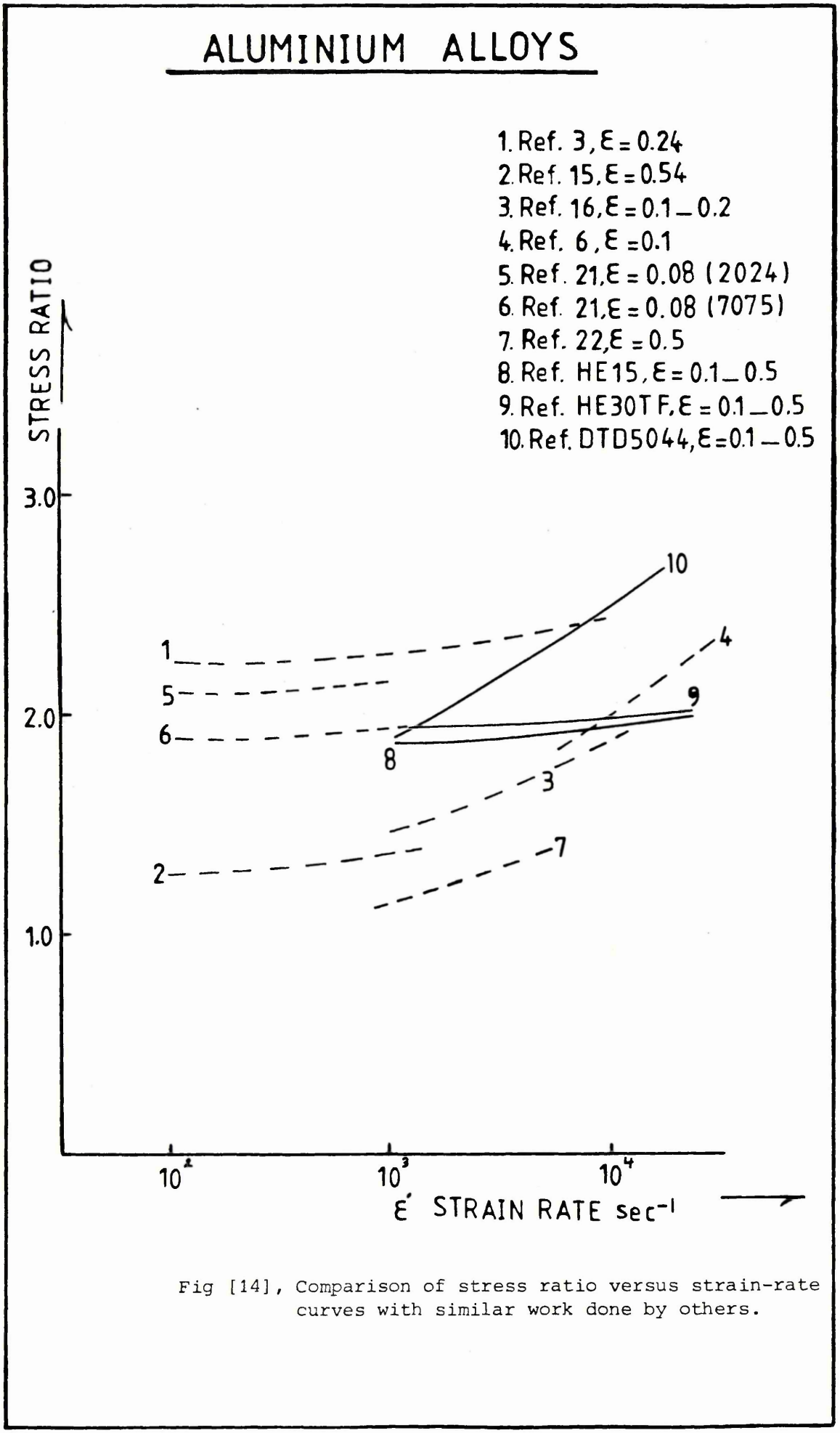

Fig [14], Comparison of stress ratio versus strain-rate curves with similar work done by others.

APPENDIX IX

CALCULATION OF TOTAL FORCE IN THE FICTITIOUS LINK MATERIALS

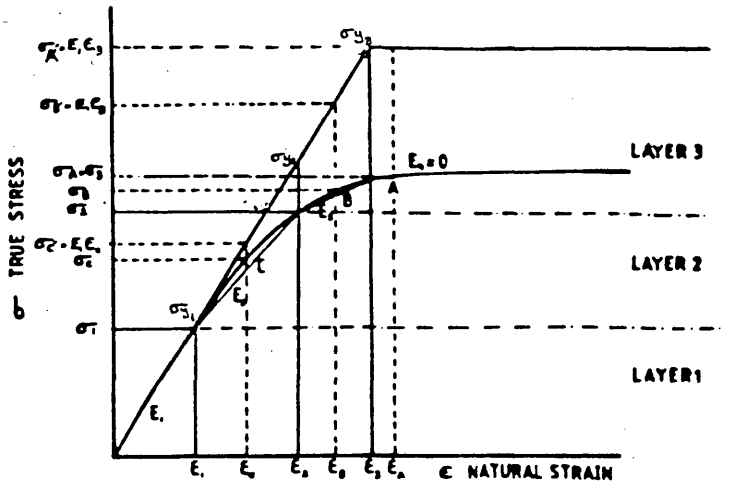

Fig (AIX) True stress-natural strain curve of link fictitious materials

The areas of the three fictitious layers of link materials are

$$A_1 = \frac{A(E_1 - E_2)}{E_1},\quad A_2 = \frac{A(E_2 - E_3)}{E_1} \text{ and } A_3 = \frac{A(E_3 - E_4)}{E_1}$$

and E_1 = elastic modulus

$$E_2 = \frac{\sigma_2 - \sigma_1}{E_2 - E_1}$$

$$E_3 = \frac{\sigma_3 - \sigma_2}{E_3 - E_2}$$

$$E_4 = 0$$

Consider Figure (AIX)

(i) For point C, strain = ε_c

The first fictitious layer of materials will become plastic, the other two layers will still be elastic

Thus the total force in the actual material

$$F_a = A\sigma_c$$

The total force in the fictitious materials

$$F_f = A_1\sigma y_1 + A_2E_1\varepsilon_c + A_3E_1\varepsilon_c$$

$$= \frac{A}{E_1}(E_1 - E_2)E_1\varepsilon_1 + \frac{A}{E_1}(E_2 - E_3)E_1\varepsilon_c + \frac{A}{E_1}(E_3 - E_4)E_1\varepsilon_c$$

$$= A[\sigma_1 + E_2(\varepsilon_c - \varepsilon_1)]$$

$$= A[\sigma_1 + \frac{\sigma_c - \sigma_1}{\varepsilon_c - \varepsilon_1} \cdot (\varepsilon_c - \varepsilon_1)$$

$= A\sigma_c$

Hence $F_a = F_f$

(ii) For point B, strain = ε_b

The first two fictitious layers of materials will become plastic - the third layer still elastic

Thus the total force in the actual material

$Fa = A\sigma_B$

Now

$$F_f = A_1\sigma y_1 + A_2\sigma y_2 + A_3\sigma_B$$

$$= \frac{A}{E_1}(E_1 = E_2)E_1\varepsilon_1 + \frac{A}{E_1}(E_2 - E_3)E_2\varepsilon_2 + \frac{A}{E_1}(E_3 - E_4)E_1\varepsilon_B$$

$$= A[E_1\varepsilon_1 - E_2\varepsilon_1 + E_2\varepsilon_2 - E_3\varepsilon_2 + E_3\varepsilon_B]$$

$$= A[\sigma_1 + E_2(\varepsilon_2 - \varepsilon_1) + E_3(\varepsilon_B - \varepsilon_2)]$$

$$= A[\sigma_1 + (\varepsilon_2 - \varepsilon_1).\left(\frac{\sigma_2 - \sigma_1}{\varepsilon_2 - \varepsilon_1}\right) + \frac{\sigma_3 - \sigma_2}{\varepsilon_B - \varepsilon_2}.(\varepsilon_B - \varepsilon_2)]$$

$$= A[\sigma_1 + \sigma_2 - \sigma_1 + \sigma_B - \sigma_2]$$

$$F_f = A\sigma_B$$

Hence $Fa = A\sigma_B = F_f$

(iii) At point A, strain = ε_A

All three fictitious layers of materials will become plastic so that

$Fa = A\sigma_3 = A\sigma a$

The total force in the fictitious materials

$$F_f = A_1\sigma y_1 + A_2\sigma y_2 + A\sigma y_3$$

$$= \frac{A}{E_1}(E_1 - E_2)E_1\varepsilon_1 + \frac{A}{E_1}(E_2 - E_3)E_1\varepsilon_2 + \frac{A}{E_1}(E_3 - E_4)E_1\varepsilon_3$$

$$= A[E_1\varepsilon_1 - E_2\varepsilon_1 + E_2\varepsilon_2 - E_3\varepsilon_2 + E_3\varepsilon_3]$$

$$= A[\sigma_1 + E_2(\varepsilon_2 - \varepsilon_1) + E_3(\varepsilon_3 - \varepsilon_2)$$

$$= A[\sigma_1 + (\varepsilon_2 - \varepsilon_1).\frac{\sigma_2 - \sigma_1}{\varepsilon_2 - \varepsilon_1} + \varepsilon_3 - \varepsilon_2.\frac{\sigma_3 - \sigma_2}{\varepsilon_3 - \varepsilon_2}]$$

$$= A[\sigma_1 + \sigma_2 - \sigma_1 + \sigma_3 - \sigma_2]$$

$$F_f = A\sigma_3 = A\sigma_A$$

Hence $F_f = Fa = A\sigma_A$